University of Oxford

Department of Chemistry



Synthesis and applications of functionalised polypropylenes

Alexander O. E. Evans

Keble College

Hilary 2025

Thesis submitted in partial fulfilment of the requirements for the degree of Doctor of Philosophy

for M. D. C.

Preface

The work described in this thesis was carried out in the Chemistry Research Laboratory at the University of Oxford, U.K. between October 2021 and February 2025 under the supervision of Professor Dermot O'Hare. All work was performed by the author unless otherwise stated, and no part has been previously submitted for any other degree.



Alexander Oscar Edward Evans

Keble College

February 2025

List of manuscripts constituting the thesis:

Chapter 2: Functionalised polypropylenes; a copolymerisation and post-modification platform, **A. Evans**, O. Casale, L. J. Morris, Z. R. Turner, D. O'Hare, *Macromolecules*, 2024, 57, 22, 10778–10791.

Chapter 3: Flame retardant phosphonate-functionalised polypropylenes, **A. Evans**, L. J. Morris, Z. R. Turner, D. O'Hare, *ACS Appl. Polym. Mater. 2025, 7, 4, 2508–2516*

Chapter 4: Functionalised polypropylene copolymers as multi-substrate hot melt adhesives, **A. Evans**, C. G. Collins-Rice, Z. R. Turner, D. O'Hare, *In review, ACS Applied Materials and Interfaces (19/11/2024).*

Chapter 5: Illuminating microplastics in cells: macro-problems for micro-barriers, **A. Evans**, R. Devereux, Z. R. Turner, A. J. Russel, D. O'Hare, *To be submitted to Nature.*

Chapter 6: Synthesis, characterisation, and magnetic properties of a permethylated manganocene, **A. Evans**, T. A. Q. Arnold, P. Ransom, S. C. Binding, W. K. Myers, A. E. Crumpton, Z. R. Turner, J-C Buffet, D. O'Hare, *Submitted to Angewandte Chemie International Edition (23/04/2025).*

Appendix A6: Boosting NIR Laser Marking Efficiency of a Transparent Epoxy Using a Layered Double Hydroxide, C. Chen, J. Wang, **A. Evans**, and D. O'Hare, *ACS Appl. Polym. Mater.*, 2024, 6, 14, 8679–8686.

Appendix A6: Strategies for enhancing the processability of UHMWPE, C. G. Collins-Rice, **A. Evans**, Z. R. Turner, J. Wattoom, and D. O'Hare, *Ind. Chem. Mater.*, 2025, 3, 178-190.

Chapters 2, 3, and 4 are also covered by the following patent applications:

"FLAME RETARDANT POLYPROPYLENE", UK Pat. Appl. GB202218265A, WO-2024121541-A1.

"FUNCTIONALISED POLYPROPYLENE COPOLYMERS", UK Pat. Appl. GB2408339.6.

Oral presentations based on parts of the work contained in this thesis were presented at the ACS Spring 2025 conference (San Diego, U.S.A), the MACRO 2024 conference (Warwick, U.K.), the CSC 2023 conference (Vancouver, Canada), and Dalton 2023 conference (Warwick, U.K.).

Abstract

Synthesis and applications of functionalised polypropylenes

Alexander O. E. Evans **D.Phil. Thesis**

Keble College **Hilary 2025**

This thesis discusses the synthesis of functionalised polypropylenes *via* a two-step copolymerisation−post-modification strategy. The resulting functionalised polypropylenes display distinctly altered bulk and surface properties, compared to polypropylene, with a specific focus on thermal stability and adhesion to metal, altered wettability, and latent reactivity; enabling applications not typically possible for polyolefins. This work broadens the understanding of functional polypropylenes and lays the foundation for the synthesis and application of novel polymer materials.

A brief review of polyolefin materials, their history, synthesis, and properties is presented in chapter 1, focusing specifically on polypropylene and its functionalisation. Functional polypropylenes are regarded as versatile building blocks for next-generation materials; however, their development has been stymied due to synthetic limitations principally caused by metallocene poisoning with polar monomers during polymerisation. Chapter 2 explores the solution-phase copolymerisation of propylene with an α,ω-bromoalkene and subsequent exploitation of the latent reactivity in one of three general synthetic routes. This is exemplified through a thorough investigation of phosphonate-modified polypropylenes for flame retardant applications in Chapter 3, evidencing significantly improved thermal stability at low loadings. Chapter 4 focuses on amine-modified polypropylenes for adhesive applications, examining the degree of functionality as a trade-off between adhesion to steel and plastic for multi-substrate adhesion.

Given the ubiquity of polyolefin materials as an environmentally pervasive contaminant, a fluorescently labelled polypropylene was synthesised and evaluated *in vitro* in Chapter 5. The method outlined contributes to understanding the degree to which concern can be levied against developing environmental plastic pollution. Finally, chapter 6 examines the synthesis, characterisation, and magnetic properties of a permethylated manganocene; a low-spin ground state Mn(II) complex that undergoes thermally accessible spin crossover.

Rational for Integrated Thesis

An integrated thesis best enables me to showcase the work completed whilst undertaking my D.Phil. as each chapter presents a complete narrative. Writing each chapter with the intent to publish as a journal article ensures an efficient and coherent presentation of the results. Principally, the research encompasses the synthesis of functionalised polypropylenes and their applications. However, due to the array of application areas, specifically the interdisciplinary nature of Chapter 5, and indeed the standalone nature of Chapter 6, the integrated format allows for adequate and appropriate introduction of the research. Additionally, I have had the privilege to collaborate in various ways over the course of my studies and an integrated format best allows me to showcase, where relevant, the incredible experimental work of my colleagues in tandem with my research.

Author Contributions

Each chapter begins with a detailed list of each authors contributions with my contributions underlined for clarity. At the end of each chapter is a statement of authorship signed by both me and Professor Dermot O'Hare to confirm the contributions made by me in each chapter are accurate.

Acknowledgements

To my colleagues, friends, and family, I can finally say in only my thirtieth year: I have finished school. Without the unwavering support, friendship, and love of many important people in my life I would not be here. All of whom I hope know who they are and how much they mean to me, and as such, thank you.

Firstly, Dermot, thank you for giving me the opportunity to study in your research group. I thoroughly enjoyed my time, be it the chemistry, the Christmas dinners, or the outrageously priced £6.65 KA Guinness. I am likewise grateful to SCG Chemicals (Thailand) for their financial support and engaging discussions.

Zoë, I am eternally grateful for your support during my DPhil, especially the time and suggestions with what I can only imagine felt like incessant proof reading regarding this thesis. I would like to extend my endless gratitude to all those who helped with this thesis in one form or another; I could not have done it without any of you. Be it the technical support: Aggy, Caitlin, Coral, James, Nick, Amber, Will, Kirsten, Steve, and Igor, or more widely the denizens of the O'Hare Group putting up with the endless dad jokes – apologies in particular to Matt, Clem, and Justin, you were only ever one chair swivel away. Incidentally, this must also include my second Oxford home, S3. Gabi, Matt, Rebecca, Peace, and last but by no means least Louis; each of you significantly contributed to my development as a polymer-cum-inorganic chemist for which I am eternally grateful. And indeed how could I forget Ollie and Lucas – your steadfast determination to teach me patience did not go unnoticed! Thank you all for not complaining about my eclectic music taste and truthfully making my time in (and out of) the lab an enjoyable experience.

There have likewise been many memorable moments outside the confines of the CRL, all of which contributed to my time at Oxford. Aisling, your enthusiasm and radiant positivity never ceased to brighten my day. Claire, Ríona, and Emma, taking you down your first blue, despite the tears, will never not be funny in hindsight. As fellow inhabitants of York Place, cooking up a daily storm with each of you, Sam, Dom, and Laura, was always a pleasure and fuelled the final push in more ways than one.

Additionally, I have had the absolute privilege to have close friends remain so for in excess of a decade. In the spirit of brevity, those belonging to *Numéro Tres*, *3MChems1MRes, consistently inconsistent, glasto fantasto*, and more specifically Rowan and Lizzie, thank you for being you, never change. I treasure each and every one of you, it has been a privilege to have you enrich my life.

Special thanks must of course be extended to Melvyn and Catherine, not least for the roof over my head but most importantly for raising my partner in crime during my time in Oxford so well. Ed, it was an absolute privilege living with you: BBQing, travelling, drinking, gigging, the list goes on. I also threatened to write one poem whilst in Oxford, so here is arguably the pièce de résistance within this body of work:

To my friends and my family so dear,
Your support has been steadfast and clear.
To my poetical mate,
Since 2007 our fate
How about we go out for a beer?

Finally, I am forever indebted to my family for their continuous help, support, and encouragement throughout the years. I would not be where I am today without each of you. No words can fully express my gratitude to my parents, Peter and Jane. And to Jack, I'll always be proud of what you've achieved and treasure memories linking chemistry and cooking together. Lastly, Grandad, to whom this thesis, laden as it is with hieroglyphics is dedicated, thank you for everything.

Abbreviations and nomenclature

$\lvert\eta^*\rvert$	Absolute value of complex viscosity
$\{^1H\}$	Proton decoupled
°C	Degrees Celsius
11-Br	11-bromo-1-undecene
Acac	Acetylacetone
Alk	Alkyl
^{a}PP	*atactic*-PP
Ar	Aryl
ATH	Aluminimum trihydroxide
ATRP	Atom transfer radical polymerisation
b	Designates a block copolymer
co	Designates an unspecified copolymer
CAD	Computer-aided design
CASSCF	Complete active space self-consistent field
CGC	Constrained geometry catalysts
COSY	Correlation spectroscopy
Cp	Cyclopentadienyl
Cp*	Permethylcyclopentadienyl
CPNQS	Cross polarization with non-quaternary suppression
CPMAS	Cross polarization magic-angle spinning
CW	Continuous-wave
Cy	Cyclohexyl
DAPI	4',6-diamidino-2-phenylindole
DBU	1,8-Diazabicyclo[5.4.0]undec-7-ene
DCC	*N,N'*-Dicyclohexylcarbodiimide
DCM	Dichloromethane
DEA	2-(ethylamino)ethanol
DEMM	Diethyl methyl malonate
DEOA	2,2'-iminodiethanol
DFT	Density functional theory
D_h	Hydrodynamic diameter
DLS	Dynamic light scattering
$Đ_M$	Dispersity
DMAP	4-Dimethylaminopyridine
DMSO	Dimethyl sulfoxide

DOSY	Diffusion-ordered NMR spectroscopy
DP	Degree of polymerisation
DLPNO-CCSD(T)	Domain-based local pair natural orbital coupled-cluster theory
DSC	Differential scanning calorimetry
DTG	Derivative thermogravimetry
EAE	2-(ethylamino)ethanol
EDA	Energy decomposition analysis
EI	Electron ionisation
Et	Ethyl
E_{Orb}	Orbital energy
EPR	Electron paramagnetic resonance
eq.	Equivalents
E_{Rep}	Repulsion energy
EVOH	Poly(ethylene-co-vinyl alcohol)
EXAFS	Extended X-ray absorption fine structure
FC	Field cooled
FG	Functional group
FP	Functional polypropylenes
FR	Flame retardant
FRP	Free radical polymerisation
FT-IR	Fourier transform infrared spectroscopy
g	Designates a graft copolymer
G'	Storage modulus
G''	Loss modulus
GPC	Gel permeation chromatography
h	Hours
HEK293T	Human embryonic kidney model cell line
HDPE	High density polyethylene
HMA	Hot melt adhesive
HMBC	Heteronuclear multiple bond correlation
HRC	Heat release capacity
HRR	Heat release rate
HSQC	Heteronuclear single quantum coherence
Hz	Hertz
Ind	Indenyl
Ind#	Hexamethylindenyl
Ind*	Permethylindenyl

^{i}PP	*isotactic* PP
^{i}Pr	*iso*-propyl
ISO	International Organization for Standardization
J	Coupling constant
L	Ligand
LAO	Linear alpha olefin
LDH	Layered double hydroxide
LDPE	Low density polyethylene
LOI	Limiting oxygen index
LR	Latent reactivity
LSS	Lap shear strength
M	Metal (II)
m	*meta* position; *meso*
M#	Metallocene
MAO	Methylaluminoxane
MBT	2-mercaptobenzothiazole
MCC	Microscale combustion calorimetry
MI	Migratory insertion
M_{n}	Molar mass; number-average molar mass
$M_{\mathrm{n,\,th}}$	Theoretical number-average molar mass
mol%	Percent by mol fraction
MS	Mass spectrometry
MSA	Multi-substrate adhesion
M_{w}	Weight-average molar mass
MWD	Molecular weight distribution
n	Number of carbon atoms in LAO
NEVPT2	Second-order *N*-electron valence state perturbation theory
NIR	Near-infrared
NMP	Nitroxide-mediated polymerisation
NMR	Nuclear magnetic resonance
NOCV	Natural orbitals for chemical valence
o	*ortho* position
p	*para* position
P	Propylene
ppm	Parts per million
PE	Polyethylene
PFG	Protected functional group

PFS	Polyferrocenylsilane
Ph	Phenyl
PHENI*	*ansa*-Permethylindenyl-phenoxy
phr	Parts per hundred rubber
pHRR	Peak heat release rate
pK_a	Acid dissociation constant
PO	Polyolefin
PP	Polypropylene
PP_{Br}	Poly(propylene)-co-(11-bromo-1-undecene)
PP_X	PP_{Br} modified by, X
PS	Polystyrene
PTFE	Polytetrafluoroethylene
r, rac	*Racemic*; Monomer reactivity ratio
RA	Rotation angle
RAFT	Reversible addition-fragmentation chain transfer
Rb	Rhodamine B
ROP	Ring-opening polymerisation
ssNMR	Solid-state nuclear magnetic resonance
SAOS	Small-amplitude oscillatory shear
SBR	Styrene-butadiene rubber
SCB/1000TC	Short chain branching profile per 1000 total carbons
SEC	Size exclusion chromatography
SEM	Scanning electron microscopy
sobEDA	EDA based on dispersion-corrected DFT
^{s}PP	*syndiotactic*-PP
SQUID	Superconducting quantum interference device
t	Time
$T_{10\%}$	Temperatures at 10% mass lost
$T_{50\%}$	Temperatures at 50% mass lost
^{t}Bu	*tert*-butyl
TEMPO	(2,2,6,6-tetramethylpiperidin-1-yl)oxyl
TGA	Thermogravimetric analysis
THF	Tetrahydrofuran
THR	Total heat release
TIBA	Triisobutylaluminum
T_m	Melt temperature
TMA	Trimethyl aluminium

T_{Max}	Temperature of maximum rate of mass loss
T_p	Polymerisation temperature
T_v	Temperature of vulcanisation onset
UHMWPE	Ultra-high molecular weight polyethylene
UL 94	Flame exposure test
UV-Vis	Ultraviolet–visible spectroscopy
VCM	Vacuum compression mould
VOC	Volatile organic compound
vPP$_{AA}$	Vulcanised PP$_{AA}$
xPP$_{AA}$	Cross-linked PP$_{AA}$
ZFC	Zero-field cooled
Zr	*rac*-ethylenebis(indenyl)zirconium dichloride
α	First position relative to functionality
β	Second position relative to functionality
γ	Shear rate; third position relative to functionality
Δ	Difference
ΔE_{HL}	Energy difference between high- and low-spin states
$\Delta_{M–C}$	Ring-slip parameter
δ	Chemical shift; Axial distortion parameter
ε	Engineering strain
ε_B	Strain at break
η	Viscosity
η*	Complex viscosity
η^x	Hapticity
θ	Angle, degrees; Weiss constant
κ′	Orbital reduction factor
λ_{Em}	Emission wavelength
λ_{Ex}	Excitation wavelength
μ_{eff}	Effective magnetic moment
μP	Microplastic
ν	Wavenumber, cm^{-1}
ξ	Spin orbit coupling
σ	Standard deviation; engineering stress
ω	Angular frequency
ω_c	Modulus crossover
χ	Flory-Huggins interaction parameter
χ_{mol}	Molar magnetic susceptibility

Table of Contents

Preface ..... **iii**
Abstract ..... **v**
Rational for Integrated Thesis ..... **vii**
Author Contributions ..... **vii**
Acknowledgements ..... **viii**
Abbreviations and nomenclature ..... **x**
Table of Contents ..... **xv**
Chapter 1 – Introduction **1**
1.1. Polyolefins 1
1.1.1. Polypropylene 2
1.1.1.1. Tacticity *3*
1.1.1.2. Molecular weights *5*
1.2. Catalysts for olefin polymerisation 6
1.2.1. Heterogenous Catalysis 6
1.2.2. Homogeneous Catalysis 8
1.2.2.1. Homogeneous polymerisation mechanism 8
1.2.2.2. Chain-end vs enantiomorphic site control 10
1.3. Polymerisation conditions 12
1.3.1. Cocatalysts 12
1.3.2. Scavengers 16
1.4. Functional polypropylenes 17
1.4.1. Direct copolymerisation of propylene with functional monomers 18
1.4.1.1. Heterogenous copolymerisation 19
1.4.1.2. Homogeneous copolymerisation 20
1.4.2. C-H bond functionalisation of polypropylenes 21
1.4.3. End group functionalisation 22
1.5. Post-polymerisation functionalisation 22
1.5.1. Small molecule transformations 22
1.5.2. Macromolecular transformations 24
1.5.2.1. Block copolymers 24
1.5.2.2. Graft copolymers 25
1.5.2.3. Living anionic polymerisation 26

1.6. Applications 28
1.6.1. Flame retardant polypropylenes 28
1.6.2. Hot melt adhesive polypropylenes 29
1.6.3. Vulcanised polypropylenes 30
1.6.4. Recycling polypropylenes 31
1.6.5. Compatibilisation of polymer blends 32
1.7. Scope of thesis 33
1.8. References 34
Chapter 2 – Functionalised polypropylenes; a copolymerisation and post-modification platform 41
2.1. Author contributions 41
2.2. Abstract 41
2.3. Introduction 42
2.4. Results and discussion 47
2.4.1. Solution-phase copolymerisation of propylene and bromoalkenes 47
2.4.2. General synthetic methodology for the post-modification of PP_{Br} 52
2.4.3. Post-polymerisation modification of PP_{Br} using forcing conditions 54
2.4.4. Post-polymerisation modification of PP_{Br} using base-mediated conditions 57
2.4.5. Post-polymerisation modification of PP_{Br} by salt metathesis 61
2.4.6. Synthesis and characterisation of synthetic rubbers *via* vulcanisation of PP_{AA} .. 63
2.4.7. Hot melt adhesive performance of hydroxyl functionalised polypropylenes 67
2.4.8. Thermal stability studies of phosphonate functionalised polypropylenes 68
2.4.9. Surface property modification 71
2.5. Conclusions 72
2.6. References 73
2.7. Statement of Authorship 76
Chapter 3 – Flame Retardant Phosphonate-functionalised Polypropylenes 77
3.1. Author contributions 77
3.2. Abstract 77
3.3. Introduction 78
3.4. Results and Discussion 81
3.4.1. Solution-phase copolymerisation of propylene and bromoalkenes 81
3.4.2. Post-polymerisation modification of bromine functionalised polypropylene using phosphite esters 84
3.4.3. Thermal stability studies of phosphonate functionalised polypropylene 85

3.4.4. Flammability studies of phosphonate-functionalised polypropylene 91
3.4.5. Polymer compounding with polypropylene and inorganic flame retardant additives 93
3.5. Conclusions 94
3.6. Experimental Details 95
3.6.1. General (co)polymer synthesis and characterisation. 95
3.6.2. General procedure for polymer compounding. 95
3.6.3. General procedure for polymer compounding with inorganic flame retardant additives. 96
3.7. References 96
3.8. Statement of Authorship 98
Chapter 4 – Functionalised polypropylene copolymers as multi-substrate hot melt adhesives 99
4.1. Author contributions 99
4.2. Abstract 99
4.3. Introduction 100
4.4. Results and Discussion 103
4.4.1. Synthesis and characterisation of functionalised polypropylenes 103
4.4.2. Rheological evaluation of functionalised polypropylenes 108
4.4.3. Hot melt adhesive performance of functionalised polypropylenes 111
4.5. Conclusion 115
4.6. References 116
4.7. Statement of Authorship 119
Chapter 5 – Illuminating microplastics in cells: macro-problems for micro-barriers 120
5.1. Author contributions 120
5.2. Abstract 120
5.3. Introduction 121
5.4. Results and discussion 124
5.4.1. Synthesis and characterisation of PP_{Rb} 124
5.4.2. Cellular Studies 126
5.4.3. Conclusionary remarks 132
5.5. References 133
5.6. Statement of Authorship 135
Chapter 6 – Synthesis, Characterisation, and Magnetic Properties of a Permethylated Manganocene 136

6.1. Author contributions 136
6.2. Abstract 137
6.3. Introduction 137
6.4. Results and Discussion 140
6.4.1. Synthesis and characterisation of Ind*$_2$Mn 140
6.4.2. Electron Paramagnetic Resonance (EPR) Studies 143
6.4.3. Magnetic Susceptibility Measurements 145
6.4.4. Computational Studies 148
6.5. Conclusion 150
6.6. Experimental 150
6.7. Acknowledgment 152
6.8. References 152
6.9. Statement of Authorship 154
Conclusions and outlook 155

Chapter 1 – Introduction

1.1. Polyolefins

Commercially, polyolefins (PO), such as polypropylene (PP)[1] and polyethylene (PE),[2] are synthesised at scale to meet the needs of a broad array of applications. PP and PE, derived from their olefinic monomers propylene and ethylene, account for 29.8 and 19.4% of the overall polymer market respectively with annual production of thermoplastic polymers in excess of 180 Mt, valued around $300 billion USD (2023, Figure 1.1).[3,4]

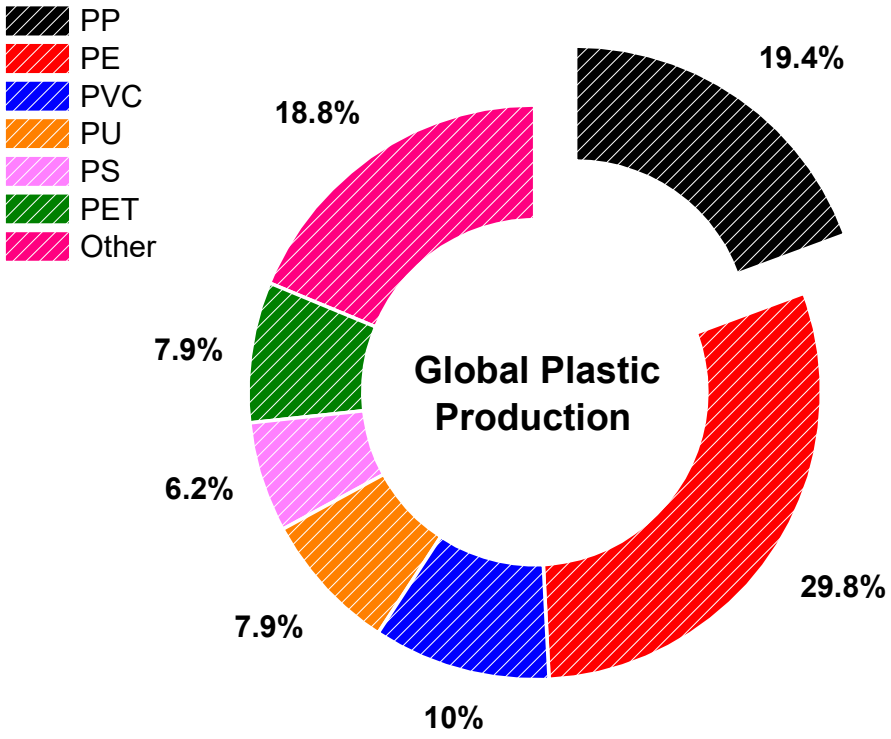

Figure 1.1 Global plastic production (2023), highlighting PP production.[3,4]

Desirable and tuneable properties coupled with low production costs are amongst the driving forces behind their utility; monomer feedstocks typically produced by petrochemical cracking of higher order fractions of crude oil enable the highly economic conversion to polymers.[5] Efforts to curtail the environmental impact from fossil-fuel

derived sources have resulted in bio-ethylene and bio-propylene from bioethanol, with limited commercialisation.[6,7] Further damaging the sustainability profile of PO materials is the tendency for utilisation in composite films that are challenging to recycle, notwithstanding the alternative traditional detrimental approaches regarding the nascent materials such as pyrolytic chemical recycling.[4,8-10] The design, synthesis, and implementation of POs requires bespoke material properties, as defined by application. Consequently, in order to keep abreast with rising demand, the generation of new materials for emerging applications continues at a rapid pace.[11] Next generation PO materials are perceived to be functional and versatile, boosting efficiencies and reducing production volumes whilst streamlining post-consumer recycling through the introduction competitive mono-materials.

1.1.1. Polypropylene

PP was discovered in 1951 by Hogan and Banks, and subsequently, in 1963, Ziegler and Natta were awarded the Nobel Prize in Chemistry "for their discoveries in the field of the chemistry and technology of high polymers"; Natta responsible for the heterogenous polymerisation of propylene to PP, $–(CH_2CH(CH_3))_n–$.[2,12,13] To this day, PP remains an important commodity and engineering material where control of key polymeric characteristics such as tacticity, branching, molar mass (M_n), and dispersities ($Đ_M$), which in turn determine physical properties, have been well studied both academically and industrially.[14] Favourable mechanical properties, chemical resistance, and cost-effectiveness enables extensive commercialisation and utility in a broad array of commercial products such as packaging materials, automotive components, textiles, and medical devices.

1.1.1.1. Tacticity

Propylene, a prochiral monomer, can polymerise in a range of microstructures consequentially impacting physical properties.[15] The arrangement of two adjacent monomer units within the polymer chain, termed a dyad, focuses on the tacticity or spatial arrangement of the methyl groups attached to the carbon backbone (Figure 1.2). There are two types of dyads: *meso* (*m*), where the methyl groups are on the same side, and *racemic* (*r*, *rac*), where they are on opposite sides. Polymer tacticity can be termed isotactic (all *m* dyads), syndiotactic (all *r* dyads), or atactic (a random mix). Expanding this concept, a pentad involves a sequence of five adjacent monomer units, offering a more detailed view of polymer tacticity. A pentad can be all *meso* (*mmmm*), all *racemic* (*rrrr*), or a mix of *meso* and *racemic* dyads (e.g., *mmrr*, *mmrm*), which provides insights into overall stereoregularity and has been extensively characterised.[16] This detailed understanding of pentads is crucial for characterising the physical properties of PP, such as crystallinity, melting temperature, and mechanical strength.

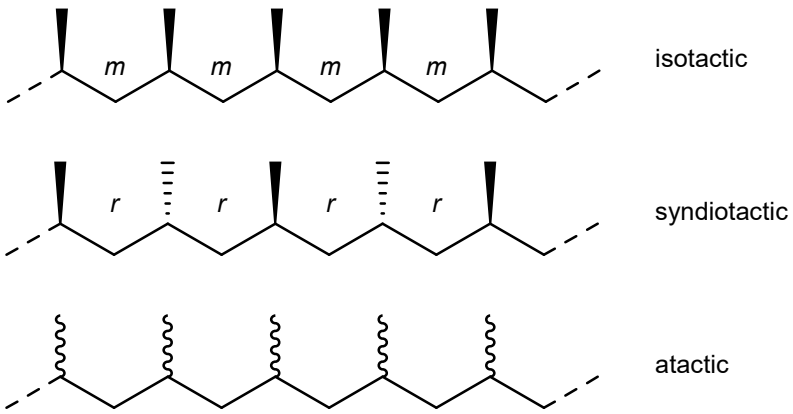

Figure 1.2 Schematic structures of isotactic, syndiotactic, and atactic polypropylene with appropriate dyad assignments.

Heterogeneous Ziegler-Natta catalysts, mixtures of transition metal and trialkylaluminium compounds such as $TiCl_4/AlEt_3$, results in highly crystalline isotactic polypropylene (^{i}PP). The resultant tacticity determined by the inherent chirality of the Ti

centres.[17] Despite a degree of ambiguity regarding the mechanism, computational modelling has elucidated the impact of steric interactions between propylene methyl groups and metal centre adjacent chlorides in the determination of tacticity control in the resultant polymer.[18] Notably, low M_n partially crystalline atactic PP (^{a}PP) is obtained as a by-product,[19] and evidence suggests that tacticity and M_n are inextricably linked.[20]

Single-site molecular catalysts such as *ansa*-metallocenes are typically used where independent control over polymer tacticity and M_n are desired (Figure 1.3).[14,21] The relationship between metallocene (a)symmetry and resulting PP tacticity is well understood,[14,22] with complexes in the C_{2v} and C_2 point groups typically producing ^{a}PP and ^{i}PP respectively (Figure 1.3b), while asymmetric C_1 complexes are reported to produce polymers with microstructures ranging from highly isotactic to atactic (Figure 1.3a).[22] For C_s-symmetric catalysts, regularly alternating propylene insertions at enantiotopic sites *via* chain-end control promote syndiotacticity (Figure 1.3c).[23-25] Constrained geometry catalysts (CGC) typically offer fast rates of polymerisation at the expense of tacticity control, producing ^{a}PP (Figure 1.3d).[26] Propylene insertion stereoselectivity results principally from enantiomorphic site control whereby ligand steric constraints impose a preference for either the *re* or *si* configuration. C_2-*ansa*-metallocenes are particularly effective, with the bridge imposing ligand conformational rigidity.[27,28]

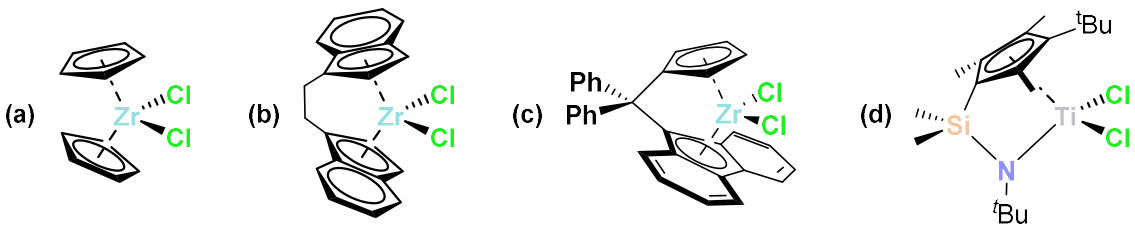

Figure 1.3 (**a**) Achiral zirconocene dichloride, chiral *ansa*-metallocenes (**b**) C_2-symmetric *rac*-ethylene-bis(4,5,6,7-tetrahydro-1-indenyl)$ZrCl_2$,[29,30] and (**c**) C_s-symmetric ^{Ph,Ph}C(cyclopentadienyl)(9-fluorenyl)$ZrCl_2$,[31] and constrained geometry catalyst (**d**) [Cp(^{t}BuMe$_2$)(SiMe$_2$N^{t}Bu)]$TiCl_2$.[32,33]

1.1.1.2. Molecular weights

PP is a product of chain growth mechanisms and consequentially is inherently a distribution of polymer chain lengths; this distribution requiring definition as statistical averages to be adequately characterised. The molecular weight distribution (MWD) comprises number-average molar mass (M_n) and weight-average molar mass (M_w) alongside molar mass dispersity ($Đ_M$) to accurately define the recorded distribution (Equation 1.1).[34,35] A value of $Đ_M = 1.00$ represents a monomodal sample where all polymer chains are of the same M_n, found typically in biological systems (e.g., proteins or DNA) or theoretical living polymerisations. Such control for the polymerisation of propylene however does not necessarily translate well to product performance, where the MWD has a critical role in mechanical, rheological, and morphological properties;[36] typically for PP, $Đ_M = 2–4$ is considered good. The influence of the MWD on PO material properties[37] can further be tuned through polymer blending,[38] bifunctional catalysts,[39-41] sequential reactivity,[42] and catalyst support composition.[43] Gel permeation chromatography (GPC), a subset of size exclusion chromatography (SEC), is the most common characterisation technique for polymer MWD determination.

$$Đ_M = \frac{M_w}{M_n}$$

$$M_n = \frac{\sum N_i M_i}{\sum N_i} \qquad M_w = \frac{\sum N_i M_i^2}{\sum N_i M_i}$$

Equation 1.1 Definitions concerning the polymer molecular weight distribution: $Đ_M$ = dispersity, M_w = weight-average molecular mass, M_n = number-average molecular mass, N_i = number of polymer chains, and M_i = molecular weight of a chain.

1.2. Catalysts for olefin polymerisation

Prior to the advent of metallocene technology, ethylene polymerisation, including copolymerisation developments with a variety of functional vinyl monomers was achieved *via* a free radical mediated process under high pressures and temperatures.[44] These processes yielded high degrees of branching due to poor control, typical of conventional free radial polymerisations. Improvements in control over both process and material properties, composition distributions and long chain branching, were realised through the development of first Ziegler–Natta and later metallocene technology. Consequentially, these polymers displayed additional material property improvements (e.g., melting point (T_m) and crystallinity) and instigated a molecular architecture approach to polymer design befitting each application through careful catalyst development and mechanistic understanding.

1.2.1. Heterogenous Catalysis

The majority of PE and ^{i}PP commercially produced are synthesised using heterogeneous Ziegler-Natta catalysts. This four-component catalytic system comprises titanium (IV) chloride, magnesium (II) chloride, an alkyl aluminium (typically $AlEt_3$), and a suitable Lewis base, in which $MgCl_2$ acts as an inert support material.[18] Despite the industrial ubiquity of Ziegler-Natta catalysis, the nature of the active sites and polymerisation mechanisms remain elusive. The Cossee-Arlman proposed mechanism (Scheme 1.1) for the polymerisation of propylene with enantiomorphic site control is generally accepted with the mechanistic understanding principally derived from polymer analysis, experimental homogeneous catalysis, and recent computational studies; importantly the mechanism is implied whilst many of the structures are unknown.[45-47] Termination mechanisms are likewise inferred from observed products *via* four pathways: β-hydride

elimination (**T1**) or chain transfer to monomer *via* a 'Zimmerman-Traxler' cyclohexane like pathway (**T2**) both producing vinyl terminated polymers; chain transfer to aluminium alkyl (cocatalyst) with the transmetallated product hydrolysing in air (**T3**); and chain transfer to hydrogen which occurs through deliberate addition of H_2 producing a saturated end group *via* σ-bond metathesis (**T4**). The inherent system complexity limiting the level of control over the final polymer, be it M_n, $Đ_M$, branching, stereochemistry, and comonomer incorporation of the resulting polymers.[48-50]

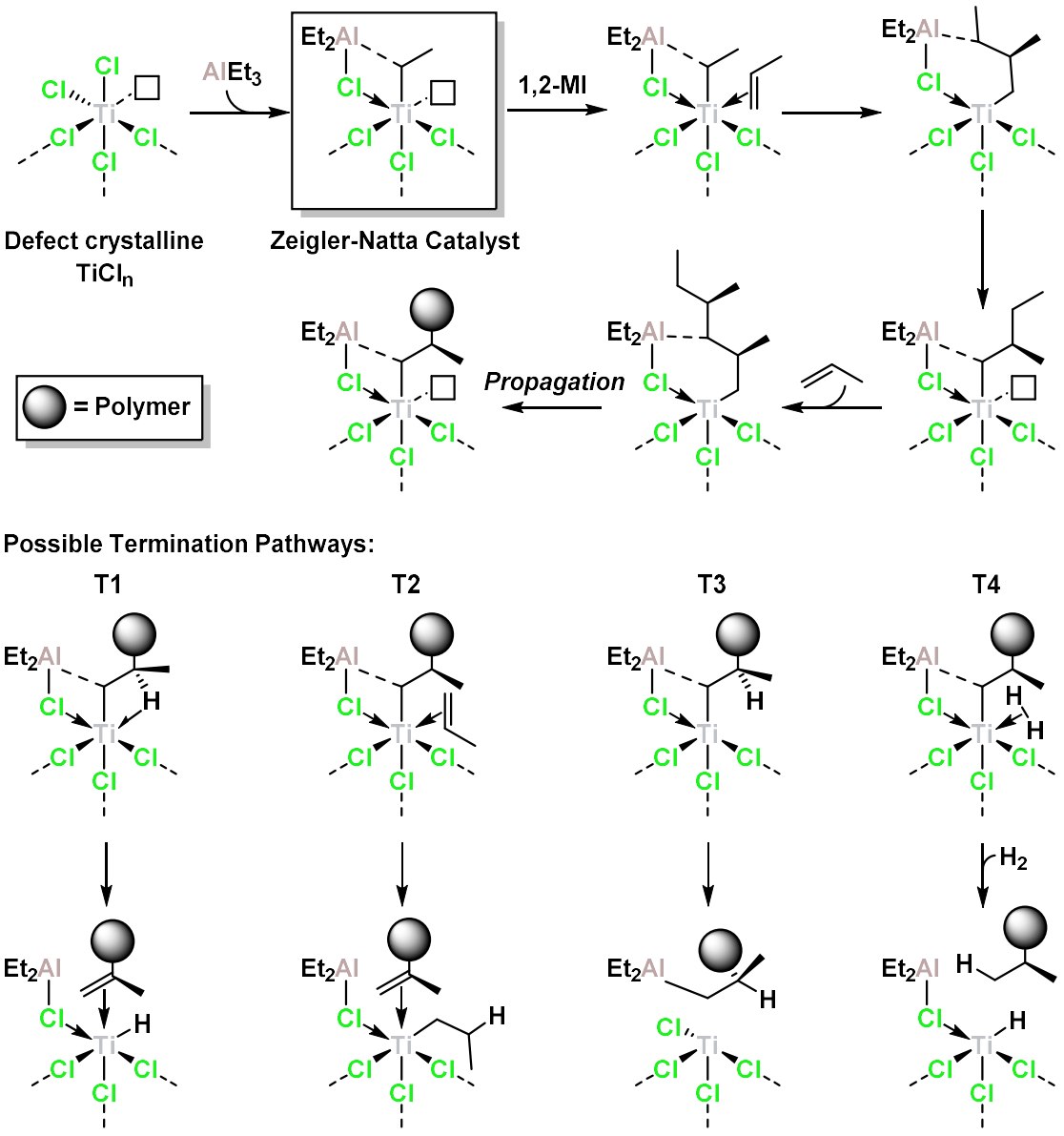

Scheme 1.1 Cossee-Arlman propylene polymerisation mechanism and four termination pathways.[45-47]

1.2.2. Homogeneous Catalysis

When polymer composition necessitates fine control over M_n, $Đ_M$, comonomer incorporation, and tacticity, traditional heterogenous catalysts are commonly superseded by Kaminsky-type metallocenes.[51,52] These metallocenes are hydrocarbon-soluble allowing for homogeneous single-site catalysis. The inherent tunability of the metallocene ligand environment has been extensively investigated yielding a plethora of catalysts affording requisite control over both the polymerisation and the resultant polymer.[53]

Until the serendipitous discovery of methylaluminoxane (MAO) by Kaminsky *et al.* in 1976 which increased metallocene polymerisation activity significantly,[54-56] metallocenes were not active enough to be exploited industrially, instead being primarily of academic interest.[57] Kaminsky demonstrated that MAO can be utilised to activate a variety of Group 4 metallocenes towards ethylene or α-olefin polymerisation, through abstraction of anionic ligands and acting as an alkylating agent to create a cationic, electrophilic, and substitutionally labile active species, whilst providing a non-interfering counter-anion (Scheme 1.2).[58,59]

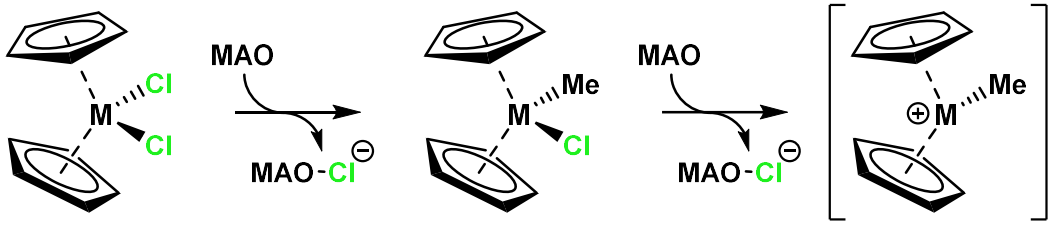

Scheme 1.2 General metallocene MAO initiation mechanism proposed by Kaminsky.[37] M = Ti, Zr, Hf.

1.2.2.1. Homogeneous polymerisation mechanism

Catalytic α-olefin polymerisation is proposed to proceed *via* the Cossee-Arlman 1,2-coordination-insertion mechanism (Scheme 1.3).[45,46] The catalyst reacts with MAO

initiator to form the electrophilic coordinatively unsaturated active species which can then coordinate the alkene in a manner described by the Dewar-Chatt-Duncanson model.[60] This is followed by successive insertion of alkene into an M-C bond at the catalyst centre.

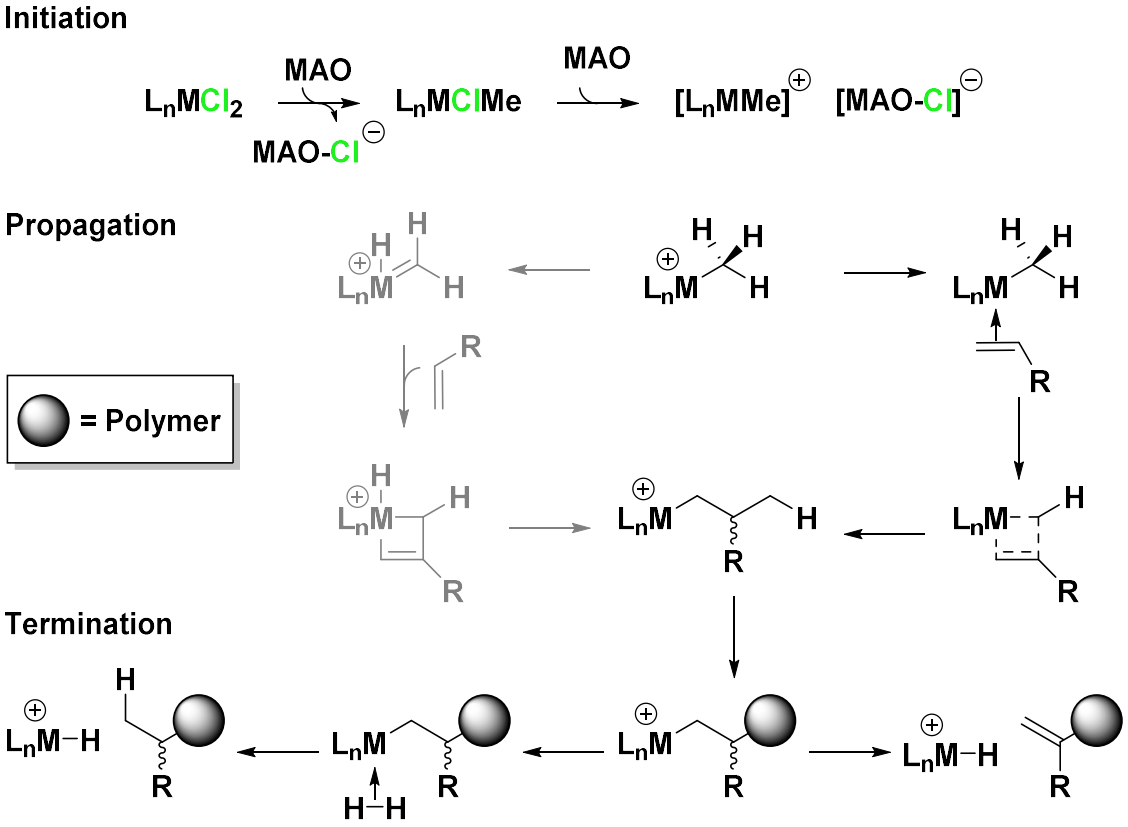

Scheme 1.3 Cossee-Arlman propagation mechanism in black[45,46] of coordination-insertion α-olefin polymerisation, with the hydrogenolysis and β-hydride elimination termination processes exemplified. Green and Rooney proposed α-elimination mechanism in grey.[61]

Whilst the Cossee-Arlman mechanism is generally accepted, subsequent developments have been postulated. Green and Rooney suggested that the polymer chain performs an α-elimination to give an alkylidene hydride.[61] This reacts with the alkene by cycloaddition followed by *cis*-elimination. Principally, the problem with this mechanistic proposal was that the metallocycle could just as easily eliminate the other M-C bond to give the unobserved ethyl-branched polymer; Grubbs later evidenced that α-elimination does not occur.[62] Further developments to the Cossee-Arlman mechanism stress the

importance of an α-agostic interaction. The most active polymerisation catalysts typically have an additional empty coordination site after alkene coordination. The modified Green-Rooney mechanism (Scheme 1.4) adds an α-agostic interaction, thought to tilt the sp^3 alkyl towards the alkene ligand and open up access to the alkene, thus promoting the migratory insertion (MI).[63,64] Note that the latter γ-agostic interaction in the product may have a role in slowing down termination by β-elimination and that the agostic interactions are involved in the termination mechanism β-hydride transfer to olefin. Recent theoretical and experimental evidence support this mechanism and is the currently accepted form.[65]

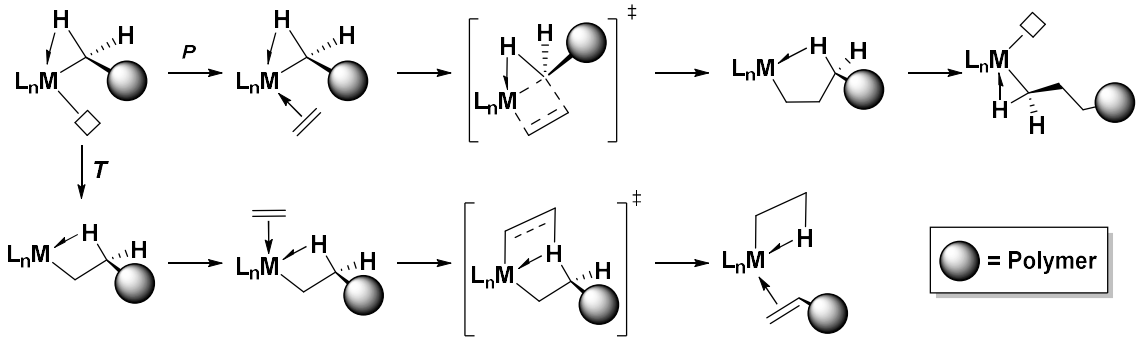

Scheme 1.4 Modified Green-Rooney mechanism highlighting the importance of α/γ-agostic interactions during propagation (*P*) and termination (*T*).

1.2.2.2. Chain-end vs enantiomorphic site control

Two mechanisms determine polymer stereospecificity when concerning single site metallocene catalysis: (1) chain-end control, the growing polymer dictates the stereochemistry of successive insertions, and (2) enantiomorphic site control, ligand-controlled tacticity (Scheme 1.5).[22] The five main symmetry categories of single site polymerisation catalysts are chain-end controlled C_{2v} and C_s, and enantiomorphic site-controlled C_s, C_2, and C_1 catalysts. Key difference in the polymerisation control is the propensity of the catalyst to propagate stereoerrors; enantiomorphic control resulting in

isolated stereoerrors in the polymer backbone whilst chain-end control yields block like microstructures as illustrated by pentad analysis *mrrm vs mmrm* for ^{i}PP.[22,66]

Enantiofacial discrimination of prochiral alkenes, like propylene, has been directly related by Ewen *et al*. to the chirality of the catalytic sites, with the R group of the α-olefin preferentially oriented in the least sterically demanding position.[27,67] Mechanisms concerning both isotactic C_2 and syndiotactic C_s catalysts undergo regular alternating insertion of olefins at the enantiotopic sites (Scheme 1.6).[68,69] Brintzinger *et al.* used α-deuterated olefins in stereokinetic studies with chiral *ansa*-zirconocenes to evidence the influence of an α-agostic interaction for monomer stereoinduction by controlling the stability of the alternative 1,2-MI transition states.[70] The preference for the *re* or *si* orientation of the incoming olefin comes from the required placement of the β carbon atom of the growing polymer chain in the least incumbered of the two positions at a rigid three-member Zr-H(α)-C(α) ring.

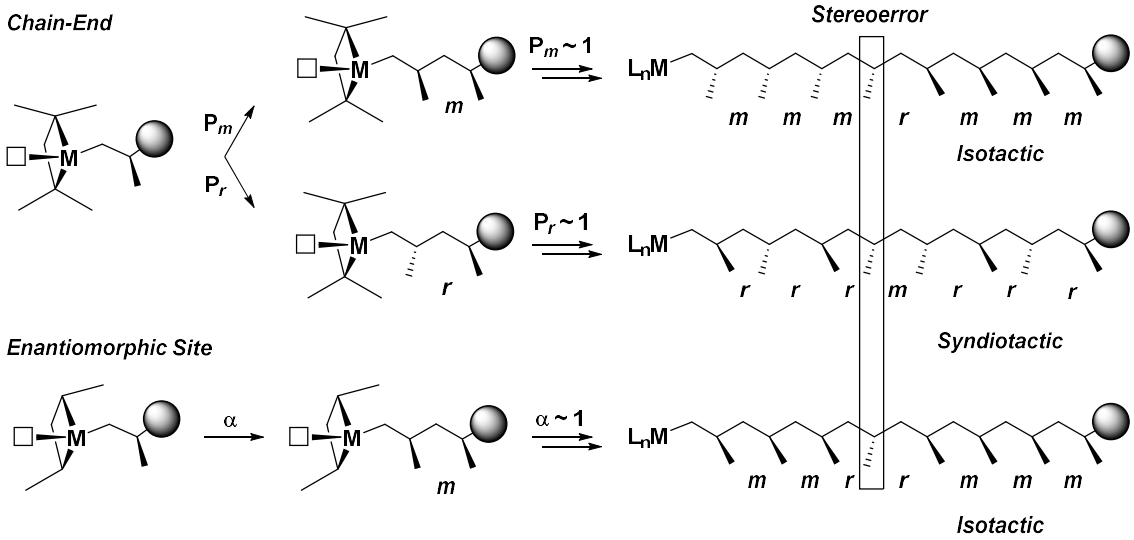

Scheme 1.5 Schematic representation of chain-end and enantiomorphic site control for single site α-olefin polymerisation catalysis and the effect on polymer tacticity.

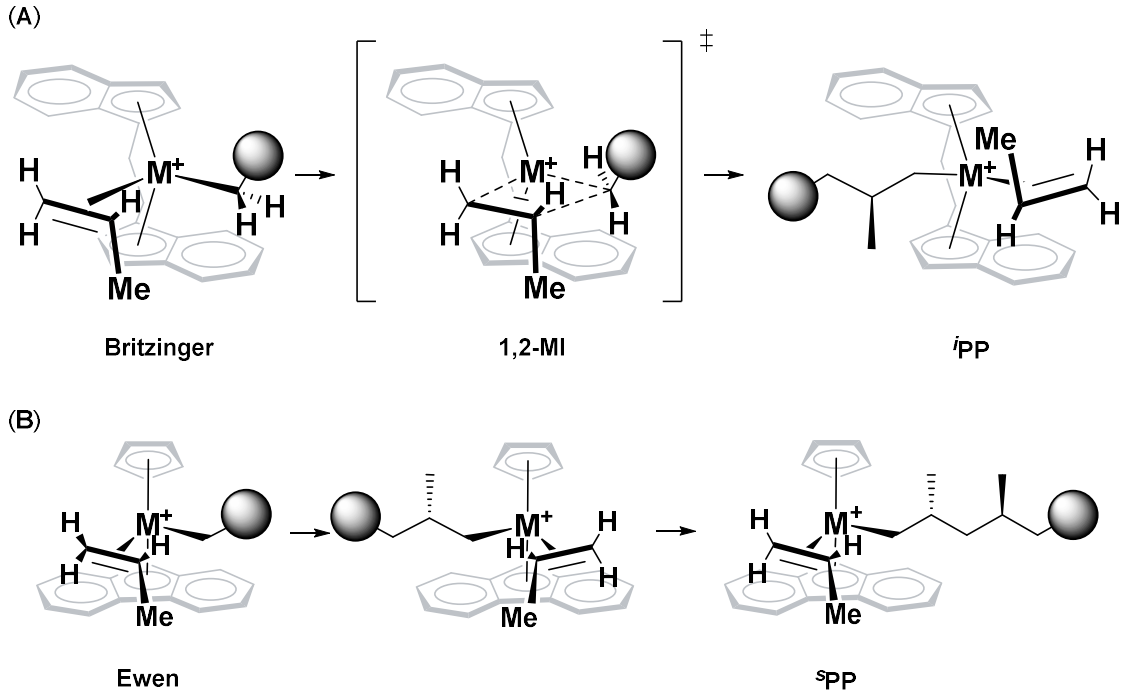

Scheme 1.6 Mechanism of C_2 (**A**) and C_s (**B**) catalysts for single site α-olefin polymerisation.

1.3. Polymerisation conditions

Homogeneous polymerisations are markedly affected by the myriad of possible reaction conditions. Variability regarding scale, agitation, pressure, temperature, and time in addition to choice and concentration of cocatalysts and scavengers lead to significantly different reported catalytic activities;[71-73] likewise notably contributing to poor inter-laboratory reproducibility.[74-76]

1.3.1. Cocatalysts

The peregrination of single-site metallocene polymerisation catalysis, driven by the axiomatic role of aluminium alkyls as activators and co-catalysts began with Natta[77] and Breslow[78] in 1957 who reported the polymerisation of ethylene by bent metallocene Cp_2TiCl_2 (Scheme 1.7). Their work laid the foundation for the widespread use of aluminium alkyls in coordination polymerisation, where these compounds function as cocatalysts by transferring alkyl groups to the metal centre, generating the active species

required for polymerisation. The serendipitous discovery of partially hydrolysed $AlMe_3$, known as methylaluminoxane (MAO), in 1976 remains fundamental with >8000 published research papers and over 20 000 patented inventions.[55,59,79] MAO serves multiple functions: alkylation of the metal chloride pre-catalyst, methide abstraction and generation of a highly electrophilic cation, provide a non-interfering counter-anion, whilst additionally acting as a scavenger for protic impurities.

Through formation of the cationic active species, a tight-contact ion pair is formed upon dissociation of the weakly-coordinating anion.[80-82] It is now generally accepted than an outer-sphere ion pair is the polymerisation-active catalyst, while bridged and bimetallic adducts are dormant species.[83,84] Additionally, the identity of the abstracted group plays a decisive role in the activation and polymerisation processes.[85,86]

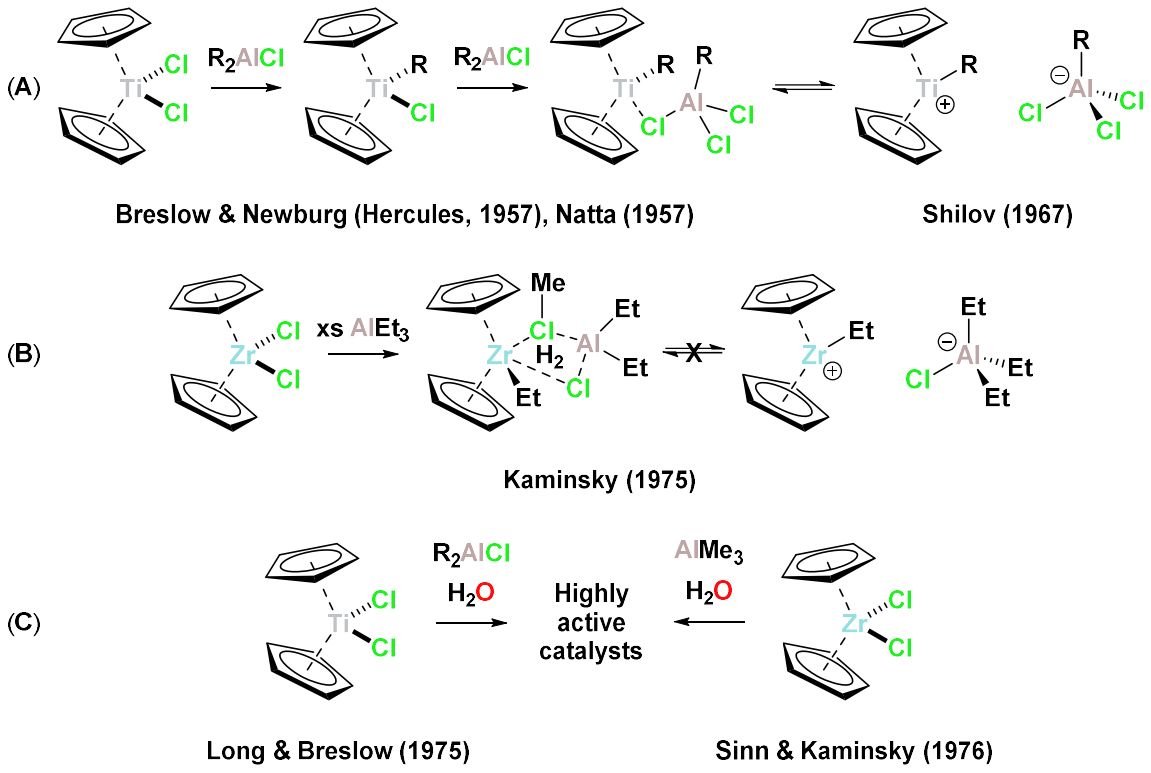

Scheme 1.7 Metallocene activators – a brief history of the free coordination site.[55,59,77,78]

Typically, highly superstoichiometric amounts of MAO are required, [Al]/[M] ≈ 102–104, which can lead to the formation inactive polymerisation species; for example, reduction of the transition metal centre and the formation of M–Al bimetallic adducts.[87,88] The presence of "free" trimethylaluminium (TMA) may also result in the formation of dormant species[85] and chain transfer to aluminium chain termination, influencing the polymer molecular weight.[83] Consequently, the MAO to metallocene ratio is a critical parameter for determining catalyst reactivity.

Despite the understanding progressing from the proposed and poorly understood structures **1**–**7** (Figure 1.4)[58] to the recent crystallographic characterisation of **9** (Figure 1.5),[79] elucidation of the full structure-property relationship regarding MAO still remains poorly understood. MAO comprises a mixture of different structures; the predominant topology reported at ambient temperatures to consist of cyclic, linear, hexagon-type clusters, or tetrameric aggregation of $[Al_4O_3(CH_3)_6]$ into various cages (Figure 1.4);[89-92] the cages of which may additionally contain "free" TMA.[93-95]

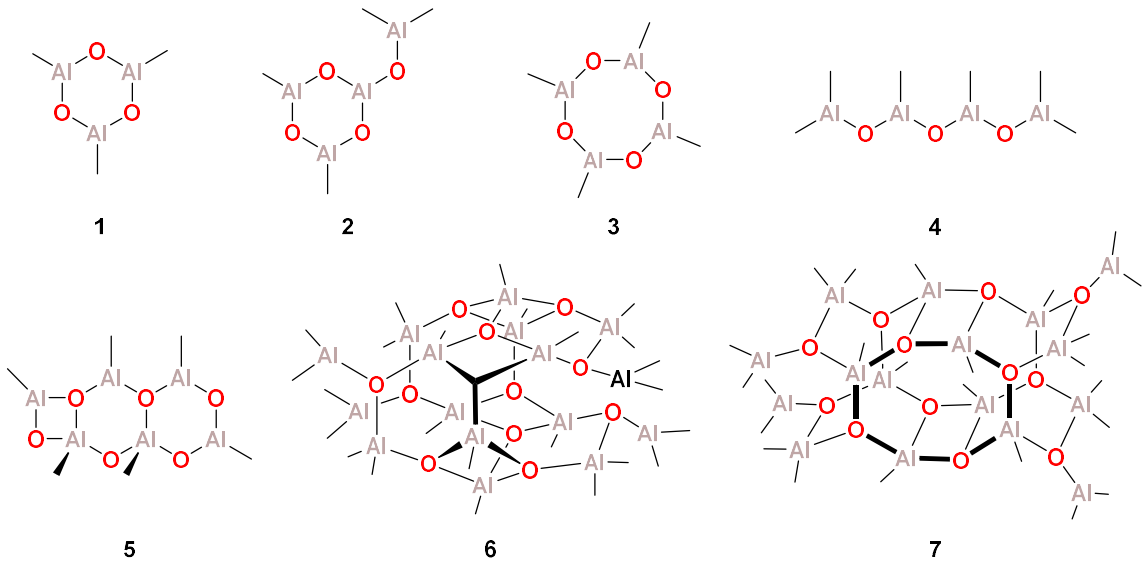

Figure 1.4 Proposed structures of MAO.[58,79]

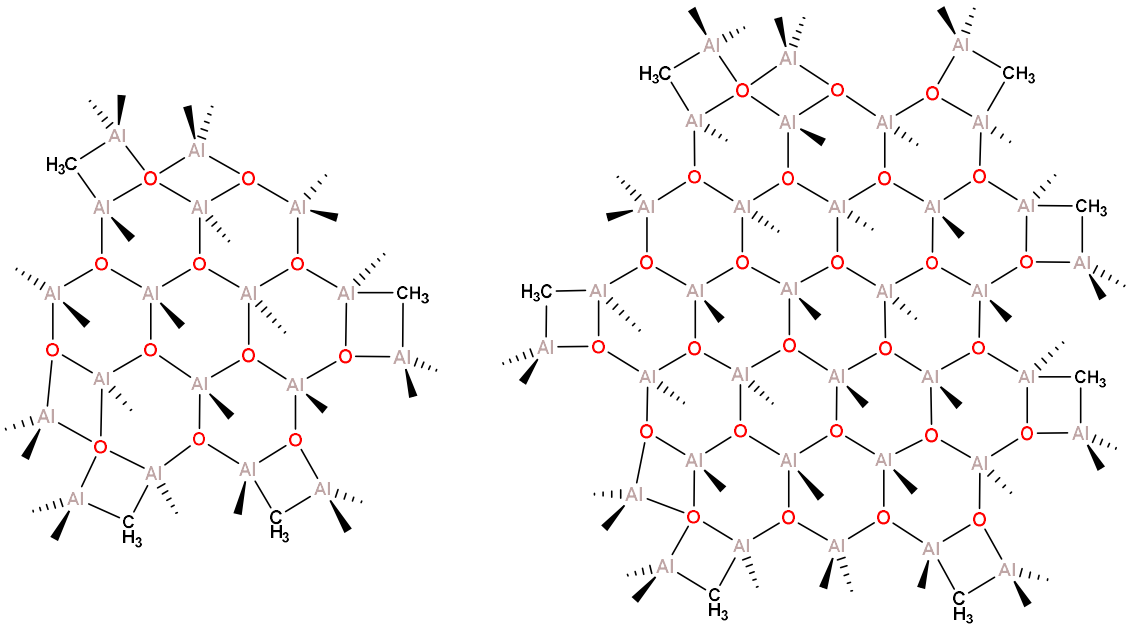

8 **9**

Figure 1.5 Examples (**8** and **9**) of soluble active components in commercial MAO solutions. Structural formula for MAO, **9**, based on a single-crystal X-ray diffraction study.[79]

Conversely, a sheet structure has been suggested for MAO molecules according to recent mass-spectrometric and computational studies and further supported by crystallographic characterisation of **9** (Figure 1.5).[96-98] However, prior to the recent work by Zabula *et al.*, none of the structures were generally accepted, especially given the structure of MAO is expected to vary both between samples, over time, and during polymerisation.[83] It is likely that the soluble active components in commercial MAO solutions consist of species **8** $[Al_{16}O_{12}(CH_3)_{24}][Al(CH_3)_3]_2$, **9** $[Al_{33}O_{26}(CH_3)_{47}][Al(CH_3)_3]_2$, and the appropriate C-to-Al ratio in between but that the derived information will aid in the rational design of next generation co-catalysts.[99-101]

Well-defined molecular analogues of MAO have been developed, such as the $[^{i}Bu_2(DMA)Al]_2(\mu\text{-}H)]^+[BAr^F{}_4]^-$ of Zaccaria *et al.*,[102] and other Lewis acids with non-coordinating counter-ions have been employed as stoichiometric activators such as trityl or anillinium borate salts as non-exhaustive examples (Scheme 1.8).[58,103-106] Borate

activators, as an alternative to aluminium counterparts, can supress chain transfer processes and result in high M_n POs.[107] It is widely regarding that the coordinating ability of the counteranion influences catalytic activity; more strongly bound ion pairs generally having lower activities.[108-110]

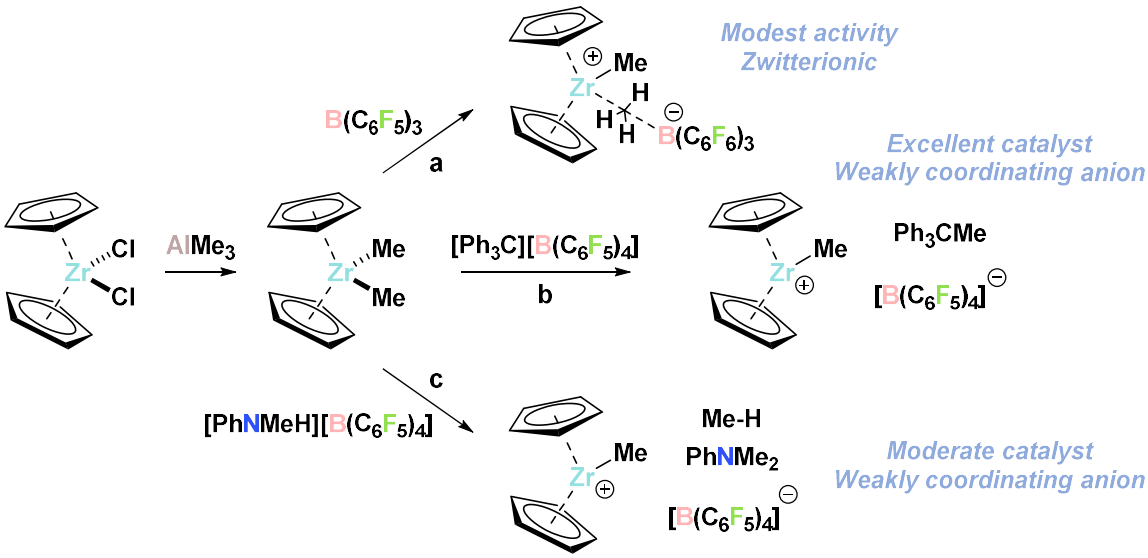

Scheme 1.8 Activator effect on catalytic activity through the generation of different active species.[58]

1.3.2. Scavengers

Scavengers are employed, additional to the co-catalyst, to remove trace impurities, principally water and oxygen, from the reaction mixture. Trialkyl aluminium scavengers (R_3Al, where R includes methyl, ethyl, *iso*-butyl and *n*-octyl) are generally used, resulting in increased activities relative to alkyl aluminium halides.[111-114] Catalyst activity and polymer M_n have both increased with the use of larger alkyl groups.[113,115] The bulkier trialkyl aluminium reagents can trap the "free" TMA in the MAO through ligand scrambling, with larger alkyl groups resulting in more active systems.[116] High [scavenger] can both deactivate the metallocene[117-119] and cause leaching of an immobilised catalyst into solution;[120,121] consequently evidencing a strong concentration dependence on the kinetic profile.

1.4. Functional polypropylenes

It is widely regarded that next generation PP materials will be functional and versatile though the incorporation of polar functionality, yet there has been limited success industrially in deviating from the ubiquitous carbon and hydrogen backbone in a controlled manner, whilst also allowing access to high molecular weights and controlled tacticity. Such functionalised PPs refer to the chemical incorporation of functional groups in order to enhance or introduce specific properties for commercial applications. Limited introduction of polar functionality has evidenced a significant impact on bulk and surface properties.[122] Consequently, synergies between base properties of PO materials and those of novel polar POs could yield significant material improvements. Such synergistic new materials may additionally circumvent leaching[123] or disrupted mechanical properties,[124] imparted through the use of additives commonly used in composite materials. Therefore, utilisation of functional PPs as additives could alleviate the negative effects when blending whilst also being utilised in place of multimaterial systems that are challenging to recycle.

PP-based functional polymers have been less widely explored with respect to PE in the literature; additional complexity for controlling C-H functionalisation chemistry resulting from the presence of methyl, methylene, and methine sp^3 C-H bonds.[125] Solubility and purity complications have additionally hindered subsequent developments.[126,127] However, a functional group (FG) containing PP copolymer may provide access to a more diverse array of functional materials in comparison with PE.

General synthetic strategies by which functional PPs can be attained can be summarised into three main groupings: direct copolymerisation of propylene and a functional

comonomer, PP post-modification *via* C-H bond or end group functionalisation. These are schematically represented in Scheme 1.9.

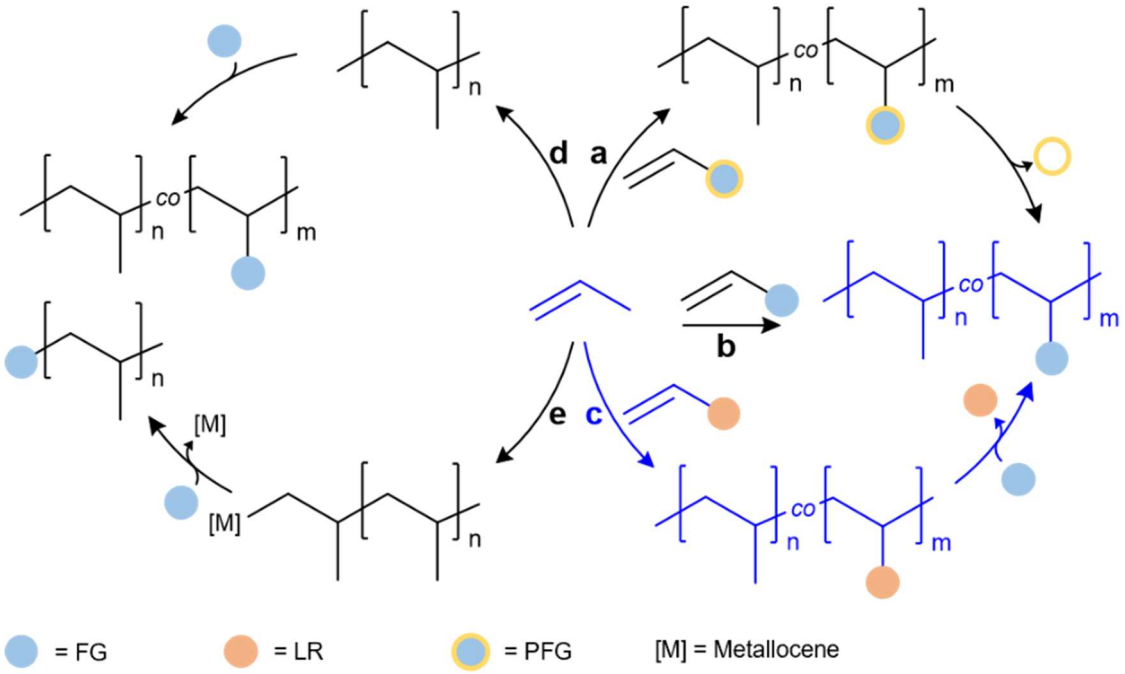

Scheme 1.9 General synthetic strategies for the preparation of functional polypropylenes: (**a**) direct copolymerisation of propylene with a protected functional group (PFG) monomer and subsequent deprotection, (**b**) direct copolymerisation of propylene with a comonomer containing the desired functional group (FG), (**c**) direct copolymerisation of propylene with a comonomer with latent reactivity (LR) and subsequent post-polymerisation modification with the desired FG, (**d**) direct post-polymerisation modification of polypropylene, and (**e**) chain-end functionalisation.

1.4.1. Direct copolymerisation of propylene with functional monomers

The copolymerisation of olefins and polar comonomers is a well-documented pathway for incorporating functionality (Scheme 1.9a-c). Three general synthetic routes are typically exploited; (a) protected functional group (PFG) monomer and subsequent deprotection,[128,129] (b) a FG containing monomer,[23] or (c) a monomer with latent reactivity (LR), exploiting successive post-modification.[130-132] A variety of polymeric architectures, principally block copolymers, with distinctly altered material properties have been synthesised in this way.[133-138] This despite the common issues associated with the copolymerisation of olefins and vinyl polar monomers *via* coordination-insertion

polymerisation which can be succinctly termed the 'polar monomer problem' (Scheme 1.10).[139,140]

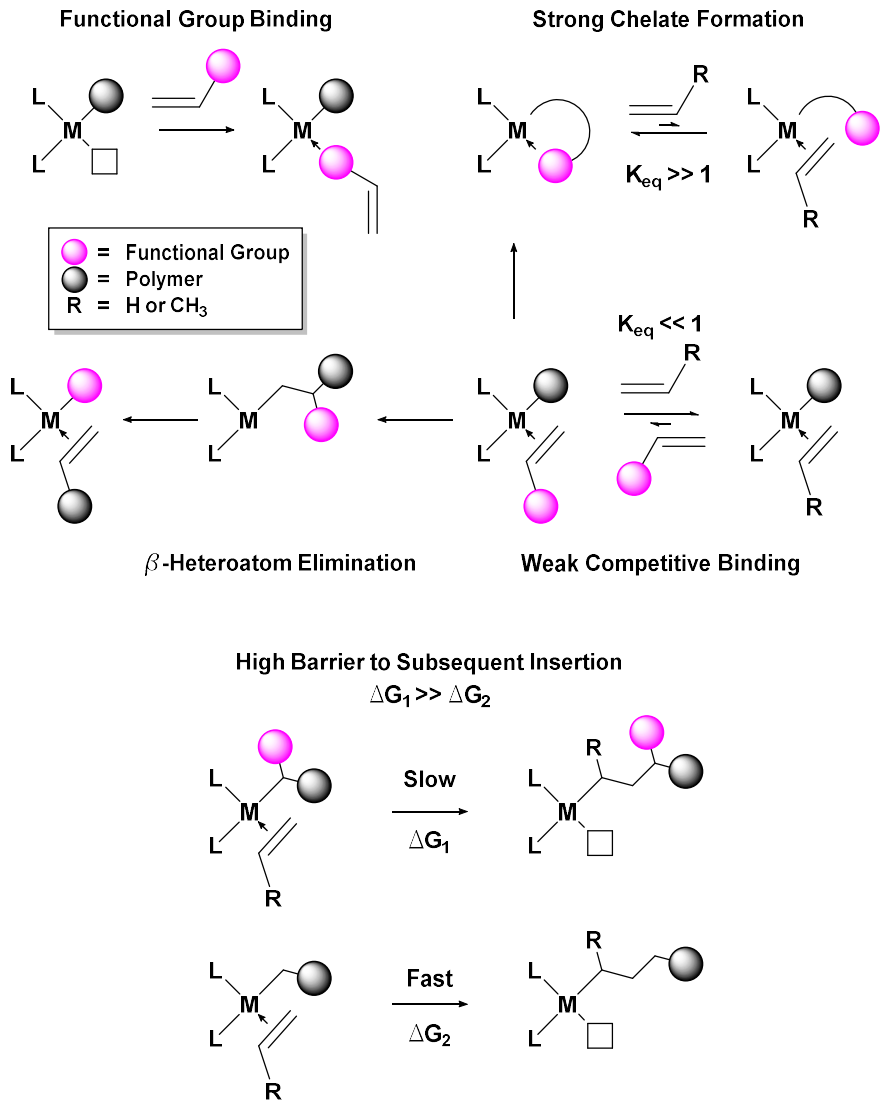

Scheme 1.10 Common issues associated with the copolymerisation of olefins and vinyl polar monomers *via* coordination-insertion polymerisation.[122, 127]

1.4.1.1. Heterogenous copolymerisation

Work by Chung *et al*. have evidenced the utility of organoborane,[141] benzylic protons,[142] and styrene moieties[143] during copolymerisation with propylene, coining the term *reactive* comonomers, to yield a range of PP materials through functional group interconversion.[134] Recent developments utilising commercial heterogenous

Ziegler–Natta catalysts have achieved polar comonomer enchainment *via* an ionic cluster strategy (Scheme 1.11).[144,145]

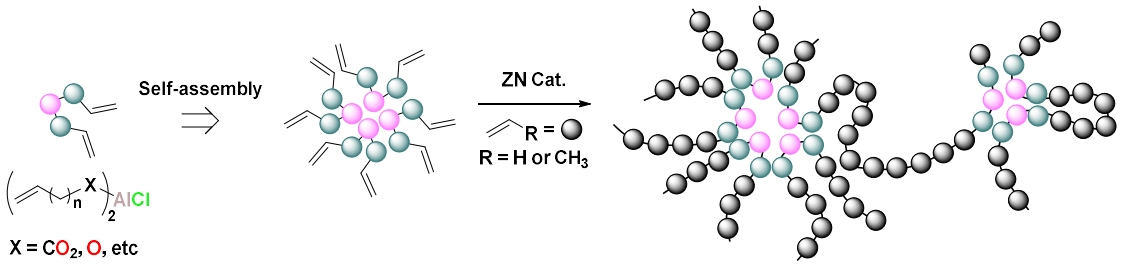

Scheme 1.11 Synthesis of polar-functionalised POs using a commercial heterogenous Ziegler–Natta catalyst, exploiting an ionic cluster strategy to drive polar monomer incorporation.[144,145]

1.4.1.2. Homogeneous copolymerisation

The direct solution phase copolymerisation of functional comonomers by widely employed early transition metal (groups III and IV) catalysts is limited by deactivation and significantly reduced activity due to ω-functional group coordination to the comonomer and backbiting oligomers to the electrophilic metal centres.[139,146] Notably, Zr catalysts have exhibited tolerability towards ω-halo coordination.[147] Increased separation, within the functional comonomer, between α-olefin and ω-FG[147-149] or excess Lewis-acidic masking reagents like methylaluminoxane (MAO) or AlR_3[150-152] have been utilised to aid comonomer enchainment. A pyridyl amido Hf catalyst has been used successfully in propylene copolymerisation with an array of hydrocarbon monomers able to undergo post-polymerisation modification with polar substituents.[153,154] Late transition metal catalysts (Ni and Pd) have been utilised more extensively for the copolymerisation of functional monomers with both propylene[155-158] and ethylene[140,159,160] due to their lower acidity and -oxophilicity than early transition metal analogues (Figure 1.6). However, cost,[161] toxicity,[162] arduous catalyst synthesis, and broad challenges to access tacticity control or high molecular weights in these systems hinder their large-scale application.

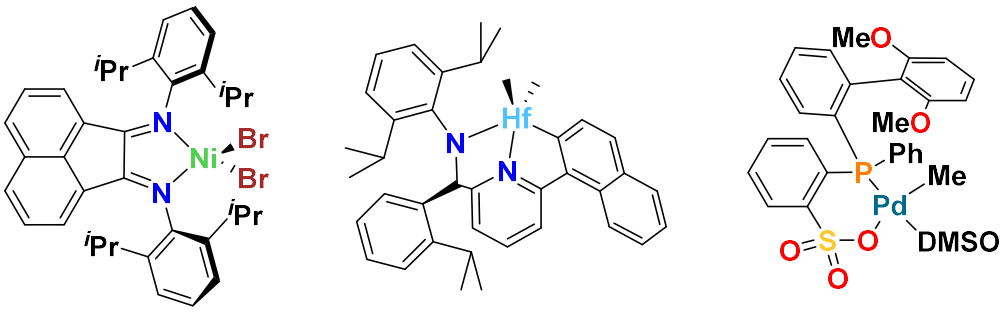

Figure 1.6 Representative examples of Ni, Hf, and Pd catalysts for functional polyolefin synthesis *via* direct olefin copolymerisation with polar monomers.[155]

1.4.2. C-H bond functionalisation of polypropylenes

To overcome low comonomer incorporation and polar monomer incompatibility, post-polymerisation modification *via* C–H functionalisation has been pursued, taking advantage of the low cost and high volume of commodity POs (Scheme 1.9d).[125,126] However, the direct and controlled functionalisation of C–H bonds is challenging as a consequence of β-scission and depolymerisation reactions. Whilst a multitude of covalent connections (C–C, C–N, C–O, C–B, C–S, and C–Halogen) are possible within polyolefin systems,[125,163,164] only radical chlorination and maleic anhydride grafting have been found to be industrially viable despite high cost, low efficiency, and the restrictions for dangerous solvents and reagents.[126,165] Recently, Cu-catalysed C–H amination has been utilised to functionalise PE with a range of functional groups, representing a key development in the controlled and selective synthesis of advanced polar PO-based materials (Scheme 1.12).[166]

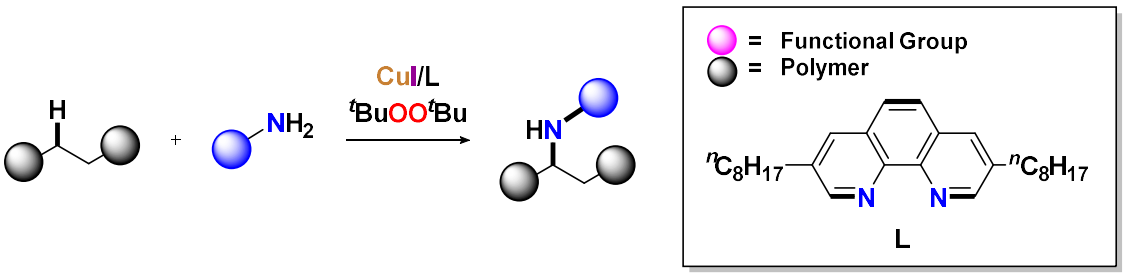

Scheme 1.12 General method for the catalytic amination of PE with nitrogen-based groups using CuI in the presence of a hydrophobic ligand (L).[166]

1.4.3. End group functionalisation

Recently reported advances concerning improved end-group functionality have been achieved by quenching metal catalysed polymerisations in the presence of air, O_2, I_2, Br_2, or S to yield PP-OH, PE-I (X = OH, I, and Br), and PE-S-PE.[167,168] PP-OH were further modified *via* esterification to yield dye modified PP and PE-I/LDPE blends investigated for PE degradability through homolysis of the C-I bond. The latent reactivity, different to traditional vinylic end groups, enables the further synthesis of a wider array of modified PO. Despite this, efforts by Schafer *et al*. have developed a strategy to amine-functionalise POs directly by Ta catalysed hydroaminoalkylation of vinyl containing POs.[169] However, a limitation of end-group post-modification is the presence of only one functional group per chain; lowering the impact of the functionality with increasing molecular weight (Scheme 1.9e).

1.5. Post-polymerisation functionalisation

Focusing on functionalisation through latent reactivity present in the nascent PO (co)polymer an array of new materials can be synthesised through a variety of modifiers for specific applications. The transformations can principally be divided into two main categories: small molecule transformations, whereby small organic molecules are bound to the (co)polymer, and macromolecular transformations, where the functionalising moiety is itself a polymer, leading to a variety of architectures, functionalities, and properties.[133,170,171]

1.5.1. Small molecule transformations

Uncontrolled small molecule transformation methods for PP functionalisation rely on high-energy radical processes to modify the polymer surface, improving adhesion, wettability, or reactivity. Techniques such as plasma treatment, flame treatment, and

corona discharge introduce oxygen-containing FGs *via* C-H bond activation and reaction with atmospheric species are commonly used industrially. These methods are widely used for surface activation in coatings, adhesives, and printing applications. However, they often lack precision, leading to inconsistent modification, degradation, or unwanted side reactions, limiting their long-term stability and reproducibility.[172,173]

Alternatively, more controlled process have been developed to introduce functionality. A variety of synthetic, often erroneously termed, 'click chemistry' pathways (thiol-halogen, thiol-ene, and thermal or Cu azide-alkyne) have likewise been employed to further increase polar group content,[174] impacting molecular weight,[175-178] or polymeric morphologies.[179] An alternate established route to functional POs has been through the functionalisation of ω-halo-α-olefin (co)polymers (halogen = Cl, Br, or I).[127,132,180,181] Modification of Br-containing PO (co)polymers with amines (pyridine or morpholine)[132] or charged analogues containing quaternised trimethylamine moieties.[181] Salt metathesis functionalisation of poly(l1-chloro-1-undecene) homopolymers yielded azide, alcohol, and ester modified polymers;[127] it is worth noting that by dealing with the homopolymers, you circumvent solubility issues predominately restricting the post-polymerisation functionalisation of ^{i}PP copolymers. Preliminary work within the O'Hare group exploiting the latent reactivity of a bromine containing PE[131] and later PP[182] evidences the synthesis and application of functionalised POs, the latter forming the basis for Chapters 2-5 in this Thesis. Modifier choice has been clearly shown to elicit vastly different material properties within the above referenced work and consequently careful consideration of functionality may yield a wide array of new and useful PP based materials.

1.5.2. Macromolecular transformations

Circumventing the limited polar group incorporation level, synthesis of PO-polar block or graft copolymers by a wide range of end group post-polymerisation techniques[133,183-187] has afforded materials able to span phase boundaries and improve immiscible polymer-polymer compatibility (Figure 1.7).[188]

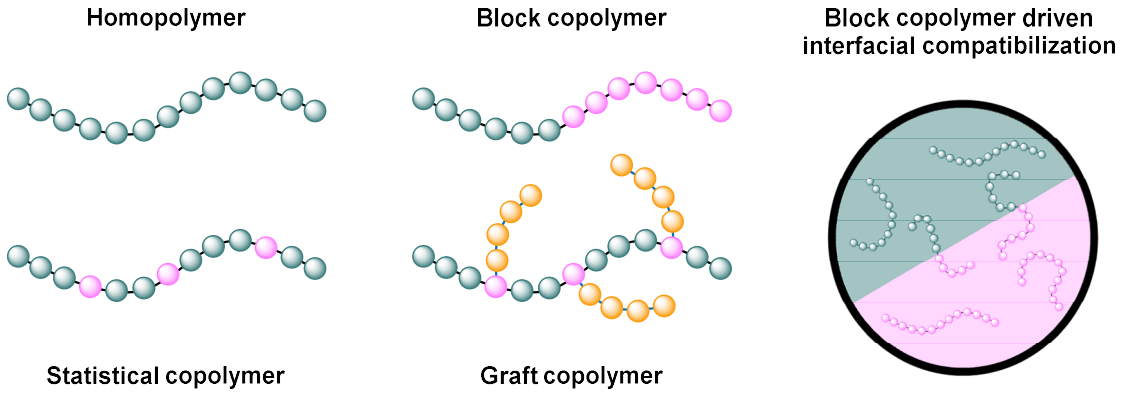

Figure 1.7 Schematic examples of (co)polymer microstructure and an illustrative example of how block copolymers can induce interfacial compatibility in blends of their respective homopolymers.

1.5.2.1. Block copolymers

Synthesis of PO-polar block copolymers are well reported through the utilisation of polymerisable ω-end groups. Traditional olefin polymerisation suffers from poor $Đ_M$ control compared to living polymerisation techniques, consequently most chain extensions have been reported *via* living polymerisations: ionic polymerisation,[183,189] nitroxide-mediated polymerisation (NMP),[184] atom transfer radical polymerisation (ATRP),[185,186] and reversible addition-fragmentation chain transfer (RAFT) polymerisation[187]. PO (co)polymers are subsequently utilised as macromonomers and the control imparted allows for fine control of final polymer properties through accurate degree of polymerisation (DP) and low $Đ_M$, hallmarks of a living polymerisation. Furthermore, such a wide array of polymerisation techniques allows for a broad monomer scope due to their respective functional group tolerances; consequently translating to unique final material properties.

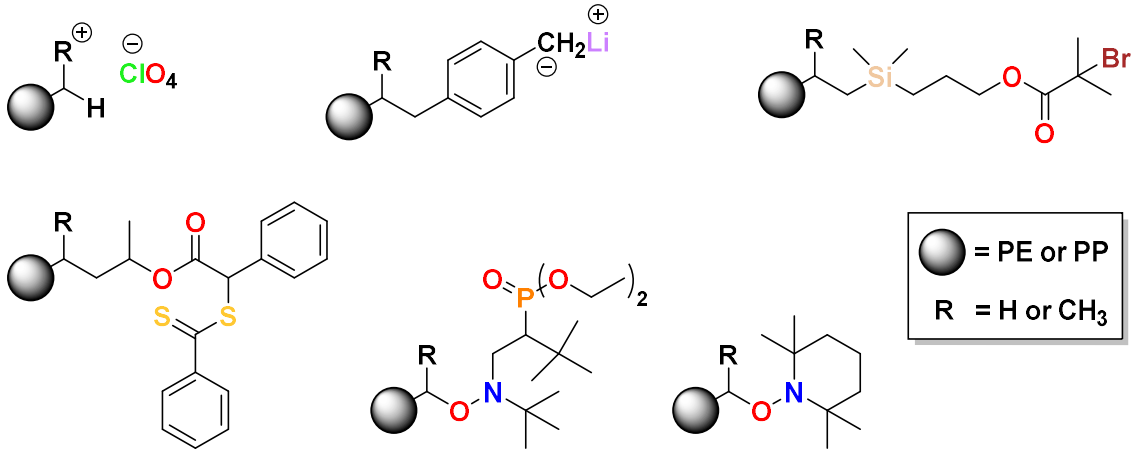

Figure 1.8 Macro-PO initiators for the synthesis of block copolymers *via* ionic polymerisation,[166, 172] ATRP,[185] RAFT polymerisation,[187] and NMP[184] methods.

Additionally, ω-end group post-polymerisation has been achieved through free radical polymerisation (FRP), a commercially relevant technique. Simple radical polymerisation in the presence of vinyl terminated PO macromonomers has been reported by Scott and co-workers to yield diblock copolymers with either acrylate, methacrylate, vinyl ester, or styrenic segments.[133] These materials exhibit interfacial phenomena, including the mediation of the mixing of immiscible polymer blends.

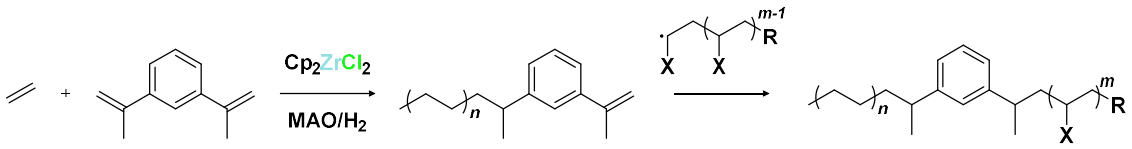

Scheme 1.13 PO-polar block copolymer synthesis by Scott *et al*..[133]

1.5.2.2. Graft copolymers

Comb polymers are a complex polymer architecture consisting of branched polymers with a linear backbone containing a tuneable proportion of pendant functionality to which living polymers can be terminated.[170,171] Comb polymers are attractive materials due to the variety of possible applications; as compatibilisers facilitating homogenisation of traditionally immiscible polymer blends to ceramic fabrication.[190-192] Yang *et al.*

synthesised comb polymers with grafted poly(methylmethacrylate), eliciting improved compatibility in poly(vinylidene fluoride)/poly(*L*-lactic acid) blends for battery fabrication.[191] Polymer blending is of great interest for production of new specialty polymeric materials as well as streamlining recycling of plastic waste.[193-195] Polypropylene-*graft*-polystyrene (PP-*g*-PS) has previously been synthesised, although poorly characterised, through living anionic polymerisation of styrene and quenching with a brominated PP copolymer.[138] This remains an area of active interest and offers the opportunity to create more varied and functional graft (co)polymers with careful monomer consideration.

1.5.2.3. Living anionic polymerisation

As alluded to in the above sections (*1.5.2.1-2*), living polymerisations have evidenced themselves as a valuable polymerisation technique and can be defined simply to proceed with a positive linear relationship between M_n of the growing polymer and monomer conversion, requiring the absence of termination. Living anionic polymerisation typically involves vinylic monomers, initiated *via* nucleophilic reaction mechanisms.[196] The relationship between initial [initiator] and [monomer] dictating the number of active chains and DP respectively, with each chain propagating at the same rate.[197] Lack of termination results in a Poisson MWD, as predicted by Flory.[198] Polymers of sufficient length (DP > 100) have been synthesised widely with $Đ_M$ = ~1.01, exhibiting far tighter control than chain or step growth polymerisations.[199] Crucially, the growing polymer chain will remain active once the supply of monomer has been exhausted. At this point further monomer can be introduced, propagating with the same or alternate monomers allowing the synthesis of higher order (multi)block polymers,[200,201] or deliberately terminated.[202-206]

A limitation of anionic living polymerisation is the fairly narrow scope of polymerisable monomers.[200] Szwarc *et al.* first reported the living anionic polymerisation of styrene in 1956[199] with subsequent studies into initiation,[207] reaction conditions,[208-211] and control over the final M_n distribution being undertaken.[198,212,213] Further to the traditional vinylic monomers, the development of anionic ring-opening polymerisations (ROP) have later been developed, expanding the library of potential monomers to include epoxides and bridged metallocenophanes as non-exhaustive examples. Manners *et al*. first reported the synthesises of silicon-bridged [1]ferrocenophane precursors and their thermally induced ROP in 1992 which has been expanded comprehensively to include anionic ROP mechanisms.[214-216] Resultant polymers, polyferrocenylsilanes, are a well-defined class of metallopolymers consisting of alternating ferrocene and organosilane units. These metallopolymers combine the processability of a stable carbon-based structure with the functionality of metal centres making them highly desirable materials;[217,218] with potential applications in catalysis, data storage, and electronics.[219-223] More interestingly, by tethering two heterogenous blocks together, block copolymers are able to undergo self-assembly into a wide array of architectures,[215,218,224] depending on the relative concentration of each polymer component, f_x, degree of polymerisation, DP, and Flory-Huggins interaction parameter, χ.[225] Careful control over DP can lead well-defined phase structures, including micelles, cylinders, and lamellar self-assembled structures (Figure 1.9).[226] Coupling this with energy dispersive imaging techniques may offer a unique insight into polymer phase behaviour during mixing, enabling the development of optimised compatibilisers for PO plastic recycling.

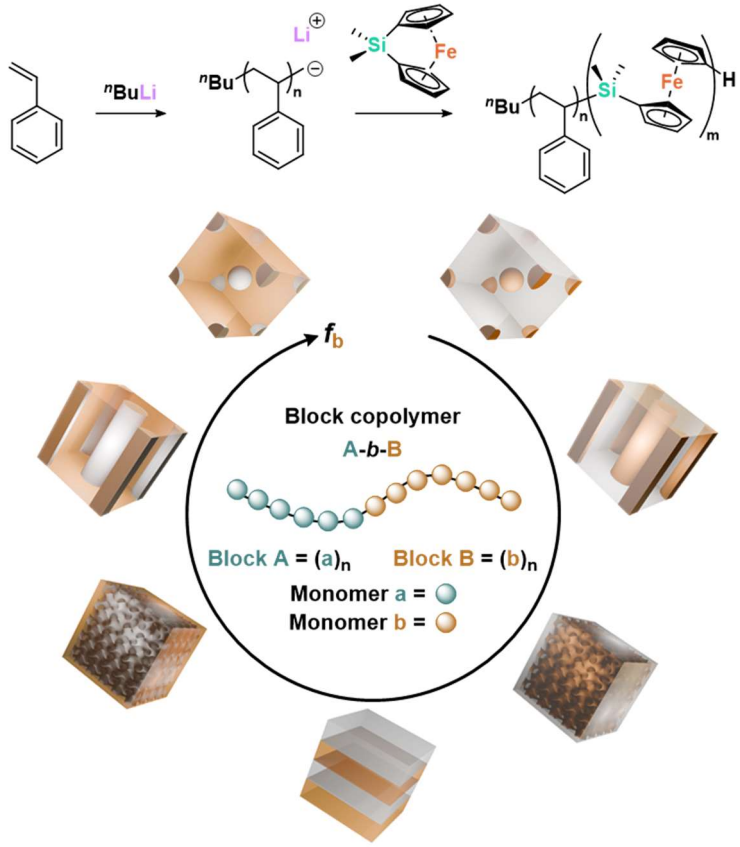

Figure 1.9 Illustrated scheme for the synthesis of diblock copolymer poly(styrene-*b*-ferrocenylsilane) and a representation of the four ordered morphologies (spheres, cylinders, discontinuous gyroid, and lamellar) of a diblock copolymer as a function of the interaction parameter, χ, and fraction of monomer B, f_B, in the diblock.[226]

1.6. Applications

The design and synthesis of polymers are driven by the need for specific material properties tailored to each application; currently the generation of new materials for emerging applications is prolific.[11] Functional polypropylenes, with varied properties through various polar group incorporation offer versatile solutions able to reduce the reliance on composite materials, simplifying recycling and reuse processes.[227,228]

1.6.1. Flame retardant polypropylenes

Common commercial non-halogenated flame retardant (FR) additives for polyolefin systems are typically based on phosphorus, boron, inorganic hydroxides, silicon, and nitrogen-based additives; which are introduced to polymer matrices during processing

(Figure 1.10).[229-233] Undesirable consequences of physical mixing include the resulting blends being prone to migration and ultimately leaching,[123] or severely disrupted mechanical properties due to poor chemical and physical compatibility within the polymer matrix.[124] Chemical incorporation of FR-functionality directly into the polymer through copolymerisation has the potential to provide good FR properties at low comonomer loadings,[234,235] avoiding migration and leaching whilst providing good mechanical performance. For example, phosphorus moieties have been incorporated *via* radical polymerisation in styrene[234] and (meth)acrylate systems[123,236,237] or Pd-catalysed copolymerisation with ethylene[159] yielding promising results.

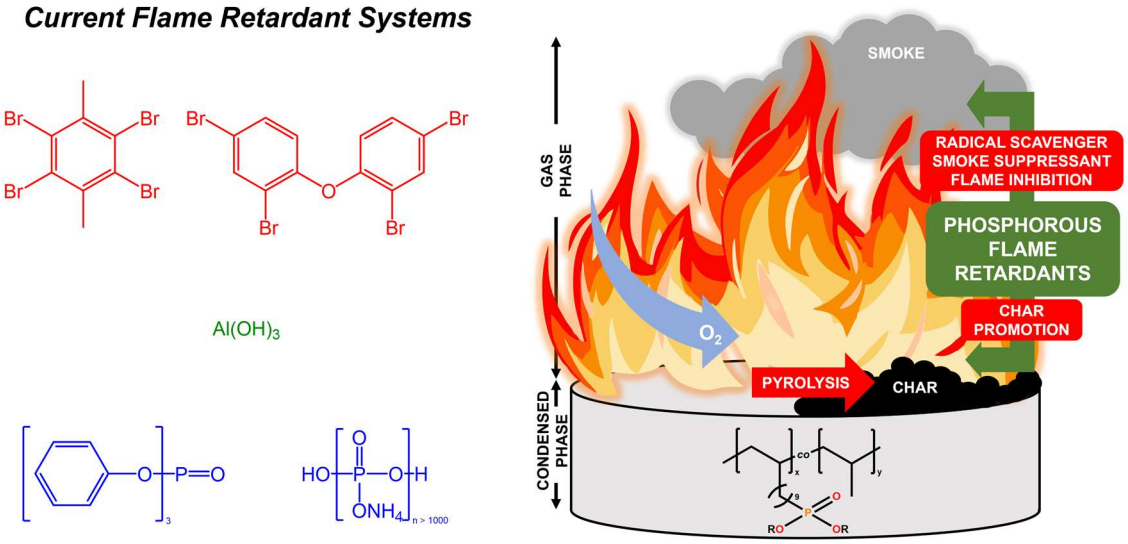

Figure 1.10 Examples of current flame retardant additives including the mechanism of action regarding phosphorus bound flame retardant materials.

1.6.2. Hot melt adhesive polypropylenes

Adhesives are vital in everyday life, with widespread applications in construction, automotive, and consumer packaging, using over 3×10^9 kg annually yet evidencing volume growth for high-performance adhesives.[238-242] Consequential to a shift industrially towards environmentally friendly, solvent- and low volatile organic compound (VOC) free adhesives,[243-247] hot melt adhesives (HMAs) are gaining prominence as they satisfy market needs for both ecological responsibility and strong

product performance.[248-252] Current adhesive strengths of commercially available ethylene−vinyl acetate or polyurethane-based HMAs are limited to 6-7 MPa.[253] Meeting demands for lightweight, high-performance products necessitates superior adhesion to diverse materials.

Numerous adhesive solutions utilise polar polymers, however bonding PO to polar substrates is challenging due to their low surface free energy, chemical inertness, and absence of functional groups.[254-256] Enhancing substrate adhesion often involves chemically or physically treating PO surfaces for increased polarity and improved wettability by means similar to the aforementioned C-H bond activation; accompanied by associated limitations.[257-260] Ongoing research focuses on advanced functional polymers, like functionalised PPs, to improve adhesion to both (non)polar substrates.[248,251] Recently reported work by Duchateau *et al*. highlighted the application of propylene-based hydroxyl-functionalised terpolymers for use as hot melt adhesives with significant adhesive performance (12.6 MPa) at low application temperatures (130 °C) despite minimal incorporation levels (≤ 0.5 mol%).[253]

1.6.3. Vulcanised polypropylenes

Cross-linking of unsaturated polymers is an established method for altering material properties; from self-assembly,[261] to industrial styrene-butadiene rubbers (SBR) with improved mechanical properties.[262] Natural Rubber and, later, SBR latexes have been routinely vulcanised in the presence of sulfur or organic peroxide crosslinking agents,[263] including propylene and ethylene based polymers (Scheme 1.14).[182,264] For ethylene-propylene-diene terpolymers, modifiers such as silica and carbon black have further been incorporated in an effort to optimise vulcanisation kinetics and mechanical and physical properties of the resultant rubber.[265,266]

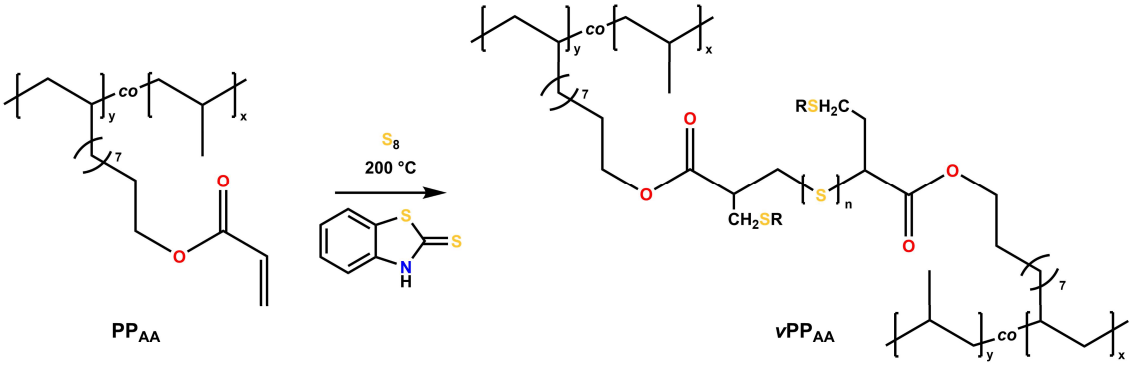

Scheme 1.14 Sulfur vulcanisation to form ***v*PP$_{AA}$**, the structure of which is adapted from the mechanism provided by Verbruggen *et al.*.[182,267]

1.6.4. Recycling polypropylenes

During the mechanical recycling processes, separation techniques have been extended to include fluorescent labelling enabling separation by specific polymeric material;[268-270] recent literature utilise fluorescently tagged PP to this avail.[271] Notably, the recycling process typically involve high temperatures and consequently careful selection of incorporated spectroscopic markers is required to avoid degradation.[271] To the best of our knowledge recent literature presents a few examples of synthesised ^{i}PP copolymers containing fluorescent units and only work by Pragliola *et al.* has evaluated them as a fluorescent marker of ^{i}PP thus far (Scheme 1.15).[272,273]

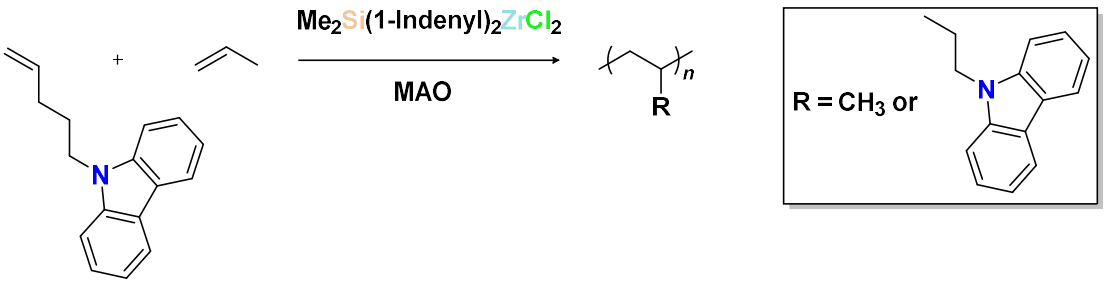

Scheme 1.15 Fluorescently labelled poly(propylene-*co*-*N*-pentenyl-carbazole) as reported by Pragliola *et al.*.[272]

1.6.5. Compatibilisation of polymer blends

Polymer blends are often immiscible, only forming thermodynamically stable mixtures in specific temperature, pressure and concentration ranges;[274] wherein a blend is defined to be comprised of two or more species, the content of each exceeding 2 wt%.[275] Mixtures of incompatible polymers display coarse morphologies, with unevenly distributed domains of each polymer usually leading to poor mechanical properties.[276,277] This is particularly prudent when considering mechanical recycling of polymer waste.[227] Blends of immiscible constituent polymers, even if only containing polymeric impurities through incorrect sorting and incorporation, yields significantly inferior properties when compared to virgin materials.[278] The entropy of mixing, often a driving force for homogenisation of small molecule mixtures, is a small factor for blends of polymers due to their high M_n.[274] Introduction of a compatibiliser, a multiphasic polymer able to act akin to a surfactant, reduces interfacial tension between different polymer domains and subsequently a reduction in heterogeneous domains whilst promoting bulk homogeneity (Figure 1.7). This imparts the blend with properties more competitive with those of virgin materials.[195,279] Block and graft copolymers have proven to be effective compatibilisers for polymer blends of their constituent polymers; with noticeable differences observed at low wt% compatibiliser incorporation.[280-282] Recent work by Chan-Seng *et al*. instead probed the compatibilisation of PE and poly(ethylene-co-vinyl alcohol) (EVOH) through radical grafting of an interfacial agent, a (2,2,6,6-tetramethylpiperidin-1-yl)oxyl-epoxy (TEMPO-epoxy), *via* the TEMPO group to PE; subsequent alcohol-induced epoxide ring-opening coupling PP to the EVOH.[283]

1.7. Scope of thesis

Polyolefin post-modification *via* simple and general nucleophilic substitution chemistry would open the door to a broader range of functional materials but requires easy access to a suitable platform polymer with electrophilic functionality. This Thesis presents a simple and generally applicable methodology for the preparation of a diverse range of FPs. Poly(propylene)-co-(11-bromo-1-undecene) (**PP$_{Br}$**) was employed as a tuneable platform copolymer which can be readily post-functionalised by utilising the latent reactivity of the brominated side-chains. This allowed for the development of a wide-ranging series of covalent connections (C–O, C–N, C–S, C–P, and C–C) *via* different substitution pathways, yielding versatile FPs with properties suitable for an array of applications (Scheme 1.9 and Scheme 1.16).

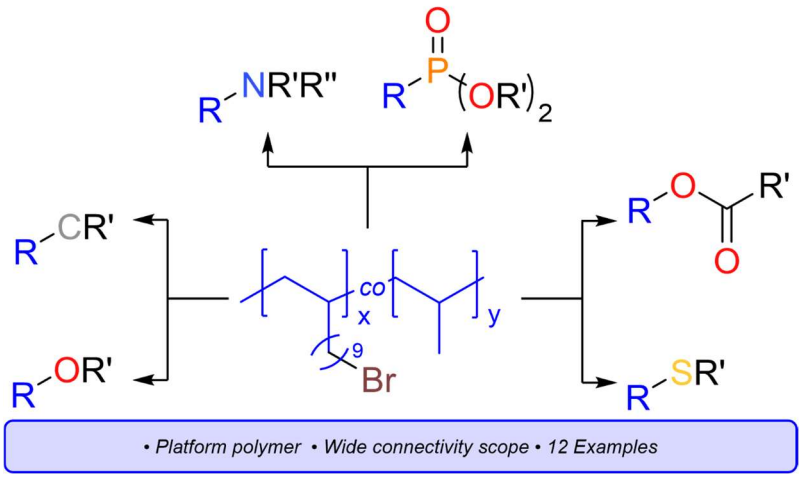

Scheme 1.16 General synthetic overview for the post-polymerisation modification of poly(propylene)-co-(11-bromo-1-undecene), **PP$_{Br}$**, *via* (**a**) forcing and (**b**) base mediated conditions, and (**c**) salt metathesis, yielding a range of covalent connections.

Chapter Two describes the optimisation of the polymerisation of propylene and 11-bromo-1-undecene by a range of metallocenes. It further explores the avenues highlighted in Scheme 1.16 for the post-polymerisation functionalisation of **PP$_{Br}$** and the subsequent material characterisation. **Chapter Three** assesses the feasibility of phosphonate modified **PP$_{Br}$** for flame retardant applications. **Chapter Four** presents the

utility of alcohol functional $\mathbf{PP_{Br}}$ as multi-substrate hot melt adhesives. **Chapter Five** showcases the development of dye functional $\mathbf{PP_{Br}}$ as a fluorescent probe for *in vitro* microplastic investigations. **Chapter Six** is a tangential project focusing on the synthesis and characterisation of a manganese sandwich complex.

1.8. References

1 G. Natta, P. Pino, P. Corradini, F. Danusso, E. Mantica, G. Mazzanti, G. Moraglio, *J. Am. Chem. Soc.*, 1955, **77**, 1708-1710.
2 K. Ziegler, E. Holzkamp, H. Breil, H. Martin, *Angew. Chem.*, 1955, **67**, 426.
3 I. A. Makaryan and I. V. Sedov, *Russ. J. Gen. Chem.*, 2020, **90**, 1141-1162.
4 A. H. Westlie, E. Y.-X. Chen, C. M. Holland, S. S. Stahl, M. Doyle, S. R. Trenor, K. M. Knauer, *Macromol. Rapid Commun.*, 2022, **43**, 2200492.
5 M. Kutz, *Applied Plastics Engineering Handbook*, Elsevier Inc., 2011.
6 M. H. Rahman and P. R. Bhoi, *J. Clean. Prod.*, 2021, **294**, 126218.
7 T. K. Phung, T. L. M. Pham, K. B. Vu, G. Busca, *J. Environ. Chem. Eng.*, 2021, **9**, 105673.
8 D. S. Achilias, C. Roupakias, P. Megalokonomos, A. A. Lappas, E. V. Antonakou, *J. Hazard. Mater.*, 2007, **149**, 536-542.
9 A. Somoza-Tornos, A. Gonzalez-Garay, C. Pozo, M. Graells, A. Espuña, G. Guillén-Gosálbez, *ACS Sustain. Chem. Eng.*, 2020, **8**, 3561-3572.
10 A. Reznichenko and A. Harlin, *SN Appl. Sci.*, 2022, **4**, 108.
11 M. Bergmann, B. C. Almroth, S. M. Brander, T. Dey, D. S. Green, S. Gundogdu, A. Krieger, M. Wagner, T. R. Walker, *Science*, 2022, **376**, 469-470.
12 H. A. Maddah, *Am. J. Polym. Sci.*, 2016, **6**, 1-11.
13 G. Natta, *Angew. Chem., Int. Ed.*, 1956, **68**, 393–403.
14 L. Resconi, L. Cavallo, A. Fait, F. Piemontesi, *Chem. Rev.*, 2000, **100**, 1253-1346.
15 G. Natta, *J. Polym. Sci.*, 1959, **34**, 531-549.
16 V. Busico, R. Cipullo, G. Monaco, M. Vacatello, A. L. Segre, *Macromolecules*, 1997, **30**, 6251-6263.
17 P. Corradini, V. Barone, R. Fusco, G. Guerra, *Eur. Polym. J.*, 1979, **15**, 1133-1141.
18 N. Bahri-Laleh, A. Hanifpour, S. A. Mirmohammadi, A. Poater, M. Nekoomanesh-Haghighi, G. Talarico, L. Cavallo, *Prog. Polym. Sci.*, 2018, **84**, 89-114.
19 Z. Zhang, R. Zhang, Y. Huang, J. Lei, Y.-H. Chen, J.-h. Tang, Z.-M. Li, *Ind. Eng. Chem. Res.*, 2014, **53**, 10144-10154.
20 A. Shamiri, M. H. Chakrabarti, S. Jahan, M. A. Hussain, W. Kaminsky, P. V. Aravind, W. A. Yehye, *Materials*, 2014, **7**, 5069-5108.
21 R. A. Collins, A. F. Russell, P. Mountford, *Appl. Petrochem. Res.*, 2015, **5**, 153-171.
22 G. W. Coates, *Chem. Rev.*, 2000, **100**, 1223-1252.
23 M. Huang, J. Chen, B. Wang, W. Huang, H. Chen, Y. Gao, T. J. Marks, *Angew. Chem. Int. Ed.*, 2020, **59**, 20522-20528.
24 L. Castro, E. Kirillov, O. Miserque, A. Welle, L. Haspeslagh, J.-F. Carpentier, L. Maron, *ACS Catalysis*, 2015, **5**, 416-425.
25 C. De Rosa, R. Di Girolamo, A. B. Muñoz-García, M. Pavone, G. Talarico, *Macromolecules*, 2020, **53**, 2959-2964.
26 C. G. Collins Rice, J. C. Buffet, Z. R. Turner, D. O'Hare, *Chem. Commun.*, 2021, **57**, 8600-8603.
27 J. A. Ewen, *J. Am. Chem. Soc.*, 1984, **106**, 6355-6364.
28 W. Spaleck, M. Antberg, J. Rohrmann, A. Winter, B. Bachmann, P. Kiprof, J. Behm, W. A. Herrmann, *Angew. Chem. Int. Ed.*, 1992, **31**, 1347-1350.
29 V. Busico, R. Cipullo, L. Caporaso, G. Angelini, A. L. Segre, *J. Mol. Catal. A: Chem.*, 1998, **128**, 53-64.
30 F. R. W. P. Wild, L. Zsolnai, G. Huttner, H. H. Brintzinger, *J. Organomet. Chem.*, 1982, **232**, 233-247.
31 L. Oliva, L. Caporaso, C. Pellecchia, A. Zambelli, *Macromolecules*, 1995, **28**, 4665-4667.
32 P. J. Shapiro, E. Bunel, W. P. Schaefer, J. E. Bercaw, *Organometallics*, 1990, **9**, 867-869.
33 J. Okuda, *Chem. Ber.*, 1990, **123**, 1649-1651.
34 H. G. B. S. Mori, *Size Exclusion Chromatography*, Springer, 1999.

35 D. J. Walton and J. P. Lorimer, *Polymers*, Oxford University Press, 2000.
36 D. T. Gentekos, R. J. Sifri, B. P. Fors, *Nat. Rev. Mater.*, 2019, **4**, 761-774.
37 C. Zou, S. Dai, C. Chen, *Macromolecules*, 2018, **51**, 49-56.
38 T. Kida, R. Tanaka, Y. Hiejima, K.-h. Nitta, T. Shiono, *Polymer*, 2021, **218**, 123526.
39 Y. Zhao, L. Wang, H. Yu, G. Jing, C. Li, Y. Chen, M. Saleem, *J. Polym. Res.*, 2014, **21**, 470.
40 M. Stürzel, T. Hees, M. Enders, Y. Thomann, H. Blattmann, R. Mülhaupt, *Macromolecules*, 2016, **49**, 8048-8060.
41 M. Stürzel, S. Mihan, R. Mülhaupt, *Chem. Rev.*, 2016, **116**, 1398-1433.
42 C. Long, Z. Dong, X. Liu, F. Yu, Y. Shang, K. Wang, S. Feng, X. Hou, C. He, Z.-R. Chen, *Polymer*, 2022, **258**, 125287.
43 P. Kenyon, D. W. J. Leung, Z. R. Turner, J.-C. Buffet, D. O'Hare, *Macromolecules*, 2022, **55**, 3408-3414.
44 P. S. Chum and K. W. Swogger, *Prog. Polym. Sci.*, 2008, **33**, 797-819.
45 P. Cossee, *J. Catal.*, 1964, **3**, 80-88.
46 E. Arlman, *J. Catal.*, 1964, **3**, 99-104.
47 L. Cavallo, G. Guerra, P. Corradini, *J. Am. Chem. Soc.*, 1998, **120**, 2428-2436.
48 K. Soga and T. Shiono, *Prog. Polym. Sci.*, 1997, **22**, 1503-1546.
49 K. H. Theopold, *Proc. Natl. Acad. Sci. U.S.A.*, 2014, **111**, 11578-11579.
50 G. G. Hlatky, *Chem. Rev.*, 2000, **100**, 1347-1376.
51 W. Kaminsky, *J. Chem. Soc., Dalton Trans.*, 1998, 1413-1418.
52 C. Copéret, A. Comas-Vives, M. P. Conley, D. P. Estes, A. Fedorov, V. Mougel, H. Nagae, F. Núñez-Zarur, P. A. Zhizhko, *Chem. Rev.*, 2016, **116**, 323-421.
53 W. Kaminsky, A. Funck, H. Hahnsen, *Dalton Trans.*, 2009, 8803-8810.
54 H. Sinn, *Macromol. Symp.*, 1995, **97**, 27-52.
55 W. P. Long and D. S. Breslow, *Justus Liebigs Ann. Chem.*, 1975, **1975**, 463-469.
56 K. H. Reichert and K. R. Meyer, *Makromol. Chem.*, 1973, **169**, 163-176.
57 W. Kaminsky, *Macromol. Chem. Phys.*, 1996, **197**, 3907-3945.
58 E. Y. Chen and T. J. Marks, *Chem. Rev.*, 2000, **100**, 1391-1434.
59 A. Andresen, H.-G. Cordes, J. Herwig, W. Kaminsky, A. Merck, R. Mottweiler, J. Pein, H. Sinn, H.-J. Vollmer, *Angew. Chem. Int. Ed.*, 1976, **15**, 630-632.
60 J. Chatt and L. A. Duncanson, *J. Chem. Soc.*, 1953, 2939-2947.
61 K. J. Ivin, J. J. Rooney, C. D. Stewart, M. L. H. Green, R. Mahtab, *J. Chem. Soc., Chem. Commun.*, 1978, 604-606.
62 L. Clawson, J. Soto, S. L. Buchwald, M. L. Steigerwald, R. H. Grubbs, *J. Am. Chem. Soc.*, 1985, **107**, 3377-3378.
63 M. Brookhart, A. F. Volpe, Jr., D. M. Lincoln, I. T. Horvath, J. M. Millar, *J. Am. Chem. Soc.*, 1990, **112**, 5634-5636.
64 M. Brookhart, M. L. H. Green, L. L. Wong, *Prog. Inorg. Chem.*, 1988, **36**, 1-124.
65 W. Guo, J. Yin, Z. Xu, W. Li, Z. Peng, C. J. Weststrate, X. Yu, Y. He, Z. Cao, X. Wen, Y. Yang, K. Wu, Y. Li, J. W. Niemantsverdriet, X. Zhou, *Science*, 2022, **375**, 1188-1191.
66 V. Busico, D. Brita, L. Caporaso, R. Cipullo, M. Vacatello, *Macromolecules*, 1997, **30**, 3971-3977.
67 J. A. Ewen, *J. Mol. Catal. A: Chem.*, 1998, **128**, 103-109.
68 R. H. Grubbs and G. W. Coates, *Acc. Chem. Res.*, 1996, **29**, 85-93.
69 L. Resconi, L. Abis, G. Franciscono, *Macromolecules*, 1992, **25**, 6814-6817.
70 H. H. Brintzinger, D. Fischer, R. Mülhaupt, B. Rieger, R. M. Waymouth, *Angew. Chem. Int. Ed.*, 1995, **34**, 1143-1170.
71 V. C. Gibson and S. K. Spitzmesser, *Chem. Rev.*, 2003, **103**, 283-316.
72 K. J. Chu, J. B. Soares, A. Penlidis, *J. Polym. Sci., Part A: Polym. Chem.*, 2000, **38**, 1803-1810.
73 P. Roos, G. B. Meier, J. J. C. Samson, G. Weickert, K. R. Westerterp, *Macromol. Rapid Commun.*, 1997, **18**, 319-324.
74 G. J. P. Britovsek, V. C. Gibson, D. F. Wass, *Angew. Chem. Int. Ed.*, 1999, **38**, 428-447.
75 M. Baker, *Nature*, 2016, **533**.
76 D. Fanelli, *Proc. Natl. Acad. Sci. U.S.A.*, 2018, **115**, 2628-2631.
77 G. Natta, P. Pino, G. Mazzanti, U. Giannini, *J. Am. Chem. Soc.*, 1957, **79**, 2975-2976.
78 D. S. Breslow and N. R. Newburg, *J. Am. Chem. Soc.*, 1957, **79**, 5072-5073.
79 L. Luo, J. M. Younker, A. V. Zabula, *Science*, 2024, **384**, 1424-1428.
80 I. Tritto, S. X. Li, M. C. Sacchi, P. Locatelli, G. Zannoni, *Macromolecules*, 1995, **28**, 5358-5362.
81 I. Tritto, R. Donetti, M. C. Sacchi, P. Locatelli, G. Zannoni, *Macromolecules*, 1997, **30**, 1247-1252.
82 I. Tritto, R. Donetti, M. C. Sacchi, P. Locatelli, G. Zannoni, *Macromolecules*, 1999, **32**, 264-269.

83 H. S. Zijlstra and S. Harder, *Eur. J. Inorg. Chem.*, 2015, **2015**, 19-43.
84 D. E. Babushkin, N. V. Semikolenova, V. A. Zakharov, E. P. Talsi, *Macromol. Chem. Phys.*, 2000, **201**, 558-567.
85 J.-N. Pédeutour, H. Cramail, A. Deffieux, *J. Mol. Catal. A: Chem.*, 2001, **174**, 81-87.
86 J.-N. Pédeutour, H. Cramail, A. Deffieux, *J. Mol. Catal. A: Chem.*, 2001, **176**, 87-94.
87 W. Kaminsky, *Macromol. Symp.*, 1995, **97**, 79-89.
88 Y. Huang, Q. Yu, S. Zhu, G. Rempel, L. Li, *J. Polym. Sci., Part A: Polym. Chem.*, 1999, **37**, 1465-1472.
89 E. Zurek and T. Ziegler, *Prog. Polym. Sci.*, 2004, **29**, 107-148.
90 S. Pasynkiewicz, *Polyhedron*, 1990, **9**, 429-453.
91 V. E. Teixeira and P. R. Livotto, *J. Mol. Graph. Model.*, 2020, **99**, 107626.
92 L. Negureanu, R. W. Hall, L. G. Butler, L. A. Simeral, *J. Am. Chem. Soc.*, 2006, **128**, 16816-16826.
93 M. Linnolahti, J. R. Severn, T. A. Pakkanen, *Angew. Chem. Int. Ed.*, 2008, **47**, 9279-9283.
94 M. Linnolahti, J. R. Severn, T. A. Pakkanen, *Angew. Chem. Int. Ed.*, 2006, **45**, 3331-3334.
95 Z. Falls, N. Tymińska, E. Zurek, *Macromolecules*, 2014, **47**, 8556-8569.
96 A. Joshi, S. Collins, M. Linnolahti, H. S. Zijlstra, E. Liles, J. S. McIndoe, *Chemistry*, 2021, **27**, 8753-8763.
97 S. Collins, G. Hasan, A. Joshi, J. S. McIndoe, M. Linnolahti, *ChemPhysChem*, 2021, **22**, 1326-1335.
98 S. Collins and M. Linnolahti, *ChemPhysChem*, 2023, **24**, e202300342.
99 H. Sinn, I. Schimmel, M. Ott, N. von Thienen, A. Harder, W. Hagendorf, B. Heitmann, E. Haupt, Metalorganic Catalysts for Synthesis and Polymerisation, Verlag, 1999.
100 D. W. Imhoff, L. S. Simeral, S. A. Sangokoya, J. H. Peel, *Organometallics*, 1998, **17**, 1941-1945.
101 A. Joshi, H. S. Zijlstra, E. Liles, C. Concepcion, M. Linnolahti, J. S. McIndoe, *Chem. Sci.*, 2021, **12**, 546-551.
102 F. Zaccaria, C. Zuccaccia, R. Cipullo, P. H. Budzelaar, A. Vittoria, A. Macchioni, V. Busico, C. Ehm, *ACS Catalysis*, 2021, **11**, 4464-4475.
103 L. Jia, X. M. Yang, A. Ishihara, T. J. Marks, *Organometallics*, 1995, **14**, 3135-3137.
104 S. Mehdiabadi, J. B. P. Soares, D. Bilbao, J. L. Brinen, *Macromol. React. Eng.*, 2011, **5**, 418-430.
105 M. Bochmann, *Organometallics*, 2010, **29**, 4711-4740.
106 J. N. Pédeutour, K. Radhakrishnan, H. Cramail, A. Deffieux, *Macromol. Rapid Commun.*, 2001, **22**, 1095-1123.
107 A. R. Siedle, W. M. Lamanna, R. A. Newmark, J. Stevens, D. E. Richardson, M. Ryan, *Makromol. Chem., Macromol. Symp.*, 1993, **66**, 215-224.
108 A. Yano, S. Hasegawa, S. Yamada, A. Akimoto, *J. Mol. Catal. A: Chem.*, 1999, **148**, 77-86.
109 V. C. Williams, G. J. Irvine, W. E. Piers, Z. Li, S. Collins, W. Clegg, M. R. J. Elsegood, T. B. Marder, *Organometallics*, 2000, **19**, 1619-1621.
110 J. Zhou, S. J. Lancaster, D. A. Walker, S. Beck, M. Thornton-Pett, M. Bochmann, *J. Am. Chem. Soc.*, 2001, **123**, 223-237.
111 N. Senso, S. Khaubunsongserm, B. Jongsomjit, P. Praserthdam, *Molecules*, 2010, **15**, 9323-9339.
112 D. G. Boucher, I. W. Parsons, R. N. Haward, *Makromol. Chem., Macromol. Chem. Phys.*, 1974, **175**, 3461-3473.
113 M. A. Bashir, V. Monteil, C. Boisson, T. F. L. McKenna, *J. Appl. Polym. Sci.*, 2018, **135**, 45670.
114 A. Muñoz-Escalona, H. García, A. Albornoz, *J. Appl. Polym. Sci.*, 1987, **34**, 977-988.
115 D. T. Lynch, M. O. Jejelowo, S. E. Wanke, *Can. J. Chem. Eng.*, 1991, **69**, 657-664.
116 R. Kleinschmidt, Y. Van der Leek, M. Reffke, G. Fink, *J. Mol. Catal. A: Chem.*, 1999, **148**, 29-41.
117 H. Hammawa, T. Mannan, D. Lynch, S. Wanke, *J. Appl. Polym. Sci.*, 2004, **92**, 3549-3560.
118 V. Busico, P. Corradini, A. Ferraro, A. Proto, *Makromol. Chem., Macromol. Chem. Phys.*, 1986, **187**, 1125-1130.
119 F. Bonini, V. Fraaije, G. Fink, *J. Polym. Sci., Part A: Polym. Chem.*, 1995, **33**, 2393-2402.
120 V. Panchenko, L. Echevkaya, V. Zakharov, M. Matsko, *Appl. Catal., A*, 2011, **404**, 47-53.
121 J. P. Turunen and T. T. Pakkanen, *J. Appl. Polym. Sci.*, 2006, **100**, 4632-4635.
122 I. Novák, E. Borsig, L. u. Hrčková, A. Fiedlerová, A. Kleinová, V. Pollák, *Polym. Eng. Sci.*, 2007, **47**, 1207-1212.
123 M. Yılmaz, A. Akar, N. Köken, N. Kızılcan, *J. Appl. Polym. Sci.*, 2020, **137**, 49023.
124 A. u. R. Shah, D.-w. Lee, Y.-q. Wang, A. Wasy, K. C. Ham, K. Jayaraman, B.-S. Kim, J.-I. Song, *T. Nonferr. Metal. Soc.*, 2014, **24**, s81-s89.
125 C. M. Plummer, L. Li, Y. Chen, *Polym. Chem.*, 2020, **11**, 6862-6872.
126 N. K. Boaen and M. A. Hillmyer, *Chem. Soc. Rev.*, 2005, **34**, 267-275.
127 S. Bruzaud, H. Cramail, L. Duvignac, A. Deffieux, *Macromol. Chem. Phys.*, 1997, **198**, 291-303.

128 M. D. Purgett and O. Vogl, *J. Polym. Sci., Part A: Polym. Chem.*, 1988, **26**, 677-700.
129 R. Tanaka, H. Fujii, T. Kida, Y. Nakayama, T. Shiono, *Macromolecules*, 2021, **54**, 1267-1272.
130 X. Wang, Y. Wang, X. Shi, J. Liu, C. Chen, Y. Li, *Macromolecules*, 2014, **47**, 552-559.
131 N. Blake, Z. R. Turner, J.-C. Buffet, D. O'Hare, *Polym. Chem.*, 2023, **14**, 3175-3185.
132 R. Bacskai, *J. Polym. Sci., Part A: Gen. Pap.*, 1965, **3**, 2491-2510.
133 C. J. Kay, P. D. Goring, C. A. Burnett, B. Hornby, K. Lewtas, S. Morris, C. Morton, T. McNally, G. W. Theaker, C. Waterson, P. M. Wright, P. Scott, *J. Am. Chem. Soc.*, 2018, **140**, 13921-13934.
134 T. C. M. Chung, *Macromol. React. Eng.*, 2014, **8**, 69-80.
135 A. Keyes, H. E. Basbug Alhan, E. Ordonez, U. Ha, D. B. Beezer, H. Dau, Y.-S. Liu, E. Tsogtgerel, G. R. Jones, E. Harth, *Angew. Chem. Int. Ed.*, 2019, **58**, 12370-12391.
136 T. C. Chung, *Prog. Polym. Sci.*, 2002, **27**, 39-85.
137 H. Wang, H. Niu, J.-Y. Dong, *Polymer*, 2017, **126**, 109-115.
138 N. Kawahara, J. Saito, S. Matsuo, H. Kaneko, T. Matsugi, S.-i. Kojoh, N. Kashiwa, *Polym. Bull.*, 2007, **59**, 177-183.
139 J. Chen, Y. Gao, T. J. Marks, *Angew. Chem. Int. Ed.*, 2020, **59**, 14726-14735.
140 Z. Chen and M. Brookhart, *Acc. Chem. Res.*, 2018, **51**, 1831-1839.
141 T. C. Chung and D. Rhubright, *Macromolecules*, 1993, **26**, 3019-3025.
142 H. L. Lu, S. Hong, T. C. Chung, *J. Polym. Sci., Part A: Polym. Chem.*, 1999, **37**, 2795-2802.
143 W. Lin, Z. Shao, J.-y. Dong, T. C. M. Chung, *Macromolecules*, 2009, **42**, 3750-3754.
144 Y. Wang, Q. Wang, C. Tan, C. Chen, *J. Am. Chem. Soc.*, 2024, **146**, 6837-6845.
145 C. Tan, C. Zou, C. Chen, *J. Am. Chem. Soc.*, 2022, **144**, 2245-2254.
146 M. Atiqullah, M. Tinkl, R. Pfaendner, M. N. Akhtar, I. Hussain, *Polym. Rev.*, 2010, **50**, 178-230.
147 X.-Y. Wang, Y.-Y. Long, Y.-X. Wang, Y.-S. Li, *J. Polym. Sci., Part A: Polym. Chem.*, 2014, **52**, 3421-3428.
148 J. Chen, A. Motta, B. Wang, Y. Gao, T. J. Marks, *Angew. Chem. Int. Ed.*, 2019, **58**, 7030-7034.
149 L. S. Boffa and B. M. Novak, *Chem. Rev.*, 2000, **100**, 1479-1494.
150 H. Hagihara, K. Tsuchihara, J. Sugiyama, K. Takeuchi, T. Shiono, *Macromolecules*, 2004, **37**, 5145-5148.
151 J.-i. Imuta, N. Kashiwa, Y. Toda, *J. Am. Chem. Soc.*, 2002, **124**, 1176-1177.
152 H. Terao, S. Ishii, M. Mitani, H. Tanaka, T. Fujita, *J. Am. Chem. Soc.*, 2008, **130**, 17636-17637.
153 X.-Y. Wang, Y.-X. Wang, Y.-S. Li, L. Pan, *Macromolecules*, 2015, **48**, 1991-1998.
154 D. Zhang, L. Pan, Y. Li, B. Wang, Y. Li, *Macromolecules*, 2017, **50**, 2276-2283.
155 B. P. Carrow and K. Nozaki, *Macromolecules*, 2014, **47**, 2541-2555.
156 S. L. J. Luckham and K. Nozaki, *Acc. Chem. Res.*, 2021, **54**, 344-355.
157 R. Nakano and K. Nozaki, *J. Am. Chem. Soc.*, 2015, **137**, 10934-10937.
158 Y. Ota, S. Ito, M. Kobayashi, S. Kitade, K. Sakata, T. Tayano, K. Nozaki, *Angew. Chem. Int. Ed.*, 2016, **55**, 7505-7509.
159 J. Gao, W. Cai, Y. Hu, C. Chen, *Polym. Chem.*, 2019, **10**, 1416-1422.
160 L. Guo, W. Liu, C. Chen, *Mater. Chem. Front.*, 2017, **1**, 2487-2494.
161 Editorial, *Nat. Catal.*, 2019, **2**, 735.
162 E. Denkhaus and K. Salnikow, *Crit. Rev. Oncol. Hematol.*, 2002, **42**, 35-56.
163 J. Y. Ko, R. M. Appa, S. Oh, N. Son, S. C. Hong, *Polym. Test.*, 2024, **136**, 108488.
164 I. Maksso, R. C. Samanta, Y. Zhan, K. Zhang, S. Warratz, L. Ackermann, *Chem. Sci.*, 2023, **14**, 8109-8118.
165 N. M. G. Franssen, J. N. H. Reek, B. de Bruin, *Chem. Soc. Rev.*, 2013, **42**, 5809-5832.
166 N. R. Ciccia, J. X. Shi, S. Pal, M. Hua, K. G. Malollari, C. Lizandara-Pueyo, E. Risto, M. Ernst, B. A. Helms, P. B. Messersmith, J. F. Hartwig, *Science*, 2023, **381**, 1433-1440.
167 M. Baier, D. Wöll, S. Mecking, *Macromolecules*, 2018, **51**, 1873-1884.
168 R. von Goetze, A. Aljaber, K.-Y. Lee, G. Hill, C. Wallis, G. J. P. Britovsek, *Polym. Chem.*, 2022, **13**, 6377-6385.
169 S. S. Scott, S.-C. Roşca, D. J. Gilmour, P. Brant, L. L. Schafer, *ACS. Macro. Lett.*, 2021, **10**, 1266-1272.
170 M. Abbasi, L. Faust, M. Wilhelm, *Adv. Mater.*, 2019, **31**, 1806484.
171 J. Roovers, *Polymer*, 1979, **20**, 843-849.
172 I. Sutherland, D. M. Brewis, R. J. Health, E. Sheng, *Surf. Interface Anal.*, 1991, **17**, 507-510.
173 D. M. Brewis and D. Briggs, *Polymer*, 1981, **22**, 7-16.
174 X.-Y. Wang, Y.-G. Li, H.-L. Mu, L. Pan, Y.-S. Li, *Polym. Chem.*, 2015, **6**, 1150-1158.
175 M. Hong, S.-R. Liu, B.-X. Li, Y.-S. Li, *J. Polym. Sci., Part A: Polym. Chem.*, 2012, **50**, 2499-2506.
176 M. Hong, J.-Y. Liu, B.-X. Li, Y.-S. Li, *Macromolecules*, 2011, **44**, 5659-5665.

177 Y.-L. Li, D.-P. Song, L. Pan, Z. Ma, Y.-S. Li, *Polym. Chem.*, 2019, **10**, 6368-6378.
178 G. Acik, E. Sey, M. Tasdelen, *Express Polym. Lett.*, 2018, **12**, 418-428.
179 H. Huang, H. Niu, J.-Y. Dong, *Macromolecules*, 2010, **43**, 8331-8335.
180 T. Toda, I. Miura, M. Miya, K. Takenaka, *Catalysts*, 2019, **9**, 660.
181 M. Zhu, Y. Su, Y. Wu, M. Zhang, Y. Wang, Q. Chen, N. Li, *J. Membr. Sci.*, 2017, **541**, 244-252.
182 A. Evans, O. Casale, L. J. Morris, Z. R. Turner, D. O'Hare, *Macromolecules*, 2024, **57**, 10778-10791.
183 Y. Doi, Y. Watanabe, S. Ueki, K. Soga, *Makromol. Chem., Rapid Commun.*, 1983, **4**, 533-537.
184 R. Godoy Lopez, C. Boisson, F. D'Agosto, R. Spitz, F. Boisson, D. Gigmes, D. Bertin, *J. Polym. Sci., Part A: Polym. Chem.*, 2007, **45**, 2705-2718.
185 K. Matyjaszewski, J. Saget, J. Pyun, M. Schlögl, B. Rieger, *J. Macromol. Sci. A*, 2002, **39**, 901-913.
186 Y. Inoue and K. Matyjaszewski, *J. Polym. Sci., Part A: Polym. Chem.*, 2004, **42**, 496-504.
187 N. Kawahara, S.-i. Kojoh, S. Matsuo, H. Kaneko, T. Matsugi, J. Saito, N. Kashiwa, *Polym. Bull.*, 2006, **57**, 805-812.
188 P. D. Goring, C. Morton, P. Scott, *Dalton Trans.*, 2019, **48**, 3521-3530.
189 T. C. Chung and J. Y. Dong, *J. Am. Chem. Soc.*, 2001, **123**, 4871-4876.
190 J. Yoshikawa, J. A. Lewis, B.-W. Chun, *J. Am. Ceram. Soc.*, 2009, **92**, S42-S49.
191 X. Yang, J. Song, H. Wang, Q. Lin, X. Jin, X. Yang, Y. Li, *Polymers*, 2020, **12**, 526.
192 M. He, J. Wang, Z. Wang, J. Mo, J. Zhang, X.-z. Fan, W. Dong, Y. Li, *Mater. Chem. Phys.*, 2021, **262**, 124219.
193 J. Wang, A. H. Tsou, H. L. Passino, B. D. Favis, *Polymer*, 2018, **138**, 92-102.
194 X. Zuo, Y. Xue, L. Wang, Y. Zhou, Y. Yin, Y.-C. Chuang, C.-C. Chang, R. Yin, M. H. Rafailovich, Y. Guo, *Macromolecules*, 2019, **52**, 7547-7556.
195 J. L. Self, A. J. Zervoudakis, X. Peng, W. R. Lenart, C. W. Macosko, C. J. Ellison, *JACS Au*, 2022, **2**, 310-321.
196 E. M. W. Tsang and S. Holdcroft, *10.35 - Alternative Proton Exchange Membranes by Chain-Growth Polymerisation*, Elsevier, Amsterdam, 2012.
197 R. B. Grubbs and R. H. Grubbs, *Macromolecules*, 2017, **50**, 6979-6997.
198 P. J. Flory, *Principles Of Polymer Chemistry*, Cornell University Press, New York, 1953.
199 M. Szwarc, *J. Polym. Sci., Part A: Polym. Chem.*, 1998, **36**, IX-XV.
200 M. Pitsikalis, *Ionic Polymerisation*, Elsevier, Athens, 2013.
201 H. Feng, X. Lu, W. Wang, N. G. Kang, J. W. Mays, *Polymers (Basel)*, 2017, **9**.
202 M. Szwarc, *Nature*, 1956, **178**, 1168-1169.
203 S. Penczek and J. B. Pretula, *Polymer Science: A Comprehensive Reference*, Elsevier, Amsterdam, 2012.
204 K. Hong, D. Uhrig, J. W. Mays, *Anionic Polymerisation*, Elsevier, Oxford, 2001.
205 P. Purohit, A. Bhatt, R. K. Mittal, M. H. Abdellattif, T. A. Farghaly, *Front. Bioeng. Biotechnol.*, 2022, **10**, 1044927.
206 J. Jagur-Grodzinski, *J. Polym. Sci., Part A: Polym. Chem.*, 2002, **40**, 2116-2133.
207 M. R. Jozaghkar, F. Ziaee, S. Jalilian, *Iran. Polym. J.*, 2022, **31**, 399-412.
208 R. Vijayaraghavan, J. M. Pringle, D. R. MacFarlane, *Eur. Polym. J.*, 2008, **44**, 1758-1762.
209 C. Stretch and G. Allen, *Polymer*, 1961, **2**, 151-160.
210 Z. Li, J. Chen, L. Su, B. Zou, P. Zhan, Y. Guan, A. Zheng, *RSC Advances*, 2017, **7**, 9933-9940.
211 D. J. Worsfold and S. Bywater, *Can. J. Chem.*, 1960, **38**, 1891-1900.
212 L. Gold, *The Journal of Chemical Physics*, 1958, **28**, 91-99.
213 W. Lee, H. Lee, J. Cha, T. Chang, K. J. Hanley, T. P. Lodge, *Macromolecules*, 2000, **33**, 5111-5115.
214 I. Manners, *Chem. Commun.*, 1999, 857-865.
215 Y. Ni, R. Rulkens, I. Manners, *J. Am. Chem. Soc.*, 1996, **118**, 4102-4114.
216 R. Rulkens, Y. Ni, I. Manners, *J. Am. Chem. Soc.*, 1994, **116**, 12121-12122.
217 J.-C. Eloi, L. Chabanne, G. R. Whittell, I. Manners, *Mater. Today*, 2008, **11**, 28-36.
218 R. L. N. Hailes, A. M. Oliver, J. Gwyther, G. R. Whittell, I. Manners, *Chem. Soc. Rev.*, 2016, **45**, 5358-5407.
219 K. Wieszczycka and K. Staszak, *Coord. Chem. Rev.*, 2017, **351**, 160-171.
220 Y.-B. Huang, J. Liang, X.-S. Wang, R. Cao, *Chem. Soc. Rev.*, 2017, **46**, 126-157.
221 Y. Yan, J. Zhang, L. Ren, C. Tang, *Chem. Soc. Rev.*, 2016, **45**, 5232-5263.
222 Z. Meng, G. Li, S.-M. Ng, H.-F. Wong, S.-C. Yiu, C.-L. Ho, C.-W. Leung, W.-Y. Wong, *Polym. Chem.*, 2016, **7**, 4467-4475.
223 Y. Wang, D. Astruc, A. S. Abd-El-Aziz, *Chem. Soc. Rev.*, 2019, **48**, 558-636.
224 D. A. Rider, K. A. Cavicchi, K. N. Power-Billard, T. P. Russell, I. Manners, *Macromolecules*, 2005, **38**, 6931-6938.

225 E. A. Men'shikov, A. V. Bol'shakova, I. V. Yaminskii, *Prot. Met. Phys. Chem. Surf.*, 2009, **45**, 295-299.
226 J. Swann and P. Topham, *Polymers*, 2010, **2**.
227 K. Ragaert, L. Delva, K. Van Geem, *Waste Manage.*, 2017, **69**, 24-58.
228 J. N. Hahladakis, C. A. Velis, R. Weber, E. Iacovidou, P. Purnell, *J. Hazard. Mater.*, 2018, **344**, 179-199.
229 H. Gao, S. Hu, H. Han, J. Zhang, *J. Appl. Polym. Sci.*, 2011, **122**, 3263-3269.
230 N. Pérez, X. L. Qi, S. Nie, P. Acuña, M. J. Chen, D. Y. Wang, *Materials (Basel)*, 2019, **12**, 152.
231 Y. Liu, J. Zhao, C.-L. Deng, L. Chen, D.-Y. Wang, Y.-Z. Wang, *Ind. Eng. Chem. Res.*, 2011, **50**, 2047-2054.
232 E. Rezvani Ghomi, F. Khosravi, Z. Mossayebi, A. Saedi Ardahaei, F. Morshedi Dehaghi, M. Khorasani, R. E. Neisiany, O. Das, A. Marani, R. A. Mensah, L. Jiang, Q. Xu, M. Försth, F. Berto, S. Ramakrishna, *Molecules*, 2020, **25**, 5157.
233 Y. Gao, J. Wu, Q. Wang, C. A. Wilkie, D. O'Hare, *J. Mater. Chem. A*, 2014, **2**, 10996-11016.
234 W. Hu, J. Zhan, N. Hong, T. R. Hull, A. A. Stec, L. Song, J. Wang, Y. Hu, *Polym. Adv. Technol.*, 2014, **25**, 631-637.
235 D. Price, K. Pyrah, T. R. Hull, G. J. Milnes, J. R. Ebdon, B. J. Hunt, P. Joseph, C. S. Konkel, *Polym. Degrad. Stab.*, 2001, **74**, 441-447.
236 D. Price, L. K. Cunliffe, K. J. Bullet, T. R. Hull, G. J. Milnes, J. R. Ebdon, B. J. Hunt, P. Joseph, *Polym. Adv. Technol.*, 2008, **19**, 710-723.
237 T. Xu, L. Zhang, Z. Cheng, X. Zhu, *Sci. China Chem.*, 2015, **58**, 1633-1640.
238 S. Wang, Z. Liu, L. Zhang, Y. Guo, J. Song, J. Lou, Q. Guan, C. He, Z. You, *Mater. Chem. Front.*, 2019, **3**, 1833-1839.
239 H. Yang, G. Du, Z. Li, X. Ran, X. Zhou, T. Li, W. Gao, J. Li, H. Lei, L. Yang, *ACS Appl. Polym. Mater.*, 2021, **3**, 1638-1651.
240 Y. Wei, J. Yao, Z. Shao, X. Chen, *ACS Sustain. Chem. Eng.*, 2020, **8**, 7668-7679.
241 C. Heinzmann, C. Weder, L. M. de Espinosa, *Chem. Soc. Rev.*, 2016, **45**, 342-358.
242 E. G. Koricho, E. Verna, G. Belingardi, B. Martorana, V. Brunella, *Int. J. Adhes. Adhes.*, 2016, **68**, 169-181.
243 Y. Zhu, C. Romain, C. K. Williams, *Nature*, 2016, **540**, 354-362.
244 H.-W. Engels, H.-G. Pirkl, R. Albers, R. W. Albach, J. Krause, A. Hoffmann, H. Casselmann, J. Dormish, *Angew. Chem. Int. Ed.*, 2013, **52**, 9422-9441.
245 S. Laurichesse and L. Avérous, *Progress in Polymer Science*, 2014, **39**, 1266-1290.
246 Y. Li, J. Krahn, C. Menon, *J. Bionic Eng.*, 2016, **13**, 181-199.
247 F. J. Díaz López and C. Montalvo, *J. Clean. Prod.*, 2015, **102**, 30-43.
248 K. Zhong, Q. Guan, W. Sun, M. Qin, Z. Liu, L. Zhang, J. Xu, F. Zhang, Z. You, *Ind. Eng. Chem. Res.*, 2021, **60**, 6925-6931.
249 G. Raos and B. Zappone, *Macromolecules*, 2021, **54**, 10617-10644.
250 B. Liu, Z. Xu, C. Fan, C. Cui, Y. Yao, M. Xiao, W. Liu, *Macromol. Rapid Commun.*, 2021, **42**, e2100010.
251 P. Sun, Y. Li, B. Qin, J.-F. Xu, X. Zhang, *ACS Materials Letters*, 2021, **3**, 1003-1009.
252 F. A. Kucherov, E. G. Gordeev, A. S. Kashin, V. P. Ananikov, *ACS Appl. Mater. Interfaces*, 2020, **12**, 45394-45403.
253 J. Kruszynski, W. Nowicka, M. Bouyahyi, Y. Liu, L. Yang, A. Rozanski, N. Anbuchezhian, L. Jasinska-Walc, R. Duchateau, *ACS Appl. Polym. Mater.*, 2023, **5**, 3875-3882.
254 Y. Liu, Y. Shigemoto, T. Hanada, T. Miyamae, K. Kawasaki, S. Horiuchi, *ACS Appl. Mater. Interfaces*, 2021, **13**, 11497-11506.
255 S. Huang, Y. Wan, X. Ming, J. Zhou, M. Zhou, H. Chen, Q. Zhang, S. Zhu, *ACS Appl. Mater. Interfaces*, 2021, **13**, 41112-41119.
256 K. Viswanathan, H. Ozhalici, C. L. Elkins, C. Heisey, T. C. Ward, T. E. Long, *Langmuir*, 2006, **22**, 1099-1105.
257 T. Sato, S. Ise, S. Horiuchi, H. Akiyama, T. Miyamae, *Int. J. Adhes. Adhes.*, 2019, **93**, 102322.
258 Y. Jia, J. Chen, H. Asahara, T.-A. Asoh, H. Uyama, *ACS Appl. Polym. Mater.*, 2019, **1**, 3452-3458.
259 H.-J. Kim, K.-J. Lee, Y. Seo, *Macromolecules*, 2002, **35**, 1267-1275.
260 S. R. Kim, *J. Appl. Polym. Sci.*, 2000, **77**, 1913-1920.
261 J. Tanaka, A. Evans, P. Gurnani, A. Kerr, P. Wilson, *Polym. Chem.*, 2020, **11**, 2519-2531.
262 R. A. Chapman, in *Handbook of Nonwovens*, ed. S. J. Russell, Woodhead Publishing, 2007, pp. 330-367.
263 N. C. Restrepo-Zapata, T. A. Osswald, J. P. Hernández-Ortiz, *Polym. Eng. Sci.*, 2015, **55**, 2073-2088.

264 C. G. Collins Rice, L. J. Morris, J.-C. Buffet, Z. R. Turner, D. O'Hare, *Chem. Commun.*, 2023, **59**, 12128-12131.
265 S. C. N. Sanches, M. Diniz, R. Lazzarini Dutra, *Polímeros*, 2014, **24**, 269-275.
266 K. C. Dao, *J. Appl. Polym. Sci.*, 1982, **27**, 4799-4806.
267 R. Winters, W. Heinen, M. A. L. Verbruggen, J. Lugtenburg, M. van Duin, H. J. M. de Groot, *Macromolecules*, 2002, **35**, 1958-1966.
268 D. Jubinville, E. Esmizadeh, S. Saikrishnan, C. Tzoganakis, T. Mekonnen, *Sustain. Mater. Technol.*, 2020, **25**, e00188.
269 E. Maris, A. Aoussat, E. Naffrechoux, D. Froelich, *Miner. Eng.*, 2012, **29**, 77-88.
270 S. Brunner, P. Fomin, C. Kargel, *Waste Manage.*, 2015, **38**, 49-60.
271 A. Arenas-Vivo, F. R. Beltrán, V. Alcázar, M. U. de la Orden, J. Martinez Urreaga, *Mater. Today Commun.*, 2017, **12**, 125-132.
272 S. Pragliola, F. Grisi, V. Vitale, O. Sacco, V. Venditto, L. Izzo, A. Grimaldi, N. Baranzini, *Polym. Chem.*, 2022, **13**, 2685-2693.
273 R. Shang, H. Gao, F. Luo, Y. Li, B. Wang, Z. Ma, L. Pan, Y. Li, *Macromolecules*, 2019, **52**, 9280-9290.
274 J. S. Higgins, J. E. G. Lipson, R. P. White, *Philos. Trans. R. Soc. A*, 2010, **368**, 1009-1025.
275 L. A. Utracki and C. A. Wilkie, *Polymer Blends Handbook*, Springer, Dordrecht, 2002.
276 F. P. La Mantia, M. Morreale, L. Botta, M. C. Mistretta, M. Ceraulo, R. Scaffaro, *Polym. Degrad. Stab.*, 2017, **145**, 79-92.
277 D. R. Paul and J. W. Barlow, *J. Macromol. Sci. C*, 1980, **18**, 109-168.
278 E. P. A. van Bruggen, R. P. Koster, S. J. Picken, K. Ragaert, 2016, **31**, 179-187.
279 D. R. Paul, *Chapter 12 - Interfacial Agents ("Compatibilizers") for Polymer Blends*, Academic Press, 1978.
280 J. Xu, J. M. Eagan, S.-S. Kim, S. Pan, B. Lee, K. Klimovica, K. Jin, T.-W. Lin, M. J. Howard, C. J. Ellison, A. M. LaPointe, G. W. Coates, F. S. Bates, *Macromolecules*, 2018, **51**, 8585-8596.
281 C. R. López-Barrón and A. H. Tsou, *Macromolecules*, 2017, **50**, 2986-2995.
282 K. Klimovica, S. Pan, T.-W. Lin, X. Peng, C. J. Ellison, A. M. LaPointe, F. S. Bates, G. W. Coates, *ACS. Macro. Lett.*, 2020, **9**, 1161-1166.
283 E. Gitzhofer, B. Vileno, M. Bouquey, D. Chan-Seng, *Polym. Chem.*, 2023, **14**, 934-942.

Chapter 2 – Functionalised polypropylenes; a copolymerisation and post-modification platform

Alexander Evans, Oliver Casale, Louis J. Morris, Zoë R. Turner, and Dermot O'Hare*

Published in Macromolecules: *Macromolecules*, 2024, 57, 22, 10778–10791

2.1. Author contributions

Alexander Evans: Performed the synthesis, analysis, and application testing. Interpreted the data. Manuscript, original draft, review and editing.

Oliver Casale: Investigation, supporting synthesis and analysis.

Louis J. Morris: Manuscript, review and editing.

Zoë R. Turner: Manuscript, review and editing. Supervision.

Dermot O'Hare: Corresponding author. Manuscript, review and editing. Supervision.

2.2. Abstract

Functional polypropylenes (FPs) are regarded as versatile building blocks for next generation materials; however, their development has been stymied due to current synthetic limitations. Here we report a diverse range of functionalised polypropylenes prepared *via* a two-step copolymerisation – post-modification strategy. Solution-phase copolymerisation of propylene and 11-bromo-1-undecene using C_2, C_1, and C_s-symmetric catalysts afforded poly(propylene)-*co*-(11-bromo-1-undecene), with tuneable comonomer incorporation levels, up to 15.5 mol%, with a range of tacticities (*iso*-, *syndio*-, and *atactic*) and wide molecular weight range (4–212 Kg mol^{-1}). Latent electrophilic reactivity of the pendent bromide has been utilised in one of three general synthetic routes, enabling incorporation of an array of polar substituents through formation of a series of covalent connections (C–O, C–N, C–S, C–P, and C–C). Resulting

FPs display distinctly altered bulk and surface properties, *vs* polypropylene: improved thermal stability and adhesion to metal, altered wettability, and latent reactivity. This strategy allows access to FPs with both high molecular weight and chosen tacticity, taking advantage of well-developed metallocene catalysts and classical organic substitution chemistry.

2.3. Introduction

Commercially, polyolefins (PO), namely polypropylene (PP)[1] and polyethylene (PE),[2] are synthesised at scale to meet the needs of a broad array of applications. Desirable and tuneable properties coupled with low production costs are amongst the driving forces behind their utility. Control of key polymeric characteristics such as branching, molar mass (M_n), and dispersities ($Đ_M$), which in turn determine physical properties, have been well studied both academically and industrially. It is widely regarded that next generation PP materials will be functional and versatile though the incorporation of polar functionality, yet there has been limited success industrially in deviating from the ubiquitous carbon and hydrogen backbone in a controlled manner, whilst also allowing access to high molecular weights and controlled tacticity. Such functionalised PPs refer to the chemical incorporation of functional groups in order to enhance or introduce specific properties for commercial applications. Limited introduction of polar functionality has evidenced a significant impact on bulk and surface properties.[3] Consequently, synergies between base properties of PO materials and those of novel polar POs could yield significant material improvements. Such synergistic new materials may additionally circumvent leaching[4] or disrupted mechanical properties,[5] imparted through the use of additives commonly used in composite materials. Therefore, utilisation of

functional PPs as additives could alleviate the negative effects when blending whilst also being utilised in place of multimaterial systems that are challenging to recycle.

The copolymerisation of olefins and polar comonomers is a well-documented pathway for incorporating functionality (Scheme 2.1a-c). Three general synthetic routes are typically exploited; (a) protected functional group (PFG) monomer and subsequent deprotection,[6,7] (b) a functional group (FG) containing monomer,[8] or (c) a monomer with latent reactivity (LR), exploiting successive post-modification.[9-11] A variety of polymeric architectures, principally block copolymers, with distinctly altered material properties have been synthesised in this way.[12-17] Work by Chung *et al*. have evidenced the utility of organoborane,[18] benzylic protons,[19] and styrene moieties[20] during copolymerisation with propylene, coining the term *reactive* comonomers, to yield a range of PP materials through functional group interconversion.[13] Recent developments utilising commercial heterogenous Ziegler–Natta catalysts have achieved polar comonomer enchainment *via* an ionic cluster strategy.[21] However, the direct solution phase copolymerisation of functional comonomers by widely employed early transition metal (groups III and IV) catalysts is limited by deactivation and significantly reduced activity due to ω-functional group coordination to the comonomer and backbiting oligomers to the electrophilic metal centres.[22,23] Notably, Zr catalysts have exhibited tolerability towards ω-halo coordination.[24] Increased separation, within the functional comonomer, between α-olefin and ω-FG[24-26] or excess Lewis-acidic masking reagents like methylaluminoxane (MAO) or AlR_3[27-29] have been utilised to aid comonomer enchainment. A pyridyl amido Hf catalyst has been utilised successfully in propylene copolymerisation with an array of hydrocarbon monomers able to undergo post-polymerisation modification with polar substituents.[30,31] Late transition metal catalysts (Ni and Pd) have been utilised more

extensively for the copolymerisation of functional monomers with both propylene[32-35] and ethylene[36-38] due to their lower acidity and oxophilicity than early transition metal analogues. However, cost,[39] toxicity,[40] arduous catalyst synthesis, and broad challenges to access tacticity control or high molecular weights in these systems hinder their large-scale application.

To overcome low comonomer incorporation and polar monomer incompatibility, post-polymerisation modification *via* C–H functionalisation has been pursued, taking advantage of the low cost and high volume of commodity POs (Scheme 2.1d). However, the direct and controlled functionalisation of C–H bonds is challenging as a consequence of β-scission and depolymerisation reactions. Whilst a multitude of covalent connections (C–C, C–N, C–O, C–B, C–S, and C–Halogen) are possible within polyolefin systems,[41-43] only radical chlorination and maleic anhydride grafting have been found to be industrially viable despite high cost, low efficiency, and the restrictions for dangerous solvents and reagents.[44,45] Recently, Cu-catalysed C–H amination has been utilised to functionalise PE with a range of functional groups, representing a key development in the controlled and selective synthesis of advanced polar PO-based materials.[46] Additionally, a variety of synthetic click chemistry pathways have been employed to further increase polar group content,[47] impacting molecular weight[48-51] or polymeric morphologies.[52]

PP-based functional polymers have been less widely explored with respect to PE in the literature; additional complexity for controlling C-H functionalisation chemistry results due to the presence of methyl, methylene, and methine sp^3 C-H bonds. Solubility and purity complications have additionally hindered subsequent developments.[44,53] However,

a FG containing PP copolymer may provide access to a more diverse array of functional materials in comparison with PE.

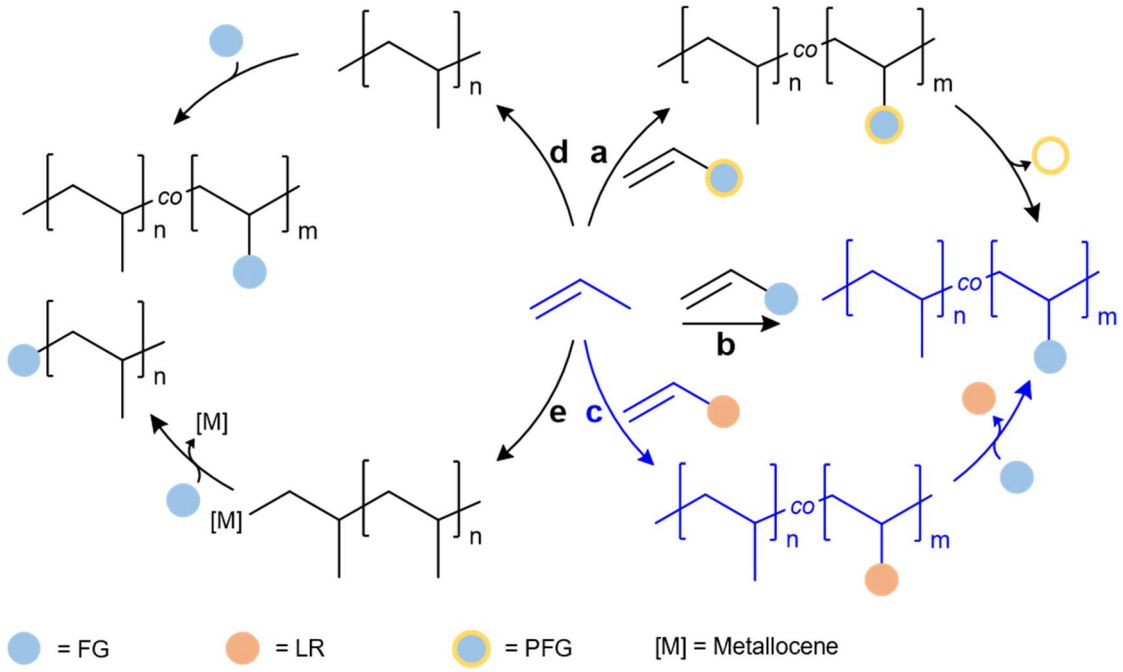

Scheme 2.1. General synthetic strategies for the preparation of functional polypropylenes: (a) Direct copolymerisation of propylene with a protected functional group (PFG) monomer and subsequent deprotection. (b) Direct copolymerisation of propylene with a comonomer containing the desired functional group (FG). (c) Direct copolymerisation of propylene with a comonomer with latent reactivity (LR) and subsequent post-polymerisation modification with the desired FG. (d) Direct post-polymerisation modification of polypropylene. (e) Chain-end functionalisation.

Recently reported advances concerning improved end-group functionality have been achieved by quenching metal catalysed polymerisations in the presence of air, O_2, I_2, Br_2, or S to yield PP-OH, PE-I (X = OH, I, and Br), and PE-S-PE.[54,55] PP-OH were further modified *via* esterification to yield dye modified PP and PE-I/LDPE blends investigated for PE degradability through homolysis of the C-I bond. The latent reactivity, different to traditional vinylic end groups, enables the further synthesis of a wider array of modified PO. However, a limitation of end-group post-modification is the presence of only one functional group per chain; lowering the impact of the functionality with increasing molecular weight (Scheme 2.1e). Circumventing the limited polar group

incorporation level, synthesis of PO-polar block copolymers by a wide range of end group post-polymerisation techniques[12,56-60] has afforded materials able to span phase boundaries and improve immiscible polymer-polymer compatibility.[61]

Polyolefin post-modification *via* simple and general nucleophilic substitution chemistry would open the door to a broader range of functional materials but requires easy access to a suitable platform polymer with electrophilic functionality. Here, we present a simple and generally applicable methodology for the preparation of a diverse range of FPs. Poly(propylene)-co-(11-bromo-1-undecene) (**PP_{Br}**) was employed as a tuneable platform copolymer which can be readily post-functionalised by utilising the latent reactivity of the brominated side-chains. This allows the development of a wide-ranging series of covalent connections (C–O, C–N, C–S, C–P, and C–C) *via* different substitution pathways, yielding versatile FPs with properties suitable for an array of applications (Scheme 2.1c and Scheme 2.2).

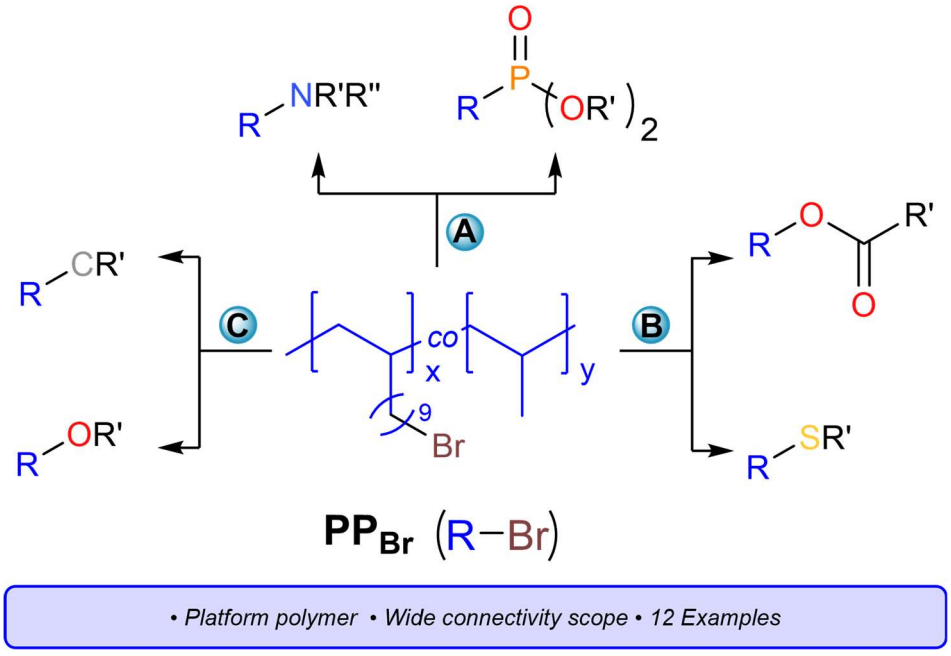

Scheme 2.2 General synthetic overview for the post-polymerisation modification of poly(propylene)-co-(11-bromo-1-undecene), PP_{Br}, *via* (a) forcing and (b) base mediated conditions, and (c) salt metathesis, yielding a range of covalent connections.

2.4. Results and discussion

2.4.1. Solution-phase copolymerisation of propylene and bromoalkenes.

The brominated copolymer poly(propylene)-*co*-(11-bromo-1-undecene) (**PP$_{Br}$**) was prepared by solution-phase copolymerisation of propylene (P, 2 bar) and 11-bromo-1-undecene (**11-Br**; 91–182 mM) using a commercially available catalyst, *rac*-ethylenebis(indenyl)zirconium dichloride (**M1**), MAO as cocatalyst, and triisobutylaluminum (TIBA) as a masking agent to aid bromoalkene enchainment with polymerisation temperatures (T_p) = 30–90 °C. Polymerisation activities up to 2628 $kg_{PP}mol_{[\mathbf{M1}]}^{-1}h^{-1}bar^{-1}$ recorded.

Successful incorporation of comonomer was identified by the presence of -C***H*$_2$**Br (δ_H = 3.49 ppm) and -C***H*$_2$**CH$_2$Br (δ_H = 1.97 ppm) resonances in the ^{1}H NMR spectrum and a C-Br stretching absorption (721 cm^{-1}) in the FT-IR spectrum (Figure A1.3 and A1.9). Enchainment levels of comonomer 2.01–8.12 mol% were determined by NMR spectroscopy (Figure A1.4), and are consistent with previously reported examples of olefin copolymerisation with ω-halo-1-alkenes.[24,62] Comonomer incorporation was found to be tuneable, related to T_p and [**11-Br**]; increasing respective reaction variables serving to increase the relative [**11-Br**]:[P] in the solution phase, providing copolymers with higher comonomer incorporation levels, albeit to the detriment of activity (Figure 2.1A, Table A1.1). With consideration to end application, we envisage polymers can be synthesised that sufficiently balance cost, efficiency, and subsequent properties. Copolymers display a reduction in melting temperature (T_m) (up to 32%) and crystallinity (up to 59%) with increasing comonomer incorporation (up to 8%), as observed by differential scanning calorimetry (DSC) (Figure A1.8), compared to the parent **PP** prepared under the same conditions.

The polymerisation catalyst displays lower tolerance for shorter chain bromoalkenes than similar ethylene systems; displaying a clear positive correlation between increasing methylene chain-length and activities, which is consistent with the literature (***n*-Br**, n = 6, 7 and 11; 0, 565 and 1686 $kg_{PP}\ mol_{[\mathbf{M1}]}^{-1}\ h^{-1}\ bar^{-1}$ respectively; Table A1.1).[10,25,33,63] The shorter-chain comonomers are more susceptible to backbiting through the formation of a chelate structure between bromine and the metal centre, which is relatively entropically favorable with respect to longer chain lengths. Overall, this decreases activity and reduces polymer M_n (Figure A1.1).[22] Considering the higher activities of **11-Br**, the same deactivation mechanism is less favorable due to the increased conformational freedom in the entropically favored unchelated state.[9] The above mechanism leading to an inactive **Zr**-Br species, supports the overall decrease in activity compared to the neat propylene system (5467 $kg_{PP}mol_{[\mathbf{M1}]}^{-1}h^{-1}bar^{-1}$; Table A1.1).[37]

Reactivity ratios pertaining to ethylene/propylene copolymerisations have been well summarised,[64] and extended for 1-hexene copolymerisations utilising three Kaminsky-Sinn-type catalysts.[65] Estimated reactivity ratios for propylene (r_P = 3.81 ± 0.14) and **11-Br** (r_B = 1.36 ± 0.33) for **M1** were obtained using the Fineman-Ross method,[66] and taking the concentration of propylene in hexanes according to Kissin's equation (Figure A1.16, Table A1.3).[67] The value $r_P \bullet r_B$ = 5.20 ± 1.26 suggests that a block-like copolymer is likely to be formed in this case. Given the low experimental number average molecular weights ($M_{n,\ SEC}$ = 4–13 Kg mol^{-1}) of $\mathbf{PP_{Br}}$ by size exclusion chromatography (SEC), a 4 mol% incorporation corresponds to 1–2 enchained **11-Br** units per polymer chain. Given $r_B \approx 1$, when accounting for standard error in the linear regression, we might reasonably expect the brominated side chains to be substantially isolated within propylene segments. $^{13}C\{^1H\}$ NMR spectroscopic data similarly supports this conclusion

with a single resonance (δ_C = 45.82 ppm) for methine carbons at the copolymer junction, consistent with isolated comonomers afforded by a single insertion of **11-Br** followed by a PP block (Figure A1.5-7). This, in conjunction with an even short chain branching profile per 1000 total carbons (SCB/1000TC) across the molecular weight distribution implies random comonomer enchainment (Figure A1.10). Reducing the duration of polymerisation further supports this observation with similar incorporation after 10 minutes (4.99 mol%), 20 minutes (4.89 mol%), and 30 minutes (3.98 mol%) (Table A1.1, Figure A1.11). The slightly reduced incorporation after longer reaction times can be explained by the decrease in [**11-Br**] relative to [propylene] with time.

All copolymers exhibited a monomodal molecular weight distribution by SEC (Figure A1.12); **M1** derived copolymers displayed relatively narrow $Đ_m$ (1.6–2.3). A range of higher M_n polymers (21–212 Kg mol^{-1}) with reasonable control ($Đ_m$ = 2.2–4.7) were also synthesised to evaluate both the robustness of the copolymerisation and the described synthetic routes to post-modification (Figure 2.1B, Table A1.2). Two *ansa*-zirconocene catalysts were employed: C_2-symmetric **M2** for highly isotactic polypropylene (^{i}PP, *mmmm* = 98%. Figure A1.14) and C_s-symmetric **M3** for syndiotactic polypropylene (^{S}PP, *rrrr* = 71%. Figure A1.13). Polymerisation by C_1-symmetric *ansa*-bridged titanium post-metallocene **M4** prepared atactic polypropylene (^{a}PP).[68] The respective copolymers were evaluated in tandem, however ^{a}**PP$_{Br}$** derived from **M4** was not further explored for post-modification due to the current unrealised commercial use of ^{a}PP. The tuneability of M_n and tacticity, in addition to comonomer incorporation, provides another dimension for targeted application through careful polymer design.

All copolymerisations display a decrease in activity (%) compared to the homopolymerisation with the degree of comonomer incorporation observed to correlate

inversely: **M1** (Δ(activity) = 28%, incorporation = 2 mol%, 2 **11–Br** units per chain), **M2** (Δ(activity) = 30%, incorporation = 1.6 mol%, 11 **11–Br** units per chain), **M3** (Δ(activity) = 51%, incorporation = 4.0 mol%, 46 **11–Br** units per chain), and **M4** (Δ(activity) = 58%, incorporation = 15.5 mol%, 338 **11–Br** units per chain). Although reduced compared to the homopolymerisation, productive catalytic activity is maintained in the presence of bromoalkene. This behavior has previously been described as the *activation and reactivation route*.[24,69] Whilst bromide coordination deactivates the cationic active species, the effect is less pronounced compared to more strongly coordinating heteroatoms. The active species can be easily regenerated due to the relatively weak M-Br bond and energetic disfavourability of the resultant 13-membered metallocyclic chelate when relevant. This is consistent with a dichlorometallocene pre-catalyst activation pathway,[24] facilitating direct **11-Br** copolymerisation.

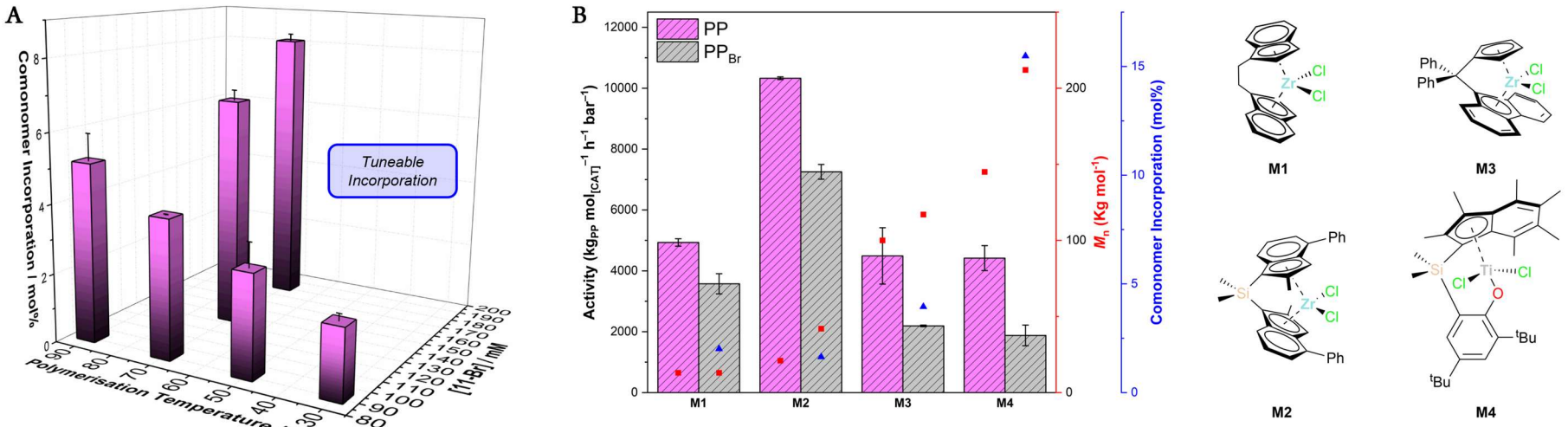

Figure 2.1. (A) Investigation into the tunable comonomer incorporation levels based on varying polymerisation temperature and [**11-Br**] for **M1**. (B) The effect of **11-Br** on activity concerning various catalysts for *iso- syndio-* and *atactic* polypropylene with corresponding M_n and incorporation data (mol%). [a]Conditions: **M1**, MAO used as a cocatalyst and scavenger with $[Al]_0$:[**M1-4**]$_0$ = 1000:1. Molar ratio of $[TIBA]_0$:[**11-Br**]$_0$ = 1:10, 0.5 mL toluene, 49.5 mL hexanes, propylene 2 bar. [b]Conditions: **M1-4** (0.024 mM, 1 mg mL^{-1} toluene), MAO used as a cocatalyst and scavenger with $[Al]_0$:[**M1-4**]$_0$ = 1000:1. Molar ratio of $[TIBA]_0$:[**11-Br**]$_0$ = 1:10, 0.50-0.75 mL toluene, 49.25-49.50 mL hexanes, propylene 2 bar, polymerisation time 20 minutes, temperature of polymerisation 50 °C. All polymerisation and analysis were performed in duplicate and mean values are reported. Comonomer incorporation determined by ^{1}H NMR spectroscopy. M_n determined by SEC.

2.4.2. General synthetic methodology for the post-modification of PP_{Br}

To our knowledge, few examples exist in the literature for the post-polymerisation functionalisation of halogen containing POs and these are typically limited to low M_n PE to combat poor polymer solubility.[10,53] We have developed transformations to afford three straightforward and generally applicable synthetic routes using **PP_{Br}** as a platform for the synthesis of functionalised polypropylene copolymers. Bulk material properties are inextricably linked to polymer M_n irrespective of functionality; modification protocols were first developed using low M_n **$^{i}PP_{Br}$**, then adapted to higher M_n analogues of **$^{i}PP_{Br}$** and $^{s}PP_{Br}$ at 1.9 and 2.4 mol% incorporation, 22 and 16 **11–Br** units per chain, respectively, to demonstrate the tunability and wide applicability of this system.

Pathways for modification can be summarised into the following categories: (A) forcing conditions using high temperature, long reaction times, and large [modifier]; (B) base-mediated mild nucleophilic substitution; (C) nucleophilic substitution by salt metathesis (Figure 2.2).

All modifications evidenced the quantitative transformation of **PP_{Br}** into the respective modified polymers (**PP_X**), which were isolated by precipitation into acidified methanol then collected by filtration in high isolated yields (>85%, Table A1.5), as confirmed through the through the absence of bromide-adjacent methylene protons (δ = 3.49 ppm) or carbon (δ = 32.81 ppm) in respective ^{1}H and $^{13}C\{^{1}H\}$ NMR spectra. Residual [Br] was evaluated *via* an oxygen combustion flask technique followed by hypochlorite amplification with an analytical uncertainty of 0.3% absolute. Due to the range of modifications, representative samples for each covalent connection were analysed, all of which support the removal of the Br (0.00–0.23 wt%) during comonomer transformation irrespective of modification pathway (Table A1.6).

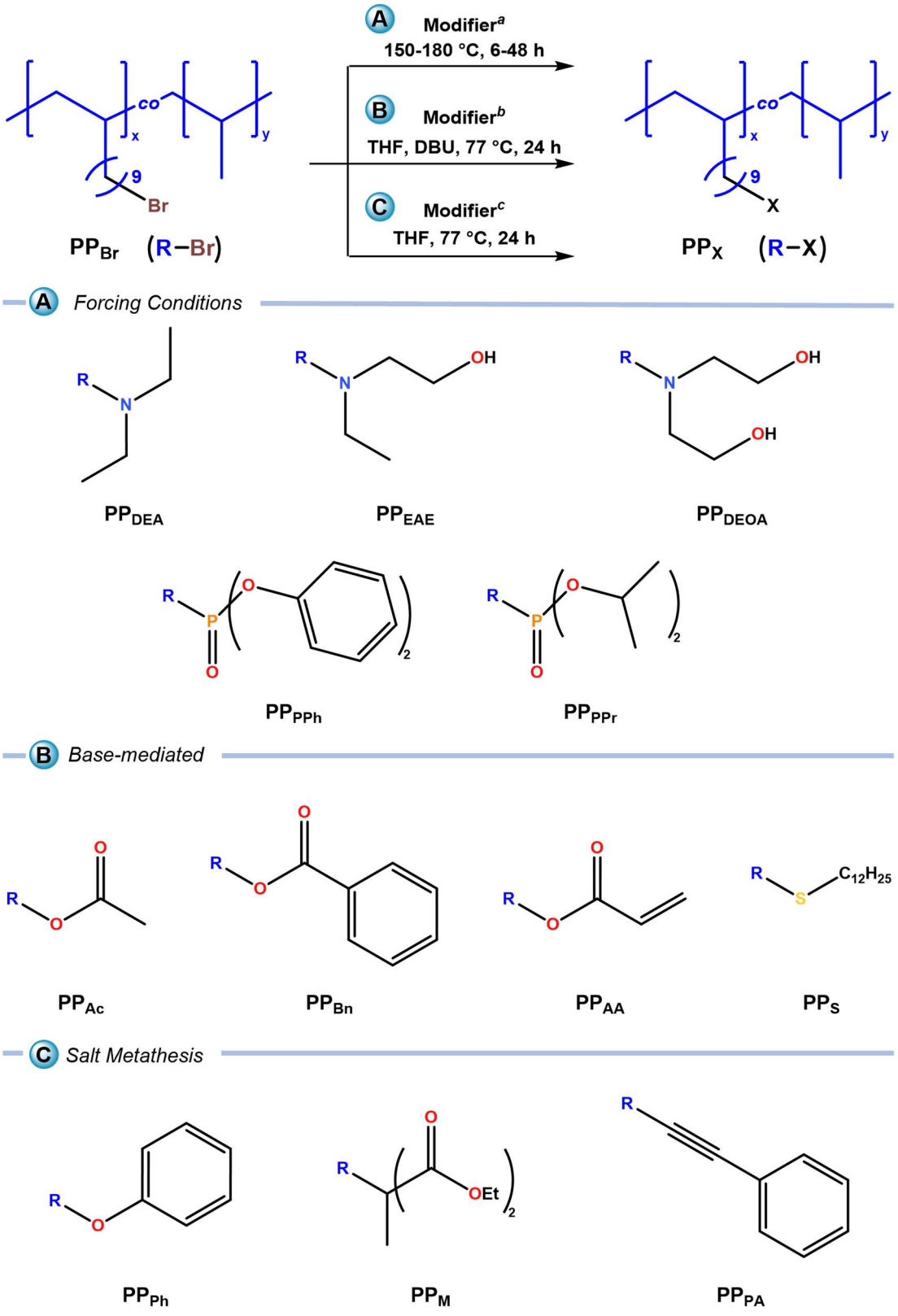

Figure 2.2 Examples of $\mathbf{PP_{Br}}$ (4 mol% incorporation unless otherwise specified; Table A1.5) which underwent post-modification *via* (**A**) forcing, (**B**) base-mediated, and (**C**) salt metathesis conditions, to yield a range of 12 modified, functional polypropylenes ($\mathbf{PP}_X$). [a]$HNEt_2$, HN(Et)(EtOH), $HN(EtOH)_2$, $P(O^iPr)_3$, or $P(OPh)_3$. [b]$MeCO_2H$, $PhCO_2H$, CH_2CHCO_2H, and $HSC_{12}H_{24}$. [c]KOPh. $KC(CH_3)(CO_2Et)_2$, and LiC_2Ph.

2.4.3. Post-polymerisation modification of PP_{Br} using forcing conditions

Functionalisation of **PP_{Br}** to provide modified polypropylene-phosphonates (**PP_{PPr}** and **PP_{PPh}**; Scheme 2.2A) with C–$P_{phosphonate}$ bonds was afforded by the quantitative Michaelis Abuzov reaction[75-77] with neat (50 eq.) triisopropyl phosphite ($P(O^iPr)_3$, 150 °C and 6 h) or triphenyl phosphite ($P(OPh)_3$, 180 °C and 48 h) in order to reach quantitative conversions. Additionally, amine modification of **PP_{Br}** in neat (50 eq.) diethylamine (DEA, 150 °C and 24 h), 2-(ethylamino)ethanol (EAE, 180 °C and 48 h), and 2,2'-iminodiethanol (DEOA, 180 °C and 48 h) resulted in formation of the corresponding C-N_{amine} bonds and generation of **PP_{DEA}**, **PP_{EAE}** and **PP_{DEOA}** respectively.

Phosphonate incorporation for **PP_{PPr}** and **PP_{PPh}** was confirmed using NMR and FT-IR spectroscopy. In the ^{1}H NMR spectrum of **PP_{PPr}**, a multiplet at $\delta_H = 4.74$ ppm corresponds to the -OC***H***$(CH_3)_2$ protons (Figure A1.17 and A1.22). Regarding **PP_{PPh}**, resonances for the -OPh***H*** ($\delta_H = 7.45–7.19$ ppm) and -C***H***$_2$P- protons ($\delta_H = 2.20–2.09$ ppm) are observed. A singlet in $^{31}P\{^1H\}$ NMR spectrum for **PP_{PPr}** ($\delta_P = 29.48$ ppm) and **PP_{PPh}** ($\delta_P = 25.21$ ppm) indicates the presence of a single phosphorus(V) environment (Figure A1.20 and A1.25);[70] notably, residual triisopropyl phosphite (*ca.* 140 ppm) and triphenyl phosphite (*ca.* 128 ppm) were not detected. Heteronuclear spin-spin coupling between phosphorus and carbon was observed in the $^{31}P\{^1H\}$ and $^{13}C\{^1H\}$ NMR spectra, further corroborating covalent functionalization. In the $^{13}C\{^1H\}$ NMR spectrum, **PP_{PPr}** displays -***C***H_2P- at $\delta_C = 27.38$ ppm (1C, $^1J_{CP} = 141.5$ Hz) and -P(***C***H)$_2$- at $\delta_C = 69.61$ ppm (2C, $^2J_{CP} = 6.9$ Hz) (Figure A118-19). **PP_{PPh}** can likewise be characterised: -***C***H_2P- $\delta_C = 26.57$ ppm (1C, $^1J_{CP} = 139.8$ Hz) and -P(*ipso*-**C**)$_2$- $\delta_C = 150.99$ ppm (2C, $^2J_{CP} = 8.7$ Hz) (Figure A1.23-24). The presence of the phosphonate moiety was demonstrated by FT-IR spectroscopy (Figure A1.21 and A1.26).

Characteristic absorption bands were found for **PP$_{PPr}$**: P=O (1245 cm^{-1}) and P–O–C (1006–981 cm^{-1}) and **PP$_{PPh}$**: P=O (1274 cm^{-1}), P–O–Ph (1191 and 927–900 cm^{-1}), and aromatic C=C (1592, 1490, 762 cm^{-1}) and C-H (681 cm^{-1}) stretching bands.

For amine functionalisation, broad resonances corresponding to the methylene environments α to N (-CH_2NR_2) in the ^{1}H and ^{13}C{^{1}H} NMR spectra can be identified for **PP$_{DEA}$** (δ_H = 2.99 ppm; δ_C = 52.03 ppm), **PP$_{EAE}$** (δ_H = 3.13 ppm; δ_C = 54.13 ppm), and **PP$_{DEOA}$** (δ_H = 3.25 ppm; δ_C = 55.54 ppm) (Figure A1.28-31, A1.33-36, and A1.38-40). For **PP$_{DEA}$** and **PP$_{EAE}$** a singlet in the quantitative ^{13}C{^{1}H} NMR spectra (δ_C = 9.11 ppm, 2C; δ_C = 8.81 ppm, 1C respectively) was assigned to the terminal -***C***H$_3$ groups of the incorporated amine. -O***H*** resonances in ^{1}H NMR spectra were not observed for **PP$_{DEOA}$** or **PP$_{EAE}$**.[53] However, increased δ with respect to -C***H$_2$***OH (δ_H = 4.13 and 4.05 ppm respectively) is consistent with deshielding by adjacent hydroxyl groups. Characteristic O-H stretches (3506–3182 cm^{-1}) were observed by FT-IR spectroscopy in addition to ascribed C-N (tertiary) absorptions (1080–1045 cm^{-1}) (Figure A1.32, A1.37, and A1.42).

Significant deviation of $M_{n,\,SEC}$ from theoretical number average molecular weights ($M_{n,\,th}$) values were observed for amine-modified polymers, suggesting severe deviation from the calibrant due to the presence of pendant amine functionality affecting both hydrodynamic volume and column interactions. All polymers displayed the same trend to lower $M_{n,\,SEC}$; **PP$_{DEA}$** (800 g mol^{-1}), **PP$_{EAE}$** (800 g mol^{-1}), and **PP$_{DEOA}$** (1000 g mol^{-1}) whilst total integrals in ^{1}H NMR spectra suggest no loss in mass. Less severe deviations from $M_{n,\,th}$ were found for phosphonate modified polymers. Monomodal SEC distributions were observed for the modified polymers with $Đ_m$ values consistent to the

parent **PP$_{Br}$** copolymer implying a controlled functionalisation (Figure A1.32, A1.37, and A1.42).

DSC is consistent with amine modification, generally increased T_m were detected respective to **PP$_{Br}$** (90.5 °C). Notably, **PP$_{DEOA}$** (98.4 °C) was elevated compared with **PP$_{DEA}$** (91.5 °C) and **PP$_{EAE}$** (93.1 °C) which could suggest that a hydrogen bonding network was developed with increasing hydroxyl groups *vs* nitrogen alone (Figure A1.32, A1.37, and A1.42). However, attempts to validate this by rheological measurements were unsuccessful due to the very low melt viscosity of all polymers.

Additional P(O^{i}Pr)$_3$ and P(OPh)$_3$ modified samples were synthesised from **M1**, varying incorporation levels (4–8 mol%), to explore the relationship between functional group incorporation and physical properties (Table A1.4, A1.7 and Figure A1.27). DSC revealed decreased crystallinity (27–11%) and lower melting temperatures (T_m = 89–77 °C for **PP$_{PPr}$**, compared to the corresponding **PP$_{Br}$**. Conversely to **PP$_{PPr}$**, DSC traces of **PP$_{PPh}$** exhibited increased crystallinity (32–24%) and T_m (95–76 °C) versus the respective **PP$_{Br}$**, possibly due a decrease in entropy due to π-π stacking of the phenyl groups; this phenomenon was likewise observed for all modified polymers containing aromatic groups.

Polymers ^{i}**PP$_{Br}$** (2.4 mol%) and ^{s}**PP$_{PPr}$** (1.9 mol%) synthesised by **M2** and **M3** were likewise post-modified with P(O^{i}Pr)$_3$ and DEA under analogous reaction conditions; increasing reaction duration was required to achieve quantitative conversion (P(O^{i}Pr)$_3$, 96 h; DEA, 48 h) (Figure A1.79-86 and A1.88). Key spectroscopic handles remained consistent relative to those derived and discussed from **M1**. M_n results deviated substantially from expected values, with DEA modified polymers both being

undetectable by GPC; behaving similarly to the lower M_n analogues, consistent with the hypothesised polymer-column interaction (Table A1.5). ^{s}**PP$_{PPr}$** ($M_{n,\ SEC}$ = 110 800 g mol^{-1}, $Đ_m$ = 2.23) displayed concordant results to theory ($M_{n,\ th}$ = 108 100 g mol^{-1}) whilst ^{i}**PP$_{PPr}$** $M_{n,\ SEC}$ = 9 500 g mol^{-1}, $Đ_m$ = 11.79) displayed a broadening in the distribution, leading to a significant deviation from theory ($M_{n,\ th}$ = 87 700 g mol^{-1}) and $Đ_m$ of the parent ^{i}**PP$_{Br}$** (2.74). Functionalised polymers evidenced negligible T_m alteration from the parent polymers at the incorporation levels investigated; ^{i}**PP$_{Br}$** = 132 °C and ^{s}**PP$_{PPr}$** = 101 °C.

Overall, modifier nucleophilicity dictated the ability to exploit the latent reactivity of the pendant bromine. Soft nucleophiles based on phosphorus and nitrogen required significant reaction times and high temperatures in neat modifier in order to reach quantitative conversion. Excess modifier was successfully recovered and can be reused for subsequent modifications.

2.4.4. Post-polymerisation modification of PP$_{Br}$ using base-mediated conditions

Sufficiently acidic protons in the presence of non-nucleophilic organic base (1,8-Diazabicyclo[5.4.0]undec-7-ene (DBU)) facilitated the transformation of **PP$_{Br}$** to a series of functionalised copolymers yielding C–O$_{ester}$ and C–S covalent connections. Acetic acid, benzoic acid, acrylic acid, and dodecanethiol where each employed as modifiers to yield **PP$_{Ac}$**, **PP$_{Bn}$**, **PP$_{AA}$**, and **PP$_{S}$** respectively under mild conditions (2 eq. modifier, 2 eq. DBU, < 24 h, and 77 °C)(Figure 2.2B).

Preparation of acetic acid and benzoic acid-modified copolymers **PP$_{Ac}$** and **PP$_{Bn}$** evidenced the facile transformation of C-Br to ester functionality under base-mediated conditions. A triplet in the ^{1}H NMR spectrum corresponds to -C***H***$_2$OC-protons (**PP$_{Ac}$**

δ_H = 4.15 ppm; **PP$_{Bn}$** δ_H = 4.41 ppm); a cross-peak in the HMBC spectrum to ***C***=O (δ_C = 170.60 ppm and δ_C = 166.54 ppm respectively) was also observed (Figure A1.43-46 and A1.48-51).

PP$_{Ac}$ displayed the FT-IR absorption bands diagnostic of C=O (1745 cm^{-1}) and C–O (1433 cm^{-1}) and **PP$_{Bn}$** exhibited complementary absorption bands for C=O (1724 cm^{-1}), C–O$_{Alk}$ (1272 cm^{-1}), and C–O$_{Ar}$ (1113 cm^{-1}) (Figure A1.47 and A1.52). Theoretical values for M_n expected by SEC were closely matched experimentally for both **PP$_{Ac}$** ($M_{n,\,th}$ = 3,800 g mol^{-1} *vs* $M_{n,\,SEC}$ = 3,100 g mol^{-1}) and **PP$_{Bn}$** ($M_{n,\,th}$ = 4,100 g mol^{-1} *vs* $M_{n,\,SEC}$ = 4,600 g mol^{-1}); similar trends in M_n were evidenced between alkyl and aryl phosphonate modified copolymers (Table A1.5).

DSC indicated increased T_m compared to **PP$_{Br}$** (**PP$_{Ac}$** = 93.2 °C; **PP$_{Bn}$** = 95.1 °C), emulating observed trends between **PP$_{PPr}$**, and **PP$_{PPh}$** that are possibly attributed to aromatic π-π stacking of the phenyl groups (Figure A1.47 and A1.52).[71] Thermogravimetric analysis (TGA) thermographs exhibit a single mass loss event with distinctions from the base copolymer being lower T_{Max} for both alkyl (421 °C) and aryl (378 °C) modified copolymers (Figure A1.47 and A1.52).

Polymers synthesised by **M2** and **M3** underwent post-modification with benzoic acid, yielding the quantitative transformation product, albeit requiring slightly higher reaction temperatures (95 °C) and longer reaction times (96 h). Key spectroscopic handles remained consistent relative to **PP$_{Bn}$** derived from **M1** (Figure A1.89-92). M_n data was consistent between **^{i}PP$_{Bn}$** ($M_{n,\,SEC}$ = 26 600 g mol^{-1}, $Đ_m$ = 7.15) and **^{s}PP$_{Bn}$** ($M_{n,\,SEC}$ = 19 600 g mol^{-1}, $Đ_m$ = 7.53), both decreasing *vs* $M_{n,\,th}$ (108 000 and 26 600 g mol^{-1} respectively) and displayed similarly increased $Đ_m$ compared to their

parent polymers (Table A1.5). As with DEA and $P(O^iPr)_3$ modified polymers, ^{i}**PP$_{Bn}$** (133 °C) and ^{s}**PP$_{Bn}$** (98 °C) T_m remained comparable to the brominated copolymers (Figure A1.92).

Acrylic acid functionalised polypropylene, **PP$_{AA}$**, displayed a triplet -C***H*$_2$OC- (δ_H = 4.25 ppm) in the ^{1}H NMR spectrum, in addition to HMBC cross-peak to ***C***=O (δ_H = 166.04 ppm) in $^{13}C\{^1H\}$ NMR spectrum, characteristic of the formation of an ester linkage (Figure A1.53-56). Further identification of vinylic protons =C***H*$_2$ (H^{cis}, δ_H = 6.43 ppm; H^{trans}, δ_H = 5.84 ppm) and =C***H*** (δ_H = 6.20 ppm), and respective carbon environments (δ_C = 129.51 ppm and 129.13 ppm) in the respective ^{1}H and $^{13}C\{^1H\}$ NMR spectra confirm successful incorporation of the acrylate functional group. In the FT-IR spectrum, absorption bands for CH= (1407, 1296, and 1267 cm^{-1}), C=C (1637 and 1058 cm^{-1}), C–O (1189 cm^{-1}), and C=O (1729 cm^{-1}) were observed (Figure A1.57). Increased M_n (4600 g mol^{-1}) and $Đ_m$ (3.59) of **PP$_{AA}$** by SEC compared with **PP$_{Br}$** and $M_{n,th}$ (3900 g mol^{-1}) suggests alternate column interaction induced by increasing polar functionality (Figure A1.57). Thermal stability by TGA (T_{Max} = 440 °C) was comparable to **PP**$_{Br}$, but T_m (98.5 °C) was increased, potentially due to long range order in the crystal structure provided by vinyl and carbonyl groups (Figure A1.57). Successive DSC cycles resulted in thermal coupling of acrylate groups to provide an insoluble cross-linked polymer ***x*PP$_{AA}$**, *vide infra*.

PPs displayed limited spectroscopic handles, with no observable C-S adsorptions in FT-IR spectroscopy. A triplet in the ^{1}H NMR spectrum (δ_H = 2.59 ppm, 4H) attributed to -C***H*$_2$SC***H*$_2$- was observed in the expected chemical shift range; *cf.* dibutyl sulfide -SC***H*$_2$- (δ_H = 2.50 ppm) (Figure A1.58). The corresponding singlet in the $^{13}C\{^1H\}$ NMR spectrum (δ_C = 32.68 ppm, 2C) integrates corroboratively, and these assignments are

additionally supported by the observation of relevant cross-peaks in the HSQC and HMBC spectra (Figure A1.59-62). Modifier chain-end -***C***H_3 groups were observed by $^{13}C\{^1H\}$ NMR spectroscopy (δ_C = 13.92 ppm, 1C). Although the corresponding methyl resonance in the ^1H NMR spectrum (δ_H = 1.00 ppm) was masked by backbone PP -C***H₃*** signals, a cross-peak at this chemical shift was positively identified in the HSQC spectrum. Good agreement between observed $M_{n,\,SEC}$ (4300 g mol^{-1}) and $M_{n,\,th}$ (4400 g mol^{-1}) further validate the successful modification (Table A1.5 and Figure A1.63). T_m (92.8 °C) and crystallinity (26%) was comparable to **PP$_{Br}$** by DSC and TGA thermographs displayed a single mass loss event in the thermographs with T_{Max} = 445 °C (Figure A1.63).

The effect of hydrophobic character on reaction rate could be readily observed. Similar modifier and polymer hydrophobicities resulted in expedited conversion, likely attributed to reduced mass transfer limitations more hydrophilic modifiers suffered from. For example, synthesis of **PP$_{DEA}$** and **PP$_{DEOA}$** were achieved in 24 h and 48 h respectively, whereas **PP$_S$** could be prepared in under 24 h.

Base mediated transformations largely outperformed the forcing conditions from an economic and environmental perspective; requiring near stoichiometric conditions, shorter reaction times, lower reaction temperatures, and evidencing greater modification versatility. However, as modifier pK_a increased, the ability to undergo base-mediated substitutions was limited. Although successful for the thiol connection (dodecanethiol, pK_a *ca.* 17.0), base-mediated nucleophilic substitution was ineffective for alcohols (phenol, trifluoroethanol, and ethanol as non-exhaustive examples; pK_a *ca.* 18.0,[72] 23.5,[73] and 29.8[74] respectively), as well as malonic ester diethyl methyl malonate (DEMM) (pK_a *ca.* 13.1[75]), resulting in limited conversion and a mixture of products. Limitations

of the base-mediated procedure for less acidic substrates were overcome *via* prior conversion into isolable alkali metal (Li and K) salts, *vide infra*.

2.4.5. Post-polymerisation modification of PP_{Br} by salt metathesis

Exemplar C–O (ether) and C–C connections were realised through facile nucleophilic substitution of **PP_{Br}** with potassium phenoxide, potassium diethylmethylmalonate, or lithium phenylacetylide in THF (2 eq. modifier, 77 °C, 24 h, Figure A1.101-104), providing facile access to the respective modified polymers **PP_{OPh}**, **PP_{M}** and **PP_{PA}**. From the perspective of industrial upscaling, this route holds significant promise regarding the scope of modifications and reasonable reaction conditions. All modified polymers were characterised similarly to previously discussed **PP_X** and displayed diagnostic features in the NMR and FT-IR spectra.

PP_{OPh} displayed a triplet (δ_H = 4.06 ppm) in the ^{1}H NMR spectrum indicative of -C***H*$_2$O-, which was found by HMBC to correlate to a resonance assigned to *ipso*-***C*$_6$**H_5 (δ_C = 159.62 ppm) in the corresponding $^{13}C\{^1H\}$ NMR spectrum (Figure A1.64-67). Malonate incorporation in **PP_{M}** was consistent with a multiplet -C***H*$_2$**$C(CH_3)(CO_2Et)_2$ (δ_H = 1.94 ppm) and singlet -C***H*$_3$** (δ_H = 1.49 ppm) in ^{1}H NMR spectrum, with HMBC cross-peaks to each respective carbon environment (δ_C = 35.93 ppm and δ_C = 20.05 ppm) in addition to carbonyl carbons (δ_C = 172.31 ppm, 2C) (Figure A1.69-72). Proton and carbon relative integrals at both α (δ_H = 4.26 ppm, 4H; δ_C = 60.93 ppm, 2C) and β (δ_C = 14.06 ppm, 2C) positions on the ethyl chains corroborate the full assignment.

Indicative FT-IR bands for **PP_{OPh}**, C_{Alk}-O (1244 cm^{-1}) and C_{Ar}-O (1080 cm^{-1}), are similar to **PP_{Bn}** and corroborate the NMR spectroscopic data, validating ether connection (Figure A1.68). The presence of the **PP_{M}** ester moiety was likewise confirmed by FT-IR

spectroscopy with absorption bands for C=O (1736 cm^{-1}) and C-O (1253 and 1115 cm^{-1}) (Figure A1.73).

Successful modification of **PP_{Br}** with lithium phenylacetylide resulted in the synthesis internal alkyne-containing **PP_{PA}**. **PP_{PA}** was similarly confirmed by salient ^1H NMR resonances: *o*-C***H*** (δ_H = 7.47 ppm), *m*/*p*-C***H*** (δ_H = 7.32 ppm), and -C***H*$_2$**≡ (δ_H = 2.49 ppm); and FT-IR ν (cm^{-1}) absorptions: 1598 and 1491 (ν (C=C)), 754 (ν (C=C_{Ar})), and (ν (C-H_{Ar})) (Figure A1.74-78). Coupling confirmation of modifier (*o*-***C***H, δ_C = 131.72 ppm**)** to copolymer side-chain (-C***H*$_2$**≡) was confirmed through cross-peaks in the HMBC spectra (Figure A1.77).

Polymer TGA thermographs displayed a singular mass loss event (Figure A1.68, A1.73, and A1.78). Thermal characterisation of **PP_{OPh}** yielded increased thermal stability compared to **PP_{Bn}** (T_{Max} = 407 °C), potentially due to the greater bond dissociation energy of ether C–O *vs* ester (Table A1.5).[76] This is consistent with the significantly greater T_{Max} of **PP_{PA}** (457 °C); the replacement of weaker C–O with thermally robust C–C connections may offer explanation. **PP_{M}** exhibited decreased thermal stability (T_{Max} = 406 °C) compared with closely related ester-modified polymer **PP_{Ac}**. DSC evidenced elevated T_m for **PP_{OPh}** (95.8 °C), **PP_{PA}** (96.3 °C), and **PP_{M}** (96.4 °C) *vs* **PP_{Br}**. Notably, T_m values for **PP_{OPh}** and **PP_{PA}** are in line with other benzyl functional polymers, which overall appear elevated *vs* alkyl functional polymers or nascent **PP_{Br}**, and can be attributed to π-π stacking of the aromatic groups.[71]

In line with prior discussed polymers, trends to increased M_n coincided with theoretical increases *vs* **PP_{Br}**. **PP_{M}**, **PP_{OPh}**, and **PP_{PA}** ($M_{n,\ SEC}$ = 5300, 4800, and 4900 g mol^{-1} respectively) (Figure A1.68, A1.73, and A1.78 and Table A1.5).

Comparative polymers isolated from polymerisation by **M2** and **M3** underwent quantitative post-modification at 95 °C within 96 h, evidencing analogous spectroscopic handles relative to **M1** derived polymers, with KOPh and KDEMM (Figure A1.93-100). Polymer M_n of all materials displayed a trend to lower masses experimentally *vs* theoretical, in addition to a marginal broadening of the distribution, whilst T_m remained consistent with the parent polymers in keeping with alternate modified ^{i}**PP$_{Br}$** and ^{s}**PP$_{Br}$** materials; ^{s}**PP$_{M}$** serves as exemplative data for these observations ($M_{n,\,SEC}$ = 85 800 g mol^{-1}, $M_{n,\,th}$ = 107 900 g mol^{-1}, $Đ_m$ = 2.31, and T_m = 103 °C) (Table A1.5).

2.4.6. Synthesis and characterisation of synthetic rubbers *via* vulcanisation of PP$_{AA}$

Cross-linking of unsaturated polymers is an established method for altering material properties; from self-assembly,[77] to industrial styrene-butadiene rubbers (SBR) with improved mechanical properties.[78] Natural Rubber and, later, SBR latexes have been routinely vulcanised in the presence of sulfur or organic peroxide crosslinking agents.[79] For ethylene-propylene-diene terpolymers, modifiers such as silica and carbon black have further been incorporated in an effort to optimise vulcanisation kinetics and mechanical and physical properties of the resultant rubber.[80,81]

DSC evidenced the accessibility and latent reactivity of the pendant vinyl functionality of **PP$_{AA}$** through successive heating cycles (Figure 2.3). Heating cycles 1 and 2 were limited to 120 °C to anneal the material prior to heating to 225 °C. In cycle 3, a clear exotherm from the spontaneous crosslinking of the vinyl groups was observed. Cycle 4 displayed no further exotherm but a decrease in T_m (84.5 °C) and crystallinity (19%) compared to **PP$_{AA}$**. The FT-IR spectrum displayed an absence of all =CH absorptions and

C=C bend (1058 cm^{-1}) associated with the nascent polymer and developed a new C=C stretch (1668 cm^{-1}) (Figure A1.110). The resultant cross-linked polymer (***x*PP$_{AA}$**) was insoluble rendering solution-phase NMR spectroscopic analysis impossible.

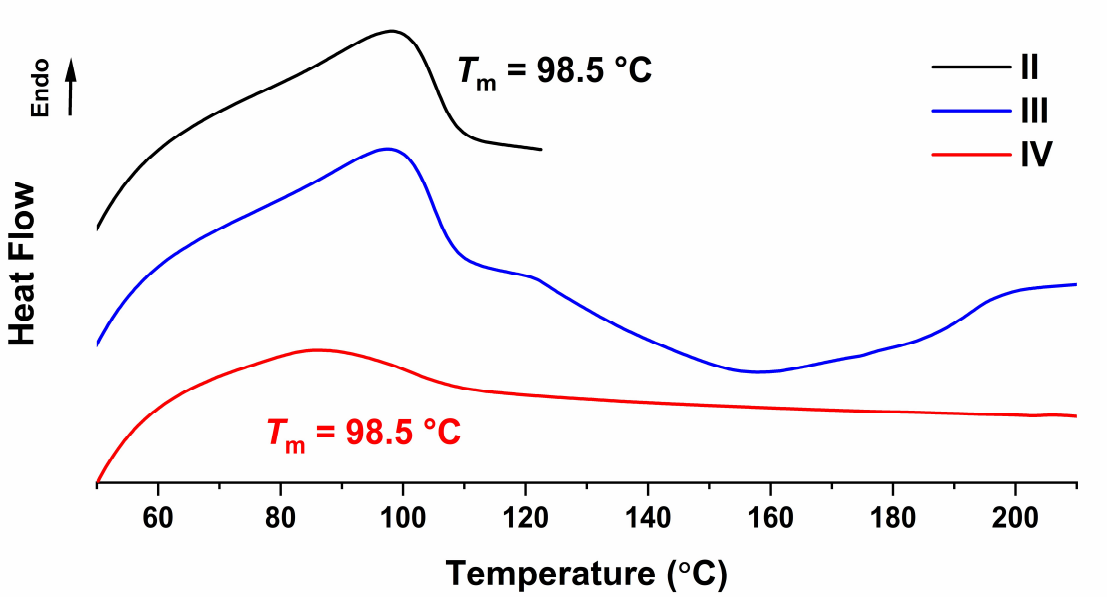

Figure 2.3 DSC curves of **PP$_{AA}$** illustrating successive heating cycles. Heating rate 20 °C min^{-1}.

Given the propensity of **PP$_{AA}$** to undergo thermally activated crosslinking, vulcanisation feasibility was investigated (Scheme 2.3). DSC studies in line with work conducted by Restrepo-Zapata *et al.*, who were able to fit simulated results and extract kinetic parameters, were investigated (Figure A1.108).[79] Relatively high loadings of S_8 (10 phr; parts per hundred rubber) and common accelerant 2-mercaptobenzothiazole ($C_6H_4(NH)SC{=}S$, MBT) (5 phr) were also used to ensure, in the absence of optimisations, sufficiently high conversion of bound acrylate moieties. Resulting thermograms display endothermic features corresponding to the melting points of sulfur (113 °C) and MBT (177–181 °C) in addition to exotherms between 180–230 °C indicative of curing proceeded by sulphur crosslinking to yield vulcanised-**PP$_{AA}$** (***v*PP$_{AA}$**). The magnitude of vulcanisation exotherms exceed those of the nascent copolymer baseline, providing

evidence for the desired transformation (Figure A1.107). Furthermore, the vulcanisation reaction was followed by dynamic rheology (Figure 2.4 and A1.108). During the initial temperature ramp, crosslinking onset (T_v) was observed at 150 °C, corresponding to an increase in the storage modulus (G'); as the reaction progresses G' increases from 18 KPa (0.5 h) to a final value of 92 KPa post 6 h of curing at 200 °C. The storage modulus is associated with the elastic response of a viscoelastic material and the observed increase in this parameter from molten **PP$_{AA}$** can be directly attributed to the formation of crosslinks which are able to store elastic potential energy. These results demonstrate that copolymers containing tuneable degrees of unsaturation can be synthesised and undergo industrially relevant post-polymerisation transformation reactions including cross-linking though conventional vulcanisation.

v*PP$_{AA}$** is a black, insoluble, rubbery material, and was characterised by TGA, FT-IR and solid-state nuclear magnetic resonance (ssNMR) spectroscopy (Figure A1.110). Analogous to ***x*PP$_{AA}$**, ***v*PP$_{AA}$** evidenced an absence of all CH= and C=C vibrations found in **PP$_{AA}$**, yet displayed new characteristic transitions: CH= (1321 cm^{-1}) and C–S (754 and 725 cm^{-1}).[82,83] Infrared S–S stretching transitions (510–450 cm^{-1}) were not observed in the wavenumber range studied. TGA analysis of ***v*PP$_{AA}$** exhibited two major mass loss events. A 70 wt% mass-loss was observed in the region 325–475 °C. This is a similar temperature to the >90% mass loss observed for both **PP$_{AA}$** and ***x*PP$_{AA}$**, confirming that the main polymeric framework is preserved during vulcanisation. The remaining mass was lost at T_{Max} = 589 °C. Furthermore, ***v*PP$_{AA}$**, like the crosslinked variant, have a minor T_{Max} = 372 °C which can be attributed to crosslinking. The solid-state ^{13}C NMR spectrum of ***v*PP$_{AA}$** shows a broad resonance around δ_C = 106–145 ppm, which is not present in the solution-phase spectrum of **PP$_{AA}$**, and corresponds to ***C–S resonances at the crosslink

junctions α to the pendant olefin. Winters *et al.* showed that broad resonances in ssNMR spectra at $\delta_C = 117$ and 151 ppm arise from ethylene propylene diene terpolymer vulcanisation, corroborating with ***v*PP$_{AA}$** and inferring successful vulcanisation to yield a propylene-based rubber.[84,85] The identified peaks were further absent in ^{13}C cross polarization magic-angle spinning (CPMAS) with non-quaternary suppression (CPNQS), whereby only signals of the non-protonated carbons and methyl groups appear in the CPNQS spectra. Mechanisms of accelerant-based vulcanisations support the presence of protons α to the C–S linkage and their subsequent characterisation herein.[86,87]

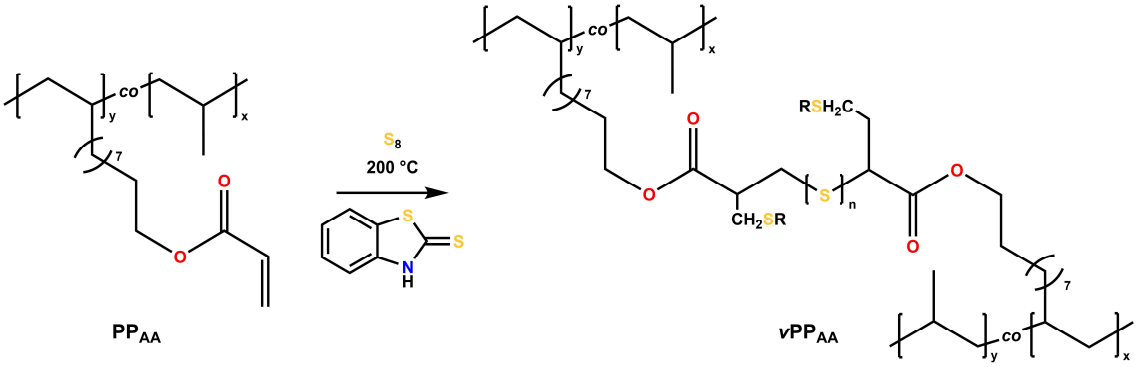

Scheme 2.3 Sulfur vulcanisation to form ***v*PP$_{AA}$**, the structure of which is adapted from the mechanism provided by Verbruggen *et al.*.[84]

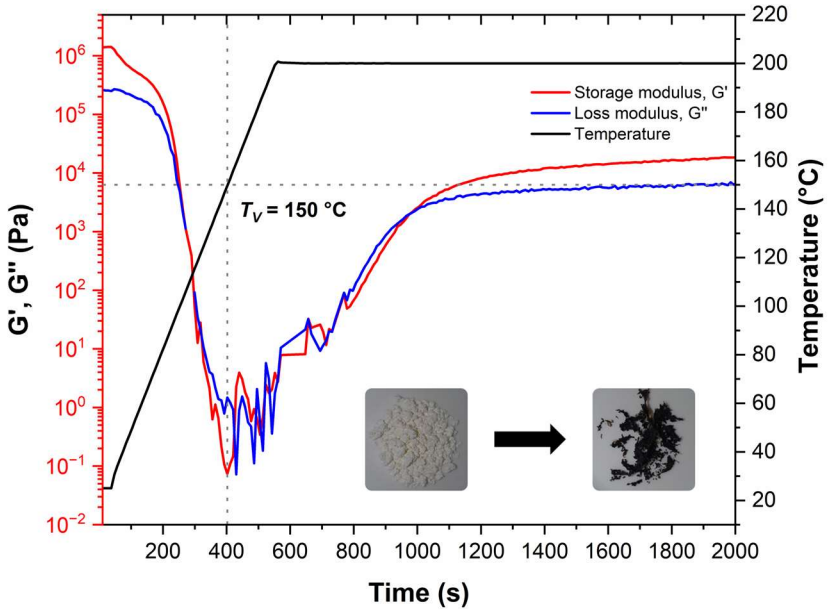

Figure 2.4 Rheometry (ω = 1 rad s^{-1}, 0.2% strain; temperature ramp 25–200 °C at 20 °C min^{-1}) as a function of time for PP$_{AA}$/S/MBT vulcanisation. Initial phase (t ≤ 2000 s) showing onset of vulcanisation at 150 °C. Dynamic crosslinking shown by increase in storage modulus over time after exceeding the polymer T_m.

2.4.7. Hot melt adhesive performance of hydroxyl functionalised polypropylenes

Interfacial adhesion is commonly investigated by lap shear strength (LSS) testing.[46,88] Recently reported work by Jasinska-Walc *et al*. highlighted the application of propylene-based hydroxyl-functionalised terpolymers for use as hot melt adhesives (HMAs).[89] Hydroxyl-functional PPs, **PP$_{EAE}$** and **PP$_{DEOA}$**, were chosen as suitable candidates for this application and compared against **PP**, **PP$_{Br}$**, and **PP$_{DEA}$**. LSS tests were conducted between aluminium and steel substrates with an application temperature of 130 °C in line with this work to quantify the effectiveness of the functional materials as HMAs (Figure 2.5 and Table A1.8).

Unfunctionalised **PP** displays significantly lower adhesive strengths (<1 MPa) to both steel and aluminium when compared with their functionalised counterparts; lending credence to the relationship between incorporated polar functionality and adhesive performance. Interestingly, all copolymers studied here evidence increased adhesion to the aluminium surface (1.8–3.9 MPa) relative to **PP.** The effect is less pronounced for steel, where **PP$_{Br}$** and **PP$_{DEA}$** have negligible improvements to adhesion. Regarding steel, increasing heteroatom content is positively correlated to increasing adhesive strength, with **PP$_{DEOA}$** recording the largest overall mean adhesive force (5.0 MPa), a 64-fold increase *vs* **PP**. The difference between observed adhesive strengths for the two metal substrates can likely be attributed to differences in morphology and polarity.[89-91] It might be reasonably inferred that lone pair containing moieties interact *via* electrostatic effects to aluminium oxides present on the surface of the aluminium. Taking the mean values, a correlation between increasing binding sites and adhesive strength is observed, but the measurement error prevents conclusive interpretation at this stage.

Given the higher incorporation of free hydroxyl groups relative to comparative materials,[46,89] adhesive strength would be expected to be far greater. However, the degree of crystallinity and low M_n of the PPs result in a low degree of entanglement, and correlates to poor adhesive performance. This is evident from frequently observed cohesive, as opposed to interfacial failure (Figure A1.107).

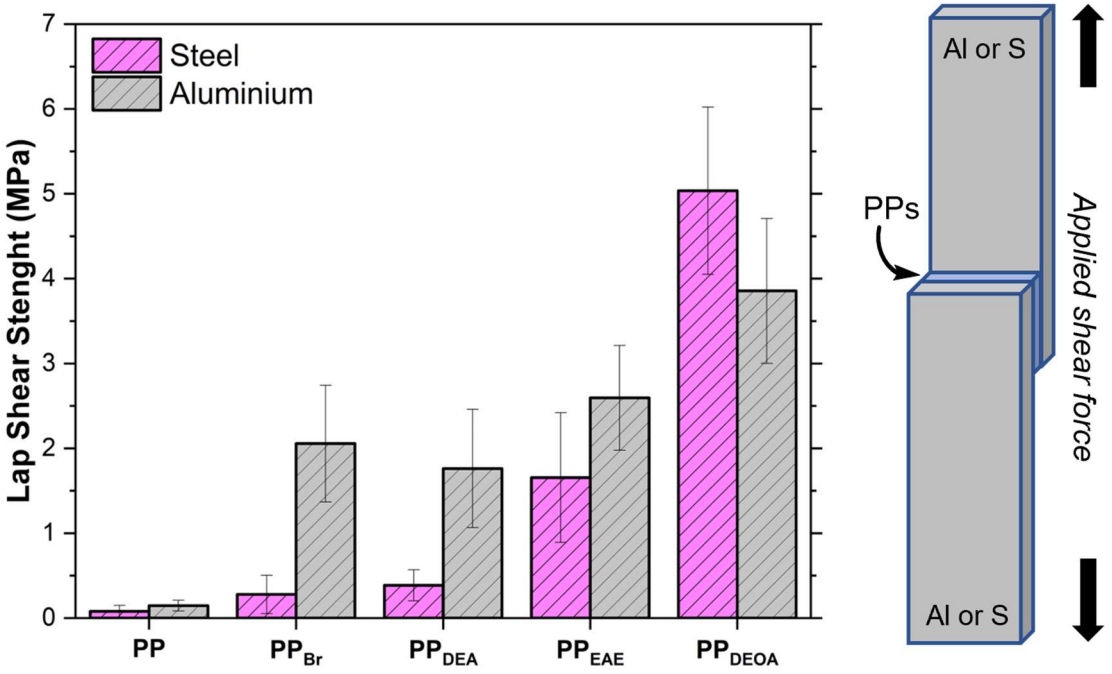

Figure 2.5 Lap shear strength tests with functional polymers as the adhesive interlayers. Error bars represent standard deviation.

2.4.8. Thermal stability studies of phosphonate functionalised polypropylenes

PP exhibits poor fire resistance, thus restricting its use in a number of applications subject to fire safety standards.[92,93] Traditionally, PP flame retardancy is improved through the additive use of halogenated compounds, often in conjunction with inorganics.[94] Undesirable consequences of physical mixing include the propensity of resulting blends to migration and leaching,[4] or severely disrupted mechanical properties due to poor chemical and physical compatibility within the polymer matrix.[5] Additionally, many brominated and chlorinated chemicals have proven to be highly persistent,

bioaccumulative, and toxic to animals and humans.[95-98] The development of halogen-free systems,[99] phosphorus based flame retardant (FR) systems in particular,[100] have been the subject of more intense investigation in order to circumvent these performance limitations and environmental concerns whilst still providing the desired material properties.

Consequently, **PP$_{PPr}$** and **PP$_{PPh}$** were assessed for their flame retardant properties. TGA is widely employed to assess thermal stability and decomposition temperatures for FR polymeric materials.[101-103] TGA analyses were performed between 50–800 °C under a synthetic air atmosphere (20:80 O_2:N_2) with heating rate of 20 °C min^{-1} (Figure A1.105). Polymers were evaluated by the temperatures at 10% and 50% weight loss ($T_{10\%}$ and $T_{50\%}$) and T_{max}. Additionally, the solid residual char yields at 700 °C were recorded as a measure of the phosphonate's activity in the condensed phase.

The phosphonate-modified polypropylenes **PP$_{PPr}$**, and **PP$_{PPh}$** displayed significantly increased thermal stability compared to **PP$_{Br}$** and **PP**, according to TGA and derivative thermogravimetry (DTG) plots (Figure 2.6 and A1.104). A two-step thermal oxidative degradation process was observed for the phosphonate-modified copolymers, in contrast to the one-step degradation of **PP** and **PP$_{Br}$**. Decomposition of the phosphonate moieties occur during the first stage, as shown by the peaks at 275 °C (**PP$_{PPr}$**) and 338 °C (**PP$_{PPh}$**) in the DTG. The higher $T_{10\%}$ of **PP$_{PPh}$** compared to **PP$_{PPr}$** (323 *vs* 273 °C; Table A1.7) is attributed to a stronger P–O–C linkage induced by the aromatic substituents in the former, which delays the first decomposition stage.[104,105] This is further supported by TGA carried out on **PP$_{PPr}$** under a N_2 atmosphere where the first of two degradation steps was attributed to P–O–C bond scission, compared with the singular degradation step of **PP$_{PPh}$** (Figure A1.106). During this process, formation of the carbonaceous char layer is proposed to shield the material from oxygen and prevent the formation of flammable

gases.[106] This provokes the second decomposition stage to occur at a significantly elevated onset temperature, compared to **PP**.

Notably, polymers exhibited comparable $T_{50\%}$ and T_{max} under an N_2 atmosphere (Figure A1.106); highlighting the impact of functionalisation on the suppression of oxidative decomposition rather than purely altered thermal stability. Evaluating $T_{50\%}$ of $\mathbf{PP_{PPr}}$ and $\mathbf{PP_{PPh}}$ against **PP** (Table A1.7) confirms improvement between of 140–160 °C and 132–175 °C, respectively. Importantly, improved thermal stability against the brominated copolymers by 47–72 °C validates beneficial characteristics of phosphonate post-modification. Furthermore, both $^{i}\mathbf{PP_{PPr}}$ and $^{s}\mathbf{PP_{PPr}}$ displayed improvements to thermal stability ($T_{50\%}$ = 416 and 413 °C, T_{max} = 438 and 437 respectively) relative to their corresponding homopolymers ($T_{50\%}$ = 331 and 353 °C, T_{max} = 337 and 370 respectively) despite low incorporation levels (1.9 and 2.4 mol% respectively) (Figure A1.87). Increased incorporation levels in both $\mathbf{PP_{PPr}}$ and $\mathbf{PP_{PPh}}$ correlated to increased thermal stability with respect to $T_{50\%}$ and T_{max}; however, plateauing at > 6.8 mol% incorporation suggests a limit in the maximum efficiency. Although $T_{50\%}$ and T_{max} showed no improvement at highest incorporation levels, the residual char for both $\mathbf{PP_{PPr}}$ and $\mathbf{PP_{PPh}}$ continued to increase with increasing phosphorus content. $\mathbf{PP_{PPr}}$ afforded the highest char yield (9.4%) whereas $\mathbf{PP_{PPh}}$ observed the highest $T_{50\%}$ (452 °C) and T_{max} (458 °C; Table A1.7).[10] Polymer blending of **PP** and $\mathbf{PP_{PPr}}$ or $\mathbf{PP_{PPh}}$ (80:20) (Figure 2.6) demonstrated tunability with respect to copolymer loadings and elicited improved thermal stability compared to the homopolymer enabling targeted applicability.

The presence of incorporated nitrogen was perceived to impact thermal stability by TGA. Thermographs of $\mathbf{PP_{DEA}}$ under an inert atmosphere evidenced a single mass loss event with increased $T_{50\%}$ (459 °C) compared to $\mathbf{PP_{Br}}$. Under a synthetic air atmosphere there

is a delayed major mass loss event ($T_{50\%}$ = 424 °C) caused by gradual initial polymer decomposition (Figure 2.6). This is attributed to generation of inert gases with functional group decomposition, serving to dilute the combustible gasses, delaying thermal oxidative decomposition.[107] Compared with phosphonated and halogenated polymers, which exhibit improved thermal stability, **PP$_{DEA}$** outperforms them with respect to $T_{50\%}$. No further synergistic improvements in thermal stability were observed by blending **PP$_{DEA}$** with **PP** or additionally with **PP$_{PPr}$**.

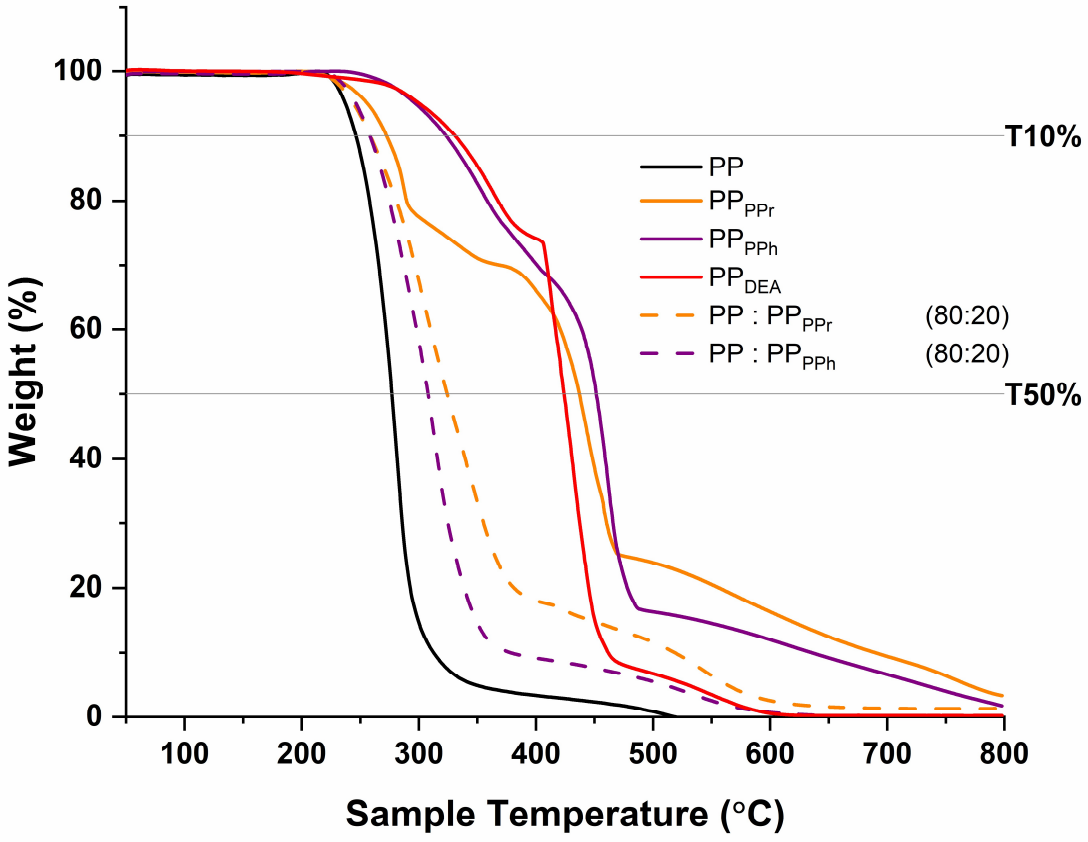

Figure 2.6 Bulk properties illustrated by **PP$_{PPh}$**, **PP$_{PPr}$**, and **PP$_{DEA}$** exhibiting improved thermal stability under a synthetic air atmosphere (20:80 O_2:N_2) with heating rate of 20 °C min^{-1} by TGA. Blending capabilities of functional copolymer and PP highlighted.

2.4.9. Surface property modification

Polymer wettability is important in coating applications. Consequently, the propensity for hydrophobic ($\theta > 90$ °) or hydrophilic ($\theta < 90$ °) character was assessed by static

water-contact angle measurements.[108] All homopolymers displayed more hydrophobic character (95-110 °) compared with their modified congeners (Table A1.5). Parent polymer M_n and tacticity evidenced some influence on the degree of altered hydrophobicity with both **^{i}PP** and **^{s}PP** displaying significant differences between homo- and modified polymers even at low incorporation (2 mol%) when compared to the subtle differences observed for **M1** derived (co)polymers; **^{i}PP$_{DEA}$**, which contains pendant tertiary amines, showed the most hydrophilic character (θ = 83 °) at this incorporation level. As anticipated, the influence of functionality on water-contact angle was related to incorporation; higher incorporation levels of heteroatoms (O, P, and N) elicited more pronounced hydrophilic character. Phosphonated polymers were assessed in this regard: **PP$_{PPr}$** θ = 82, 80, and 71 (4, 6, and 8 mol% respectively) and **^{i}PP$_{PPr}$** θ = 93, 90, and 84 ° (2, 4, and 6 mol% respectively) (Figure 2.7).

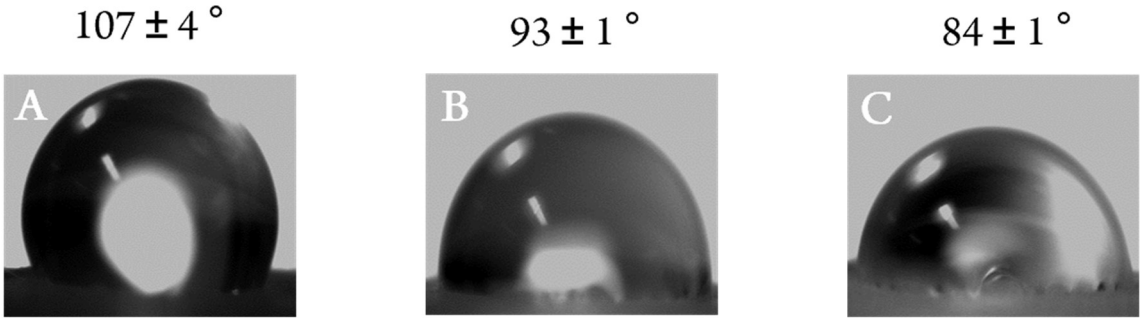

Figure 2.7 Water contact angles of (A) **^{i}PP$_{Br}$** (2 mol%), (B) **^{i}PP$_{PPr}$** (2 mol%), and **^{i}PP$_{PPr}$** (6 mol%).

2.5. Conclusions

A general methodology for the preparation of a diverse range of FPs has been developed. A brominated polypropylene was utilised as a tuneable and versatile platform copolymer that can be readily post-functionalised by simple nucleophilic substitution protocols. The developed methodology is applicable to **PP** materials of differing molecular weight and tacticity, and the resultant functional polymers exhibit significantly altered bulk thermal

and rheological, and surface properties compared to **PP**. Modified **PP** with pendant acrylate functionality was crosslinked by vulcanisation. The diverse properties of the FPs have been explored in the context of applications including flame retardancy and hot-melt adhesion. We envisage this inexpensive, modular, and widely applicable copolymerisation – post-modification approach will aid in the development of high-value next generation functional polyolefins, whereby bespoke designer polymers can be synthesised to target precise applications.

2.6. References

1 G. Natta, P. Pino, P. Corradini, F. Danusso, E. Mantica, G. Mazzanti, G. Moraglio, *J. Am. Chem. Soc.*, 1955, **77**, 1708-1710.
2 K. Ziegler, E. Holzkamp, H. Breil, H. Martin, *Angew. Chem.*, 1955, **67**, 426.
3 I. Novák, E. Borsig, L. u. Hrčková, A. Fiedlerová, A. Kleinová, V. Pollák, *Polym. Eng. Sci.*, 2007, **47**, 1207-1212.
4 M. Yılmaz, A. Akar, N. Köken, N. Kızılcan, *J. Appl. Polym. Sci.*, 2020, **137**, 49023.
5 A. u. R. Shah, D.-w. Lee, Y.-q. Wang, A. Wasy, K. C. Ham, K. Jayaraman, B.-S. Kim, J.-I. Song, *T. Nonferr. Metal. Soc.*, 2014, **24**, s81-s89.
6 M. D. Purgett and O. Vogl, *J. Polym. Sci., Part A: Polym. Chem.*, 1988, **26**, 677-700.
7 R. Tanaka, H. Fujii, T. Kida, Y. Nakayama, T. Shiono, *Macromolecules*, 2021, **54**, 1267-1272.
8 M. Huang, J. Chen, B. Wang, W. Huang, H. Chen, Y. Gao, T. J. Marks, *Angew. Chem. Int. Ed.*, 2020, **59**, 20522-20528.
9 X. Wang, Y. Wang, X. Shi, J. Liu, C. Chen, Y. Li, *Macromolecules*, 2014, **47**, 552-559.
10 N. Blake, Z. R. Turner, J.-C. Buffet, D. O'Hare, *Polym. Chem.*, 2023, **14**, 3175-3185.
11 R. Bacskai, *J. Polym. Sci., Part A: Gen. Pap.*, 1965, **3**, 2491-2510.
12 C. J. Kay, P. D. Goring, C. A. Burnett, B. Hornby, K. Lewtas, S. Morris, C. Morton, T. McNally, G. W. Theaker, C. Waterson, P. M. Wright, P. Scott, *J. Am. Chem. Soc.*, 2018, **140**, 13921-13934.
13 T. C. M. Chung, *Macromol. React. Eng.*, 2014, **8**, 69-80.
14 A. Keyes, H. E. Basbug Alhan, E. Ordonez, U. Ha, D. B. Beezer, H. Dau, Y.-S. Liu, E. Tsogtgerel, G. R. Jones, E. Harth, *Angew. Chem. Int. Ed.*, 2019, **58**, 12370-12391.
15 T. C. Chung, *Prog. Polym. Sci.*, 2002, **27**, 39-85.
16 H. Wang, H. Niu, J.-Y. Dong, *Polymer*, 2017, **126**, 109-115.
17 N. Kawahara, J. Saito, S. Matsuo, H. Kaneko, T. Matsugi, S.-i. Kojoh, N. Kashiwa, *Polym. Bull.*, 2007, **59**, 177-183.
18 T. C. Chung and D. Rhubright, *Macromolecules*, 1993, **26**, 3019-3025.
19 H. L. Lu, S. Hong, T. C. Chung, *J. Polym. Sci., Part A: Polym. Chem.*, 1999, **37**, 2795-2802.
20 W. Lin, Z. Shao, J.-y. Dong, T. C. M. Chung, *Macromolecules*, 2009, **42**, 3750-3754.
21 Y. Wang, Q. Wang, C. Tan, C. Chen, *J. Am. Chem. Soc.*, 2024, **146**, 6837-6845.
22 J. Chen, Y. Gao, T. J. Marks, *Angew. Chem. Int. Ed.*, 2020, **59**, 14726-14735.
23 M. Atiqullah, M. Tinkl, R. Pfaendner, M. N. Akhtar, I. Hussain, *Polym. Rev.*, 2010, **50**, 178-230.
24 X.-Y. Wang, Y.-Y. Long, Y.-X. Wang, Y.-S. Li, *J. Polym. Sci., Part A: Polym. Chem.*, 2014, **52**, 3421-3428.
25 J. Chen, A. Motta, B. Wang, Y. Gao, T. J. Marks, *Angew. Chem. Int. Ed.*, 2019, **58**, 7030-7034.
26 L. S. Boffa and B. M. Novak, *Chem. Rev.*, 2000, **100**, 1479-1494.
27 H. Hagihara, K. Tsuchihara, J. Sugiyama, K. Takeuchi, T. Shiono, *Macromolecules*, 2004, **37**, 5145-5148.
28 J.-i. Imuta, N. Kashiwa, Y. Toda, *J. Am. Chem. Soc.*, 2002, **124**, 1176-1177.
29 H. Terao, S. Ishii, M. Mitani, H. Tanaka, T. Fujita, *J. Am. Chem. Soc.*, 2008, **130**, 17636-17637.
30 X.-Y. Wang, Y.-X. Wang, Y.-S. Li, L. Pan, *Macromolecules*, 2015, **48**, 1991-1998.

31 D. Zhang, L. Pan, Y. Li, B. Wang, Y. Li, *Macromolecules*, 2017, **50**, 2276-2283.
32 B. P. Carrow and K. Nozaki, *Macromolecules*, 2014, **47**, 2541-2555.
33 S. L. J. Luckham and K. Nozaki, *Acc. Chem. Res.*, 2021, **54**, 344-355.
34 R. Nakano and K. Nozaki, *J. Am. Chem. Soc.*, 2015, **137**, 10934-10937.
35 Y. Ota, S. Ito, M. Kobayashi, S. Kitade, K. Sakata, T. Tayano, K. Nozaki, *Angew. Chem. Int. Ed.*, 2016, **55**, 7505-7509.
36 J. Gao, W. Cai, Y. Hu, C. Chen, *Polym. Chem.*, 2019, **10**, 1416-1422.
37 Z. Chen and M. Brookhart, *Acc. Chem. Res.*, 2018, **51**, 1831-1839.
38 L. Guo, W. Liu, C. Chen, *Mater. Chem. Front.*, 2017, **1**, 2487-2494.
39 Editorial, *Nat. Catal.*, 2019, **2**, 735.
40 E. Denkhaus and K. Salnikow, *Crit. Rev. Oncol. Hematol.*, 2002, **42**, 35-56.
41 C. M. Plummer, L. Li, Y. Chen, *Polym. Chem.*, 2020, **11**, 6862-6872.
42 J. Y. Ko, R. M. Appa, S. Oh, N. Son, S. C. Hong, *Polym. Test.*, 2024, **136**, 108488.
43 I. Maksso, R. C. Samanta, Y. Zhan, K. Zhang, S. Warratz, L. Ackermann, *Chem. Sci.*, 2023, **14**, 8109-8118.
44 N. K. Boaen and M. A. Hillmyer, *Chem. Soc. Rev.*, 2005, **34**, 267-275.
45 N. M. G. Franssen, J. N. H. Reek, B. de Bruin, *Chem. Soc. Rev.*, 2013, **42**, 5809-5832.
46 N. R. Ciccia, J. X. Shi, S. Pal, M. Hua, K. G. Malollari, C. Lizandara-Pueyo, E. Risto, M. Ernst, B. A. Helms, P. B. Messersmith, J. F. Hartwig, *Science*, 2023, **381**, 1433-1440.
47 X.-Y. Wang, Y.-G. Li, H.-L. Mu, L. Pan, Y.-S. Li, *Polym. Chem.*, 2015, **6**, 1150-1158.
48 M. Hong, S.-R. Liu, B.-X. Li, Y.-S. Li, *J. Polym. Sci., Part A: Polym. Chem.*, 2012, **50**, 2499-2506.
49 M. Hong, J.-Y. Liu, B.-X. Li, Y.-S. Li, *Macromolecules*, 2011, **44**, 5659-5665.
50 Y.-L. Li, D.-P. Song, L. Pan, Z. Ma, Y.-S. Li, *Polym. Chem.*, 2019, **10**, 6368-6378.
51 G. Acik, E. Sey, M. Tasdelen, *Express Polym. Lett.*, 2018, **12**, 418-428.
52 H. Huang, H. Niu, J.-Y. Dong, *Macromolecules*, 2010, **43**, 8331-8335.
53 S. Bruzaud, H. Cramail, L. Duvignac, A. Deffieux, *Macromol. Chem. Phys.*, 1997, **198**, 291-303.
54 M. Baier, D. Wöll, S. Mecking, *Macromolecules*, 2018, **51**, 1873-1884.
55 R. von Goetze, A. Aljaber, K.-Y. Lee, G. Hill, C. Wallis, G. J. P. Britovsek, *Polym. Chem.*, 2022, **13**, 6377-6385.
56 Y. Doi, Y. Watanabe, S. Ueki, K. Soga, *Makromol. Chem., Rapid Commun.*, 1983, **4**, 533-537.
57 R. Godoy Lopez, C. Boisson, F. D'Agosto, R. Spitz, F. Boisson, D. Gigmes, D. Bertin, *J. Polym. Sci., Part A: Polym. Chem.*, 2007, **45**, 2705-2718.
58 K. Matyjaszewski, J. Saget, J. Pyun, M. Schlögl, B. Rieger, *J. Macromol. Sci. A*, 2002, **39**, 901-913.
59 Y. Inoue and K. Matyjaszewski, *J. Polym. Sci., Part A: Polym. Chem.*, 2004, **42**, 496-504.
60 N. Kawahara, S.-i. Kojoh, S. Matsuo, H. Kaneko, T. Matsugi, J. Saito, N. Kashiwa, *Polym. Bull.*, 2006, **57**, 805-812.
61 P. D. Goring, C. Morton, P. Scott, *Dalton Trans.*, 2019, **48**, 3521-3530.
62 Y. Wang, L. Jiang, X. Ren, F. Guo, Z. Hou, *J. Polym. Sci.*, 2021, **59**, 2324-2333.
63 Y. Konishi, W.-j. Tao, H. Yasuda, S. Ito, Y. Oishi, H. Ohtaki, A. Tanna, T. Tayano, K. Nozaki, *ACS. Macro. Lett.*, 2018, **7**, 213-217.
64 P. J. T. Tait and I. G. Berry, in *Comprehensive Polymer Science and Supplements*, eds. G. Allen and J. C. Bevington, Pergamon, Amsterdam, 1989, pp. 575-584.
65 T. Uozumi and K. Soga, *Makromol. Chem.*, 1992, **193**, 823-831.
66 M. Fineman and S. D. Ross, *J. Polym. Sci.*, 1950, **5**, 259-262.
67 Y. V. Kissin, L. A. Rishina, E. I. Vizen, *J. Polym. Sci., Part A: Polym. Chem.*, 2002, **40**, 1899-1911.
68 C. G. Collins Rice, J. C. Buffet, Z. R. Turner, D. O'Hare, *Chem. Commun.*, 2021, **57**, 8600-8603.
69 W. Zhao, B. Wang, B. Dong, H. Liu, Y. Hu, M. S. Eisen, X. Zhang, *Organometallics*, 2020, **39**, 3983-3991.
70 H. Pizova and P. Bobal, *Tetrahedron Lett.*, 2015, **56**, 2014-2017.
71 G. N. Kangovi and S. Lee, *Macromolecules*, 2017, **50**, 8678-8687.
72 F. G. Bordwell, R. J. McCallum, W. N. Olmstead, *J. Org. Chem.*, 1984, **49**, 1424-1427.
73 F. G. Bordwell, *Acc. Chem. Res.*, 1988, **21**, 456-463.
74 W. N. Olmstead, Z. Margolin, F. G. Bordwell, *J. Org. Chem.*, 1980, **45**, 3295-3299.
75 E. M. Arnett, S. G. Maroldo, S. L. Schilling, J. A. Harrelson, *J. Am. Chem. Soc.*, 1984, **106**, 6759-6767.
76 J. A. Dean, *Lange's Handbook of Chemistry*, 15 edn., McGraw-Hill Professional, 1998.
77 J. Tanaka, A. Evans, P. Gurnani, A. Kerr, P. Wilson, *Polym. Chem.*, 2020, **11**, 2519-2531.
78 R. A. Chapman, in *Handbook of Nonwovens*, ed. S. J. Russell, Woodhead Publishing, 2007, pp. 330-367.

79 N. C. Restrepo-Zapata, T. A. Osswald, J. P. Hernández-Ortiz, *Polym. Eng. Sci.*, 2015, **55**, 2073-2088.
80 S. C. N. Sanches, M. Diniz, R. Lazzarini Dutra, *Polímeros*, 2014, **24**, 269-275.
81 K. C. Dao, *J. Appl. Polym. Sci.*, 1982, **27**, 4799-4806.
82 F. J. Linnig and J. E. Stewart, *Rubber Chem. Technol.*, 1958, **31**, 719-736.
83 G. Socrates, *Infrared and Raman Characteristic Group Frequencies*, 3 edn., John Wiley & Sons Ltd, 2001.
84 R. Winters, W. Heinen, M. A. L. Verbruggen, J. Lugtenburg, M. van Duin, H. J. M. de Groot, *Macromolecules*, 2002, **35**, 1958-1966.
85 C. G. Collins Rice, L. J. Morris, J.-C. Buffet, Z. R. Turner, D. O'Hare, *Chem. Commun.*, 2023, **59**, 12128-12131.
86 A. Y. Coran, in *The Science and Technology of Rubber (Fourth Edition)*, eds. J. E. Mark, B. Erman and C. M. Roland, Academic Press, Boston, 2013, pp. 337-381.
87 P. Ghosh, S. Katare, P. Patkar, J. M. Caruthers, V. Venkatasubramanian, K. A. Walker, *Rubber Chem. Technol.*, 2003, **76**, 592-693.
88 Y. Boutar, S. Naïmi, S. Mezlini, L. F. M. Da Silva, M. Hamdaoui, M. Ben Sik Ali, *J. Adhes. Sci. Technol.*, 2016, **30**, 1913-1929.
89 J. Kruszynski, W. Nowicka, M. Bouyahyi, Y. Liu, L. Yang, A. Rozanski, N. Anbuchezhian, L. Jasinska-Walc, R. Duchateau, *ACS Appl. Polym. Mater.*, 2023, **5**, 3875-3882.
90 J. Haubrich, M. Löbbecke, P. Watermeyer, F. Wilde, G. Requena, J. da Silva, *Appl. Surf. Sci.*, 2018, **433**, 546-555.
91 S. Horiuchi, Y. Liu, T. Hanada, H. Akiyama, *Appl. Surf. Sci.*, 2022, **599**, 153964.
92 M. J. John, in *Green Composites for Automotive Applications*, eds. G. Koronis and A. Silva, Woodhead Publishing, 2019, pp. 43-58.
93 A. K. Sen, B. Mukherjee, A. S. Bhattacharya, L. K. Sanghi, P. P. De, A. K. Bhowmick, *J. Appl. Polym. Sci.*, 1991, **43**, 1673-1684.
94 V. I. Babushok, P. Deglmann, R. Krämer, G. T. Linteris, *Combust. Sci. Technol.*, 2017, **189**, 290-311.
95 I. T. Cousins, C. A. Ng, Z. Wang, M. Scheringer, *Environ. Sci. Process. Impacts*, 2019, **21**, 781-792.
96 R. J. Law, A. Covaci, S. Harrad, D. Herzke, M. A. Abdallah, K. Fernie, L. M. Toms, H. Takigami, *Environ. Int.*, 2014, **65**, 147-158.
97 P. Schmid, M. Kohler, A. C. Gerecke, E. Gujer, M. Zennegg, M. Wolfensberger, *CHIMIA*, 2003, **57**, 509.
98 M. Venier, A. Salamova, R. A. Hites, *Acc. Chem. Res.*, 2015, **48**, 1853-1861.
99 Y. Z. Wang, in *Advances in Fire Retardant Materials*, eds. A. R. Horrocks and D. Price, Woodhead Publishing, 2008, pp. 67-94.
100 S. V. Levchik and E. D. Weil, in *Advances in Fire Retardant Materials*, eds. A. R. Horrocks and D. Price, Woodhead Publishing, 2008, pp. 41-66.
101 M. Hussain, R. J. Varley, Z. Mathys, Y. B. Cheng, G. P. Simon, *J. Appl. Polym. Sci.*, 2004, **91**, 1233-1253.
102 K. Wazarkar, M. Kathalewar, A. Sabnis, *Polym. Compos.*, 2017, **38**, 1483-1491.
103 S. Yang, Y. Hu, Q. Zhang, *High Perform. Polym.*, 2019, **31**, 186-196.
104 Z. Bai, L. Song, Y. Hu, R. K. K. Yuen, *Ind. Eng. Chem. Res.*, 2013, **52**, 12855-12864.
105 L. Wang, B. Yang, Y. Guo, Y. Zhang, N. Wang, F. Li, H. Yu, J. Cui, J. Guo, B. Mu, L. Tian, *High Perform. Polym.*, 2020, **32**, 1169-1180.
106 I. van der Veen and J. de Boer, *Chemosphere*, 2012, **88**, 1119-1153.
107 A. B. Morgan and C. A. Wilkie, *The Non-Halogenated Flame Retardant Handbook*, John Wiley & Sons, Incorporated, Newark, UNITED STATES, 2014.
108 K.-Y. Law, *J. Phys. Chem. Lett.*, 2014, **5**, 686-688.

2.7. Statement of Authorship

Title of Paper	Functionalised polypropylenes; a copolymerisation and post-modification platform
Publication Status	Published in *Macromolecules*
Publication Details	Published in Macromolecules: *Macromolecules*, 2024, 57, 22, 10778–10791

Student Confirmation

Student Name:	Alexander Oscar Edward Evans
Contribution to the Paper	Performed the synthesis, analysis, and application testing. Interpreted the data. Wrote the manuscript, original draft, with review and editing contributions from all authors.

Signature 	Date 02/01/2025

Supervisor Confirmation

Supervisor name and title: Professor Dermot O'Hare
Supervisor comments: I can confirm that the candidate's contribution to this paper is as described above.

Signature 	Date 19/01/2025

Chapter 3 – Flame Retardant Phosphonate-functionalised Polypropylenes

Alexander Evans, Louis J. Morris, Zoë R. Turner, and Dermot O'Hare*

Published in ACS Applied Polymer Materials: *ACS Appl. Polym. Mater.*, 2025, 7, 4, 2508-2516.

3.1. Author contributions

Alexander Evans: Performed the synthesis and analysis of all samples aside from microscale combustion calorimetry and quantitative Br analysis. Interpreted the data. Wrote the manuscript, original draft, review and editing.

Louis J. Morris: Manuscript, review and editing.

Zoë R. Turner: Manuscript, review and editing. Supervision.

Dermot O'Hare: Corresponding author. Manuscript, review and editing. Supervision.

3.2. Abstract

Phosphonate-modified polypropylenes (**PP$_R$**; R = PPr, P(O)(O^{i}Pr)$_2$; PPh, P(O)(OPh)$_2$) have been prepared *via* a two-step synthesis, and display enhanced thermal stability, offering potential as compatible flame-retardant additives for polypropylene (PP) systems. PP typically displays high flammability and poor fire resistance which consequently restricts applications. We find that solution-phase copolymerisation of propylene and 11-bromo-1-undecene using commercial *rac*-ethylenebis(indenyl)zirconium dichloride afforded poly(propylene)-*co*-(11-bromo-1-undecene) with tuneable comonomer incorporation levels up to 8.1 mol%. Solvent-free, quantitative, post-modification of pendant bromine with phosphite esters yielded alkyl (**PP$_{PPr}$**) and aryl (**PP$_{PPh}$**) phosphonate-modified PPs. Increased thermal stability (higher $T_{10\%}$, $T_{50\%}$, T_{max} and %residue at 700 °C) in a synthetic air atmosphere were

determined by TGA with respect to **PP**. Microscale combustion calorimetry (MCC) of both $\mathbf{PP_{PPr}}$ and $\mathbf{PP_{PPh}}$ indicate lower values of heat release capacity (HRC), peak heat release rate (pHRR), and total heat release (THR) compared to those of **PP**, indicating enhanced flame retardancy. Both $\mathbf{PP_{PPr}}$ or $\mathbf{PP_{PPh}}$ can be easily blended with **PP** at **PP**:$\mathbf{PP_R}$ weight ratios 80:20, 90:10, 95:5, and 99:1 respectively. The polymer blends demonstrated higher thermal stability than the homopolymer and so $\mathbf{PP_R}$ offer an alternate strategy for improving the flame-retardant properties of PP-based materials which circumvents additive leaching.

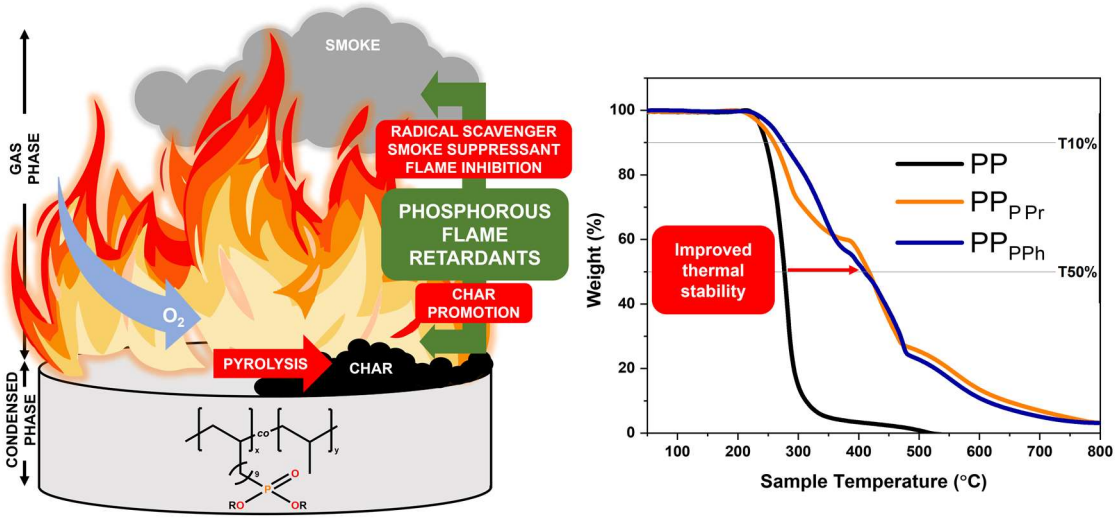

3.3. Introduction

Polyolefins are ubiquitous in everyday life. Since its inception,[1] polypropylene (PP) has been one of the most manufactured polymers in the world; second only to polyethylene (PE).[2] Desirable chemical and mechanical resistance, low toxicity, relative ease of processability, and low production costs have led to widespread utilisation in a plethora of applications. Despite this, pristine PP exhibits poor fire resistance as characterised by limiting oxygen index (LOI), heat release rate (HRR), and flame exposure tests (UL 94);[3-5] thus restricting its use in a number of applications subject to fire safety standards.[6,7]

The flame retardancy of polymers is traditionally improved through the additive use of halogenated compounds, often in conjunction with inorganics such as aluminimum trihydroxide (ATH), magnesium hydroxide, and antimony trioxide.[8] However, many brominated and chlorinated chemicals have proven to be highly persistent, bioaccumulative, and toxic to animals and humans.[9-12] development of halogen-free systems,[13] phosphorus-based flame retardant (FR) systems in particular,[14] have been the subject of more intense investigation in order to circumvent these environmental concerns whilst still providing the desired material properties.

The effectiveness of phosphorus-based FR systems can be attributed to their chemical versatility, low required loadings, and multiple mechanisms by which flammability is reduced in both the condensed and gas-phase.[15-19] Char formation in the condensed phase is stimulated by phosphorous moieties such as phosphite esters ($PO(OR)_3$), phosphonates ($PO(OR)_2R$), and phosphinates ($PO(OR)R_2$), which act as acid precursors and lead to esterification and dehydration. This mechanism serves to blockade oxygen from the substrate whilst additionally preventing the formation of flammable gases.[20] Further improved FR characteristics can be gained from tandem gas-phase mechanisms, whereby $PO^{\cdot}$ acts as a radical scavenger during combustion.[21,22]

Common commercial non-halogenated FR additives for polyolefin systems are typically based on phosphorus, boron, inorganic hydroxides, silicon, and nitrogen-based additives; which are introduced to polymer matrices during processing.[5,23-26] Undesirable consequences of physical mixing include the resulting blends being prone to migration and ultimately leaching,[27] or severely disrupted mechanical properties due to poor chemical and physical compatibility within the polymer matrix.[28] Chemical incorporation of FR-functionality directly into the polymer through copolymerisation has the potential

to provide good FR properties at low comonomer loadings,[29,30] avoiding migration and leaching whilst providing good mechanical performance. For example, phosphorus moieties have been incorporated *via* radical polymerisation in styrene[29] and (meth)acrylate systems[27,31,32] or Pd-catalysed copolymerisation with ethylene[33] yielding promising results.

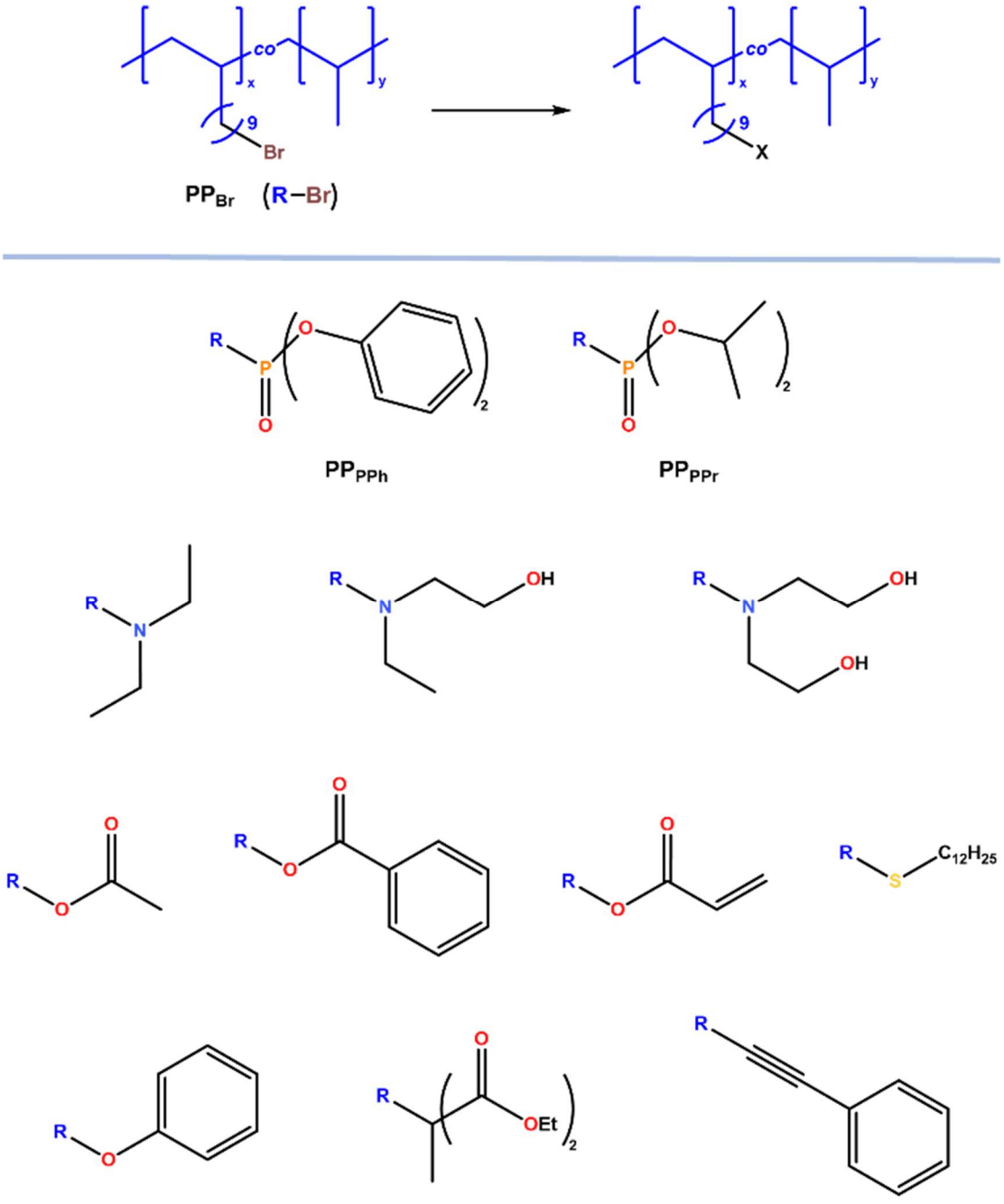

Scheme 3.1 Recently reported synthetic strategy for the post-modificaiton of **PP$_{Br}$** yielding a variety of modified PPs, including **PP$_{PPh}$** and **PP$_{PPr}$**.[34]

However, polyolefin post-modification *via* traditional small molecule nucleophilic substitution chemistry presents solubility and purity complications and is subsequently less developed.[35,36] Our recent report concerning the development of phosphonate-functionalised polypropylene *via* quantitative post-modification of a brominated copolymer with aryl or alkyl phosphite esters (**PP$_R$**; R = PPr, P(O)(O^{i}Pr)$_2$; PPh, P(O)(OPh)$_2$, Scheme 3.1) highlighted potential FR properties.[34] Herein, we build on our previous results regarding the phosponate-modified polymers, offering a more comprehensive study of the materials. Both **PP$_{PPr}$** and **PP$_{PPh}$** have been fully characterised, focusing on thermal stability and their FR efficacy, and displayed significantly improved thermal stability and FR properties when blended with pristine PP.

3.4. Results and Discussion

3.4.1. Solution-phase copolymerisation of propylene and bromoalkenes

The brominated copolymer poly(propylene)-*co*-(11-bromo-1-undecene) (**PP$_{Br}$**) was first prepared by copolymerisation of propylene and 11-bromo-1-undecene (**11-Br**) using a commercially available catalyst, *rac*-ethylenebis(indenyl)zirconium dichloride (**Zr**) (Scheme 3.2a). Subsequent copolymer post-modification was carried out with triisopropyl phosphite (P(O^{i}Pr$_3$)) and triphenyl phosphite (P(OPh$_3$)) according to previously reported work (Scheme 3.2b).[34]

The copolymerisation of propylene and **11-Br** was carried out and results summarised in Table 3.1. Successful incorporation of comonomer was identified by the presence of -C***H$_2$***Br (δ = 3.49 ppm) and -C***H$_2$***CH$_2$Br (δ = 1.97 ppm) in ^{1}H NMR spectra and C–Br stretching frequency (721 cm^{-1}) in the FT-IR spectrum; 3.99–8.12 mol% as judged by

NMR spectroscopy (Figures A2.1–3); enchainment levels of comonomer were consistent with previously reported examples of olefin copolymerisation with ω-halo-1-alkenes[37,38]

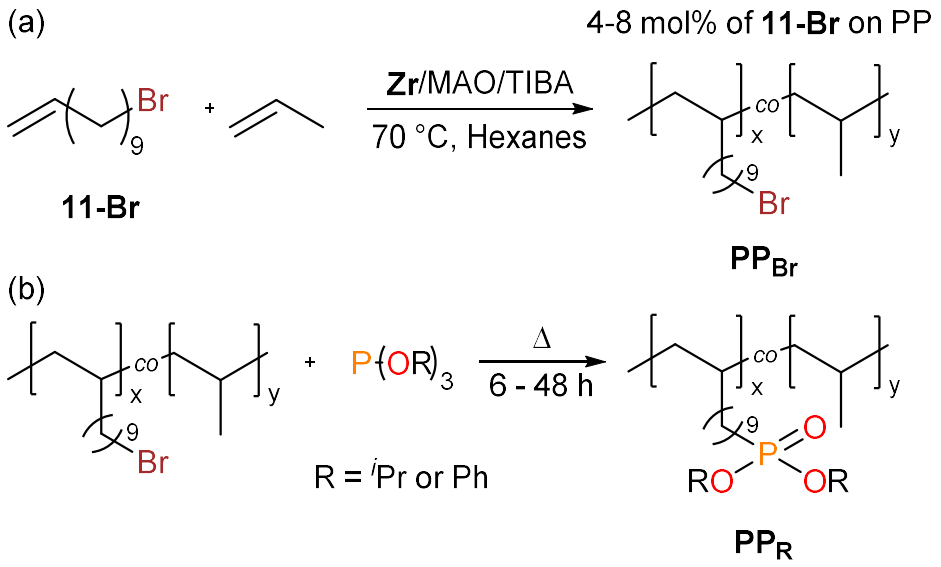

Scheme 3.2 Synthesis of phosphonate-functionalised polypropylenes by (a) copolymerisation and subsequent (b) post-modification.

All copolymers exhibited a monomodal M_n distribution by SEC (Figures A2.4) with narrow polydispersities ($Đ_m$) (1.7–2.2). Under a given set of conditions, the copolymer M_n is lower than polypropylene (Table 3.1, entries 1; 13 600 g mol^{-1} and 2; 5 000 g mol^{-1}) but displays narrower $Đ_m$, yet changing [**11-Br**] had little impact on M_n or $Đ_m$. The reduction of copolymer M_n could be attributed to the chain transfer reactions induced by the spatial active site of **Zr**. Additionally, chain transfer to aluminium alkyl, β-H transfer to metal and monomer are also significant in **Zr** polymerisation.[37,39] Competing coordination of **11-Br** and propylene to the metal centre may accelerate chain transfer reactions, further decreasing copolymer M_n.

Table 3.1 (Co)polymerisation data of propylene and **11-Br**.[a]

Entry	**11-Br** (mM)	Activity[b]	Productivity[c]	Yield (g)	Incorporation[d] (mol%)	M_n[e, f] (g mol^{-1})	$Đ_m$[e]	T_m[g] (°C)	Crystallinity[g] (%)
1	0	5467	26.1	6.53	0.00	13 600	2.2	114	44
2	91	1686	8.1	2.01	3.98	5 000	1.9	90	43
3	137	1594	7.6	1.90	6.63	4 500	1.7	81	41
4	182	1025	4.9	1.22	8.12	5 200	1.7	78	18

[a]Conditions: *rac*-ethylenebis(indenyl)zirconium dichloride ([**Zr**] = 0.024 mM), MAO used as a cocatalyst and scavenger with $[Al]_0$:$[\mathbf{Zr}]_0$ = 1000:1. Molar ratio of $[TIBA]_0$:$[\mathbf{11\text{-}Br}]_0$ = 1:10, 0.5 mL toluene, 49.5mL hexanes, propylene 2 bar, polymerisation time = 30 min, polymerisation temperature = 70 °C. Polymerisation and analysis were performed in duplicate and mean values are reported [b]kg_{PP} mol_{Zr}^{-1} h^{-1} bar^{-1}. [c]kg_{PP} g_{Zr}^{-1} h. [d]Determined by ^{1}H NMR. [e]Determined by SEC. [f]g mol^{-1}. [g]Determined by DSC.

3.4.2. Post-polymerisation modification of bromine functionalised polypropylene using phosphite esters

Our previously reported studies evidence the C-Br bond transformation to C-P[34] *via* the Michaelis Arbuzov reaction.[40-42] Characterisation was found to be fully consistent with the phosphonate group being covalently bound to the polymer and quantitatively converted (Figure A2.5, A2.7, and A2.8). The reaction of **PP$_{Br}$** with neat triisopropyl phosphite (P(O^{i}Pr)$_3$) or triphenyl phosphite (P(OPh)$_3$) led to corresponding polypropylene-phosphonates (**PP$_{PPr}$** and **PP$_{PPh}$**; Table 3.2, Scheme 3.2b**).** Full conversion was achieved within 6 h and 48 h respectively, as confirmed by ^{1}H NMR spectroscopy through the absence of the methylene protons adjacent to the bromide (Figures A2.7 and A2.8), irrespective of incorporation levels. Complimentary convection compensated diffusion experiments support the modifier-polymer coupling with key modifier ^{1}H NMR resonances (eg: **PP$_{PPr}$** = δ 4.80–4.68 ppm –OC***H***Me$_2$ and **PP$_{PPh}$** = 7.39–7.23 ppm –OAr***H***) displaying the same diffusion coefficient to that of polymer backbone resonances (**PP$_{PPr}$** = 2.8x10^{-6} cm^2 s^{-1} and **PP$_{PPh}$** = 2.1x10^{-6} cm^2 s^{-1}; Figure 3.1, Figure A2.1).

Monomodal SEC distributions were observed for the modified polymers with consistent $Đ_m$ to the parent copolymer (Figure A2.6). However, a significant deviation between $M_{n,\,th}$ and $M_{n,\,SEC}$ (Table A2.1) was evidenced and can be attributed to altered polymer polarity affecting polymer-column interaction. Since the Mark-Houwink correlation is not known for functionalised PP, and the presence of the polar group is likely to affect the radius of gyration in solution, this may explain the experimental data;[43] however it is assumed that the backbone chain length is unchanged during post-polymerisation modification. Quantitative Br analysis evidenced removal of the Br functionality in **PP$_{PPr}$** and **PP$_{PPh}$** (Table 3.2, entries 5 and 8); 0.23 ± 0.2 and 0.12 ± 0.1 wt% brominated comonomer

respectively post modification. **PP$_{Br}$** (Table 3.1, entry 4) exhibited 23.7 ± 3.7 wt% comonomer incorporation level, which tracks with 18.7 wt% incorporation as determined by ^{1}H NMR spectroscopy.

Differential scanning calorimetry (DSC) (Table 3.2: entries 5–7) revealed decreased crystallinity (27–11%) and lower melting temperatures (T_m = 89–77 °C; S23) for **PP$_{PPr}$**, compared to the corresponding **PP$_{Br}$**. Conversely to **PP$_{PPr}$**, DSC traces of **PP$_{PPh}$** (Table 3.2: entries 8–10) exhibited increased crystallinity (32–24%) and T_m (95–76 °C) (Figure A2.5) versus the corresponding **PP$_{Br}$**, possibly due a decrease in entropy due to π-π stacking of the phenyl groups.

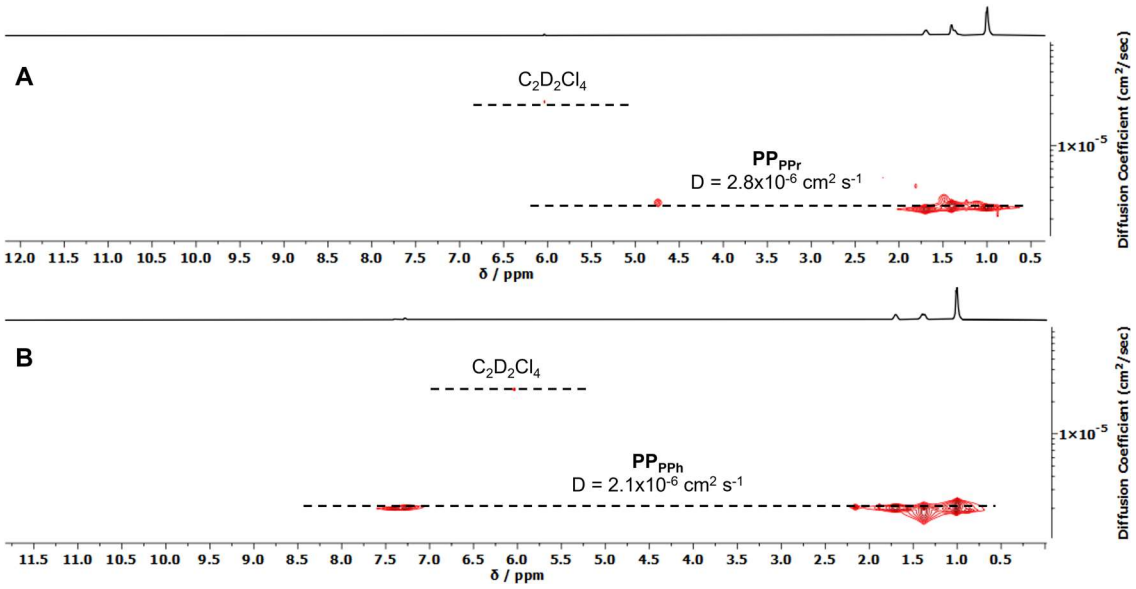

Figure 3.1 DOSY ^{1}H NMR spectra (500 MHz, $C_2D_2Cl_4$, 393 K)of **PP$_{PPr}$** (**A**) and **PP$_{PPh}$** (**B**).

3.4.3. Thermal stability studies of phosphonate functionalised polypropylene

Thermal gravimetric analysis (TGA) is widely employed to assess thermal stability and decomposition temperatures for FR polymeric materials.[41,42,44] TGA analyses were performed between 50–800 °C under a synthetic air atmosphere (20:80 O_2:N_2) with heating rate of 20 °C min^{-1} (Figure 3.2 and Table 3.2). Polymers were evaluated by the

temperatures at 10% and 50% weight loss ($T_{10\%}$ and $T_{50\%}$) and the temperature of maximum rates of weight loss (T_{max}). Additionally, the solid residual char yields at 700 °C were recorded as a measure of the phosphonate's activity in the condensed phase. Notably, polymers exhibited comparable $T_{50\%}$ and T_{max} under an N_2 atmosphere (Figure A2.9); highlighting the impact of functionalisation on the suppression of oxidative decomposition rather than purely altered thermal stability.

The phosphonate-modified polypropylenes **PP$_{PPr}$**, and **PP$_{PPh}$** displayed significantly increased thermal stability compared to **PP$_{Br}$** and **PP**, according to TGA and derivative thermogravimetry (DTG) plots (Figure 3.2 and Table 3.2). A two-step thermal oxidative degradation process was observed for the phosphonate-modified copolymers, in contrast to the one-step degradation of **PP** and **PP$_{Br}$**. Decomposition of the phosphonate moieties occur during the first stage, as shown by the peaks at 275 °C (**PP$_{PPr}$**) and 338 °C (**PP$_{PPh}$**) in the DTG. The higher $T_{10\%}$ of **PP$_{PPh}$** compared to **PP$_{PPr}$** (323 *vs* 273 °C; Table 2, entries 7 and 10) is attributed to a stronger P–O–C linkage induced by the aromatic substituents in the former, which delays the first decomposition stage.[45,46] This is further supported by TGA carried out on **PP$_{PPr}$** under a N_2 atmosphere where the first of two degradation steps was attributed to P–O–C bond scission, compared with the singular degradation step of **PP$_{PPh}$** (Figure A2.9). During this process, formation of the carbonaceous char layer serves to shield the material from oxygen and prevent the formation of flammable gases.[16] This provokes the second decomposition stage to be at a significantly elevated temperature compared to **PP**. Evaluating $T_{50\%}$ of **PP$_{PPr}$** (Table 3.2, entries 5–7) and **PP$_{PPh}$** (Table 3.2, entries 8–10) against **PP** (Table 3.2, entry 1) confirms improvement between of 140–160 °C and 132–175 °C respectively. Importantly, improved thermal stability against the brominated copolymers (Table 2, entries 2-4) by 47–72 °C validates beneficial

characteristics of phosphonate post-modification. Increased incorporation levels in both **PP$_{PPr}$** and **PP$_{PPh}$** correlated to increased thermal stability with respect to $T_{50\%}$ and T_{max}; however, plateauing at > 6.8 mol% incorporation suggests a limit in the maximum efficiency. Although $T_{50\%}$ and T_{max} showed no improvement at highest incorporation levels the residual char for both **PP$_{PPr}$** and **PP$_{PPh}$** continued to increase. **PP$_{PPr}$** (Table 3.2, entry 7) afforded the highest char yield (9.4%) whereas **PP$_{PPh}$** observed the highest $T_{50\%}$ (452 °C) and T_{max} (458 °C; Table 3.2, entry 10).

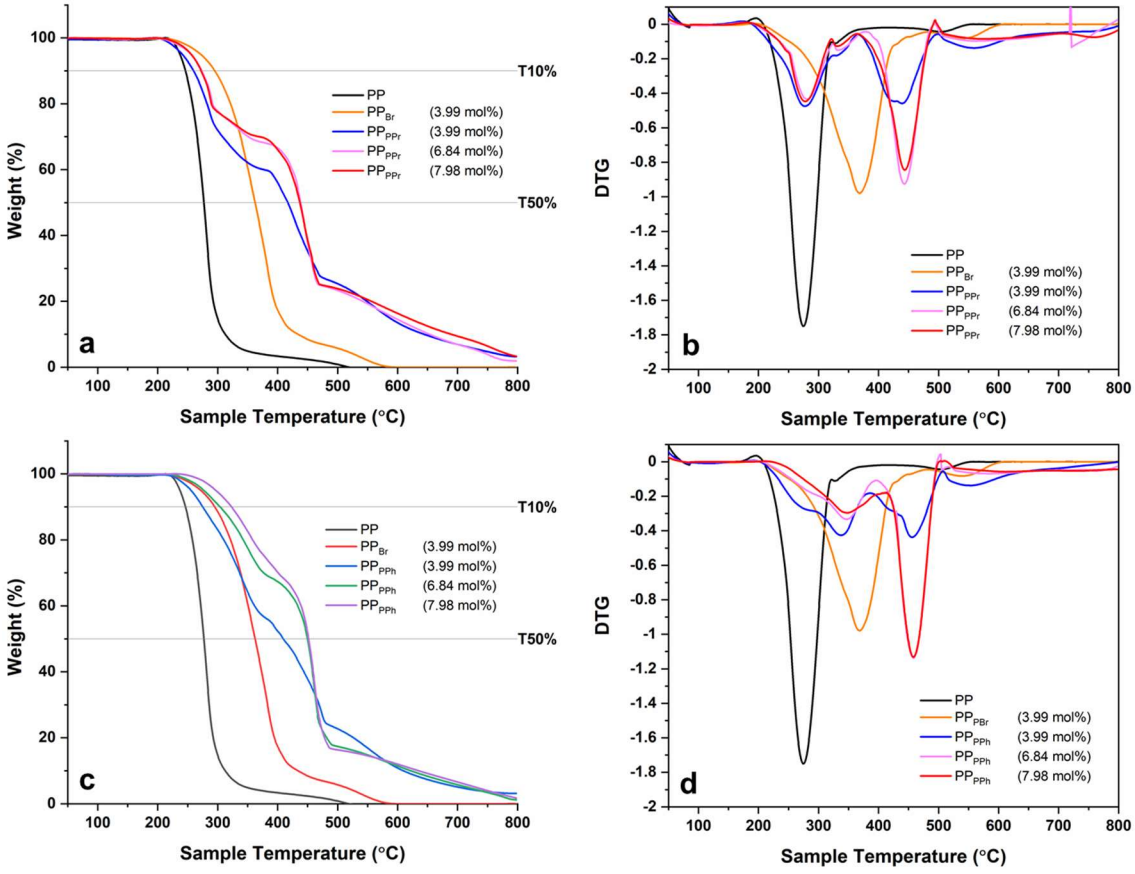

Figure 3.2 TGA curves and DTG plots of **PP$_{PPr}$** (a-b) and **PP$_{PPh}$** (c-d) under a synthetic air atmosphere (20:80 O_2:N_2) with heating rate of 20 °C min^{-1}.

Table 3.2 Thermal characterisation data of polymers.[a]

Entry	Functionality	Incorporation[a] (mol%)	T_m[b] (°C)	Crystallinity[b] (%)	$T_{10\%}$[c] (°C)	$T_{50\%}$[c] (°C)	Residue[c,d]	$T_{max\ (1)}$[c] (°C)	$T_{max\ (2)}$[c] (°C)
1	**PP**	0.00	111	38	246	277		275	
2	**PP_{Br}**	3.99	91	27	295	362		369	
3		6.84	83	22	294	376		380	
4		7.98	77	19	302	380		388	
5	**PP_{PPr}**	3.99	89	27	260	417	6.9	277	440
6		6.84	77	20	274	438	6.9	281	443
7		7.98	77	11	273	437	9.4	279	443
8	**PP_{PPh}**	3.99	95	32	275	409	5.1	337	456
9		6.84	84	24	304	450	5.8	346	458
10		7.98	76	26	323	452	6.6	346	458

[a]Determined by ^{1}H NMR. [b]Determined by DSC. [c]TGA analyses were performed between 50-800 °C under a synthetic air atmosphere (20:80 O_2:N_2) with heating rate of 20 °C min^{-1} with values reported in °C. [d]Residue (%) at 700 °C

Table 3.3 MCC data of propylene (co)polymers.

Entry	Functionality	Incorporation (mol%)	HRC ($J\ g^{-1}\ K^{-1}$)	pHRR ($W\ g^{-1}$)	THR ($kJ\ g^{-1}$)	T_{pHRR} (°C)
1	**PP**	0.00	1245.2 (47.2)	1047.2 (24.6)	48.3 (4.4)	468.5 (1.7)
2	**PP_{Br}**	3.98	577.2 (126.2)	501.5 (113.0)	43.6 (4.4)	428.0 (5.7)
4		8.12	715.8 (55.9)	615.6 (53.4)	41.5 (2.9)	430.0 (0.4)
5	**PP_{PPr}**	3.98	812.1 (79.6)	688.3 (54.3)	39.9 (3.8)	470.9 (2.6)
7		8.12	911.4 (8.8)	778.9 (3.9)	42.5 (3.6)	473.8 (1.0)
8	**PP_{PPh}**	3.98	949.3 (23.5)	840.9 (10.9)	43.6 (1.7)	473.6 (2.3)
10		8.12	975.9 (24.8)	832.2 (18.7)	41.8 (0.5)	470.0 (1.2)

Each sample repeated in triplicate and error, one standard deviation, shown in brackets (σ).

Table 3.4 Thermal characterisation data of polymer blends.[a]

Sample	wt%	T_m[b] (°C)	Crystallinity[b] (%)	$T_{10\%}$[c]	$T_{50\%}$[c]	Residue[c,d]	$T_{max\ (1)}$[c]	$T_{max\ (2)}$[c]
PP		111	38	246	277		275	
PP$_{PPr}$		89	27	260	417	6.94	277	440
PP$_{PPh}$		95	32	275	409	5.11	337	456
PP : **PP$_{PPr}$**	80 : 20	108	30	270	338	0.80	312	450
	90 : 10	109	50	266	320	0.00	327	
	95 : 5	111	33	271	323	0.87	329	
	99 : 1	113	38	257	307	0.62	312	
PP : **PP$_{PPh}$**	80 : 20	115	27	264	324	0.74	329	
	90 : 10	114	35	276	326	0.02	333	
	95 : 5	113	33	267	317	0.40	319	
	99 : 1	112	36	242	282	0.91	281	
PP : ATH	80 : 20	109	26	256	297	14.03	290	
PP : ATH : **PP$_{PPr}$**	80 : 10 : 10	112	32	265	315	7.58	311	
PP : ATH : **PP$_{PPh}$**	80 : 10 : 10	113	31	259	308	6.41	307	
PP : LDH	80 : 20	109	30	265	315	5.68	311	
PP : LDH : **PP$_{PPr}$**	80 : 10 : 10	110	27	260	312	3.36	313	
PP : LDH : **PP$_{PPh}$**	80 : 10 : 10	114	28	273	325	6.34	324	

[a]**PP$_{PPr}$** and **PP$_{PPh}$** phosphonate incorporation 4 mol%. [b]Determined by DSC. [c]TGA analyses were performed between 50-800 °C under a synthetic air atmosphere (20:80 O_2:N_2) with heating rate of 20 °C min^{-1} with values reported in °C. [d]Residue (%) at 700 °C.

.

3.4.4. Flammability studies of phosphonate-functionalised polypropylene

Microscale combustion calorimetry (MCC) is a thermal analysis method for predicting flame resistance and fire behaviour of flame-retardant materials, commonly utilised as a screening tool. The MCC method directly measures the heat of combustion of the gases evolved during controlled heating of milligram-sized samples.[47] MCC was carried out in triplicate for **PP**, $\mathbf{PP_{Br}}$, $\mathbf{PP_{PPr}}$, and $\mathbf{PP_{PPh}}$ of 4 and 8 mol% functionality (Figure A2.10-11); averaged values for heat release capacity (HRC), peak heat release rate (pHRR), total heat release (THR) and temperature at pHRR (T_{pHRR}) with accompanying error are summarised in Table 3.3 and illustrated in Figure 3.3.

PP yields high values concerning HRC (1245.2 J g^{-1} K), pHRR (1047.2 W g^{-1}), and THR (48.3 kJ g^{-1}) indicating substantial release of flammable products; these values are consistent with those reported in the literature.[47-49] Improved HRC and pHRR of $\mathbf{PP_{PPr}}$ (36 and 34% respectively) and $\mathbf{PP_{PPh}}$ (24 and 20% respectively) for 4 mol% incorporated polymers compared with PP indicate incorporation of the phosphonate group increases the flame retardancy performance. Increased performance was not attained *via* increased incorporation levels, as suggested by TGA, despite improvements to HRC and pHRR of $\mathbf{PP_{PPr}}$ (27 and 26% respectively) and $\mathbf{PP_{PPh}}$ (22 and 21% respectively) for 8 mol% incorporated polymers compared with **PP**. This is surprising and implies an alternate contributing effect, perhaps attributable to polymer molecular weight given the low M_n; this trend was likewise observed for both $\mathbf{PP_{Br}}$ samples. Comparing both modified polymers to their parent $\mathbf{PP_{Br}}$ we can isolate the effect of increasing modifier incorporation. HRC of $\mathbf{PP_{PPr}}$ and $\mathbf{PP_{PPh}}$ with respect to $\mathbf{PP_{Br}}$ were observed to be higher in all instances, but the difference was minimised for samples with higher incorporation (41 and 64% *vs* 27 and 36% respectively). Given the mechanism of action for the

phosphonated samples largely relies on the surface effects brought on by the char layer formation, increasing the proportion of modifier likely prompts this response. Highlighting the effect of M_n on MCC test results, synthesis of high M_n **PP$_R$** could contribute substantially to further improving the flammability performance. Preliminary synthesis of a modified high M_n PP (M_n = 54,300 g mol^{-1}, 6.2 mol%) supports this, evidencing an increased $T_{50\%}$ (477 °C) (Figure A2.21) *vs* $T_{50\%}$ = 438 °C for **PP$_{PPr}$** (7.98 mol%).

Heat release profile for **PP$_{PPr}$** suggests a two-step decomposition pathway in line with observed TGA data under oxidative conditions whilst a single decomposition peak was observed for the remaining polymers. **PP$_{Br}$** evidences a substantial drop in HRC (54 %) and pHRR (52 %) but also exhibits significant error and peak broadness compared to the other materials. This implies an inconsistent FR mechanism when compared with both **PP$_{PPr}$** and **PP$_{PPh}$**, all of which display lower errors.

HRC can be utilised to predict the fire behaviour and flame resistance of flame-retardant polymers.[47] Given the HRC of both **PP$_{PPr}$** and **PP$_{PPh}$** are > 400 J g^{-1} K^{-1} they are still currently characterised as flammable; plastics with HRC above 400 J g^{-1} K^{-1} typically will continue to burn after a brief exposure to a small flame and correlate to a limiting oxygen index below 21% or Underwriters Laboratory HB rating.[6] MCC has been shown to correlate well to the fire properties of homopolymers, however, Stoliarov *et. al.* have highlighted that MCC cannot be solely used to accurately assess polymer flame retardancy for a broad range of chemical compositions.[50] Consequently further evaluation by alternate methods, preferably at larger scale, should be undertaken to more accurately determine the material FR characteristics.

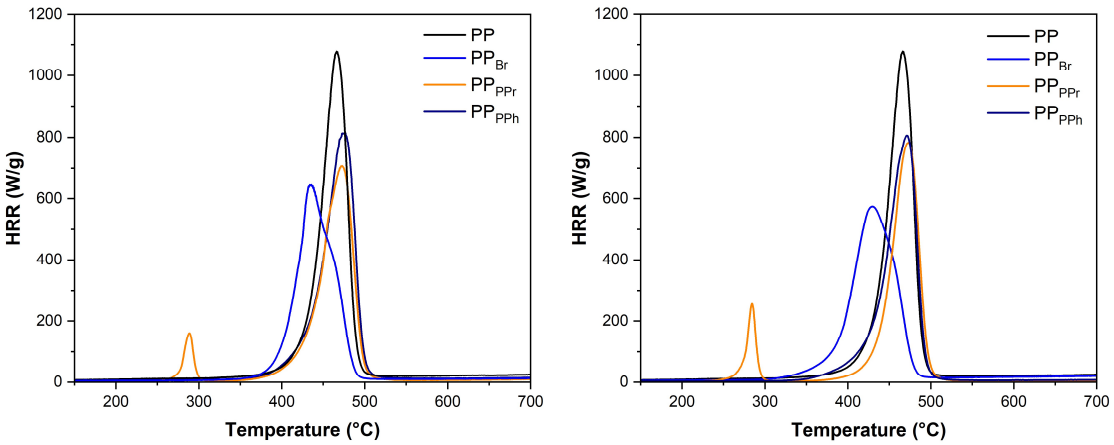

Figure 3.3 Representative microscale combustion calorimetry of **PP**, **PP$_{Br}$**, **PP$_{PPr}$**, and **PP$_{PPh}$**, at 3.98 (left) and 8.12 mol% incorporation (right).

3.4.5. Polymer compounding with polypropylene and inorganic flame retardant additives

PP was blended with 20, 10, 5, or 1 wt% **PP$_{PPr}$** or **PP$_{PPh}$**, and assessed against blends containing inorganic FR additives, ATH or FR layered double hydroxide (FR-LDH), by DSC and TGA under an air atmosphere (Figure 3.4 and Table 3.4; Figures A2.9, A2.12–20 and Table A2.2–3).

TGA data on the polymer blends (Figure 3.4 and Table 3.4) show a minor increase in $T_{10\%}$, $T_{50\%}$ and T_{max} values compared to **PP**, for 1 wt% blends of 4 mol% phosphonate-modified copolymer. This effect is more pronounced at loadings > 5 wt%. This clearly demonstrates that very low overall phosphonate loadings could be highly effective in imparting polypropylene with tuneable FR properties whilst mitigating any degradation in mechanical properties. ATH is used as an FR additive in commercial polyethylene formulations for electrical applications, due to the endothermic decomposition and liberation of water vapour between 220-400 °C. This slows the combustion process, diluting the flammable gases and shielding the polymer surface from oxygen.[51] Given low melt processing temperatures (< 200 °C) for blending, synthesised (co)polymer blends with ATH were investigated. Synergies between ATH and phosphorus have been

extensively investigated due to different FR mechanisms of action.[52-55] Blending **PP** with **PP$_{PPr}$** or **PP$_{PPh}$** and inorganic FR additives ATH or LDH (80:10:10 wt% respectively), however, afforded no significant improvement in thermal stability by TGA, compared to pure phosphonate-copolymers (Table 3.4). This is unsurprising given the high loading of ATH (> 35 wt%) typically required to elicit a significant response. Such high inorganic contents result in a significant trade-off between flame retardancy and mechanical properties.[28] By contrast, the low required loading of **PP$_R$**, as a propylene copolymer similar in chemistry to pure PP, should limit the impact on mechanical properties, making phosphonate-copolymers a promising alternative.

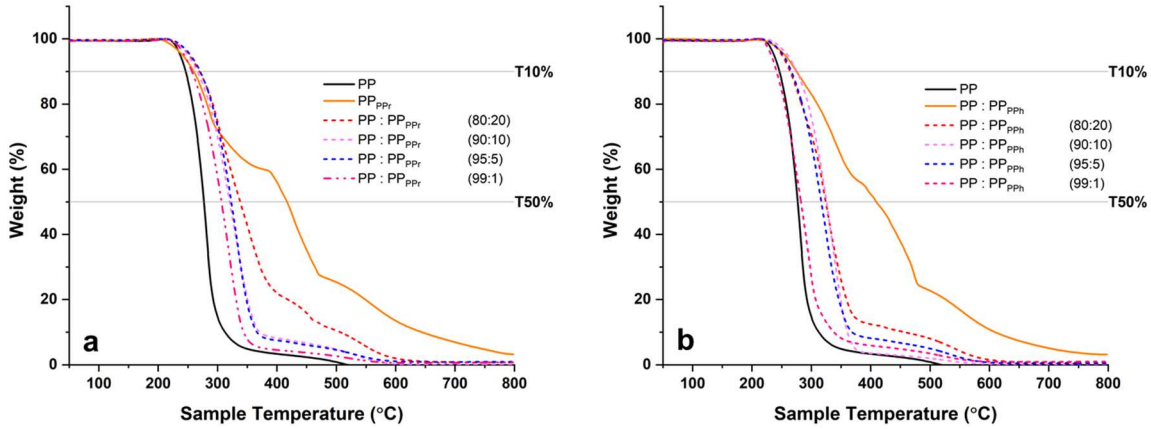

Figure 3.4 TGA thermographs of **PP$_{PPr}$** (4 mol%) (**a**), **PP$_{PPh}$** (4 mol%) (**b**), and associated blends with **PP** under a synthetic air atmosphere (20:80 O_2:N_2) with heating rate of 20 °C min^{-1}

3.5. Conclusions

Synthesis and characterisation of a range of phosphonate-functionalised PP *via* quantitative post-modification of **PP$_{Br}$** with aryl and alkyl phosphite esters under neat conditions has been achieved. Significantly improved thermal stability of the phosphonate-PP was evidenced by TGA in a synthetic air atmosphere when compared to unmodified **PP**; evaluated by T_{max}, $T_{10\%}$, $T_{50\%}$, and residual char residue at 700 °C. Modified polymers exhibited a two-stage oxidative degradation whilst a single decomposition step was observed for **PP**. MCC of both **PP$_{PPr}$** and **PP$_{PPh}$** indicate lower

values of HRC, pHRR, and THR compared to those of **PP**, indicating enhanced flame retardancy. Polymer blending of **PP** and **PP$_{PPr}$** or **PP$_{PPh}$** demonstrated that very low copolymer loadings (≥ 1 wt%) elicited improved thermal stability compared to the homopolymer. Whilst no significant improvement in thermal stability was identified with blends including ATH or FR-LDH, at similar loadings, the phosphonate-functionalised polymers outperformed the commercial inorganic additives.

These single component FR materials hold promise over commonly utilised FR-additives; removing toxicity and environmental concerns of halogenated additives, not requiring high loadings of inorganic materials that compromise polymer mechanical properties and by being resistant to leaching by virtue of the covalent tethering of the phosphonate group. Additionally, the ability to readily synthesise alternate functionalised PP and to further increase comonomer incorporation can now be investigated to further boost polyolefin FR efficacy.

3.6. Experimental Details

3.6.1. General (co)polymer synthesis and characterisation.

General procedure for the solution-phase copolymerisation of propylene with bromoalkenes and subsequent post-modification of poly(propylene)-*co*-(11-bromo-1-undecene) with triisopropyl phosphite or triphenyl phosphite was carried out according to literature.[34]

3.6.2. General procedure for polymer compounding.

In a vial with a magnetic stirrer bar, phosphite-post-modified poly(propylene)-*co*-(11-bromo-1-undecene) was combined with poly(propylene) in a known ratio by weight and melted in xylenes (5 mL) at 120 °C. The blend was subsequently precipitated in acidified

methanol (2 wt% HCl) before being collected by filtration, washed with methanol (20 mL), then acetone (2 x 20 mL), and dried *in vacuo* at 40 °C to a constant weight.

3.6.3. General procedure for polymer compounding with inorganic flame retardant additives.

Phosphite-post-modified poly(propylene)-co-(11-bromo-1-undecene) was combined with polypropylene and alumina trihydroxide (ATH) or layered double hydroxide (LDH), in known ratios by weight in a vial with a magnetic stirrer bar. The mixture was melted in xylenes (5 mL) at 120 °C, and precipitated in acidified methanol (2 wt% HCl) before being collected by filtration, washed with methanol (20 mL), then acetone (2 x 20 mL), and dried *in vacuo* at 40 °C to a constant weight.

3.7. References

1 G. Natta, P. Pino, P. Corradini, F. Danusso, E. Mantica, G. Mazzanti, G. Moraglio, *J. Am. Chem. Soc.*, 1955, **77**, 1708-1710.
2 K. Ziegler, E. Holzkamp, H. Breil, H. Martin, *Angew. Chem.*, 1955, **67**, 426.
3 D. Hohenwarter, H. Mattausch, C. Fischer, M. Berger, B. Haar, *Materials (Basel)*, 2020, **13**.
4 A. A. Younis, *Egypt. J. Pet.*, 2017, **26**, 1-7.
5 E. Rezvani Ghomi, F. Khosravi, Z. Mossayebi, A. Saedi Ardahaei, F. Morshedi Dehaghi, M. Khorasani, R. E. Neisiany, O. Das, A. Marani, R. A. Mensah, L. Jiang, Q. Xu, M. Försth, F. Berto, S. Ramakrishna, *Molecules*, 2020, **25**, 5157.
6 M. J. John, in *Green Composites for Automotive Applications*, eds. G. Koronis and A. Silva, Woodhead Publishing, 2019, pp. 43-58.
7 A. K. Sen, B. Mukherjee, A. S. Bhattacharya, L. K. Sanghi, P. P. De, A. K. Bhowmick, *J. Appl. Polym. Sci.*, 1991, **43**, 1673-1684.
8 V. I. Babushok, P. Deglmann, R. Krämer, G. T. Linteris, *Combust. Sci. Technol.*, 2017, **189**, 290-311.
9 I. T. Cousins, C. A. Ng, Z. Wang, M. Scheringer, *Environ. Sci. Process. Impacts*, 2019, **21**, 781-792.
10 R. J. Law, A. Covaci, S. Harrad, D. Herzke, M. A. Abdallah, K. Fernie, L. M. Toms, H. Takigami, *Environ. Int.*, 2014, **65**, 147-158.
11 P. Schmid, M. Kohler, A. C. Gerecke, E. Gujer, M. Zennegg, M. Wolfensberger, *CHIMIA*, 2003, **57**, 509.
12 M. Venier, A. Salamova, R. A. Hites, *Acc. Chem. Res.*, 2015, **48**, 1853-1861.
13 Y. Z. Wang, in *Advances in Fire Retardant Materials*, eds. A. R. Horrocks and D. Price, Woodhead Publishing, 2008, pp. 67-94.
14 S. V. Levchik and E. D. Weil, in *Advances in Fire Retardant Materials*, eds. A. R. Horrocks and D. Price, Woodhead Publishing, 2008, pp. 41-66.
15 L. Chen and Y.-Z. Wang, *Polym. Adv. Technol.*, 2010, **21**, 1-26.
16 I. van der Veen and J. de Boer, *Chemosphere*, 2012, **88**, 1119-1153.
17 S. Hörold, in *Polymer Green Flame Retardants*, eds. C. D. Papaspyrides and P. Kiliaris, Elsevier, Amsterdam, 2014, pp. 221-254.
18 M. M. Velencoso, A. Battig, J. C. Markwart, B. Schartel, F. R. Wurm, *Angew. Chem. Int. Ed.*, 2018, **57**, 10450-10467.
19 B. Schartel, *Materials*, 2010, **3**, 4710-4745.
20 S. Rabe, Y. Chuenban, B. Schartel, *Materials*, 2017, **10**, 455.

21 J. Green, *J. Fire Sci.*, 1992, **10**, 470-487.
22 J. Green, *J. Fire Sci.*, 1996, **14**, 426-442.
23 H. Gao, S. Hu, H. Han, J. Zhang, *J. Appl. Polym. Sci.*, 2011, **122**, 3263-3269.
24 N. Pérez, X. L. Qi, S. Nie, P. Acuña, M. J. Chen, D. Y. Wang, *Materials (Basel)*, 2019, **12**, 152.
25 Y. Liu, J. Zhao, C.-L. Deng, L. Chen, D.-Y. Wang, Y.-Z. Wang, *Ind. Eng. Chem. Res.*, 2011, **50**, 2047-2054.
26 Y. Gao, J. Wu, Q. Wang, C. A. Wilkie, D. O'Hare, *J. Mater. Chem. A*, 2014, **2**, 10996-11016.
27 M. Yılmaz, A. Akar, N. Köken, N. Kızılcan, *J. Appl. Polym. Sci.*, 2020, **137**, 49023.
28 A. u. R. Shah, D.-w. Lee, Y.-q. Wang, A. Wasy, K. C. Ham, K. Jayaraman, B.-S. Kim, J.-I. Song, *T. Nonferr. Metal. Soc.*, 2014, **24**, s81-s89.
29 W. Hu, J. Zhan, N. Hong, T. R. Hull, A. A. Stec, L. Song, J. Wang, Y. Hu, *Polym. Adv. Technol.*, 2014, **25**, 631-637.
30 D. Price, K. Pyrah, T. R. Hull, G. J. Milnes, J. R. Ebdon, B. J. Hunt, P. Joseph, C. S. Konkel, *Polym. Degrad. Stab.*, 2001, **74**, 441-447.
31 D. Price, L. K. Cunliffe, K. J. Bullet, T. R. Hull, G. J. Milnes, J. R. Ebdon, B. J. Hunt, P. Joseph, *Polym. Adv. Technol.*, 2008, **19**, 710-723.
32 T. Xu, L. Zhang, Z. Cheng, X. Zhu, *Sci. China Chem.*, 2015, **58**, 1633-1640.
33 J. Gao, W. Cai, Y. Hu, C. Chen, *Polym. Chem.*, 2019, **10**, 1416-1422.
34 A. Evans, O. Casale, L. J. Morris, Z. R. Turner, D. O'Hare, *Macromolecules*, 2024, **57**, 10778-10791.
35 N. K. Boaen and M. A. Hillmyer, *Chem. Soc. Rev.*, 2005, **34**, 267-275.
36 N. Blake, Z. R. Turner, J.-C. Buffet, D. O'Hare, *Polym. Chem.*, 2023, **14**, 3175-3185.
37 X.-Y. Wang, Y.-Y. Long, Y.-X. Wang, Y.-S. Li, *J. Polym. Sci., Part A: Polym. Chem.*, 2014, **52**, 3421-3428.
38 Y. Wang, L. Jiang, X. Ren, F. Guo, Z. Hou, *J. Polym. Sci.*, 2021, **59**, 2324-2333.
39 L. Resconi, L. Cavallo, A. Fait, F. Piemontesi, *Chem. Rev.*, 2000, **100**, 1253-1346.
40 H. Pizova and P. Bobal, *Tetrahedron Lett.*, 2015, **56**, 2014-2017.
41 M. Hussain, R. J. Varley, Z. Mathys, Y. B. Cheng, G. P. Simon, *J. Appl. Polym. Sci.*, 2004, **91**, 1233-1253.
42 K. Wazarkar, M. Kathalewar, A. Sabnis, *Polym. Compos.*, 2017, **38**, 1483-1491.
43 L. K. Kostanski, D. M. Keller, A. E. Hamielec, *J. Biochem. Biophys. Methods*, 2004, **58**, 159-186.
44 S. Yang, Y. Hu, Q. Zhang, *High Perform. Polym.*, 2019, **31**, 186-196.
45 Z. Bai, L. Song, Y. Hu, R. K. K. Yuen, *Ind. Eng. Chem. Res.*, 2013, **52**, 12855-12864.
46 L. Wang, B. Yang, Y. Guo, Y. Zhang, N. Wang, F. Li, H. Yu, J. Cui, J. Guo, B. Mu, L. Tian, *High Perform. Polym.*, 2020, **32**, 1169-1180.
47 R. E. Lyon, R. N. Walters, S. I. Stoliarov, *Polym. Eng. Sci.*, 2007, **47**, 1501-1510.
48 X. Chen and C. Jiao, *Polym. Adv. Technol.*, 2011, **22**, 817-821.
49 Q. Tai, Y. Hu, R. K. K. Yuen, L. Song, H. Lu, *J. Mater. Chem.*, 2011, **21**, 6621-6627.
50 R. E. Lyon, R. N. Walters, S. I. Stoliarov, *Polym. Eng. Sci.*, 2007, **47**, 1501-1510.
51 E. A. Coleman, in *Applied Plastics Engineering Handbook (Second Edition)*, ed. M. Kutz, William Andrew Publishing, 2017, pp. 489-500.
52 P. Khalili, K. Y. Tshai, D. Hui, I. Kong, *Compos. B. Eng.*, 2017, **114**, 101-110.
53 Z. Qin, D. Li, Q. Li, R. Yang, *Mater. Des.*, 2016, **89**, 988-995.
54 Z.-s. Xu, L. Yan, L. Chen, *Procedia Eng.*, 2016, **135**, 631-636.
55 L. Yan, Z. Xu, X. Wang, N. Deng, Z. Chu, *J. Coat. Technol. Res.*, 2018, **15**, 1357-1369.

3.8. Statement of Authorship

Title of Paper	Flame retardant phosphonate-functionalised polypropylenes
Publication Status	*ACS Appl. Polym. Mater., 2025, 7, 4, 2508-2516.*
Publication Details	**A. Evans**, L. J. Morris, Z. R. Turner, D. O'Hare.

Student Confirmation

Student Name:	Alexander Oscar Edward Evans
Contribution to the Paper	Performed the synthesis and analysis of all samples aside from microscale combustion calorimetry and quantitative Br analysis. Interpreted the data. Wrote the manuscript, original draft, with review and editing contributions from all authors.

Signature 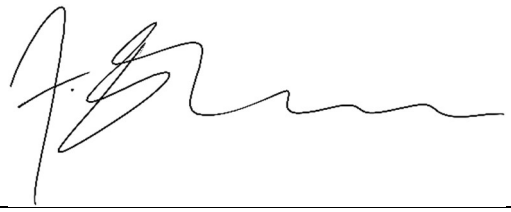	Date 02/01/2025

Supervisor Confirmation

Supervisor name and title: Professor Dermot O'Hare
Supervisor comments: I can confirm that the candidate's contribution to this paper is as described above.

Signature 	Date 19/01/2025

Chapter 4 – Functionalised polypropylene copolymers as multi-substrate hot melt adhesives

Alexander Evans, Clement G. Collins Rice, Zoë R. Turner, and Dermot O'Hare*

Submitted to ACS Applied Materials and Interfaces (19/11/2024)

4.1. Author contributions

Alexander Evans: Project conceptualisation. Performed the synthesis, analysis, and application testing of all samples. Led the rheological investigation. Interpreted all data. Wrote the manuscript, original draft, review and editing.

Clement G. Collins Rice: Rheology formal analysis. Manuscript, review and editing.

Zoë R. Turner: Manuscript, review and editing. Supervision.

Dermot O'Hare: Corresponding author. Manuscript, review and editing. Supervision.

4.2. Abstract

Amine-modified polypropylenes (**PP_R**, R = $NH(Et)_2$ (DEA); $NH(Et)(CH_2CH_2OH)$ (EAE); $NH(CH_2CH_2OH)_2$ (DEOA) have been prepared *via* a two-step synthesis and display enhanced adhesive performance with respect to both steel and polypropylene (PP) substrates. PP typically displays poor adhesion to polar substrates which consequently restricts its utility as a hot melt adhesive (HMA). Solvent-free, quantitative post-modification of poly(propylene)-*co*-(11-bromo-1-undecene) (range of comonomer incorporations (3–9 mol%)) with secondary amines yielded amine-modified PPs **PP_{DEA}**, **PP_{EAE}**, and **PP_{DEOA}**. Rheological and FT-IR characterisation identified the presence of a PP-based supramolecular hydrogen bonding network. (Co)polymers were evaluated as HMAs by lap shear strength between steel-steel and steel-plastic substates. **PP_{EAE}** and **PP_{DEOA}** both performed well as HMAs between steel, recording the largest mean

adhesive forces of 16.8 and 17.4 MPa respectively, **PP$_{DEOA}$** displaying a 252-fold increase *vs* **PP**. The adhesive failure mode in multi-substrate adhesion was found to be a function of interfacial effects, depending on the relative ability of the HMAs to bind to the polar steel surface and diffuse into the plastic substrate. **PP$_{DEA}$** and **PP$_{EAE}$** were found to be optimal in this case, with failure by stock break indicative of adhesion greater than the tensile strength of the substrate and consequently appropriate for the application. This study now allows further sets of functionalised PPs to be readily prepared to meet a diverse array of multi-substrate adhesive requirements.

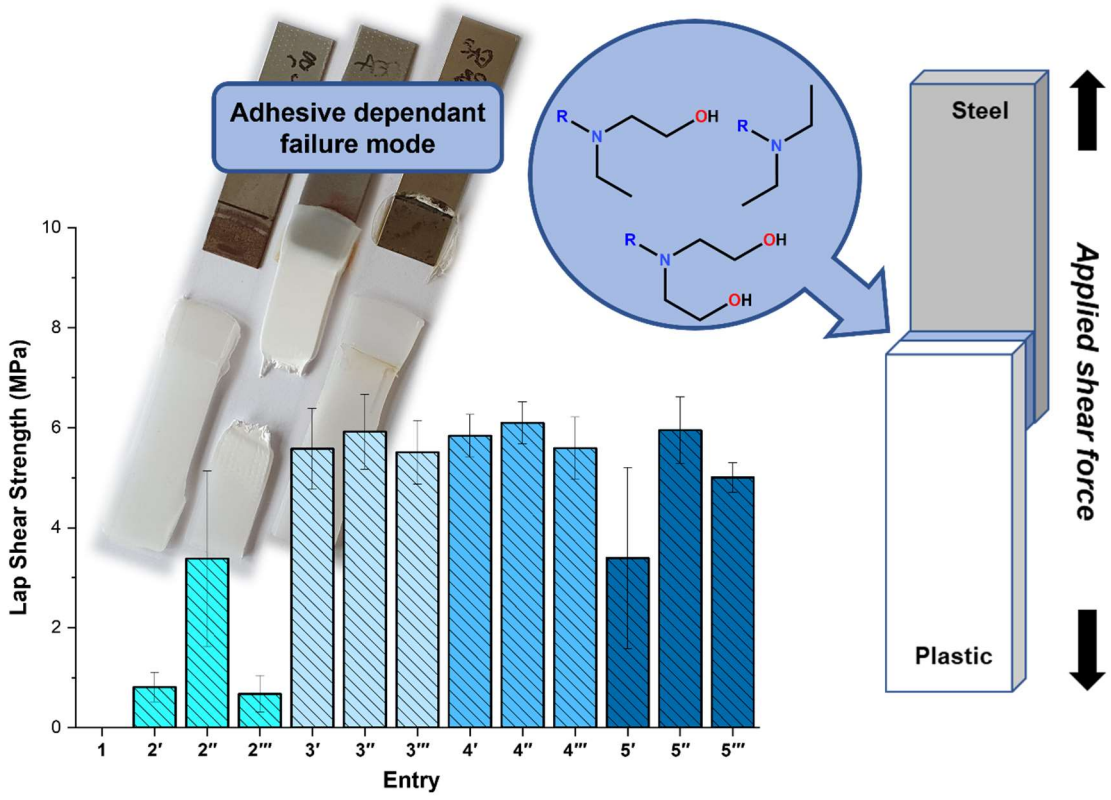

4.3. Introduction

Adhesives are vital in everyday life, with widespread applications in construction, automotive, and consumer packaging, using over 6 billion lbs annually yet evidencing volume growth for high-performance adhesives.[1-5] Consequential to an industry shift

towards environmentally friendly, solvent- and volatile organic compound- (VOC) free adhesives,[6-10] hot melt adhesives (HMAs) are gaining prominence as they satisfy market needs for both ecological responsibility and strong product performance.[11-15] Current adhesive strengths of commercially available ethylene vinyl acetate or polyurethane-based HMAs are limited to 6–7 MPa.[16] Meeting demands for lightweight, high-performance products necessitates superior adhesion to diverse materials: plastics, metals, and wood.

Numerous adhesive solutions utilise polar polymers, however bonding polyolefins (POs) to polar substrates is challenging due to their low surface free energy, chemical inertness, and absence of functional groups.[17-19] Enhancing substrate adhesion often involves chemically or physically treating PO surfaces for increased polarity and improved wettability, accompanied by associated limitations such as limited control and functionality.[20-23] Bonding to both high (metals) and low (plastic) surface free energy substrates, termed multi-substate adhesion (MSA), presents a unique challenge. MSA through the use of HMAs has gained traction as an alternative to conventional mechanical and adhesive bonding methods. Unlike mechanical fastening, which can add weight, damage, and weaken the material, or standard adhesive joints requiring surface pre-treatment and curing time,[24-26] HMAs provide a fast, effective, and damage-free alternative. As such, there are numerous potential commercial applications for functional PPs as hot-melt adhesives, particularly as light-weight alternatives to traditional fastenings methods in the automotive industry. Ultimately, such effective light-weight hot-melt adhesive joints can further contribute to the amelioration of carbon emissions.

POs have the potential to become attractive materials for adhesive applications because of their low density and production costs, and tuneable material properties. However, the

nonpolar and highly crystalline properties of isotactic PP are generally considered hallmarks of poor adhesives that have the potential to hinder its application in multi-material assemblies. Surface modifications and functionalised adhesives have been developed to overcome these limitations by enhancing polymer interfacial compatibility with other materials, particularly metals.[16, 27-29] Ongoing research focuses on advanced functional polymers to improve adhesion to both polar and nonpolar substrates.[11, 14, 28] Recently reported work by Duchateau and co-workers highlighted the application of propylene-based hydroxyl-functionalised terpolymers for use as HMAs with improved adhesive performance (12.6 MPa) at low application temperatures (130 °C) despite minimal incorporation levels ($\leq$ 0.5 mol%);[16] however, direct copolymerisation as a method to access these materials is likely to have a limited range of functionality that can be incorporated. As an alternative to improving the polymer wetting, focus has likewise been directed at enhancing the wettability and bonding strength of the metal substate, with recent work evidencing superior joint strengths up to 25 MPa by creating a surface texture that complements the adhesive properties of polymers.[25, 26]

An additional complexity in polymer-metal bonding lies in the interphase, the three-dimensional boundary region where two materials meet.[30-34] Understanding the interphase is critical for predicting and enhancing adhesive performance from an industrial perspective.[30, 31, 35, 36] Advanced techniques like sum frequency generation vibrational spectroscopy have facilitated non-destructive analysis of these buried interfacial regions, revealing details about hydrogen bonding, acid-base interactions, and other molecular behaviours that contribute to interfacial adhesion strength.[37, 38] Nishino *et al.* recently described improved isotactic PP-rubber adhesion stemming from crystalline growth and the formation of lamellae interlock in the interphase region.[27]

Functional PP materials therefore offer a unique opportunity, able to provide binding sites to the metallic substate whilst adhering to plastic substrates through the diffusion of molecular chains at the interface. The use of HMAs for multi-substrate applications provides an innovative approach to lightweight construction. By addressing interfacial challenges between metals and polymers, HMAs can enable the production of reliable, high-strength hybrid components for structural and functional parts in various sectors such as construction and transport.

We now build upon our recent report of the synthesis of a set of low molecular weight amine- and amino alcohol-functionalised polypropylenes, prepared using a two-step copolymerisation and post-functionalisation methodology, which were utilised as HMAs for steel-steel adhesion in preliminary studies.[29] Herein, we synthesise and characterise a library of amine-modified polypropylene-based copolymers, spanning different incorporation levels and molecular weights, allowing for effective assessment of their adhesion as HMAs to steel and commercial PP; in particular, their utility in multi-substrate adhesion is highlighted.

4.4. Results and Discussion

4.4.1. Synthesis and characterisation of functionalised polypropylenes

The synthesis of brominated polypropylene copolymer, poly(propylene)-*co*-(11-bromo-1-undecene) (**PP$_{Br}$**) by solution-phase copolymerisation of propylene and 11-bromo-1-undecene (**11-Br**), and subsequent transformations by diethylamine (DEA), 2-(ethylamino)ethanol (EAE), and 2,2'-iminodiethanol (DEOA) resulted in the formation of **PP$_{DEA}$**, **PP$_{EAE}$** and **PP$_{DEOA}$** respectively, as previously reported (Scheme 4.1).[29]

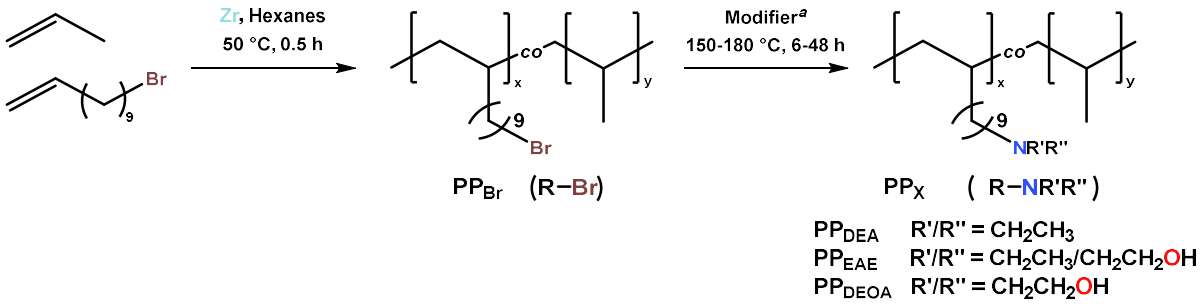

Scheme 4.1 Synthesis of $\mathbf{PP_{Br}}$ by solution-phase copolymerisation. **Zr** = dimethylsilylene bis(2–methyl–4–phenyl–1–indenyl) zirconium(IV) dichloride ([**Zr**] = 0.024 mM), [**11-Br**] = 91, 137, or 182 mM yielding comonomer incorporation of 2.96, 4.78, and 9.10 mol% respectively as determined by ^{1}H NMR spectroscopy. [a]Modifier = DEA, EAE, or DEOA

Table 4.1 (Co)polymerisation of propylene (and 11-bromo-1-undecene).[a]

Entry	[**11-Br**] (mM)	Activity[b]	Productivity[c]	Yield (g)	Incorporation (mol%)[d]	M_w (g mol^{-1})[e]	$Đ_M$[e]
1	0	10 094	32.10	8.03	0.00	98 000	4.7
2′	91	3 581	11.39	4.27	2.96	225 500	2.8
2″	137	2 090	6.65	2.49	4.78	171 700	2.7
2‴	182	1 232	3.92	1.47	9.10	162 600	2.5

[a]Conditions: dimethylsilylene bis(2–methyl–4–phenyl–1–indenyl) zirconium dichloride (**Zr**), MAO used as a cocatalyst and scavenger with $[Al]_0$:[**Zr**]$_0$ = 1000:1. Molar ratio of $[TIBA]_0$:[**11-Br**]$_0$ = 1:10, 0.5 mL toluene, 49.5 mL hexanes, propylene 2 bar, polymerisation temperature = 50 °C, 0.5 h. Polymerisation were performed at least in duplicate and mean values reported. [b]kg_{PP} mol_{Zr}^{-1} h^{-1} bar^{-1}. [c]kgPP g_{Zr}^{-1} h^{-1}. [d]Determined by ^{1}H NMR. [e]Determined by SEC using the Mark-Howink correction for PP.

Our previously reported inchoate studies utilised low molar mass (M_n) functionalised PPs (*ca*. 4000 g mol^{-1}) produced by *rac*-ethylenebisindenyl zirconium (IV) dichloride as hot melt adhesives.[29] Unfortunately, the predominant failure mode during lap shear strength analysis was cohesive failure, as opposed to interfacial failure. This was attributed to the low M_n of the PPs resulting in a low ultimate tensile strength, less than that of the adhesive interfacial strength. Consequently, it was hypothesised that synthesising high M_n analogues, with increased tensile strength, would enable a thorough assessment of the materials as hot melt adhesives. The synthesis of $\mathbf{PP_{Br}}$ copolymers with increased M_n was achieved using dimethylsilylene bis(2–methyl–4–phenyl–1–indenyl) zirconium (IV)

dichloride (**Zr**); molar mass was determined by size exclusion chromatography ($M_{n,\,SEC}$ = 81 400–63 500 g mol^{-1}; Table 4.1, Figure A3.1). The range of **PP$_{Br}$** copolymers was achieved by varying [**11-Br**] (91–182 mM), eliciting differences in incorporation to evaluate the degree to which polar functionality contributes to adhesion. **PP$_{Br}$** copolymers containing 2.96, 4.78, and 9.10 mol% incorporation of **11-Br**, as determined by ^{1}H NMR spectroscopy, were isolated and all subsequently functionalised with one of DEA, EAE, or DEOA and characterised (Table 4.2, Figures A3.1–6). The presence of the comonomer branches, in addition to the modifier R-groups, generally suppresses crystallinity leading to reduced melt temperatures (T_m) and crystallinity with respect to **PP**. Since the Mark-Houwink correlation is not known for functionalised PP, and the presence of a polar and hydrogen bondable group is likely to affect the radius of gyration in solution, SEC was not obtained for the amine-modified polymers but it is assumed that the backbone chain length is unchanged during post-polymerisation modification.[29, 39-43]

Table 4.2 Characterisation and adhesive data for propylene (co)polymers.

Entry	Modifier	Incorporation[a] (mol%)	T_m[b] (°C)	Crystallinity[b] (%)	G′[c] (kPa)	G″[c] (kPa)	|η*|[c] (Pa·s)	Steel Plastic[d] (MPa)	Steel Steel[d] (MPa)
1		0	139	73	0.5	2.6	147	[e]	0.1 ± 0.0
2′	11-Br	2.96	120	33	23.6	34.1	2330	0.8 ± 0.3[f]	3.6 ± 1.8
2″		4.78	104	17	9.0	19.2	1190	3.4 ± 1.8[f]	1.8 ± 1.0
2‴		9.10	96	5	2.3	7.3	428	0.7 ± 0.4[f]	7.6 ± 3.7
3′	DEA	2.96	121	27	120.1	38.4	7090	5.6 ± 0.8[g]	1.5 ± 0.9
3″		4.78	105	25	113.7	46.9	6920	5.9 ± 0.7[g]	7.6 ± 3.1
3‴		9.10	99	5	71.5	36.4	4510	5.5 ± 0.6[h]	6.1 ± 2.9
4′	EAE	2.96	119	30	211.5	85.7	12 800	5.8 ± 0.4[g]	6.7 ± 2.6
4″		4.78	106	21	183.4	84.4	11 400	6.1 ± 0.4[g]	15.2 ± 2.2
4‴		9.10	101	14	123.8	63.2	7820	5.6 ± 0.6[h]	16.8 ± 0.9
5′	DEOA	2.96	116	29	352.8	110.4	20 800	3.4 ± 1.8[h]	9.1 ± 2.6
5″		4.78	101	11	204.6	64.9	12 100	6.0 ± 0.7[h]	15.3 ± 1.4
5‴		9.10	93	1	190.9	66.6	11 400	5.0 ± 0.3[h]	17.4 ± 1.6

[a]Determined by ^{1}H NMR spectroscopy. [b]Determined by DSC. [c]ω = 17.7829 rad s^{-1}, measured at 180 °C. [d]Determined by lap shear strength, mean adhesion ± one standard deviation reported. [e]Measurement not possible due to lack of adhesion. [f]Adhesive failure to metal. [g]Stock break failure. [h]Adhesive failure to plastic.

Fourier transform infrared (FT-IR) spectroscopy of the copolymers determined the presence of hydrogen bonding. A broad absorption band between 3600–3080 cm^{-1} can be attributed to the presence of O–H stretches between hydrogen bonded hydroxyl units in all samples of **PP$_{EAE}$** and **PP$_{DEOA}$** (Figure 4.1, Figure A3.3);[40] the observed peak broadness corresponds to the distribution of OH···O bond angles. Isolated hydroxyl groups were not observed, suggesting essentially complete participation in hydrogen bonded networks. **PP$_{DEA}$**, samples 3″ and 3‴ (Table 4.2), however both display a broad peak at 3410 cm^{-1} (Figure 4.1, Figure A3.3), in the region of an aliphatic N···H hydrogen bonding environment despite the lack of H-bond donor groups.[44] Given the apparent rheological network and adhesion results, *vide infra*, we attribute this to an exogenous hydrogen bond donor, likely to be aluminium hydroxide resulting from the hydrolysis of residual MAO despite purification by reprecipitation;[45] an observed broad absorbance between 670–400 cm^{-1} may be attributed to these Al–O residues.[46]

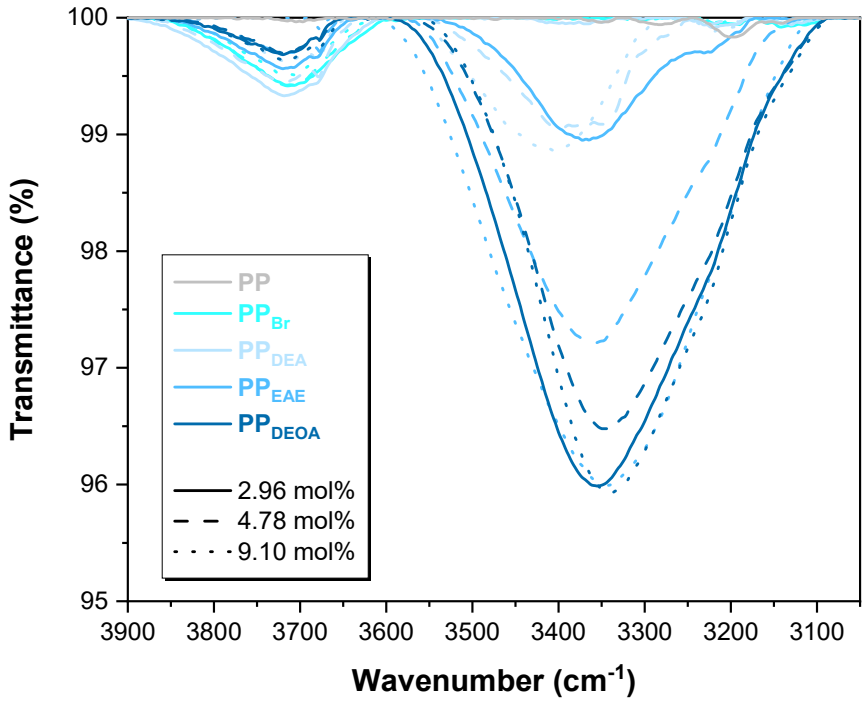

Figure 4.1 FT-IR spectrum of **PP**, **PP$_{Br}$**, **PP$_{DEA}$**, **PP$_{EAE}$**, and **PP$_{DEOA}$** at 2.96, 4.78, and 9.10 mol% incorporation, shown between 3050–3900 cm^{-1}

4.4.2. Rheological evaluation of functionalised polypropylenes

The thermoresponsive viscoelastic behaviour of PP is well documented when accounting for M_n and crystallinity differences.[47] It is important to note that direct comparisons between different mol% incorporation level copolymers and their functionalised analogues is complex for this reason, in addition to the variation in functionality. Recently, rheology and simulations have demonstrated the effects of hydroxyl-functionalised POs, with stable hydrogen bonding networks and nanophase hydroxyl aggregation expected in the polymer melt even at relatively low [OH].[40, 48]

Small-amplitude oscillatory shear (SAOS) rheometry was conducted for all samples (Table 4.2, Figures A3.4–8) to evaluate the presence of a dynamic crosslinked PP network. Hydrogen bonding effects are expected to be more pronounced in the low shear regime, where the network reassociation time is faster than ω_c^{-1} and hydrogen bonds are in dynamic equilibrium Experiments were completed at 180 °C, the application temperature for later lap shear strength testing, and in the frequency (ω) range 10^{-2}–10^{2} rad s^{-1}. **PP** and **PP$_{Br}$** behaved as expected with loss modulus (G'') greater than storage modulus (G'), indicative of a "liquid-like" viscosity dominated regime, and crossover frequency, $\omega_c > 10^2$ rad s^{-1} (relaxation time $\tau < 0.01$ s). With respect to increasing **11-Br** incorporation levels, **PP$_{Br}$** generally displayed increasing complex viscosity (η^*) which may be attributed to increased branching density and comonomer-promoted entanglements as well as dipolar interactions.[49, 50]

Evaluating G' at a specific ω (17.7829 rad s^{-1}), for functional group conversions of the same parent polymers, it is possible to isolate the effects of [heteroatom] and the impact of both hydrogen donor and acceptor moieties from molecular weight effects since the molecular weight distributions are identical (Figure 4.2). When accounting for each

parent **PP$_{Br}$**, each modification yields increasing G': at 2.98 mol% incorporation **PP$_{Br}$** = 0.0236 MPa, **PP$_{DEA}$** = 0.1201 MPa, **PP$_{EAE}$** = 0.2115 MPa, and **PP$_{DEOA}$** = 0.3528 MPa (Table 4.2). This observed increasing trend in G' was likewise observed for the 4.78 mol% and 9.10 mol% polymers. It follows logically that increased G' occurs due to restricted mobility and an enhancement to the polymer network in amine-modified polymers where hydrogen bonding is possible, either through intermolecular interactions or exogeneous H-bond donors. By comparison with de-ashed polymers, prior studies have evidenced the impact of catalyst residues on rheological behaviours, with dynamic crosslinks proposed to originate from hydrogen bonding and electrostatic interactions.[16] Structural adhesives, especially ones able to undergo adhesion to low and high surface energy materials, typically require high G' to effectively resist deformation and maintain a bond between structural components, enabling it to carry and distribute loads without significant creep or deformation.[51, 52] This is critical in applications like automotive, aerospace, and construction, where adhesives experience sustained forces over time.[53]

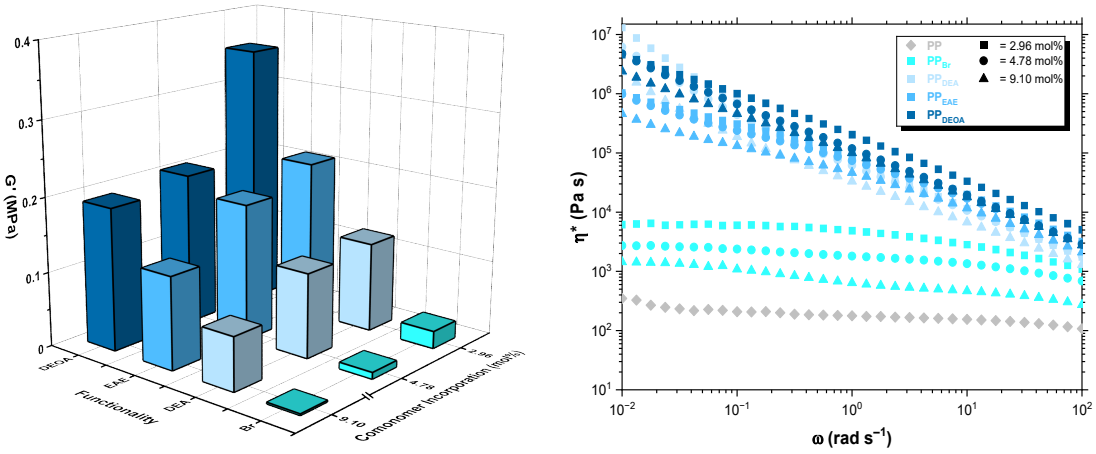

Figure 4.2 Small-amplitude oscillatory shear rheology of propylene copolymers. (Left) where G' is reported at ω = 17.7829 rad s^{-1}, measured at 180 °C, and related to comonomer incorporation and polymer functionality. (Right) complex viscosity, |η*|, as a function of oscillation frequency, ω.

All **PP$_{DEA}$** and **PP$_{DEOA}$** samples display an inverted relationship between G' and G'' compared to **PP$_{Br}$** whereby $G' > G''$, consistent with $\omega_c < 10^{-2}$ rad s^{-1}. The longer relaxation times that this suggests ($\tau > 100$ s) imply a "solid-like" material with a stable network that resists deformation over time even under relatively high shear. All **PP$_{EAE}$** samples evidence a modulus crossover (ω_c; $4' = 0.2371$ rad s^{-1}, $4'' = 0.3162$ rad s^{-1}, and $4''' = 0.7499$ rad s^{-1}; Figures A3.5–7). Given lower ω_c can also suggest higher M_n or greater chain entanglement, both of which increase the resistance to flow and favor elastic behaviour,[54-57] in isolation this data doesn't offer additional support for the presence of hydrogen bonding. However, a lower ω_c generally indicates a higher level of crosslinking or stronger interactions within the material as it maintains an elastic behaviour even at lower frequencies. Interestingly, there is no observable crossover ω for all **PP$_{DEOA}$** samples as $G' > G''$ consistent with $\omega_c < 10^{-2}$ rad s^{-1}. Isolating the impact of M_n effects and taken in conjunction with observed **PP$_{EAE}$** data, we can infer that all **PP$_{DEOA}$** materials are dynamically crosslinked through hydrogen bonding to a greater extent than **PP$_{EAE}$** by virtue of the increased hydroxyl concentration, and both show orders of magnitude greater interactions than in the parent **PP$_{Br}$** polymers. The increased elasticity of these amine-functionalised PPs may in part be attributable to supramolecular networking effects mediated by intermolecular hydrogen bonding. In the case of **PP$_{DEA}$** the presence of exogeneous H-bond donors, observed by FT-IR spectroscopy, may be responsible for the observed network effect; alternatively polar-induced nanophase aggregates may act as supramolecular crosslinks to produce a transient network.[40, 48]

The strongest evidence for the existence of supramolecular hydrogen bonding networks arises from shear-thinning phenomena. At low shear rates the network maintains equilibrium (the association time is less than ω^{-1} and hydrogen bonds quickly reform)

and viscosity equals the zero-shear value ($\eta = \eta_0$); shear thinning is attributable to the disruption of the equilibrium network which decreases viscosity. The shear sensitivity, measured as the slope of the shear-thinning region of η/η_0 as a function of shear rate, is therefore indicative of the extent of supramolecular networking as well as normalising the effects of M_n and dispersity. This analysis was applied to SAOS complex viscosity η^*/η^*_0 as a function of ω and to steady-shear viscosity η/η_0 as a function of $\dot{\gamma}$ with the zero-shear viscosities modelled according to the Carreau equation (Figures A3.9–11).[58] It is clear that amine-functionalised PPs have significantly greater zero-shear viscosities and display more pronounced shear-thinning, both of which are consistent with a dynamic supramolecular hydrogen bonded network in the melt phase.[40]

4.4.3. Hot melt adhesive performance of functionalised polypropylenes

Interfacial adhesion is commonly investigated by lap shear strength (LSS) testing.[59, 60] Recently reported work by Duchateau *et al*. highlighted the application of propylene-based hydroxyl-functionalised terpolymers for use as hot melt adhesives (HMAs).[16] Furthermore, we recently reported the LSS of low molecular weight hydroxyl-functional PPs, **PP$_{EAE}$** and **PP$_{DEOA}$**, compared against **PP**, **PP$_{Br}$**, and **PP$_{DEA}$**.[29] However, as expected given the low M_n, cohesive failure was the predominate failure mode for the conducted LSS tests between aluminium and steel substrates. As such, the synthesis and application of higher M_n congeners was targetted to more accurately evaluate the efficiency of the propylene-based copolymers as HMAs by transitioning to adhesive failure modes. Given the increased T_m and viscosity *vs* the previous work, an application temperature of 180 °C was selected for two reasons: (1) to maximise the obtained adhesive force[16] and (2) to promote diffusion of molecular chains between sample copolymers and plastic substrate;[27] the plastic being an untreated commercially supplied PP sheet. To this end,

testing was completed between steel-steel and steel-plastic substrates to evaluate adhesion to both high and low surface energy substrates, aiming to exemplify the copolymers as multi-substrate HMAs.

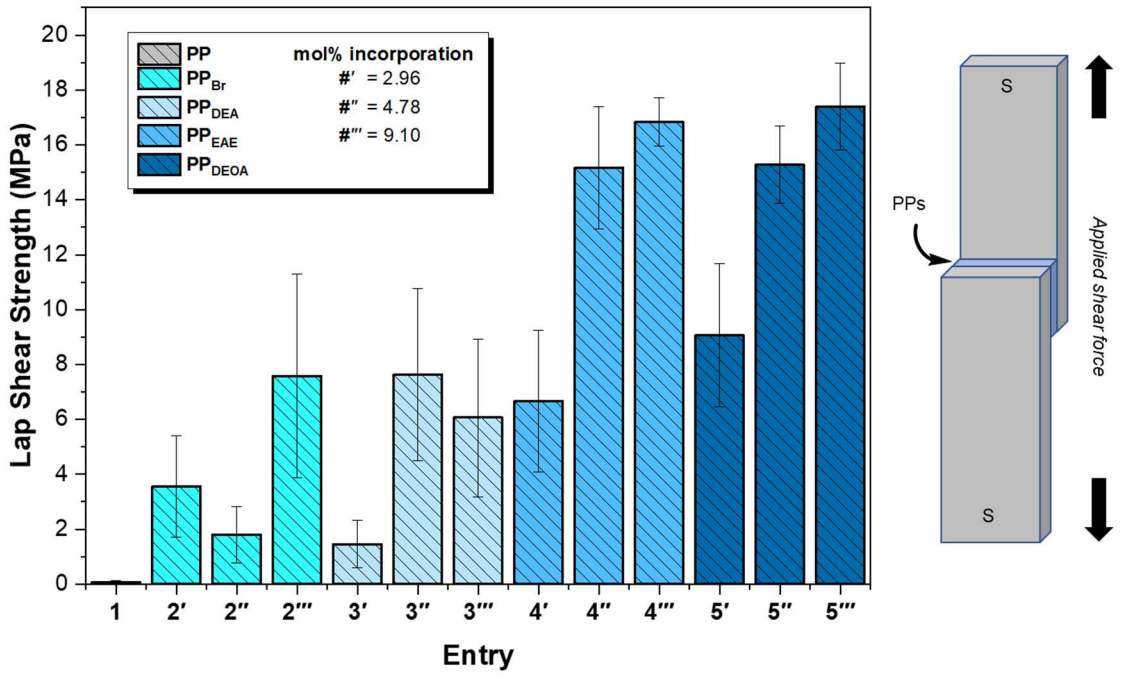

Figure 4.3 Lap shear strength tests with functional polymers as the adhesive interlayers between steel. Error bars represent standard deviation.

The general trend in initial LSS test results between steel sheets (Figure 4.3, Table 4.2) were analogous to our previously reported work,[29] albeit displaying significantly stronger cohesive forces and each sample failing at the copolymer-steel interface. The measured LSS is therefore indicative of the adhesive strength of the polymers. Unfunctionalised **PP** was found to be a poor HMA recording a very low mean adhesive force (<0.1 MPa). **PP$_{Br}$** displayed mean adhesives strengths greater than anticipated, mean values somewhat increasing with [Br]. On inspection of the steel substrate after adhesive failure, a tarnish is present on the surface that this is only observed for **PP$_{Br}$** samples. We anticipate this is a result of the generation of corrosive bromine species formed under the high temperature and pressure hot melt conditions, increasing the overall surface area at the interface by damaging the steel.[61] **PP$_{DEA}$** displayed adhesive strengths similar to **PP$_{Br}$** (1.5–7.6 MPa)

with no observable trend within the sample set beyond the lowest incorporation sample clearly performing the worst. The improvement compared with **PP** may be attributed to the enhanced polarity afforded by the diethylamine functionality. $\mathbf{PP_{EAE}}$ and $\mathbf{PP_{DEOA}}$ both performed well as HMAs, recording the largest mean adhesive forces as 16.8 and 17.4 MPa respectively; $\mathbf{PP_{DEOA}}$ displaying a 252-fold increase *vs* **PP**. It might be reasonably inferred that lone pair containing moieties interact *via* electrostatic effects to oxides present on the surface of the steel and subsequently improving adhesion; similarly, the available polymer functionality eliciting the observed supramolecular network by rheological evaluation. Current commercial one- and two-component structural adhesives from a range of epoxy, urethane, methacrylate, and acrylic chemistries offer adhesive strengths between 9.6–42.7 MPa ($\bar{x}$ = 22 MPa) by LSS for steel connections.[53] Within each sample subset, mean increased adhesive performance can be ostensibly attributed to increasing [heteroatoms] within the polymer matrix: 4′ = 6.7 MPa, 4″ = 15.2 MPa, and 4‴ = 16.8 MPa; 5′ = 9.1 MPa, 5″ = 15.3 MPa, and 5‴ = 17.4 MPa (Table 4.2).

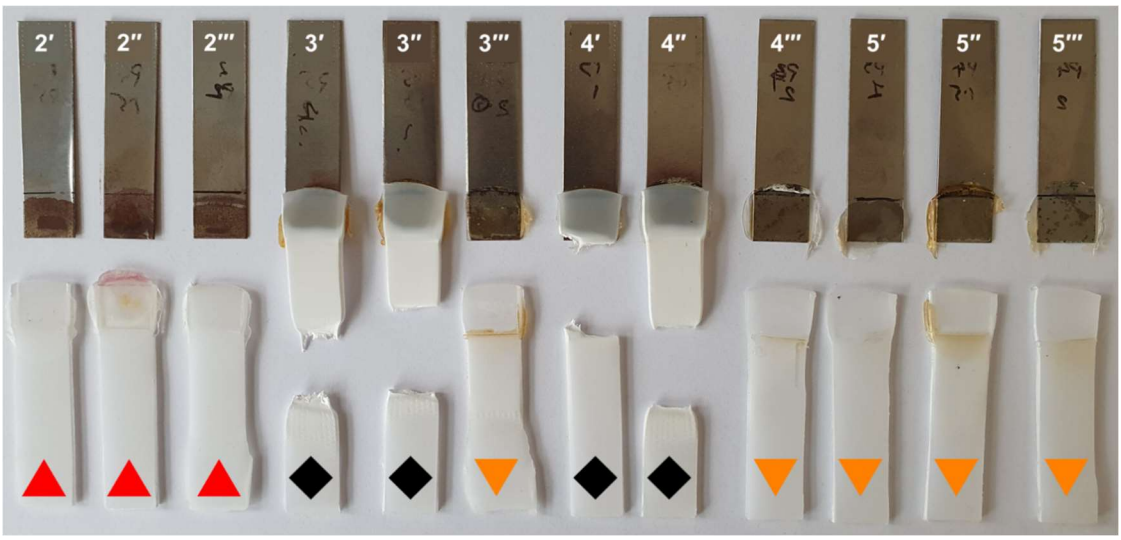

Figure 4.4 Lap shear strength samples evidencing failure modes: ▲ = Adhesive (steel), ◆ = Stock break, and ▼ = Adhesive (plastic).

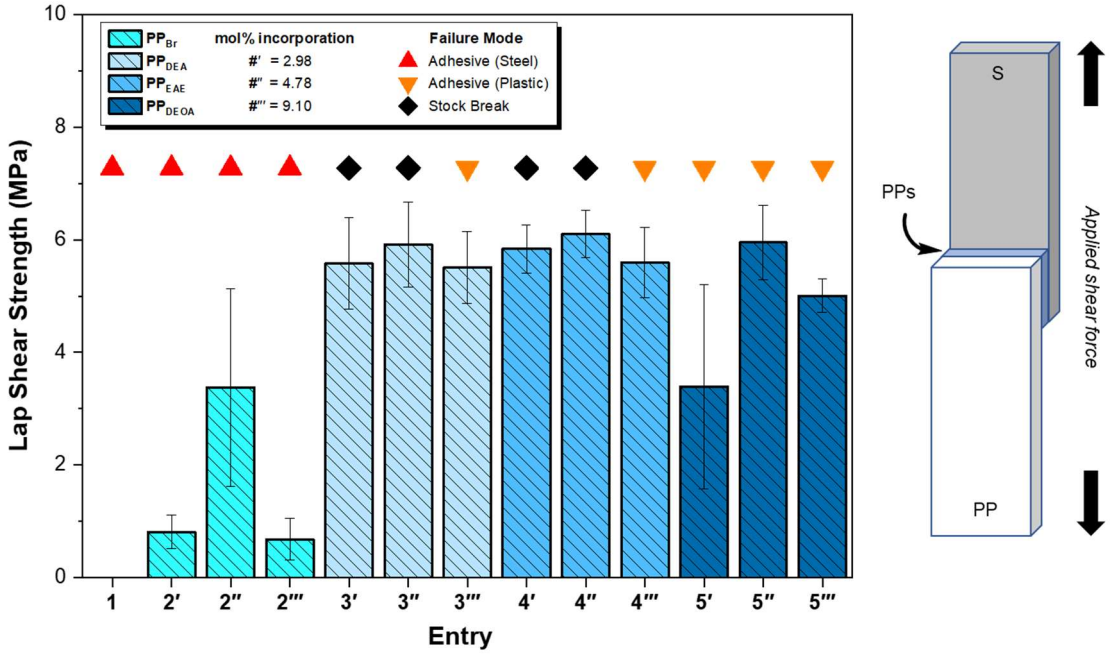

Figure 4.5 Lap shear strength tests with functional polymers as the adhesive interlayers between steel and commercial polypropylene. Error bars represent standard deviation.

Functionalised POs offer a unique opportunity for MSA between plastic and steel through entanglements and electrostatic interactions respectively. The LSS results between steel-plastic substrates are summarised in in Table 4.2 and presented in Figures 4.4–5.

Unsurprisingly, unfunctionalised **PP** was a poor HMA with no samples able to be tested due to a lack of adhesion to steel. **PP$_{Br}$** was likewise poor across the sample subset, with low adhesion to steel, and the same tarnished steel indicative of corrosion. Interestingly the failure mode, perhaps as expected, was adhesive failure to steel, with the **PP$_{Br}$** in all cases remaining adhered to the PP sheet. The observed failure mode however for **PP$_{DEA}$** (3′ and 3″) was stock break, whereby the PP sheet broke before the adhesive joint failed. This was not observed for 3‴ however there was severe stress to the PP, evidenced by an increase in PP opacity, implying that the joint adhesion was only marginally weaker than that of the PP sheet under the experimental conditions. All but the greatest incorporation levels of **PP$_{EAE}$** likewise failed by stock break. 9.10 mol% incorporated **PP$_{EAE}$** and all **PP$_{DEOA}$** samples however underwent an alternate failure mode, this time adhesive failure

to plastic due to decreased compatibility with the propylene homopolymer. As observed in the steel LSS results, the increase in [heteroatom] correlates well with increased adhesion to steel.

The mean adhesive force values for stock break failure modes are largely uninformative, instead measuring the tensile strength of the PP sheet and indicating that adhesion strength is suitable for the substrate utilised. However, given the difference in failure modes across the series, it is likely that selection of an optimal adhesive between steel and plastic can be obtained with the use of a plastic substrate with higher tensile strength. Furthermore, the trend can be qualitatively correlated to copolymer polarity similarly to that discussed in the steel-steel LSS results. There is a trade-off between increasing functionality to improve steel adhesion (also at the expense of M_n and crystallinity) and compatibility with the plastic substrate. Functionalised polymers with reduced polarity are able to form sufficient entanglements with the PP sheet and yet insufficiently adhere to metal, whilst those with the greatest degree of functionality are poorly miscible at the polymer interface yet retain significant adhesion to steel through the presence of heteroatoms. Therefore, the materials that failed by stock break, **PP$_{DEA}$** and **PP$_{EAE}$**, sit in an optimal window regarding adhesive performance between both steel and plastic. The knowledge gained now allows further sets of functionalised PPs to be readily prepared to meet a diverse array of multi-substrate adhesive requirements.

4.5. Conclusion

We have reported the synthesis and characterisation of a library of amine-modified polypropylene copolymers to assess effectively their adhesion to steel and commercial PP substrates. Rheological characterisation evidenced viscoelastic phenomena believed to be the result of supramolecular hydrogen bonding. The increasing concentration of

hydrogen bond acceptor and donor moieties is directly attributed to increases in elasticity and shear sensitivity. The presence of functionality further contributed to adhesive strength with hydroxyl functionality having a pronounced effect on LSS adhesion to steel. A maximum mean adhesive strength recorded of 17.4 MPa is comparable to those of two-component epoxy resins. The dependency of adhesion between plastic and steel displayed an unexpected structure-functionality property relationship; observed failure modes transition from adhesive failure at the steel interface, to stock break, and finally adhesive failure at the plastic interface with increasing copolymer functionality. Tensile failure by stock break in this regime demonstrates that the adhesive joint strength is greater than the tensile strength of the substrate itself, rendering it wholly appropriate for adhesion to this material.

We have demonstrated that multi-substrate adhesion can be maximised by controlling the molecular weight, and nature and amount of functionality of PP; balancing entanglements to the PP substrate and polar-binding to the metal substrate. The two-step copolymerisation and post-modification platform utilised has already been shown to be capable of producing diverse functionalised PPs and can readily expand this class of holt-melt adhesives. We believe that this allows for the preparation of broad classes of HMAs, that can be deployed dependent on the multi-substrate system of choice.

4.6. References

1. S. Wang, Z. Liu, L. Zhang, Y. Guo, J. Song, J. Lou, Q. Guan, C. He and Z. You, *Mater. Chem. Front.*, 2019, **3**, 1833-1839.
2. H. Yang, G. Du, Z. Li, X. Ran, X. Zhou, T. Li, W. Gao, J. Li, H. Lei and L. Yang, *ACS Appl. Polym. Mater.*, 2021, **3**, 1638-1651.
3. Y. Wei, J. Yao, Z. Shao and X. Chen, *ACS Sustain. Chem. Eng.*, 2020, **8**, 7668-7679.
4. C. Heinzmann, C. Weder and L. M. de Espinosa, *Chem. Soc. Rev.*, 2016, **45**, 342-358.
5. E. G. Koricho, E. Verna, G. Belingardi, B. Martorana and V. Brunella, *Int. J. Adhes. Adhes.*, 2016, **68**, 169-181.
6. Y. Zhu, C. Romain and C. K. Williams, *Nature*, 2016, **540**, 354-362.
7. H.-W. Engels, H.-G. Pirkl, R. Albers, R. W. Albach, J. Krause, A. Hoffmann, H. Casselmann and J. Dormish, *Angew. Chem. Int. Ed.*, 2013, **52**, 9422-9441.

8. S. Laurichesse and L. Avérous, *Progress in Polymer Science*, 2014, **39**, 1266-1290.
9. Y. Li, J. Krahn and C. Menon, *J. Bionic Eng.*, 2016, **13**, 181-199.
10. F. J. Díaz López and C. Montalvo, *J. Clean. Prod.*, 2015, **102**, 30-43.
11. K. Zhong, Q. Guan, W. Sun, M. Qin, Z. Liu, L. Zhang, J. Xu, F. Zhang and Z. You, *Ind. Eng. Chem. Res.*, 2021, **60**, 6925-6931.
12. G. Raos and B. Zappone, *Macromolecules*, 2021, **54**, 10617-10644.
13. B. Liu, Z. Xu, C. Fan, C. Cui, Y. Yao, M. Xiao and W. Liu, *Macromol. Rapid Commun.*, 2021, **42**, e2100010.
14. P. Sun, Y. Li, B. Qin, J.-F. Xu and X. Zhang, *ACS Materials Letters*, 2021, **3**, 1003-1009.
15. F. A. Kucherov, E. G. Gordeev, A. S. Kashin and V. P. Ananikov, *ACS Appl. Mater. Interfaces*, 2020, **12**, 45394-45403.
16. J. Kruszynski, W. Nowicka, M. Bouyahyi, Y. Liu, L. Yang, A. Rozanski, N. Anbuchezhian, L. Jasinska-Walc and R. Duchateau, *ACS Appl. Polym. Mater.*, 2023, **5**, 3875-3882.
17. Y. Liu, Y. Shigemoto, T. Hanada, T. Miyamae, K. Kawasaki and S. Horiuchi, *ACS Appl. Mater. Interfaces*, 2021, **13**, 11497-11506.
18. S. Huang, Y. Wan, X. Ming, J. Zhou, M. Zhou, H. Chen, Q. Zhang and S. Zhu, *ACS Appl. Mater. Interfaces*, 2021, **13**, 41112-41119.
19. K. Viswanathan, H. Ozhalici, C. L. Elkins, C. Heisey, T. C. Ward and T. E. Long, *Langmuir*, 2006, **22**, 1099-1105.
20. T. Sato, S. Ise, S. Horiuchi, H. Akiyama and T. Miyamae, *Int. J. Adhes. Adhes.*, 2019, **93**, 102322.
21. Y. Jia, J. Chen, H. Asahara, T.-A. Asoh and H. Uyama, *ACS Appl. Polym. Mater.*, 2019, **1**, 3452-3458.
22. H.-J. Kim, K.-J. Lee and Y. Seo, *Macromolecules*, 2002, **35**, 1267-1275.
23. S. R. Kim, *J. Appl. Polym. Sci.*, 2000, **77**, 1913-1920.
24. K. van der Straeten, J. Sparla, A. Olowinsky and A. Gillner, *Welding in the World*, 2019, **63**, 1431-1441.
25. K. van der Straeten, A. Olowinsky and A. Gillner, *Journal of Laser Applications*, 2018, **30**.
26. K. van der Straeten, I. Burkhardt, A. Olowinsky and A. Gillner, *Physics Procedia*, 2016, **83**, 1137-1144.
27. T. Matsumoto, Y. Shimizu and T. Nishino, *Macromolecules*, 2021, **54**, 7226-7233.
28. A. Hanifpour, N. Bahri-Laleh and M. Nekoomanesh-Haghighi, *Polym. Adv. Technol.*, 2020, **31**, 922-931.
29. A. Evans, O. Casale, L. J. Morris, Z. R. Turner and D. O'Hare, *Macromolecules*, 2024, **57**, 10778-10791.
30. B. Pukánszky, *Eur. Polym. J.*, 2005, **41**, 645-662.
31. L. H. Sharpe, *The Journal of Adhesion*, 1972, **4**, 51-64.
32. S.-J. Park and J.-S. Jin, *J. Colloid Interface Sci.*, 2001, **242**, 174-179.
33. K. W. Stöckelhuber, A. S. Svistkov, A. G. Pelevin and G. Heinrich, *Macromolecules*, 2011, **44**, 4366-4381.
34. T. Matsumoto, Y. Nakanishi, C. Hongo, H. Hakukawa, S. Horiuchi and T. Nishino, *Polymer*, 2018, **137**, 63-71.
35. L. F. Boesel, C. Greiner, E. Arzt and A. del Campo, *Adv. Mater.*, 2010, **22**, 2125-2137.
36. E. M. Liston, L. Martinu and M. R. Wertheimer, *J. Adhes. Sci. Technol.*, 1993, **7**, 1091-1127.
37. J. N. Myers and Z. Chen, *The Journal of Adhesion*, 2017, **93**, 1081-1103.
38. Z. Chen, *Progress in Polymer Science*, 2010, **35**, 1376-1402.
39. L. K. Kostanski, D. M. Keller and A. E. Hamielec, *J. Biochem. Biophys. Methods*, 2004, **58**, 159-186.
40. S. Gupta, X. Yuan, T. C. Mike Chung, M. Cakmak and R. A. Weiss, *Polymer*, 2016, **107**, 223-232.
41. J. Chen, A. Motta, B. Wang, Y. Gao and T. J. Marks, *Angew. Chem. Int. Ed.*, 2019, **58**, 7030-7034.
42. D. M. Meunier, J. H. Wade, M. Janco, R. Cong, W. Gao, Y. Li, D. Mekap and G. Wang, *Anal. Chem.*, 2021, **93**, 273-294.
43. A. Ginzburg, T. Macko, F. Malz, M. Schroers, I. Troetsch-Schaller, J. Strittmatter and R. Brüll, *J. Chromatogr. A*, 2013, **1285**, 40-47.
44. G. Socrates, *Infrared and Raman Characteristic Group Frequencies*, John Wiley & Sons Ltd, 3 edn., 2001.
45. J. B. Knight, P. D. Calvert and N. C. Billingham, *Polymer*, 1985, **26**, 1713-1718.
46. M.-C. Jodin-Caumon, B. Humbert, N. Phambu and F. Gaboriaud, *Spectrochim. Acta A Mol. Biomol. Spectrosc.*, 2009, **72**, 959-964.
47. S. Kurzbeck, F. Oster, H. Münstedt, T. Q. Nguyen and R. Gensler, *J. Rheol.*, 1999, **43**, 359-374.
48. M. Misra, M. Agarwal, D. W. Sinkovits, S. K. Kumar, C. Wang, G. Pilania, R. Ramprasad, R. A. Weiss, X. Yuan and T. C. M. Chung, *Macromolecules*, 2014, **47**, 1122-1129.

49. Y. Li, Z. Yao, Z.-h. Chen, S.-l. Qiu, C. Zeng and K. Cao, *Ind. Eng. Chem. Res.*, 2013, **52**, 7758-7767.
50. A. D. Gotsis, B. L. F. Zeevenhoven and C. Tsenoglou, *J. Rheol.*, 2004, **48**, 895-914.
51. M. R. Maheri and R. D. Adams, *Int. J. Adhes. Adhes.*, 2002, **22**, 119-127.
52. R. A. Pethrick, *Proc. Inst. Mech. Eng. L: J. Mater.: Des. Appl.*, 2015, **229**, 349-379.
53. K. Sullivan and K. D. Peterman, *J. Constr. Steel Res.*, 2024, **213**, 108405.
54. C. Carrot and J. Guillet, *J. Rheol.*, 1997, **41**, 1203-1220.
55. R. H. Colby, L. J. Fetters and W. W. Graessley, *Macromolecules*, 1987, **20**, 2226-2237.
56. R. R. Rahalkar, *Rheol. Acta*, 1989, **28**, 166-175.
57. H. Niu, Y. Wang, X. Liu, Y. Wang and Y. Li, *Polym. Test.*, 2017, **60**, 260-265.
58. P. J. Carreau, *T. Soc. Rheol.*, 1972, **16**, 99-127.
59. Y. Boutar, S. Naïmi, S. Mezlini, L. F. M. Da Silva, M. Hamdaoui and M. Ben Sik Ali, *J. Adhes. Sci. Technol.*, 2016, **30**, 1913-1929.
60. N. R. Ciccia, J. X. Shi, S. Pal, M. Hua, K. G. Malollari, C. Lizandara-Pueyo, E. Risto, M. Ernst, B. A. Helms, P. B. Messersmith and J. F. Hartwig, *Science*, 2023, **381**, 1433-1440.
61. M. A. Kappes, *Corros. Rev.*, 2020, **38**, 1-24.

4.7. Statement of Authorship

Title of Paper	Functionalised polypropylene copolymers as multi-substrate hot melt adhesives
Publication Status	*Submitted to ACS Applied Materials and Interfaces* (19/11/2024)
Publication Details	**A. Evans**, C. G. Collins-Rice, Z. R. Turner, D. O'Hare.

Student Confirmation

Student Name:	Alexander Oscar Edward Evans
Contribution to the Paper	Project conceptualisation. Performed the synthesis, analysis, and application testing of all samples. Led the rheological investigation but was assisted by Collins-Rice for formal analysis. Interpreted all data. Wrote the manuscript, original draft, with review and editing contributions from all authors.

Signature 	Date 02/01/2025

Supervisor Confirmation

Supervisor name and title: Professor Dermot O'Hare	
Supervisor comments: I can confirm that the candidate's contribution to this paper is as described above.	
Signature 	Date 19/01/2025

Chapter 5 – Illuminating microplastics in cells: macro-problems for micro-barriers

Alexander Evans, Ríona M. Devereux, Zoë R. Turner, Angela J. Russell,* and Dermot O'Hare*

To be submitted to Nature.

5.1. Author contributions

Alexander Evans: Project conceptualisation. Performed the polymer synthesis and analysis. Interpreted the polymer data and assisted the *in vitro* analysis. Wrote the manuscript, original draft, review and editing.

Ríona M. Devereux: Led the investigation and formal analysis for the *in vitro* research. Manuscript, review and editing.

Zoë R. Turner: Manuscript, review and editing. Supervision.

Angela J. Russell: Corresponding author. Manuscript, review and editing. Supervision.

Dermot O'Hare: Corresponding author. Manuscript, review and editing. Supervision.

5.2. Abstract

Polypropylene (PP) is the second most produced plastic globally and is environmentally pervasive in the form of microplastics (μP). The cellular localisation and fate of μPs within biological systems remain poorly understood. We present a method for the covalent fluorescent labelling of PP functionalised with rhodamine B (**Rb**), **PP$_{Rb}$**, and subsequent μP evaluation in a human embryonic kidney model cell line (HEK293T). **Rb** was successfully coupled under Steglich esterification conditions and characterised, the resulting polymer utilised *in vitro*, offering a significantly improved μP model to conventional staining methods that can definitively locate μP in human cells. Cellular uptake of **PP$_{Rb}$** was rapid (≤ 1 h), non-toxic up to 70 μM, and was not observed to

localise within the nucleus. Increased mean lysosomal fluorescence intensity suggested an endosomal uptake mechanism with significant exocytosis implied over a 48 h period.

5.3. Introduction

Commercially, polyolefins (PO), namely polypropylene (PP)[1] and polyethylene (PE),[2] are synthesised at scale to meet the needs of a broad array of applications; with PP accounting for 17% of global plastic production.[3] Desirable and tuneable properties as a result of branching, molecular mass (M_n), and dispersities ($Đ_M$), coupled with low production costs are amongst the driving forces behind their widespread utility.[4] Although PP is recyclable, a significant proportion enter landfill or the environment.[5-7] An abundance of PP waste is converted to microplastics (μP),[8] or indeed nanoplastics,[9] *via* slow degradation due to (a)biotic factors.[7] Detection of PO μP is widely reported, and the μP highly prevalent.[10, 11] Plastic debris is an environmentally persistent and complex contaminant (e.g. varying in size, morphology, chemical constituency),[12] whilst μP detection remains challenging.[13, 14] Consequently, recent legislative efforts have been introduced in the U.K. to curtail the prevalence of single use plastics given the emergence of μP as a pressing environmental concern due to their ubiquity, potential ecological ramifications, and associated risk.[10, 14-17]

The impact of μP on macroscopic organisms have been extensively studied with recent reports evaluating effects on mice,[18, 19] fish,[20-22] and humans.[23] Reports detailing μP entry into aquatic and terrestrial food chains *via* biomagnification and bioaccumulation,[12, 24-26] and detection in fish, birds, and mammals feeding on aquatic organisms or living in aquatic environments has been the subject of further investigation.[22, 27] Perturbation to ecological processes may align with other anthropogenic pollutants despite the lack of lethality; reduced fecundity and growth at the first trophic level may cause persistent

reduction of biomass.[28, 29] Additionally, investigations into which animals can ingest μP and the mechanism by which this occurs has been reported.[30, 31] However, the marked chemical inertness severely hampers evaluation on living species; the incorporation of a fluorescent probe circumvents μP detection issues in organic tissues.[32-37]

However, the effects on single-celled organisms, which constitute fundamental components of aquatic ecosystems, remain relatively underexplored. These minute organisms, encompassing diverse taxa such as phytoplankton and protozoa, play pivotal roles in nutrient cycling and food web dynamics.[29, 38-40] The ingestion of microplastics by single-celled organisms can lead to various detrimental outcomes, including altered feeding behaviours, impaired metabolic functions, and compromised reproductive success. Furthermore, the sorption of toxic chemicals onto microplastics introduces an additional layer of risk, as the bioavailability of these pollutants increases upon ingestion by these microorganisms,[13, 16, 28, 33, 41] although disputed.[10] Despite the limited research in this area, the potential for cascading effects throughout aquatic ecosystems underscores the urgency to comprehensively elucidate the consequences of microplastic exposure on single-celled organisms. Ascertaining an understanding of the posed risk is crucial for the educated development of policy. Current methods for μP evaluation predominantly utilise staining,[42] due to the relative synthetic simplicity,[43] although some are covalently bound.[37] *In vitro* assays on mice[44] and human[45] cell lines utilise polystyrene (PS) for this purpose. However, this methodology has drawbacks, primarily leaching of free dye, potentially leading to the presence of artefacts, confounding the results.[46-48] Subsequently, reports with claims of sample purity, or indeed covalent coupling of dye moieties, are not supported by adequate rigorous characterisation data leading to the ambiguous interpretation of results.

In the field of mechanical recycling, separation techniques have been extended to include fluorescent labelling enabling separation by specific polymeric material;[49-51] recent reports utilise fluorescently tagged PE in this way.[52] Notably, recycling process typically involve high temperatures and consequently careful selection of incorporated spectroscopic markers is required to avoid degradation.[52] To the best of our knowledge, recent literature presents a few examples of synthesised *isotactic*-PP copolymers containing fluorescent units, and only work by Pragliola *et al*. has evaluated them as a fluorescent marker of PP thus far.[32, 53] Fluorescent probe coupled PP may be used to mimic the *in vivo* behaviour of PP-derived μP pollutants on a cellular level.

Several Norwegian institutions and initiatives have pioneered extensive studies in evaluating μP research;[54] despite a plethora of published articles, it is posited that a lack of standardisation and validated methods, particularly for the smallest plastic particles, hamper conclusive and harmonised research.[55] Given the interdisciplinary nature of the problem, it is well within the remit of polymer scientists to design, synthesise, and provide specific model polymers for μP analysis in collaboration with relevant academic disciplines. We have recently reported a general two-step methodology to functionalise PP, creating a wide range of covalent linkages, something traditionally difficult to achieve in a controlled manner.[56] Consequently, we present a method for the covalent fluorescent labelling of rhodamine B (**Rb**) functionalised PP, $\mathbf{PP_{Rb}}$, and subsequent μP evaluation in a human kidney cell line. We believe that this work provides a new methodology for covalently bound fluorescent tags on a PO system which allows confident analysis of any polymer–cell interaction. This has the potential to offer a harmonised approach for the study of related polymeric materials and enable conclusive evaluation of the interaction of such ubiquitous materials within cells and organisms.

5.4. Results and discussion

5.4.1. Synthesis and characterisation of PP_{Rb}

PP_{Rb} was synthesised *via* the transformation of previously reported alcohol-functionalised PP copolymer (**PP_{EAE}**) under Steglich esterification conditions (DMAP 0.3 eq., DCC 2 eq., DCM, 80 °C, 72 h) with **Rb** (2 eq.) (Figure 5.1).[56, 57]

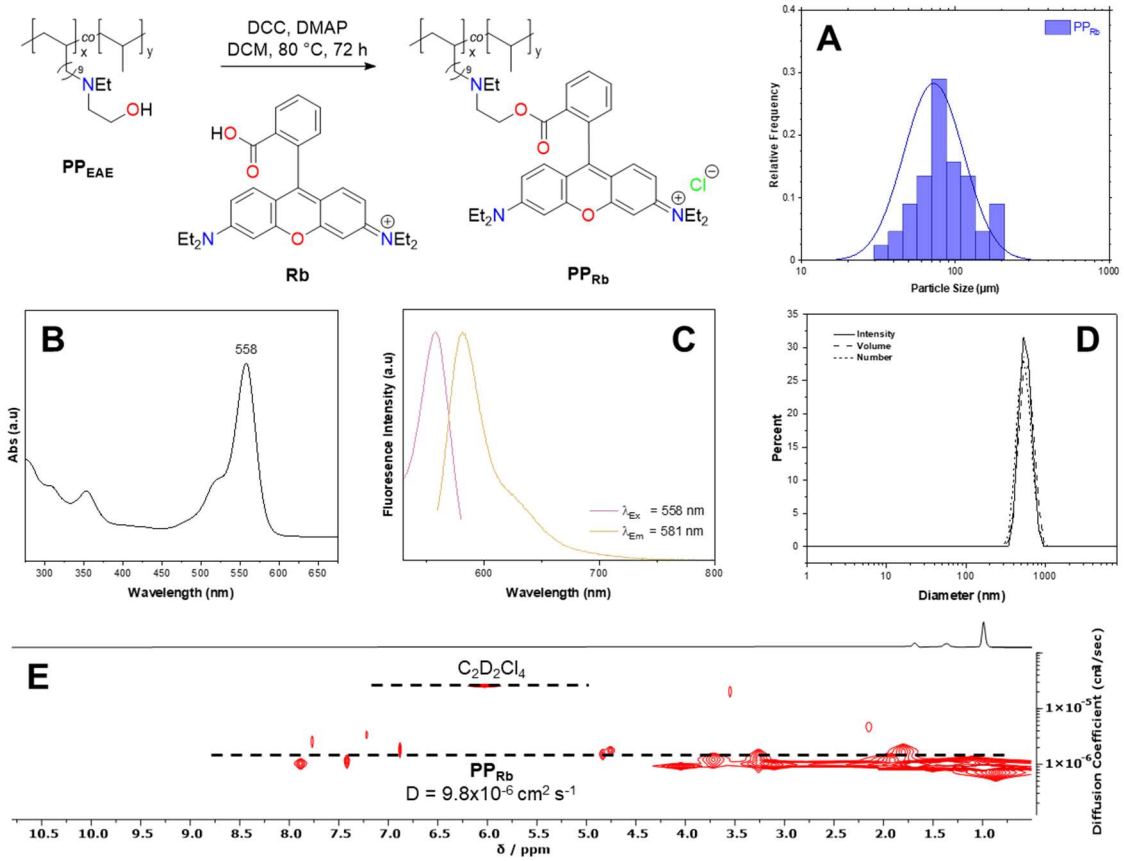

Figure 5.1 Scheme: Synthesis of **PP_{Rb}** under Steglich esterification conditions, (**A**) Solid particle size distribution histogram as determined by SEM (Figure A4.9), (**B**) UV-Vis spectrum of **PP_{Rb}** solution (0.5 mg mL^{-1}, chloroform), (**C**) Fluorescence spectrum of **PP_{Rb}** solution (0.5 mg mL^{-1}, chloroform), (**D**) DLS analysis of **PP_{Rb}** solution (1 mg mL^{-1}, toluene), and (**E**) DOSY ^{1}H NMR spectrum (500 MHz, $C_2D_2Cl_4$, 393 K).of **PP_{Rb}**.

Following extensive purification by water Soxhlet extraction, **PP_{Rb}** with 1.87 mol% covalently-bound dye incorporation was isolated and fully characterised. Key ^{1}H NMR spectroscopic handles evidence the presence of dye; six aromatic resonances between 6.37–7.91 ppm integrate appropriately (Figure A4.1). Convection compensated diffusion

experiments support the conclusion that **Rb** is bound to a higher molecular weight species with a diffusion coefficient of 9.8×10^{-6} cm^2 s^{-1}, which is comparable to the parent copolymer (*ca.* 9.9×10^{-6} cm^2 s^{-1}) and considerably different from the free dye (*ca.* 6.2×10^{-6} cm^2 s^{-1}) as tracked by aromatic protons and distinct quartet assigned to -NC***H***$_2$CH$_3$ (3.44 ppm) (Figure A4.1–2). **PP$_{Rb}$** solution in chloroform (0.5 mg mL^{-1}) displays an excitation wavelength (λ_{Ex}) at 558 nm by ultraviolet-visible (UV-Vis) spectroscopy (Figure 5.1). Significantly, the polymer was also shown to be fluorescent with an emission wavelength (λ_{Em}) at 581 nm (Figure 5.1). Crucially, λ_{Ex} and λ_{Em} are distinctly altered when compared to derivative **Rb** (λ_{Ex} = 569 nm, λ_{Em} = 592 nm) in comparable molar concentration of fluorophore in chloroform (Figure A4.8).

The polymer was further characterised by Fourier transform infrared spectroscopy (ν = 1736 cm^{-1} (C=O) and 808 cm^{-1} (C=C$_{Ar}$)), differential scanning calorimetry (T_m = 113 °C), and evidenced a single decomposition step (T_{max} = 431 °C) by thermogravimetric analysis (Figure A4.4). M_n analysis by size exclusion chromatography (SEC) was unsuccessful, with **PP$_{Rb}$** not eluting within the calibration window; however, theoretical molar mass ($M_{n,\,th}$) is predicted *ca.* 14 700 g mol^{-1} based on parent copolymer experimental molar mass ($M_{n,\,SEC}$ = 13 800 g mol^{-1}) (Figure A4.6). Since the Mark Houwink correlation is not known for functionalised PP, and the presence of a polar group is likely to affect the radius of gyration in solution, but it is reasonable to assume that the backbone chain length is unchanged during post polymerisation modification.[58] Dynamic light scattering (DLS) suggests that **PP$_{Rb}$** aggregates in the solution state, common for amphiphilic copolymers and potentially induced by the ionic nature of the fluorophore.[59] **PP$_{Rb}$** in toluene solution (1 mg mL^{-1}) displayed good agreement between number, volume, and intensity values for hydrodynamic diameter (D_h), *ca.* 570 nm, and

increased from the parent copolymer *ca*. 140 nm, supporting a micellar arrangement in solution with increasing hydrophilic character (Figure 5.1, Figure A4.7, and Table A4.1). It is worth noting that this may subsequently affect the permeability of $\mathbf{PP_{Rb}}$ towards the cell membrane; however, existing *in vitro* experiments employ charged, colloidally stable PS particles[44] and we believe our approach offers an alternate with significantly reduced impact (*vide infra*). Additionally, some $\mathbf{PP_{Rb}}$ was cryofractured ($^{c}\mathbf{PP_{Rb}}$) in an attempt to simulate accelerated weathering (Figure A4.10); such that the irregularities in size and shape of μP found within the environment could be rudimentally assessed.[32]

5.4.2. Cellular Studies

Incorporating fluorophores directly into microplastic models marks a critical advancement in visualising and understanding μP interactions within biological systems. Fluorophore incorporation on PP enabled an *in vitro* investigation in a human embryonic kidney (HEK293T) model cell line where $\mathbf{PP_{Rb}}$ is utilised as a model for μP, overcoming imaging issues suffered by traditional polyolefins. Through the covalent linkage of the dye moiety, it can be concluded that any observations arise due to the presence of dye-bound polymer and not through leaching; other methods previously reported suffer from this drawback.[42, 48, 60]

HEK293T cells were chosen as the model cell line to investigate uptake and localisation *via* confocal microscopy. The primary entry points for μPs into the human body are ingestion, inhalation, and dermal contact.[61, 62] Once internalised, μPs can enter the circulatory system, potentially accumulating in organs such as the gut, liver, and kidneys.[63] Given the kidney's role in filtering and detoxifying various substances, including environmental contaminants like μPs, the HEK293T cell line serves as a relevant model for examining cellular defence mechanisms in response to μPs.[64]

The acute cytotoxicity of **PP$_{Rb}$** was assessed *in vitro* using the alamarBlue™ Cell Viability Assay in HEK293T cells. Cells were exposed to a range of [**PP$_{Rb}$**] for 24 h, with cell viability measured across the concentration gradient. No significant cytotoxic effects were observed up to the highest concentration tested (**PP$_{Rb}$** = 70 μM), as compared to the control group (**PP$_{Rb}$** = 0 μM) (Figure 5.2). Additionally, bright-field microscopy of cells treated with 35 μM **PP$_{Rb}$** for 24 hours revealed no signs of cell death or structural abnormalities relative to untreated control cells (Figure 5.2 and A4.12). It is worth noting that **PP$_{Rb}$** was rigorously purified prior to cell treatment. In environmental contexts, however, μPs often act as sorbents, potentially concentrating harmful and toxic materials on their surfaces, which may influence their biological effects.[33, 65-67]

To assess the uptake and localisation of **PP$_{Rb}$** *in vitro*, HEK293T cells were incubated with either 35 μM of unbound fluorophore (**Rb**) or fluorophore-bound **PP$_{Rb}$** for 1 h and 24 h, respectively, and compared with untreated control cells (Figure 5.3). At both time points, a detectable signal was observed in the 555 nm channel for both **Rb** and **PP$_{Rb}$**, with minimal background fluorescence in the negative control group. Notably, cells treated with **PP$_{Rb}$** exhibited a higher signal intensity compared to those treated with free **Rb**, indicating a consistent cellular uptake of **PP$_{Rb}$** without removal upon washing. The 1 h treatment period demonstrates rapid cellular uptake and accumulation of **PP$_{Rb}$** within HEK293T cells. The dye-bound polymer, **PP$_{Rb}$**, exhibits directed labelling within cells due to its polymeric structure, in contrast to the free **Rb** dye, which results in a more diffuse cellular distribution. Accumulation of **PP$_{Rb}$** within cells was evident, as confirmed by z-stack imaging (Figure 5.3), highlighting the polymer's capacity for localised uptake and retention compared with the less structured, widespread labelling

pattern observed with free **Rb**. The different observed cellular behaviours of both **Rb** and **PP$_{Rb}$** are consistent with the absence of ester hydrolysis and dye liberation from **PP$_{Rb}$**.[68]

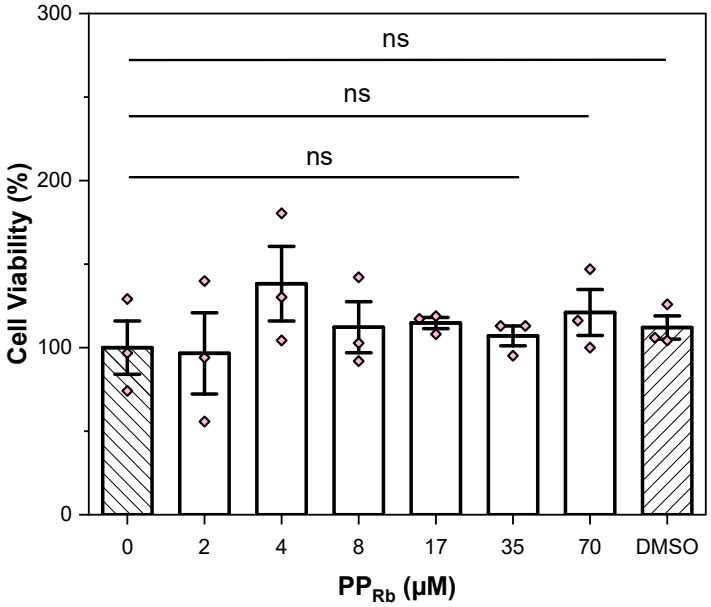

Figure 5.2 *In vitro* cytotoxicity assessment of **PP$_{Rb}$** in HEK293 cells using the alamarBlue™ Cell Viability Assay. (Top) Cell viability (%) in response to various concentrations of **PP$_{Rb}$** (0–70 μM) after 24 h of treatment, as compared to the DMSO control group. Data are represented as mean ± standard error of the mean (n = 3). "ns" indicates no statistically significant difference ($p > 0.05$) relative to the control (0 μM **PP$_{Rb}$**).

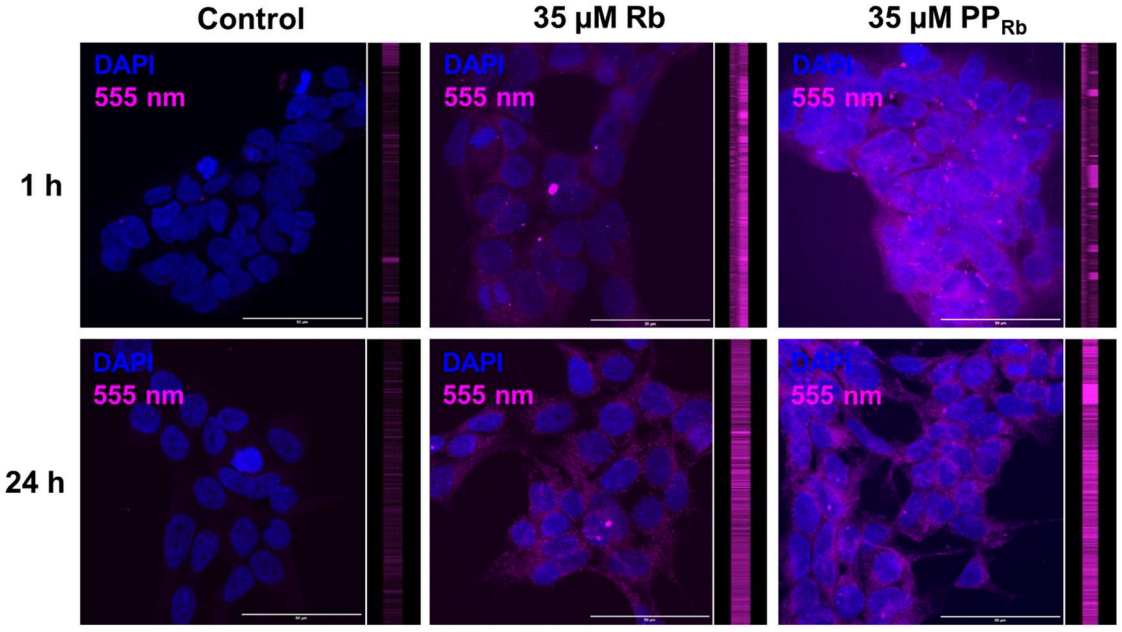

Figure 5.3 Confocal microscopy images showing the cellular uptake and localisation of **Rb** and dye-bound polymer **PP$_{Rb}$** in HEK293T cells. Cells were incubated with either 35 μM of free **Rb** or **PP$_{Rb}$** for 1 h (top) and 24 h (bottom) and compared with untreated control cells. The images display fluorescence representing the presence of **Rb** or **PP$_{Rb}$** (magenta) and DAPI nuclear staining (blue). Z-stack panels (side view) illustrate the spatial distribution of fluorescence within the cells. Scale bars = 50 μm.

After 24 h, cellular labelling of **PP$_{Rb}$** is reduced compared to the 1 h time point, suggesting a potential decrease in intracellular retention (Figure 5.3). This reduction in labelling may indicate that **PP$_{Rb}$** is being actively removed from the cell through a cellular clearance pathway, possibly *via* an endosomal recycling pathway.[69]

A competition assay was conducted to assess the influence of the parent alcohol-functionalised copolymer, **PP$_{EAE}$**, on the cellular localisation of **PP$_{Rb}$** (Figure 5.4, Figure A4.11). The results indicated that cellular localisation of **PP$_{Rb}$** is directed by the parent polymer, as fluorescence was significantly decreased upon co-incubation with 35 μM **PP$_{EAE}$**. This further supports the limited impact of the charged fluorophore driving cellular uptake, strengthening the role of **PP$_{Rb}$** as a model μP. Notably, this competitive reduction in fluorescence was not observed with the **Rb** fluorophore alone, underscoring that **PP$_{EAE}$**, and not **Rb**, modulates the intracellular dynamics of **PP$_{Rb}$** localisation.

Furthermore, a sample of **PP$_{Rb}$** was subjected to cryogenic fracturing to produce **^{c}PP$_{Rb}$**, a model intended to simulate accelerated environmental degradation.[32] However, data showed no significant difference in cellular localisation between **^{c}PP$_{Rb}$** and the original **PP$_{Rb}$** sample (Figure A4.8). Importantly, across all timepoints, there was no observed co-localisation of **PP$_{Rb}$** and nuclear stain, DAPI (Figure A4.9). Excluding certain molecules or structures from the nucleus can prevent potential disruptions to nuclear architecture or DNA stability, safeguarding essential cellular processes.[70]

It was hypothesised that, due to the polymer size and relatively low M_n, the polymer, or any nanoparticles formed through self-assembly, would enter the cells through an energy-dependent mechanism involving trafficking through a probable endosomal pathway.[71] It is, therefore, reasonable to infer possible trafficking of **PP$_{Rb}$** to the lysosomes upon

cellular entry. To investigate this, HEK293T cells were stained with LysoTracker, an acidic vesicle-labelling dye, and incubated with **PP_{Rb}** for 1, 24, and 48 h (Figure 5.5). The mean LysoTracker fluorescence intensity for **PP_{Rb}**, **$^{c}PP_{Rb}$** and free **Rb** increased relative to the control at 1 and 24 h, suggesting a potential endosomal uptake mechanism. By 48 h, however, the mean fluorescence intensity of LysoTracker in **PP_{Rb}** samples returned to control levels, while fluorescence for free **Rb** remained elevated. These observations, along with earlier dosing data showing reduced **PP_{Rb}** localisation by 24 h (Figure 5.3), suggest that cells may actively work to clear the polymer over time.

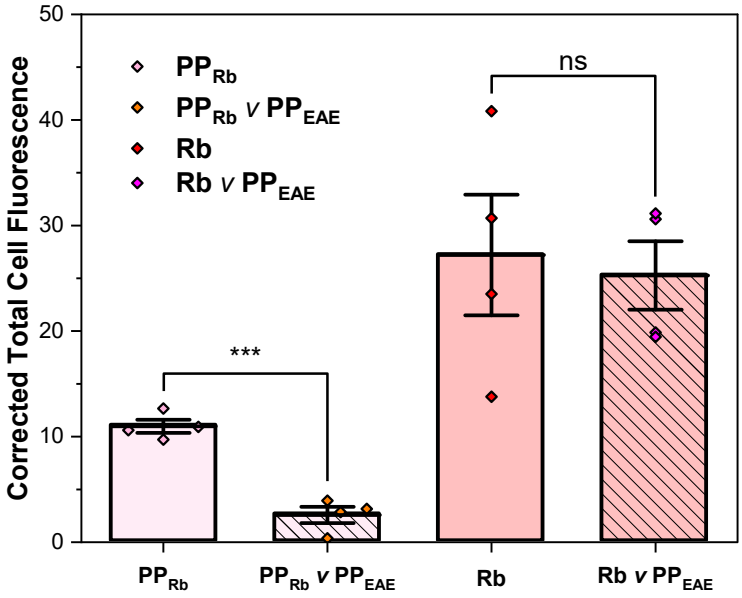

Figure 5.4 Comparison of Corrected Total Cell Fluorescence at 555 nm for **PP_{Rb}**, the competition condition (**PP_{Rb}** *vs* **PP_{EAE}**), free **Rb**, and **Rb** co-incubated with **PP_{EAE}** (**Rb** *vs* **PP_{EAE}**) in a fluorescence competition experiment (n = 3). Confocal microscopy analysis showed a significant reduction in fluorescence for the competition condition **PP_{Rb}** *vs* **PP_{EAE}** compared to PP_{Rb}, indicating that fluorescent labelling is outcompeted by the parent compound **PP_{EAE}**. The fluorescence of free **Rb** remains unchanged with cotreatment with **PP_{EAE}** (**Rb** *vs* **PP_{EAE}**). *** $p < 0.001$, ns $p > 0.05$.

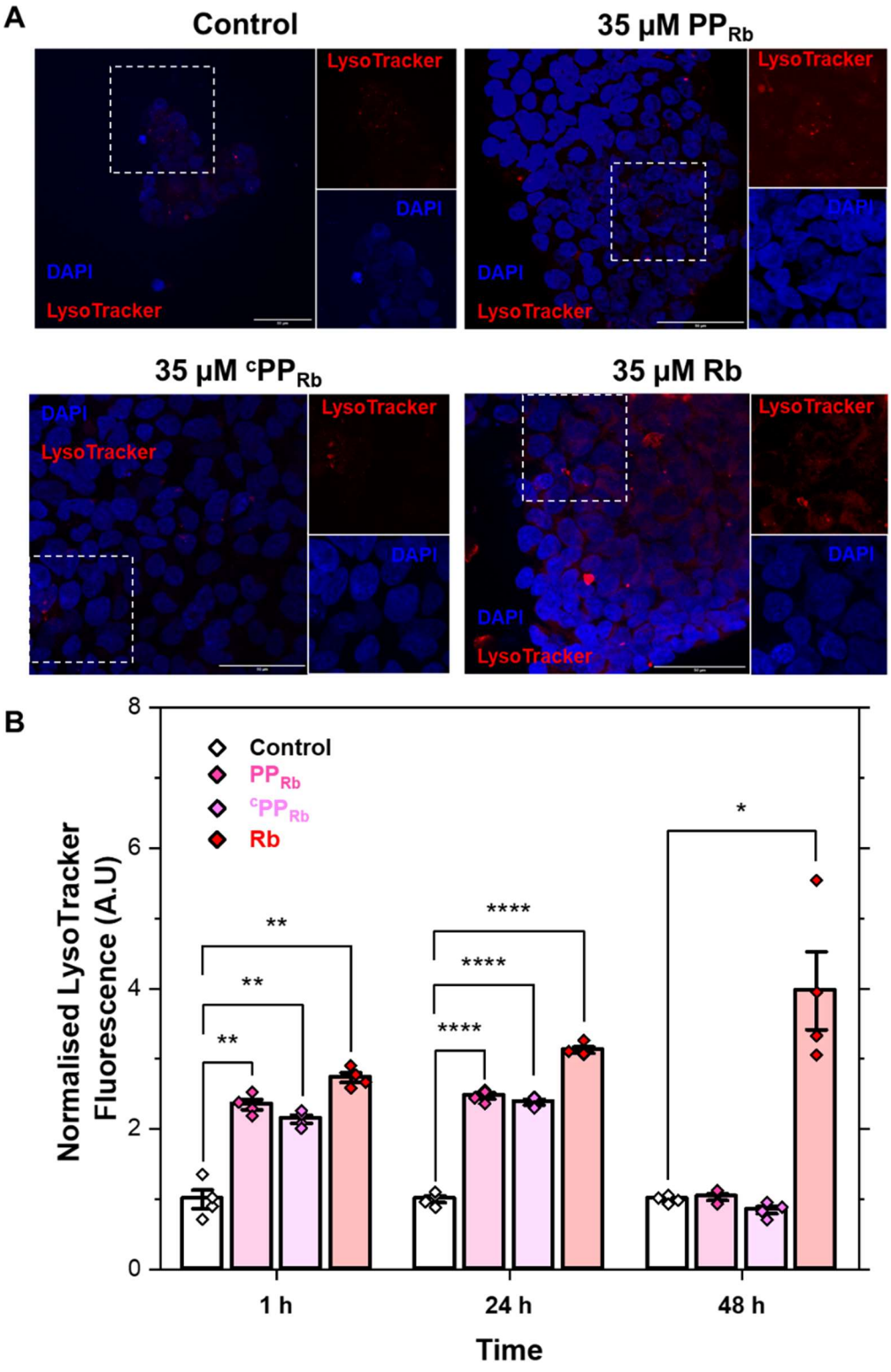

Figure 5.5 Quantification of lysosome formation in HEK293T cells following treatment with **PP_{Rb}**, **$^{c}PP_{Rb}$**, and free **Rb**. (**A**) Confocal microscopy images showing lysosomal staining with LysoTracker (red) and nuclear staining with DAPI (blue) in control cells and cells treated with 35 μM of **PP_{Rb}**, **$^{c}PP_{Rb}$**, or free **Rb** for 1 h. Dashed white boxes indicate magnified regions (×3 magnification). (**B**) Normalised LysoTracker fluorescence intensity (A.U.) was quantified over time (1, 24, and 48 h) for each treatment group. Data are represented as mean ± SEM (n = 3).**p < 0.01, ***p < 0.001, and ****p < 0.0001, compared to control. Scale bars = 50 μm.

5.4.3. Conclusionary remarks

Polypropylene with covalently-bound fluorescent rhodamine B tag, **PP$_{Rb}$**, was synthesised and characterised for *in vitro* studies against a HEK293T cell line and evaluated by confocal microscopy. The two-step copolymerisation – post-modification strategy employed is facile and, importantly, allows preparation of rigorously purified model polymer samples that do not undergo dye leaching.

Incubation with **PP$_{Rb}$** resulted in rapid cellular uptake (1 h) whilst remaining non-toxic up to 70 μM. Crucially no observed localisation within the nucleus was observed. Initial investigations into the uptake mechanism and efficacy as a PP μP model were undertaken. Increased mean lysosomal fluorescence intensity following **PP$_{Rb}$** treatment suggests an endosomal uptake mechanism with significant exocytosis implied over a 48 h period. Cellular localisation of **PP$_{Rb}$** is directed by the parent alcohol-functionalised copolymer, as evidenced by competition studies, indicating that **PP$_{Rb}$** is a valuable model for **PP** cell interaction. Optimistically, accounting for the constraints of our investigation, **PP$_{Rb}$** acts as an inert orthogonal species within the cell. However, it is important to investigate this further, especially by probing the polymer species as a vector for harmful environmental substances.

We believe this method for the synthesis and application of covalently bound dye moieties can elucidate the degree to which concern can be levied against the developing environmental plastic pollution. More broadly, this blueprint can enable a precise and confident interlaboratory analysis of polymer-cell interactions through the targeted synthesis of dye-modified polymers of interest. Additionally, this method offers many investigative opportunities, be it an *in vitro* cell line or *in vivo* studies of more complex organisms, including their ecological surroundings.

5.5. References

1. G. Natta, P. Pino, P. Corradini, F. Danusso, E. Mantica, G. Mazzanti and G. Moraglio, *J. Am. Chem. Soc.*, 1955, **77**, 1708-1710.
2. K. Ziegler, E. Holzkamp, H. Breil and H. Martin, *Angew. Chem.*, 1955, **67**, 426.
3. A. H. Westlie, E. Y.-X. Chen, C. M. Holland, S. S. Stahl, M. Doyle, S. R. Trenor and K. M. Knauer, *Macromol. Rapid Commun.*, 2022, **43**, 2200492.
4. L. Resconi, L. Cavallo, A. Fait and F. Piemontesi, *Chem. Rev.*, 2000, **100**, 1253-1346.
5. R. Francis, *Recycling of Polymers: Methods, Characterisation and Applications*, John Wiley & Sons, 2016.
6. V. V. Narmadha, J. Jose, S. Patil, M. O. Farooqui, B. Srimuruganandam, S. Saravanadevi and K. Krishnamurthi, *Int. J. Environ. Res.*, 2020, **14**, 629-640.
7. M. Potrykus, V. Redko, K. Głowacka, A. Piotrowicz-Cieślak, P. Szarlej, H. Janik and L. Wolska, *Sci. Total Environ.*, 2021, **758**, 143649.
8. J. P. G. L. Frias and R. Nash, *Mar. Pollut. Bull.*, 2019, **138**, 145-147.
9. J. Gigault, A. T. Halle, M. Baudrimont, P. Y. Pascal, F. Gauffre, T. L. Phi, H. El Hadri, B. Grassl and S. Reynaud, *Environ. Pollut.*, 2018, **235**, 1030-1034.
10. E. E. Burns and A. B. A. Boxall, *Environ. Toxicol. Chem.*, 2018, **37**, 2776-2796.
11. J. Sun, X. Dai, Q. Wang, M. C. M. van Loosdrecht and B.-J. Ni, *Water Res.*, 2019, **152**, 21-37.
12. A. A. Horton, A. Walton, D. J. Spurgeon, E. Lahive and C. Svendsen, *Sci. Total Environ.*, 2017, **586**, 127-141.
13. S. O. Fakayode, T. F. Mehari, V. E. Fernand Narcisse, C. Grant, M. E. Taylor, G. A. Baker, N. Siraj, M. Bashiru, I. Denmark, A. Oyebade, D. K. Bwambok, C. Kuedukey, T. Alonge and D. Anum, *Appl. Spectrosc. Rev.*, 2024, **59**, 1183-1277.
14. G. Chen, Q. Feng and J. Wang, *Sci. Total Environ.*, 2020, **703**, 135504.
15. A. A. Koelmans, P. E. Redondo-Hasselerharm, N. H. M. Nor, V. N. de Ruijter, S. M. Mintenig and M. Kooi, *Nat. Rev. Mater.*, 2022, **7**, 138-152.
16. P. Liu, X. Zhan, X. Wu, J. Li, H. Wang and S. Gao, *Chemosphere*, 2020, **242**, 125193.
17. K. Liu, X. Wang, T. Fang, P. Xu, L. Zhu and D. Li, *Sci. Total Environ.*, 2019, **675**, 462-471.
18. Y. Jin, L. Lu, W. Tu, T. Luo and Z. Fu, *Sci. Total Environ.*, 2019, **649**, 308-317.
19. L. Lu, Z. Wan, T. Luo, Z. Fu and Y. Jin, *Sci. Total Environ.*, 2018, **631-632**, 449-458.
20. L. Lei, S. Wu, S. Lu, M. Liu, Y. Song, Z. Fu, H. Shi, K. M. Raley-Susman and D. He, *Sci. Total Environ.*, 2018, **619-620**, 1-8.
21. A. Batel, F. Linti, M. Scherer, L. Erdinger and T. Braunbeck, *Environ. Toxicol. Chem.*, 2016, **35**, 1656-1666.
22. L. C. de Sá, M. Oliveira, F. Ribeiro, T. L. Rocha and M. N. Futter, *Sci. Total Environ.*, 2018, **645**, 1029-1039.
23. N. Chartres, C. B. Cooper, G. Bland, K. E. Pelch, S. A. Gandhi, A. BakenRa and T. J. Woodruff, *Environ. Sci. Technol.*, 2024, DOI: 10.1021/acs.est.3c09524.
24. Y. Huang, Q. Liu, W. Jia, C. Yan and J. Wang, *Environ. Pollut.*, 2020, **260**, 114096.
25. F. Shahul Hamid, M. S. Bhatti, N. Anuar, N. Anuar, P. Mohan and A. Periathamby, *Waste Manage. Res.*, 2018, **36**, 873-897.
26. A. A. de Souza Machado, W. Kloas, C. Zarfl, S. Hempel and M. C. Rillig, *Global Change Biology*, 2018, **24**, 1405-1416.
27. N. Baranzini, L. Pulze, C. Bon, L. Izzo, S. Pragliola, V. Venditto and A. Grimaldi, *Fish Shellfish Immunol.*, 2022, **127**, 492-507.
28. T. S. Galloway, M. Cole and C. Lewis, *Nat. Ecol. Evol.*, 2017, **1**, 0116.
29. P. Raju, P. Santhanam, S. S. Pandian, M. Divya, A. Arunkrishnan, K. N. Devi, S. Ananth, J. Roopavathy and P. Perumal, *Arch. Microbiol.*, 2021, **204**, 84.
30. S. Anbumani and P. Kakkar, *Environ. Sci. Pollut. Res.*, 2018, **25**, 14373-14396.
31. H. S. Auta, C. U. Emenike and S. H. Fauziah, *Environ. Int.*, 2017, **102**, 165-176.
32. S. Pragliola, F. Grisi, V. Vitale, O. Sacco, V. Venditto, L. Izzo, A. Grimaldi and N. Baranzini, *Polym. Chem.*, 2022, **13**, 2685-2693.
33. C. Campanale, C. Massarelli, I. Savino, V. Locaputo and V. F. Uricchio, *Int. J. Environ. Res. Public Health*, 2020, **17**.
34. T. Maes, R. Jessop, N. Wellner, K. Haupt and A. G. Mayes, *Sci. Rep.*, 2017, **7**, 44501.
35. L. Nalbone, A. Panebianco, F. Giarratana and M. Russell, *Mar. Pollut. Bull.*, 2021, **172**, 112888.
36. E. G. Karakolis, B. Nguyen, J. B. You, P. J. Graham, C. M. Rochman and D. Sinton, *Environ. Sci. Technol.*, 2018, **5**, 62-67.

37. B. Nguyen and N. Tufenkji, *Environ. Sci. Technol.*, 2022, **56**, 6426-6435.
38. S. Rist, A. Baun and N. B. Hartmann, *Environ. Pollut.*, 2017, **228**, 398-407.
39. M. Long, I. Paul-Pont, H. Hégaret, B. Moriceau, C. Lambert, A. Huvet and P. Soudant, *Environ. Pollut.*, 2017, **228**, 454-463.
40. Y. Mao, H. Ai, Y. Chen, Z. Zhang, P. Zeng, L. Kang, W. Li, W. Gu, Q. He and H. Li, *Chemosphere*, 2018, **208**, 59-68.
41. M. Gao, Y. Liu and Z. Song, *Chemosphere*, 2019, **237**, 124482.
42. E. G. Karakolis, B. Nguyen, J. B. You, C. M. Rochman and D. Sinton, *Environ. Sci. Technol.*, 2019, **6**, 334-340.
43. S. Morgana, B. Casentini, V. Tirelli, F. Grasso and S. Amalfitano, *Trends Anal. Chem.*, 2024, **172**, 117559.
44. B.-K. Jung, S.-W. Han, S.-H. Park, J.-S. Bae, J. Choi and K.-Y. Ryu, *Neurotoxicology*, 2020, **81**, 189-196.
45. Y. Zhang, S. Wang, V. Olga, Y. Xue, S. Lv, X. Diao, Y. Zhang, Q. Han and H. Zhou, *Chemosphere*, 2022, **291**, 132714.
46. M. T. Sturm, E. Myers, D. Schober, A. Korzin and K. Schuhen, *Analytica*, 2023, **4**, 27-44.
47. W. J. Shim, S. H. Hong and S. E. Eo, *Anal. Methods.*, 2017, **9**, 1384-1391.
48. G. Malafaia, T. M. d. Luz, M. A. I. Ahmed, S. Karthi and A. P. d. C. Araújo, *J. Hazard. Mater. Adv.*, 2022, **6**, 100054.
49. D. Jubinville, E. Esmizadeh, S. Saikrishnan, C. Tzoganakis and T. Mekonnen, *Sustain. Mater. Technol.*, 2020, **25**, e00188.
50. E. Maris, A. Aoussat, E. Naffrechoux and D. Froelich, *Miner. Eng.*, 2012, **29**, 77-88.
51. S. Brunner, P. Fomin and C. Kargel, *Waste Manage.*, 2015, **38**, 49-60.
52. A. Arenas-Vivo, F. R. Beltrán, V. Alcázar, M. U. de la Orden and J. Martinez Urreaga, *Mater. Today Commun.*, 2017, **12**, 125-132.
53. R. Shang, H. Gao, F. Luo, Y. Li, B. Wang, Z. Ma, L. Pan and Y. Li, *Macromolecules*, 2019, **52**, 9280-9290.
54. A. L. Lusher, R. Hurley, H. P. H. Arp, A. M. Booth, I. L. N. Bråte, G. W. Gabrielsen, A. Gomiero, T. Gomes, B. E. Grøsvik, N. Green, M. Haave, I. G. Hallanger, C. Halsband, D. Herzke, E. J. Joner, T. Kögel, K. Rakkestad, S. B. Ranneklev, M. Wagner and M. Olsen, *Environ. Int.*, 2021, **157**, 106794.
55. A. Bakir, A. R. McGoran, B. Silburn, J. Russell, H. Nel, A. L. Lusher, R. Amos, R. S. Shadrack, S. J. Arnold, C. Castillo, J. F. Urbina, E. Barrientos, H. Sanchez, K. Pillay, L. Human, T. Swartbooi, M. R. Cordova, S. Y. Sani, T. W. A. W. Wijesinghe, A. A. D. Amarathunga, J. Gunasekara, S. Somasiri, K. Mahatantila, S. Liyanage, M. Müller, Y. Y. Hee, D. F. Onda, K. M. Jansar, Z. Shiraz, H. Amir and A. G. Mayes, *Sci. Rep.*, 2024, **14**, 12714.
56. A. Evans, O. Casale, L. J. Morris, Z. R. Turner and D. O'Hare, *Macromolecules*, 2024, **57**, 10778-10791.
57. B. Neises and W. Steglich, *Angew. Chem. Int. Ed.*, 1978, **17**, 522-524.
58. L. K. Kostanski, D. M. Keller and A. E. Hamielec, *J. Biochem. Biophys. Methods*, 2004, **58**, 159-186.
59. C. J. Kay, P. D. Goring, C. A. Burnett, B. Hornby, K. Lewtas, S. Morris, C. Morton, T. McNally, G. W. Theaker, C. Waterson, P. M. Wright and P. Scott, *J. Am. Chem. Soc.*, 2018, **140**, 13921-13934.
60. Z. Gao, K. Wontor and J. V. Cizdziel, *Molecules*, 2022, **27**, 7415.
61. J. C. Prata, *Environ. Pollut.*, 2018, **234**, 115-126.
62. M. Revel, A. Châtel and C. Mouneyrac, *Curr. Opin. Environ. Sci. Health*, 2018, **1**, 17-23.
63. R. Gautam, J. Jo, M. Acharya, A. Maharjan, D. Lee, P. B. K.C, C. Kim, K. Kim, H. Kim and Y. Heo, *Sci. Total Environ.*, 2022, **838**, 156089.
64. N. Jourde-Chiche, F. Fakhouri, L. Dou, J. Bellien, S. Burtey, M. Frimat, P.-A. Jarrot, G. Kaplanski, M. Le Quintrec, V. Pernin, C. Rigothier, M. Sallée, V. Fremeaux-Bacchi, D. Guerrot and L. T. Roumenina, *Nat. Rev. Nephrol.*, 2019, **15**, 87-108.
65. K. Lu, R. Qiao, H. An and Y. Zhang, *Chemosphere*, 2018, **202**, 514-520.
66. L. G. A. Barboza, L. R. Vieira, V. Branco, N. Figueiredo, F. Carvalho, C. Carvalho and L. Guilhermino, *Aquat. Toxicol.*, 2018, **195**, 49-57.
67. L. Bradney, H. Wijesekara, K. N. Palansooriya, N. Obadamudalige, N. S. Bolan, Y. S. Ok, J. Rinklebe, K.-H. Kim and M. B. Kirkham, *Environ. Int.*, 2019, **131**, 104937.
68. J. Tanaka, A. Evans, P. Gurnani, A. Kerr and P. Wilson, *Polym. Chem.*, 2020, **11**, 2519-2531.
69. L. Shang, K. Nienhaus and G. U. Nienhaus, *J. Nanobiotechnology*, 2014, **12**, 5.
70. B. M. Webster and C. P. Lusk, *Trends Cell Biol.*, 2016, **26**, 29-39.
71. G. J. Doherty and H. T. McMahon, *Annu Rev Biochem*, 2009, **78**, 857-902.

5.6. Statement of Authorship

Title of Paper	Illuminating microplastics in cells: macro-problems for micro-barriers
Publication Status	Draft manuscript, to be submitted to Nature.
Publication Details	**A. Evans**, R. Devereux, Z. R. Turner, A. J. Russel, D. O'Hare.

Student Confirmation

Student Name:	Alexander Oscar Edward Evans
Contribution to the Paper	Project conceptualisation. Performed the polymer synthesis and analysis. Interpreted the polymer data and assisted the *in vitro* analysis. Wrote the manuscript, original draft, with review and editing contributions from all authors.

Signature 	Date 02/01/2025

Supervisor Confirmation

Supervisor name and title: Professor Dermot O'Hare
Supervisor comments: I can confirm that the candidate's contribution to this paper is as described above.

Signature 	Date 19/01/2025

Chapter 6 – Synthesis, Characterisation, and Magnetic Properties of a Permethylated Manganocene

Alexander Evans, Thomas A. Q. Arnold, Paul Ransom, Samantha C. Binding, William K. Myers, Agamemnon E. Crumpton, Zoë R. Turner, Jean-Charles Buffet, and Dermot O'Hare*

Submitted to Angewandte Chemie International Edition (23/04/2025).

6.1. Author contributions

Alexander Evans: Project conceptualisation. Performed the ligand and complex synthesis. Lead crystallographer. Performed the SQUID investigation but was assisted by co-author (Binding). Interpreted the requisite data. Wrote the manuscript, original draft, review and editing.

Thomas A. Q. Arnold: Improved ligand synthesis and complex synthesis investigation and formal analysis. Manuscript, review and editing.

Paul Ransom: Improved ligand synthesis investigation and formal analysis. Manuscript, review and editing.

Samantha C. Binding: Investigation and formal analysis of SQUID. Manuscript, review and editing.

William K. Myers: Investigation and formal analysis of EPR. Manuscript, original draft of EPR section, review and editing.

Agamemnon E. Crumpton: Performed the quantum chemical calculations. Manuscript, review and editing.

Zoë R. Turner: Manuscript, review and editing. Supervision.

Jean-Charles Buffet: Manuscript, review and editing. Supervision.

Dermot O'Hare: Corresponding author. Manuscript, review and editing. Supervision.

6.2. Abstract

The heptamethylindenyl ligand (Ind*) has been used to synthesise the manganese complex, Ind*$_2$Mn, by lithiation of the proligand and subsequent salt metathesis with $MnCl_2$. The solid state molecular structure indicates a low-spin (S = ½) ground state for the Mn^{2+} metal centre at 100 K. Solution EPR spectroscopy, solid state magnetic susceptibility measurements, and computational investigation suggest the complex undergoes thermally accessible spin-crossover to a high-spin (S = $^5/_2$) ground state.

6.3. Introduction

Following the discovery of the prototypical metallocene complex, ferrocene,[1-3] the cyclopentadienyl anion (Cp) has become ubiquitous in the isostructural transition metal metallocenes (η^5–Cp_2)M (*e.g.*: M = V–Ni),[4-6] and further existing in complexes exhibiting a range of hapticities.[7] Cp_2M metallocene sandwich complexes, were later expanded to include s-block (Cp_2Mg)[8,9] and p-block (Cp_2Sn and Cp_2Pb) metals.[10-12] More recently, homo- and heterobimetallic sandwich complexes have been reported in the literature from across the periodic table utilising Cp or sterically and electronically tuned derivatives.[13-16] Additionally, increased steric bulk provided by Cp permethylation, Cp*, yields increased kinetic stability compared to their Cp analogues.[17]

The indenyl anion (Ind), formally a benzannulated derivative of Cp, displays significantly altered chemistry from Cp, predominantly due to its flexibility in binding modes, and has become an important ligand framework in organometallic chemistry. Transition metal bis(η^5–Ind) complexes are well documented, with Ind_2Fe and Ind_2Co first reported in 1954;[18] however, it is notable that Ind_2Mn has eluded characterisation as a non-THF adduct. To date η^6-, η^3-, η^2- and η^1-indenyl transition metal complexes have also been

reported[19,20] in addition to mixed complexation modes with Nesmeyanov *et al.* reporting the synthesis of a tungsten complex displaying both η^3- and η^5-bound Ind ligands to the same metal centre.[21] An array of substituted manganocenes were reported by Hanusa and co-workers in 2010 and later by Maekawa *et al.*.[22,23] A spectrum of binding modes was reported, but five compounds ($Ind^R{}_2Mn$, R = 2-$SiMe_3$, 1,3-$SiMe_3$, 1,3-^{i}Pr, 1,3-^{t}Bu and 1,3-Cy) displayed η^5- binding. Magnetic studies and DFT clearly illustrate that the above species all contain high-spin manganese, mirroring the original discovery concerning Cp_2Mn.

In many cases, indenyl metallocene, and indeed indenyl metallocenophane, complexes, exhibit significantly divergent reactivities compared to their Cp counterparts.[24] This is reasoned to be caused by the ability of the indenyl group to undergo η^5,η^3-haptotropic ring slip while maintaining the aromaticity of the benzene ring. This phenomenon is commonly referred to as the "indenyl effect".[25] The η^5-η^3 ring slip is formally a two-electron oxidation of the metal which becomes electrophilic and coordinatively unsaturated, allowing concomitant associative substitution processes not common for 18 electron complexes,[26] leading to a several-thousand-fold increase in the rate of ligand substitution.[27] This differing reactivity is classically exemplified in the S_N2 (associative) substitution of PPh_3 into the rhodium complex, $IndRh(CO)_2$, which proceeds 10^8 times faster than its Cp analogue.[28]

Similarly to Cp, permethylation confers kinetic stability to permethylindenyl (Ind*) complexes through increased steric bulk. This reduces the propensity for reactive collision, and the positive inductive effect of the methyl groups through $\sigma_{CH} \rightarrow \pi^*_{CC}$ hyperconjugation generally increases the thermodynamic stability.[29] The synthesis of the bulky Ind*H ligand precursor from (2*E*)-2-methylbut-2-enoic acid is well established,[29]

enabling its use in the preparation of Ind* metallocenes (Ind*$_2$M) for a variety of d- and f-block elements through reactions with alkali metal Ind* salts and metal sources (such as Co(acac)$_2$ or FeCl$_2$.*x*THF).[30-36] The electronic properties of the Ind* ligand in Ind*$_2$Fe have been studied by O'Hare *et al.* – a combined electrochemical and photoelectron spectroscopic approach showed quantitatively the electron donating nature of the Ind* ligand by a reduction in the first ionisation energies and redox potentials compared to Cp*$_2$Fe.[30]

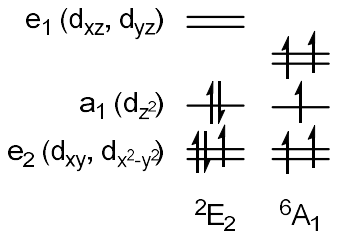

Figure 6.1 Mn d^5 ground states in distorted O_h fields.[37-41]

Manganocene, and its methyl-substituted derivatives, have been extensively studied due to their unique property of having two energetically accessible spin states (Figure 6.1).[37-41] These can be readily interconverted, induced by external stimuli such as light, pressure, or temperature, in a phenomenon known as spin-crossover.[42] It has been found that while Cp$_2$Mn is a high-spin (^{6}A$_{1g}$) species and its permethylated counterpart Cp*$_2$Mn occupies an S = ½ (^{2}E$_{2g}$) ground state, whereas a singularly methylated Cp complex Cp′$_2$Mn varies the occupation of the two spin states quite significantly with temperature.[43-48] Work by Walter *et al*. has examined the high temperature spin-crossover behaviours of a variety of manganocenes using both EXAFS and solid-state magnetic measurements,[49] whilst recent studies have investigated the low-spin d^5 metallocene as a photoredox agent.[50] Herein, we report the synthesis and characterisation of the manganese sandwich complex, Ind*$_2$Mn – the first indenyl-containing manganocene to display thermally induced variation in the Mn^{2+} spin state.

6.4. Results and Discussion

6.4.1. Synthesis and characterisation of Ind*$_2$Mn

Two procedures for the preparation of proligand Ind*H were used in this work: (1) methylation of hexamethylindene (Ind$^{\#}$H) by the action of MeI on the lithiated precursor (Ind$^{\#}$Li), and (2) an improved synthesis following the previously reported route, minimising reaction steps and optimising reagents (Appendix 5.2).[13] In both cases Ind*H was subsequently deprotonated with ^{n}BuLi at –78 °C in THF and isolated as a solid powder. Synthesis of Ind*$_2$Mn was achieved by adding two equivalents of Ind*Li to a stirred THF solution of $MnCl_2$ at –78 °C, allowing to warm room temperature overnight (Scheme 6.1). Work-up afforded Ind*$_2$Mn as a purple solid.

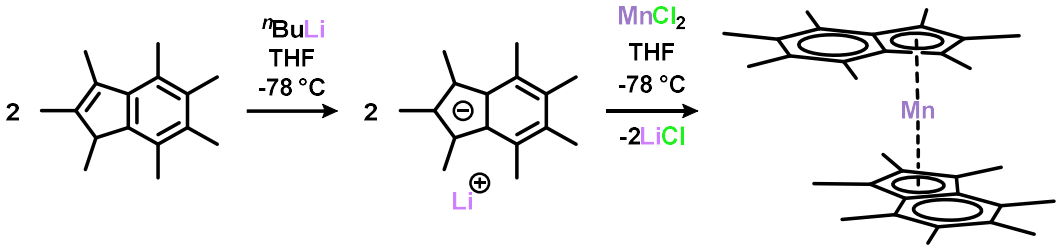

Scheme 6.3 Synthesis of Ind*$_2$Mn.

The solution phase ^{1}H NMR spectrum was paramagnetically broadened as expected for a d^5 Mn^{2+} centre (Figure A5.4). On further investigation by variable temperature ^{1}H NMR spectroscopy (Figure 6.2), the manganocene's wing tip methyl (Me_2) resonance demonstrated a dramatic response to temperature ($\Delta\delta$ = 9.8 ppm between 333 and 233 K) whilst other Me resonances varied slightly ($\Delta\delta$ = 0.18 ppm) over the same temperature range. The temperature dependence of the chemical shifts did not obey the Curie law ($\delta \propto T^{-1}$) and we were unable to extract meaningful quantitative data (*vide infra;* Figure A5.12). This has been similarly observed by Ashley *et al.* for the paramagnetic bimetallic chromium permethylpentalene complex.[51]

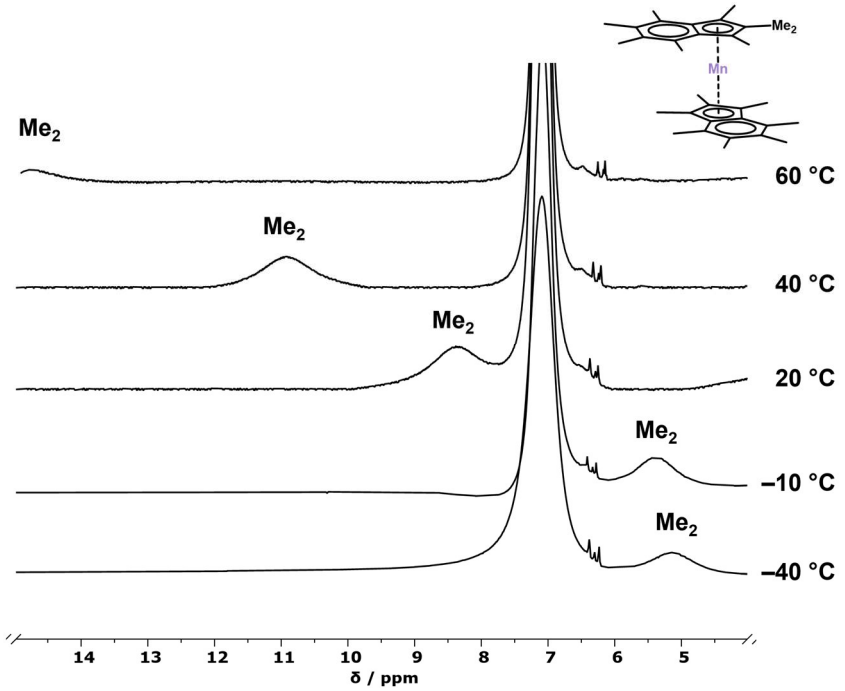

Figure 6.2 Variable-temperature ^{1}H NMR spectra of Ind*$_2$Mn in toluene-d_8 solution.

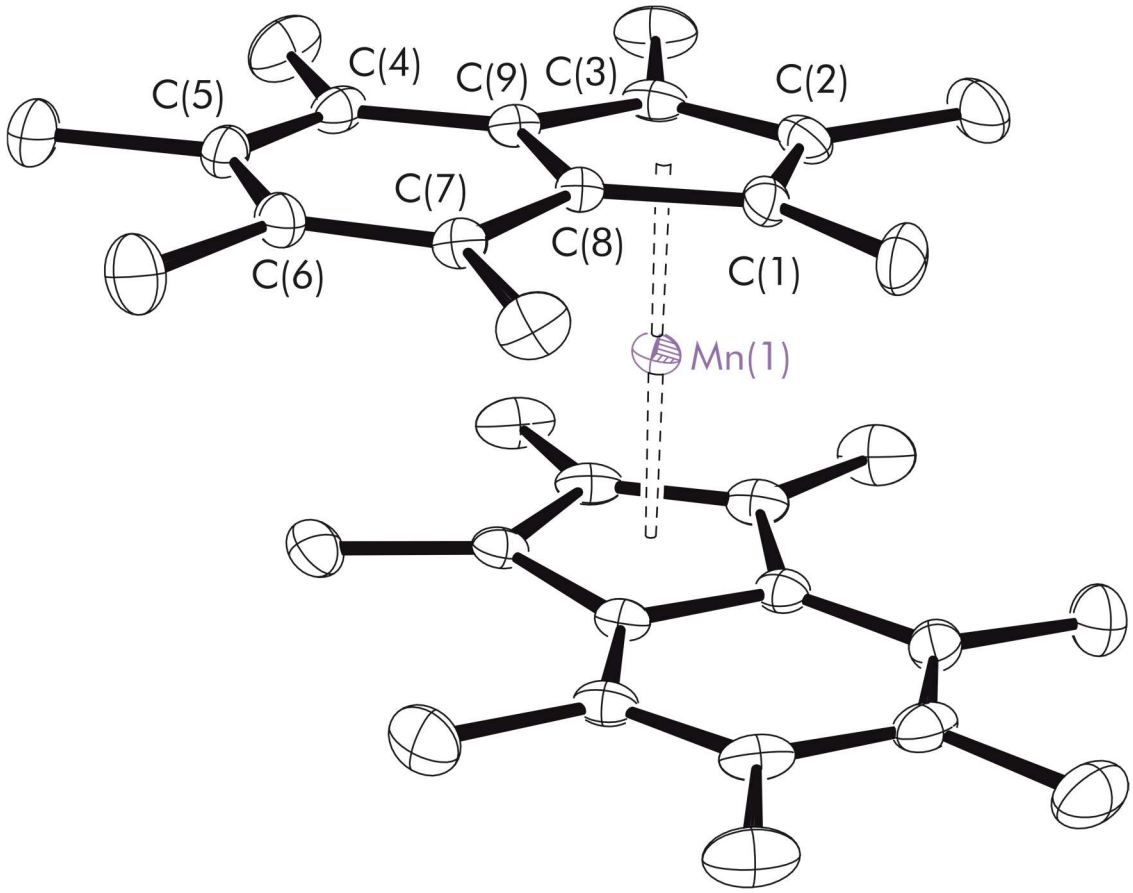

Figure 6.3 Molecular structure of Ind*$_2$Mn. For clarity, hydrogens atoms were omitted (displacement ellipsoids are drawn at 30% probability). Selected distances (Å) and angles (°): Mn-Cp$_{cent}$ 1.7400(6), $\Delta_{M\text{-}C}$ 0.073, $\Delta_{M\text{-}C}$ 0.077, RA 85.2(2), C_6-C_5 1.443(2), C_{21}-C_{22} 1.441(2). [b]Ring-slip parameter ($\Delta_{M\text{-}C}$) defined in Equation A5.1. Rotation angle (RA) based on adapted torsion angle, visually defined in Figure A5.8.[52]

Single crystals suitable for X-ray diffraction were obtained from a concentrated hexanes solution after cooling to –24 °C overnight. The molecular structure is depicted in Figure 6.3. The molecule crystallises in the triclinic space group $P\bar{1}$; alternate views are shown in Figure A5.7, and relevant bond lengths and angles are given in Table A5.2. Scrutinising the molecular structure, the Ind* ligands are nearly coplanar, as shown by the low value of the fold angles about the C_6-C_5 ring junctions (1.91(6) and 2.68(6)°) and a tilt angle = 4.80(5)°. Crystal structures previously reported for neutral Ind*$_2$M complexes of the first row transition-metals are those of Ind*$_2$Cr,[31] and Ind*$_2$Fe.[53] The expected trend in decreasing average M-C distance is observed across the period (Cr = 2.182 Å, Mn = 2.1272(13) Å, Fe = 2.074 Å). The average Mn-C distance is significantly different from the values observed for all other structurally characterised alkyl manganocenes, Ind$^R_2$Mn where R = 2-SiMe$_3$, 1,3-SiMe$_3$, 1,3-^{i}Pr, 1,3-^{t}Bu and 1,3-cyclohexyl (Table 6.1), where the reported average Mn-C distance is 2.41 Å.[22,23] Furthermore, the average Mn-Cp$_{cent}$ distance is 1.7400(6) Å for Ind*$_2$Mn compared to 2.05 Å for the other Ind$^R_2$Mn complexes. By both measures, the Ind*$_2$Mn distance is 0.3 Å shorter, clearly indicating a major change in the electronic structure. In fact, the measured Mn-Cp$_{cent}$ distance much more closely matches the value for Cp*$_2$Mn (1.734 Å), a low-spin manganocene.[54] A DFT analysis conducted by Maekawa *et al*. on the effect of the spin state of Mn in their bis(indenyl) analogue suggested dramatically different values for the M-Cp$_{cent}$ distance in the low- and high-spin cases, encouraging us to investigate the effect of Ind* computationally.[23] Interestingly, the rotation angle (RA) for Ind*$_2$Mn is 85.2(2)°, whereas that for the chromium and iron species are 180° and 151° respectively; this value is similar to that found for the cationic cobalt and chromium species, and does not fit previous conclusions that the RA for permethylindenyl complexes fall broadly into two regions: 180° for the neutral species and 90° for the

cations.[31] However, it is in good agreement with the observed and calculated values for $Ind^{R}{}_2Mn$, where R = 1,3-^{t}Bu and 1,3-$SiMe_3$ are reported as 86.0° and 83.7° respectively.[22,23] It was noted that the ring-slip parameter values ($\Delta_{M\text{-}C}$ = 0.073 and 0.077 Å) were within the range of literature values (0.07–0.156 Å).

Table 6.3 Comparison of relevant parameters for other crystallographically characterised indenyl manganocenes.[a]

$Ind^{R}{}_2Mn$	M-C avg. (Å)	Cp_{cent}-M (Å)	$\Delta_{M\text{-}C}$[b] (Å)	RA[c] (°)
R = 1,2,3,4,5,6,7-Me	2.127	1.740	0.075	85.2
R = 2-$SiMe_3$[22]	2.409	2.079	0.14	180
R = 1,3-$SiMe_3$[22]	2.42	2.085	0.12	83.7
R = 1,3-^{i}Pr[22]	2.4	2.04	0.07	176
R = 1,3-^{t}Bu[23]	2.42	2.10	0.156	86.0
R = 1,3-cyclohexyl[23]	2.383	1.96	0.148	91.35

[a]Contents calculated according to Equation A5.1 and Figure A5.8. [b]Ring-slip parameter ($\Delta_{M\text{-}C}$) defined in Equation A5.1. [c]Rotation angle (RA) based on adapted torsion angle, visually defined in Figure A5.8.[52]

6.4.2. Electron Paramagnetic Resonance (EPR) Studies

The temperature dependence of the X-band CW-EPR signal for $Ind^*{}_2Mn$ was studied between 4.5–160 K in a toluene glass. Representative spectra are shown in Figure 6.4. At 12 K, the signal is characteristic of low-spin Mn^{2+}. As the temperature approaches 100 K, the unresolved outer manifold transitions of high-spin Mn^{2+}, $M_S = \pm^5/_2 \leftrightarrow M_S = \pm^3/_2$ and $M_S = \pm^3/_2 \leftrightarrow M_S = \pm^1/_2$, are apparent on either side of the sextet of ^{55}Mn hyperfine lines at g = 2 from the low-spin Mn^{2+} and $M_S = \pm^1/_2 \leftrightarrow M_S = \pm^1/_2$ of high-spin Mn^{2+}. Double integration of the total EPR signal over the temperatures studied reveals an increasing amplitude with temperature as the high-spin state is populated. The low-spin signal was simulated, shown in Figure A5.13, providing g-values of $g_{\parallel}$ = 2.56 and $g_{\perp}$ = 1.975, while

the ^{55}Mn hyperfine simulations were $A_{||}(^{55}\text{Mn})$ = 206 MHz and $A_{\perp}(^{55}\text{Mn})$ = 80 MHz. The theory of Maki and Berry has a separation of $g_{||}$ and $g_{\perp}$ defined as follows.[55]

$$\begin{gathered} g_{||} = 2 + 4\kappa'(1-\zeta^2)/(1+\zeta^2) \\ g_{\perp} = 4\zeta/(1+\zeta^2) \\ \zeta = (\delta/\xi)/\left(1+\sqrt{(1+(\delta/\xi)^2)}\right) \end{gathered} \quad (1)$$

Here, the observed g-values of $g_{||}$ and $g_{\perp}$ are described with respect to the orbital reduction factor, κ', effective spin orbit coupling parameter, $\xi = \kappa'\xi_0$, and an axial distortion parameter, δ. It was found that this molecule has an axial distortion of $|\delta|$ = 1700 cm^{-1}, with κ' = 0.89, using the literature spin orbit coupling of ξ_0 = 305 cm^{-1}.

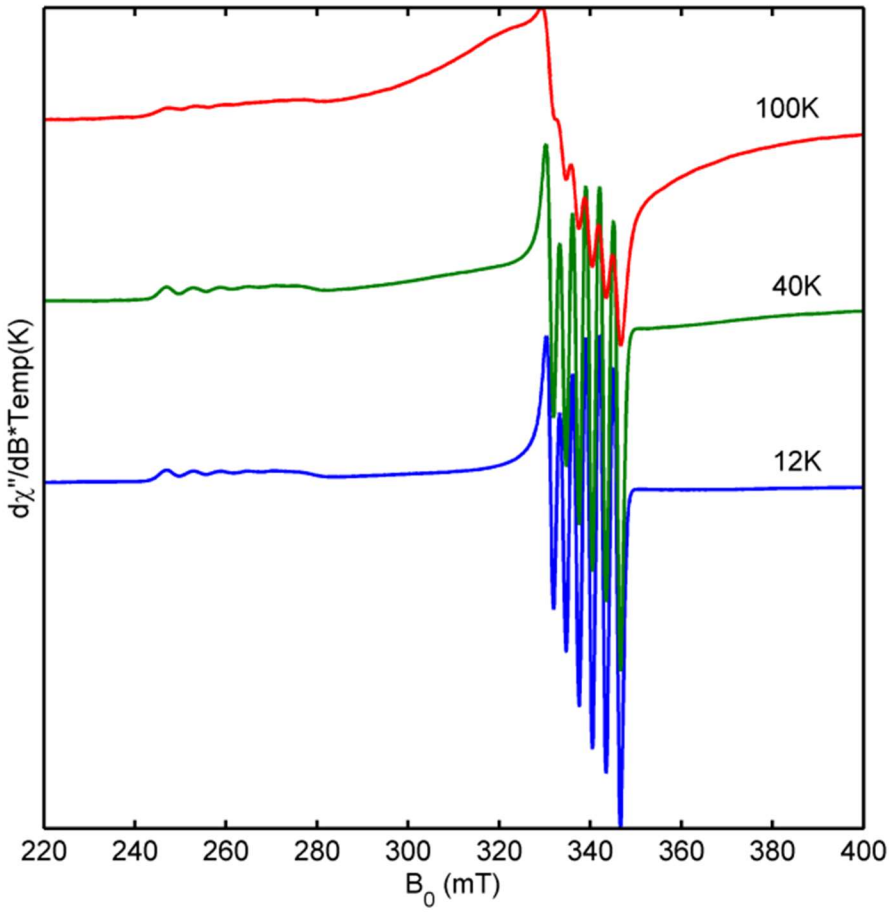

Figure 6.4 X-band CW-EPR of the Ind*$_2$Mn complex at 12, 40 and 100 K. Conditions were a microwave power of 50 μW, 100 kHz modulation amplitude of 0.8 mT, microwave frequency of 9.372(4) GHz and a time constant of 20.48 ms.

According to Equation 1, the Ind* ligand provides a new extreme of an axial distortion, shown in Figure. A5.8. Comparison of the g-values of Ind*$_2$Mn with those of Cp$_2$Mn, Cp*$_2$Mn, and Cp′$_2$Mn reveals a clear trend.[48] The g-value of the lowest symmetry ligand, Cp′, is most similar to that of Ind*, followed by Cp* and Cp. On a lesser note, samples in frozen solution provide g-values that are closer than samples in magnetically-dilute solids.

6.4.3. Magnetic Susceptibility Measurements

The solid state magnetic susceptibility of Ind*$_2$Mn has been measured between 6-300 K (Figure 6.5). No difference was observed between the magnetic susceptibility data of a zero-field cooled (ZFC) compared to a field cooled (FC) sample over this temperature range. Attempts to fit the data to the Curie-Weiss law either gave very poor agreement or unrealistic values. For example, a least squares fit to the magnetic susceptibility data between 50 and 200 K gives a Weiss constant, $\theta = -76$ K, and an effective magnetic moment, $\mu_{eff} = 4.18\ \mu_B$. Such a large value for the Weiss constant is not reasonable for a metallocene of this type (Figure A5.10).

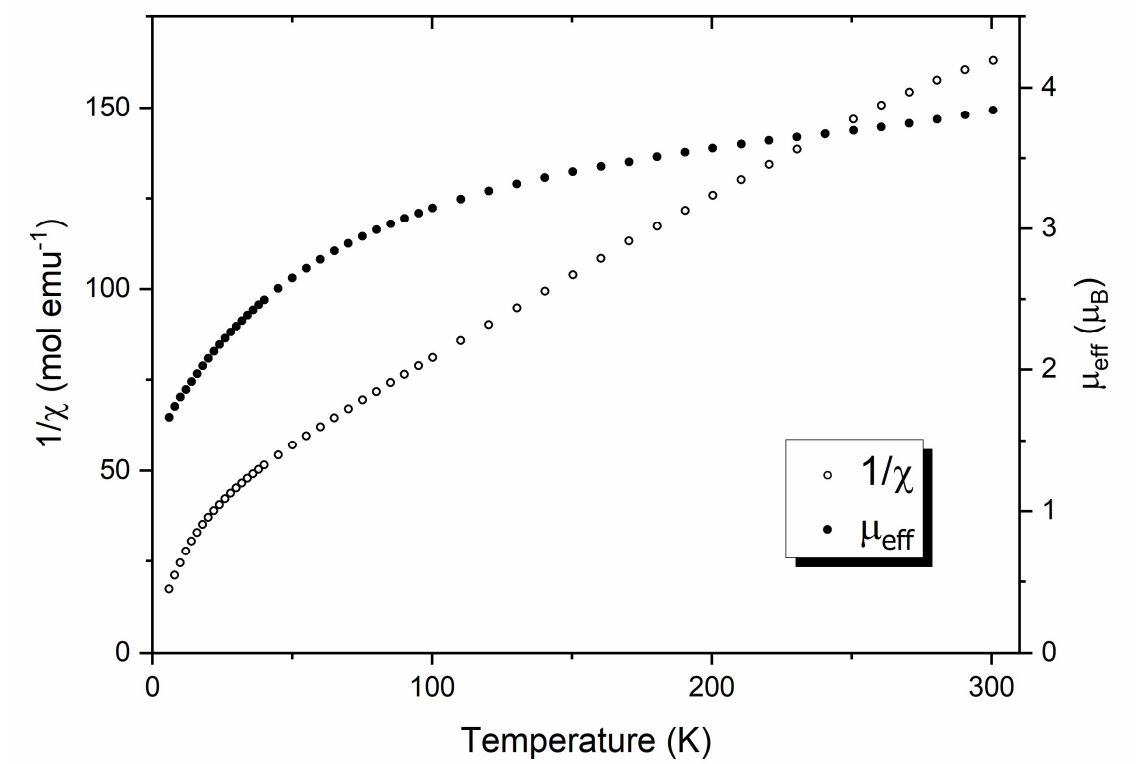

Figure 6.5 Temperature dependence of reciprocal molar magnetic susceptibility ($1/\chi_{mol}$) and effective magnetic moment (μ_{eff}) for Ind*$_2$Mn.

In the solid state, Ind*$_2$Mn undergoes a thermally induced spin-crossover. At 6 K, $\mu_{eff} = 1.67\ \mu_B$ which is close to the value predicted on the basis of the low temperature EPR ($\mu_{eff} = 1.89\ \mu_B$. $S = {}^1/_2$; <g> = 2.19). Between 6 K and 300 K, the effective magnetic moment of the sample steadily increases, reaching a $\mu_{eff} = 3.85\ \mu_B$ at 300 K, which is consistent with a thermally induced partial population of a high-spin, $S = {}^5/_2$ state. Assuming an ideal high-spin excited state with a $\mu_{eff} = 5.92$, the magnetic moment at 300 K is consistent with a 36% population of this high temperature form.[47] A derived Arrhenius plot ($\ln K$ *vs* T^{-1}) over the studied temperature range enabled reasonable extraction of thermodynamic parameters *via* a linear fit regression (Figure A5.11; $R^2 = 0.992$, $\Delta H = 0.485 \pm 0.007$ kJ mol^{-1}, and $\Delta S = -7.98 \pm 0.17$ J mol^{-1}).[49] Negligible enthalpic contributions in the solid state suggest an entropy driven process towards the thermally induced spin-crossover. Variable-temperature single-crystal X-ray diffraction was also employed to probe the system; however, all crystal structures exhibit largely the

same unit cell parameters, with only minor variations attributed to thermal expansion. Notably, there were no significant changes to the RA, suggesting that any geometry induced spin-state transition does not manifest in the crystalline phase; however the complex may behave differently in a toluene glass/solution due to reduced conformational rigidity. Consequently, we believe the magnetometry studies isolate the thermodynamic data associated with purely the spin-crossover phenomena, whilst the NMR data includes a second regime related to the ligand geometry, supported by DFT (*vide infra*), confounding the extraction of thermodynamic parameters.

Solution phase effective magnetic moment was measured at 298 K using the Evans method[56] and found to be 2.53 μ_B in a range of hydrocarbon solvents. Negligible variation of the moment over the accessible temperature range, 193–333 K, was observed. The existence of a low-spin configuration contrasts all previously reported manganese *bis*(indenyl) complexes which have high-spin, $S = {}^5/_2$ ground states from 4–300 K: $(Ind^R{}_2)_2Mn$ (R = ^{i}Pr, ^{t}Bu, or Cy), μ_{eff} = 5.25–5.9 μ_B.[4,5]

The magnetic susceptibility behaviour of $Ind^*{}_2Mn$ reflects the trend observed with *bis*(indenyl)chromium(II) complexes studied by Hanusa, Yee and co-workers, where the staggered and eclipsed conformations favour high-spin ground states, and the gauche conformations are generally associated with low-spin complexes.[57] In addition, they also report a general correlation between increasing methylation and a propensity for low-spin ground states; this trend is mirrored in magnetic studies on the manganocenes Cp_2Mn, $Cp^*{}_2Mn$, and $Cp'{}_2Mn$.[43-48] Extrapolating from these observations, $Ind^*{}_2Mn$ would be expected to favour a low-spin configuration.

6.4.4. Computational Studies

Magnetometry measurements at 300 K indicate that 36% of the complex exists in the high-spin state.[47] At 130 K, EPR spectroscopy reveals the loss of hyperfine splitting, suggesting the presence of a high-spin complex. This observation is consistent with the expectation that a significant high-spin population would overwhelm the signal from the low-spin state. Given the discrepancies between observed spin-crossover behaviours in the NMR, EPR, and SQUID measurements, the complex was investigated computationally in order to probe the ligand influence on the Mn spin-state.

Accurate computational prediction of relative spin state energy levels for metal complexes are notoriously difficult to obtain.[58,59] Screening a variety of density functional theory (DFT) functionals from the crystallographically-defined coordinates of Ind*$_2$Mn yielded a wide range of electronic energy difference between the low- and high-spin states (approximately 420 kJ mol^{-1} ΔE_{HL}; Table A5.4). Given the disparity in ΔE_{HL}, similarly observed in the literature for manganese spin-crossover complexes,[42] more accurate methods were utilised to ascertain an appropriate functional for the reactive surface. Consequently, complete active space self-consistent field with second-order *N*-electron valence state perturbation theory (CASSCF/NEVPT2) along with domain-based local pair natural orbital coupled-cluster theory (DLPNO-CCSD(T)) were selected due to their increased reliability in determining ΔE_{HL}: CASSCF-NEVPT2 ΔE_{HL} = 117 kJ mol^{-1} and CCSD(T) ΔE_{HL} = 134 kJ mol^{-1}.[42] Reasonable agreement between the methods (ΔE = 17 kJ mol^{-1}) prompted selection of the DFT functional MN15 (ΔE = 138 kJ mol^{-1}), due to its alignment with CCSD(T).[42] Consequently optimised geometries were performed, with a scan across the RA for the optimised low- and high-spin structures where single point calculations were performed at DLPNO-CCSD(T)

(Figure 6.6). The potential energy surfaces of the high-spin and low-spin states were found to intersect, supporting the experimental observation that Ind*$_2$Mn undergoes thermally induced spin-crossover.

In order to probe the differences in the nature of the Cp* and Ind* ligand architectures, supplementary energy decomposition analysis (EDA), *via* sobEDA, of L_2Mn (R = Ind* and Cp*) was carried out. The total energy interaction was found to be broadly similar (Table A5.7). While both ligands stabilise the manganese centre through electrostatic and orbital (E_{orb}) interactions, the Ind* ligand contributes both larger Pauli repulsive (E_{rep}) and orbital attractive forces, markedly counteracting one another. Increased E_{rep} is reasonably explained by the imposed sterics of the benzannulated ring. Further decomposition of E_{orb} was undertaken using EDA-NOCV. The pairwise deformation densities reveal that, in the Ind* complex, the benzene ring contributes additional electron density to the Mn centre through its extended π-system (Figure A5.16).

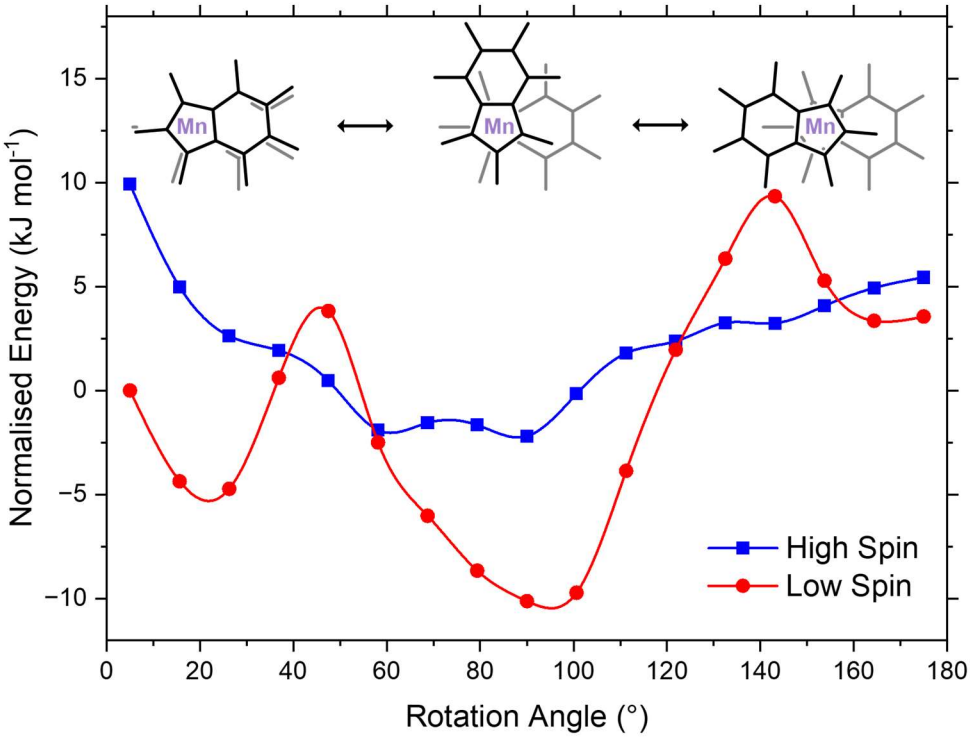

Figure 6.6 Single point calculations performed at CCSD(T) for both high- and low-spin Ind*$_2$Mn, energies normalised to the low-spin complex at 5°.

6.5. Conclusion

The solid state structure and the low temperature magnetic responses of Ind*$_2$Mn suggest that it is the first indenyl manganese complex with a low-spin ground state. At room temperature the solid state magnetic moment suggest that a high-spin ($S = {}^5/_2$) configuration is significantly populated. Given the ubiquity of Cp*, certain circumstances likely demand increased steric constraint; consequently use of Ind* as an alternate ligand framework may provide attractive complex properties and we hope this puts into greater focus the work being done already within the group.[60,61]

6.6. Experimental

Synthesis of Ind*H. 7.40 g 1,2,4,5,6,7-hexamethyl-1*H*-indene (Ind$^{\#}$H, 36.9 mmol, 1 eq.) was dissolved in 150 mL THF and was cooled, in a 300 mL schlenk under N_2, to −78 °C before fast dropwise addition of 23.1 mL n-butyllithium (1.6 M in hexanes; 36.93 mmol, 1 eq.). The reaction mixture was allowed to warm to room temperature over 16 h before cooling to −78 °C and 2.53 mL MeI (40.63 mmol, 1.1 eq.) added dropwise. The reaction mixture was allowed to warm to room temperature over 2 h. THF was removed *in vacuo* and the residue dissolved in DCM and transferred to a separating funnel containing brine solution. Product was extracted in 3 × 50 mL DCM, dried over $MgSO_4$, DCM removed by rotary evaporation before placing the oil in a −4 °C freezer. Crystalline solid product was isolated by Buchner filtration and recrystallised from EtOH at −4 °C yielding 7.35 g (92%) yellow, crystalline 1,2,3,4,5,6,7-heptamethylindene (Ind*H). **^{1}H NMR** (Benzene-*d*$_6$, 298 K, 400 MHz) δ (ppm): 3.03 (q, 1H, $^3J_{HH}$ = 7.5, C***H***), 2.44 (s, 3H, Ar-**Me**), 2.21 (s, 3H, Ar-**Me**), 2.18-2.13 (m, 9H, Ar-**Me** and Cp-**Me**), 1.82 (s, 3H, Cp-**Me**), 2.43 (d, 3H, $^3J_{HH}$ = 7.5, Cp-**Me**).

Synthesis of Ind*$_2$Mn. One equivalent of $MnCl_2$ (0.27 g, 2.18 mmol) was stirred in an ampoule in 30 mL THF for 16 hours, yielding a white suspension. This mixture was cooled to –78 °C and a slurry of two equivalents of Ind*Li (1.00 g, 4.36 mmol) in 30 mL THF added. The yellow-brown mixture was allowed to warm to room temperature and stirred for 15 hours, affording a brown-orange solution. The solvent was removed under vacuum to give a brown-orange solid. Extraction with hexane gave a purple solution, which was filtered through celite and dried *in vacuo* affording a purple solid in 60% yield (0.543 g, 1.30 mmol). **^{1}H NMR** (benzene-d_6, 298 K, 499.9 MHz) δ (ppm): 9.06, 3.05, 2.44, 2.16, 1.82, 1.18 (all broad). **^{13}C{^{1}H} NMR** (benzene-d_6, 298 °K, 499.9 MHz) δ (ppm): 145.3, 142.3, 141.2, 133.5, 132.7, 130.6, 128.6, 126.5, 46.6, 16.8, 16.4, 16.3, 16.3, 16.1, 15.5, 12.3. **MS** (EI): Calc: 481.2667 Found: 481.2301. **UV/Vis**: λ_{max}(*n*-hexanes) = 533.1 nm ($\varepsilon = 5.30 \times 10^2$ mol^{-1} dm^3 cm^{-1}). **FT-IR** (KBr, cm^{-1}): 2965 (s), 1616 (m), 1447 (m), 1385 (s), 1261 (s), 1093 (m), 1022 (m), 801 (s). **CHN** analysis (calculated, found; %): C = 79.79,79.91; H = 8.80, 8.83.

X-ray crystallography details. Colourless single crystals of Ind*H were isolated from concentrated pentane solution at room temperature. $C_{16}H_{22}$, M_r = 214.33, monoclinic, $P2_1/c$, a = 13.0353(4) Å, b = 10.9285(4) Å, c = 9.0453(3) Å, $\alpha = 90°$, $\beta = 91.765(3)°$, $\gamma = 90°$, V = 1287.95(7) Å^3, Z = 4, T = 150 K, block, colourless, 5161 independent reflections, R_1 = 0.0470, wR_2 = 0.1368 [I>=2σ(I)]. CCDC deposition number: 2421030 Dark purple single crystals of Ind*$_2$Mn were isolated from a concentrated solution (hexanes) after cooling to –24 °C overnight. $C_{32}H_{42}Mn$, M_r = 481.59, triclinic, $P\bar{1}$, a = 9.05120(10) Å, b = 10.43980(10) Å, c = 15.81240(10) Å, $\alpha = 73.2730(10)°$, $\beta = 84.7780(10)°$, $\gamma = 63.9150(10)°$, V = 1284.09(2) Å^3, Z = 2, T = 100 °K, block,

purple, 5238 independent reflections, $R(\text{int}) = 0.0279$, $R_1 = 0.0290$, $wR_2 = 0.0801$ [I>=2σ(I)]. CCDC deposition number: 2421029

6.7. Acknowledgment

The authors would like to thank SCG Chemicals plc. (Thailand) for financial support. Thanks to Louis J. Morris for crystallographic assistance with regards to the Ind*H data collection and structure refinement. Thanks to Stephen Boyer of London Metropolitan University for the elemental analysis. We gratefully acknowledge the EPSRC for a Strategic Equipment Grant (EP/V028995/1).

6.8. References

1 T. J. Kealy and P. L. Pauson, *Nature*, 1951, **168**, 1039-1040.
2 S. A. Miller, J. A. Tebboth, J. F. Tremaine, *J. Chem. Soc.*, 1952, 632-635.
3 H. Werner, *Angew. Chem. Int. Ed.*, 2012, **51**, 6052-6058.
4 P. J. Chirik and J. E. Bercaw, *Metallocenes: Synthesis Reactivity Applications*, Wiley-VCH, Weinheim, 1998.
5 P. L. Pauson, *Q. Rev. Chem. Soc.*, 1955, **9**, 391-414.
6 G. Wilkinson, P. L. Pauson, F. A. Cotton, *J. Am. Chem. Soc.*, 1954, **76**, 1970-1974.
7 J. M. O'Connor and C. P. Casey, *Chem. Rev.*, 1987, **87**, 307-318.
8 E. O. Fischer and W. Hafner, *Z. Naturforsch., B*, 1954, **9**, 503-505.
9 G. Wilkinson and F. A. Cotton, *Chem. Ind. (London)*, 1954, 307.
10 L. Wirtz and A. Schäfer, *Chem. Eur. J.*, 2021, **27**, 1219-1230.
11 E. O. Fischer and U. Piesbergen, *Z. Naturforsch., B*, 1956, **11**, 758-759.
12 E. O. Fischer and H. Grubert, *Z. Anorg. Allg. Chem.*, 1956, **286**, 237-242.
13 I. Resa, E. Carmona, E. Gutierrez-Puebla, A. Monge, *Science*, 2004, **305**, 1136-1138.
14 J. T. Boronski, A. E. Crumpton, L. L. Wales, S. Aldridge, *Science*, 2023, **380**, 1147-1149.
15 I.-A. Bischoff, S. Danés, P. Thoni, B. Morgenstern, D. M. Andrada, C. Müller, J. Lambert, E. C. J. Gießelmann, M. Zimmer, A. Schäfer, *Nat. Chem.*, 2024, **16**, 1093-1100.
16 T. Piou, F. Romanov-Michailidis, M. Romanova-Michaelides, K. E. Jackson, N. Semakul, T. D. Taggart, B. S. Newell, C. D. Rithner, R. S. Paton, T. Rovis, *J. Am. Chem. Soc.*, 2017, **139**, 1296-1310.
17 D. C. Calabro, J. L. Hubbard, C. H. Blevins, A. C. Campbell, D. L. Lichtenberger, *J. Am. Chem. Soc.*, 1981, **103**, 6839-6846.
18 P. L. Pauson and G. Wilkinson, *J. Am. Chem. Soc.*, 1954, **76**, 2024-2026.
19 I. A. Lobanova and V. I. Zdanovich, *Russ. Chem. Rev.*, 1988, **57**, 967-980.
20 M. Stradiotto and M. J. McGlinchey, *Coord. Chem. Rev.*, 2001, **219-221**, 311-378.
21 A. N. Nesmeyanov, N. A. Ustynyuk, L. G. Makarova, V. G. Andrianov, Y. T. Struchkov, S. Andrae, Y. A. Ustynyuk, S. G. Malyugina, *J. Organomet. Chem.*, 1978, **159**, 189-199.
22 J. A. Crisp, R. M. Meier, J. S. Overby, T. P. Hanusa, A. L. Rheingold, W. W. Brennessel, *Organometallics*, 2010, **29**, 2322-2331.
23 M. Maekawa, C. G. Daniliuc, M. Freytag, P. G. Jones, M. D. Walter, *Dalton Trans.*, 2012, **41**, 10317-10327.
24 V. Cadierno, J. n. Díez, M. Pilar Gamasa, J. Gimeno, E. Lastra, *Coord. Chem. Rev.*, 1999, **193-195**, 147-205.
25 E. O. Fischer, D. Seus, R. Jira, *Z. Naturforsch., B*, 1953, **8**, 692-693.
26 A. J. Hart-Davis and R. J. Mawby, *J. Chem. Soc. A*, 1969, **0**, 2403-2407.
27 A. J. Hart-Davis, C. White, R. J. Mawby, *Inorg. Chim. Acta*, 1970, **4**, 441-446.

28 M. E. Rerek, L.-N. Ji, F. Basolo, *J. Chem. Soc., Chem. Commun.*, 1983, 1208-1209.
29 T. K. Miyamoto, M. Tsutsui, L.-B. Chen, *Chem. Lett.*, 1981, **10**, 729-730.
30 D. Ohare, J. C. Green, T. Marder, S. Collins, G. Stringer, A. K. Kakkar, N. Kaltsoyannis, A. Kuhn, R. Lewis, C. Mehnert, P. Scott, M. Kurmoo, S. Pugh, *Organometallics*, 1992, **11**, 48-55.
31 D. O'Hare, V. J. Murphy, N. Kaltsoyannis, *J. Chem. Soc., Dalton Trans.*, 1993, 383-392.
32 T. M. Frankcom, J. C. Green, A. Nagy, A. K. Kakkar, T. B. Marder, *Organometallics*, 1993, **12**, 3688-3697.
33 D. Ohare, V. Murphy, G. M. Diamond, P. Arnold, P. Mountford, *Organometallics*, 1994, **13**, 4689-4694.
34 T. M. Trnka, J. B. Bonanno, B. M. Bridgewater, G. Parkin, *Organometallics*, 2001, **20**, 3255-3264.
35 M. Tsutsui, L. B. Chen, D. E. Bergbreiter, T. K. Miyamoto, *J. Am. Chem. Soc.*, 1982, **104**, 855-856.
36 D. O'Hare, V. Murphy, G. M. Diamond, P. Arnold, P. Mountford, *Organometallics*, 1994, **13**, 4689-4694.
37 N. Hebendanz, F. H. Koehler, G. Mueller, J. Riede, *J. Am. Chem. Soc.*, 1986, **108**, 3281-3289.
38 D. Cozak and F. Gauvin, *Organometallics*, 1987, **6**, 1912-1917.
39 J. H. Ammeter, R. Bucher, N. Oswald, *J. Am. Chem. Soc.*, 1974, **96**, 7833-7835.
40 S. Evans, M. L. H. Green, B. Jewitt, G. H. King, A. F. Orchard, *J. Chem. Soc., Faraday Trans. 2*, 1974, **70**, 356-376.
41 J. A. Bandy, F. G. N. Cloke, G. Copper, J. P. Day, R. B. Girling, R. G. Graham, J. C. Green, R. Grinter, R. N. Perutz, *J. Am. Chem. Soc.*, 1988, **110**, 5039-5050.
42 M. Drosou, C. A. Mitsopoulou, D. A. Pantazis, *Polyhedron*, 2021, **208**, 115399.
43 F. Engelmann, *Z. Naturforsch., B*, 1953, **8**, 775-776.
44 E. O. Fischer and H. Leipfinger, *Z. Naturforsch., B*, 1955, **10**, 353-355.
45 L. T. Reynolds and G. Wilkinson, *J. Inorg. Nucl. Chem.*, 1959, **9**, 86-92.
46 G. Wilkinson, F. A. Cotton, J. M. Birmingham, *J. Inorg. Nucl. Chem.*, 1956, **2**, 95-113.
47 M. E. Switzer, R. Wang, M. F. Rettig, A. H. Maki, *J. Am. Chem. Soc.*, 1974, **96**, 7669-7674.
48 J. L. Robbins, N. M. Edelstein, S. R. Cooper, J. C. Smart, *J. Am. Chem. Soc.*, 1979, **101**, 3853-3857.
49 M. D. Walter, C. D. Sofield, C. H. Booth, R. A. Andersen, *Organometallics*, 2009, **28**, 2005-2019.
50 A. M. May, M. Deegbey, K. Edme, K. J. Lee, R. N. Perutz, E. Jakubikova, J. L. Dempsey, *Inorg. Chem.*, 2024, **63**, 1858-1866.
51 A. E. Ashley, A. R. Cowley, D. O'Hare, *Eur. J. Org. Chem.*, 2007, **2007**, 2239-2242.
52 M. J. Calhorda, V. Félix, L. s. F. Veiros, *Coord. Chem. Rev.*, 2002, **230**, 49-64.
53 S. A. Westcott, A. K. Kakkar, G. Stringer, N. J. Taylor, T. B. Marder, *J. Organomet. Chem.*, 1990, **394**, 777-794.
54 D. P. Freyberg, J. L. Robbins, K. N. Raymond, J. C. Smart, *J. Am. Chem. Soc.*, 1979, **101**, 892-897.
55 A. H. Maki and T. E. Berry, *J. Am. Chem. Soc.*, 1965, **87**, 4437-4441.
56 D. F. Evans, *J. Chem. Soc.*, 1959, 2003-2005.
57 M. B. Meredith, J. A. Crisp, E. D. Brady, T. P. Hanusa, G. T. Yee, M. Pink, W. W. Brennessel, V. G. Young, Jr., *Organometallics*, 2008, **27**, 5464-5473.
58 J. Cirera, M. Via-Nadal, E. Ruiz, *Inorg. Chem.*, 2018, **57**, 14097-14105.
59 S. Gómez-Coca and E. Ruiz, *Dalton Trans.*, 2024, **53**, 11895-11902.
60 C. G. Collins Rice, L. J. Morris, J.-C. Buffet, Z. R. Turner, D. O'Hare, *Chem. Commun.*, 2023, **59**, 12128-12131.
61 P. Ransom, A. E. Ashley, N. D. Brown, A. L. Thompson, D. O'Hare, *Organometallics*, 2011, **30**, 800-814.

6.9. Statement of Authorship

Title of Paper	Synthesis, characterisation, and magnetic properties of a permethylated manganocene
Publication Status	*Submitted to Angewandte Chemie International Edition (23/04/2025).*
Publication Details	**A. Evans**, T. A. Q. Arnold, P. Ransom, S. C. Binding, W. K. Myers A. E. Crumpton, Z. R. Turner, J-C Buffet, D. O'Hare

Student Confirmation

Student Name:	Alexander Oscar Edward Evans
Contribution to the Paper	Project conceptualisation. Performed the ligand and complex synthesis. Lead crystallographer. Performed the SQUID investigation but was assisted by co-author (Binding). Interpreted the requisite data. Wrote the manuscript, original draft, with review and editing contributions from all authors.

Signature 	Date 02/01/2025

Supervisor Confirmation

Supervisor name and title: Professor Dermot O'Hare	
Supervisor comments: I can confirm that the candidate's contribution to this paper is as described above.	
Signature 	Date 19/01/2025

Conclusions and outlook

The research discussed in this thesis broadly covers five topics: the synthesis of a range of brominated copolymers *via* solution-phase copolymerisation, subsequent post-modification with a range of functional moieties, and specific use case application testing. Additionally, fluorophore-modified propylene copolymer as a tool for *in vitro* studies of microplastics, and finally the synthesis of a manganese sandwich complex. A summary of each topic and areas for further investigation are outlined below.

i. Copolymerisation of propylene and 11-bromo-1-undecene

Solution-phase copolymerisation of propylene and 11-bromo-1-undecene using C_2, C_1, and C_s-symmetric catalysts afforded poly(propylene)-*co*-(11-bromo-1-undecene), with tuneable comonomer incorporation levels, up to 15.5 mol%, with a range of tacticities (*iso*-, *syndio*-, and *atactic*) and a wide molecular weight span (4−212 kg mol^{-1}). The copolymerisation and polymers were extensively characterised and provide the framework for application specific polymer composition. The copolymerisation of a range of functional comonomers with orthogonal latent reactivity would be an ideal iteration. The ability to selectively functionalise the same terpolymer could provide a platform for more complex physical properties and unique performance.

ii. Post-modification of brominated propylene copolymers

The latent electrophilic reactivity of the pendent bromide has been utilised in one of three general synthetic routes, enabling the incorporation of an array of polar substituents through the formation of a series of covalent connections (C−O, C−N, C−S, C−P, and C−C) with 12 example functionalisations. The resulting functional polypropylenes (PPs) display distinctly altered bulk and surface properties, compared to PP: improved thermal

stability and adhesion to metal, altered wettability, and latent reactivity. This strategy allows access to functional PPs with both high molecular weight and chosen tacticity, overcoming major limitations of the polar monomer problem whilst taking advantage of well-developed metallocene catalysts and organic substitution chemistry.

Preliminary work has been undertaken for alternate functionalisations but not included herein. Small molecule thermally activated radical thiol-Michael addition between 3-mercaptopropanoic acid and vinyl functional PP was successful and could be applied to future propylene copolymer systems in an effort to synthesis anionic PPs. Potential application areas for such a polymer concern either improved Li ion transport as a separator in electrochemical cells, or to chelate Ag ions and elicit antimicrobial responses. The synthesis of graft copolymers was also investigated using the living chains from the anionic synthesis of polystyrene or polyferrocenylsilane in the nucleophilic post-modification of propylene copolymers. Further investigation concerning graft copolymers could potentially utilise the attractive material properties of PPs in conjunction with desirable grafted copolymers properties, specifically focusing on their potential utility as compatibilising additives for recycling various plastic waste streams.

iii. Application-driven functional copolymers

Following the synthesis of a range of functional polymers, specific application testing was desirable to validate the value of the copolymerisation and post-modification platform. Consequently, phosphonate-functionalised PPs were evaluated as flame-retardant additives whilst an array of amine-modified PPs were used as multi-substrate adhesives.

Alkyl (**PP$_{PPr}$**) and aryl (**PP$_{PPh}$**) phosphonate-modified PPs displayed increased thermal stability in a synthetic air atmosphere with respect to PP, and microscale combustion calorimetry indicated enhanced flame retardancy. Both **PP$_{PPr}$** or **PP$_{PPh}$** can be easily blended with PP, enhancing thermal stability and offering an alternate strategy for improving the flame-retardant properties of PP-based materials which circumvents additive leaching. Evaluation of the effectiveness of these materials necessitates expanded characterisation such as cone calorimetry. This requires large quantities of material and consequently future work should address the scalability of copolymerisation and funcitonalisation.

Amine-modified copolymers were evaluated as hot melt adhesives by lap shear strength between steel-steel and steel-plastic substates. Modifiers containing pendent hydroxyl functionality showed strong adhesion to steel, recording the largest mean adhesive force of 17.4 MPa, a 252-fold increase *vs* control PP. The adhesive failure mode between plastic-steel substrates was found to be a function of interfacial effects, depending on the relative ability of the polymeric adhesives to bind to the polar steel surface and diffuse into the plastic substrate. Tertiary alkyl amine modifiers performed best in this regard with failure by stock break indicative of adhesive strength being greater than the tensile strength of the plastic substrate. Future work for multi-substrate adhesion should further optimise the polymer molecular weight, degree of functionality, and modifier used whilst also expanding the application testing to a wider array of commercially relevant procedures.

iv. *In vitro* microplastic evaluation of dyed polypropylene

Given the widespread production of polyolefins including PP, microplastics (μP) are environmentally pervasive however remain poorly understood. The covalent fluorescent

labelling of PP functionalised with rhodamine B **PP$_{Rb}$** enabled *in vitro* studies of the interaction between μP and a human embryonic kidney model cell line (HEK293T). Cellular uptake of **PP$_{Rb}$** was rapid (≤ 1 h), non-toxic up to 70 μM, and was not observed to localise within the nucleus. Increased mean lysosomal fluorescence intensity suggested an endosomal uptake mechanism with significant exocytosis implied over a 48 h period.

An alternative route to photoactive polymers would ideally focus on chain-end functionalisation, with precisely one fluorophore per chain and a lessened impact on the chemical properties of the polymer. Further to this, rhodamine B is ionic in nature which may have an impact on the polymer's ability to cross cellular membranes. A neutral fluorophore bound to the polymer through a hydrolytically stable bond would be preferable. Preliminary work not included in this thesis to synthesise a fluorescent polymer addressing the discussed limitations was undertaken *via* synthesis of a vinyl terminated PP and subsequent thiol-Michael addition with 2-napthalenethiol; this would be a good starting point for future developments.

v. Synthesis of sandwich complexes

Finally, the heptamethylindenyl ligand (Ind*) has been used to synthesise the manganese complex, Ind*$_2$Mn. The solid-state molecular structure indicates a low spin (S = ½) ground state for the Mn^{2+} metal center at 100 K. Solution EPR spectroscopy, solid state magnetic susceptibility measurements, and computational investigation suggest the complex undergoes thermally accessible spin crossover to a high spin (S = $^5/_2$) ground state. Computational assessment of the Ind* ligand displayed increased steric and orbital interactions compared to the ubiquitous Cp* ligand. Preliminary work not included in this thesis explored the synthesis of Ind*$_2$M (M = Ca and Sn). The synthesis of transition metal complexes utilising the Ind* ligand is relatively well understood, but there remains

scope for unexplored coordination chemistry in main group systems. Furthermore, the presence of the benzene ring may potentially afford heterobimetallic complexes through reduction of the Ind*$_2$M complex (eg: K(I)) or intercalation (eg: Ni(0)).

University of Oxford

Department of Chemistry



Synthesis and applications of functionalised polypropylenes

Appendix of Characterisation Data

Alexander O. E. Evans

Keble College

Hilary 2025

Thesis submitted in partial fulfilment of the requirements for the degree of Doctor of Philosophy

Appendices

Appendix A **A-4**

A1. Supplementary data for Chapter Two A-4

A1.1. General details and instrumentation A-4

A1.2. Solution-phase copolymerisation of propylene and bromoalkenes A-8

A1.3. Fineman-Ross analysis A-18

A1.4. Synthesis and characterisation of functional polypropylenes A-20

A1.5. Synthesis of potassium salts A-81

A1.6. Thermal stability studies of phosphonate functionalised polypropylene A-84

A1.7. Lap shear strength A-85

A1.8. Cross-linking and vulcanisation of PP_{AA} A-86

A1.9. References A-88

A2. Supplementary data for Chapter Three A-89

A2.1. General details and instrumentation A-89

A2.2. Solution-phase copolymerisation of propylene and bromoalkenes A-91

A2.3. Post-polymerisation modification of bromo-functionalised polypropylene using phosphite esters A-93

A2.4. Thermal stability studies of phosphonate functionalised polypropylene A-95

A2.5. Flammability studies of phosphonate functionalised polypropylene A-95

A2.6. Polymer compounding with polypropylene and inorganic flame retardant additives… A-97

A2.7. Higher molecular weight PP_{PPr} TGA analysis A-102

A2.8. Reference A-102

A3. Supplementary data for Chapter Four A-103

A3.1. General details and instrumentation A-103

A3.2. Polymer NMR, DSC, SEC, and FT-IR characterisation A-106

A3.3. Polymer Rheology A-108

A3.4. Lap shear strength A-112

A3.5. Modifier polarity assessment A-112

A3.6. References A-113

A4. Supplementary data for Chapter Five A-114

A4.1. General details and instrumentation A-114

A4.2. Synthesis and characterisation A-118

A4.3. Cellular studies A-125

A4.4. References A-127

A5. Supplementary data for Chapter Six A-128
A5.1. Experimental A-128
A5.2. Synthesis and Characterisation A-130
A5.3. Computational details A-141
A5.4. References A-149
A6. Device fabrication A-151
A6.1. Introduction A-151
A6.2. Vacuum compression moulding devices fabrication A-152
A6.3. Silicone mould design and fabrication A-157
A6.4. Tensile strength testing A-159
A6.5. Boosting NIR Laser Marking Efficiency of a Transparent Epoxy Using a Layered Double Hydroxide[1] A-159
A6.6. Strategies for enhancing the processability of UHMWPE[2] A-161
A6.7. References A-164
A6.8. Statement of Authorship A-165
Appendix B B-1
Crystallographic information file B-1
B1. Ind*H B-1
B2. Ind*$_2$Mn B-1
Appendix C C-1

Appendix A

A1. Supplementary data for Chapter Two

Functionalized polypropylenes; a copolymerization and post-modification platform

Alexander Evans, Oliver Casale, Louis. J. Morris, Zoë R. Turner, and Dermot O'Hare

A1.1. General details and instrumentation

General procedures. Air- and moisture-sensitive compounds were manipulated under an inert atmosphere of nitrogen, using standard Schlenk line techniques[1] on a dual manifold vacuum/nitrogen line or in an MBraun Labmaster 100 glovebox.

Hexanes and toluene were dried using an MBraun SPS 800 solvent purification system, stored over a potassium mirror, and degassed under partial vacuum before use.

Commercially supplied materials. 11-Bromo-1-undecene (Sigma Aldrich) was dried over pre-activated 3 Å molecular sieves, filtered and freeze-pump-thaw degassed before use. Propylene (N2.5) was supplied by BOC Ltd. and was used as received. MAO was supplied by Chemtura Corporation as a slurry in toluene which was dried under vacuum before use. *rac*-ethylenebis(indenyl)zirconium dichloride was used as supplied by SGC Chemicals PLC. Triphenyl phosphite, triisopropyl phosphite, xylene, 1,1,2,2-tetrachloroethane-d_2, triisobutylaluminium, were used as received from Sigma Aldrich. Aluminium (A23.5, smooth mill finish, Q-Panel) and steel (QD23.5, smooth mill finish, Q-Panel) were employed as surfaces for adhesive experiments from Q-LAB.

Solution NMR spectroscopy. NMR spectra were recorded on a Bruker NEO 600 (14.1 T, 600.4 MHz) with a broadband helium cryoprobe. Spectra were recorded at 393 K

and referenced internally to the residual *protio* solvent resonance. Chemical shifts, δ, are reported in parts per million (ppm) relative to tetramethylsilane (δ = 0 ppm). Quantitative ^{13}C NMR spectroscopy was performed using an inverse-gated ^{1}H decoupling pulse sequence, a relaxation delay of 60 s, and 2.8 mg mL^{-1} $Cr(acac)_3$ as a T_1 relaxation agent. Limited solubility of **^{i}PP**, **^{s}PP**, and functionalised derivates incorporation observed poor signal-noise ratio in $^{13}C\{^{1}H\}$ NMR spectra due to high M_n and low mol% incorporation, hence some known peaks, observed in HSQC or HMBC, were not observed $^{13}C\{^{1}H\}$ NMR spectra.

Gel permeation chromatography. Gel permeation chromatography (GPC) was performed by Ms Liv Thobru, Ms Sara Rund Herum, and Ms Rita Jenssen (Norner AS, Norway) on a high temperature gel permeation chromatograph with an IR5 infrared detector (GPC-IR5). Samples were prepared by dissolution in 1,2,4-trichlorobenzene (TCB) containing 300 ppm of 3,5-di-*tert*-buty-4-hydroxytoluene (BHT) at 160 °C for 90 minutes and then filtered with a 10 μm SS filter before being passed through the GPC column. The samples were run under a flow rate of 0.5 mL min^{-1} using TCB containing 300 ppm of BHT as mobile phase with 1 mg mL^{-1} BHT added as a flow rate marker. The GPC column and detector temperature were set at 145 and 160 °C respectively.

Differential scanning calorimetry. Differential scanning calorimetry was performed on a Perkin Elmer DSC 4000 System, unless otherwise stated, within a temperature range of 30-200 °C at a rate of 20 K min^{-1}. Polymer samples were sealed in 50 μL aluminium crucibles. An empty crucible was used as a reference, and the DSC was calibrated using indium and zinc. Vulcanisation: polymer, sulfur, and MBT were combined in agitated hot toluene prior to vacuum drying. Vulcanisations were performed in 50 μL DSC pans, and the reactions were followed by dynamic DSC protocols established through the work

of Restrepo-Zapata *et al*., who were able to fit simulated results and extract kinetic parameters.[2] Samples were heated at a constant rate (2.5–20 °C min^{-1}) to 300 °C, then cooled to ambient temperature at the same rate. A second cycle was performed to obtain the baseline for the experiment.

Thermogravimetry. Thermogravimetric analysis was performed on a Perkin Elmer TGA 8000 thermogravimetric analyser within a temperature range of 50-800 °C. Polymer samples were loaded into pre-weighed ceramic pans and heated at a rate of 20 K min^{-1} unless otherwise stated. A purge gas of either dry nitrogen or synthetic air (20% O_2 in N_2) was used.

Fourier-Transform Infrared Spectroscopy. Fourier-Transform Infrared Spectroscopy spectra were collected on a Bruker VERTEX 80 FT-IR spectrometer fitted with a DuraSamplIR Diamond ATR. Before the sample scans, 128 scans were taken as a background over the range 4000-400 cm^{-1}. Transmittance was recorded at a resolution of 4 cm^{-1} over the range 4000-400 cm^{-1} for 128 scans.

Quantitative bromine analysis. Quantitative bromine analysis was performed by Mr R. A. Croxall and Mr K. Bhamber (EAI Exeter Analytical, UK) in accordance with bromine method covered by ISO 17025 UKAS. An accurately weighed sample containing greater than 2 mg bromine is combusted in an oxygen flask over sodium meta-bisulphite solution. This process yields the sample into a gaseous form which is then immersed into the absorbent. The solution is acidified and boiled to dispel any chlorine fumes and titrated with silver nitrate. The end point of the titration is measured at the inflection point of the titration curve with an analytical uncertainty of 0.3% absolute.

Lap shear strength. Samples were prepared *via* vacuum compression-molding the polymer. Propylene-based copolymers were loaded between the substrates: Steel QD35 and Aluminum A35 with overlap of 12.5 mm (312.5 mm^2 bonding area). Then, the compression-heating cycle was applied: (i) heating to 130 °C (ii) stabilizing for 5 min with no force applied, (iii) applying for 5 min with 100 kN (2 MPa) normal force and cooling down to 40 °C under 100 kN (0.6 MPa) normal force. Before measurements, samples were conditioned for 7 days at room temperature. The measurements were performed using an Instron 5582 tensile tester equipped with a 5 kN load cell. The tests were performed on specimens (51 cm × 12.7 cm) with surface overlapping 10 mm at room temperature. A grip-to-grip separation of 140 mm was used. The samples were pre-stressed to 3 N, then loaded with a constant cross-head speed 100 mm/min. To calculate the lap shear strength the reported force value divided by the bonding surface (127 mm^2) of the specimens. The reported values are an average of at least 4 measurements of each composition.

Dynamic Rheology. Rheology was performed on a TA Instruments Discovery HR-2 hybrid rheometer using a temperature controlled stainless steel Peltier plate and a flat parallel plate geometry (20 mm diameter) with a working gap of 1000 μm. Approximately 180 mg **PP_{AA}** /S/MBT were pressed using a pellet press under 10 tons of pressure which was then placed on the rheometer plate at 25 °C. Under continuous oscillation (ω = 1 rad s^{-1}; 0.2% strain), the temperature was raised to 200 °C at a heating rate of 20 °C min^{-1} and held for 6 hours.

Contact angle. Measurement of contact angle was recorded on an ITConcept tracker.

A1.2. Solution-phase copolymerisation of propylene and bromoalkenes

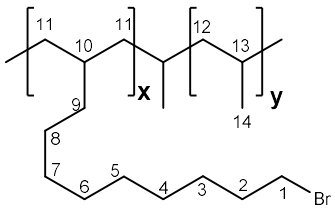

General procedure for the solution-phase copolymerisation of propylene with bromoalkenes. A catalyst stock solution of **M1-4** (24 μmol) in toluene (10 mL) was prepared. Prescribed quantities of catalyst stock solutions were added into an ampoule containing a hexane solution of cocatalyst MAO and magnetic stirrer bar. In the ampoule side arm, n-bromoalkene, TIBA and hexane were added. The polymerisation ampoule was then stirred in a preheated oil bath and evacuated before simultaneous additions of the n-bromoalkene and TIBA solution, and exposure to proplyene (2 bar) for the duration of the polymerisation. After the above procedure, the reaction mixture was degassed and the mixture was precipitated in acidified methanol (2 wt% HCl) before being collected by filtration, washed with methanol (20 mL), then acetone (2 x 20 mL), and dried *in vacuo* at 40 °C to a constant mass. Comonomer incorporation (mol%) and conversion calculated according to Figure S4. **PP$_{Br}$** (3.99 mol%). **^{1}H NMR (600 MHz, C$_2$D$_2$Cl$_4$, 393 K)**: δ 4.84 (0.14H, s, H^{15}), 4.77 (0.14H, s, H^{15}), 3.49 (2H, t, $^3J_{HH}$ = 6.8 Hz, H^1), 1.97 (2H, p, $^3J_{HH}$ = 6.9 Hz, H^2), 1.75-1.58 ppm (25H, br m, H^{13}), 1.58-1.50 (4H, m, H^3 and H^a), 1.50-1.06 (46H, m, H^a, H^4, and H^{12} (^{anti})), 1.05-0.84 ppm (95H, br d, H^{14} and H^{12} (^{syn})). **^{13}C{^{1}H} NMR (151 MHz, C$_2$D$_2$Cl$_4$, 393 K)**: δ 120.54, 99.91, 45.82 (1C, s, C^{10}), 45.43 (C^{13}), 42.94 (2C, s, C^{11}), 35.14 (1C, s, C^9), 32.87 (1C, s, C^a), 32.81 (1C, s, C^1), 32.37 (1C, s, C^2), 29.45 (1C, s, C^a), 28.87 (1C, s, C^a), 28.77 (1C, s, C^a), 28.13 (1C, s, C^4), 27.90 (C^{12}), 27.64 (1C, s, C^3), 26.11 (1C, s), 21.80-19.65 (26.5C, C^{14}, *mmmm* = 83%^{b}). ^{a}Resonances corresponding to C$^{5\text{-}8}$. ^{b}Assigned according to literature.[3] **FTIR**: *v* (cm^{-1}) = 2950, 2867, and 1456 (*v* (C-H, CH$_3$)), 2917, 2838, and 1377 (*v* (C-H, CH$_2$)), 2917, 2838, and 1377 (*v* (CH$_2$)), 721 (*v* (CBr)).

Table A1.1 Copolymerisation optimisation data of propylene and **n-Br** (n = 6, 7, and 11) using M1.[a]

Entry	n-**Br**		**M1**	Temp.	Time	Activity[b]	Productivity[c]	Yield	Incorporation[d]	M_w[e]	$Đ_m$[e]	T_m[f]	Crystallinity[f]
	(n)	(mM)	(mM)	(°C)	(min)			(g)	(mol%)	(g mol^{-1})		(°C)	(%)
1	0	0	0.024	70	30	5467	26.1	6.53	0	13 600	2.2	114	44
2	6	91	0.024	70	30	0	0	0.00	0				
3	7	91	0.024	70	30	565	2.7	0.67	5.06	5800	1.6	88	24
4	11	91	0.024	70	30	1686	8.1	2.01	3.98	9400	1.9	90	43
5	11	91	0.024	30	30	2377	11.4	2.84	2.01	32 100	2.3	113	53
6	11	91	0.024	50	30	2202	10.5	2.63	2.94	17 400	2.1	104	45
7	11	91	0.024	90	30	350	1.7	0.42	5.15	6300	1.6	79	44
8	11	91	0.012	70	30	606	2.9	0.36	4.36	13 300	1.7	93	41
9	11	91	0.048	70	30	1666	8.0	3.65	3.42	7000	1.7	94	41
10	11	137	0.024	70	30	1594	7.6	1.90	6.63	7700	1.7	81	41
11	11	182	0.024	70	30	1025	4.9	1.22	8.12	8600	1.7	78	18
12	11	91	0.024	70	20	1770	8.5	1.41	4.86	9000	1.7	86	23
13	11	91	0.024	70	10	2628	12.6	1.05	4.99	7700	1.7	87	40

[a]Conditions: *rac*-ethylenebis(indenyl)zirconium dichloride (**M1**), MAO used as a cocatalyst and scavenger with $[Al]_0$:$[\mathbf{M1}]_0$ = 1000:1. Alpha olefins denoted **n-Br**, where n is equal to the number of carbons in the monomer. Molar ratio of $[TIBA]_0$:$[\mathbf{n\text{-}Br}]_0$ = 1:10, 0.5 mL toluene, 49.5 mL hexanes, propylene 2 bar. Polymerisation and analysis were performed in duplicate and mean values are reported [b]$kg_{PP}\ mol_{[\mathbf{M1}]}^{-1}\ h^{-1}\ bar^{-1}$. [c]$kg_{PP}\ g_{[\mathbf{M1}]}^{-1}\ h$. [d]Determined by ^1H NMR. [e]Determined by SEC. [f]Determined by DSC.

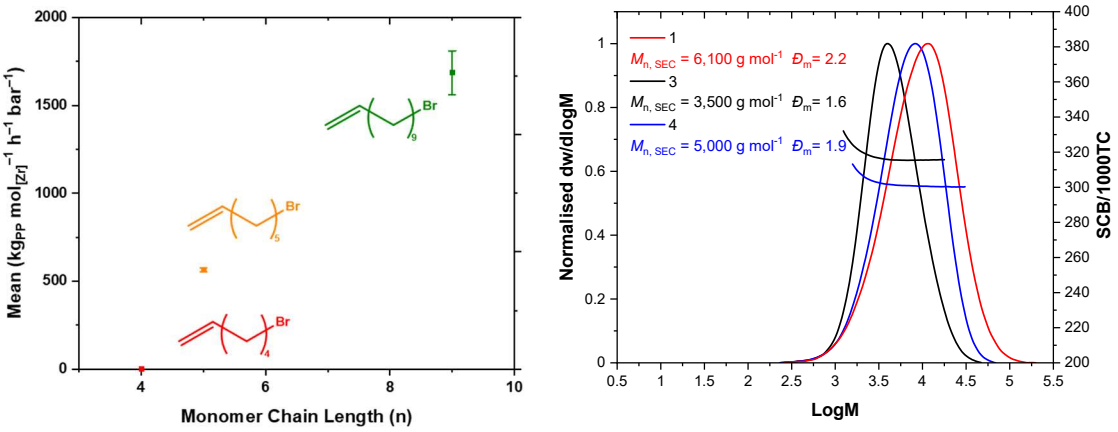

Figure A1.1 (Left) Activity plot for the copolymerisation of propylene and **n-Br** (Table 1, entries 2-4). (Right) SEC traces and SCB profiles of **PP** and **PP_{Br}** polymerised using **n-Br** (Table 1, entries 1-4).

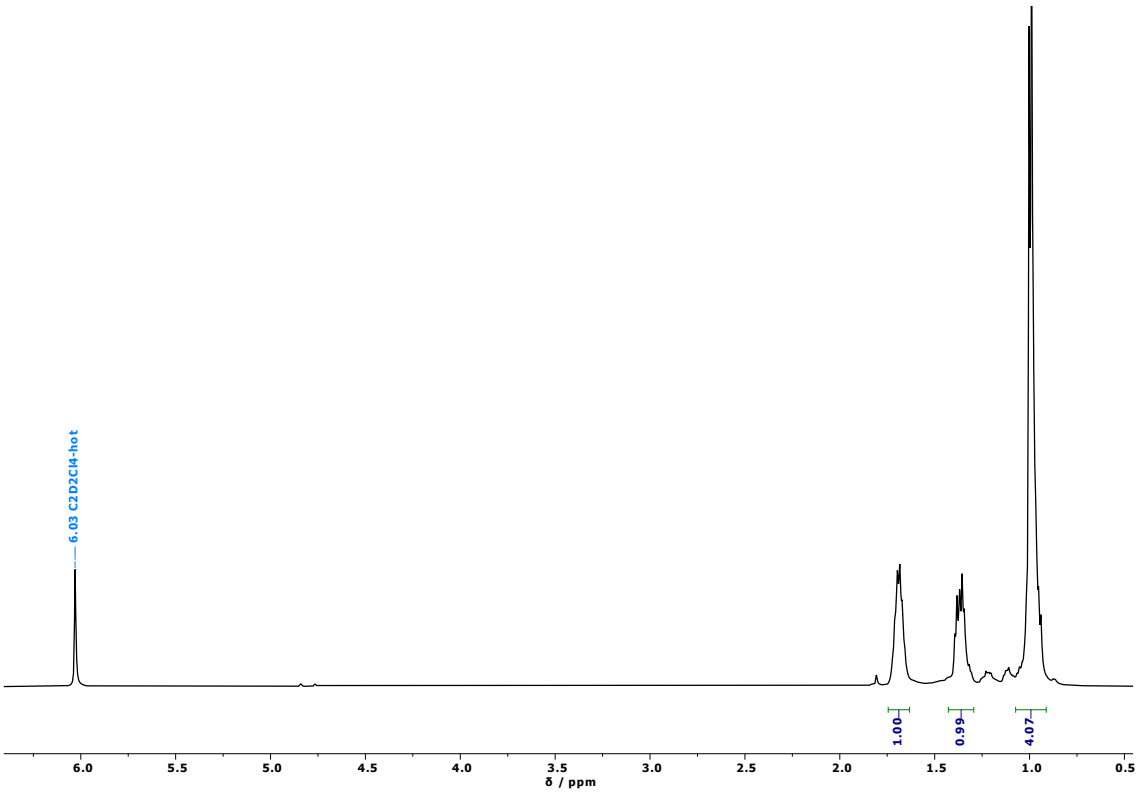

Figure A1.2 PP ^{1}H NMR (600 MHz, $C_2D_2Cl_4$, 393 K).

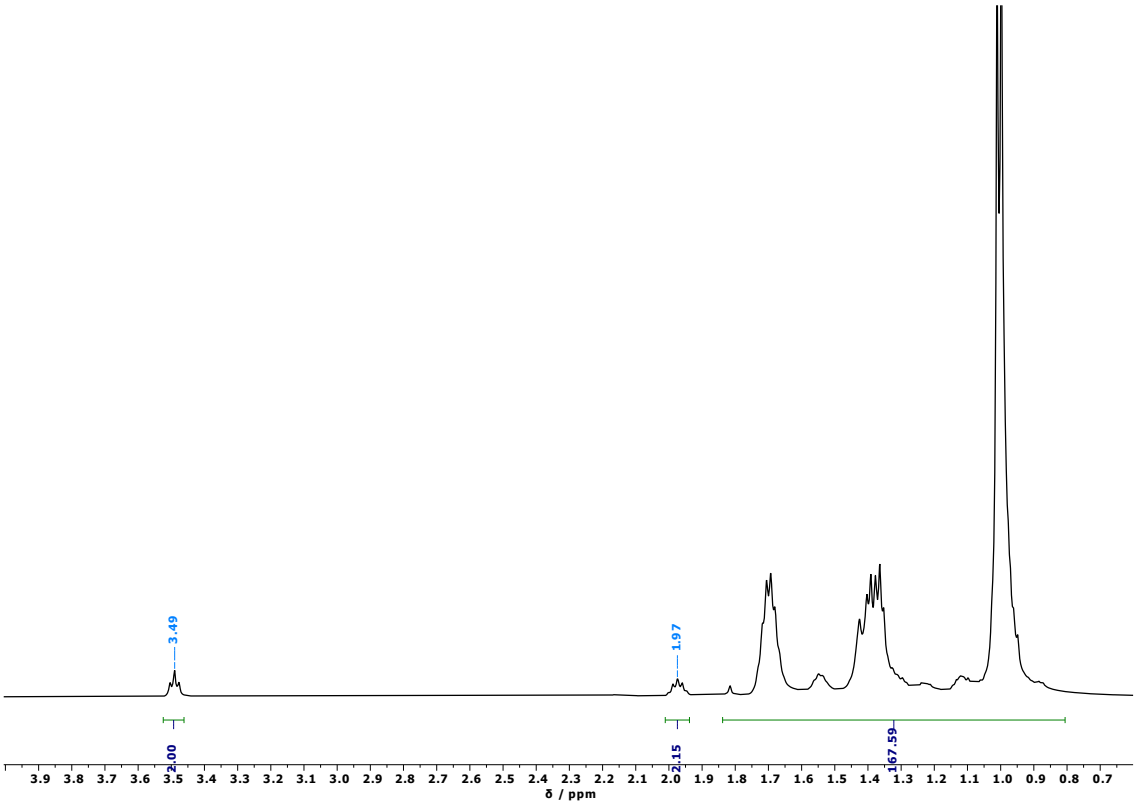

Figure A1.3 PP_{Br} ^{1}H NMR (600 MHz, $C_2D_2Cl_4$, 393 K).

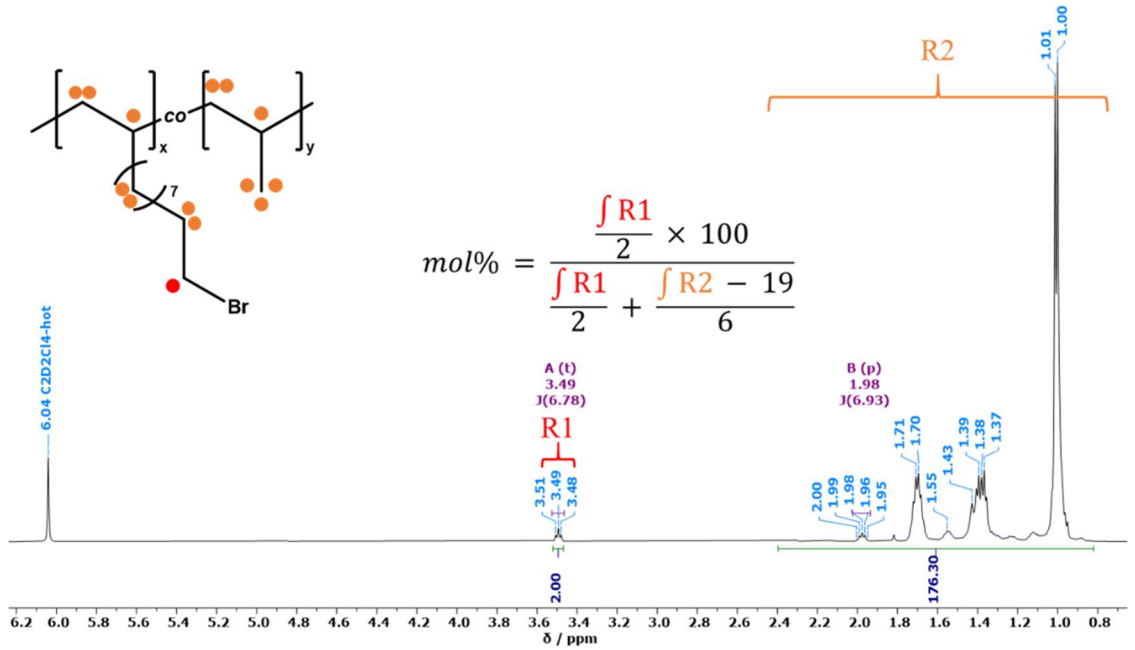

Figure A1.4 PP_{Br} mol% incorporation calculation.

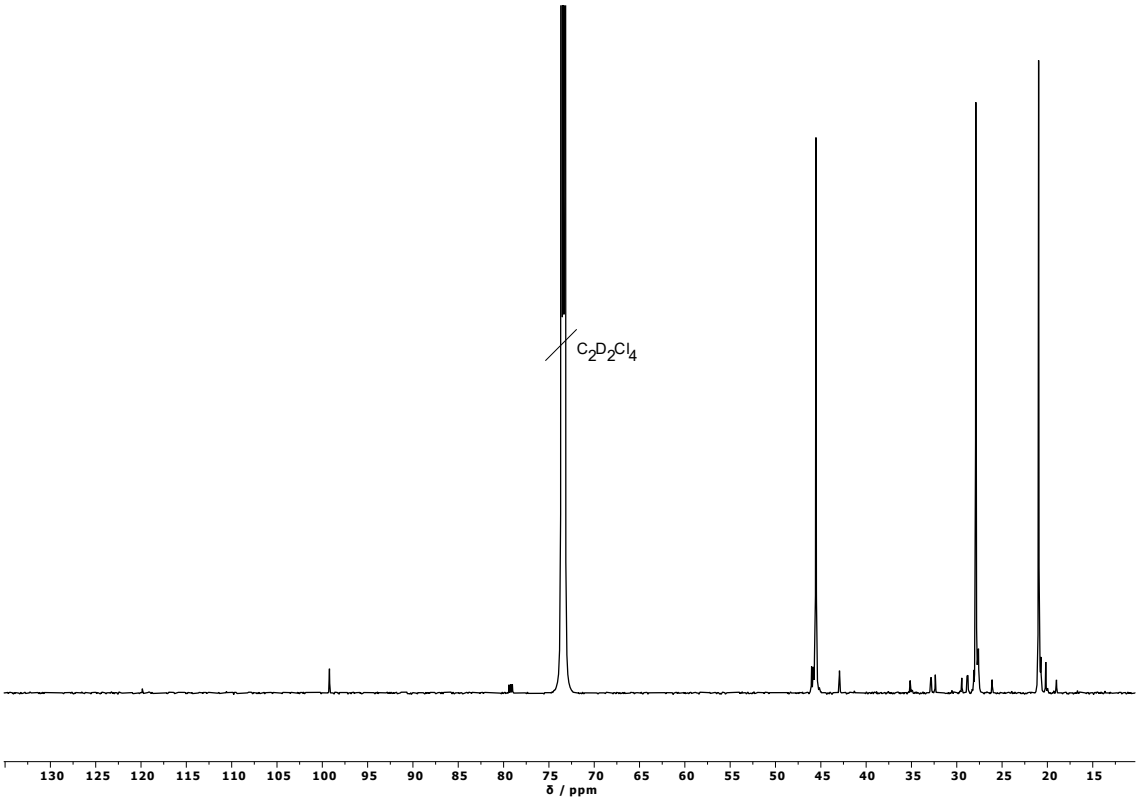

Figure A1.5 PP$_{Br}$ $^{13}C\{^1H\}$ NMR (151 MHz, $C_2D_2Cl_4$, 393 K), full spectrum.

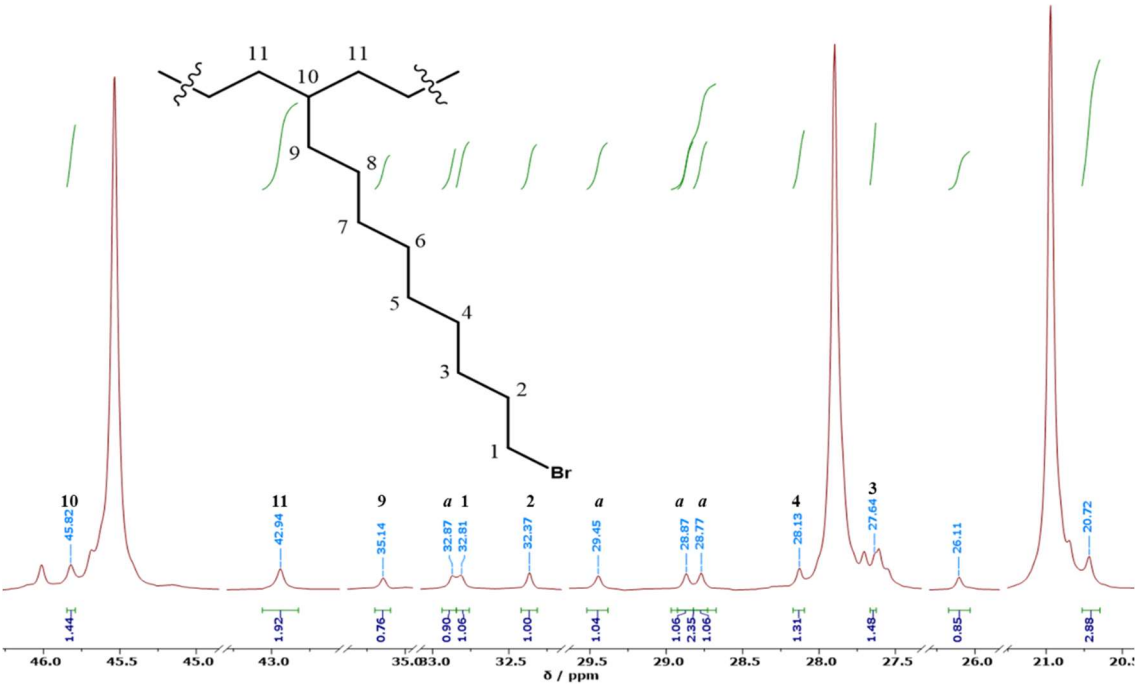

Figure A1.6 PP$_{Br}$ $^{13}C\{^1H\}$ NMR (151 MHz, $C_2D_2Cl_4$, 393 K), expanded comonomer region with assigned carbons. Where assignment was inconclusive, *a* has been used to indicate a comonomer -CH_2-.

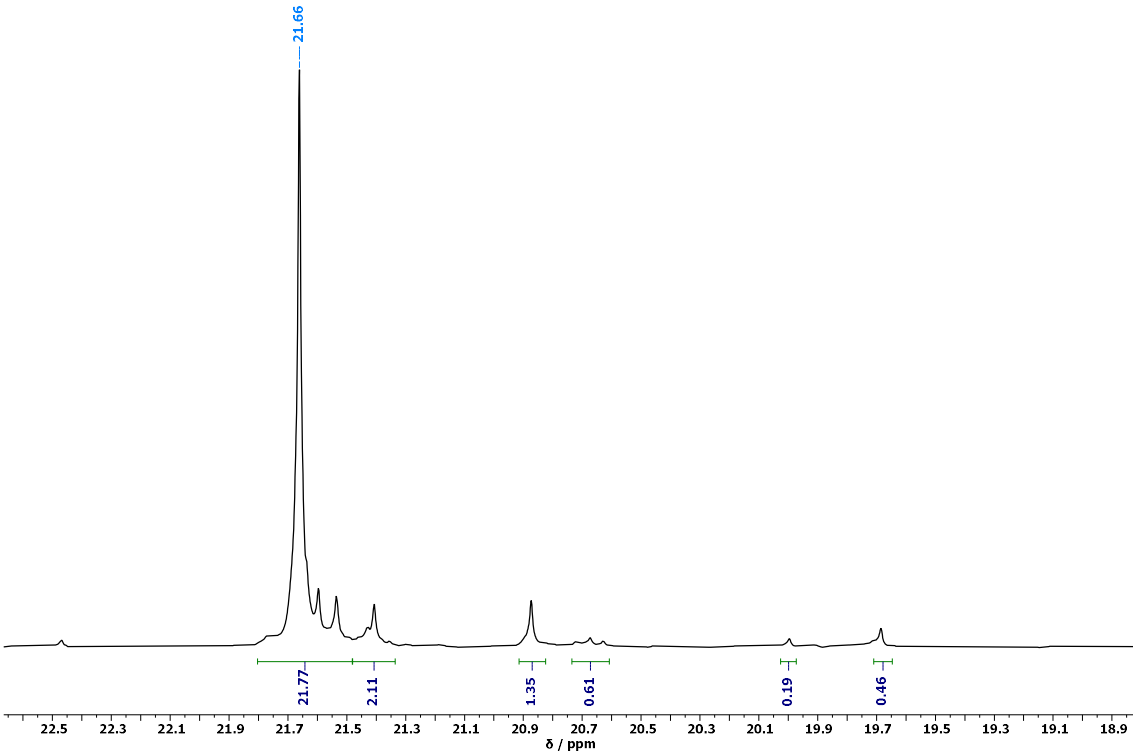

Figure A1.7 PP$_{Br}$ $^{13}C\{^{1}H\}$ NMR (151 MHz, $C_2D_2Cl_4$, 393 K), expanded methyl region.[3]

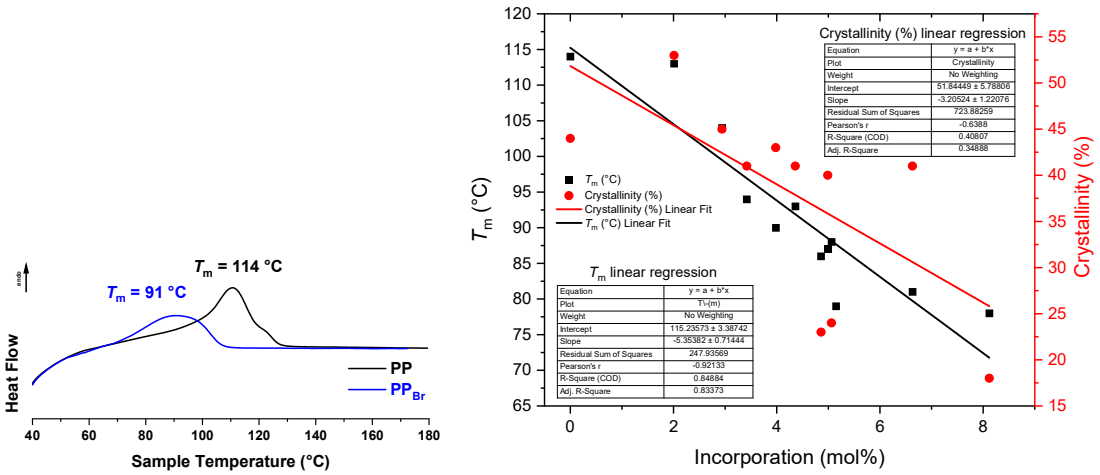

Figure A1.8 DSC 2nd heating curve of **PP** and **PP$_{Br}$** (Left). Plot of the relationship between **11-Br** incorporation level and both T_m and crystallinity (Right).

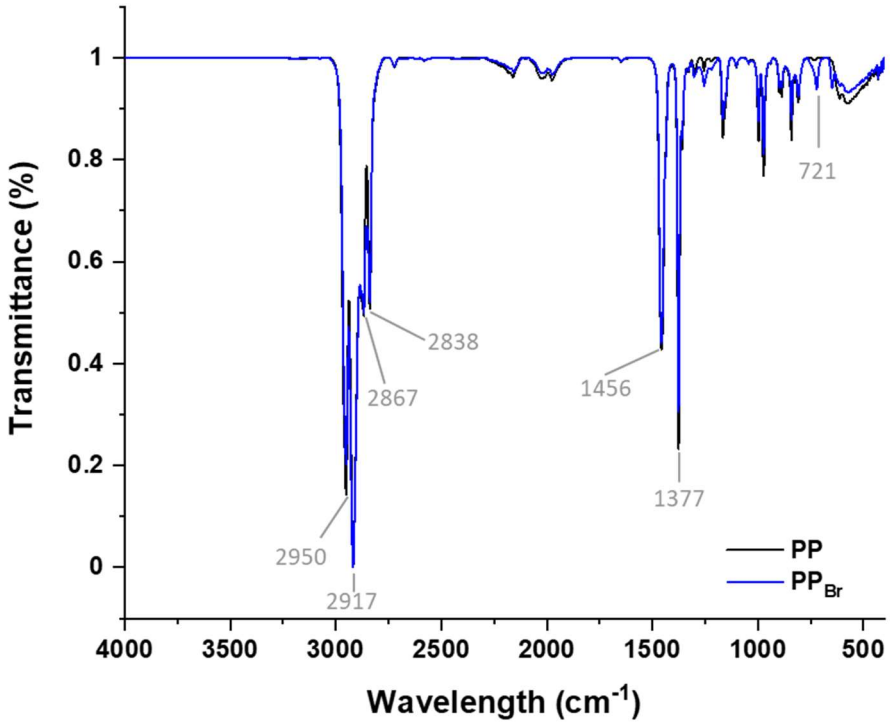

Figure A1.9 FT-IR spectrum overlay of **PP** and **PP$_{Br}$**.

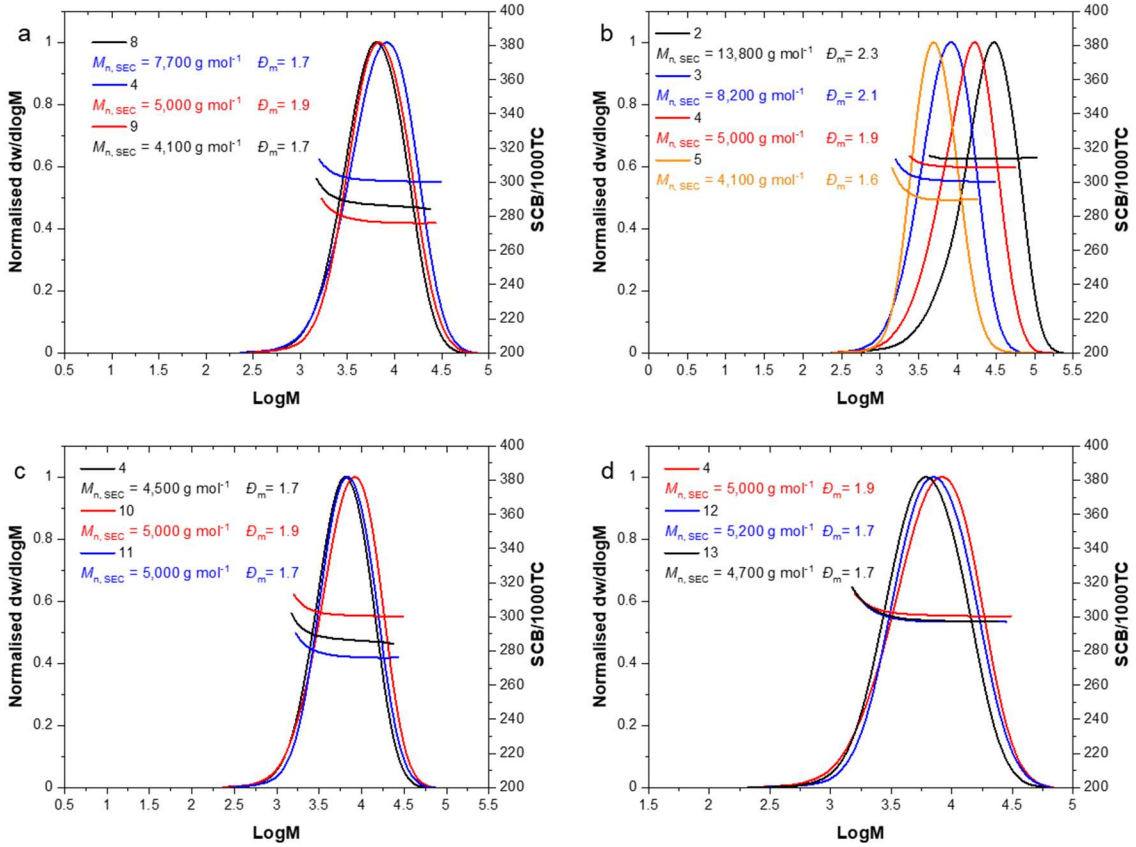

Figure A1.10 SEC traces and SCB profiles of **PP$_{Br}$** with (a) varying [**M1**] (b) differing polymerisation temperatures (c) varying [**11-Br**] and (d) differing polymerisation time (Table A1.1, entries 4-13).

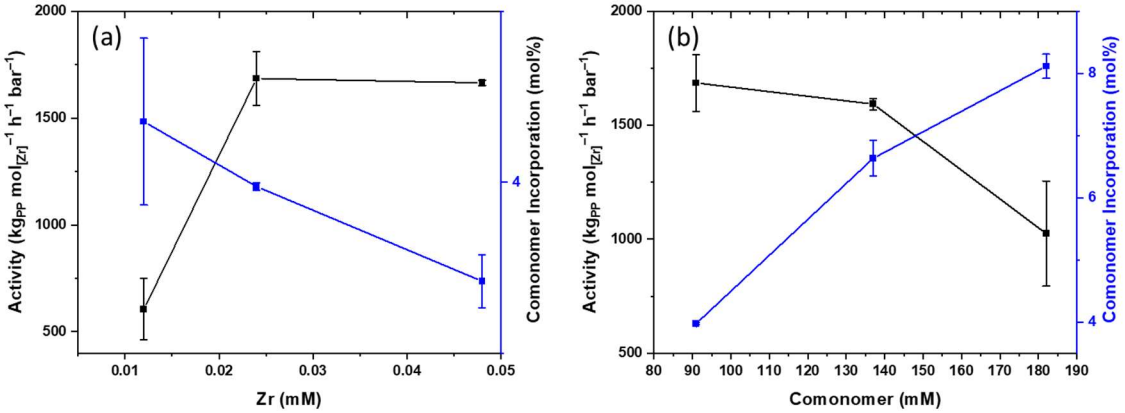

Figure A1.11 Activity plots for the copolymerisation of propylene and **11-Br** with varying (a) [**M1**] and (b) [**11-Br**] (Table A1.1, entries 4, 7-8, and 10-11).

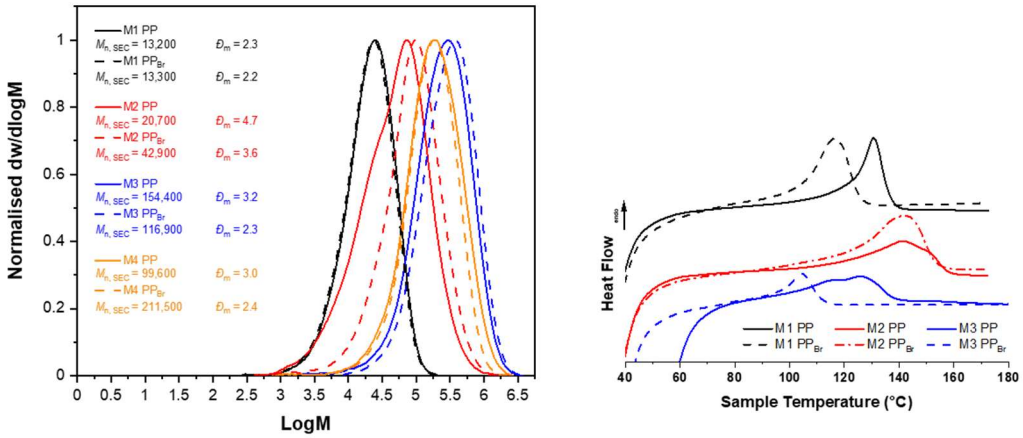

Figure A1.12 (Left) SEC traces and (right) DSC curves of **PP** and **PP_{Br}** synthesised by **M1-4**.

Table A1.2 (Co)polymerisation data of propylene (and **11-Br**) using **M1-4**.[a]

Entry	Catalyst (**MX**)	**11-Br** (mM)	Activity[b]	Productivity[c]	Yield (g)	Incorporation[d] (mol%)	M_W[e] (g mol^{-1})	$Đ_m$[e]	T_m[f] (°C)	Crystallinity[f] (%)	Major pentad[d]
1	**M1**		4932	15.7	3.92		30 100	2.3	131	54	mmmm (86.8%)
2	**M1**	45.5	3575	11.4	2.84	2.01	28 500	2.2	116	30	
3	**M2**		10 328	32.8	8.21		98 000	4.7	141	78	mmmm (98.4%)
4	**M2**	45.5	7254	23.1	5.77	1.64	152 200	3.6	142	54	
5	**M3**		4491	14.3	3.19		318 800	3.2	126	23	rrrr (71.7%)
6	**M3**	45.5	2192	7.6	1.69	3.95	271 600	2.3	104	16	
7	**M4**		4419	15.3	3.51		433 700	3.0			
8	**M4**	45.5	1879	6.5	1.49	15.48	508 600	2.4			

[a]Conditions: **M1-4** (0.024 mM, 1 mg mL^{-1} **t**oluene**)**, MAO used as a cocatalyst and scavenger with $[Al]_0$:$[\mathbf{MX}]_0$ = 1000:1. Molar ratio of $[TIBA]_0$:$[\mathbf{11\text{-}Br}]_0$ = 1:10, 0.50–0.75 mL toluene, 49.25–49.50 mL hexanes, propylene 2 bar, T_p = 50 °C, 20 min^{-1}. Polymerisation and analysis were performed in duplicate and mean values are reported [b]$kg_{PP}\ mol_{[\mathbf{MX}]}^{-1}\ h^{-1}\ bar^{-1}$. [c]$kg_{PP}\ g_{[\mathbf{MX}]}^{-1}\ h$. [d]Determined by ^1H NMR. [e]Determined by SEC. [f]Determined by DSC.

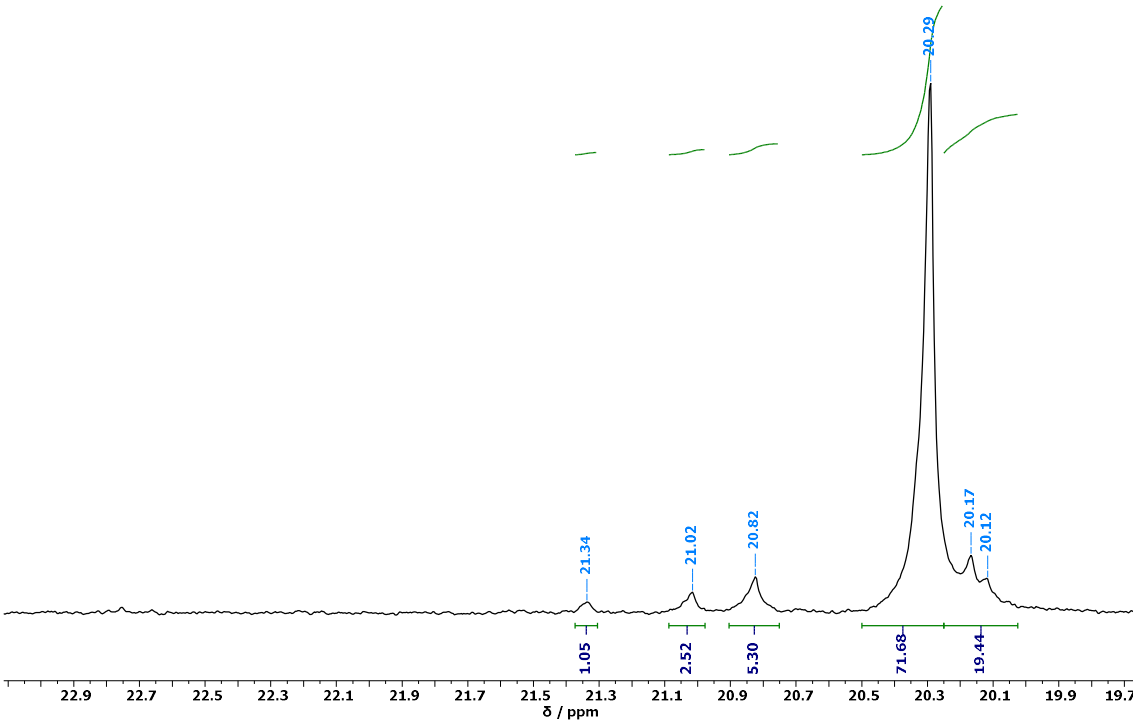

Figure A1.13 $^{13}C\{^{1}H\}$ NMR (151 MHz, $C_2D_2Cl_4$, 393 K) **PP** synthesised by **M3**, expanded methyl region.[3]

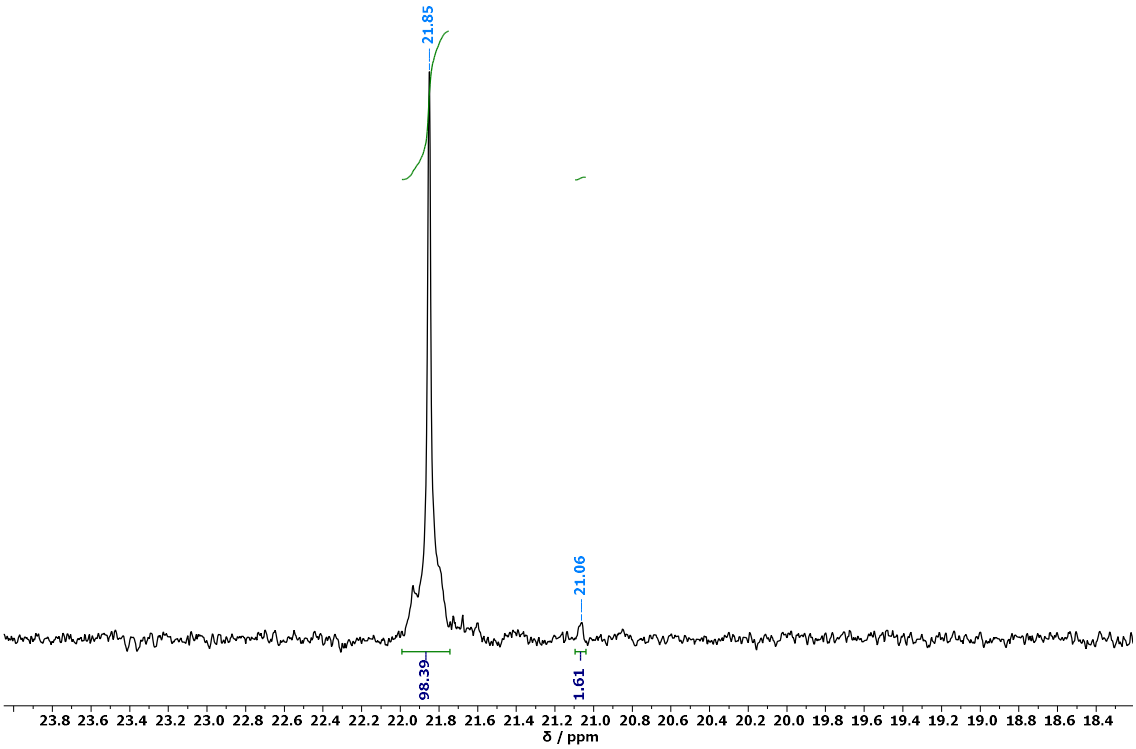

Figure A1.14 $^{13}C\{^{1}H\}$ NMR (151 MHz, $C_2D_2Cl_4$, 393 K) **PP** synthesised by **M2**, expanded methyl region.[3]

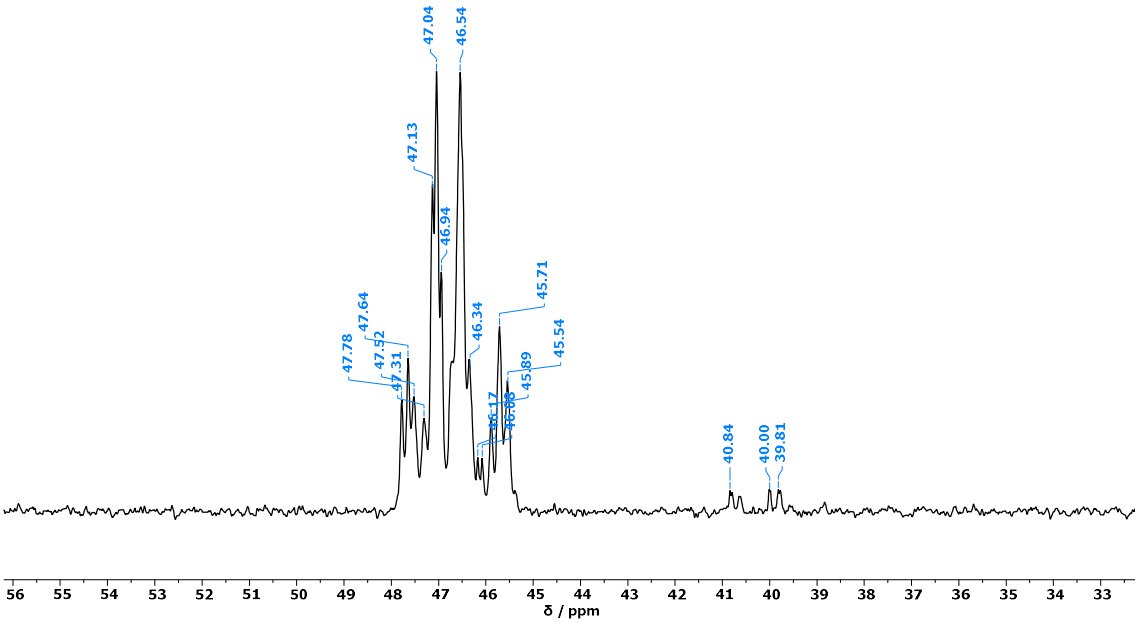

Figure A1.15 $^{13}C\{^{1}H\}$ NMR (151 MHz, $C_2D_2Cl_4$, 393 K) **PP** synthesised by **M4**, expanded methyleneregion.[3]

A1.3. Fineman-Ross analysis

Using the Fineman-Ross method,[4] and taking the concentration of propylene, [P], in hexanes according to Kissin's equation, $[P] \approx p \cdot 0.00272 \cdot exp\left(\frac{3260}{1.98 \cdot T}\right)$ for partial pressure, p, in bar and absolute temperature T,[5] it is possible to estimate the reactivity ratios.

$$f = F\frac{r_1 F + 1}{r_2 + F} \Rightarrow \frac{F}{f}(f-1) = r_1\frac{F^2}{f} - r_2$$

$$r_1 = \frac{k_{11}}{k_{12}};\ r_2 = \frac{k_{22}}{k_{21}}$$

where F = [P]/[11-Br] in feed, f = [P]/[11-Br] in copolymer, and knm is the rate constant for the insertion of monomer m after monomer n.

Table A1.3 Fineman-Ross data for P/11-Br copolymerisation. F = [P]/[11-Br] in feed, f = [P]/[11-Br] ($= \frac{1}{x_{11-}} - 1$) in copolymer. [P] calculated from Kissin's equation, for partial pressure, p, in bar and absolute temperature T: $[P] \approx p \cdot 0.00272 \cdot exp\left(\frac{3260}{1.98 \cdot T}\right)$.[5] [a]Polymerisation conditions: rac-ethylenebis(indenyl)zirconium dichloride (**M1**), MAO used as a cocatalyst and scavenger with $[Al]_0$:[**Zr**]$_0$ = 1000:1. Molar ratio of $[TIBA]_0$:[**11-Br**]$_0$ = 1:10, 0.5 mL toluene, 49.5 mL hexanes, propylene 2 bar. Polymerisation and analysis were performed in duplicate and mean values are reported.

11-Br /μL	T /°C	[P] /mM	[**11-Br**] /mM	$x_{\mathbf{11\text{-}Br}}$ /mol%	F	f
1000	30	1242	91	2.01	3.83	13.34
1000	50	888	91	2.94	2.88	9.46
1000	70	660	91	3.98	2.18	6.95
1000	90	507	91	5.15	1.68	5.26
1500	70	660	137	6.63	1.65	4.47
2000	70	660	182	8.12	1.16	3.30

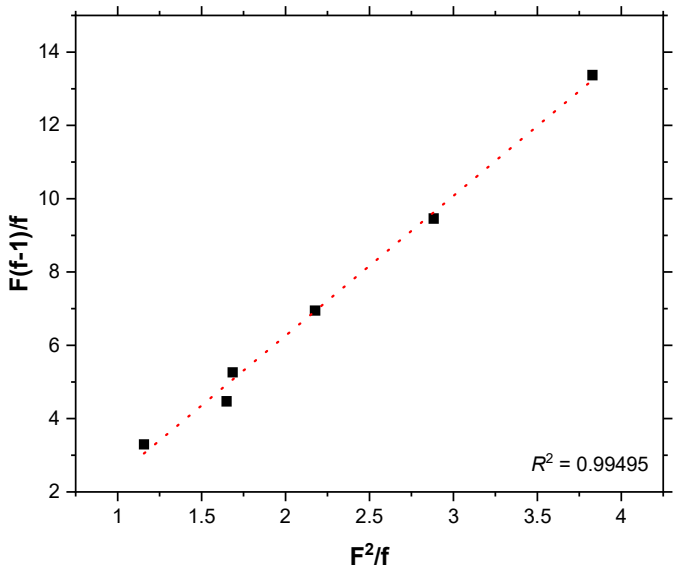

Figure A1.16 Fineman-Ross plot for propylene/**11-Br** copolymerisation at T_p = 30-90 °C, using **M1**.

A1.4. Synthesis and characterisation of functional polypropylenes

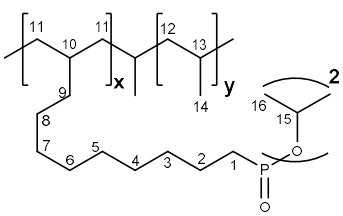

Synthesis of triisopropyl phosphite modified PP_{Br}, PP_{PPr}. Triisopropyl phosphite ($P(O^iPr)_3$, 50 equiv.) was added to poly(propylene)-*co*-(11-bromo-1-undecene) (0.5 g). The reaction mixture was heated and stirred at 180 °C for 6 h in an ampoule. Aliquots were taken periodically and dried *in vacuo* at 40 °C. The final polymer was precipitated in acidified methanol (2 wt% HCl) before being collected by filtration, washed with methanol (20 mL), then acetone (2 x 20 mL), and dried *in vacuo* at 40 °C to a constant mass. $\mathbf{PP_{PPr}}$ (3.99 mol%). **^{1}H NMR (600 MHz, $C_2D_2Cl_4$, 393 K)**: δ 4.80-4.68 (2H, m, H^{15}), 1.77-1.51 (27H, br m, H^{13}), 1.55-1.45 (4H, m, H^a) 1.44-1.06 (54H, m, H^a, $H^{12\ (anti)}$ and H^{16}), 1.05-0.84 ppm (80H, br m, H^{14} and $H^{12\ (syn)}$) ppm. **^{13}C{^{1}H} NMR (151 MHz, $C_2D_2Cl_4$, 393 K):** 120.53, 99.89, 69.61 (2C, d, $^2J_{CP}$ = 6.9 Hz, C^{15}), 46.21 (C^{13}), 35.88 (1C, s, C^a), 30.59 (1C, d, $^3J_{CP}$ = 15.2 Hz, C^3), 30.20 (1C, s, C^a), 29.66 (1C, s, C^a), 29.50 (1C, s, C^a), 29.18 (1C, s, C^a), 28.58 (C^{12}), 27.38 (1C, d, $^1J_{CP}$ = 141.5 Hz, C^1), 24.09 (2C, dd, $^3J_{CP}$ = 7.8, 3.62 Hz, C^{16}), 22.70 (1C, d, $^2J_{CP}$ = 5.5 Hz, C^2), 21.64 (C^{14}). *a*Resonances corresponding to unassigned CH_2. **^{31}P{^{1}H} NMR (243 MHz, $C_2D_2Cl_4$, 393 K)**: 28.80 ppm (s, O=***P***($O^iPr)_2$). **FTIR**: *v* (cm^{-1}) = 2950, 2867, and 1456 (*v* (C-H, CH_3)), 2917, 2838, and 1377 (*v* (C-H, CH_2)), 1245 (*v* (P=O)), 1006 and 981 (*v* (P-O-C)).

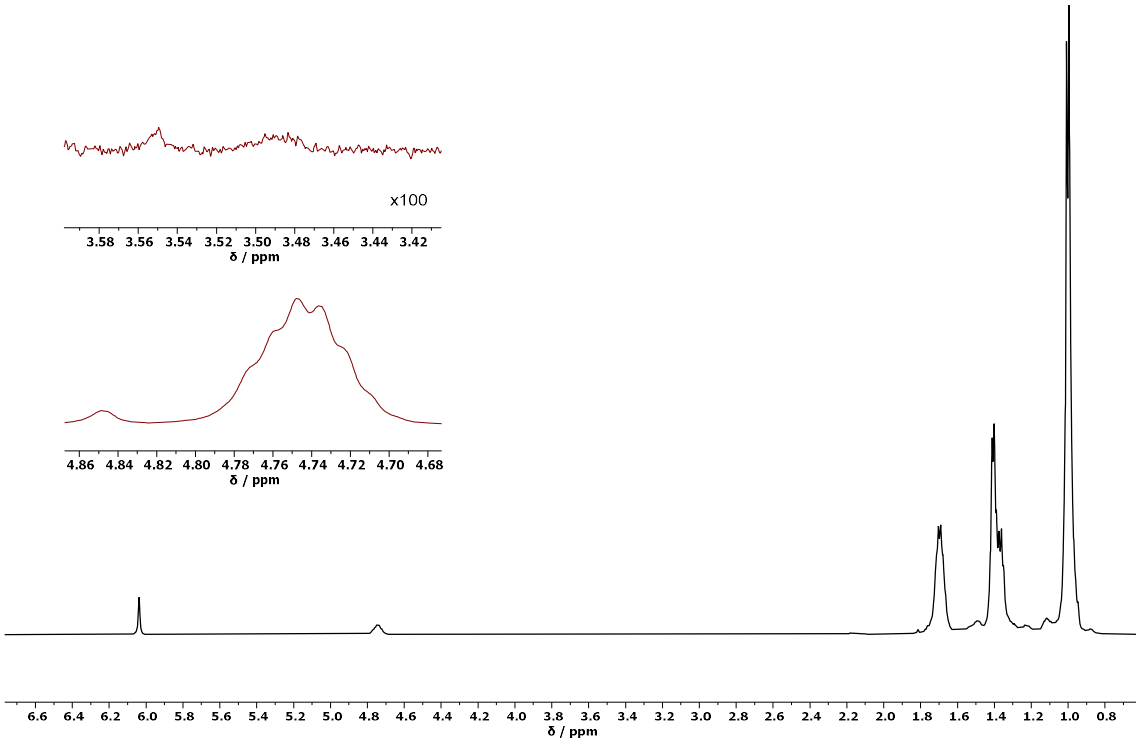

Figure A1.17 PP_{PPr} ^{1}H NMR (600 MHz, $C_2D_2Cl_4$, 393 K).

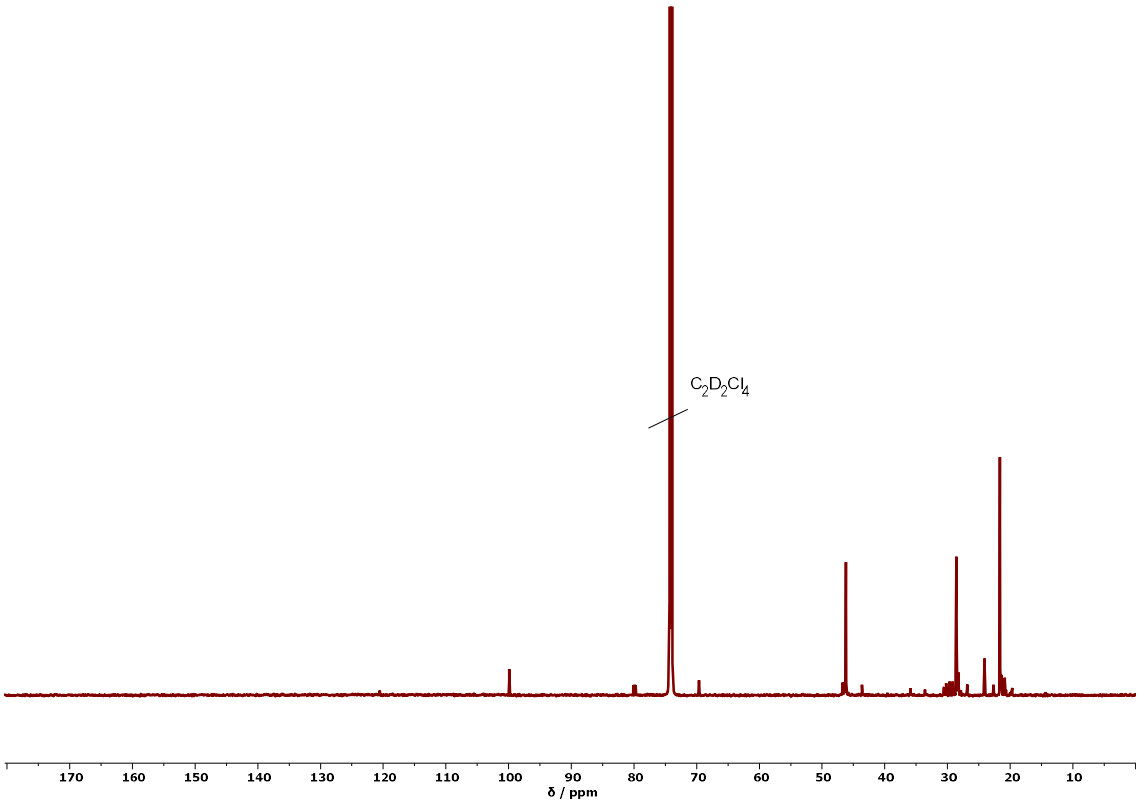

Figure A1.18 PP_{PPr} $^{13}C\{^{1}H\}$ NMR (151 MHz, $C_2D_2Cl_4$, 393 K), full spectrum.

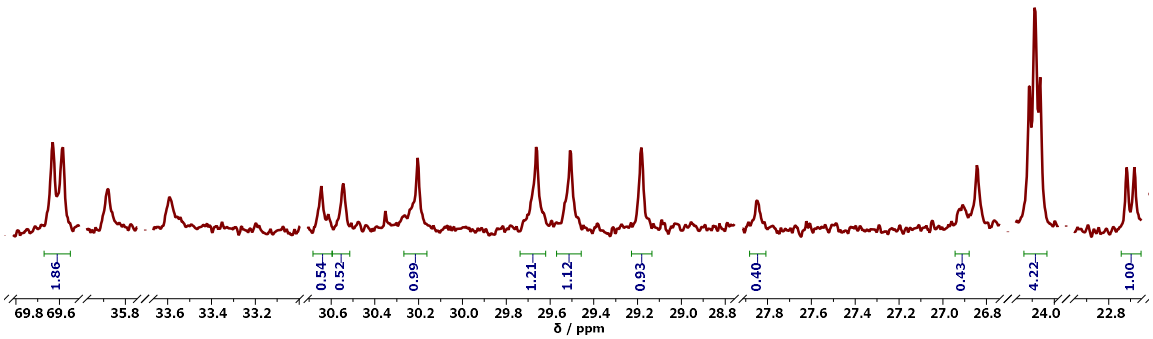

Figure A1.19 PP$_{PPr}$ $^{13}C\{^{1}H\}$ NMR (151 MHz, $C_2D_2Cl_4$, 393 K), expanded comonomer region.

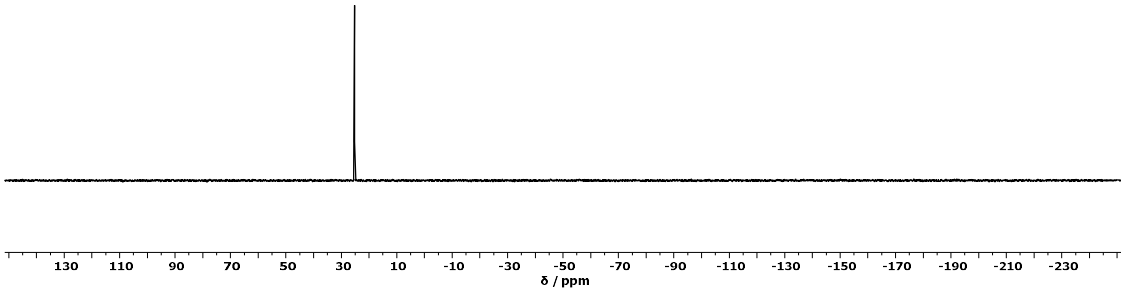

Figure A1.20 PP$_{PPr}$ $^{31}P\{^{1}H\}$ NMR (243 MHz, $C_2D_2Cl_4$, 393 K).

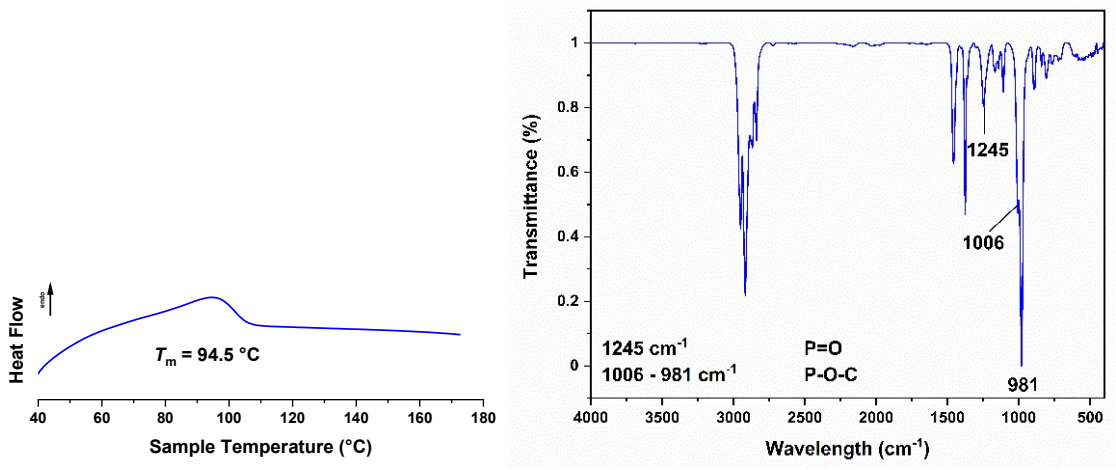

Figure A1.21 (Left) **PP$_{PPr}$** DSC 2nd heating curve and (right) FT-IR spectrum of **PP$_{PPr}$**.

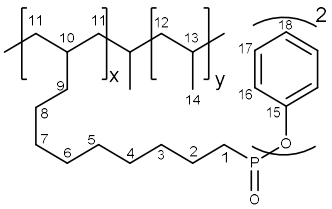

Synthesis of triphenyl phosphite modified PP$_{Br}$, PP$_{PPh}$. Triphenyl phosphite ($P(OPh)_3$, 50 equiv.) were added to poly(propylene)-*co*-(11-bromo-1-undecene) (0.5 g) heated and stirred at 180 °C for 48 h in an ampoule. Aliquots were taken periodically and dried *in vacuo* at 40 °C. The final polymer was precipitated in acidified methanol (2 wt% HCl) before being collected by filtration, washed with methanol (20 mL), then acetone (2 x 20 mL), and dried *in vacuo* at 40 °C to a constant mass. **PP$_{PPh}$** (3.99 mol%). **^{1}H NMR (600 MHz, $C_2D_2Cl_4$, 393 K)**: δ 7.39 (4H, t, $^3J_{HH}$ 7.7 Hz, H^{17}), 7.27 (4H, d, $^3J_{HH}$ = 7.8 Hz, H^{16}), 7.23 (2H, t, $^3J_{HH}$ = 7.4 Hz, H^{18}), 2.19-2.09 (2H, br m, H^1), 1.92-1.82 (2H, br m, H^2), 1.75-1.60 (20H, br m, H^{13}), 1.59-1.06 (44H, m, H^a and H^{12} (*anti*)), 1.04-0.84 ppm (78H, br m, H^a, H^{14} and H^{12} (*syn*)). **^{13}C{^{1}H} NMR (151 MHz, $C_2D_2Cl_4$, 393 K):** 150.99 (2C, d, $^2J_{CP}$ = 8.7, C^{15}), 129.70 (4C, s, C^{17}), 124.94 (2C, s, C^{18}), 120.62 (4C, d, $^3J_{CP}$ = 4.4 Hz, C^{16}), 99.89, 46.21 (C^{13}), 43.64 (2C, s C^b), 35.90 (1C, s, C^a), 33.60 (1C, s, C^a), 30.44 (1C, d, $^3J_{CP}$ = 15.8 Hz, C^3), 30.19 (1C, s, C^a), 29.63 (1C, s, C^a), 29.44 (1C, s, C^a), 29.09 (1C, s, C^a), 28.58 (C^{12}), 26.84 (1C, s, C^a), 26.57 (1C, d, $^1J_{CP}$ = 139.8 Hz, C^1), 22.45 (1C, d, $^2J_{CP}$ = 5.5 Hz, C^2), 21.64 (C^{14}). *a*Peaks corresponding to unassigned CH_2. **^{31}P{^{1}H} NMR (243 MHz, $C_2D_2Cl_4$, 393 K)**: 24.52

ppm (s, O=***P***$(OPh)_2$). **FTIR**: *v* (cm^{-1}) = 2950, 2867, and 1456 (*v* (C-H, CH_3)), 2917, 2838, and 1377 (*v* (C-H, CH_2)), 1274 (*v* (P=O)), 1191, 927, 900 (*v* (P-O-Ph)), 762 (*v* ($C=C_{Ar}$)), and 681(*v* ($C\text{-}H_{Ar}$)).

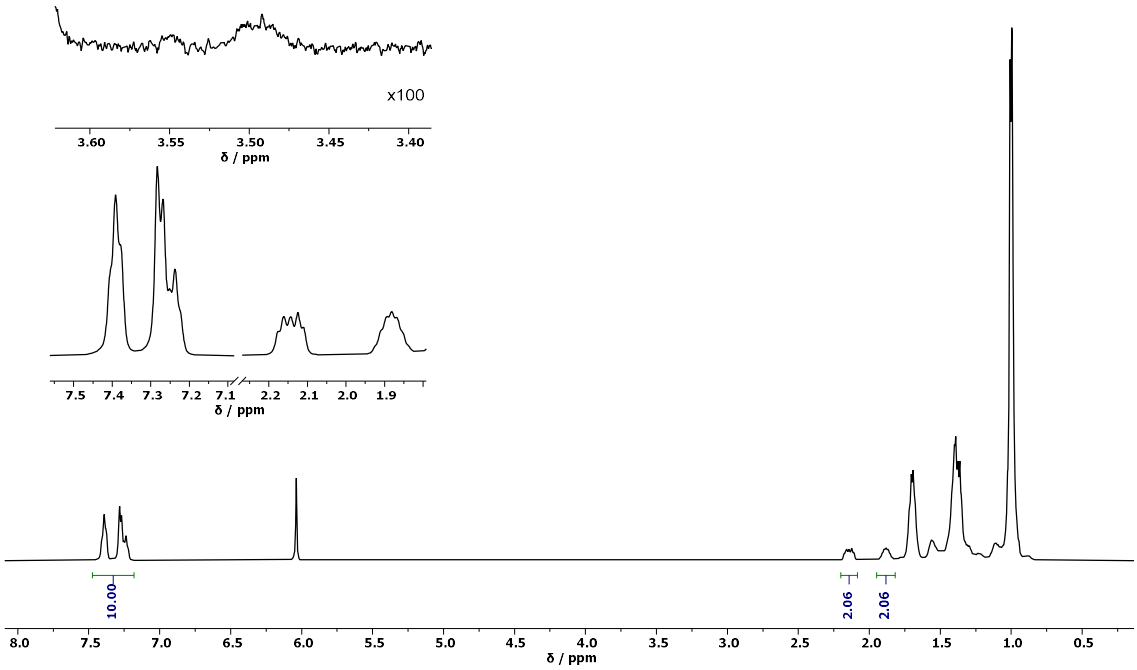

Figure A1.22 PP_{Pph} ^1H NMR (600 MHz, $C_2D_2Cl_4$, 393 K).

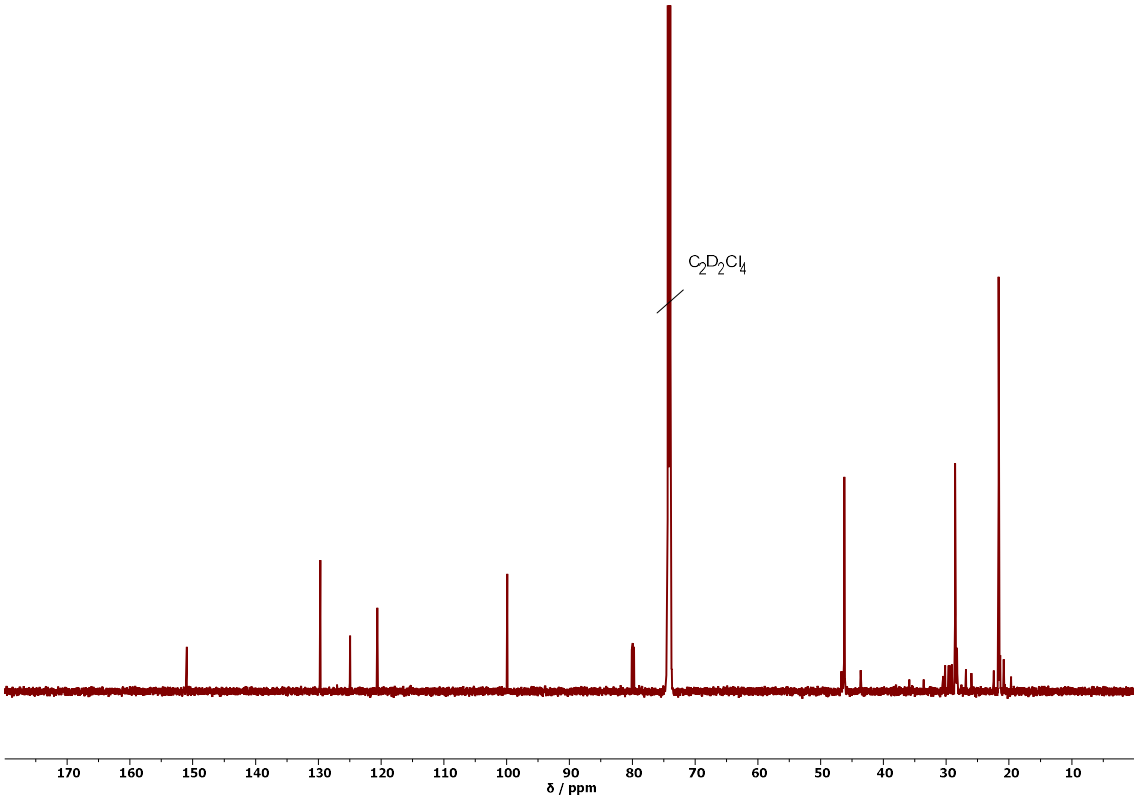

Figure A1.23 PP$_{PPh}$ $^{13}C\{^{1}H\}$ NMR (151 MHz, $C_2D_2Cl_4$, 393 K), full spectrum.

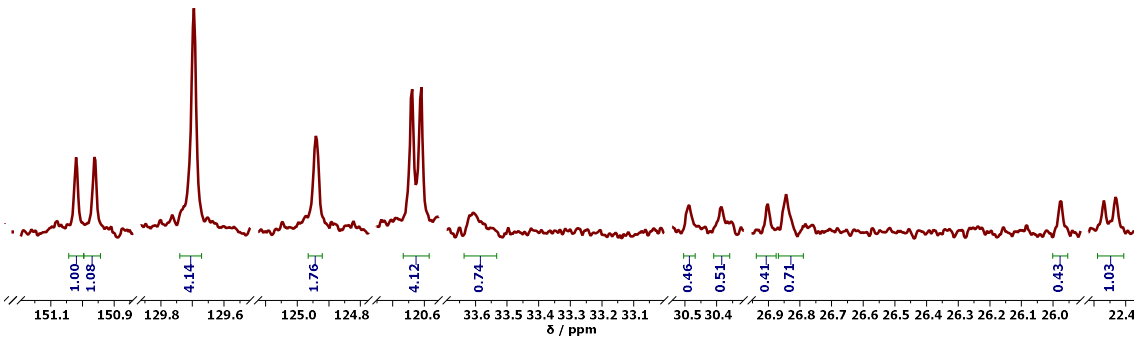

Figure A1.24 PP$_{PPh}$ $^{13}C\{^{1}H\}$ NMR (151 MHz, $C_2D_2Cl_4$, 393 K), expanded comonomer region.

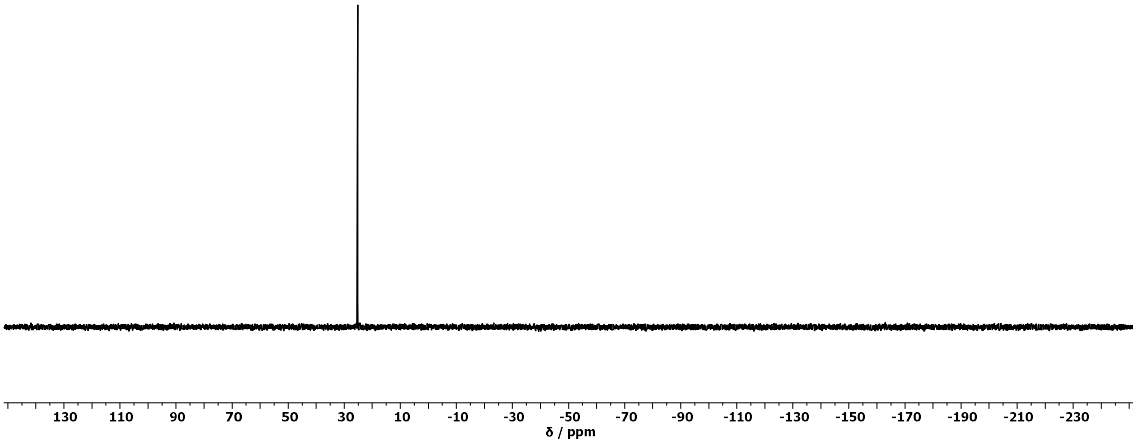

Figure A1.25 PP$_{PPh}$ $^{31}P\{^{1}H\}$ NMR (243 MHz, $C_2D_2Cl_4$, 393 K).

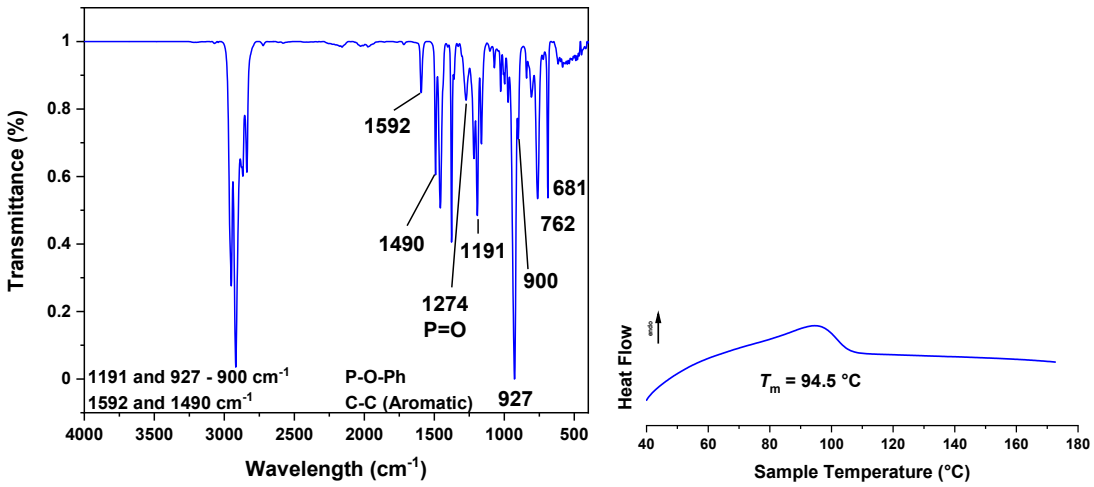

Figure A1.26 (Left) FT-IR spectrum of **PP$_{PPh}$**. (Right) **PP$_{PPh}$** DSC 2nd heating curve.

Table A1.4 SEC data of $\mathbf{PP_{Br}}$, $\mathbf{PP_{PPh}}$, and $\mathbf{PP_{PPr}}$ with varying incorporation levels.

Polymer	Incorporation[a] (mol%)	Conv.[a]	$M_{n,\,th}$[b] (g mol^{-1})	$M_{n,\,SEC}$[c] (g mol^{-1})	$Đ_m$[c]
$\mathbf{PP_{Br}}$	3.99			9,400	1.9
$\mathbf{PP_{PPr}}$		>99%	9,700	5,200	2.0
$\mathbf{PP_{PPh}}$		>99%	10,000	8,000	1.9
$\mathbf{PP_{Br}}$	6.84			7,700	1.7
$\mathbf{PP_{PPr}}$		>99%	8,400	4,000	1.9
$\mathbf{PP_{PPh}}$		>99%	8,800	7,100	1.7
$\mathbf{PP_{Br}}$	7.98			8,600	1.7
$\mathbf{PP_{PPr}}$		>99%	9,500	3,700	1.9
$\mathbf{PP_{PPh}}$		>99%	10,000	9,100	1.8

[a]Determined by ^{1}H NMR. [b]Calculated: $\mathbf{PP_{PPr}}$ ($M_{n,\,SEC}$–(mol%×79.9)+(mol%×165.2)) and $\mathbf{PP_{PPh}}$ ($Mn_{,\,SEC}$–(mol%×79.9)+(mol%×233.19)). [c]Determined by SEC.

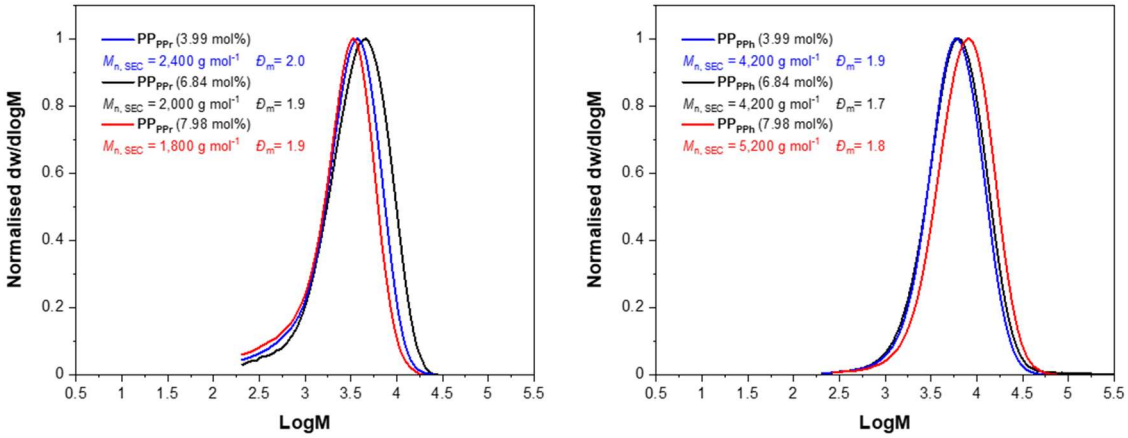

Figure A1.27 SEC traces of $\mathbf{PP_{PPr}}$ (left) and $\mathbf{PP_{PPh}}$ (right) at varying incorporation levels, relating to Table S4.

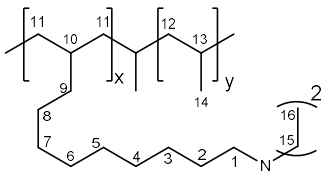

Synthesis of *N*-ethylethanamine (DEA) modified $\mathbf{PP_{Br}}$, $\mathbf{PP_{DEA}}$. DEA (50 equiv.) were added to $\mathbf{PP_{Br}}$ (0.5 g) heated and stirred at 150 °C for 24 h in an ampoule. The final polymer was precipitated in acidified methanol (2wt% HCl) before being collected by filtration on a glass sintered frit (porosity 3), washed with methanol, then acetone, and dried in vacuo at 60 °C to a constant weight. $\mathbf{PP_{DEA}}$ (3.99 mol%). **^{1}H NMR (600 MHz,**

$C_2D_2Cl_4$, 393 K): 3.12 (4H, br s, H^{15})^a, 2.99 (2H, br s, H^1)^a, 1.89 (2H, br s, H^2)^a, 1.75-1.58 (19H, br m, H^{13}), 1.57-1.06 (49H, br m, H^b, H^{12} (*anti*) and H^{16})^a, 1.05-0.84 ppm (70H, br m, H^b, H^{12} (*syn*), and H^{14}). **$^{13}C\{^1H\}$ NMR (151 MHz, $C_2D_2Cl_4$, 393 K):** 123.92, 120.52, 52.03 (1C, s, C^1)^a, 47.39 (2C, s, C^{15})^a, 46.19 (C^{13}), 43.63 (1C, s, C^b), 35.91 (1C, s, C^b), 33.63 (1C, s, C^b), 30.16 (1C, s, C^b), 29.55 (1C, s, C^b), 29.48 (1C, s, C^b), 29.11 (1C, s, C^b), 28.56 (C^{12}), 27.23 (1C, s, C^b), 26.84 (1C, s, C^b), 23.66 (1C, s, C^2)^a, 21.63 (C^{14}), 9.11 (2C, s, C^{16})^a. ^{a}Nitrogen adjacent ^{1}H and ^{13}C NMR peaks appear broad. This observation is potentially explained by an increase in the relaxation rate caused by quadrupolar Nitrogen. A lack of HMBC cross-peaks whilst still evidencing HSQC cross-peaks support this. Experimentally, HSQC equivalent delays were optimised for 145 Hz (3 ms delay) whereas HMBC experiments were optimised for a 125 ms delay, giving the nuclei sufficient time to relax and preventing the appearance of any cross-peak to carbons adjacent to nitrogen.[6, 7] ^{b}Peaks corresponding to unassigned CH_2. **FTIR**: ν (cm^{-1}) = 2950, 2867, and 1456 (ν (C-H, CH_3)), 2917, 2838, and 1377 (ν (C-H, CH_2)), 1203 (ν (CN)).

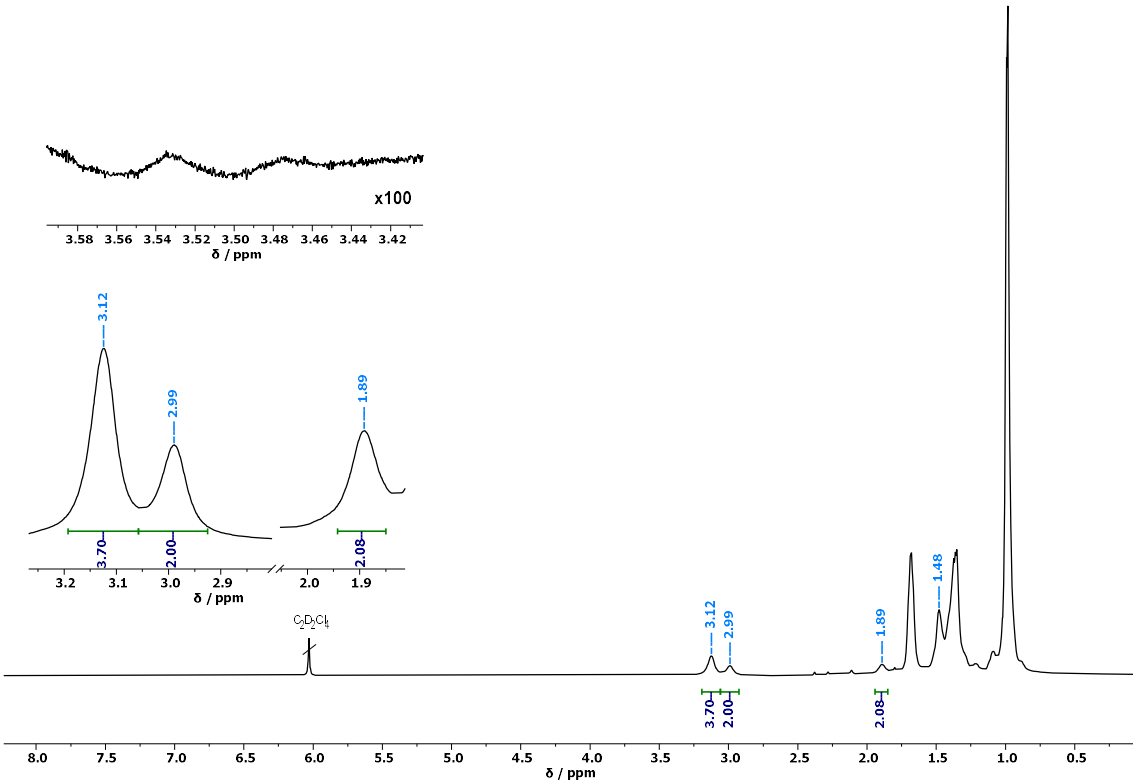

Figure A1.28 PP_{DEA} ^{1}H NMR (600 MHz, $C_2D_2Cl_4$, 393 K).

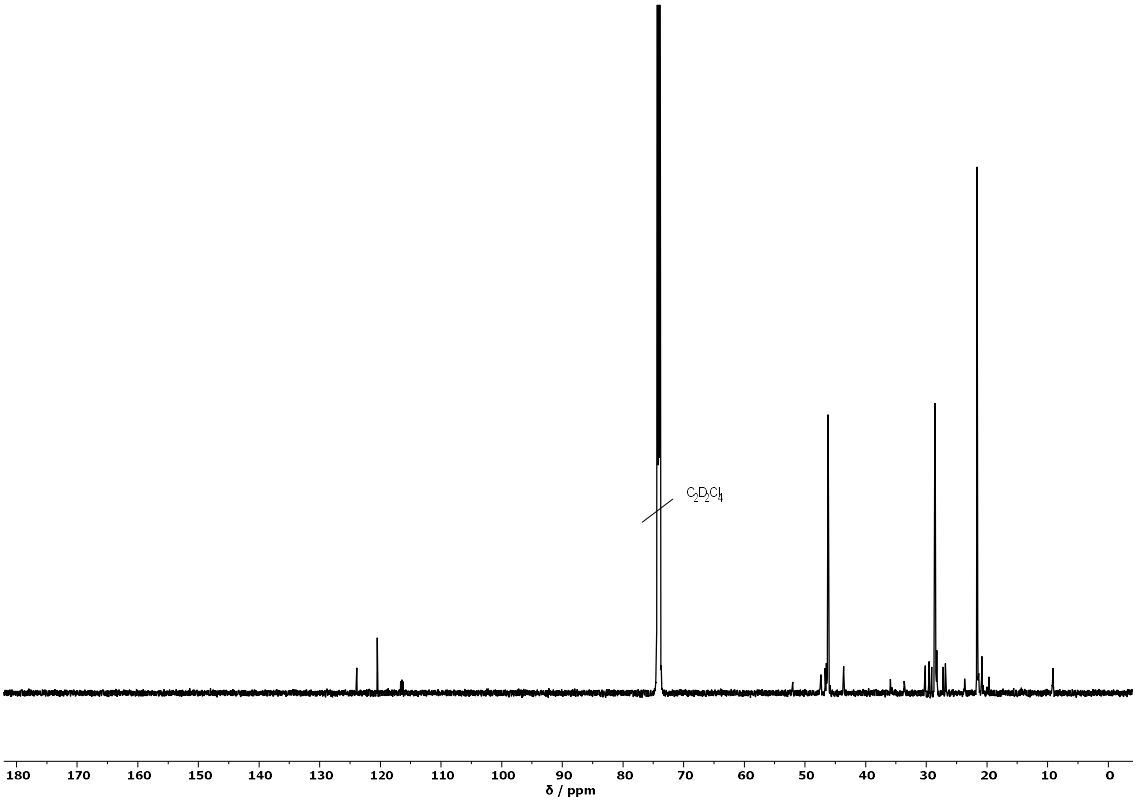

Figure A1.29 PP_{DEA} $^{13}C\{^{1}H\}$ NMR (151 MHz, $C_2D_2Cl_4$, 393 K), full spectrum.

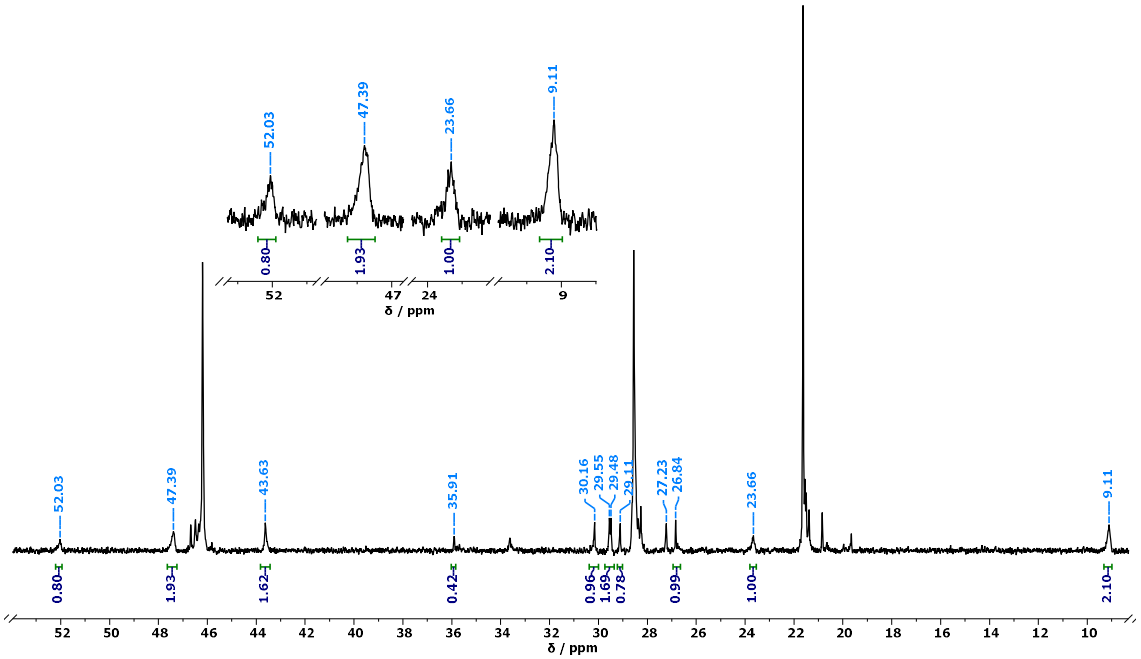

Figure A1.30 PP_{DEA} $^{13}C\{^{1}H\}$ NMR (151 MHz, $C_2D_2Cl_4$, 393 K), expanded comonomer region.

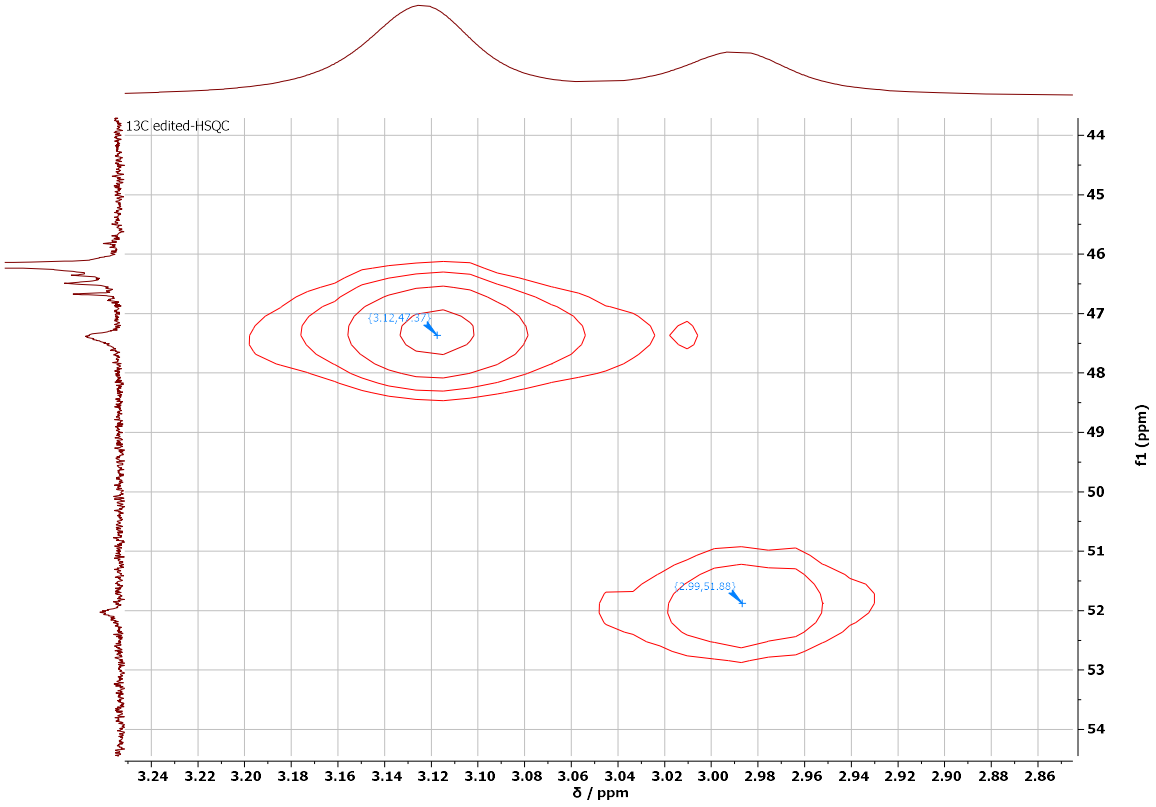

Figure A1.31 PP_{DEA} HSQC ^{1}H-^{13}C NMR spectrum.

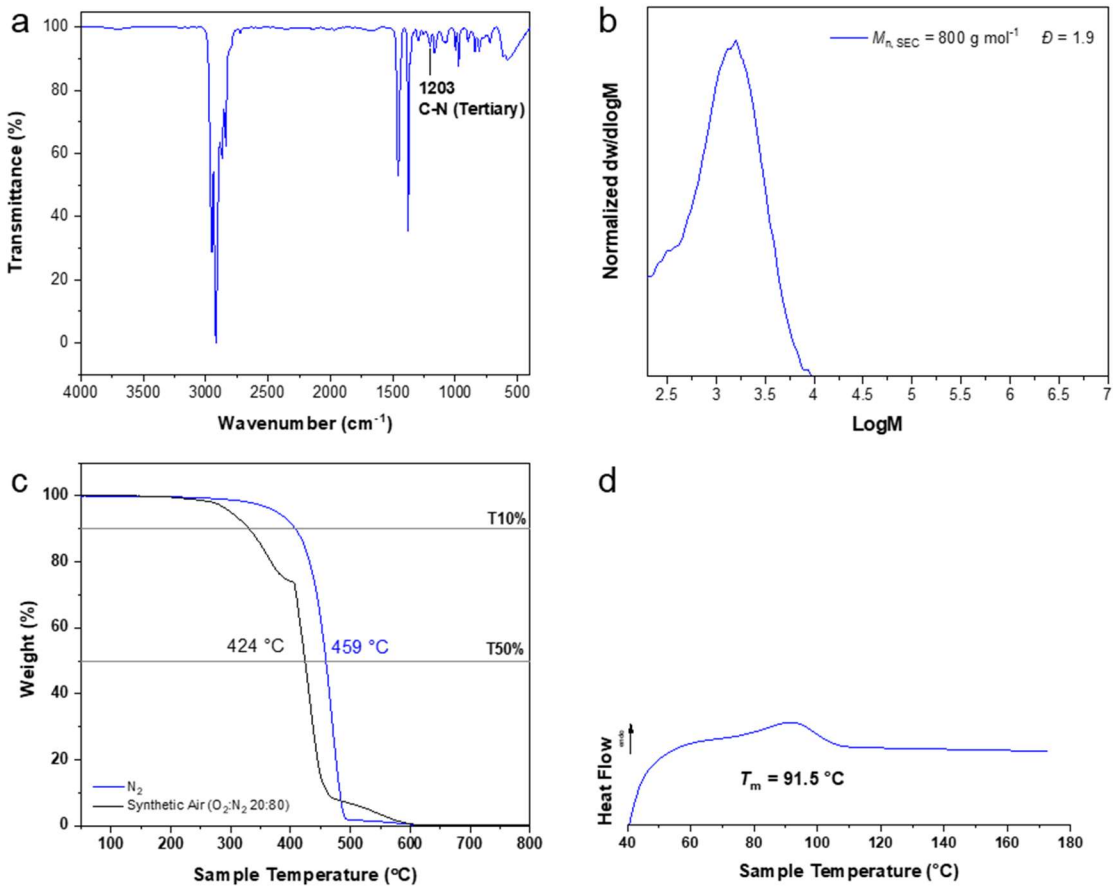

Figure A1.32 (a) FT-IR spectrum (b) SEC trace (c) TGA thermograph and (d) DSC 2nd heating curve of **PP$_{DEA}$**.

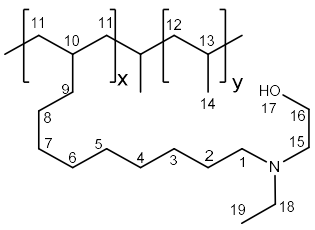

Synthesis of 2,2'-iminodiethanol (EAE) modified PP$_{Br}$, PP$_{EAE}$. EAE (50 equiv.) were added to **PP$_{Br}$** (0.5 g) heated and stirred at 180 °C for 48 h in an ampoule. The final polymer was precipitated in acidified methanol (2wt% HCl) before being collected by filtration on a glass sintered frit (porosity 3), washed with methanol, then acetone, and dried *in vacuo* at 60 °C to a constant weight. **PP$_{EAE}$** (3.99 mol%). **^{1}H NMR (600 MHz, C$_2$D$_2$Cl$_4$, 393 K)**: 4.05 (2H, br s, H^{16})^a, 3.27 (2H, br s, H^{15})^a, 3.18 (2H, br s, H^{18})^a, 3.13 (2H, br s, H^1)^a, 1.92 (2H, br s, H^2)^a, 1.75-1.62 (33H, br m, H^{13}), 1.55-1.06 (72H, br m, H^b, H$^{3\text{-}4}$, H^{12} $^{(anti)}$, and H^{19}), 1.05-0.84 ppm (135H, br m, H^{14} and H^{12} $^{(syn)}$). **^{13}C{^{1}H} NMR (151 MHz, C$_2$D$_2$Cl$_4$, 393 K)**: 144.85, 123.93, 111.22, 99.88, 57.49

(1C, br s, C^{18})[a], 56.75 (1C, s, C^{16}), 54.13 (1C, s, C^{1}), 49.40 (1C, s, C^{15}), 46.51 (1C, s, C^{10}), 46.21 (C^{13}), 43.65 (1C, s, C^{a}), 39.53 (1C, s, C^{a}), 35.93 (1C, s, C^{a}), 33.66 (1C, s, C^{a}), 30.16 (1C, s, C^{a}), 29.09 (1C, s, C^{a}), 28.57 (C^{12}), 27.05, 26.85, 23.47 (1C, s, C^{2})[a], 21.64 (C^{14}), 20.85, 19.67, 8.81 (1C, s, C^{19}). **FT-IR**: ν (cm^{-1}) = 2950, 2867, and 1456 (ν (CH, CH_3)), 2917, 2838, and 1377 (ν (CH, CH_2)), 1110-1014 (ν (CN)). [a]Nitrogen adjacent ^{1}H and ^{13}C NMR peaks appear broad. This observation is potentially explained by an increase in the relaxation rate caused by quadrupolar Nitrogen. A lack of HMBC cross-peaks whilst still evidencing HSQC cross-peaks support this. Experimentally, HSQC equivalent delays were optimised for 145 Hz (3 ms delay) whereas HMBC experiments were optimised for a 125 ms delay, giving the nuclei sufficient time to relax and preventing the appearance of any cross-peak to carbons adjacent to nitrogen.[6, 7] [b]Peaks corresponding to unassigned CH_2.

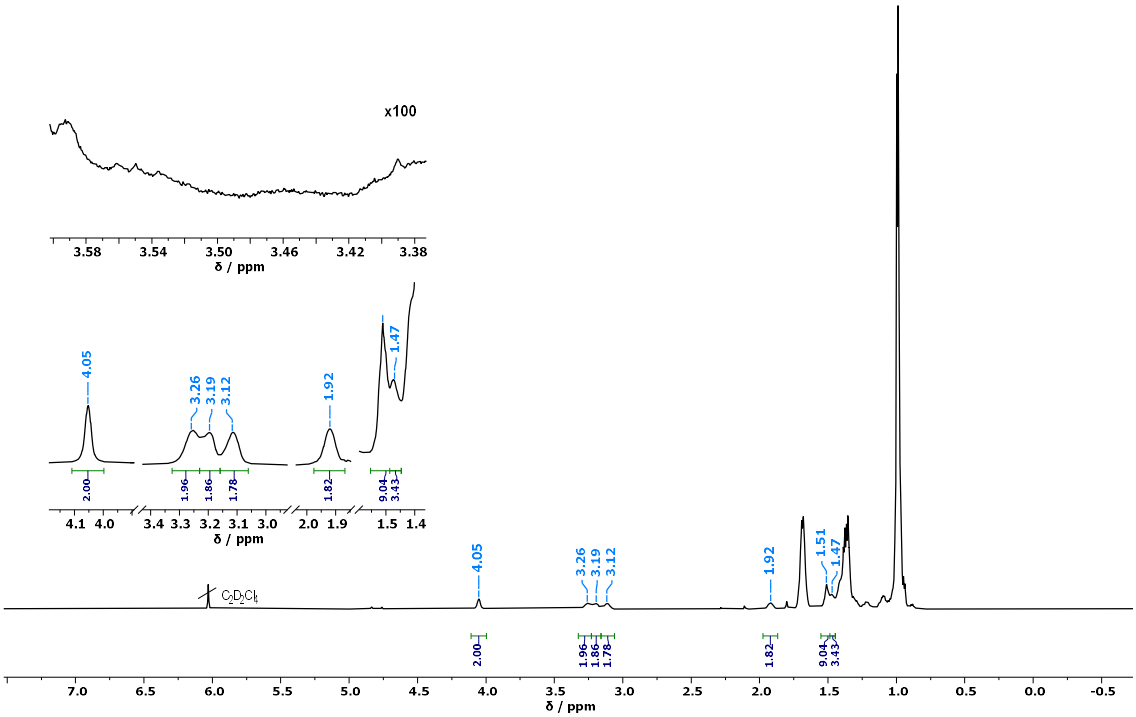

Figure A1.33 PP_{EAE} ^{1}H NMR (600 MHz, $C_2D_2Cl_4$, 393 K).

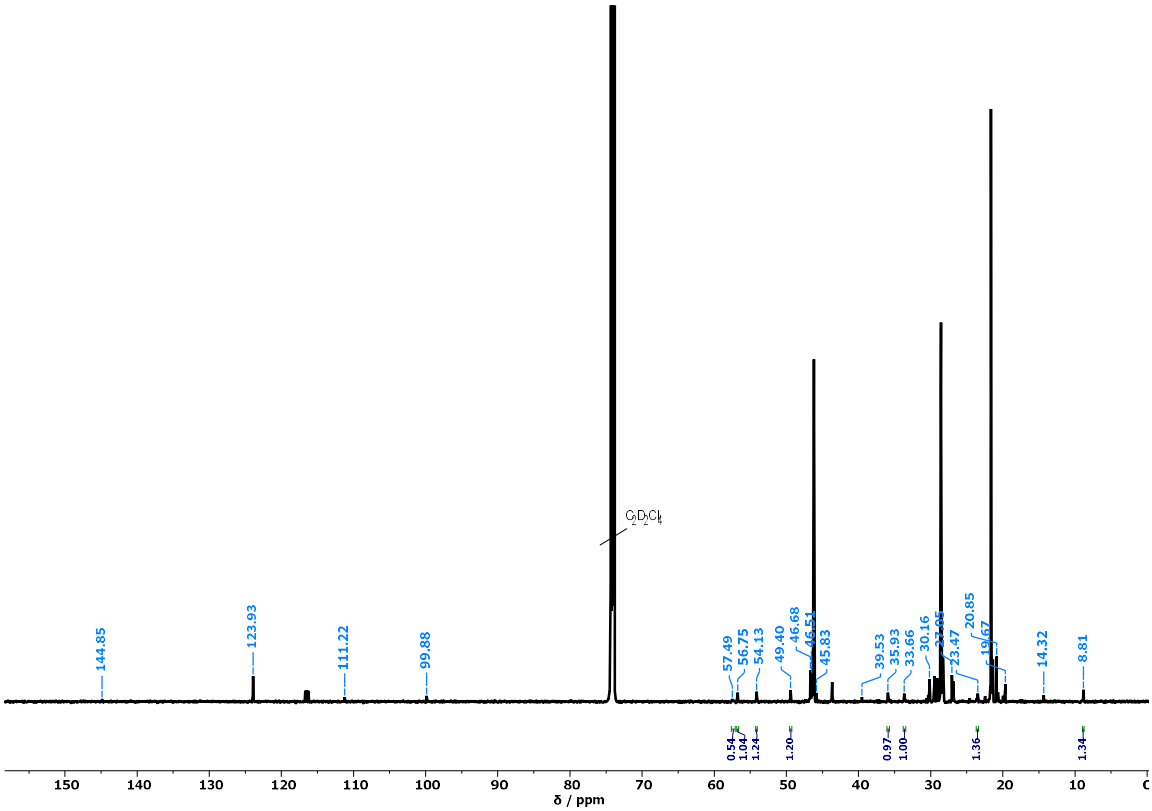

Figure A1.34 PP$_{EAE}$ $^{13}C\{^{1}H\}$ NMR (151 MHz, $C_2D_2Cl_4$, 393 K), full spectrum.

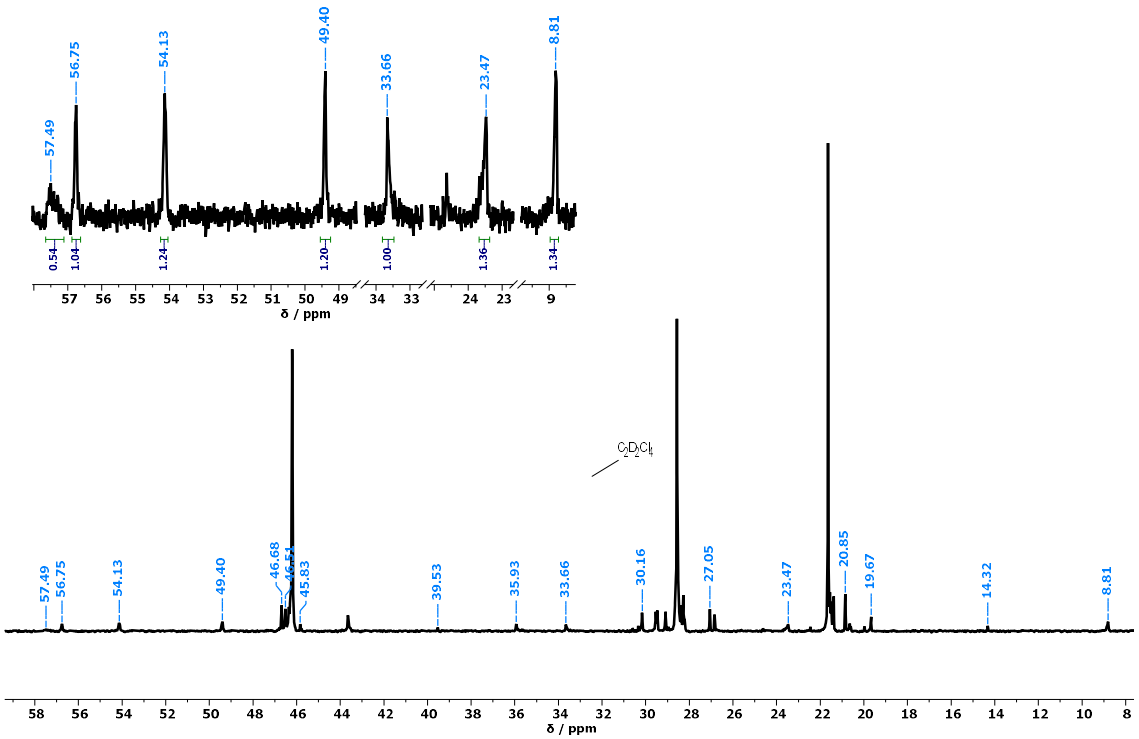

Figure A1.35 PP$_{EAE}$ $^{13}C\{^{1}H\}$ NMR (151 MHz, $C_2D_2Cl_4$, 393 K), expanded comonomer region.

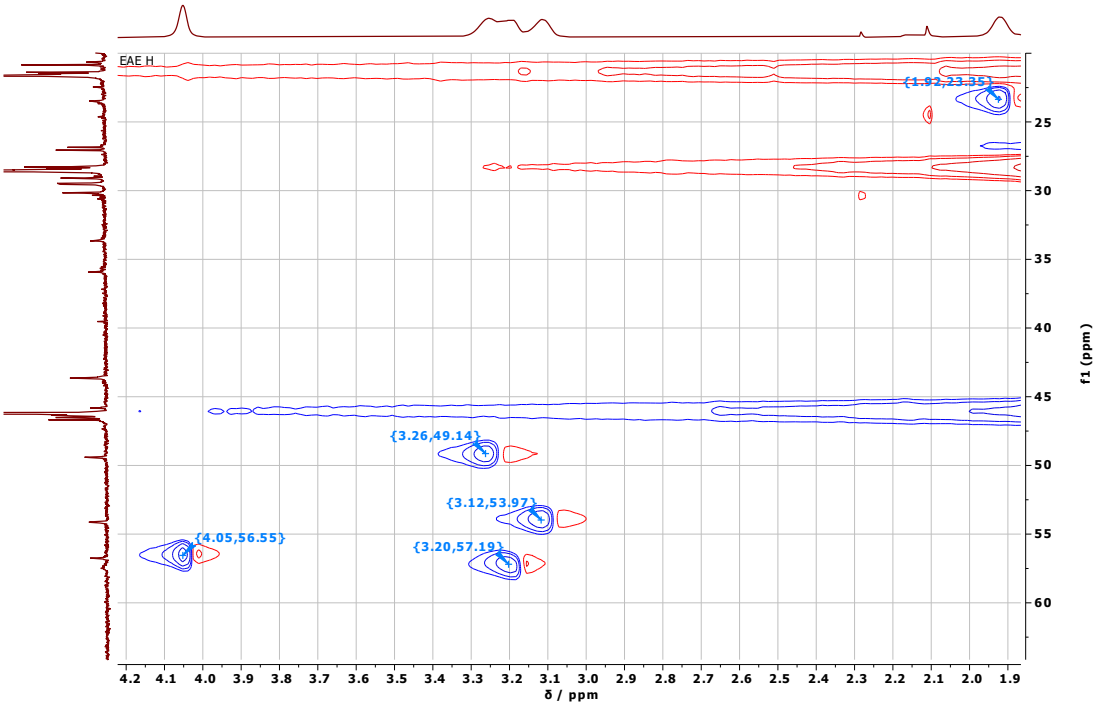

Figure A1.36 PP$_{EAE}$ HSQC ^{1}H-^{13}C NMR spectrum.

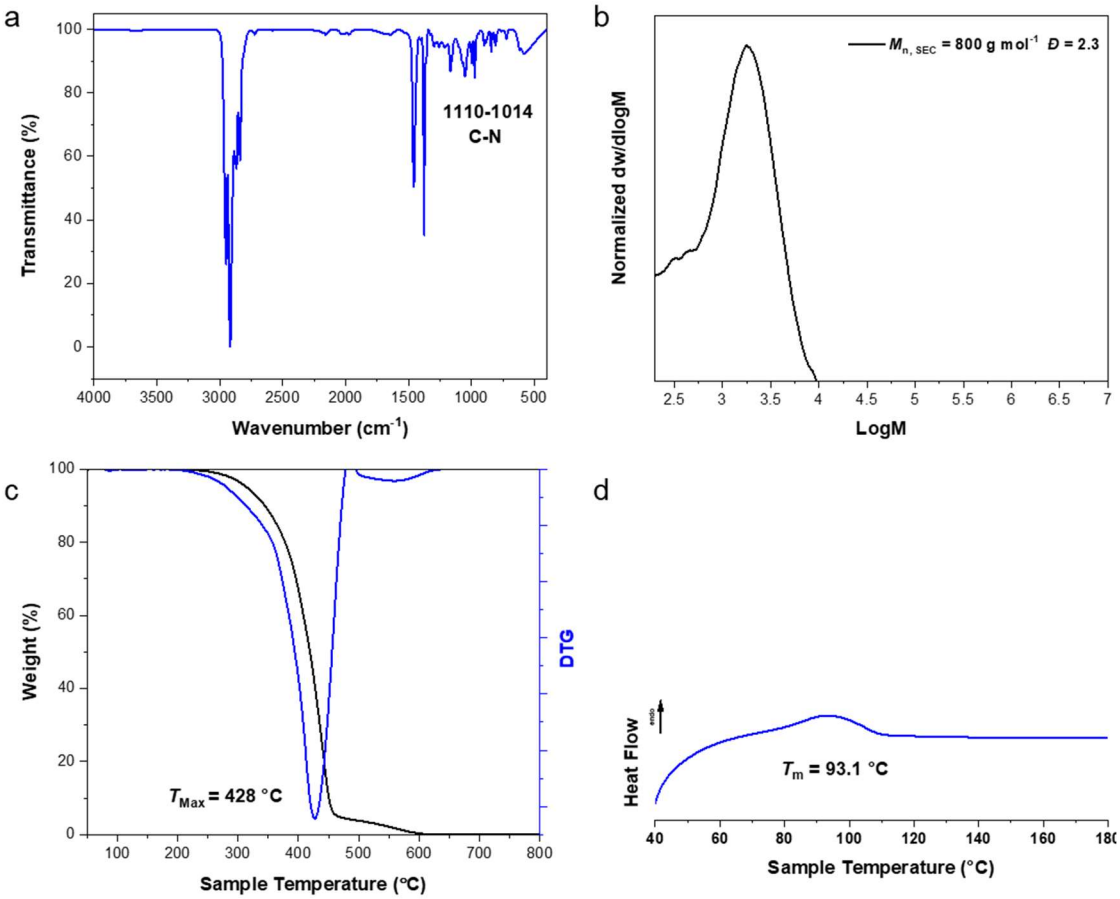

Figure A1.37 (a) FT-IR spectrum (b) SEC trace (c) TGA thermograph and (d) DSC 2nd heating curve of **PP$_{EAE}$**.

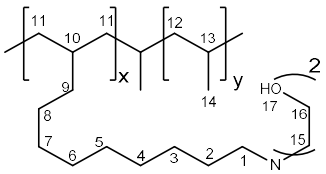

Synthesis of 2,2'-iminodiethanol (DEOA) modified PP_{Br}, PP_{DEOA}. DEOA (50 equiv.) were added to **PP_{Br}** (0.5 g) heated and stirred at 180 °C for 48 h in an ampoule. The final polymer was precipitated in acidified methanol (2wt% HCl) before being collected by filtration on a glass sintered frit (porosity 3), washed with methanol, then acetone, and dried in vacuo at 60 °C to a constant weight. **PP_{DEOA}** (3.99 mol%). **^{1}H NMR (600 MHz, $C_2D_2Cl_4$, 393 K)**: 4.13 (4H, br s, H^{16})^a, 3.37 (4H, br s, H^{15})^a, 3.25 (2H, br s, H^1)^a, 1.93 (2H, br s, H^2)^a, 1.75-1.62 (40H, br m, H^{13}), 1.55-1.06 (78H, br m, H^b, $H^{3\text{-}4}$ and H^{12} (*anti*)), 1.05-0.84 ppm (162H, br m, H^{14} and H^{12} (*syn*)). **^{13}C{^{1}H} NMR (151 MHz, $C_2D_2Cl_4$, 393 K):** 123.93, 120.53, 116.47, 111.23, 99.88, 58.72 (2C, br s, C^{15})^a, 56.90 (2C, br s, C^{16})^a, 55.54 (1C, br s, C^1)^a, 46.21 (C^{13}), 45.83, 45.38 (1C, s, C^4), 43.66, 39.52, 35.96, 33.68, 28.58 (C^{12}), 26.99, 23.67 (1C, br s, C^2)^a, 22.45, 21.64 (C^{14}), 19.66, 14.32. ^{a}Nitrogen adjacent ^{1}H and ^{13}C NMR peaks appear broad. This observation is potentially explained by an increase in the relaxation rate caused by quadrupolar Nitrogen. A lack of HMBC cross-peaks whilst still evidencing HSQC cross-peaks support this. Experimentally, HSQC equivalent delays were optimised for 145 Hz (3 ms delay) whereas HMBC experiments were optimised for a 125 ms delay, giving the nuclei sufficient time to relax and preventing the appearance of any cross-peak to carbons adjacent to nitrogen.[6, 7] ^{b}Peaks corresponding to unassigned CH_2. **FTIR**: ν (cm^{-1}) = 3506-3182 (ν (OH)), 2950, 2867, and 1456 (ν (C-H, CH_3)), 2917, 2838, and 1377 (ν (C-H, CH_2)), 1080-1045 (ν (CN)).

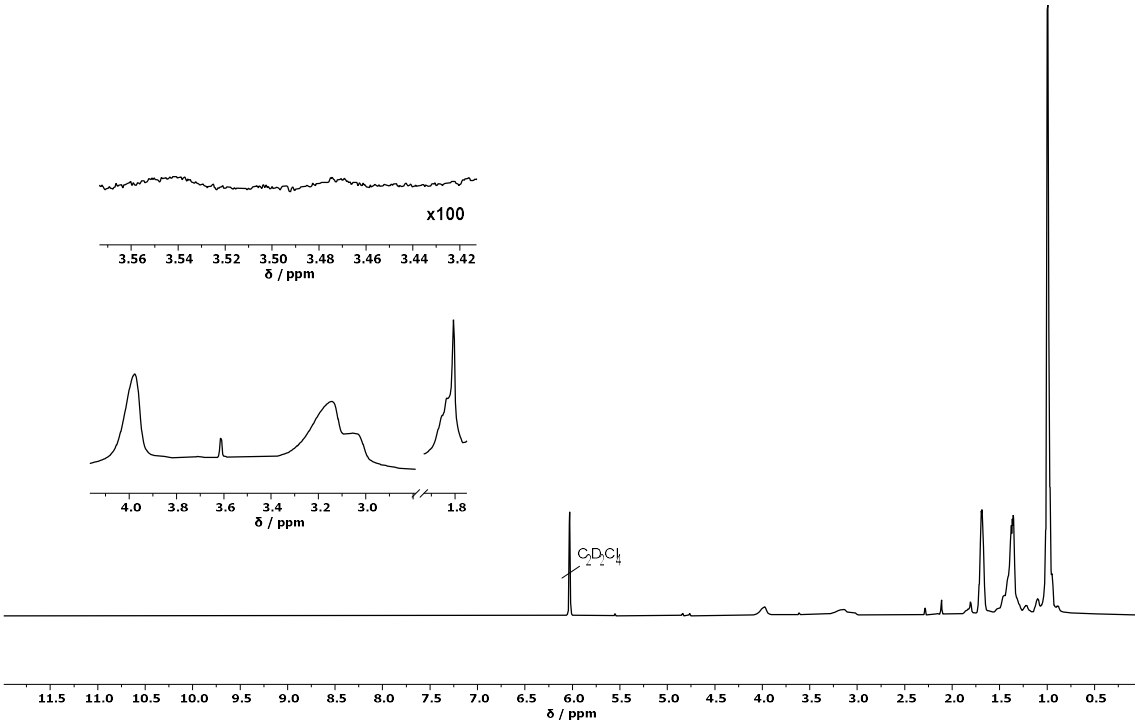

Figure A1.38 PP_{DEOA} ^{1}H NMR (600 MHz, $C_2D_2Cl_4$, 393 K).

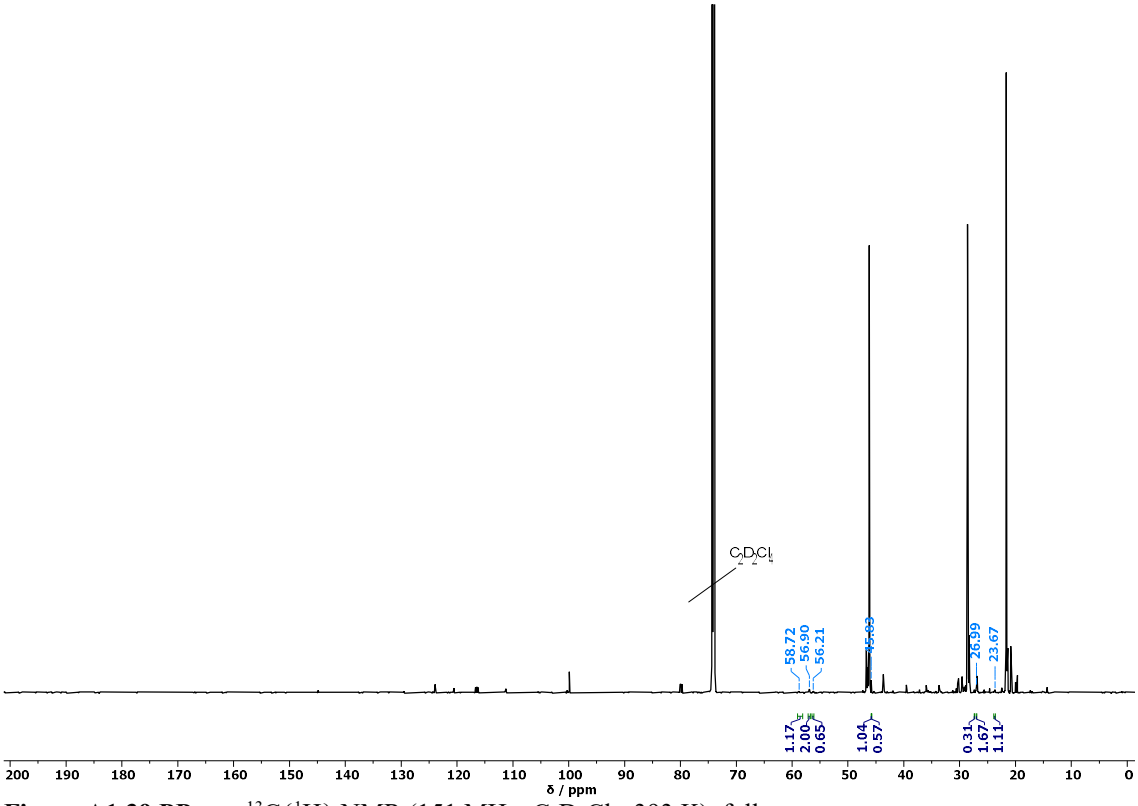

Figure A1.39 PP_{DEOA} $^{13}C\{^{1}H\}$ NMR (151 MHz, $C_2D_2Cl_4$, 393 K), full spectrum.

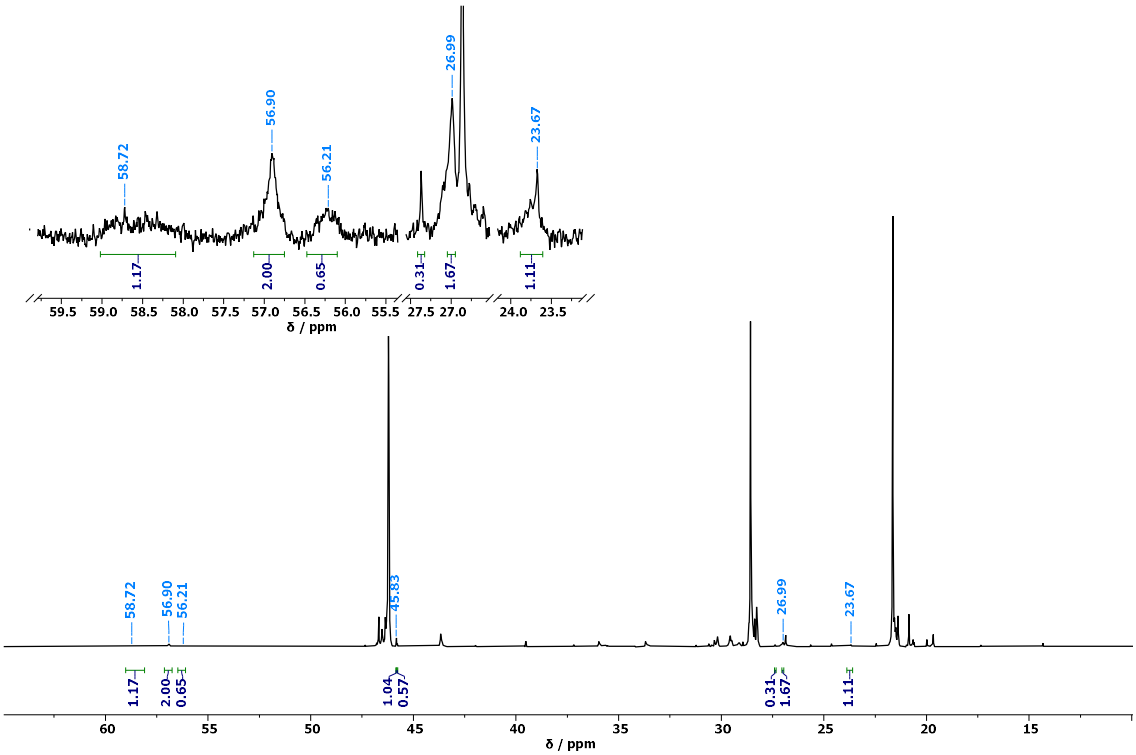

Figure A1.40 PP$_{DEOA}$ $^{13}C\{^{1}H\}$ NMR (151 MHz, $C_2D_2Cl_4$, 393 K), expanded comonomer region.

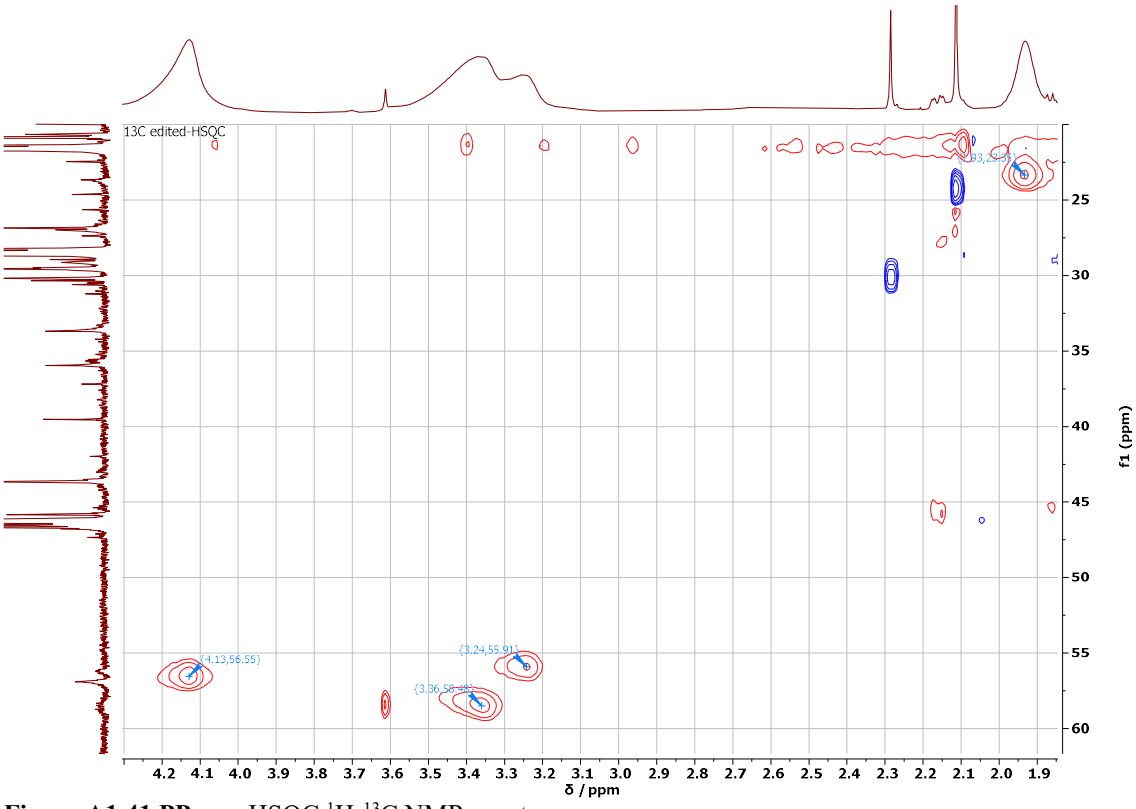

Figure A1.41 PP$_{DEOA}$ HSQC ^{1}H-^{13}C NMR spectrum.

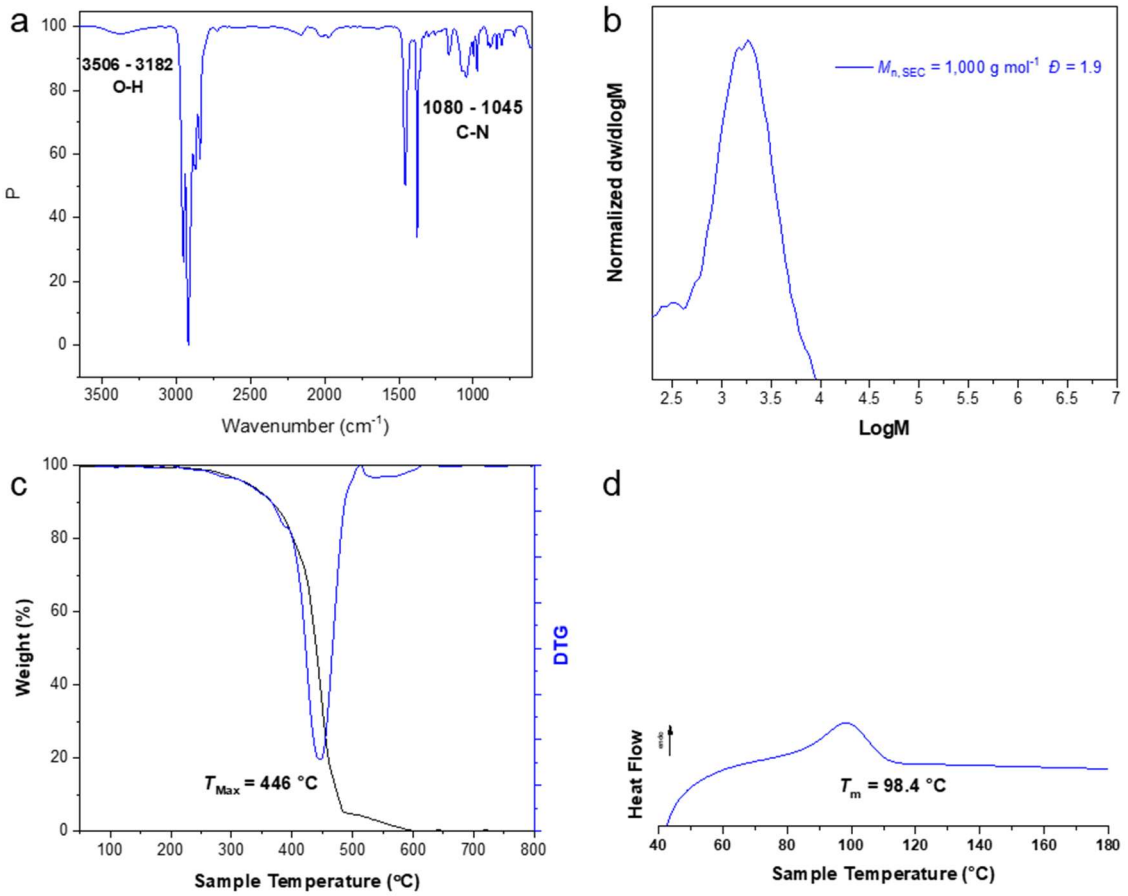

Figure A1.42 (a) FT-IR spectrum (b) SEC trace (c) TGA thermograph and (d) DSC 2nd heating curve of **PP_{DEOA}**.

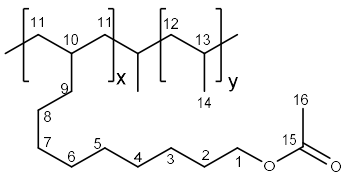

Synthesis of ethanoic acid modified PP_{Br}, PP_{Ac}. 2,3,4,6,7,8,9,10-octahydropyrimido[1,2-*a*]azepine (DBU, 2 equiv.) were added to a THF (1 ml) solution of ethanoic acid (2 equiv.) and **PP_{Br}** (0.25 g) in an ampoule before being heated and stirred at 77 °C for 24 h. The final polymer was precipitated in acidified methanol (2wt% HCl) before being collected by filtration on a glass sintered frit (porosity 3), washed with methanol, then acetone, and dried in vacuo at 60 °C to a constant weight. **PP_{Ac}** (3.99 mol%). **^{1}H NMR (600 MHz, $C_2D_2Cl_4$, 393 K)**: 4.15 (2H, t, $^3J_{HH}$ = 6.7 Hz, H^1), 2.09 (3H, s, H^{16}), 1.74-1.58 (25H, br m, H^{13}), 1.58-1.06 (45H, br m, H^a, H^2 and $H^{12\ (anti)}$), 1.05-0.84 ppm (67H, br m, H^{14} and $H^{12\ (syn)}$). **^{13}C{^{1}H} NMR (151 MHz, $C_2D_2Cl_4$, 393 K):** 170.60 (1C, s, C^{15}), 120.53, 99.89, 64.59 (1C, s, C^1), 46.21 (C^{13}), 43.63 (1C, s, C^a), 35.85 (1C, s, C^a),

33.57 (1C, s, C^a), 30.17 (1C, s, C^a), 29.68 (1C, s, C^a), 29.59 (1C, s, C^a), 29.54 (1C, s, C^a), 29.28 (1C, s, C^3), 28.88 (1C, s, C^2), 28.58 (C^{12}), 26.81 (1C, s, C^a), 26.04 (1C, s, C^4), 21.64 (C^{14}), 20.76 (1C, s, C^{16}). [a]Peaks corresponding to unassigned CH_2. **FTIR**: ν (cm^{-1}) = 2950, 2867, and 1456 (ν (C-H, CH_3)), 2917, 2838, and 1377 (ν (C-H, CH_2)), 1745 (ν (C=O)), 1433 (ν (C-O)).

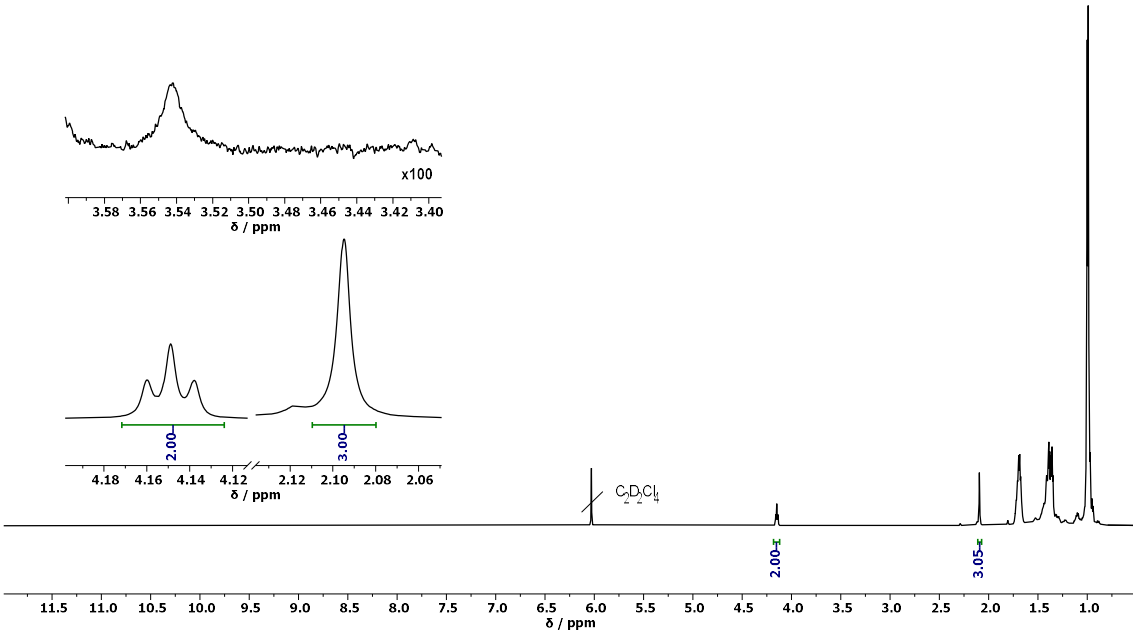

Figure A1.43 PP_{Ac} ^{1}H NMR (600 MHz, $C_2D_2Cl_4$, 393 K).

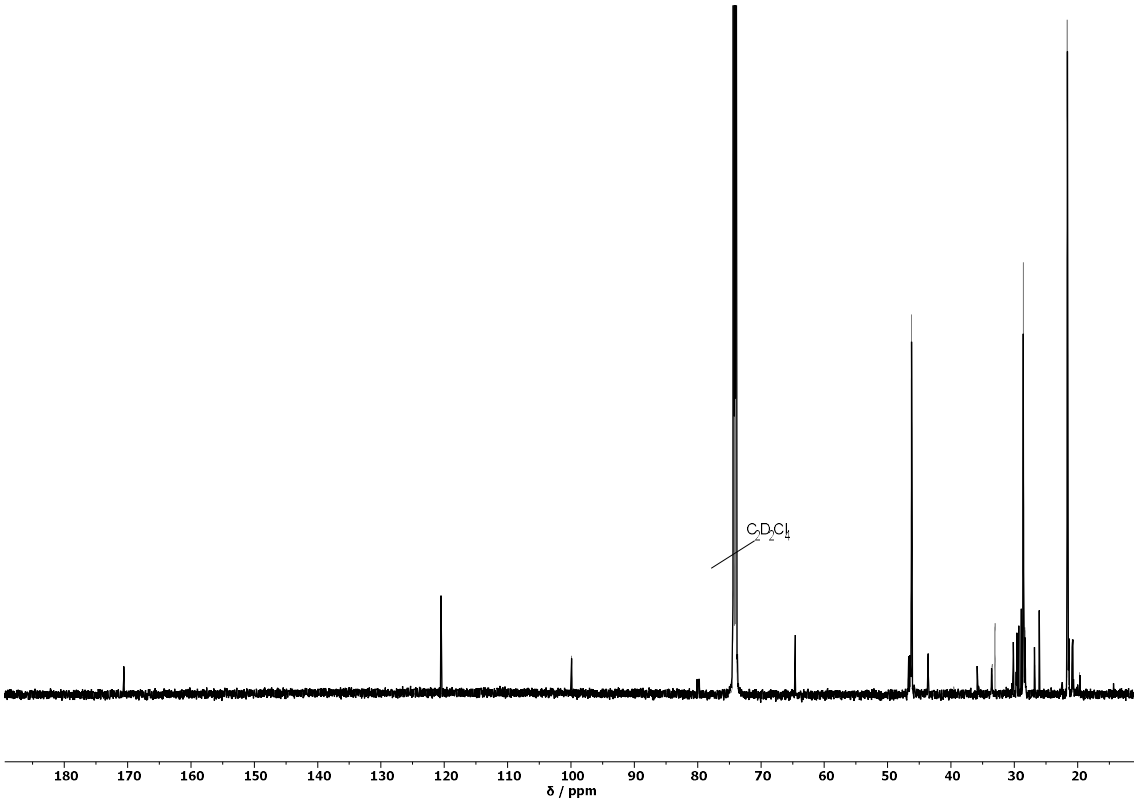

Figure A1.44 PP$_{Ac}$ $^{13}C\{^1H\}$ NMR (151 MHz, $C_2D_2Cl_4$, 393 K), full spectrum.

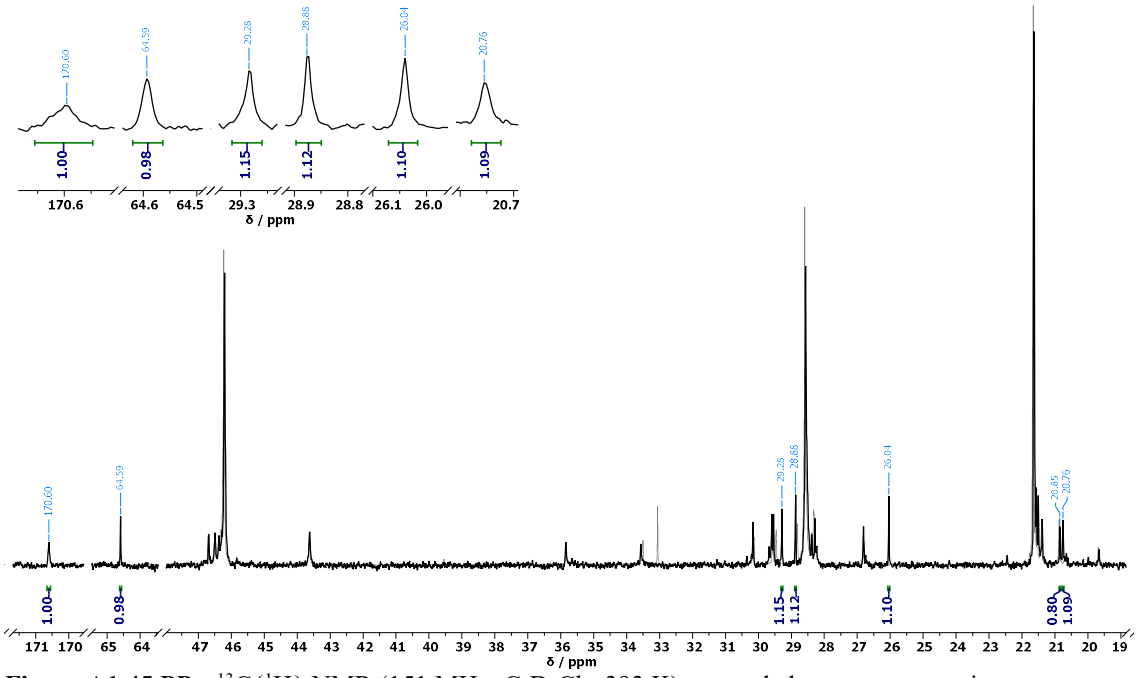

Figure A1.45 PP$_{Ac}$ $^{13}C\{^1H\}$ NMR (151 MHz, $C_2D_2Cl_4$, 393 K), expanded comonomer region.

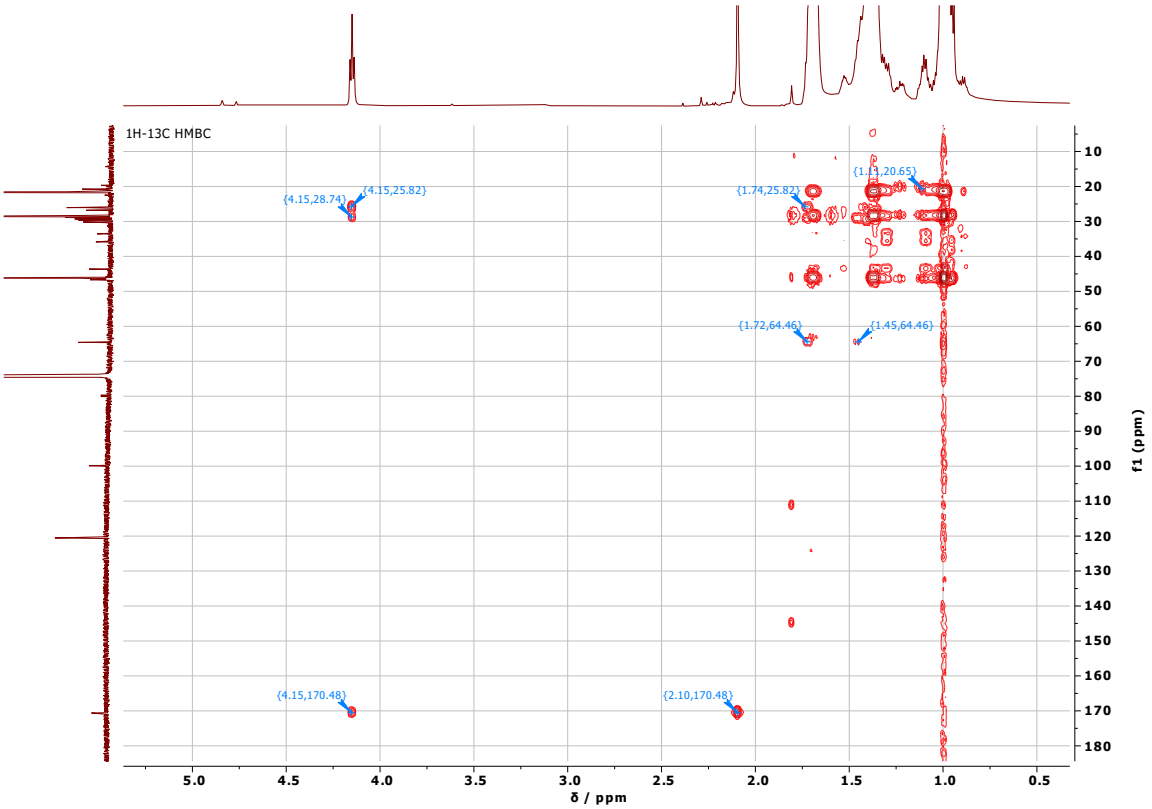

Figure A1.46 PP_{Ac} HMBC ^{1}H-^{13}C NMR spectrum.

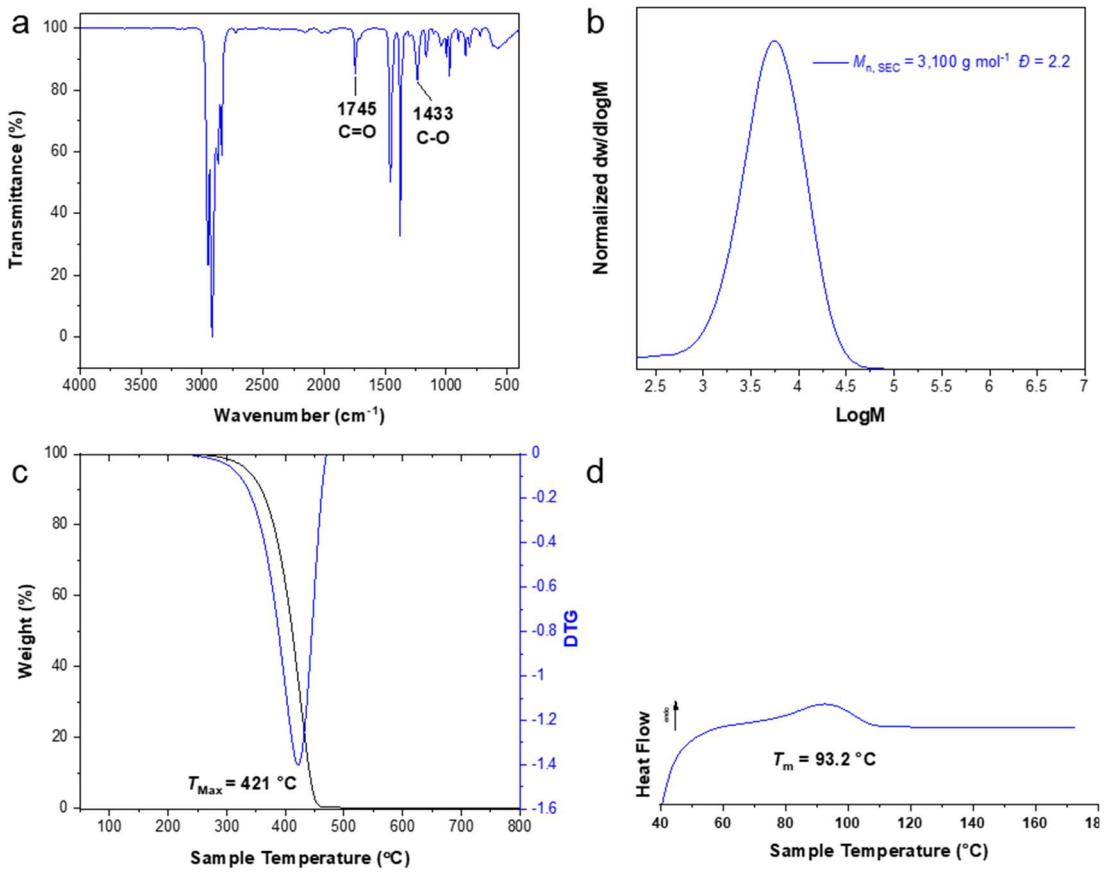

Figure A1.47 (a) FT-IR spectrum (b) SEC trace (c) TGA thermograph and (d) DSC 2nd heating curve of **PP_{Ac}**.

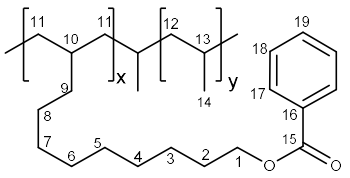

Synthesis of benzoic acid modified PP_{Br}, PP_{Bn}. DBU (2 equiv.) were added to a THF (1 ml) solution of benzoic acid (2 equiv.) and **PP_{Br}** (0.25 g) in an ampoule before being heated and stirred at 77 °C for 24 h. The final polymer was precipitated in acidified methanol (2wt% HCl) before being collected by filtration on a glass sintered frit (porosity 3), washed with methanol, then acetone, and dried in vacuo at 60 °C to a constant weight. **PP_{Bn}** (3.99 mol%). **^{1}H NMR (500 MHz, $C_2D_2Cl_4$, 393 K)**: 8.11 (2H, d, $^3J_{HH}$ = 7.4 Hz, H^{17}), 7.61 (1H, t, $^3J_{HH}$ = 6.7 Hz, H^{19}), 7.50 (2H, t, $^3J_{HH}$ = 7.5 Hz, H^{18}), 4.41 (2H, t, $^3J_{HH}$ = 6.6 Hz, H^1), 1.87 (2H, m, H^2), 1.75-1.58 (23H, br m, H^{13}), 1.58-1.06 (52H, br m, H^a, H^2, and H^{12} (*anti*)), 1.04-0.93 ppm (88H, br m, H^{14} and H^{12} (*syn*)). **$^{13}C\{^1H\}$ NMR (151 MHz, $C_2D_2Cl_4$, 393 K):** 166.54 (1C, s, C^{15}), 132.61 (1C, s, C^{16}), 131.21 (1C, s, C^{19}), 129.60 (2C, s, C^{18}), 128.33 (2C, s, C^{17}), 120.54, 99.89, 65.21 (1C, s, C^1), 46.21 (C^{13}), 43.63 (1C, s, C^a), 39.54 (1C, s, C^a), 35.87 (1C, s, C^a), 33.59 (1C, s, C^a), 30.18 (1C, s, C^a), 29.62 (1C, s, C^a), 29.58 (1C, s, C^a), 29.33 (1C, s, C^3), 28.98 (1C, s, C^2), 28.58 (C^{12}), 26.82 (1C, s, C^a), 26.16 (1C, s, C^4), 21.64 (C^{14}). *a*Peaks corresponding to unassigned CH_2. **FTIR**: *v* (cm^{-1}) = 2950, 2867, and 1456 (*v* (C-H, CH_3)), 2917, 2838, and 1377 (*v* (C-H, CH_2)), 1724 (*v* (C=O)), 1272 (*v* (C_{Al}-O)), 1113 (*v* (C_{Ar}-O)), and 709 (*v* (C=C_{Ar})).

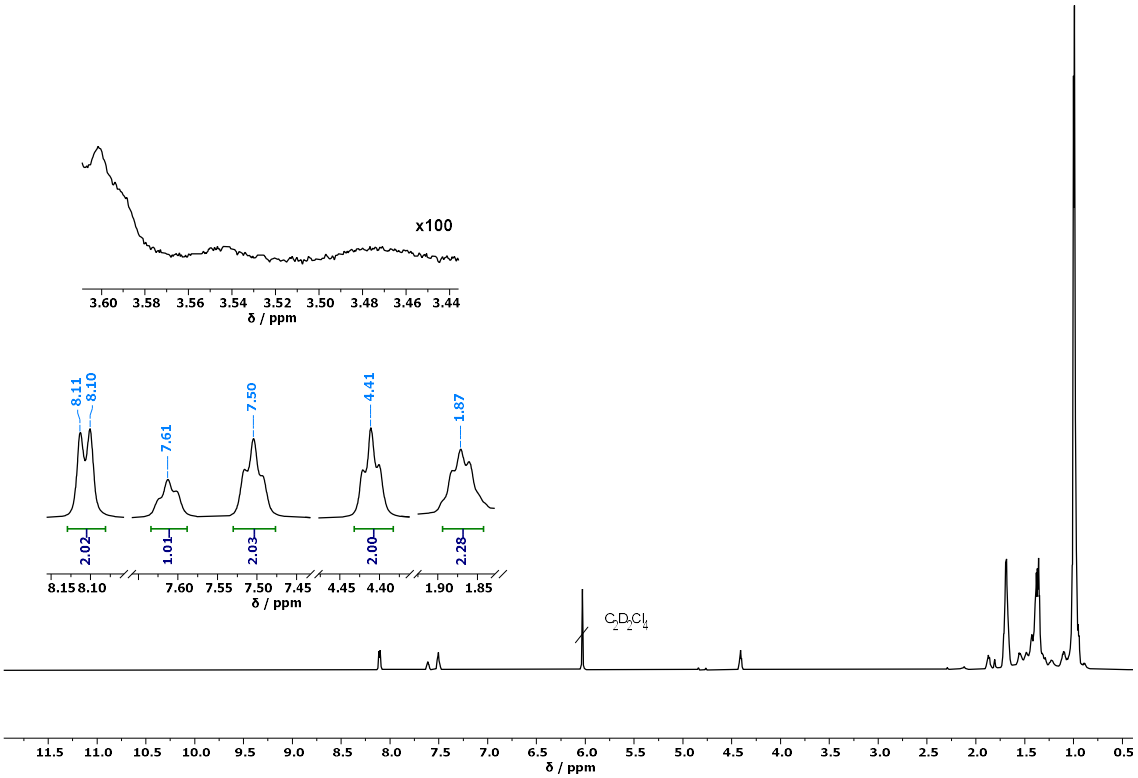

Figure A1.48 PP_{Bn} ^{1}H NMR (600 MHz, $C_2D_2Cl_4$, 393 K).

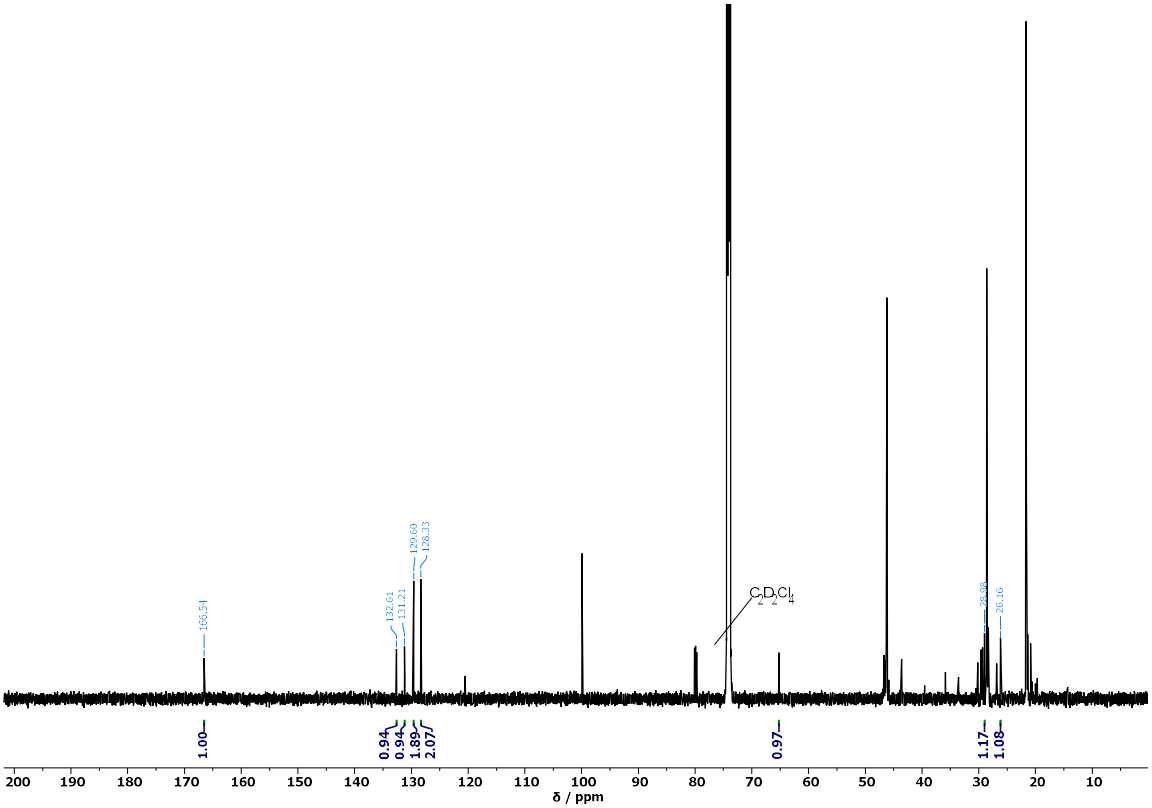

Figure A1.49 PP_{Bn} $^{13}C\{^{1}H\}$ NMR (151 MHz, $C_2D_2Cl_4$, 393 K), full spectrum.

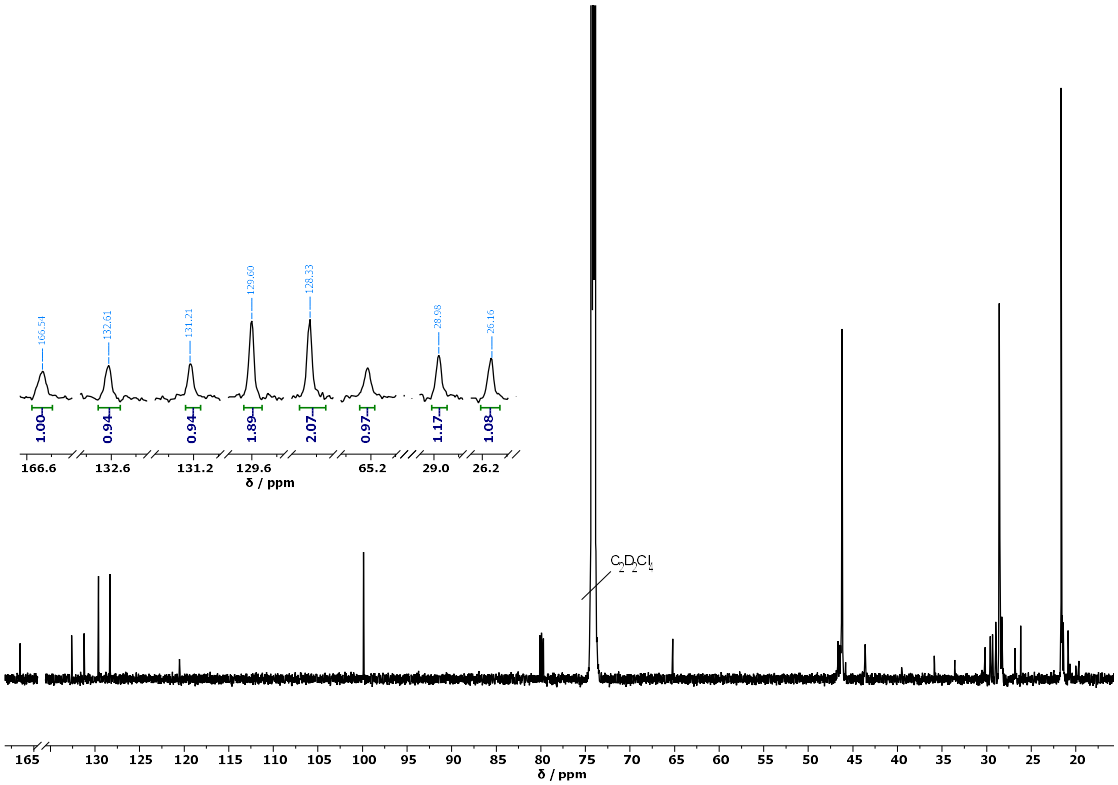

Figure A1.51 PP$_{Bn}$ $^{13}C\{^{1}H\}$ NMR (151 MHz, $C_2D_2Cl_4$, 393 K), expanded comonomer region.

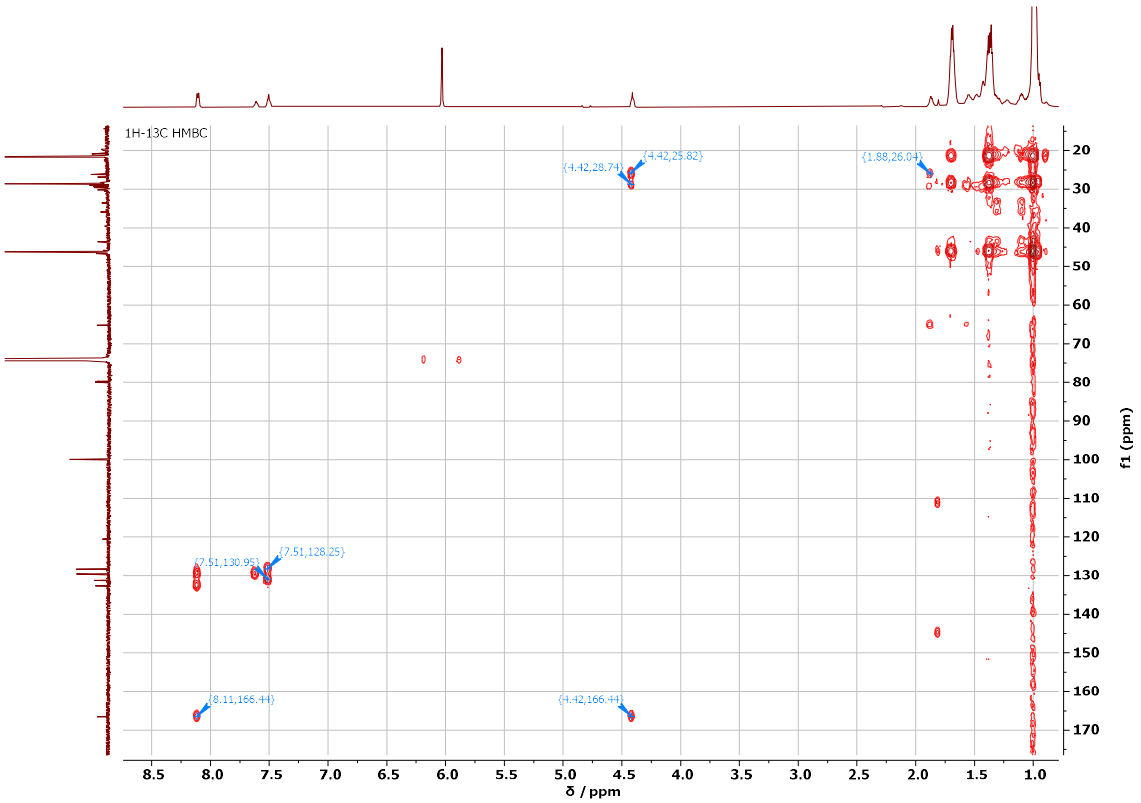

Figure A1.51 PP$_{Bn}$ HMBC ^{1}H-^{13}C NMR spectrum.

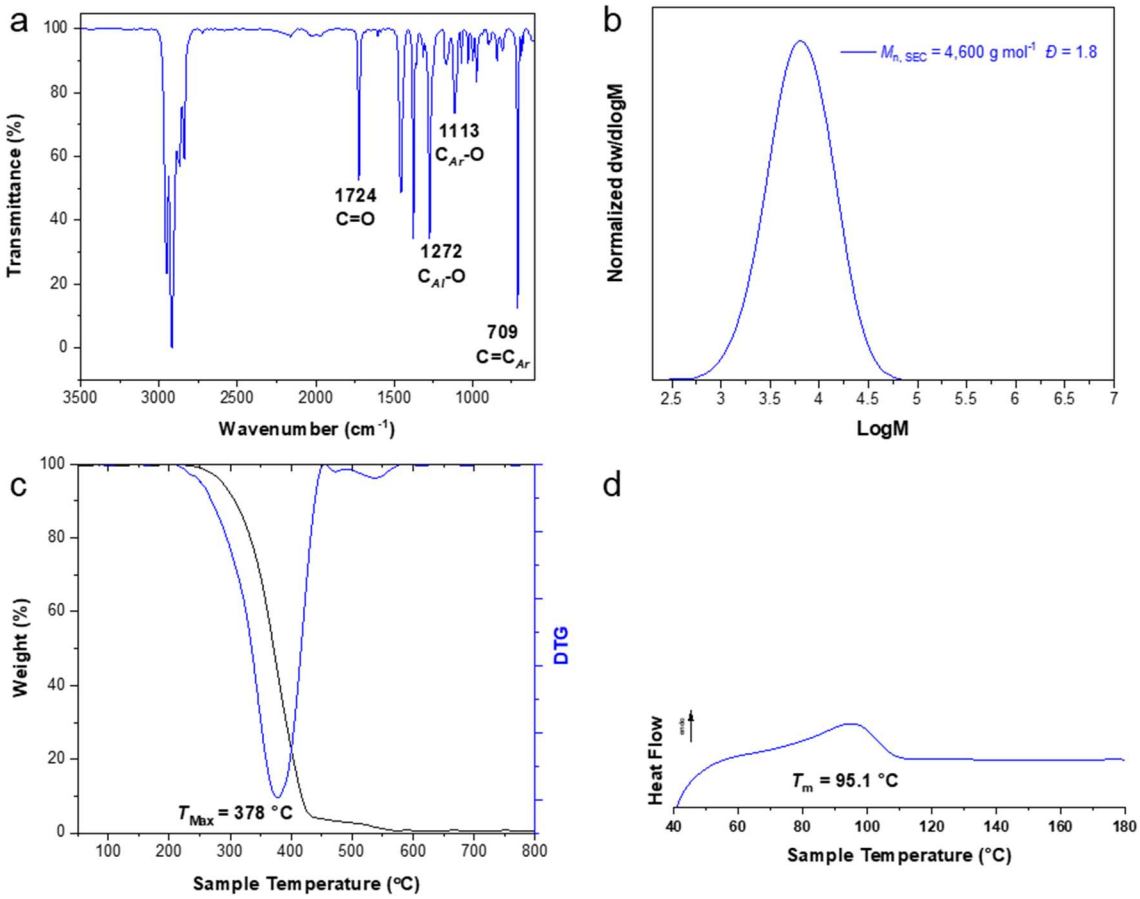

Figure A1.52 (a) FT-IR spectrum (b) SEC trace (c) TGA thermograph and (d) DSC 2nd heating curve of **PP_{Bn}**.

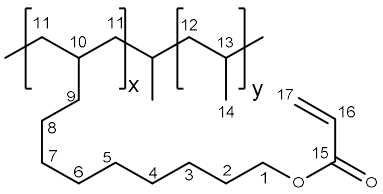

Synthesis of acrylic acid modified PP_{Br}, PP_{AA}. DBU (2 equiv.) were added to a THF (5 ml) solution of propenoic acid (2 equiv.) and **PP_{Br}** (0.25 g) in an ampoule, sparged with N_2 for 15 minutes before being heated and stirred at 77 °C for 96 h. The final polymer was precipitated in acidified methanol (2wt% HCl) before being collected by filtration on a glass sintered frit (porosity 3), washed with methanol, then acetone, and dried in vacuo at 60 °C to a constant weight. **PP_{AA}** (3.99 mol%). **^{1}H NMR (600 MHz, $C_2D_2Cl_4$, 393 K)**: 6.43 (1H, d, $^3J_{HH}$ = 17.3 Hz, $H^{17\ (cis)}$), 6.20 (1H, dd, $^3J_{HH}$ = 17.3 and 10.3 Hz, H^{16}), 5.84 (1H, d, $^3J_{HH}$ = 10.3 Hz, $H^{17\ (trans)}$), 4.25 (2H, t, $^3J_{HH}$ = 6.6 Hz, H^1), 1.76 (2H, m, H^2), 1.75-1.58 (30H, br m, H^{13}), 1.48-1.32 (68H, br m, H^a and $H^{12\ (anti)}$), 1.04-0.93 ppm (110H, br m, H^{14} and $H^{12\ (syn)}$). **^{13}C{^{1}H} NMR (151 MHz, $C_2D_2Cl_4$, 393**

K): 166.04 (1C, s, C^{15}), 129.51 (1C, s, C^{17}), 129.13 (1C, s, C^{16}), 64.72 (1C, s, C^{1}), 46.21 (C^{13}), 43.62 (2C, s, C^{a}), 35.85 (1C, s, C^{a}), 33.57 (1C, s, C^{a}), 30.16 (1C, s, C^{a}), 29.67-29.53 (3C, m, C^{a}), 29.28 (1C, s, C^{3}), 28.86 (1C, s, C^{2}), 28.58 (C^{12}), 26.81 (1C, s, C^{a}), 26.05 (1C, s, C^{4}), 21.64 (C^{14}). *a*Peaks corresponding to unassigned CH_2. **FTIR**: ν (cm^{-1}) = 2950, 2867, and 1456 (ν (C-H, CH_3)), 2917, 2838, and 1377 (ν (C-H, CH_2)), 1729 (ν (C=O)), 1637 (ν (C=C)), 1407, 1296, and 1267 (ν (CH=)), 1189 (ν (C-O)).

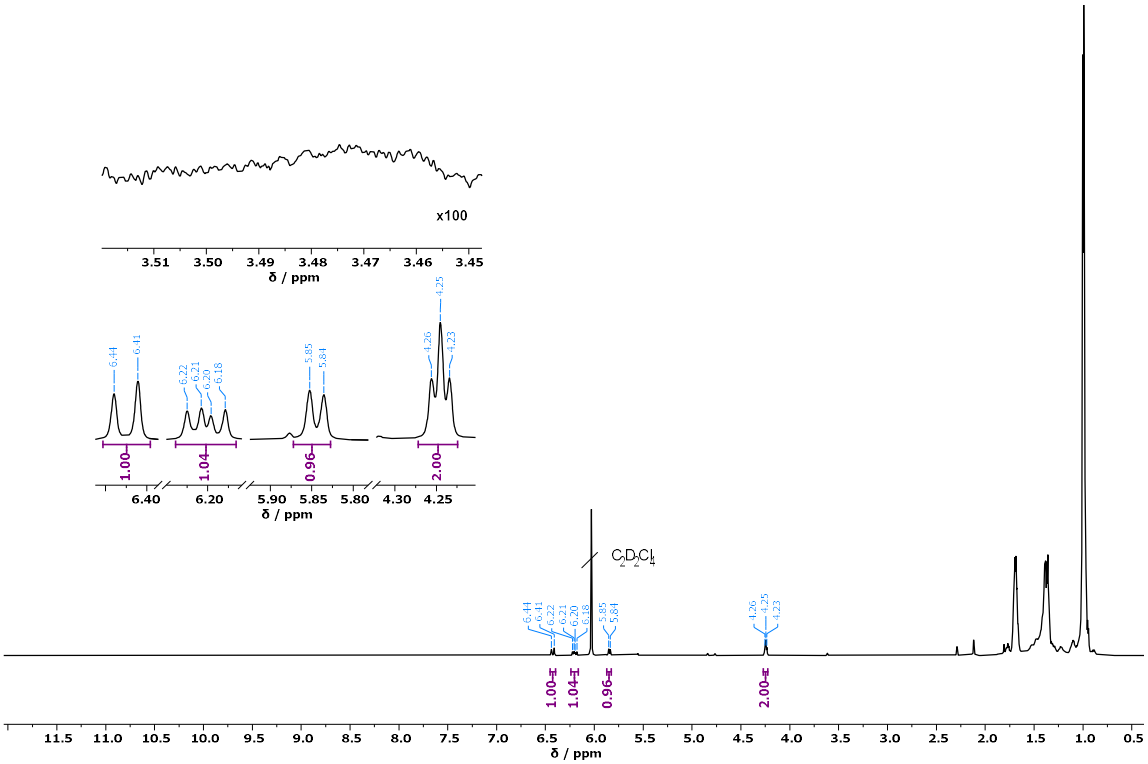

Figure A1.53 PP_{AA} ^{1}H NMR (600 MHz, $C_2D_2Cl_4$, 393 K).

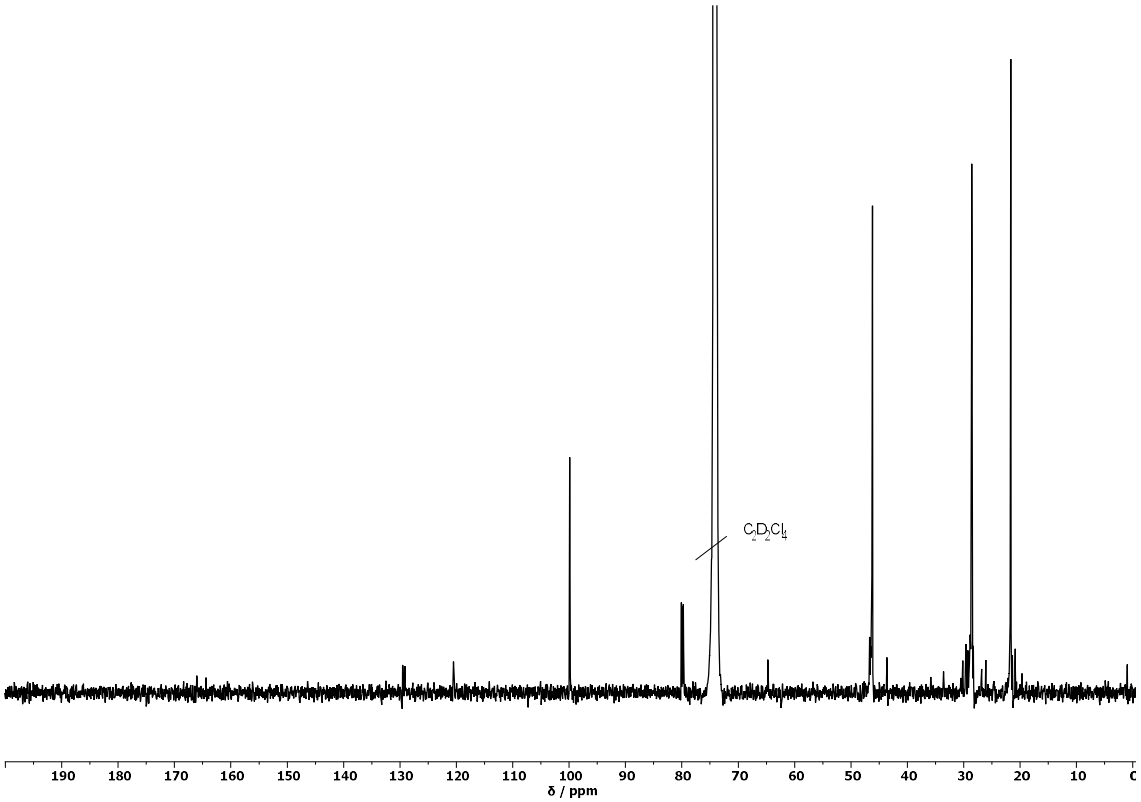

Figure A1.54 PP$_{AA}$ $^{13}C\{^{1}H\}$ NMR (151 MHz, $C_2D_2Cl_4$, 393 K), full spectrum.

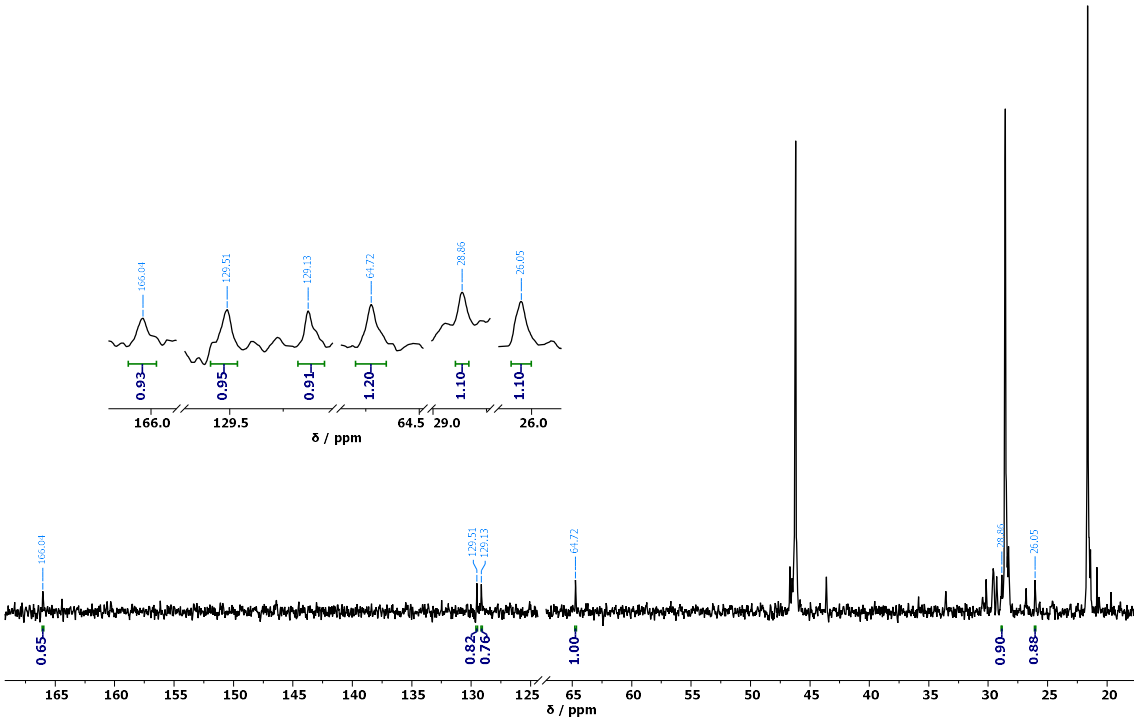

Figure A1.55 PP$_{AA}$ $^{13}C\{^{1}H\}$ NMR (151 MHz, $C_2D_2Cl_4$, 393 K), expanded comonomer region.

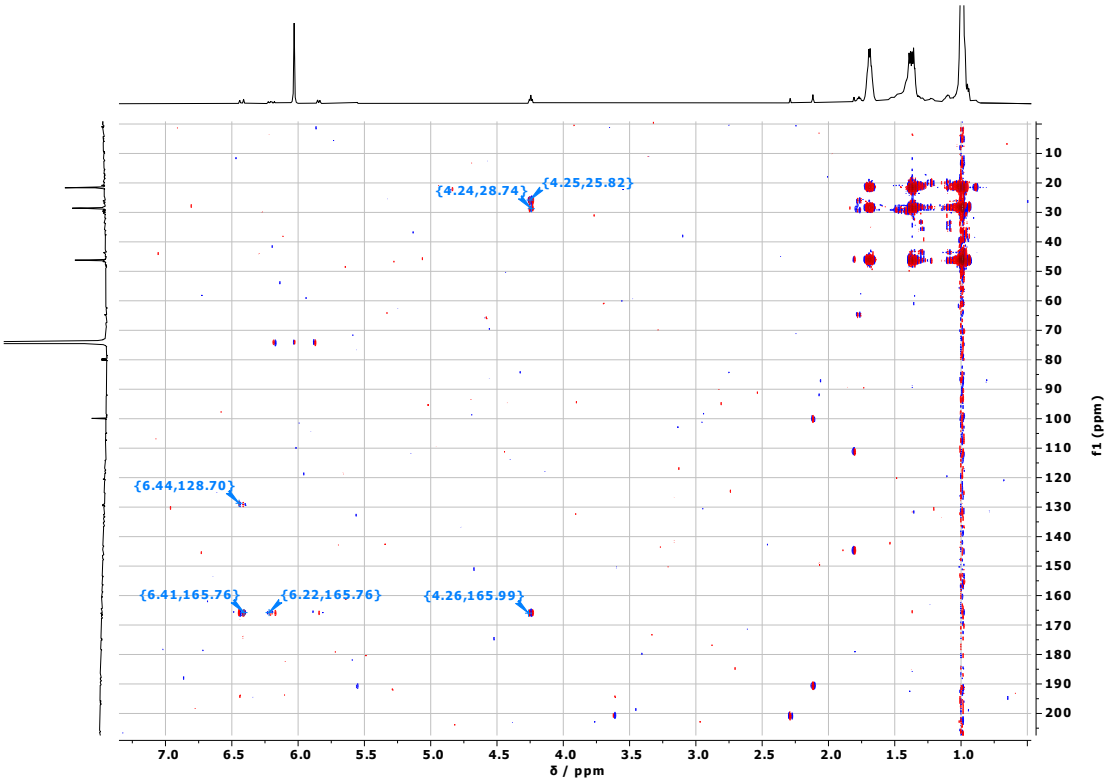

Figure A1.56 PP_{AA} HMBC ^{1}H-^{13}C NMR spectrum.

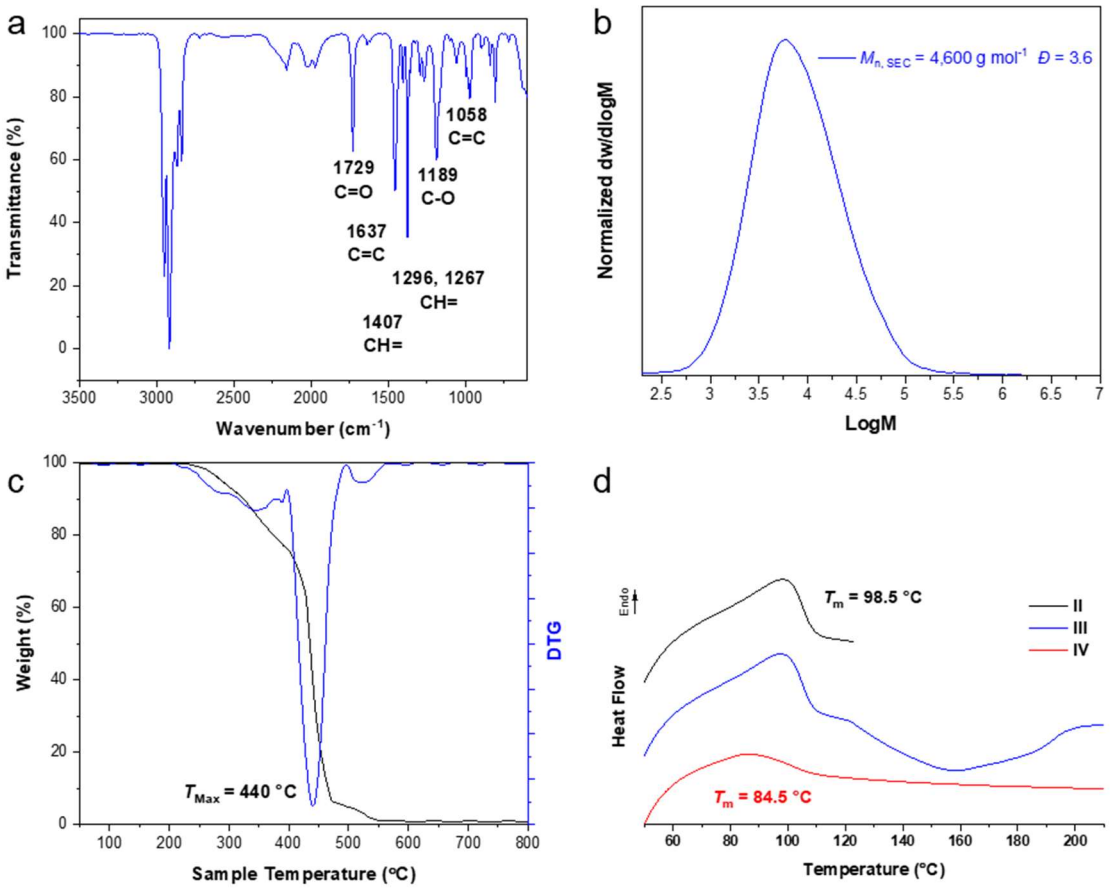

Figure A1.57 (a) FT-IR spectrum (b) SEC trace (c) TGA thermograph and (d) DSC 2nd, 3rd, and 4th heating curve of **PP_{AA}**.

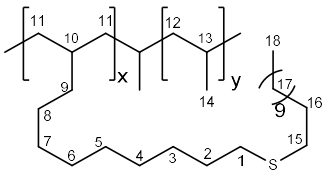

Synthesis of 1-dodecanethiol modified PP_{Br}, PP_S. DBU (50 equiv.) were added to a THF (5 ml) solution of 1-dodecanethiol (50 equiv.) and **PP_{Br}** (0.5 g) in an ampoule before being heated and stirred at 77 °C for 24 h. The final polymer was precipitated in acidified methanol (2wt% HCl) before being collected by filtration on a glass sintered frit (porosity 3), washed with methanol, then acetone, and dried in vacuo at 60 °C to a constant weight. **PP_S** (3.99 mol%). **^{1}H NMR (600 MHz, $C_2D_2Cl_4$, 393 K)**: 2.59 (4H, t, $^3J_{HH}$ = 7.2 Hz, H^1 and H^{15}), 1.75-1.58 (27H, br m, H^2, H^{13}, and H^{16}), 1.55-1.46 (8H, br m, H^3 and H^a), 1.46-1.06 (66H, br m, H^a and $H^{12\ (anti)}$), 1.05-0.84 ppm (87H, br m, H^{18}, H^{14} and $H^{12\ (syn)}$). **^{13}C{^{1}H} NMR (151 MHz, $C_2D_2Cl_4$, 393 K):** 120.54, 99.90, 46.21 (C^{13}), 43.63 (2C, s, C^a), 35.87 (1C, s, C^a), 33.58 (1C, s, C^a), 32.68 (2C, s, C^1 and C^{15}), 31.91 (1C, s, C^a), 30.30-29.98 (4C, m, C^a), 29.78-29.42 (8C, m, C^a, C^2 and C^{16}), 29.4-29.12 (4C, m, C^a), 29.02 (2C, s, C^3 and C^a), 28.58 (C^{12}), 26.83 (1C, s, C^a), 22.60 (2C, s, C^a), 21.64 (C^{14}), 13.92 (1C, s, C^{18}). *a*Peaks corresponding to unassigned CH_2. **FTIR**: ν (cm^{-1}) = 2950, 2867, and 1456 (ν (C-H, CH_3)), 2917, 2838, and 1377 (ν (C-H, CH_2)).

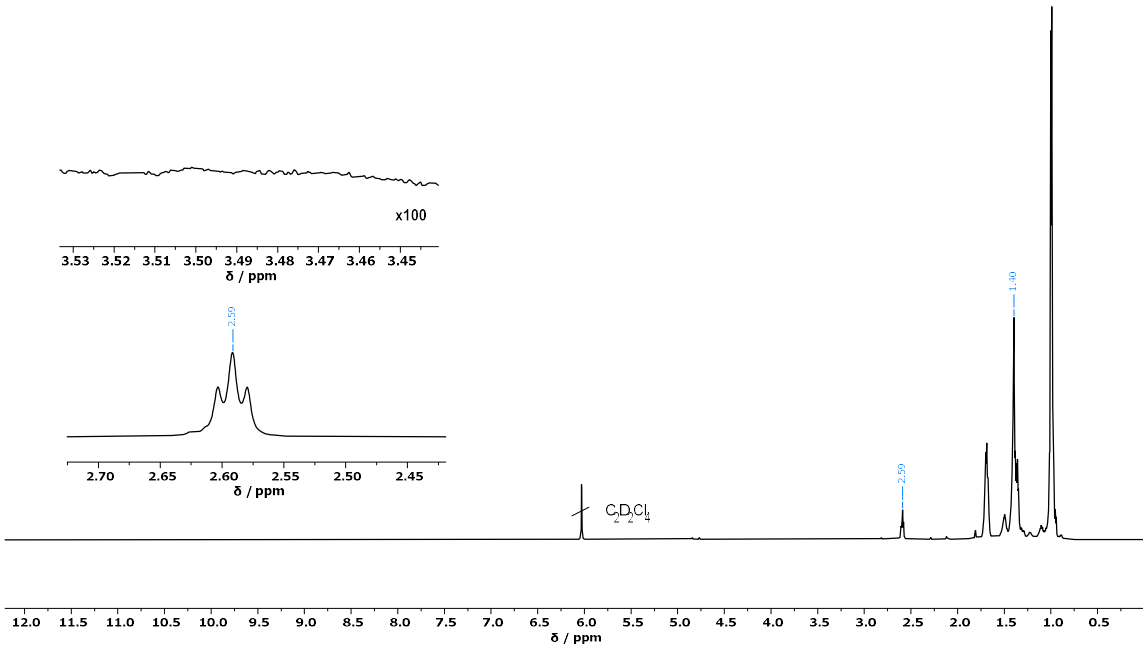

Figure A1.58 PPs ^{1}H NMR (600 MHz, $C_2D_2Cl_4$, 393 K).

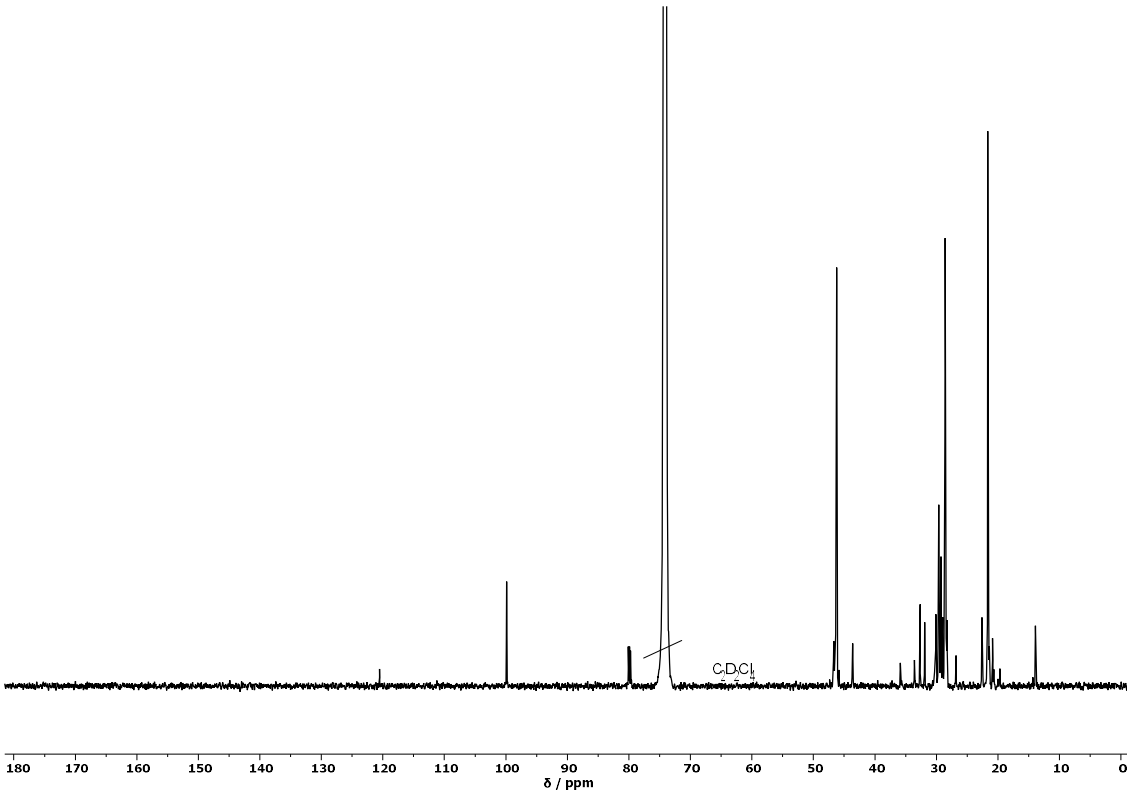

Figure A1.59 PPs ^{13}C{^{1}H} NMR (151 MHz, $C_2D_2Cl_4$, 393 K), full spectrum.

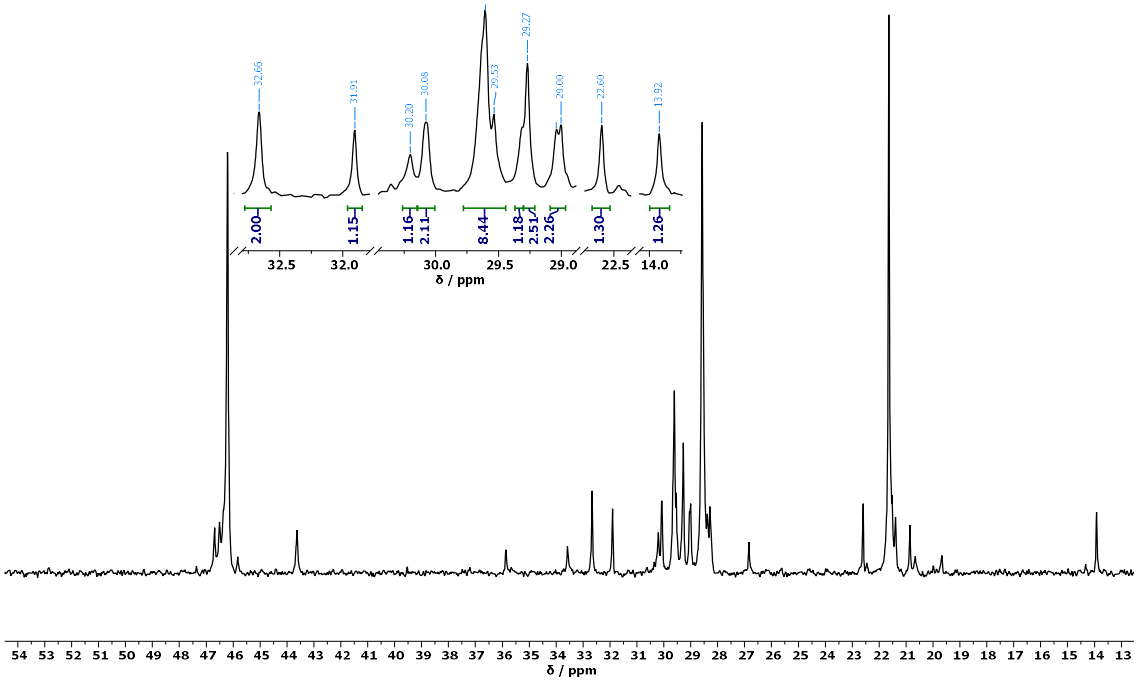

Figure A1.60 PPs $^{13}C\{^{1}H\}$ NMR (151 MHz, $C_2D_2Cl_4$, 393 K), expanded comonomer region.

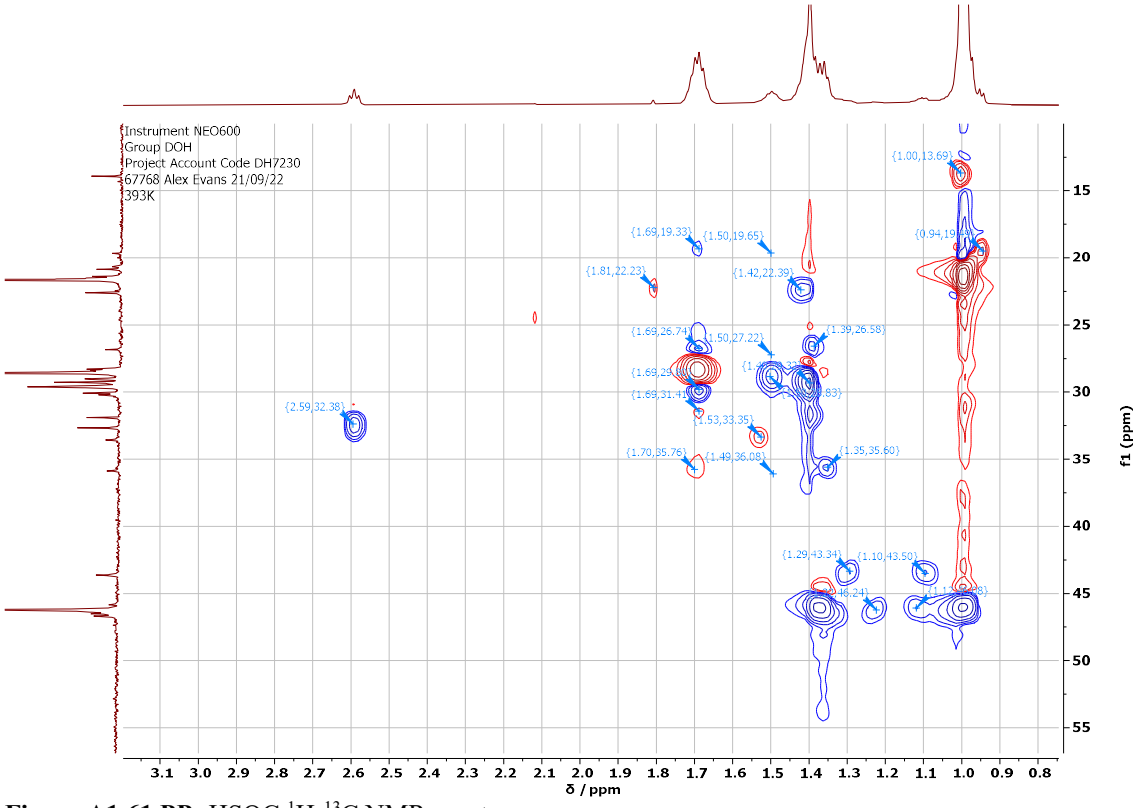

Figure A1.61 PPs HSQC ^{1}H-^{13}C NMR spectrum.

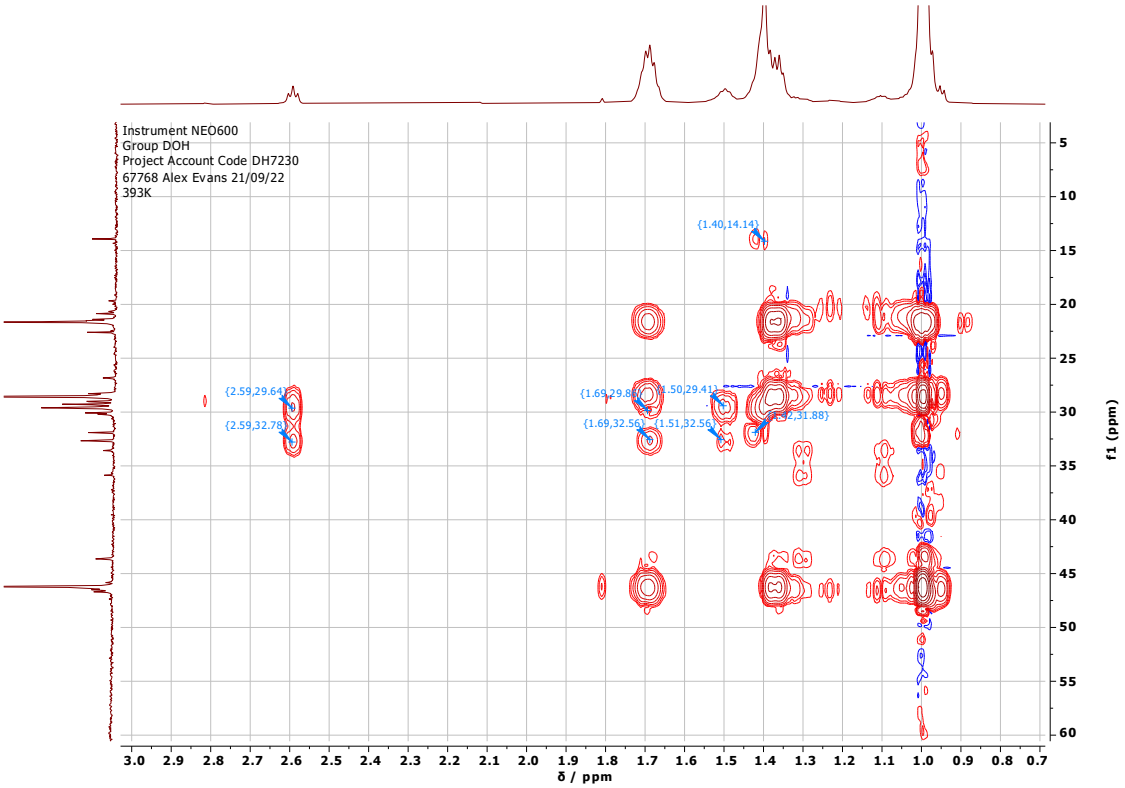

Figure A1.62 PP_S HMBC ^{1}H-^{13}C NMR spectrum.

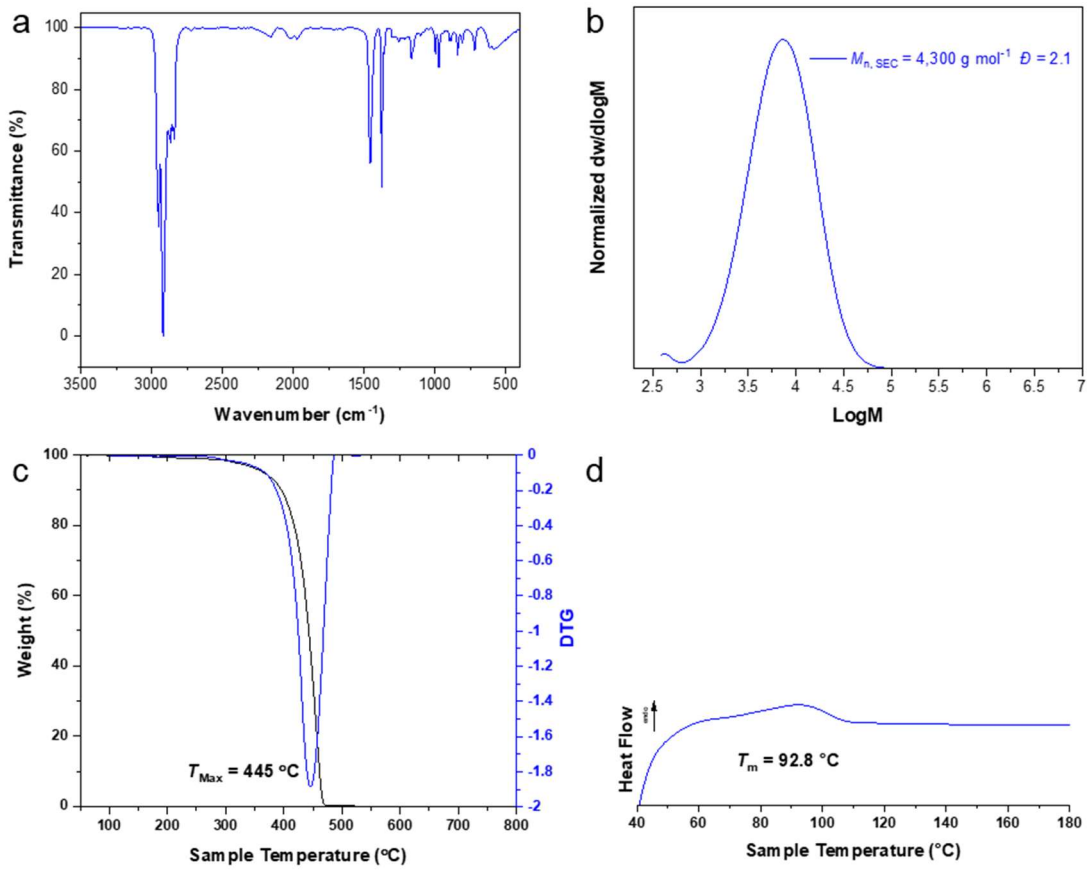

Figure A1.63 (a) FT-IR spectrum (b) SEC trace (c) TGA thermograph and (d) DSC 2nd heating curve of **PPS**.

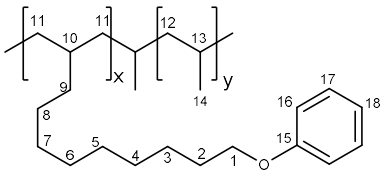

Synthesis of potassium phenoxide (KOPh) modified PP_{Br}, PP_{OPh}. KOPh (2 equiv.) were added under an inert atmosphere to a THF (4 ml) solution of **PP_{Br}** (0.2 g) in an ampoule before being heated and stirred at 77 °C for 24 h. The final polymer was precipitated in acidified methanol (2wt% HCl) before being collected by filtration on a glass sintered frit (porosity 3), washed with methanol, then acetone, and dried in vacuo at 60 °C to a constant weight. **PP_{OPh}** (3.99 mol%). **^{1}H NMR (600 MHz, $C_2D_2Cl_4$, 393 K)**: 7.33 (2H, t, $^3J_{HH}$ = 7.4 Hz, H^{17}), 6.99 (3H, m, H^{16} and H^{18}), 4.06 (2H, t, $^3J_{HH}$ = 6.3 Hz, H^1), 1.86 (2H, m, H^2), 1.75-1.58 (br m, H^{13}), 1.58-1.06 (50H, br m, H^a and H^{12} (*anti*)), 1.05-0.84 ppm (88H, br m, H^{14} and H^{12} (*syn*)). **$^{13}C\{^1H\}$ NMR (151 MHz, $C_2D_2Cl_4$, 393 K):** 159.62 (1C, s, C^{15}), 129.40 (2C, s, C^{17}), 120.70 (2C, s, C^{16}), 115.31 (2C, s, C^{18}), 159.62, 129.40, 120.74, 115.31, 99.89, 68.59 (1C, s, C^1), 46.21 (C^{13}), 43.63 (1C, s, C^a), 35.85 (1C, s, C^a), 33.57 (1C, s, C^a), 30.19 (1C, s, C^a), 29.62 (2C, s, C^a), 29.54 (1C, s, C^a), 29.44 (1C, s, C^a), 29.62 (C^2), 28.58 (C^{12}), 26.82 (1C, s, C^a), 26.18 (1C, s, C^3), 21.64 (C^{14}). *a*Peaks corresponding to unassigned CH_2. **FTIR**: ν (cm^{-1}) = 2950, 2867, and 1456 (ν (C-H, CH_3)), 2917, 2838, and 1377 (ν (C-H, CH_2)), 1601 and 1497 (ν (C=C)), 1244 (ν (C_{Al}-O)), 1080 (ν (C_{Ar}-O)), and 752 (ν (C=C_{Ar})), and 690 (ν (C-H_{Ar})).

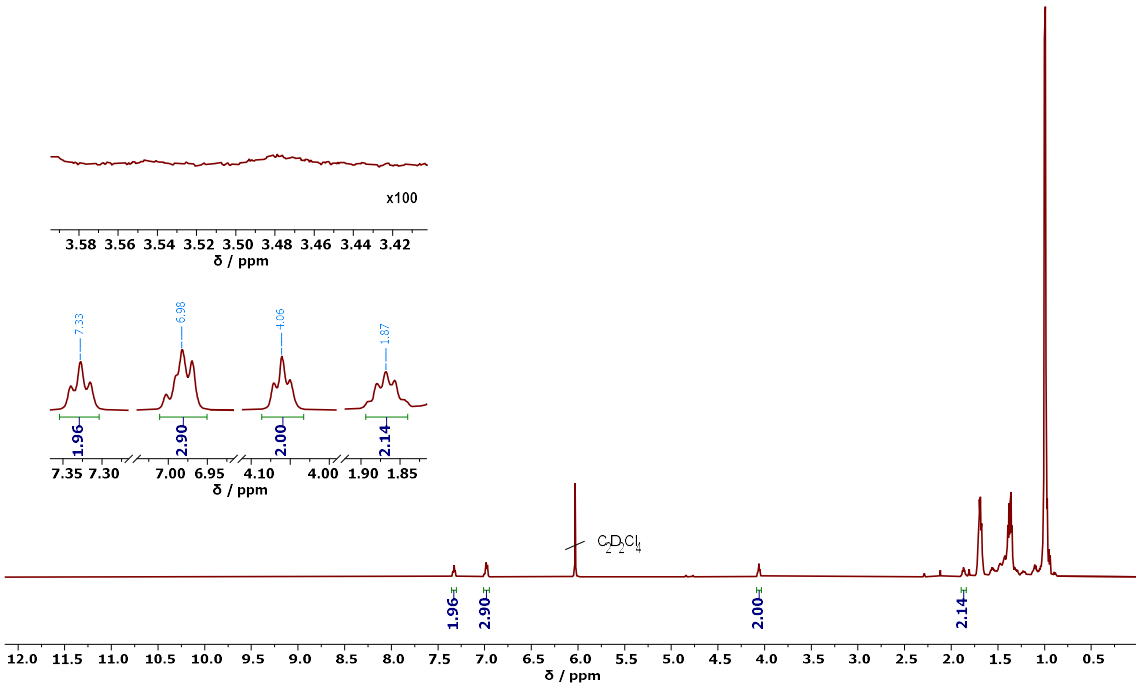

Figure A1.64 PP$_{OPh}$ ^{1}H NMR (600 MHz, $C_2D_2Cl_4$, 393 K).

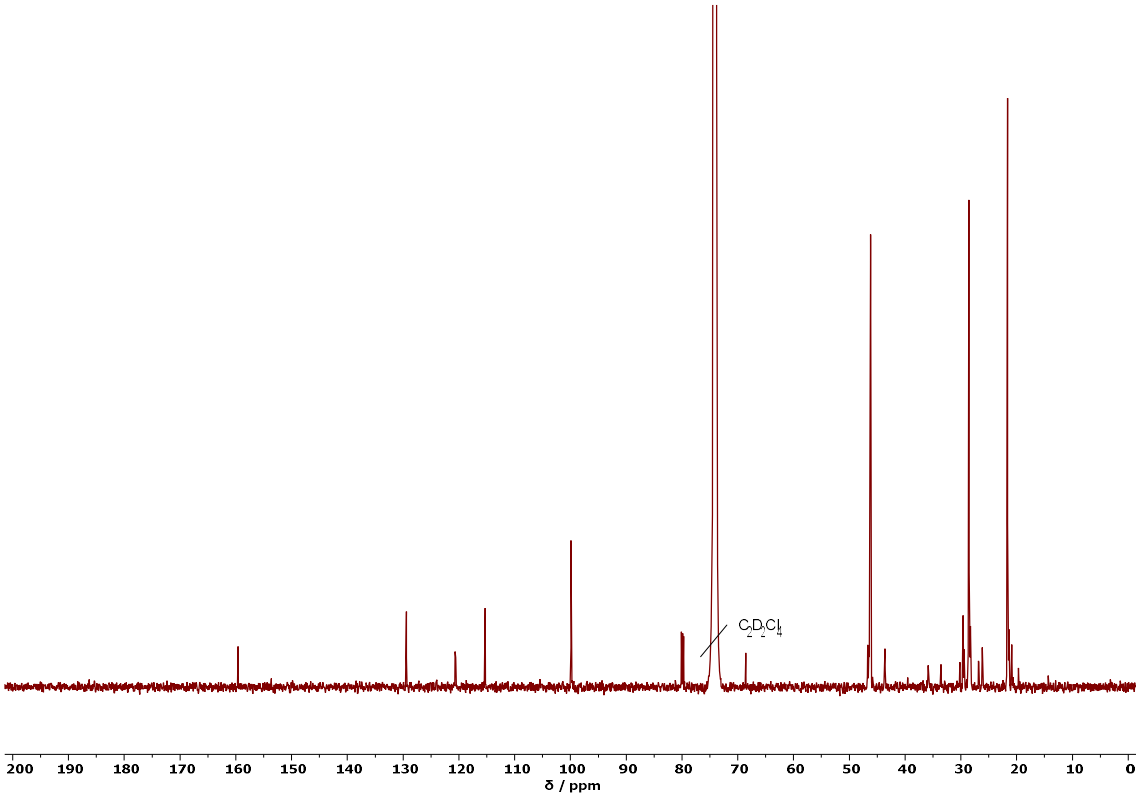

Figure A1.65 PP$_{OPh}$ $^{13}C\{^{1}H\}$ NMR (151 MHz, $C_2D_2Cl_4$, 393 K), full spectrum.

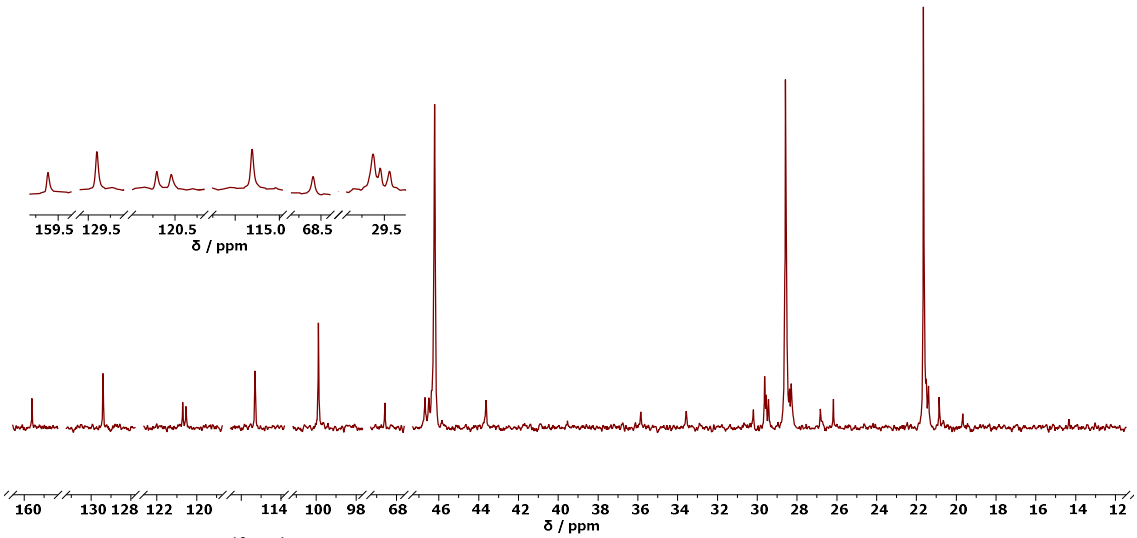

Figure A1.66 PP$_{OPh}$ $^{13}C\{^{1}H\}$ NMR (151 MHz, $C_2D_2Cl_4$, 393 K), expanded comonomer region.

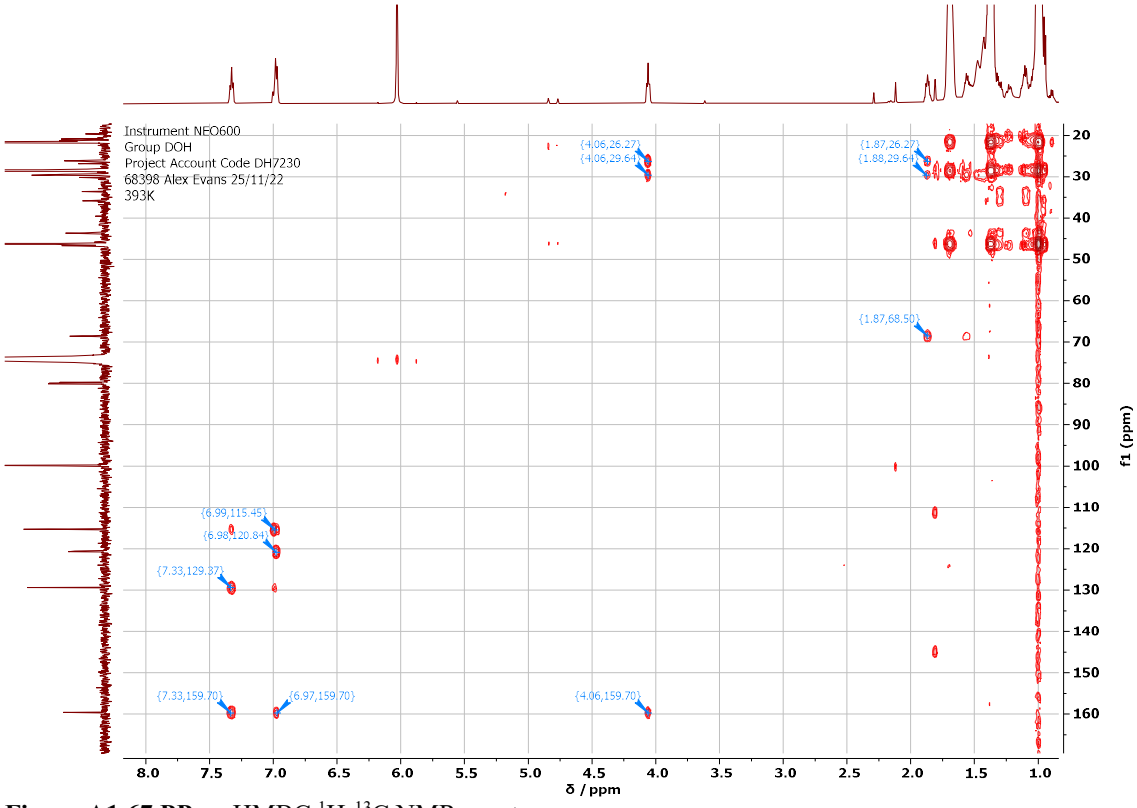

Figure A1.67 PP$_{OPh}$ HMBC ^{1}H-^{13}C NMR spectrum.

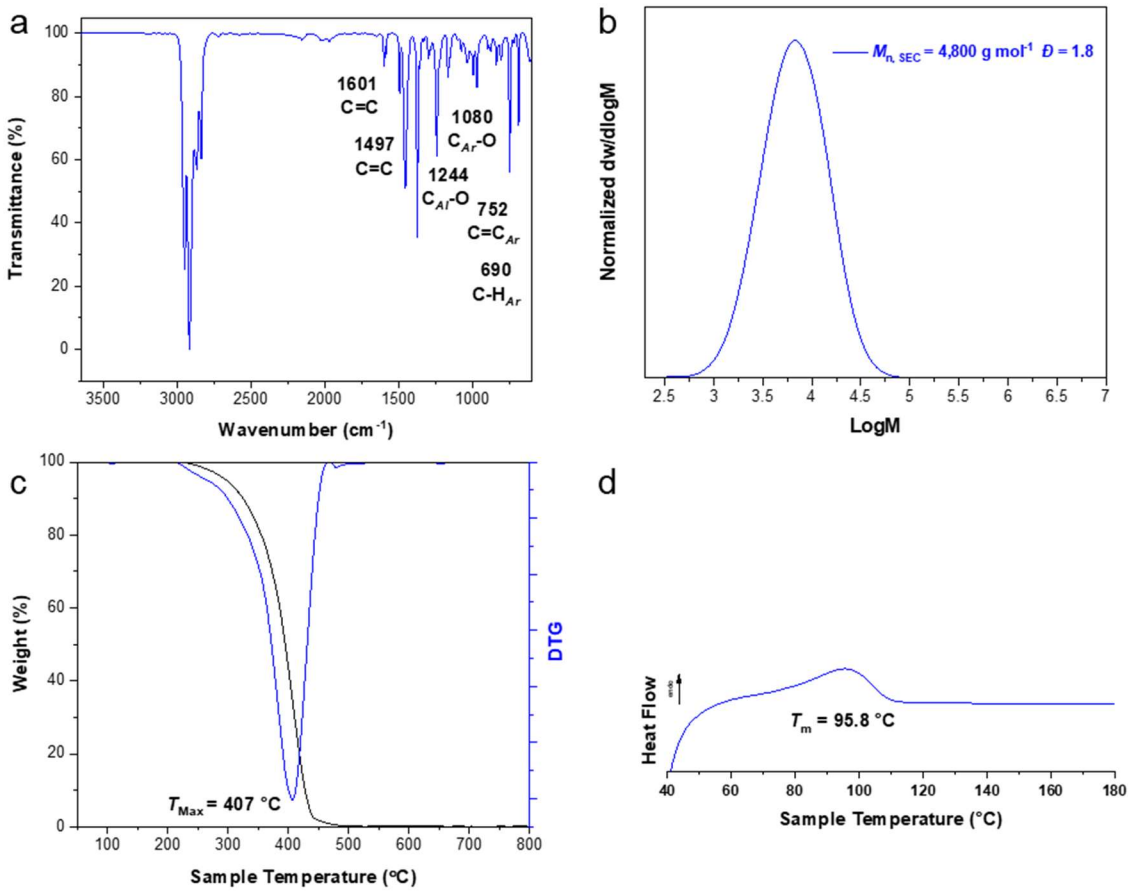

Figure A1.68 (a) FT-IR spectrum (b) SEC trace (c) TGA thermograph and (d) DSC 2nd heating curve of **PP$_{OPh}$.**

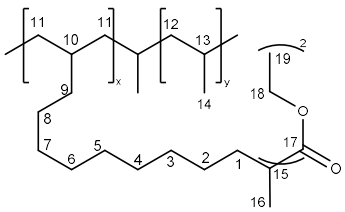

Synthesis of potassium 1,3-diethoxy-2-methyl-1,3-dioxopropan-2-ide (KDEMM) modified PP$_{Br}$, PP$_{M}$. KDEMM (2 equiv.) was added under an inert atmosphere to a THF (4 ml) solution of **PP$_{Br}$** (0.2 g) in an ampoule before being heated and stirred at 77 °C for 24 h. The final polymer was precipitated in acidified methanol (2wt% HCl) before being collected by filtration on a glass sintered frit (porosity 3), washed with methanol, then acetone, and dried in vacuo at 60 °C to a constant weight. **PP$_{M}$** (3.99 mol%). **^{1}H NMR (600 MHz, C$_2$D$_2$Cl$_4$, 393 K)**: 4.26 (4H, q, $^{3}J_{HH}$ = 7.0 Hz, H^{18}), 1.94 (2H, m, H^{1}), 1.75-1.58 (22H, br m, H^{13}), 1.58-1.29 (63H, br m, H^{a}, H^{2}, H^{19}, and H^{12} (*anti*)), 1.05-0.84 ppm (83H, br m, H^{14} and H^{12} (*syn*)). **^{13}C{^{1}H} NMR (151 MHz, C$_2$D$_2$Cl$_4$, 393 K):** 172.31 (2C, s, C^{17}), 120.54, 99.89, 60.93 (2C, s, C^{18}), 54,14

(1C, s, C^{15}), 46.21 (C^{13}), 43.63 (1C, s, C^{a}), 35.93 (1C, s, C^{1}), 30.23 (1C, s, C^{a}), 30.03 (1C, s, C^{a}), 29.67 (1C, s, C^{a}), 29.63 (1C, s, C^{a}), 29.42 (1C, s, C^{a}), 28.58 (C^{12}), 26.58 (1C, s, C^{2}), 24.45 (1C, s, C^{a}), 21.64 (C^{14}), 20.05 (1C, s, C^{16}), 14.06 (2C, s, C^{19}). [a]Peaks corresponding to unassigned CH_2. **FTIR**: ν (cm^{-1}) = 2950, 2867, and 1456 (ν (C-H, CH_3)), 2917, 2838, and 1377 (ν (C-H, CH_2)), 1736 (ν (C=O)), 1253 and 1115 (ν (C-O)).

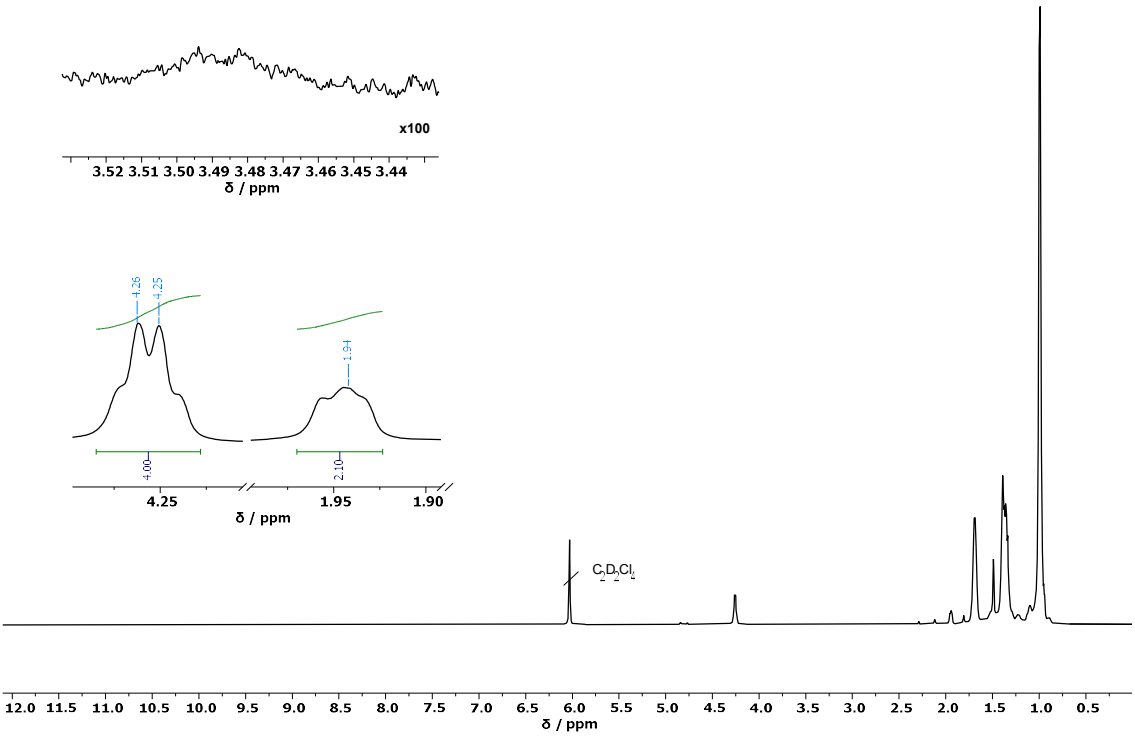

Figure A1.69 PP_M ^{1}H NMR (600 MHz, $C_2D_2Cl_4$, 393 K).

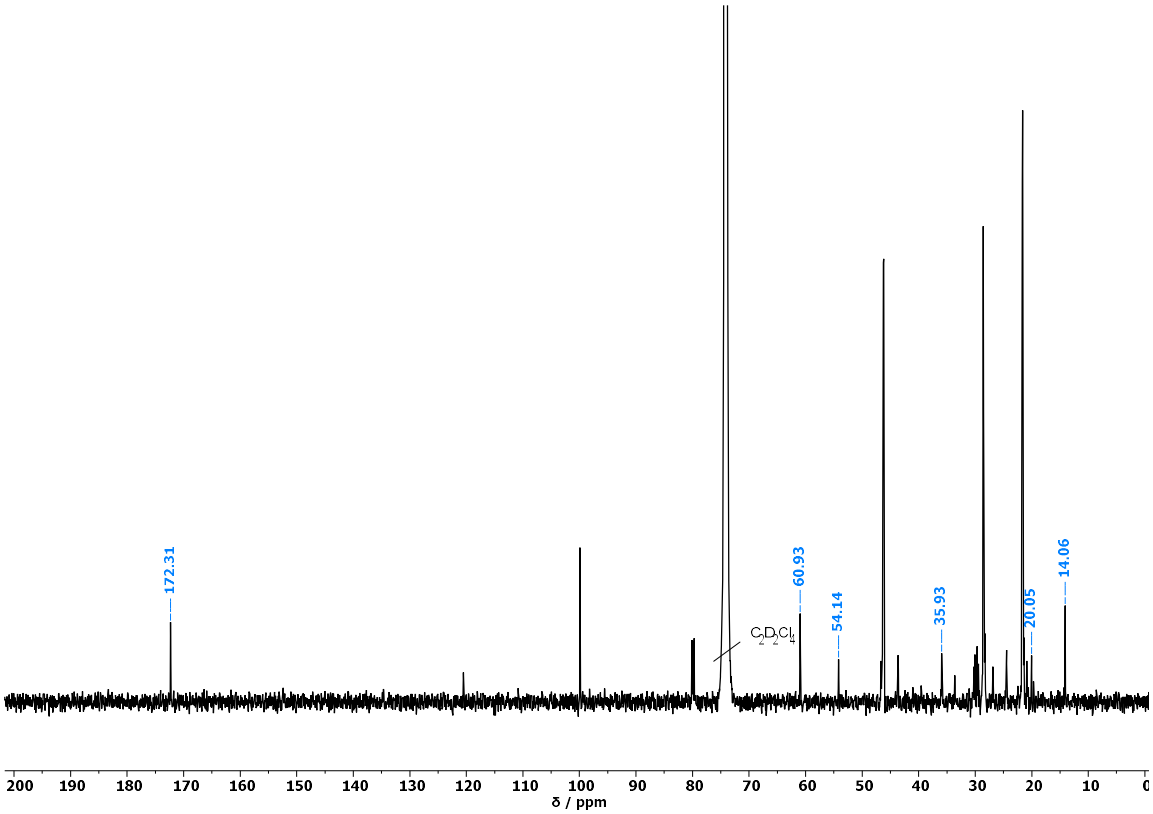

Figure A1.70 PP$_M$ $^{13}C\{^1H\}$ NMR (151 MHz, $C_2D_2Cl_4$, 393 K), full spectrum.

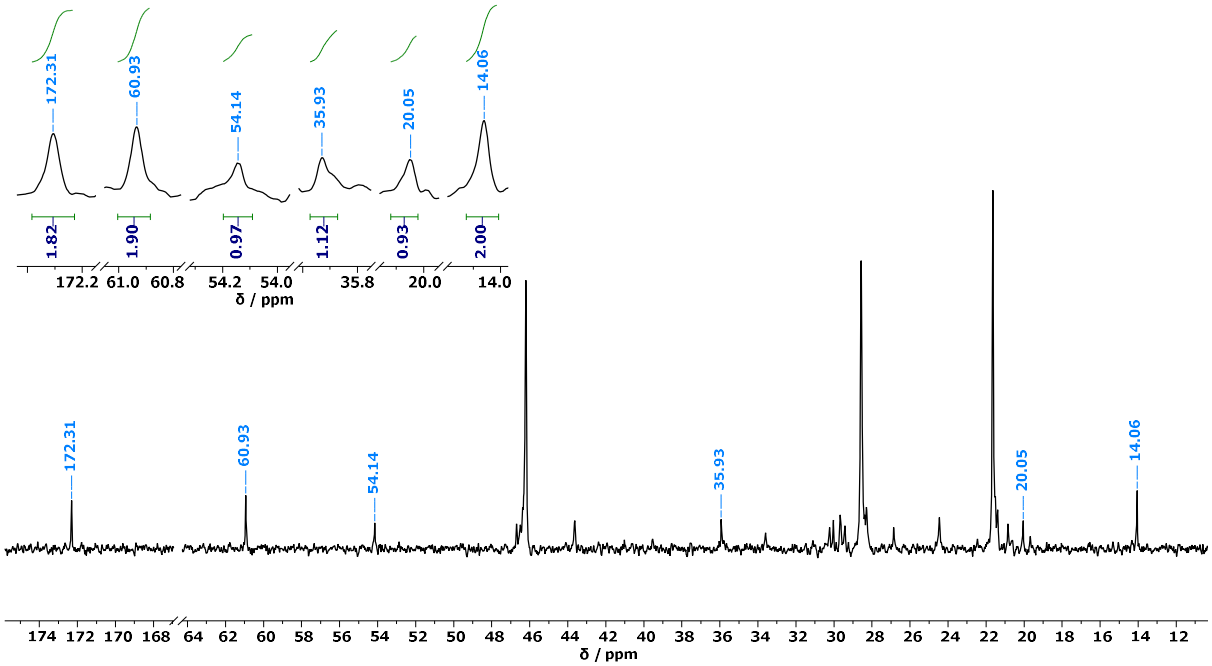

Figure A1.71 PP$_M$ $^{13}C\{^1H\}$ NMR (151 MHz, $C_2D_2Cl_4$, 393 K), expanded comonomer region.

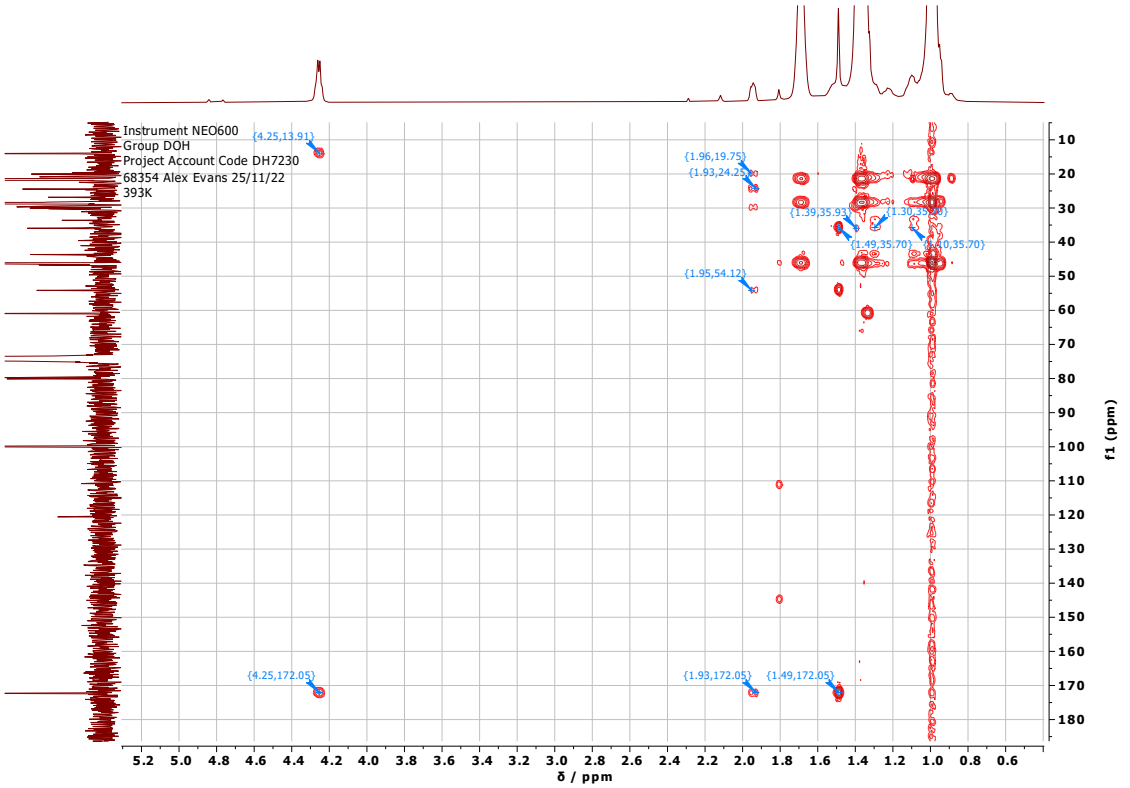

Figure A1.72 PP$_M$ HMBC ^{1}H-^{13}C NMR spectrum.

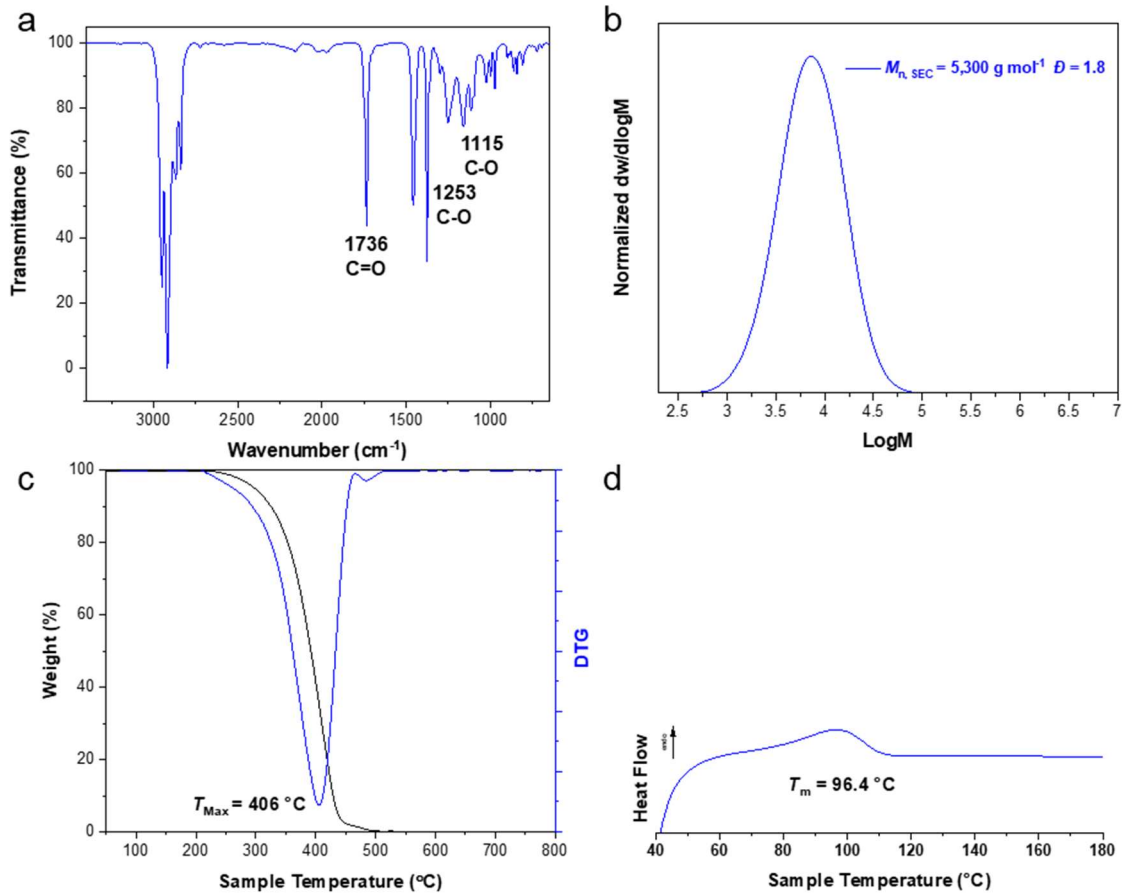

Figure A1.73 (a) FT-IR spectrum (b) SEC trace (c) TGA thermograph and (d) DSC 2nd heating curve of **PP$_M$**.

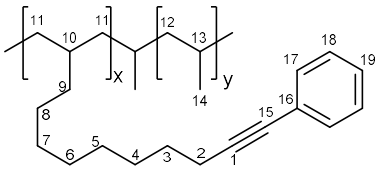

Synthesis of lithium phenylacetylide (LiPA) modified PP_{Br}, PP_{PA}. LiPA (2 equiv.) was added under an inert atmosphere to a THF (4 ml) solution of $\mathbf{PP_{Br}}$ (0.2 g) in an ampoule before being heated and stirred at 77 °C for 24 h. The final polymer was precipitated in acidified methanol (2wt% HCl) before being collected by filtration on a glass sintered frit (porosity 3), washed with methanol, then acetone, and dried in vacuo at 60 °C to a constant weight. $\mathbf{PP_{PA}}$ (3.99 mol%). **^{1}H NMR (600 MHz, $C_2D_2Cl_4$, 393 K)**: 7.47 (2H, d, $^3J_{HH}$ = 6.5 Hz, H^{17}), 7.32 (3H, m, H^{18} and H^{19}), 2.49 (2H, t, $^3J_{HH}$ = 6.8 Hz, H^2), 1.75-1.63 (24H, br m, H^3 and H^{13}), 1.63-1.05 (57H br m, H^a, and $H^{12\ (anti)}$), 1.05-0.84 (89H, br m, H^{14} and $H^{12\ (syn)}$). **^{13}C{^{1}H} NMR (151 MHz, $C_2D_2Cl_4$, 393 K):** 131.72 (2C, s, C^{17}), 128.15 (2C, s, C^{18}), 127.37 (1C, s, C^{19}), 124.69 (1C, s, C^{16}), 90.83 (1C, s, C^1), 80.96 (1C, s, C^{15}), 46.21 (C^{13}), 33.57 (1C, s, C^a), 30.20 (1C, s, C^a), 29.67 (1C, s, C^a), 29.59 (1C, s, C^a), 29.20 (1C, s, C^a), 29.02 (1C, s, C^a), 29.01 (1C, s, C^a), 28.58 (C^{12}), 26.83 (1C, s, C^a), 21.64 (C^{14}), 19.55 (1C, s, C^2). *a*Peaks corresponding to unassigned CH_2.**FTIR**: ν (cm^{-1}) = 2950, 2867, and 1456 (ν (C-H, CH_3)), 2917, 2838, and 1377 (ν (C-H, CH_2)), 1598 and 1491 (ν (C=C)), 754 (ν (C=C_{Ar})), and 690 (ν (C-H_{Ar})).

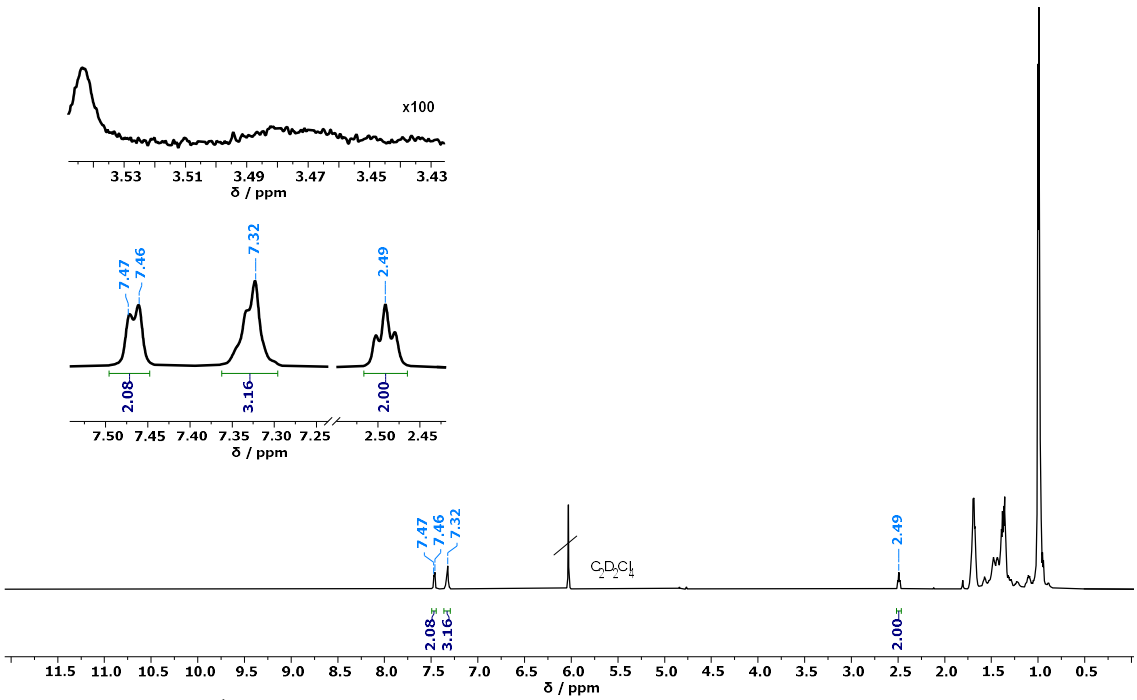

Figure A1.74 PP$_{PA}$ ^{1}H NMR (600 MHz, $C_2D_2Cl_4$, 393 K).

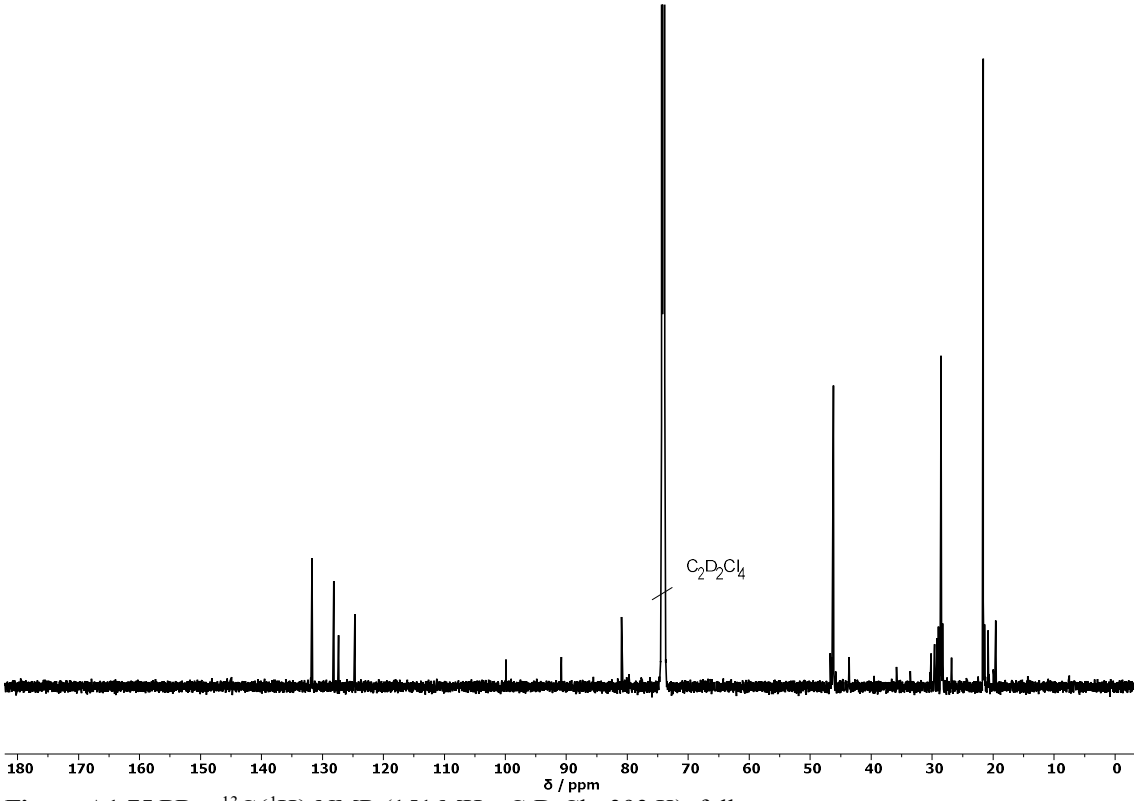

Figure A1.75 PP$_{PA}$ $^{13}C\{^{1}H\}$ NMR (151 MHz, $C_2D_2Cl_4$, 393 K), full spectrum.

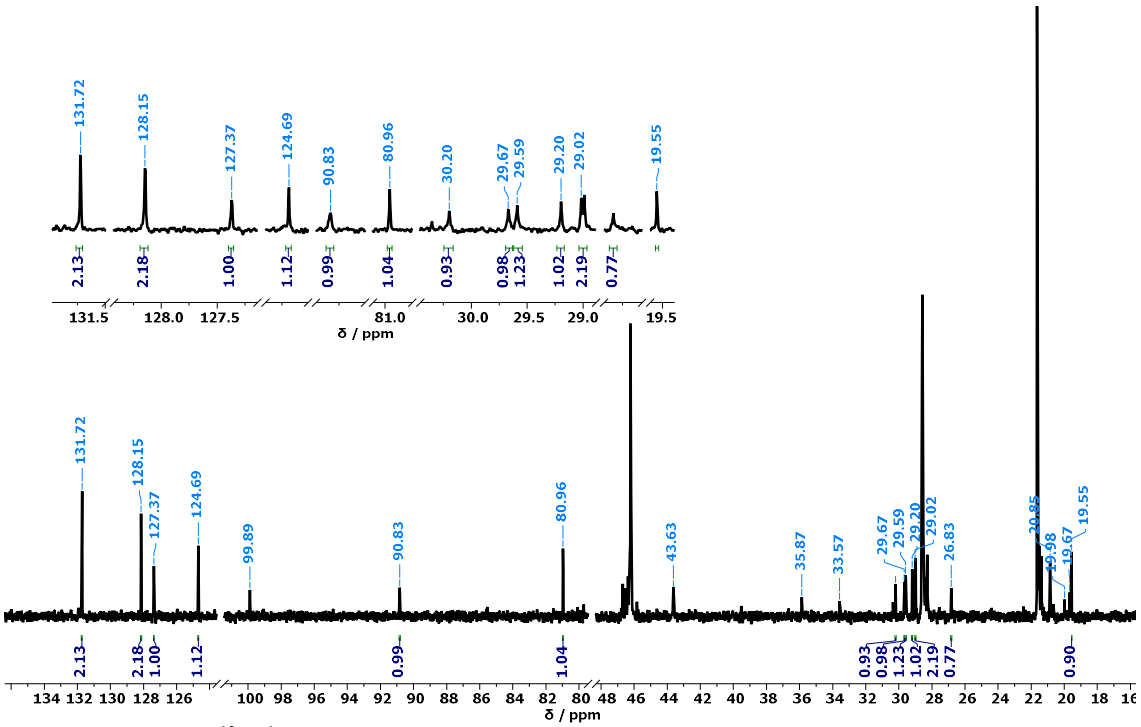

Figure A1.76 PP$_{PA}$ $^{13}C\{^{1}H\}$ NMR (151 MHz, $C_2D_2Cl_4$, 393 K), expanded comonomer region.

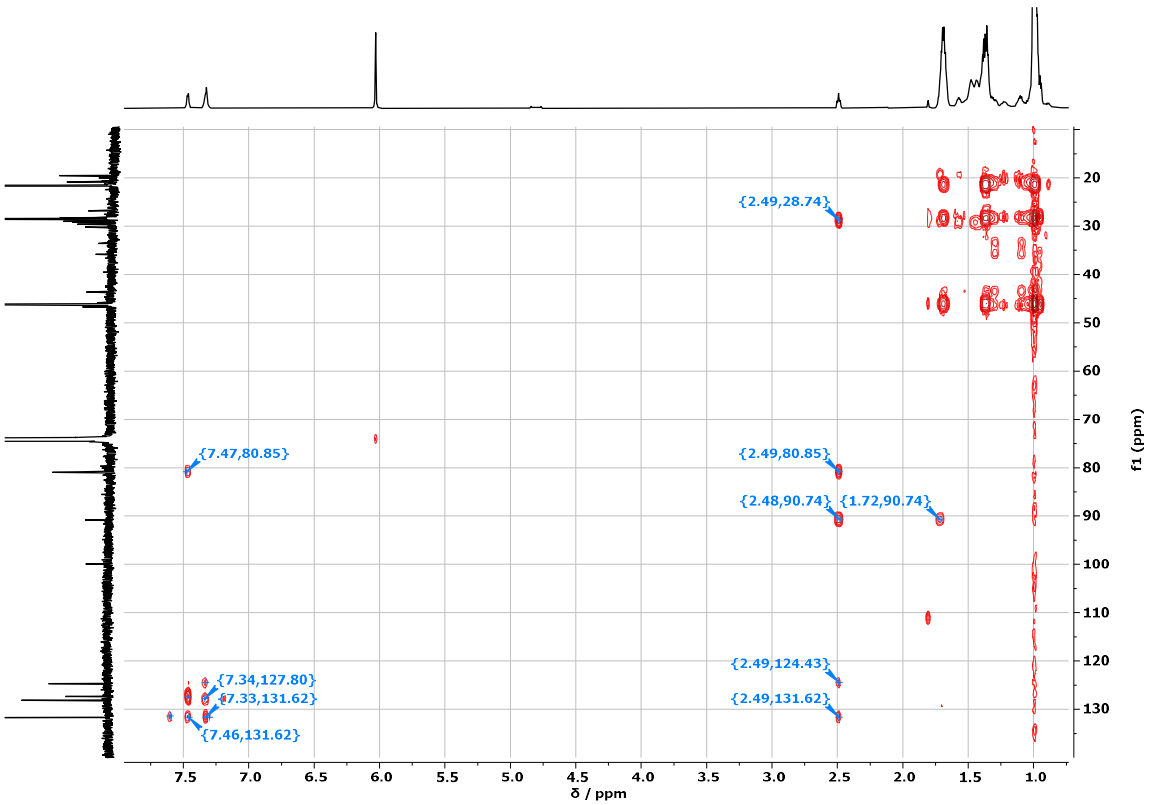

Figure A1.77 PP$_{PA}$ HMBC ^{1}H-^{13}C NMR spectrum.

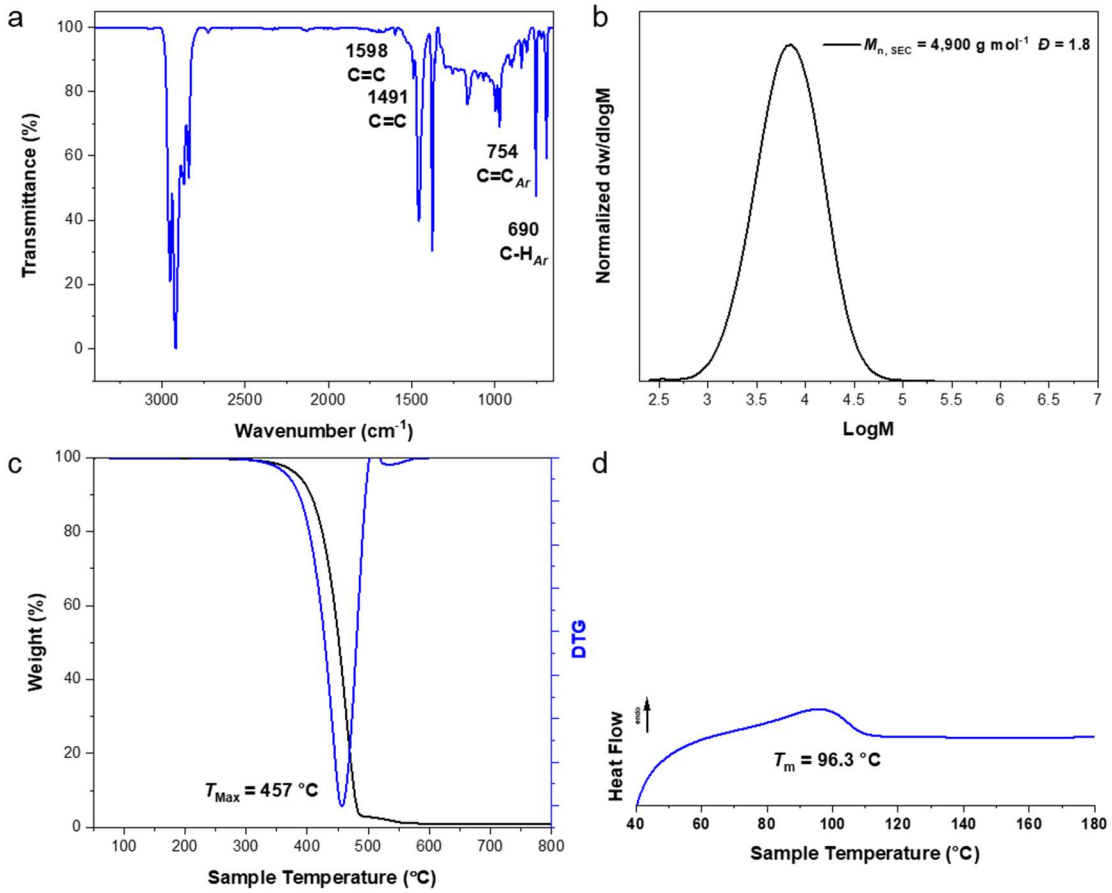

Figure A1.78 (a) FT-IR spectrum (b) SEC trace (c) TGA thermograph and (d) DSC 2nd heating curve of **PP$_{PA}$**.

Table A1.1. Characterisation of post-modified polymers based on **PP$_{Br}$** (3.99 mol%), ^{i}**PP$_{Br}$** (2.42 mol%), and ^{s}**PP$_{Br}$** (1.88 mol%).

Polymer	Conv.[a]	Isolated Yield (%)	$M_{n,\,th}$ [b] (g mol^{-1})	$M_{n,\,SEC}$[c] (g mol^{-1})	$Đ_m$[c]	T_m[d] (°C)	Crystallinity[d] (%)	T_{max}[e] (°C)	Contact angle (°)	σ
PP				6 100	2.20	114.0	44	393	94	
PP$_{Br}$	>99%			3 900	1.97	90.5	27	448	91	3
PP$_{PPr}$	>99%	90	4 200	2 000	1.96	89.2	27	485	82	2
PP$_{PPh}$	>99%	86	4 400	4 400	1.70	94.5	32	487	90	2
PP$_{DEA}$	>99%	96	3 900	800	1.91	91.5	22	465	91	1
PP$_{DEOA}$	>99%	85	4 000	1 000	1.85	98.4	32	446	93	1
PP$_{Ac}$	>99%	90	3 800	3 100	2.18	93.2	20	421	95	1
PP$_{Bn}$	>99%	95	4 100	4 600	1.82	95.1	26	378	84	4
PP$_{AA}$	>99%	85	3 900	4 600	3.59	98.5	31	440	97	2
PP$_{OPh}$	>99%	96	4 000	4 800	1.81	95.8	27	407	90	2
PP$_{S}$	>99%	92	4 400	4 300	2.10	92.8	26	445	94	1
PP$_{M}$	>99%	87	4 300	5 300	1.77	96.4	22	406	85	1
PP$_{EAE}$	>99%	94	3 900	800	2.29	93.1	31	414	90	2
PP$_{PA}$	>99%	97	4 000	4 900	1.83	96.3	28	457	93	2
^{s}**PP$_{Br}$**	>99%			107 900	2.18	100.8	18	410	102	1
^{s}**PP$_{DEA}$**	>99%	92	107 900	N/D		97.9	10	428	87	1
^{s}**PP$_{PPr}$**	>99%	97	108 100	110 800	2.23	101.9	17	447	88	2
^{s}**PP$_{Bn}$**	>99%	98	108 000	19 600	7.53	97.9	12	388	87	1
^{s}**PP$_{OPh}$**	>99%	90	107 900	85 800	2.31	102.8	16	392	95	2
^{s}**PP$_{M}$**	>99%	98	108 100	93 000	2.67	100.5	11	380	89	1
^{i}**PP$_{Br}$**	>99%			87 500	2.74	132.0	64	407	105	5
^{i}**PP$_{DEA}$**	>99%	89	87 500	N/D		131.5	60	423	83	4
^{i}**PP$_{PPr}$**	>99%	86	87 700	9 500	11.79	133.4	57	454	93	1
^{i}**PP$_{Bn}$**	>99%	82	87 600	26 600	7.15	133.4	61	353	87	2
^{i}**PP$_{OPh}$**	>99%	94	87 500	80 900	3.05	132.5	64	380	95	1
^{i}**PP$_{M}$**	>99%	87	87 700	92 700	3.02	133.4	59	352	87	1

[a]Determined by ^{1}H NMR. [b]Calculated: PP_X ($M_{w,\,SEC}$–(mol%×79.9)+(mol%×X (g mol^{-1}))). [c]Determined by SEC. [d]Determined by DSC. [e]Determined by TGA.

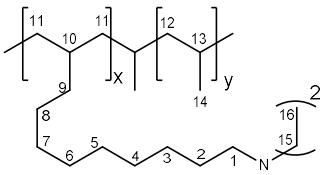

Synthesis of DEA modified ^{i}PP$_{Br}$ and ^{s}PP$_{Br}$, ^{i}PP$_{DEA}$ and ^{s}PP$_{DEA}$. DEA, (50 equiv.) and **PP$_{Br}$** (200 mg) were added to an ampoule. The reaction mixture was heated at 150 °C and agitated for 48 hrs. The final polymer was precipitated in acidified methanol (2wt% HCl) before being collected by filtration on a glass sintered frit (porosity 3), washed with methanol, then acetone, and dried *in vacuo* at 60 °C to a constant weight. Polymer isolated: 178 mg ^{i}**PP$_{DEA}$** (2.42 mol%) and 183 mg ^{s}**PP$_{DEA}$** (1.88 mol%). ^{i}**PP$_{DEA}$: ^{1}H NMR (600 MHz, C$_2$D$_2$Cl$_4$, 393 K)**: δ 3.13 (4H, br s, H^{15})^{b}, 3.00 (2H, br s, H^{1})^{b}, 2.30, 2.13, 1.91 (2H, br s, H^{2})^{b}, 1.75-1.63 (48.5H, br m, H^{13}), 1.63-1.23 (93H, br m, H^{3}, H$^{12(anti)}$, H^{16} and H^{a})^{b}, 1.20-0.81 (196H, br m, H$^{12\,(syn)}$, H^{14}). **^{13}C{^{1}H} NMR (151 MHz, C$_2$D$_2$Cl$_4$,**

393 K): δ 123.94, 120.54, 99.89, 51.88 (C^{1}), 47.36 (C^{15}), 47.04 (C^{15}), 46.20 (C^{12}), 43.63, 42.75, 35.92, 29.55, 29.49, 28.56 (C^{13}), 27.21, 23.52 (C^{2}), 21.64 (C^{14}), 8.85 (C^{16}). **FTIR**: *v* (cm^{-1}) = 2951, 2868 and 1456 (*v* (C-H, CH_3)), 2918, 2839 and 1376 (*v* (C-H, CH_2)), 1228 (*v* (C-N)). **^{s}PP$_{DEA}$: ^{1}H NMR (600 MHz, $C_2D_2Cl_4$, 393 K)**: δ 3.13 (4H, br s, H^{15})^{b}, 3.01 (2H, br s, H^{1})^{b}, 2.30, 2.13, 1.91 (2H, br s, H^{2})^{b}, 1.75-1.63 (53H, br m, H^{13}), 1.63-1.26 (64H, br m, H^{3}, H^{16} and H^{a})^{b}, 1.26-1.03 (103H, br m, H^{12} and H^{a}), 1.03-0.82 (155H, br m, H^{14}). **^{13}C{^{1}H} NMR (151 MHz, $C_2D_2Cl_4$, 393 K)**: δ 120.53, 99.88, 51.55 (C^{1}), 47.04 (C^{15}), 46.93 (C^{12}), 28.14 (C^{13}), 23.19 (C^{2}), 20.09 (C^{14}), 8.69 (C^{16}). **FTIR**: *v* (cm^{-1}) = 2956, 2868 and 1462 (*v* (C-H, CH_3)), 2914, 2839 and 1377 (*v* (C-H, CH_2)), 1232 (*v* (C-N)). ^{a}Resonances corresponding to unassigned CH_2. ^{b} Peaks refer to ^{1}H atoms adjacent to the Nitrogen which appear broad, this could be attributed to the effect of the quadrupolar ^{14}N on the relaxation rate.[1]

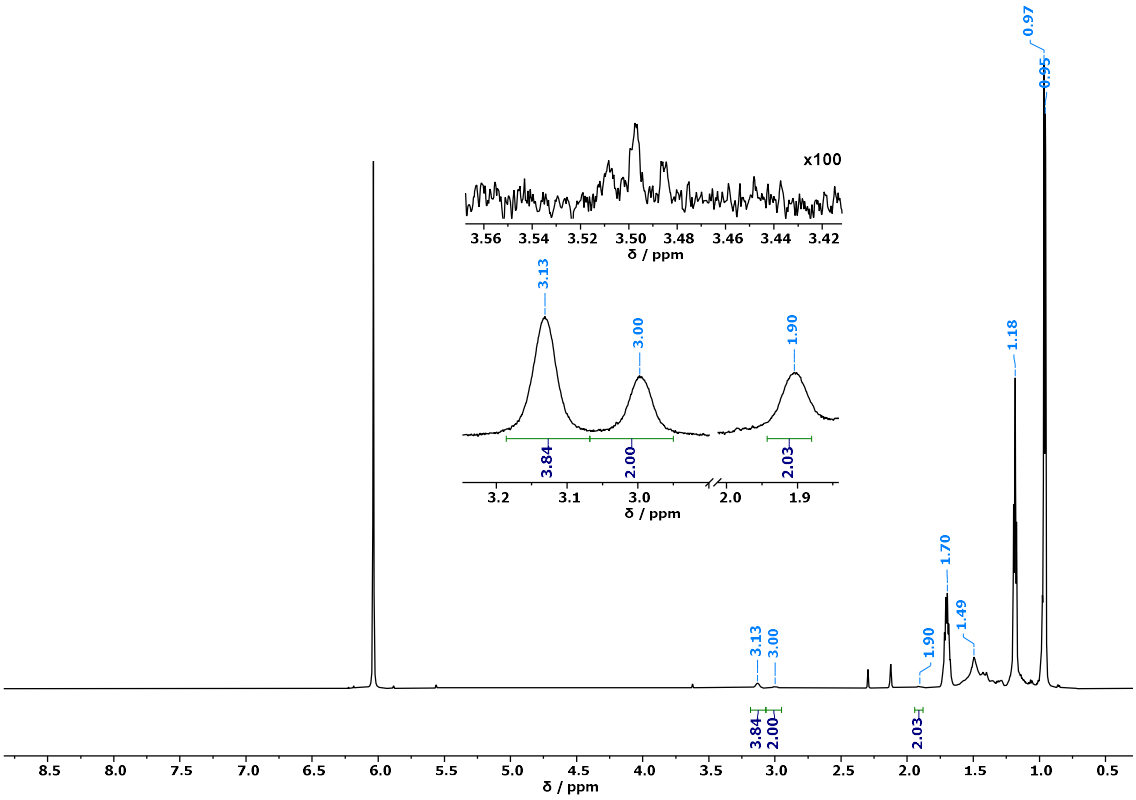

Figure A1.79 ^{s}PP$_{DEA}$ ^{1}H NMR (600 MHz, $C_2D_2Cl_4$, 393 K).

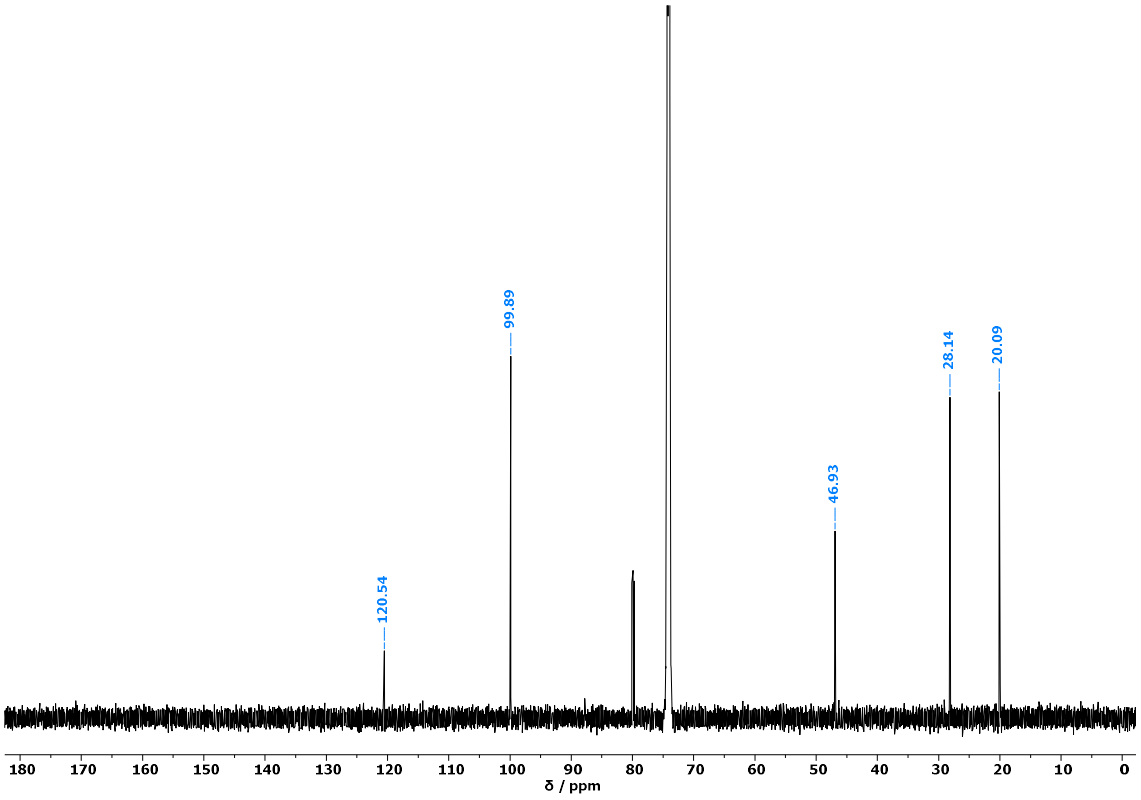

Figure A1.80 ^{s}**PP$_{DEA}$** $^{13}C\{^{1}H\}$ NMR (151 MHz, $C_2D_2Cl_4$, 393 K).



Figure A1.81 ^{s}**PP$_{DEA}$** HSQC ^{1}H-^{13}C NMR spectrum.

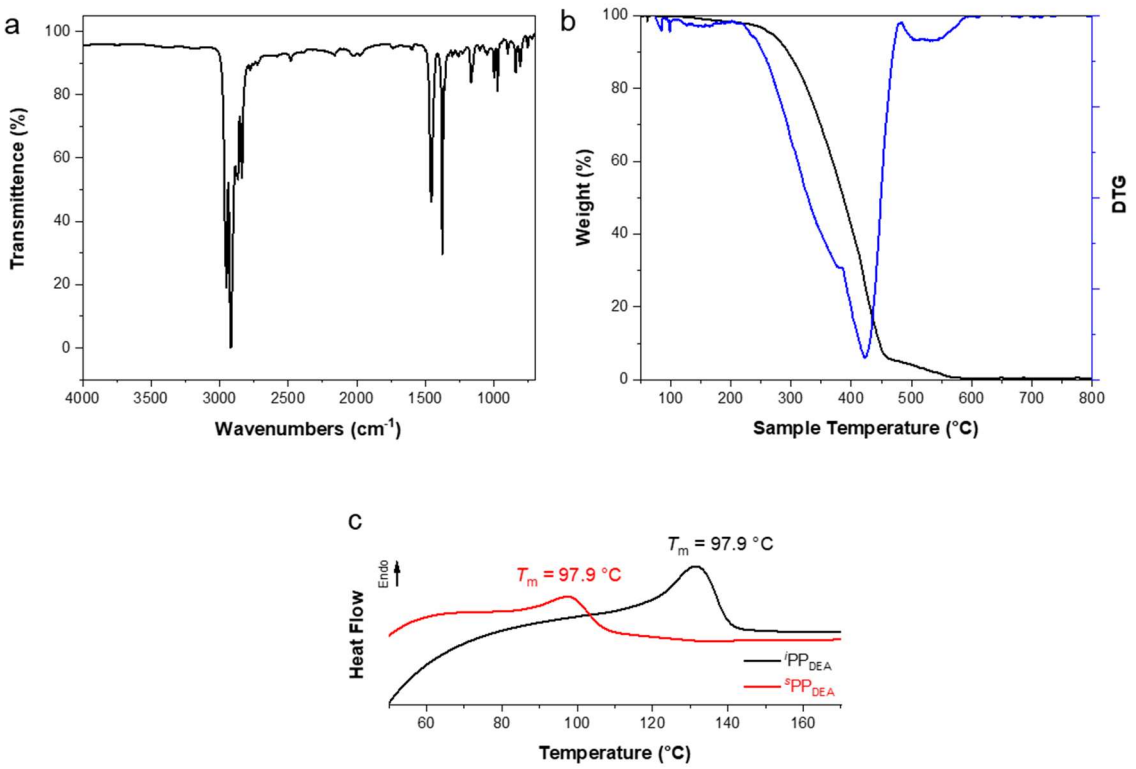

Figure A1.82 (a) FT-IR spectrum and (b) TGA thermograph of $^{i}PP_{DEA}$ and (c) DSC 2nd heating curves of $^{i}\mathbf{PP_{DEA}}$ and $^{s}\mathbf{PP_{DEA}}$.

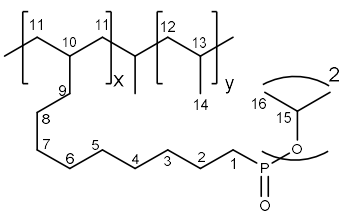

Synthesis of P(O^{i}Pr)$_3$ modified $^{i}\mathbf{PP_{Br}}$ and $^{s}\mathbf{PP_{Br}}$, $^{i}\mathbf{PP_{PPr}}$ and $^{s}\mathbf{PP_{PPr}}$. P(O^{i}Pr)$_3$ (50 equiv.) and **PP$_{Br}$** (200 mg) were added to an ampoule. The reaction mixture was heated at 150 °C and agitated for 96 hrs. The final polymer was precipitated in acidified methanol (2wt% HCl) before being collected by filtration on a glass sintered frit (porosity 3), washed with methanol, then acetone, and dried *in vacuo* at 60 °C to a constant weight. Polymer isolated: 172 mg of $^{i}\mathbf{PP_{PPr}}$ (2.42 mol%) and 193 mg of $^{s}\mathbf{PP_{PPr}}$ (1.88 mol%). **^{i}PP$_{PPr}$: ^{1}H NMR (600 MHz, C$_2$D$_2$Cl$_4$, 393 K)**: δ 4.73 (2H, m, H^{15}), 2.90, 2.12, 1.84-1.63 (66H, br m, H^{1}, H^{13} and H^{a}), 1.63-1.24 (105H, br m, H$^{12\ (anti)}$, H^{16} and H^{a}), 1.24-0.83 (252H, br m, H$^{12\ (syn)}$ and H^{14}). **^{13}C{^{1}H} NMR (151 MHz, C$_2$D$_2$Cl$_4$, 393 K)**: δ 120.54, 99.89, 69.58 (C^{15}), 46.21 (C^{12}), 43.64(C^{a}), 35.88(C^{a}), 33.59(C^{a}), 32.50 (C^{a}), 29.66 (C^{a}), 29.51 (C^{a}), 29.19 (C^{a}), 28.58 (C^{13}), 26.90 (C^{a}), 26.84 (C^{a}), 24.63 (C^{a}), 24.11(C^{a}), 24.09

(C^{a}), 23.84 (C^{16}), 21.64 (C^{14}). **$^{31}P\{^{1}H\}$ NMR (243 MHz, $C_2D_2Cl_4$, 393 K)**: δ 29.49. **FTIR**: *v* (cm^{-1}) 2951, 2868 and 1458 (*v* (C-H, CH_3)), 2920, 2838 and 1377 (*v* (C-H, CH_2)), 1250 (*v* (P=O)), 1109 (*v* (C-O)), 982 (*v* (P-O-C)). **$^{s}PP_{PPr}$:^{1}H NMR (600 MHz, $C_2D_2Cl_4$, 393 K)**: δ 4.74 (2H, h, H^{15}), 2.30, 2.12, 1.86-1.62 (68H, br m, H^{13}, H^{1} and H^{a}), 1.62-1.26 (59H, br m, H^{16} and H^{a}), 1.26- 1.03 (126H, br m, H^{12} and H^{a}), 1.03-0.75 (190H, br m, H^{14}). **$^{13}C\{^{1}H\}$ NMR (151 MHz, $C_2D_2Cl_4$, 393 K)**: δ 120.54, 99.90, 69.28 (C^{15}), 46.93 (C^{12}), 46.29, 46.16, 44.15, 28.14 (C^{13}), 24.09, 23.84 (C^{16}), 20.81, 20.62, 20.46, 20.09(C^{14}). **$^{31}P\{^{1}H\}$ NMR (243 MHz, $C_2D_2Cl_4$, 393 K)**: δ 29.63. **FTIR**: *v* (cm^{-1}) 2956, 2868 and 1464 (*v* (C-H, CH_3)), 2914, 2839 and 1377 (*v* (C-H, CH_2)), 1246 (*v* (P=O)), 1109 (*v* (C-O)), 982 (*v* (P-O-C)). ^{a}Peaks corresponding to unassigned CH_2.

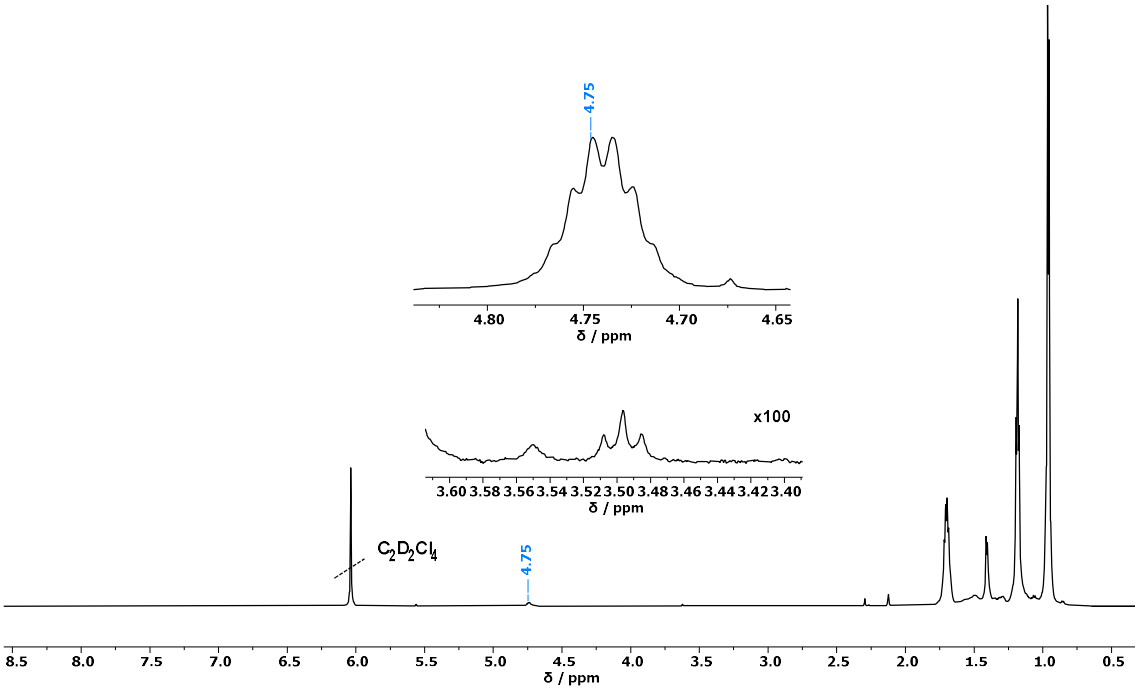

Figure A1.83 $^{s}PP_{PPr}$ ^{1}H NMR (600 MHz, $C_2D_2Cl_4$, 393 K).

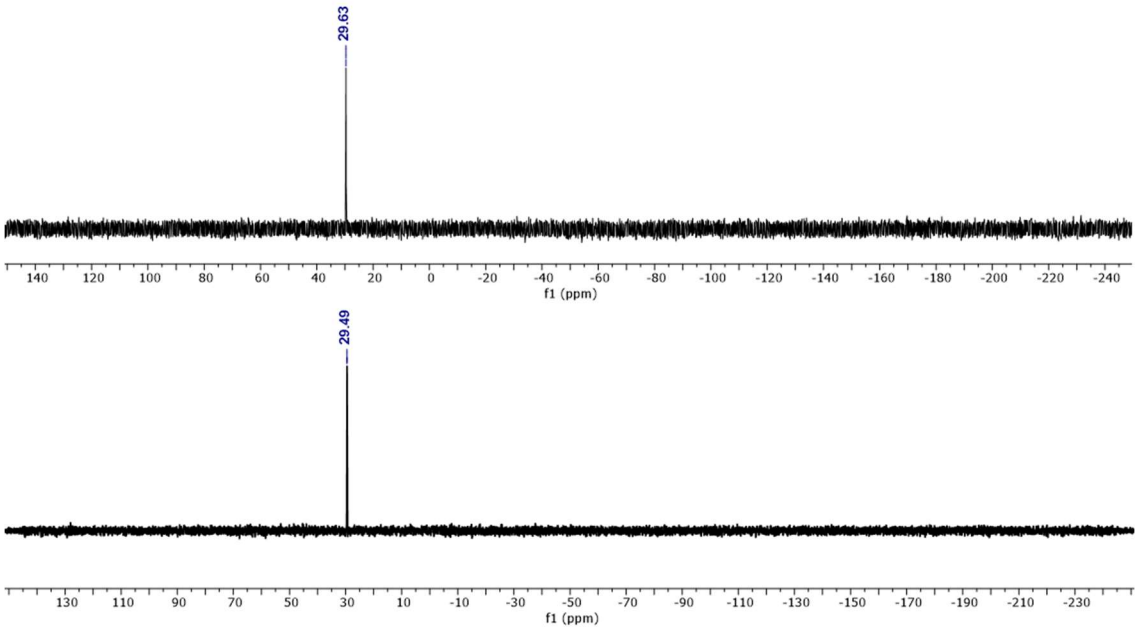

Figure A1.84 ^{i}**PPP$_{PPr}$** (top) and ^{s}**PP$_{PPr}$** (bottom) $^{31}P\{^{1}H\}$ NMR (243 MHz, $C_2D_2Cl_4$, 393 K)**.**

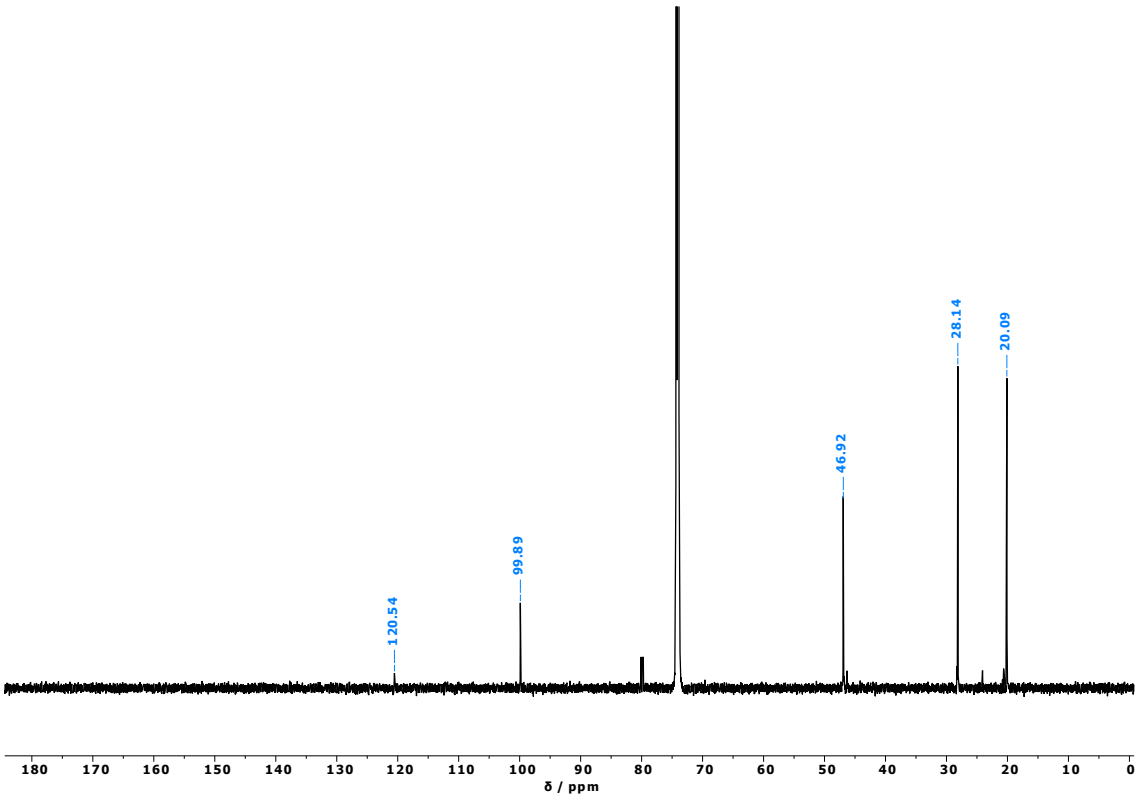

Figure A1.85 ^{s}**PP$_{PPr}$** $^{13}C\{^{1}H\}$ NMR (151 MHz, $C_2D_2Cl_4$, 393 K).

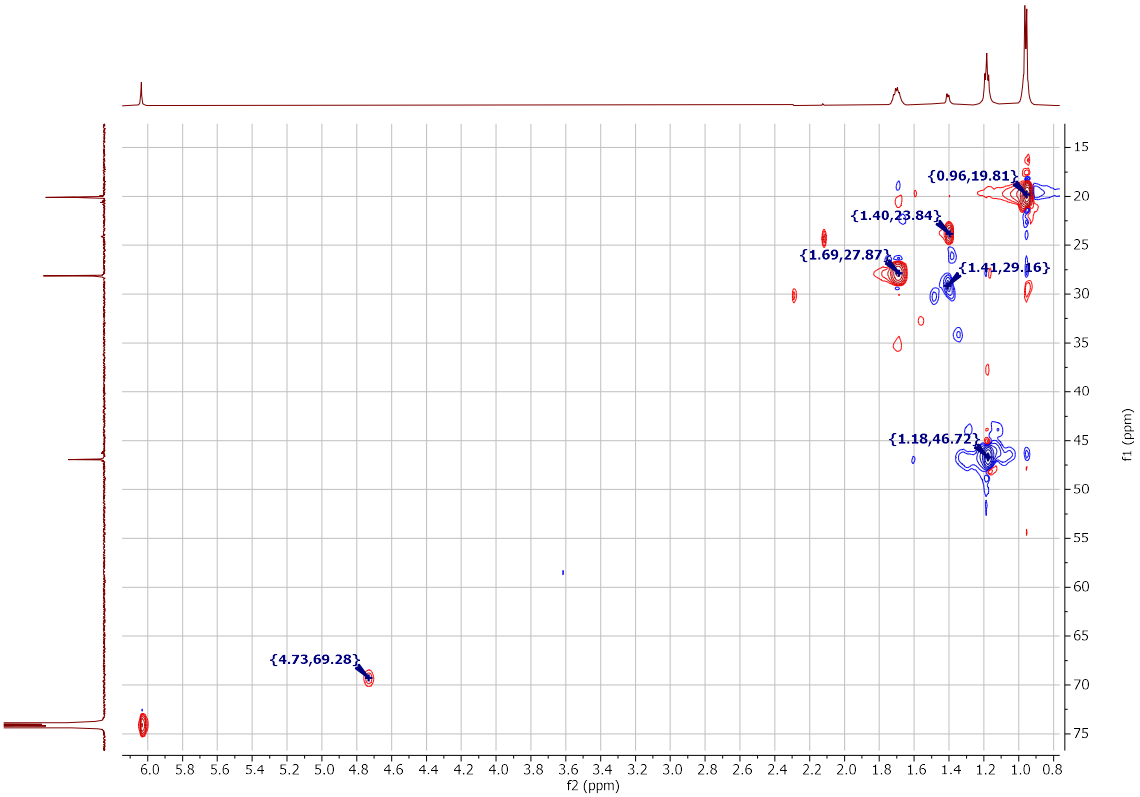

Figure A1.86 ^{s}**PP$_{PPr}$** HSQC ^{1}H-^{13}C NMR spectrum.

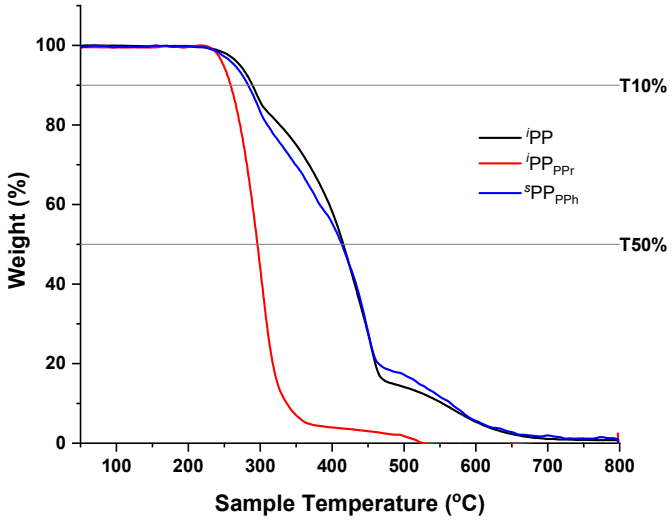

Figure A1.87 ^{i}**PP$_{PPr}$** and ^{s}**PP$_{PPr}$** TGA analyses, performed between 50-800 °C under a synthetic air atmosphere (20:80 O_2:N_2) with heating rate of 20 °C min^{-1}

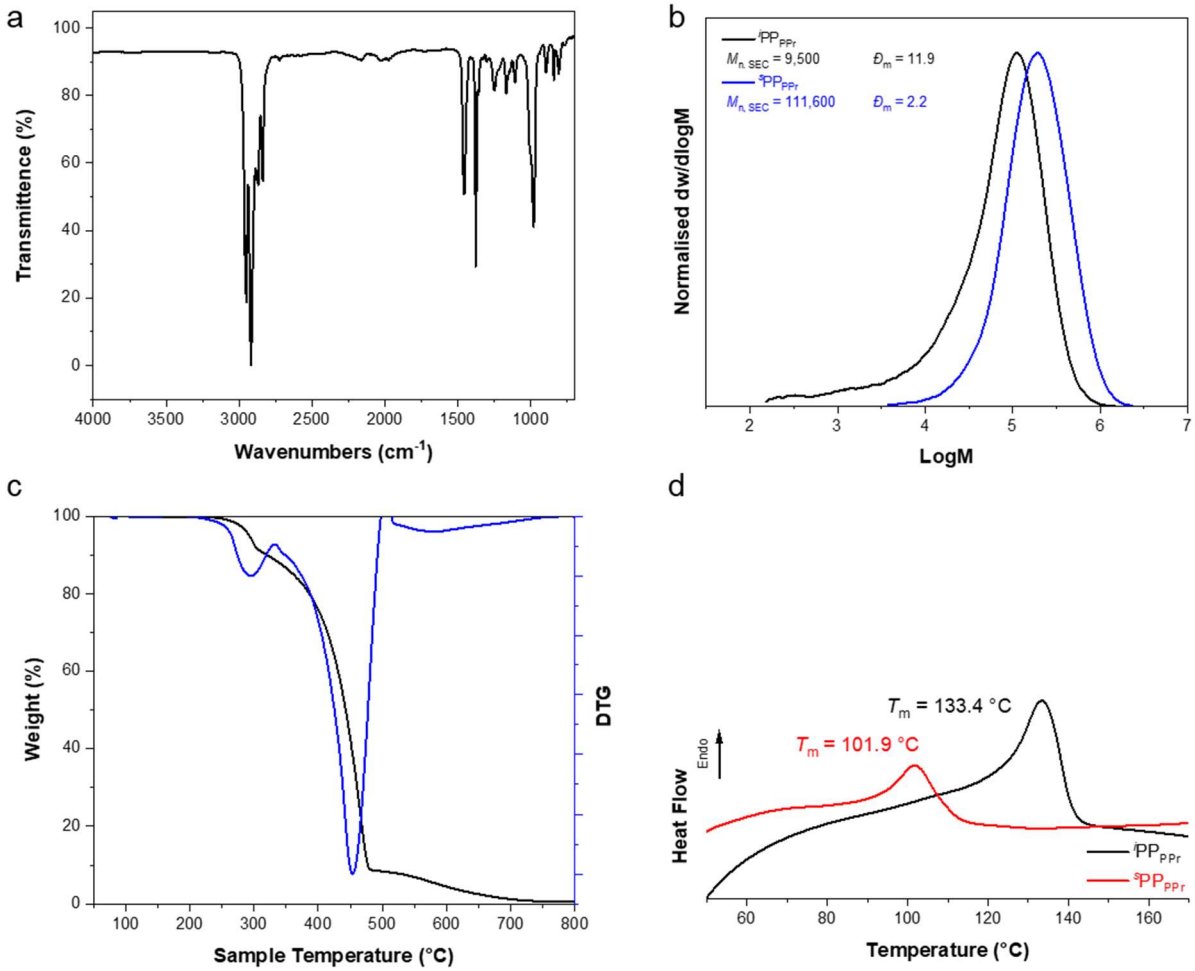

Figure A1.88 (a) FT-IR spectrum and (b) TGA thermograph of ^{i}**PP$_{PPr}$** and (c) SEC trace and (d) DSC 2nd heating curves of ^{i}**PP$_{PPr}$** and ^{s}**PP$_{PPr}$**.

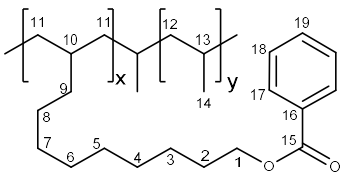

Synthesis of Bn modified ^{i}PP$_{Br}$ and ^{s}PP$_{Br}$, ^{i}PP$_{Bn}$ and ^{s}PP$_{Bn}$. Bn (2 equiv.) and DBU (2 equiv.) were added to an ampoule containing **PP$_{Br}$** (200 mg) and THF (5 mL). The reaction mixture was heated at 95 °C and agitated for 96 hrs. The final polymer was precipitated in acidified methanol (2wt% HCl) before being collected by filtration on a glass sintered frit (porosity 3), washed with methanol, then acetone, and dried *in vacuo* at 60 °C to a constant weight. Polymer isolated:163 mg of ^{i}**PP$_{Bn}$** and 205 mg of ^{s}**PP$_{Bn}$**. ^{i}**PP$_{Bn}$: ^{1}H NMR (600 MHz, C$_2$D$_2$Cl$_4$, 393 K)** : δ 8.11 (2H, d, $^{3}J_{HH}$ = 7.4 Hz, H^{17}), 7.62 (1H, t, $^{3}J_{HH}$ = 7.4 Hz, H^{19}), 7.51 (2H, t, $^{3}J_{HH}$ = 7.4 Hz, H^{18}), 4.42 (2H, t, $^{3}J_{HH}$ = 6.6 Hz, H^{1}), 1.88 (2H, p, $^{3}J_{HH}$ = 7.2 Hz, H^{2}), 1.75-1.64

(54H, br m, H^{13}),1.58-1.33 (81H, br m, H^3, H^4, $H^{12\,(anti)}$ and H^a), 1.07-0.92 (213H, br m, $H^{12\,(syn)}$, H^{14}). **$^{13}C\{^1H\}$ (151 MHz, $C_2D_2Cl_4$, 393 K)**: δ 166.53 (C^{15}) 132.60 (C^{19}), 131.21 (C^{16}) 129.60 (C^{17}), 128.32 (C^{18}), 120.54, 99.89, 65.21 (C^1), 46.21 (C^{12}), 43.62(C^a), 38.23(C^a), 33.58(C^a), 30.18(C^a), 29.62(C^a), 29.57(C^a), 29.33 (C^4) 28.98 (C^2), 28.57 (C^{13}), 26.83 (C^a), 26.16 (C^3), 21.64 (C^{14}). **FTIR**: ν (cm^{-1}) = 2950, 2867 and 1456 (ν(C-H, CH_3)), 2917, 2839 and 1376 (ν (C-H, CH_2)), 1726 (ν (C=O)), 1272 (ν (C_{Alk}-O)), 1111 (ν (C_{Ar}-O)). **$^sPP_{Bn}$: ^1H NMR (600 MHz, $C_2D_2Cl_4$, 393 K)**: δ 8.11 (2H, d, $^3J_{HH}$ = 7.5 Hz, H^{17}), 7.62 (1H, t, $^3J_{HH}$ = 7.4 Hz, H^{19}), 7.51 (2H, t, $^3J_{HH}$ = 7.6 Hz, H^{18}), 4.42 (2H, t, $^3J_{HH}$ = 6.6 Hz, H^1), 1.88 (2H, p, $^3J_{HH}$ = 6.8 Hz, H^2), 1.78-1.63 (25H, br m, H^{13}), 1.63-1.26 (20H, br m, H^3, H^4 and H^a), 1.26-1.03 (49H, br m, H^{12} and H^a), 1.03-0.83 (75H, br m, H^{14}). **$^{13}C\{^1H\}$ NMR (151 MHz, $C_2D_2Cl_4$, 393 K)**: δ 165.93 (C^{15}), 132.61 (C^{19}), 131.21 (C^{16}), 129.60 (C^{17}), 128.32 (C^{18}), 120.54, 99.89, 65.21 (C^1), 46.92 (C^{12}), 44.15, 38.95, 32.68, 32.24, 29.56, 28.97 (C^2), 28.14 (C^{13}), 27.54, 25.93 (C^3), 20.62, 20.09 (C^{14}). **FTIR**: ν (cm^{-1}) = 2956, 2868 and 1464 (ν(C-H, CH_3)), 2915, 2841 and 1377 (ν (C-H, CH_2)), 1726 (ν (C=O)), 1273 (ν (C_{Alk}-O)), 1111 (ν (C_{Ar}-O)). ^{a}Peaks corresponding to unassigned CH_2.

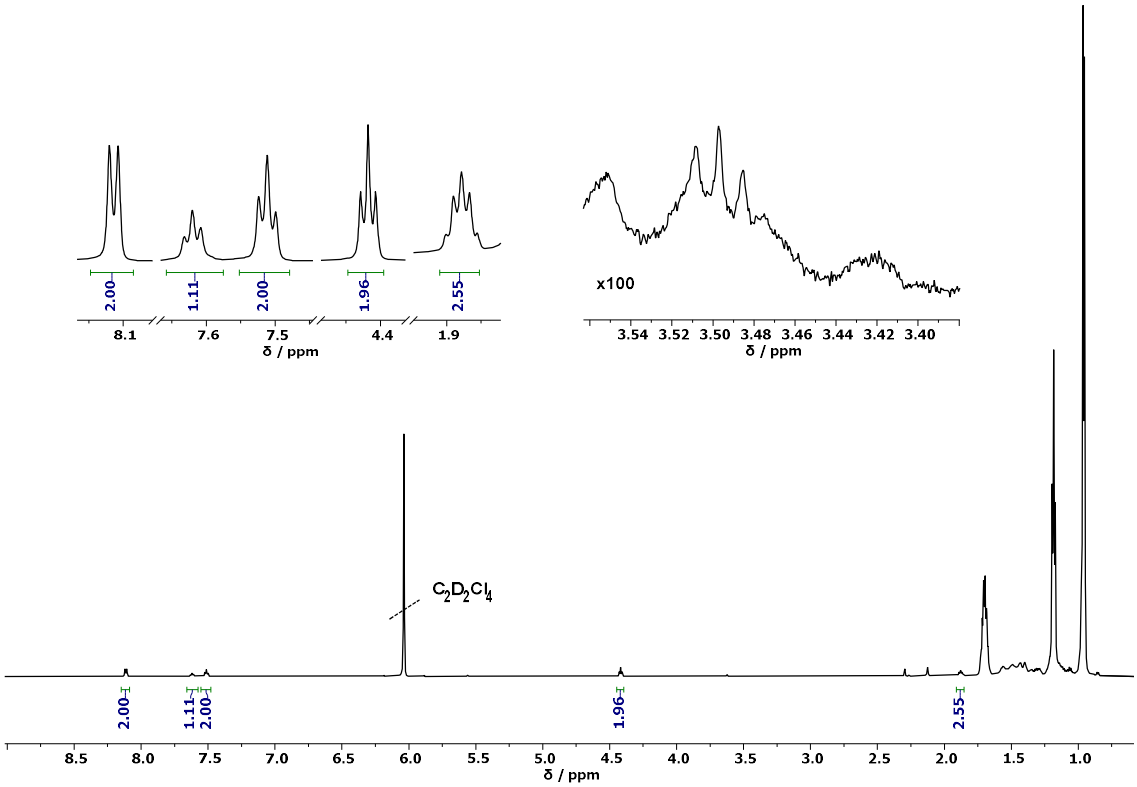

Figure A1.89 ^{s}**PP$_{Bn}$** ^{1}H NMR (600 MHz, $C_2D_2Cl_4$, 393 K).

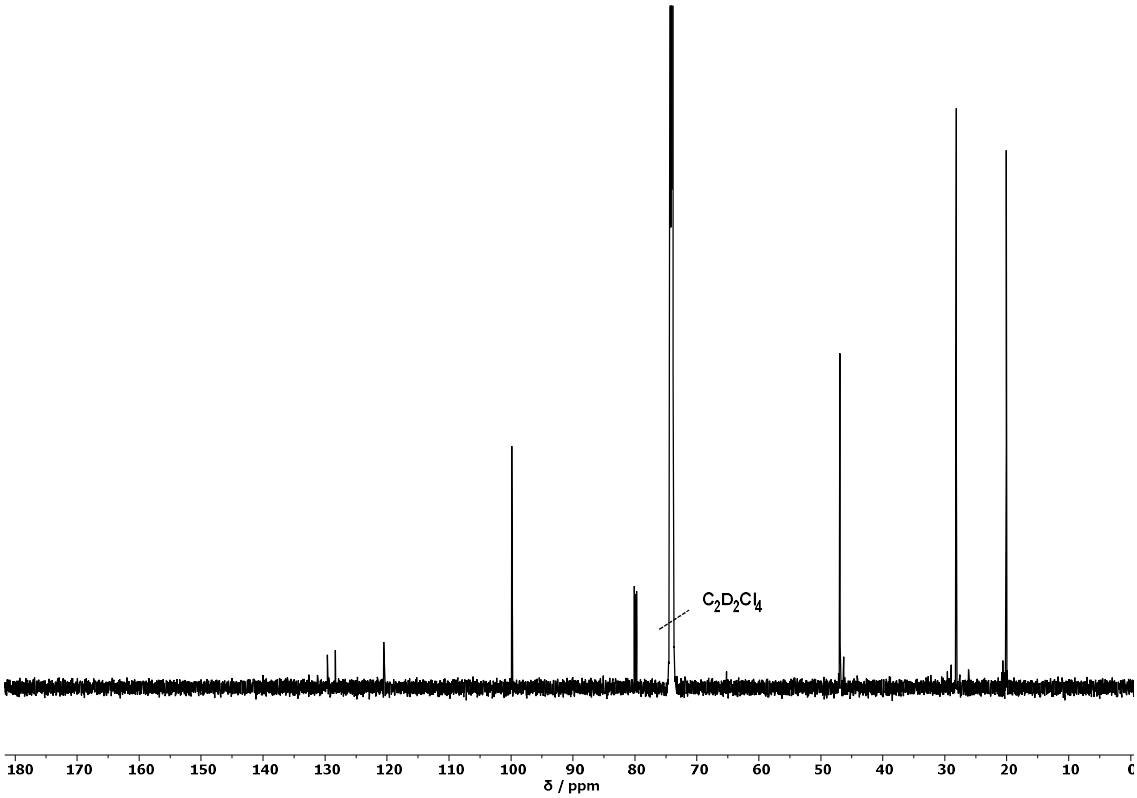

Figure A1.90 ^{s}**PP$_{Bn}$** ^{13}C{^{1}H} NMR (151 MHz, $C_2D_2Cl_4$, 393 K).

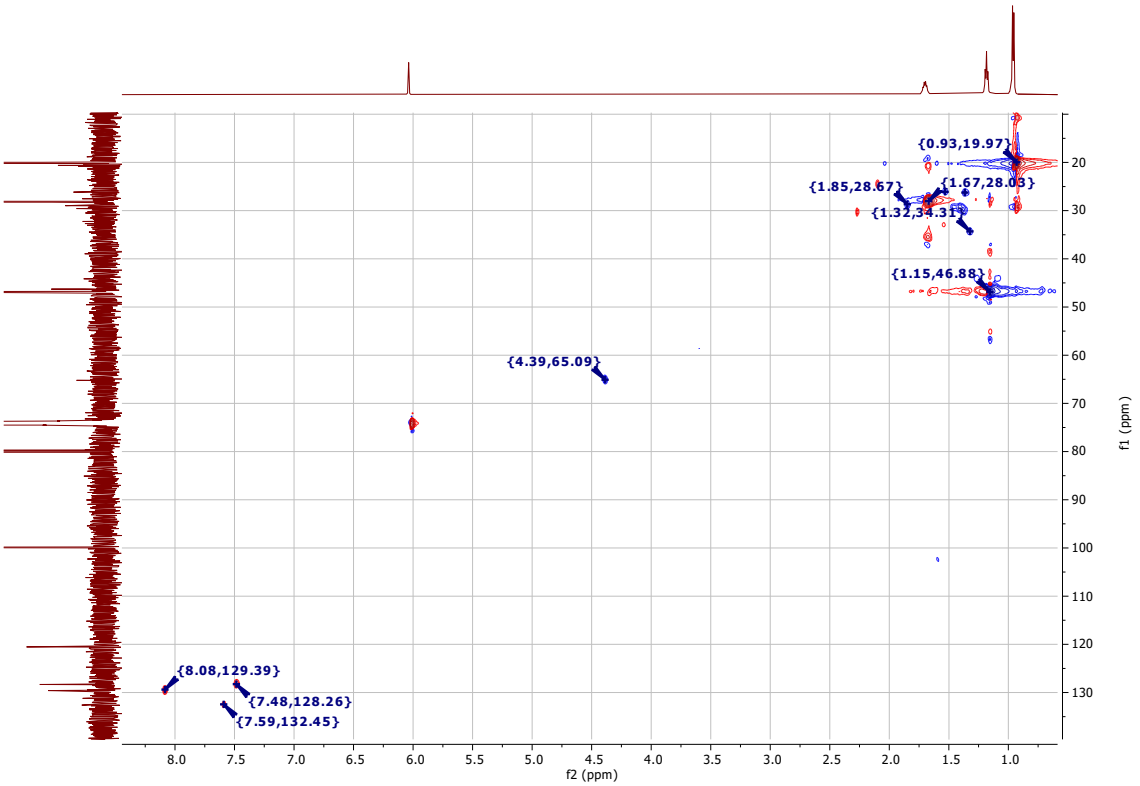

Figure A1.91 ^{s}**PP$_{Bn}$** HSQC ^{1}H-^{13}C NMR spectrum.

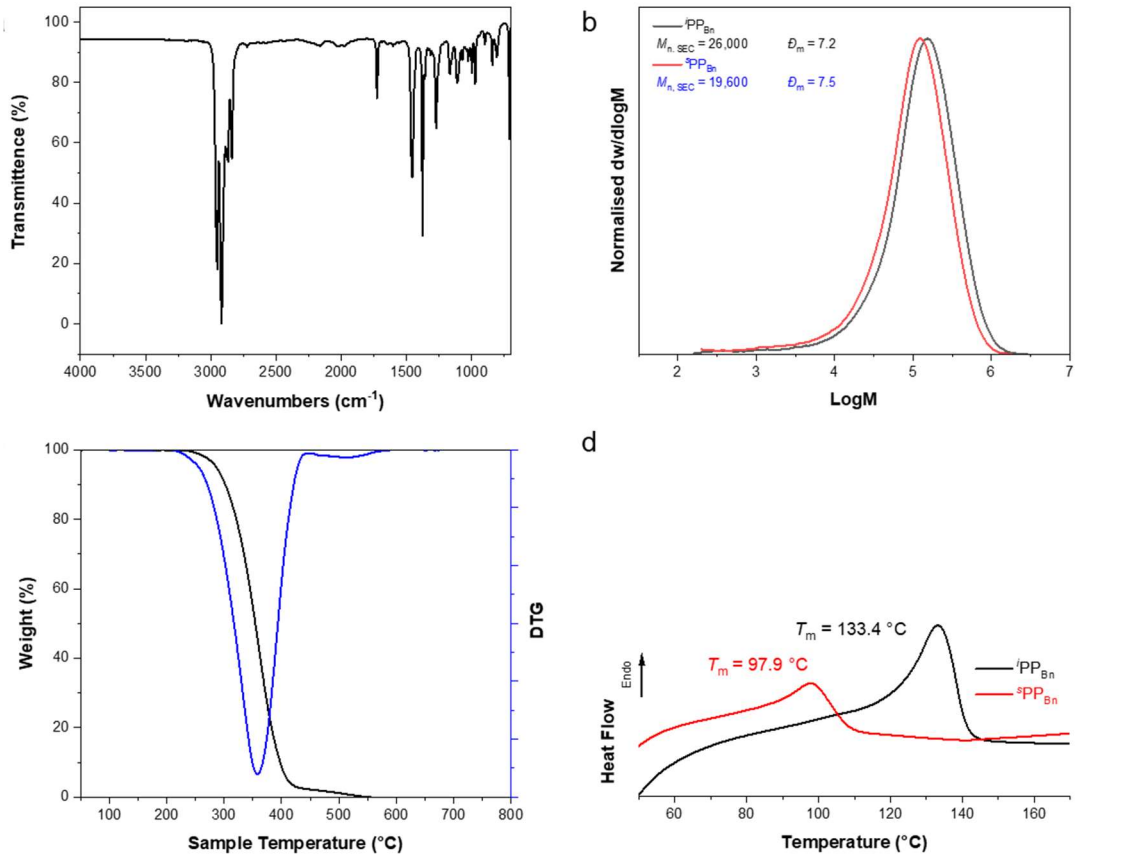

Figure A1.92 (a) FT-IR spectrum and (b) TGA thermograph of ^{i}**PP$_{Bn}$** and (c) SEC trace and (d) DSC 2nd heating curves of ^{i}**PP$_{Bn}$** and ^{s}**PP$_{Bn}$**.

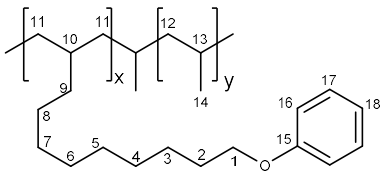

Synthesis of KOPh modified ^{i}PP$_{Br}$ and ^{s}PP$_{Br}$, ^{i}PP$_{OPh}$ and ^{s}PP$_{OPh}$. Under an inert nitrogen atmosphere, pre-prepared **KOPh** (2 equiv.), **PP$_{Br}$** (200 mg) and THF (5 mL) were added to an ampoule and sealed with a Teflon tap. The reaction mixture was heated at 95 °C and agitated for 96 hrs. The polymer formed was worked up with the relevant procedure, yielding 187 mg of ^{i}**PP$_{OPh}$** and 179 mg of ^{s}**PP$_{OPh}$**. ^{i}**PP$_{OPh}$: ^{1}H NMR (600 MHz, C$_2$D$_2$Cl$_4$,393 K)**: δ 7.33 (2H, t, $^{3}J_{HH}$ = 7.6 Hz, H^{17}), 6.99 (3H, dd, $^{3}J_{HH}$ = 12.8, 7.4 Hz, H^{16} and H^{18}), 4.07 (2H, t, $^{3}J_{HH}$ = 7.6 Hz, H^{1}), 2.30, 2.12, 1.87 (2H, p, $^{3}J_{HH}$ = 6.8 Hz, H^{2}), 1.83-1.62 (59H, br m, H^{13}), 1.63-1.21 (91H, br m, H^{3}, H^{4}, H$^{12(anti)}$ and H^{a}) 1.21-0.74 (240H, br m, H$^{12\,(syn)}$ and H^{14}). **^{13}C{^{1}H } (151 MHz, C$_2$D$_2$Cl$_4$, 393 K)**: δ 159.61 (C^{15}), 129.41 (C^{17}), 120.70 (C^{18}), 116.94 (C^{16}), 99.89, 68.59 (C^{1}), 47.73, 46.21 (C^{12}), 43.63, 35.85, 34.96, 34.24, 33.93, 33.91, 29.62, 29.54 28.66, 28.57 (C^{13}), 21.89, 21.65 (C^{14}). **FTIR**: *v* (cm^{-1}) = 2951, 2868 and 1456 (*v* (C-H, CH$_3$)), 2918, 2839 and 1377 (*v* (C-H, CH$_2$)), 1601 and 1497 (*v* (C=C)), 1246 (*v* (C$_{Alk}$-O)), 1043 (*v* (C$_{Ar}$-O)). ^{s}**PP$_{OPh}$: ^{1}H NMR (600 MHz, C$_2$D$_2$Cl$_4$, 393 K)**: δ 7.33 (2H, t, $^{3}J_{HH}$ = 7.7 Hz, H^{17}), 6.99 (3H, dd, $^{3}J_{HH}$ = 12.6, 7.4 Hz, H^{16} and H^{18}), 4.07 (2H, t, $^{3}J_{HH}$ = 6.5 Hz, H^{1}), 2.30, 2.13, 1.88 (2H, p, $^{3}J_{HH}$ = 6.8 Hz, H^{2}), 1.77-1.62 (53H, br m, H^{13}), 1.62-1.26 (30H, br m, H^{3} and H^{a}), 1.26-1.03 (107H, br m, H^{12} and H^{a}), 1.03-0.8 (165H, br m, H^{14}). **^{13}C{^{1}H} (151 MHz, C$_2$D$_2$Cl$_4$, 393 K)**: δ 159.62 (C^{15}), 129.40 (C^{17}), 120.70 (C^{18}), 120.54, 115.31 (C^{16}), 99.89, 68.59 (C^{1}), 46.93 (C^{12}), 46.30, 46.16, 44.16 (C^{a}), 43.47 (C^{a}), 34.77 (C^{a}), 29.61 (C^{2}), 29.54 (C^{a}), 29.43 (C^{a}), 28.14 (C^{13}), 26.27 (C^{a}), 26.17 (C^{a}), 20.82 (C^{a}), 20.63, 20.48 (C^{a}), 20.09 (C^{14}). **FTIR**: *v* (cm^{-1}) = 2954, 2868 and 1462 (*v* (C-H, CH$_3$)), 2914, 2839 and 1377 (*v* (C-H, CH$_2$)), 1602 and 1497 (*v* (C=C)), 1244 (*v* (C$_{Alk}$-O)), 1038 (*v* (C$_{Ar}$-O)). ^{a}Peaks corresponding to unassigned CH$_2$.

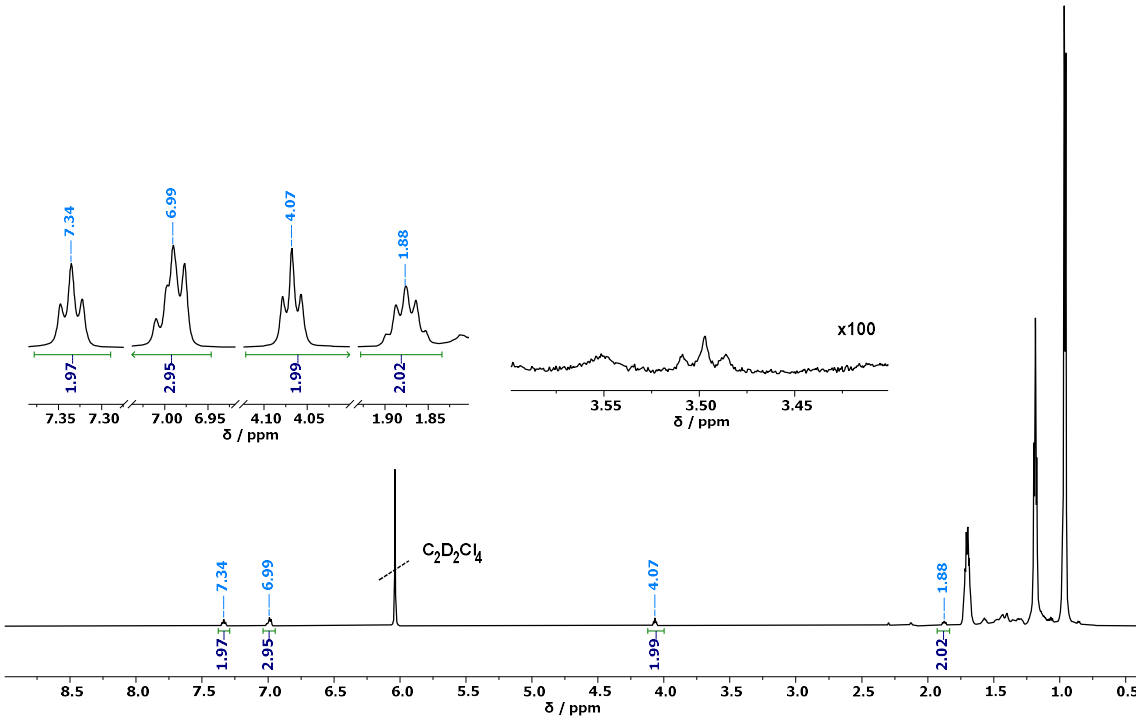

Figure A1.93 ^{s}**PP$_{OPh}$** ^{1}H NMR (600 MHz, $C_2D_2Cl_4$, 393 K).

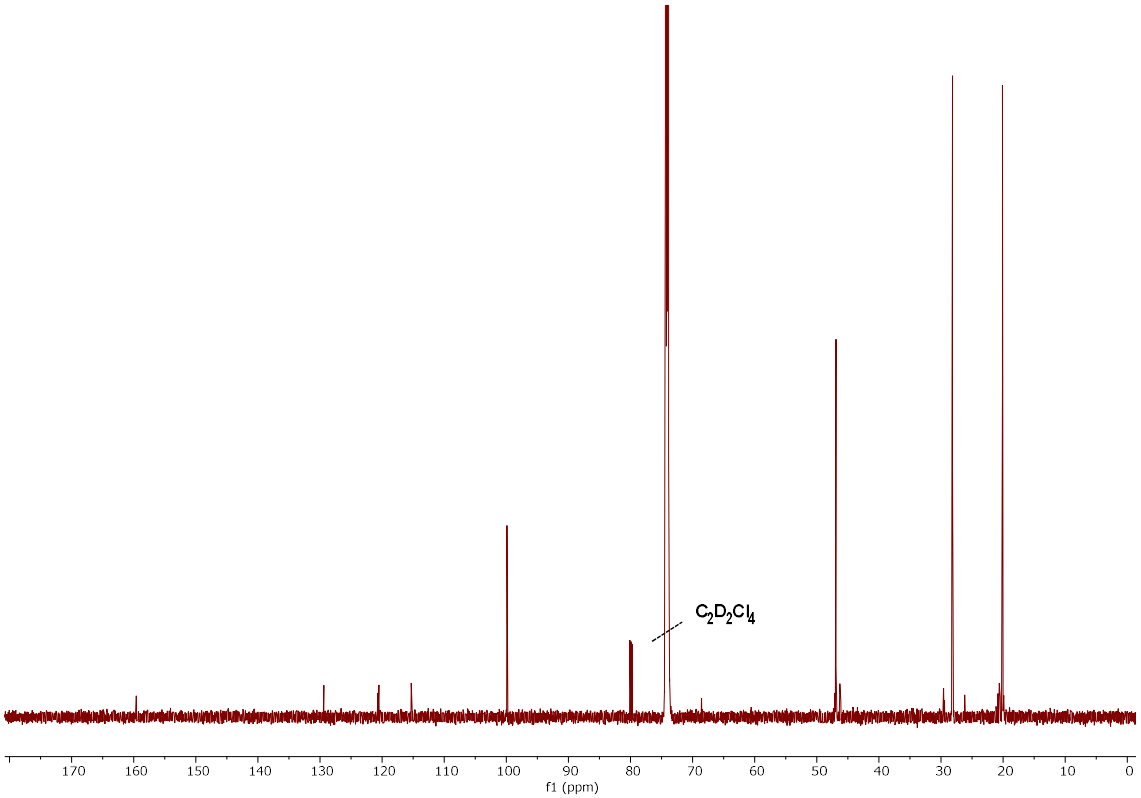

Figure A1.94 ^{s}**PP$_{OPh}$** ^{13}C{^{1}H} NMR (151 MHz, $C_2D_2Cl_4$, 393 K).

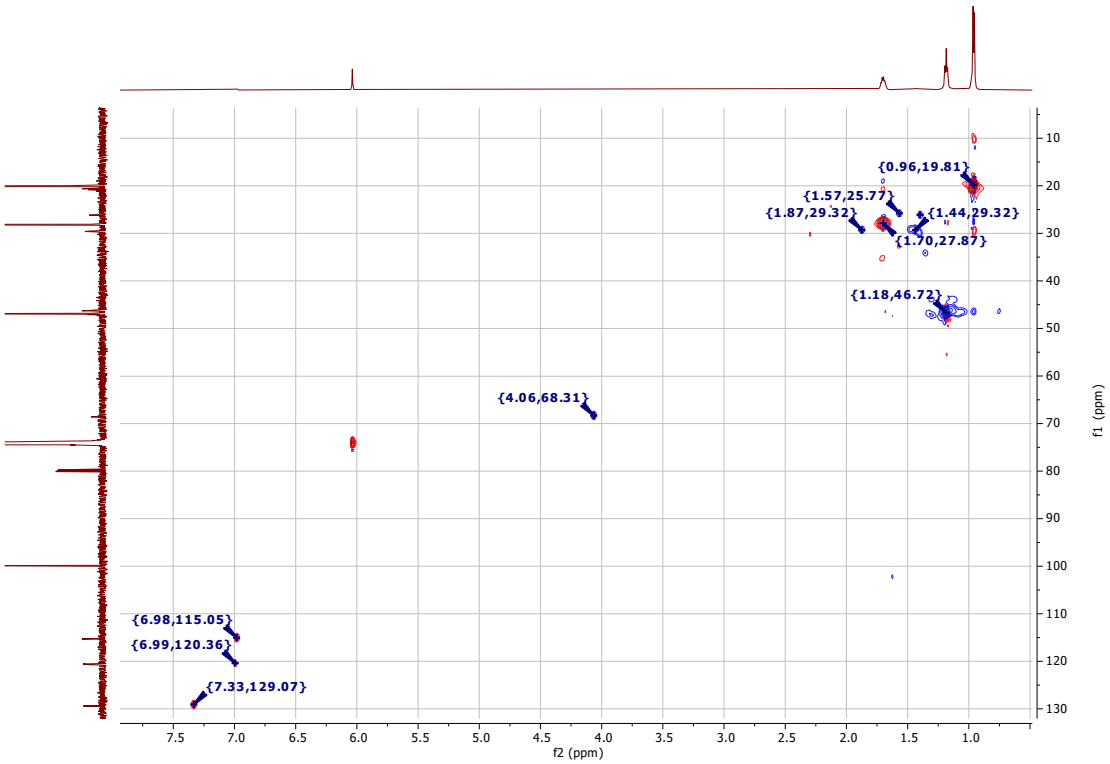

Figure A1.95 ^{s}**PP$_{OPh}$** HSQC ^{1}H-^{13}C NMR spectrum.

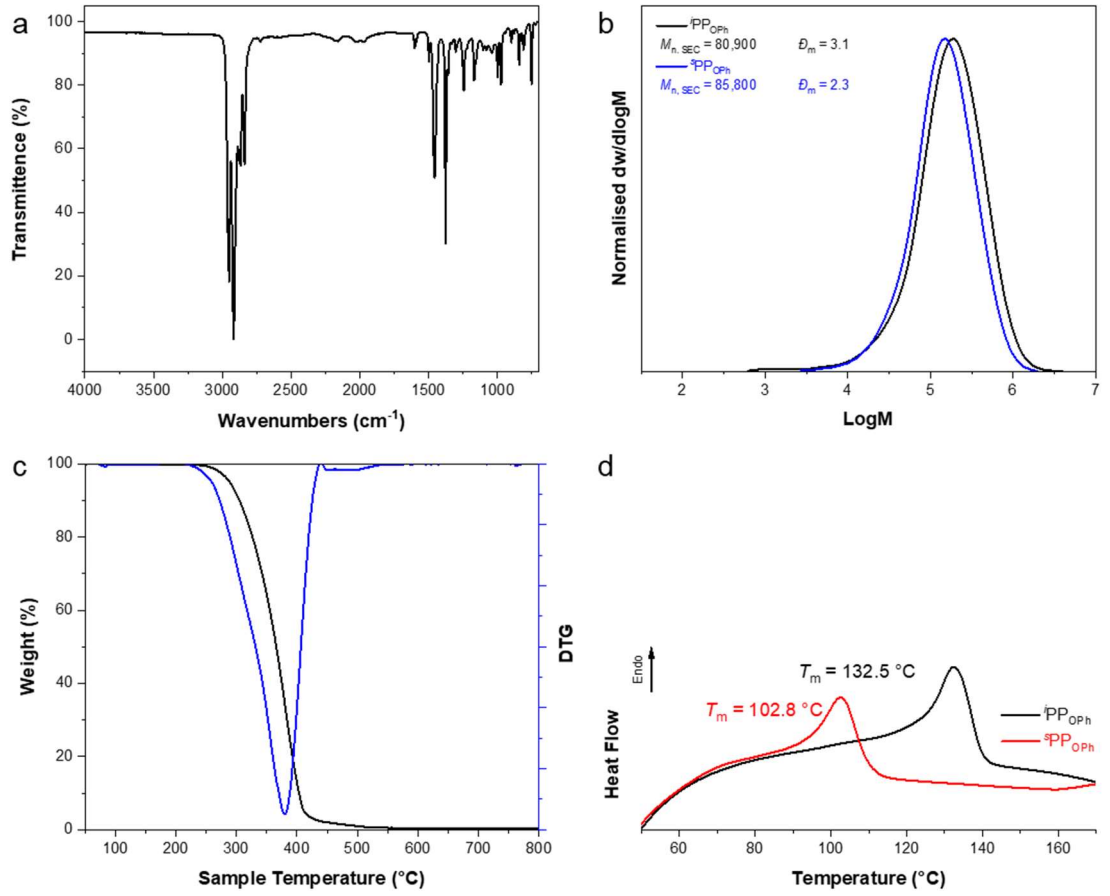

Figure A1.96 (a) FT-IR spectrum and (b) TGA thermograph of ^{i}**PP$_{OPh}$** and (c) SEC trace and (d) DSC 2nd heating curves of ^{i}**PP$_{OPh}$** and ^{s}**PP$_{OPh}$**.

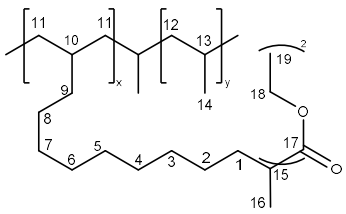

Synthesis of KDEMM modified ^{i}PP$_{Br}$ and ^{s}PP$_{Br}$, ^{i}PP$_{M}$ and ^{s}PP$_{M}$. Under an inert nitrogen atmosphere, KDEMM salt (2 equiv.), **PP$_{Br}$** (200 mg) and THF (5 mL) were added to an ampoule and sealed with a Teflon tap. The reaction mixture was heated at 95 °C and agitated for 96 hrs. The final polymer was precipitated in acidified methanol (2wt% HCl) before being collected by filtration on a glass sintered frit (porosity 3), washed with methanol, then acetone, and dried *in vacuo* at 60 °C to a constant weight. Polymer isolated: 173 mg of ^{i}**PP$_{M}$** and 210 mg of ^{s}**PP$_{M}$**. ^{i}**PP$_{M}$: ^{1}H NMR (600 MHz, C$_2$D$_2$Cl$_4$, 393 K)**: δ 4.26 (4H, q, $^{3}J_{HH}$ = 7.0 Hz, H^{18}), 2.30, 2.13, 1.95 (2H, m, H^{1}), 1.90-1.63 (67H, br m, H^{13}), 1.63-1.24 (90H, br m, H^{2}, H$^{12(anti)}$, H^{15}, H^{19} and H^{a}), 1.24-0.86 (225H, br m, H$^{12(syn)}$ and H^{14}). **^{13}C{^{1}H} (151 MHz, C$_2$D$_2$Cl$_4$, 393 K)**: δ 172.30 (C^{17}), 99.89, 60.93 (C^{18}), 54.14 (C^{15}), 46.21 (C^{12}), 43.63 (C^{a}), 35.93 (C^{1}), 30.22 (C^{a}), 30.03 (C^{a}), 29.68 (C^{a}), 26.63 (C^{a}), 29.41 (C^{a}), 28.57 (C^{13}), 26.85 (C^{a}), 25.64 (C^{a}), 24.45 (C^{2}), 21.64 (C^{14}), 20.05 (C^{16}), 15.81, 14.06 (C^{19}). **FTIR**: ν (cm^{-1}) = 2951, 2868 and 1458 (ν (C-H, CH$_3$)), 2918, 2839, and 1377 (ν (C-H, CH$_2$)), 1735 (ν (C=O)), 1255 and 1113 (ν (C-O)). ^{s}**PP$_{M}$: ^{1}H NMR (600 MHz, C$_2$D$_2$Cl$_4$, 393 K)**: δ 4.26 (4H, q, $^{3}J_{HH}$ = 7.0 Hz, H^{18}), 2.30. 2.13, 1.95 (2H, m, H^{1}), 1.89-1.63 (56H, br m, H^{13}), 1.63-1.26 (52H, br m, H^{2}, H^{15}, H^{19} and H^{a}), 1.26-1.03 (109H, br m, H^{12} and H^{a}), 1.03-0.82 (165H, br m, H^{14}). **^{13}C{^{1}H} (151 MHz, C$_2$D$_2$Cl$_4$, 393 K)**: δ 172.30 (C^{17}), 120.54, 99.89, 60.93 (C^{18}), 54.14 (C^{15}), 46.92 (C^{12}), 46.29, 42.37, 29.66, 28.14 (C^{13}), 24.44 (C^{2}), 20.82, 20.62, 20.46, 20.09 (C^{14}), 19.65 (C^{16}), 14.06 (C^{19}). **FTIR**: ν (cm^{-1}) = 2956, 2868 and 1468 (ν (C-H, CH$_3$)), 2914, 2839 and 1377 (ν (C-H, CH$_2$)), 1736 (ν (C=O)), 1246 and 1113 (ν (C-O)). ^{a}Peaks corresponding to unassigned CH$_2$.

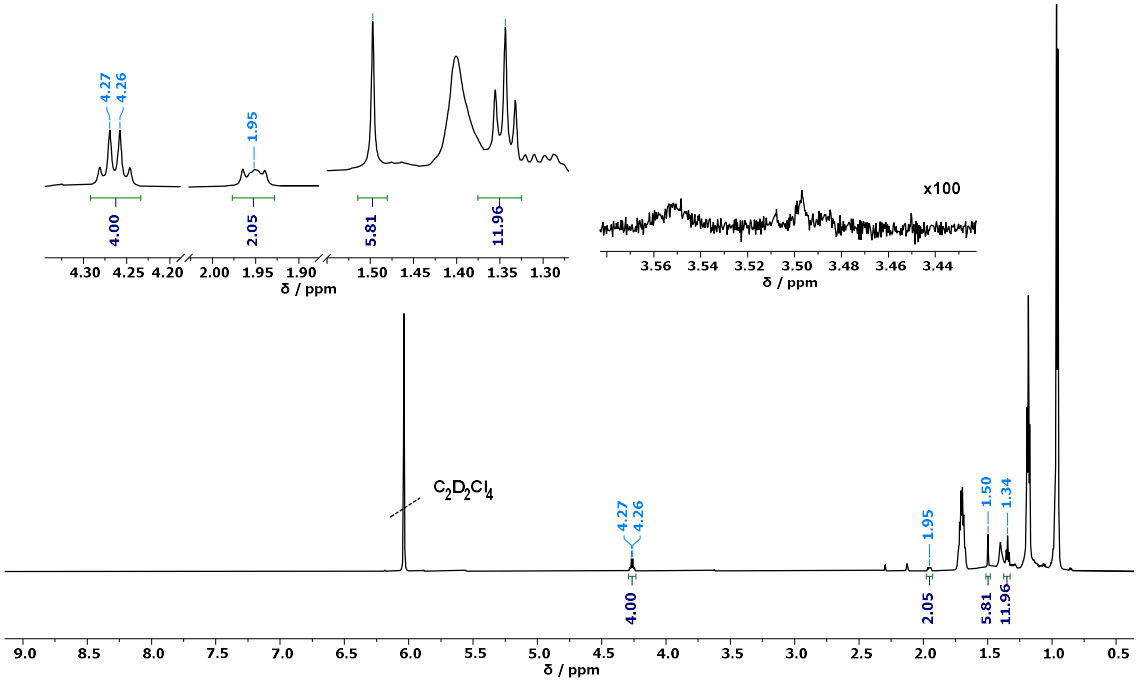

Figure A1.97 **^{s}PP$_{M}$** ^{1}H NMR (600 MHz, $C_2D_2Cl_4$, 393 K).

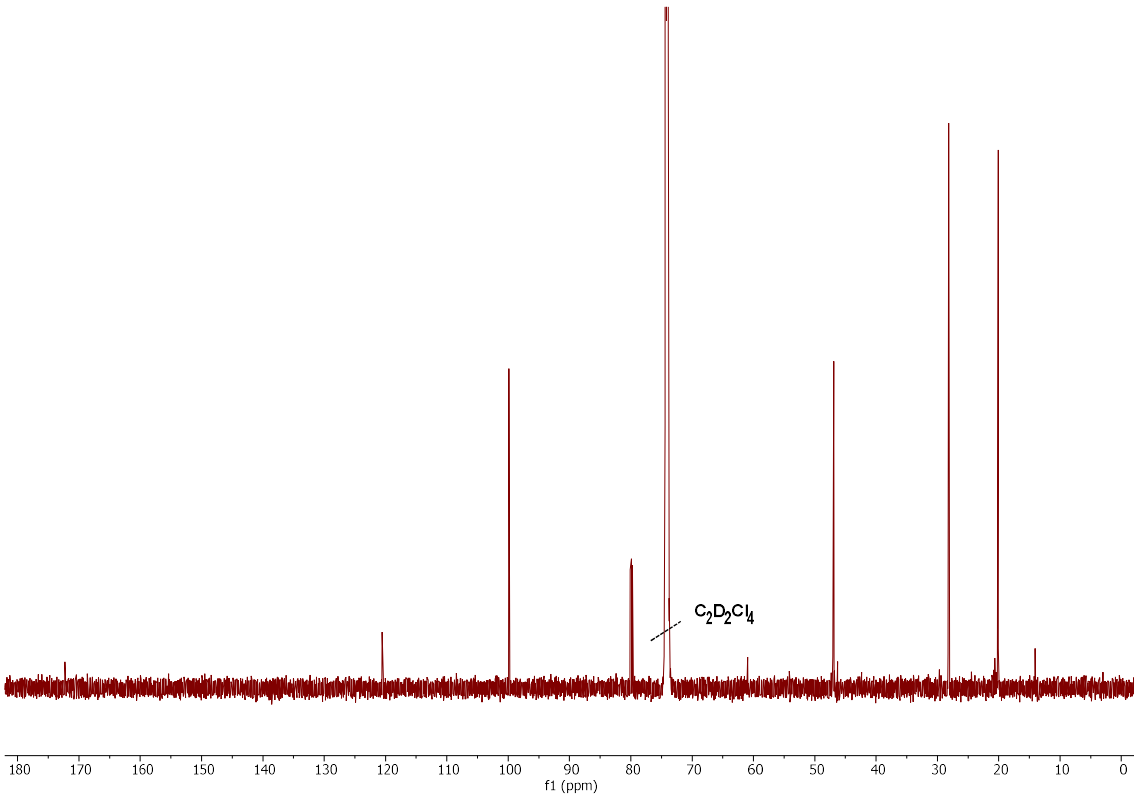

Figure A1.98 **^{s}PP$_{M}$** ^{13}C{^{1}H} NMR (151 MHz, $C_2D_2Cl_4$, 393 K).

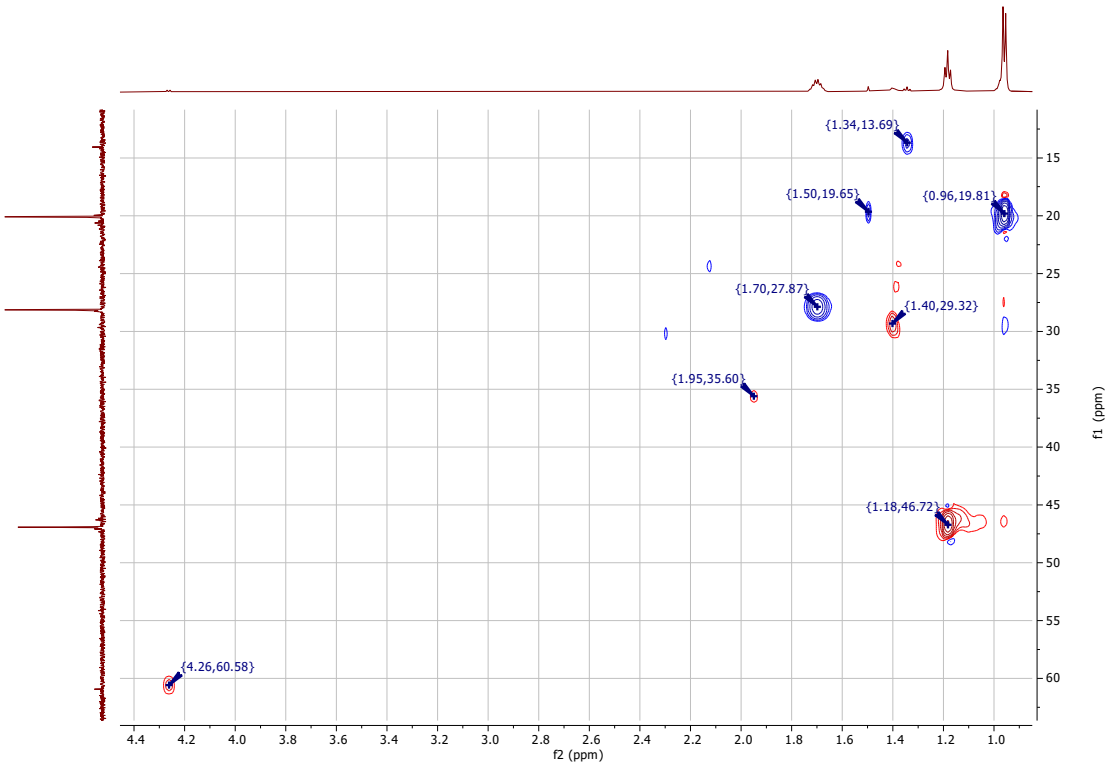

Figure A1.99 ^{s}**PP$_{M}$** HSQC ^{1}H-^{13}C NMR spectrum.

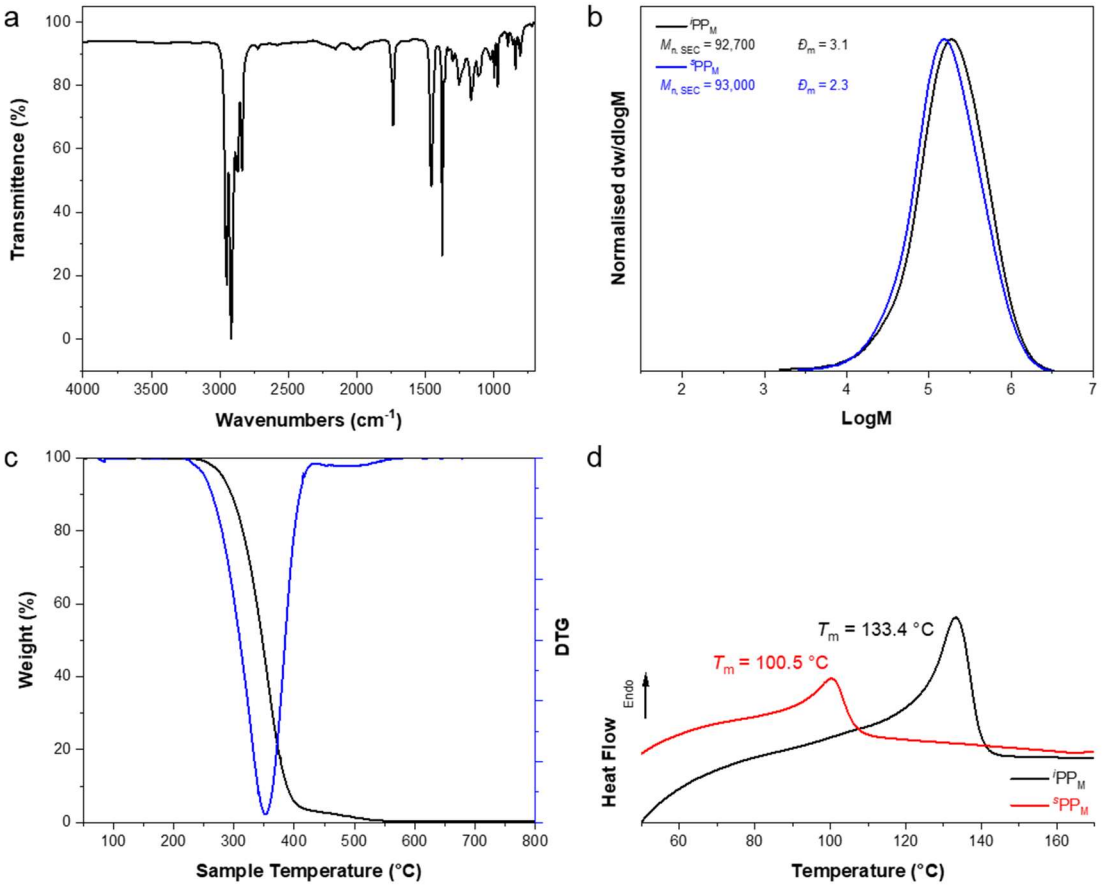

Figure A1.100 (a) FT-IR spectrum and (b) TGA thermograph of ^{i}**PP$_{M}$** and (c) SEC trace and (d) DSC 2nd heating curves of ^{i}**PP$_{M}$** and ^{s}**PP$_{M}$**.

Table A1.2 Quantitative bromine analysis.

Entry	[Br][a]	
PP_{Br}	23.67	(3.74)
PP_{PPr}	0.23	(0.20)
PP_{PPh}	0.12	(0.10)
PP_{Ac}	0.00	(0.00)
PP_{DEA}	0.00	(0.00)
PP_{S}	0.13	(0.13)
PP_{M}	0.19	(0.07)
PP_{OPh}	0.00	(0.00)

[a]wt% brominated comonomer extrapolated from residual bromine %wt/wt of the parent polymer. One standard deviation, shown in brackets (σ).

A1.5. Synthesis of potassium salts

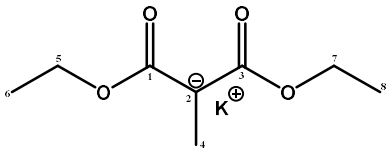

Synthesis of potassium 1,3-diethoxy-2-methyl-1,3-dioxopropan-2-ide (KDEMM). Potassium *t*-butoxide (1.2 g, 1 eq.) were dissolved in THF (12 ml) in a schlenk and diethyl methyl malonate (DEMM, 2 ml, 1.2 eq.) added dropwise *via* cannula transfer. After stirring for 16 h volatiles were removed *in vacuo* and the solid washed with pentane (3 x 20 ml) and dried *in vacuo* to yield a yellow? solid (96.20 %), mp 164-166 °C. ^{1}H NMR (500 MHz, THF-d_8, 298 K): δ = 3.89 (q, ^{3}J = 7.1 Hz, 4H, $H^{5, 7}$), 1.67 (s, 3H, H^{4}), 1.14 (t, ^{3}J =7.1 Hz, 6H, $H^{6, 8}$); $^{13}C\{^{1}H\}$ NMR (126 MHz, THF-d_8, 298 K): δ = 172.1 ($C^{1,3}$), 61.0 (C^{2}), 57.3 ($C^{5,7}$), 15.7 (C^{4}), 12.2 ($C^{6,8}$).

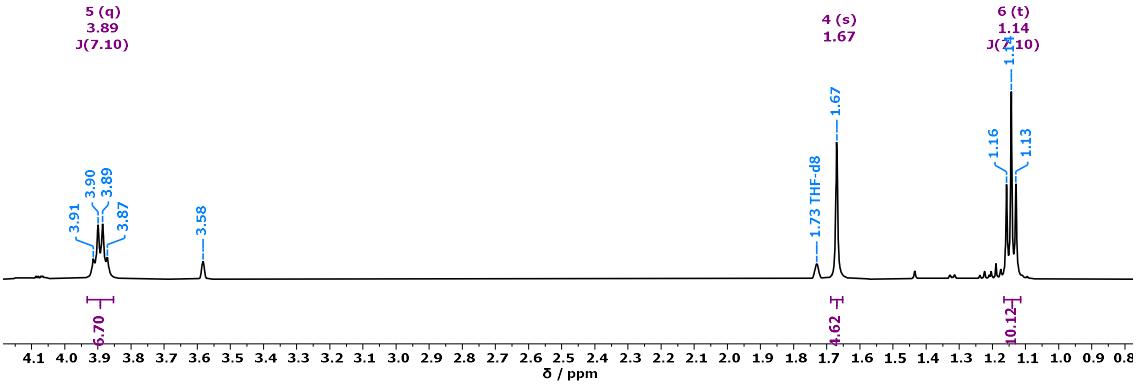

Figure A1.101 KDEMM ^{1}H NMR (500 MHz, d_8-THF, 298 K).

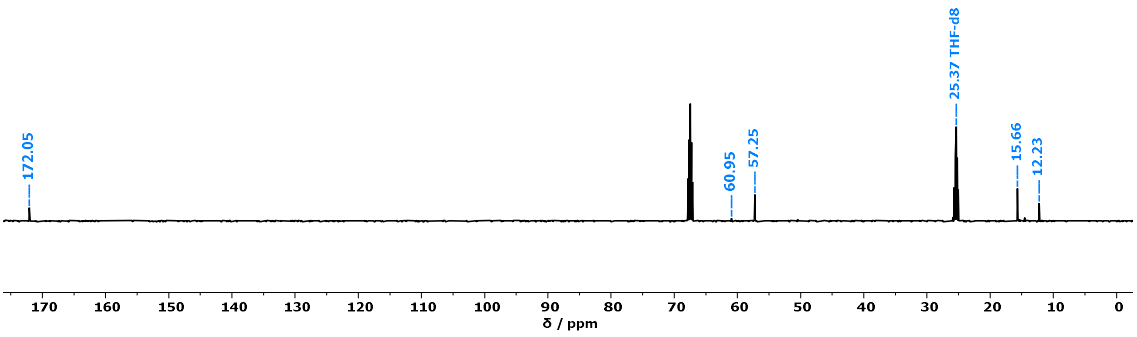

Figure A1.102 KDEMM ^{13}C{^{1}H} NMR (126 MHz, d_8-THF, 298 K).

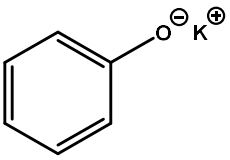

Synthesis of potassium phenolate (KOPh). Phenol (3 g, 1.5 eq.) were dissolved in THF (6 ml) in a schlenk and added dropwise *via* cannula transfer to a schlenk containing a slurry of potassium hydride (0.85 g, 1 eq.) in THF (6 ml). After stirring for 16 h volatiles were removed *in vacuo* and the solid washed with pentane (3 x 20 ml) and dried *in vacuo* to yield a white solid (96.16 %), mp 103-104 °C. ^{1}H NMR (500 MHz, THF-d_8, 298 K): δ = 6.53 (m, 2H, *o*-C$_6$***H***$_5$), 6.51 (dd, J = 8.4, 0.80 Hz, 2H, *m*-C$_6$***H***$_5$), 6.25 (tt, J = 7.2, 1.2 Hz, 1H, *p*-C$_6$***H***$_5$); ^{13}C{^{1}H} NMR (126 MHz, THF-d_8, 298 K): δ = 168.3 (C^{1}), 130.0 (C^{3,5}), 118.7 (C^{2,6}), 113.0 (C^{4}).

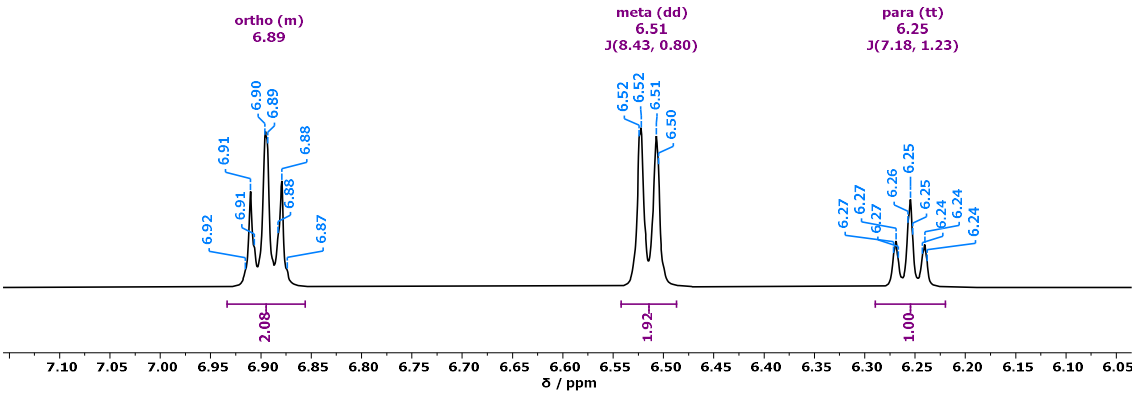

Figure A1.103 KOPh ^{1}H NMR (500 MHz, d_8-THF, 298 K).

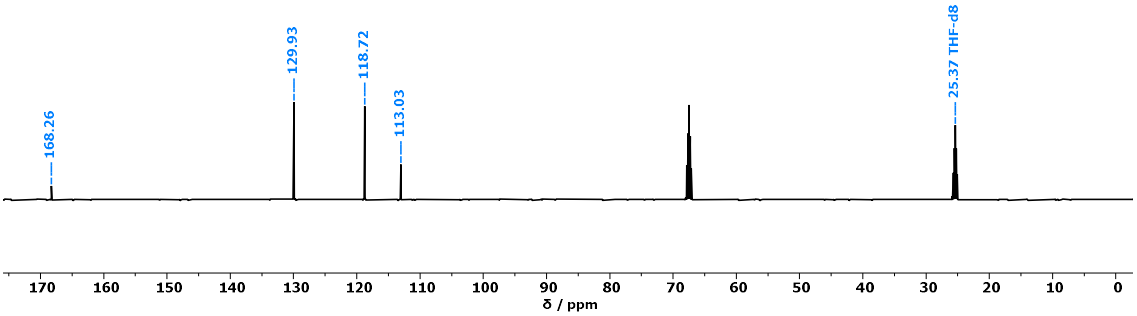

Figure A1.104 KOPh $^{13}C\{^{1}H\}$ NMR (126 MHz, d_8-THF, 298 K).

Lithium phenyl acetylide synthesised according to literature.[8]

A1.6. Thermal stability studies of phosphonate functionalised polypropylene

Table A1.3 Thermal characterisation data of polymers.

Functionality	Incorporation[a] (mol%)	T_m[b] (°C)	Crystallinity[b] (%)	$T_{10\%}$[c]	$T_{50\%}$[c]	Residue[c,d]	$T_{max\ (1)}$[c]	$T_{max\ (2)}$[c]
PP		111	38	246	277		275	
PP$_{Br}$	3.99	91	27	295	362		369	
	6.84	83	22	294	376		380	
	7.98	77	19	302	380		388	
PP$_{PPr}$	3.99	89	27	260	417	6.9	277	440
	6.84	77	20	274	438	6.9	281	443
	7.98	77	11	273	437	9.4	279	443
PP$_{PPh}$	3.99	95	32	275	409	5.1	337	456
	6.84	84	24	304	450	5.8	346	458
	7.98	76	26	323	452	6.6	346	458

[a]Determined by ^{1}H NMR. [b]Determined by DSC. [c]TGA analyses were performed between 50-800 °C under a synthetic air atmosphere (20:80 O_2:N_2) with heating rate of 20 °C min^{-1} with values reported in °C. [d]Residue (%) at 700 °C

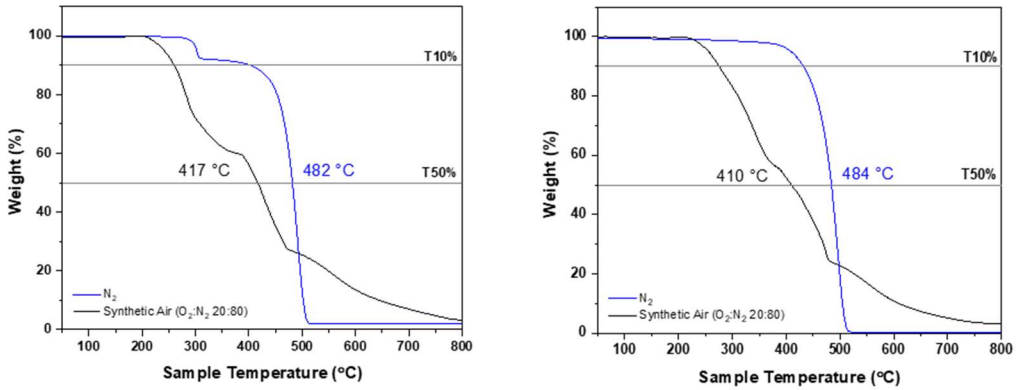

Figure A1.105 (left) **PP$_{PPr}$** and (right) **PP$_{PPh}$** TGA analyses, performed between 50-800 °C with heating rate of 20 °C min^{-1}

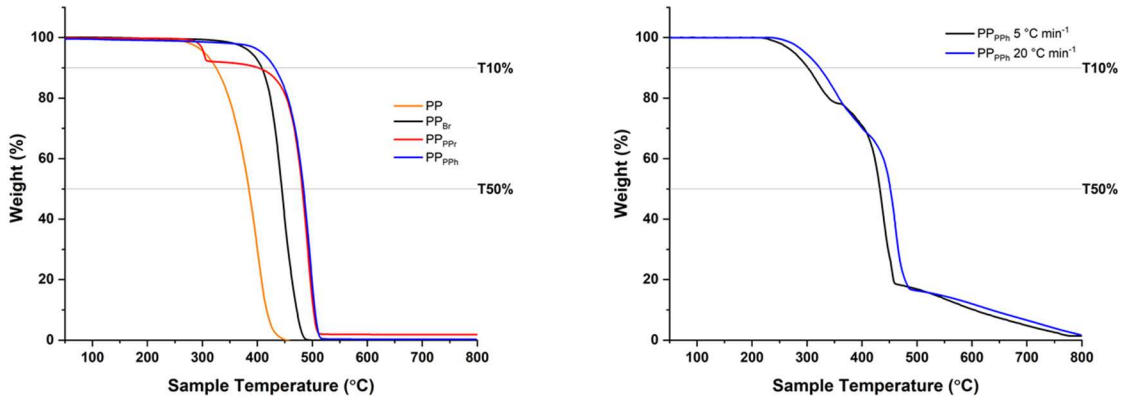

Figure A1.106 TGA curves of (left) (co)polymers under a N_2 atmosphere and (right) **PP$_{PPh}$** under a synthetic air atmosphere with different heating rates.

A1.7. Lap shear strength

Table A1.4 LSS measured adhesive forces

Entry	Steel		Aluminium	
PP	0.07983	(0.06995)	0.14622	(0.06299)
PP$_{Br}$	0.27859	(0.2268)	2.05613	(0.68799)
PP$_{DEA}$	0.38582	(0.18388)	1.76286	(0.69736)
PP$_{EAE}$	1.65481	(0.76366)	2.59508	(0.61809)
PP$_{DEOA}$	5.03594	(0.9856)	3.85552	(0.85359)

Values reported in MPa. One standard deviation, shown in brackets (σ).



Figure A1.107 Cohesive failure of **PP$_{DEOA}$** between steel plates.

A1.8. Cross-linking and vulcanisation of PP$_{AA}$

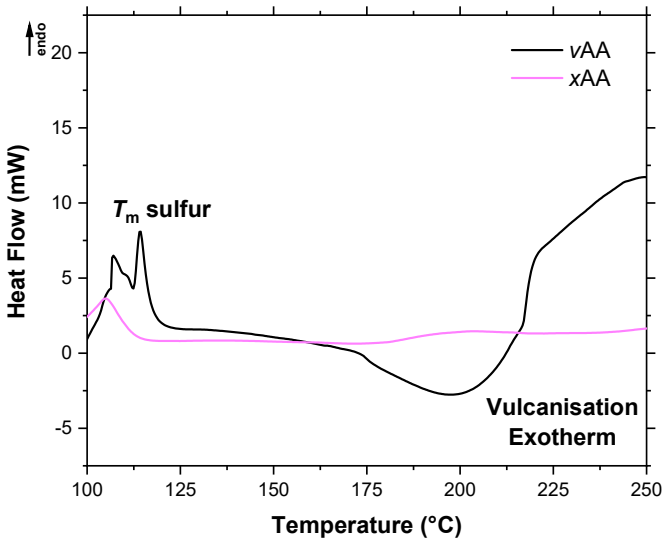

Figure A1.108 DSC thermograms for **PP$_{AA}$**/S/MBT vulcanisation at a heating rate of 20 °C min^{-1} under and inert atmosphere.

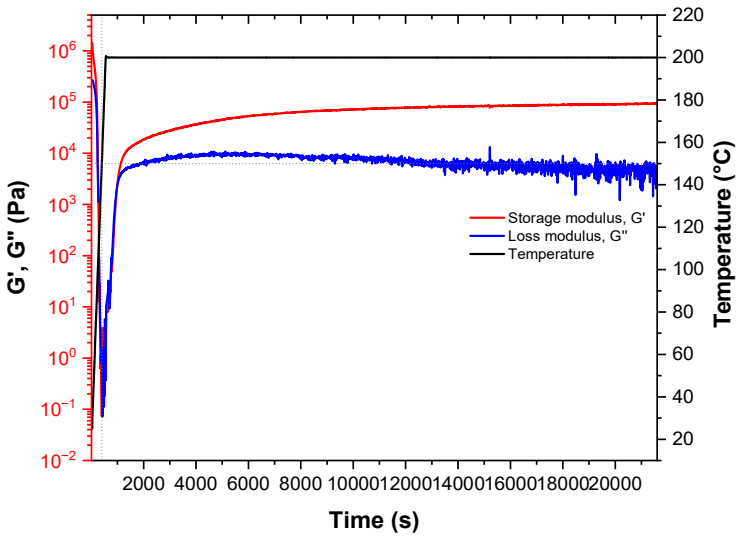

Figure A1.109 Rheometry (ω = 1 rad s^{-1}, 0.2% strain; temperature ramp 25–200 °C at 20 °C min^{-1}) as a function of time for PP_{AA}/S/MBT vulcanisation. Full experimental: 6 h cure time at 200 °C. Dynamic crosslinking shown by increase in storage modulus, G', over time. Storage modulus, G'; loss modulus, G''.

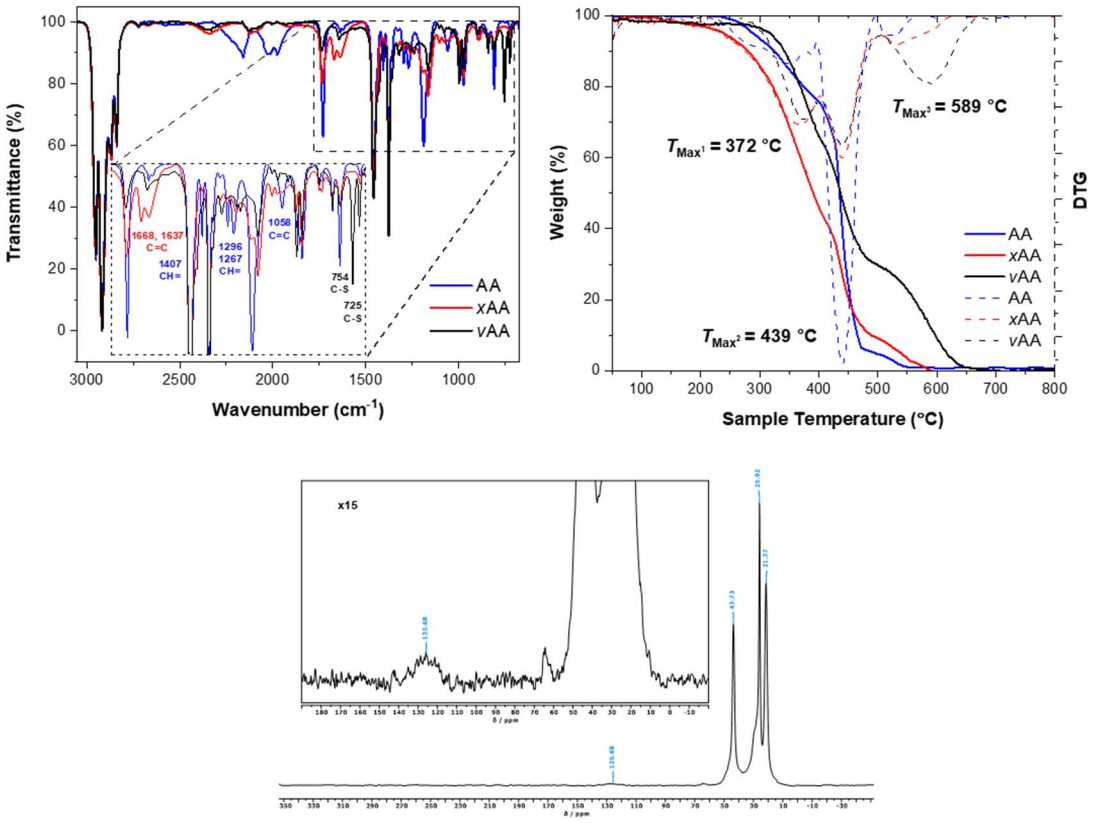

Figure A1.110 Characterisation of ***v*PP$_{AA}$** (black): FT-IR spectrum (top left), TGA thermograph (top right), and solid state (101 MHz, 10 kHz, 298 K) $^{13}C\{^{1}H\}$ NMR spectroscopy. **PP$_{AA}$** (blue) and ***x*PP$_{AA}$** (red) are overlayed in both FT-IR and TGA graphs for comparison.

A1.9. References

1 D. F. Shriver and M. A. Drezdon, *The Manipulation of Air-Sensitive Compounds*, 2 edn., Wiley, 1986.
2 N. C. Restrepo-Zapata, T. A. Osswald, J. P. Hernández-Ortiz, *Polym. Eng. Sci.*, 2015, **55**, 2073-2088.
3 V. Busico, R. Cipullo, G. Monaco, M. Vacatello, A. L. Segre, *Macromolecules*, 1997, **30**, 6251-6263.
4 M. Fineman and S. D. Ross, *J. Polym. Sci.*, 1950, **5**, 259-262.
5 Y. V. Kissin, L. A. Rishina, E. I. Vizen, *J. Polym. Sci., Part A: Polym. Chem.*, 2002, **40**, 1899-1911.
6 T. C. Wong, L. R. Collazo, F. S. Guziec, *Tetrahedron*, 1995, **51**, 649-656.
7 J. A. Jarvis, I. M. Haies, P. T. Williamson, M. Carravetta, *Phys. Chem. Chem. Phys.*, 2013, **15**, 7613-7620.
8 M. Witanowski and G. A. Webb, in *Annual Reports on NMR Spectroscopy*, ed. E. F. Mooney, Academic Press, 1972, vol. 5, pp. 395-464.
9 C. Jiang, P. J. Young, C. B. Durr, T. F. Spilker, M. H. Chisholm, *Inorg. Chem.*, 2016, **55**, 5836-5844.

A2. Supplementary data for Chapter Three

Synthesis, characterisation, thermal property, and flame retardancy of phosphonate functionalised polypropylenes

Alexander Evans, Louis. J. Morris, Zoë R. Turner, and Dermot O'Hare

A2.1. General details and instrumentation

General procedures. Air- and moisture-sensitive compounds were manipulated under an inert atmosphere of nitrogen, using standard Schlenk line techniques[1] on a dual manifold vacuum/nitrogen line or in an MBraun Labmaster 100 glovebox.

Hexanes and toluene were dried using an MBraun SPS 800 solvent purification system, stored over a potassium mirror, and degassed under partial vacuum before use.

Commercially supplied materials. 11-Bromo-1-undecene (Sigma Aldrich) was dried over pre-activated 3 Å molecular sieves, filtered and freeze-pump-thaw degassed before use. Propylene (N2.5) was supplied by BOC Ltd. and was used as received. MAO was supplied by Chemtura Corporation as a slurry in toluene which was dried under vacuum before use. *rac*-ethylenebis(indenyl)zirconium dichloride and layered double hydroxide was used as supplied by SGC Chemicals PLC. Triphenyl phosphite, triisopropyl phosphite, xylene, 1,1,2,2-tetrachloroethane-d_2, triisobutylaluminium, and alumina trihydroxide were used as receive from Sigma Aldrich.

Solution NMR spectroscopy. NMR spectra were recorded on a Bruker AVD 500 MHz. Spectra were recorded at 393 K and referenced internally to the residual *protio* solvent resonance ($C_2D_2Cl_4$). Chemical shifts, δ, are reported in parts per million (ppm) relative to tetramethylsilane (δ = 0 ppm). Convection compensated diffusion experiment was

carried out using Bruker pulse program "dstebpgp3s" on a Bruker AVD 500 MHz, $C_2D_2Cl_4$, 393 K.

Gel permeation chromatography. Gel permeation chromatography (GPC) was performed by Ms Liv Thobru, Ms Sara Rund Herum, and Ms Rita Jenssen (Norner AS, Norway) on a high temperature gel permeation chromatograph with an IR5 infrared detector (GPC-IR5). Samples were prepared by dissolution in 1,2,4-trichlorobenzene (TCB) containing 300 ppm of 3,5-di-*tert*-buty-4-hydroxytoluene (BHT) at 160 °C for 90 minutes and then filtered with a 10 μm SS filter before being passed through the GPC column. The samples were run under a flow rate of 0.5 mL min^{-1} using TCB containing 300 ppm of BHT as mobile phase with 1 mg mL^{-1} BHT added as a flow rate marker. The GPC column and detector temperature were set at 145 and 160 °C respectively.

Differential scanning calorimetry. Differential scanning calorimetry was performed on a Perkin Elmer DSC 4000 System within a temperature range of 30-200 °C at a rate of 20 K min^{-1}. Polymer samples were sealed in 100 μL aluminium crucibles. An empty crucible was used as a reference, and the DSC was calibrated using indium and zinc.

Thermogravimetry. Thermogravimetric analysis was performed on a Perkin Elmer TGA 8000 thermogravimetric analyser within a temperature range of 50-800 °C. Polymer samples were loaded into pre-weighed ceramic pans and heated at a rate of 20 K min^{-1} unless otherwise stated. A purge gas of either dry nitrogen or synthetic air (20% O_2 in N_2) was used.

Fourier-Transform Infrared Spectroscopy. Fourier-Transform Infrared Spectroscopy spectra were collected on a Bruker VERTEX 80 FT-IR spectrometer fitted with a DuraSamplIR Diamond ATR. Before the sample scans, 128 scans were taken as a

background over the range 4000-400 cm^{-1}. Transmittance was recorded at a resolution of 4 cm^{-1} over the range 4000-400 cm^{-1} for 128 scans.

Microscale combustion calorimetry. Microscale Combustion Calorimetry was performed by Mr C. Chong and Mr S. Kumar (Interscience Communications, UK) in accordance with the procedure specified in clause 4.3 Method B of ASTM D 7309-19.

Quantitative bromine analysis. Quantitative bromine analysis was performed by Mr R. A. Croxall and Mr K. Bhamber (EAI Exeter Analytical, UK) in accordance with bromine method covered by ISO 17025 UKAS. An accurately weighed sample containing greater than 2 mg bromine is combusted in an oxygen flask over sodium meta-bisulphite solution. This process yields the sample into a gaseous form which is then immersed into the absorbent. The solution is acidified and boiled to dispel any chlorine fumes and titrated with silver nitrate. The end point of the titration is measured at the inflection point of the titration curve with an analytical uncertainty of 0.3% absolute.

A2.2. Solution-phase copolymerisation of propylene and bromoalkenes

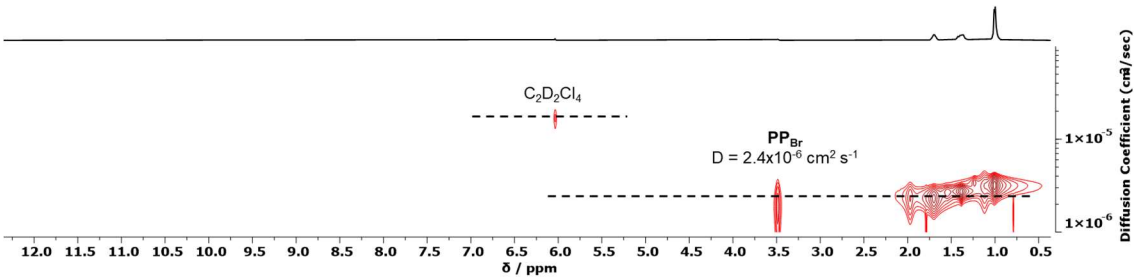

Figure A2.1 DOSY ^{1}H NMR spectra (500 MHz, $C_2D_2Cl_4$, 393 K).of $\mathbf{PP_{Br}}$.

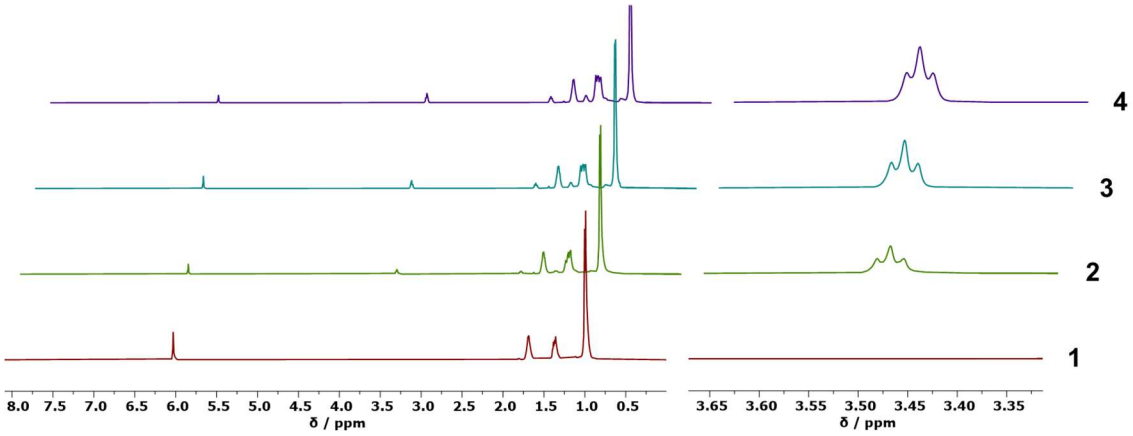

Figure A2.2 Stacked **PP** and **PP$_{Br}$** ^{1}H NMR (500 MHz, $C_2D_2Cl_4$, 393 K) spectra of entries 1-4 (Table 2): Full spectra (left), expanded characteristic functional group peaks (middle), x100 zoom on -C*H*$_2$Br region (right).

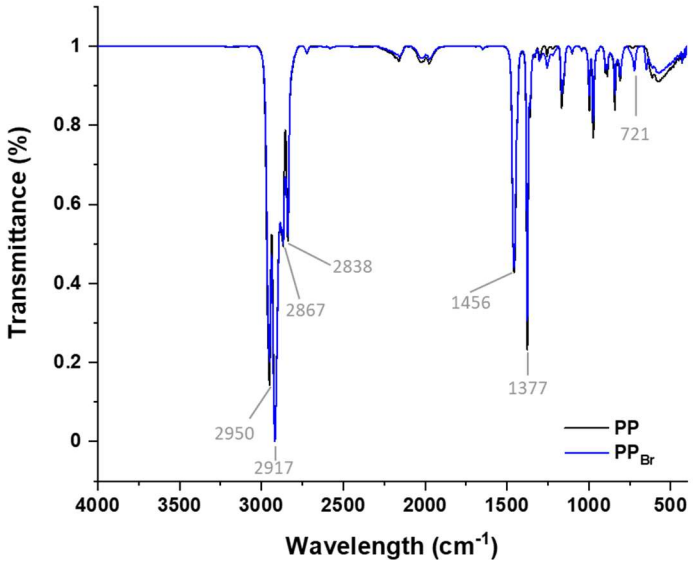

Figure A2.3 FT-IR spectrum overlay of **PP** and **PP$_{Br}$**.

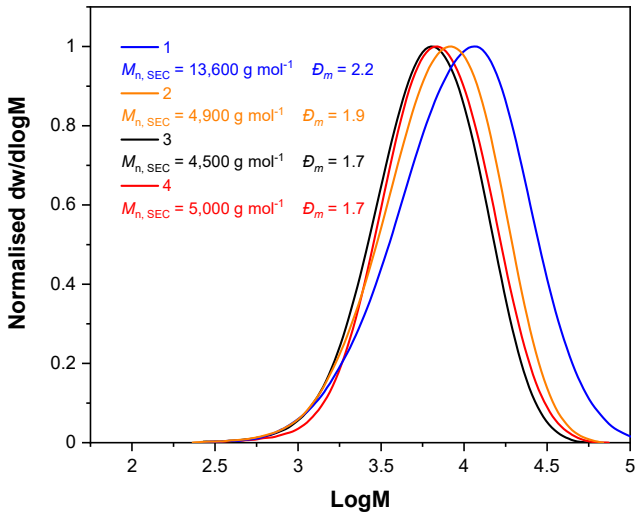

Figure A2.4 SEC traces of **PP** and **PP$_{Br}$** with varying [**11-Br**] (Table 1).

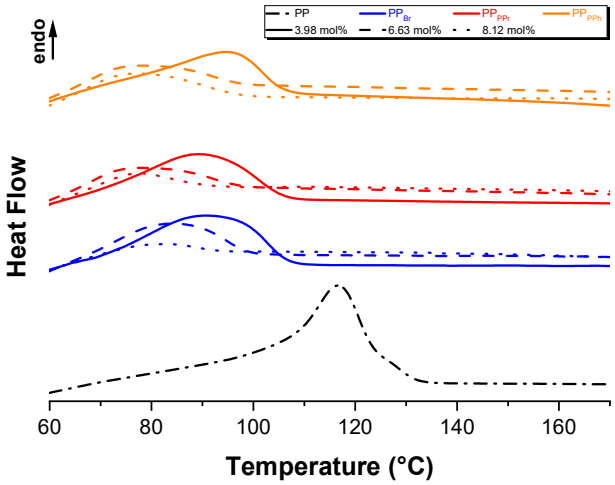

Figure A2.5 DSC traces of **PP**, **PP$_{Br}$**, **PP$_{PPr}$**, and **PP$_{PPh}$** at various mol% incorporation (Table 2).

A2.3. Post-polymerisation modification of bromo-functionalised polypropylene using phosphite esters

Table A2.5 SEC data of **PP$_{Br}$**, **PP$_{PPr}$**, and **PP$_{PPh}$** with varying incorporation levels.

Entry	Polymer	Incorporation[a] (mol%)	Con.[a] (%)	$M_{n,\,th}$[b] (g mol^{-1})	$M_{n,\,SEC}$[c] (g mol^{-1})	$Đ_m$[c]
2	**PP$_{Br}$**	3.98			5 000	1.9
5	**PP$_{PPr}$**		>99%	5 300	2 600	2.0
8	**PP$_{PPh}$**		>99%	5 600	4 200	1.9
3	**PP$_{Br}$**	6.63			4 500	1.7
6	**PP$_{PPr}$**		>99%	5 100	2 100	1.9
9	**PP$_{PPh}$**		>99%	5 500	4 200	1.7
4	**PP$_{Br}$**	8.12			5 200	1.7
7	**PP$_{PPr}$**		>99%	5 900	2 000	1.9
10	**PP$_{PPh}$**		>99%	6 400	5 100	1.8

[a]Determined by ^{1}H NMR. [b]Calculated: **PP$_{PPr}$** ($M_{n,\,SEC}$–(mol%×79.9)+(mol%×165.2)) and **PP$_{PPh}$** ($M_{n,\,SEC}$–(mol%×79.9)+(mol%×233.19)). [c]Determined by SEC.

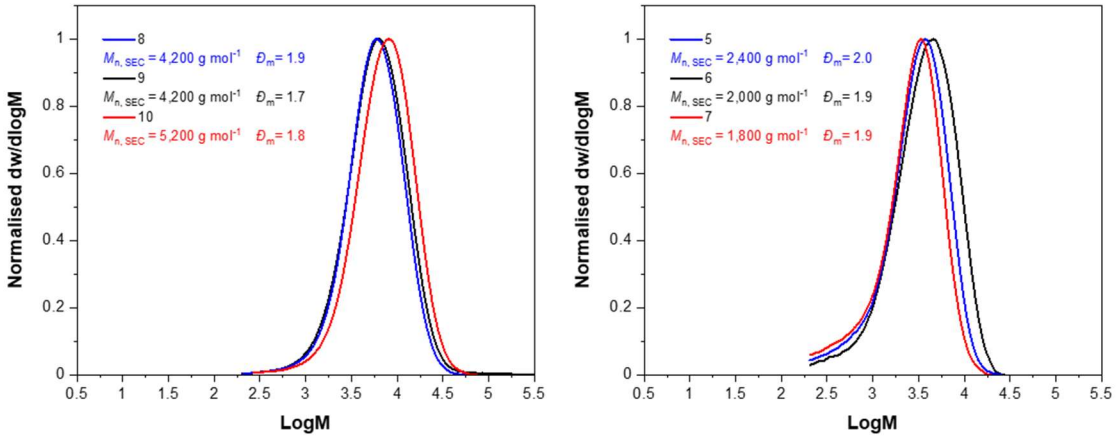

Figure A2.6 SEC traces of (left) **PP$_{PPh}$** and (right) **PP$_{PPr}$** at varying incorporation levels, relating to Table A2.1.

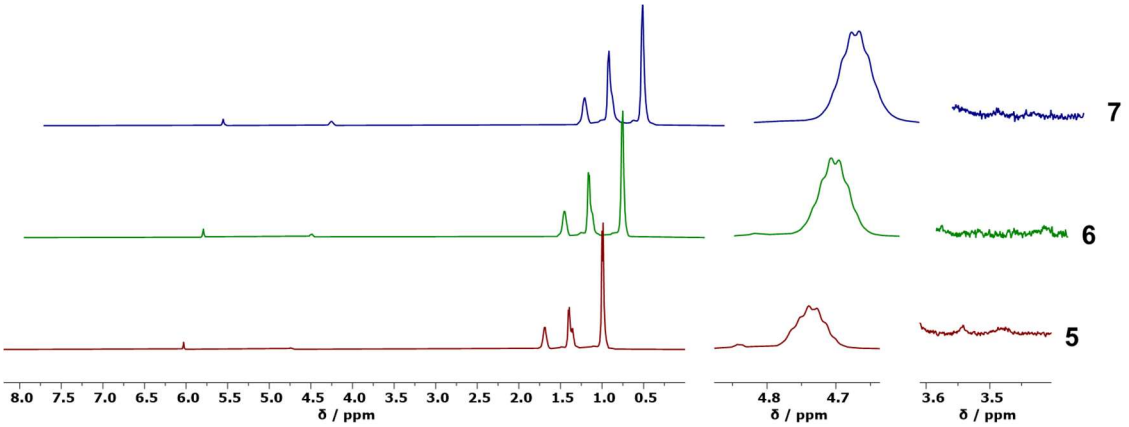

Figure A2.7 Stacked **PP$_{PPr}$** ^{1}H NMR (500 MHz, $C_2D_2Cl_4$, 393 K) spectra of entries 5-7 (Table 2): Full spectra (left), expanded characteristic functional group peaks (middle), x100 zoom on -C*H*$_2$Br region (right).

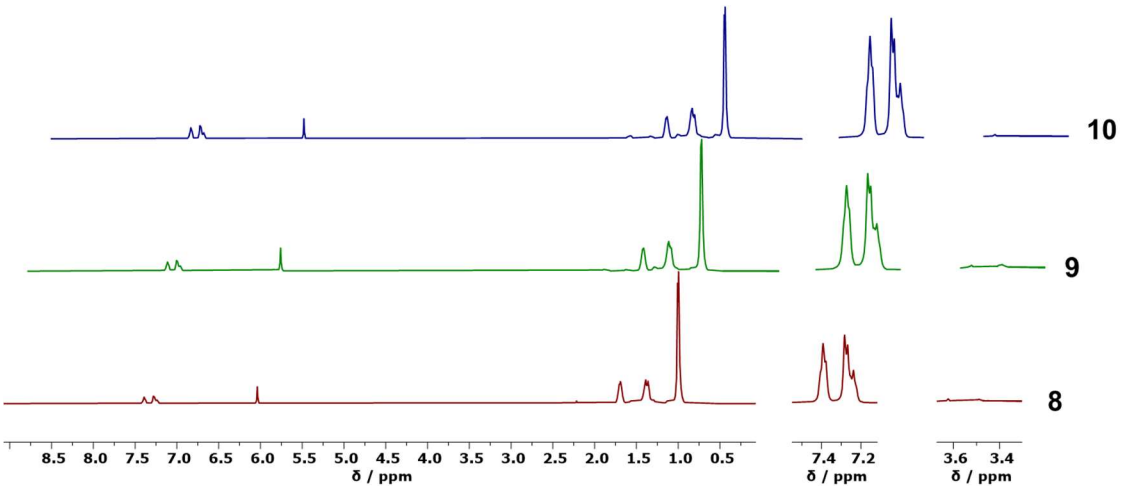

Figure A2.8 Stacked **PP$_{PPh}$** ^{1}H NMR (500 MHz, $C_2D_2Cl_4$, 393 K) spectra of entries 8-10 (Table 2): Full spectra (left), expanded characteristic functional group peaks (middle), x100 zoom on -C*H*$_2$Br region (right).

A2.4. Thermal stability studies of phosphonate functionalised polypropylene

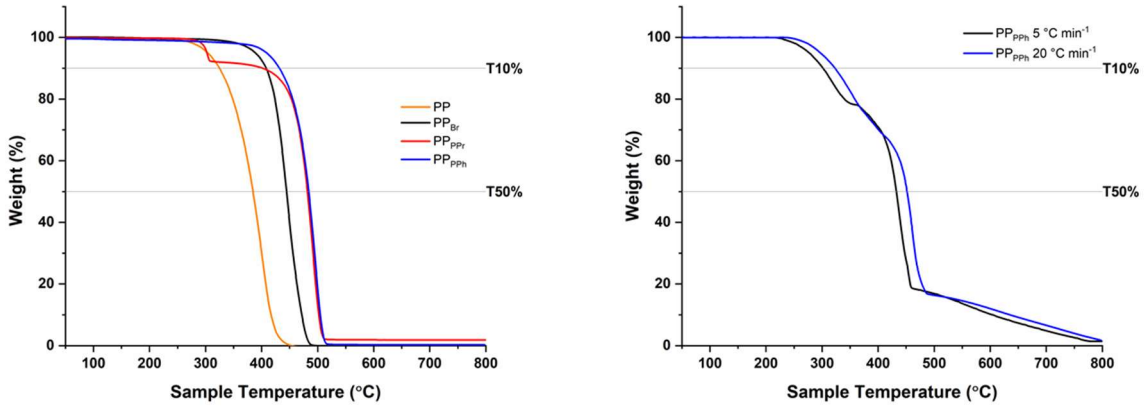

Figure A2.9 TGA curves of (left) (co)polymers under a N_2 atmosphere and (right) **PP$_{PPh}$** under a synthetic air atmosphere with different heating rates.

A2.5. Flammability studies of phosphonate functionalised polypropylene

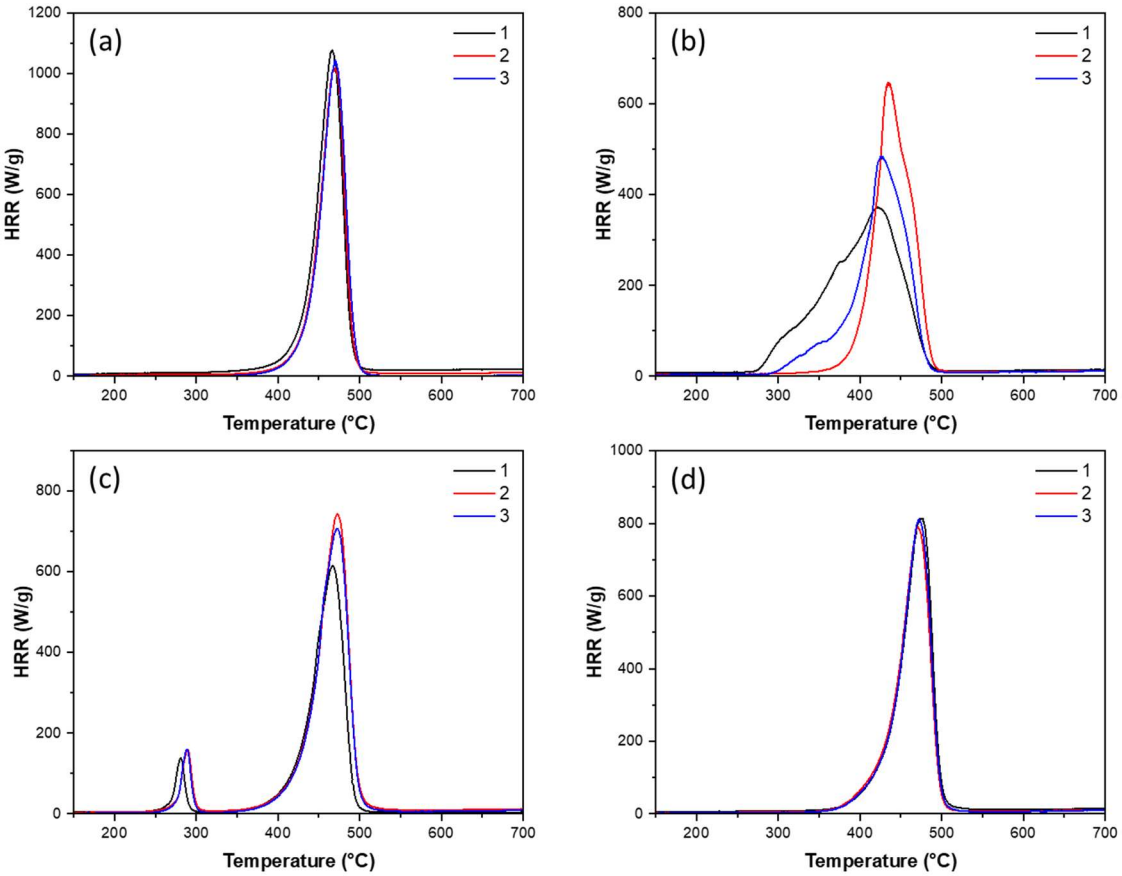

Figure A2.10 MCC plots of (a) **PP**, (b) **PP$_{Br}$**, (c) **PP$_{PPr}$**, and (d) **PP$_{PPh}$** (co)polymers (3.99 mol%) in triplicate.

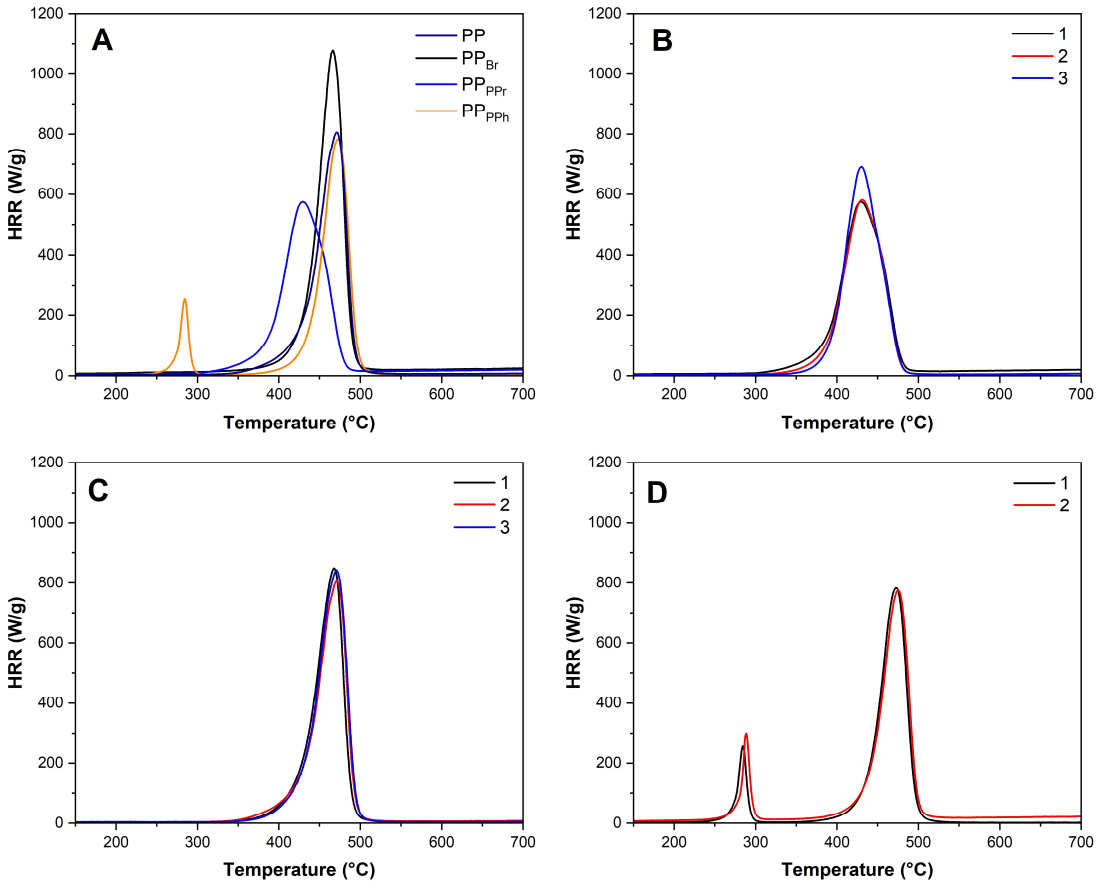

Figure A2.11 MCC plots of (a) **PP**, (b) **PP$_{Br}$**, (c) **PP$_{PPh}$**, and (d) **PP$_{PPr}$** (co)polymers (8.12 mol%).

A2.6. Polymer compounding with polypropylene and inorganic flame retardant additives…

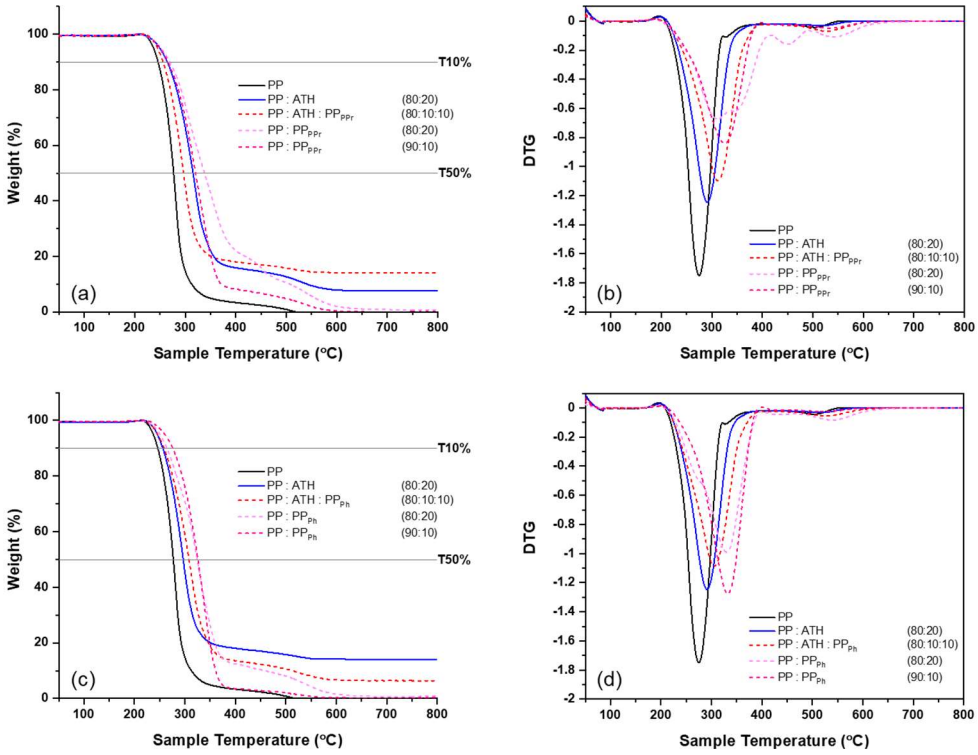

Figure A2.12 TGA curves and DTG plots of blends with modified polymers (3.99 mol%) and ATH. **PP$_{PPr}$** (a-b) and **PP$_{PPh}$** (c-d) with **PP** and ATH under a synthetic air atmosphere (20:80 O_2:N_2) with heating rate of 20 °C min^{-1}.

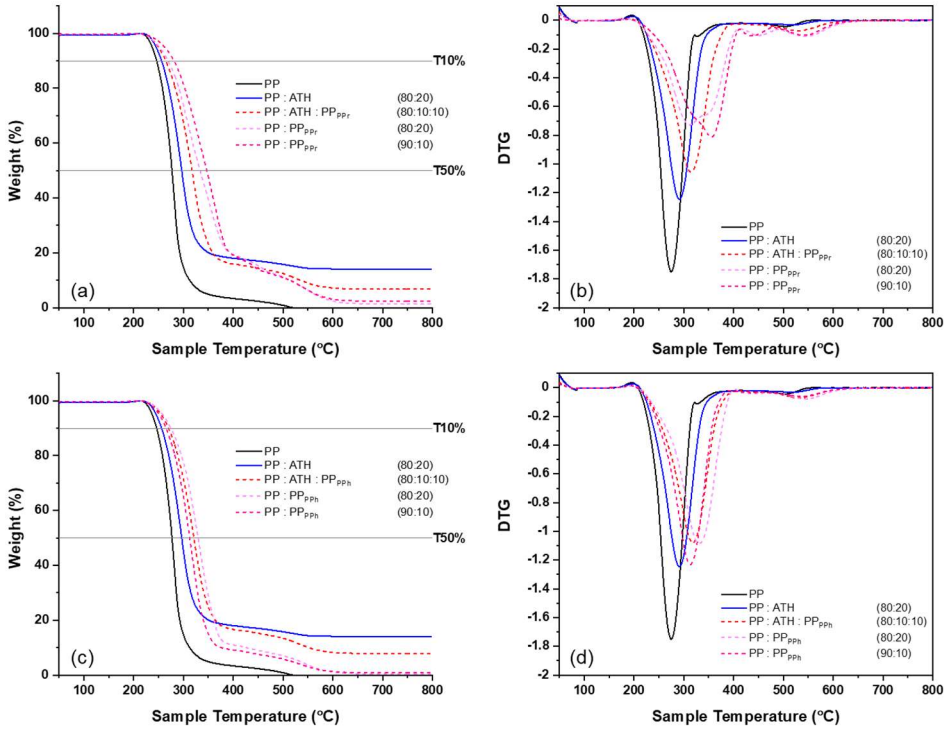

Figure A2.13 TGA curves and DTG plots of blends with modified polymers (6.84 mol%) and ATH. **PP$_{PPr}$** (a-b) and **PP$_{PPh}$** (c-d) with **PP** and ATH under a synthetic air atmosphere (20:80 O_2:N_2) with heating rate of 20 °C min^{-1}.

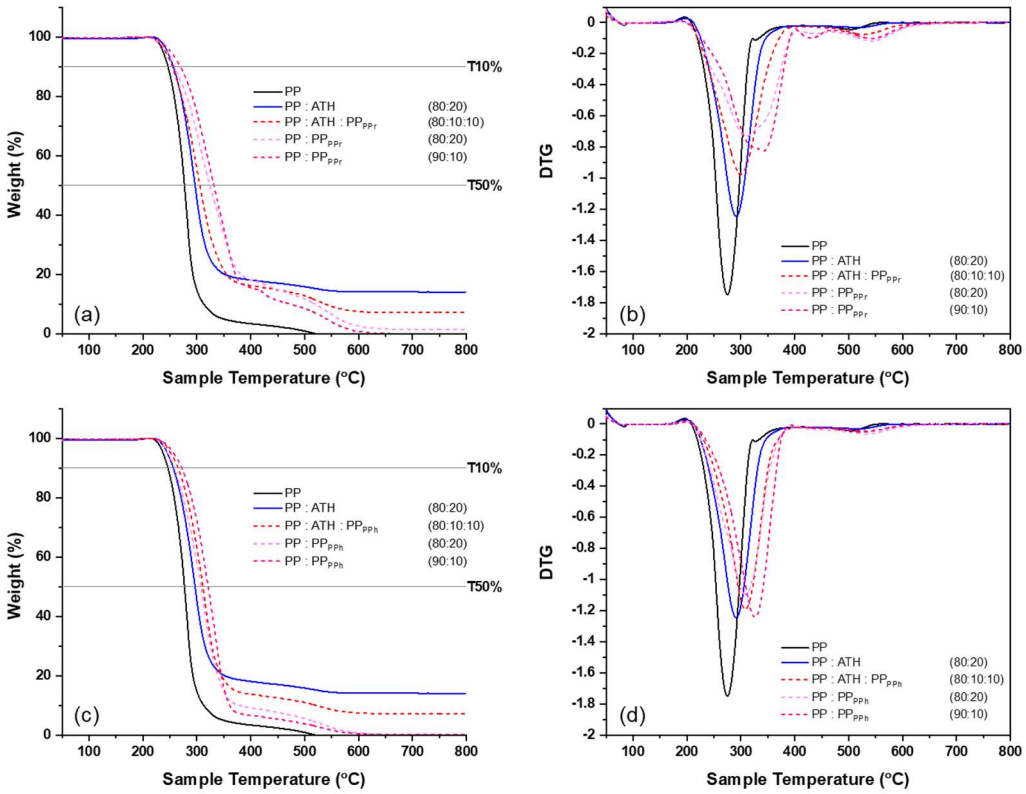

Figure A2.14 TGA curves and DTG plots of blends with modified polymers (7.98 mol%) and ATH. **PP$_{PPr}$** (a-b) and **PP$_{PPh}$** (c-d) with **PP** and ATH under a synthetic air atmosphere (20:80 O_2:N_2) with heating rate of 20 °C min^{-1}.

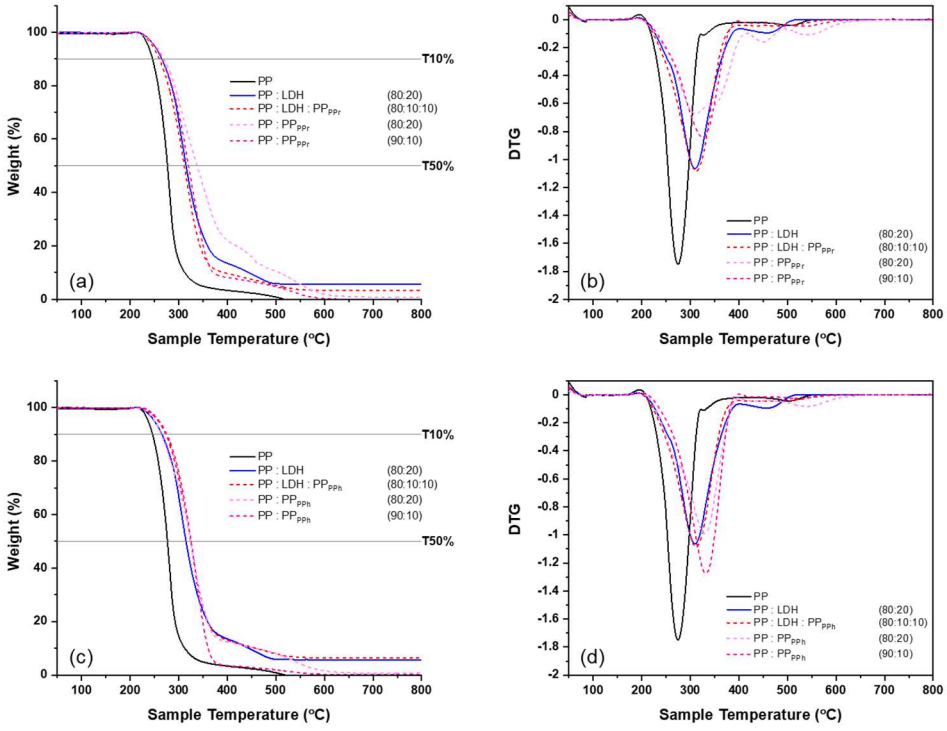

Figure A2.15 TGA curves and DTG plots of blends with modified polymers (3.99 mol%) and LDH. **PP$_{PPr}$** (a-b) and **PP$_{PPh}$** (c-d) with **PP** and LDH under a synthetic air atmosphere (20:80 O_2:N_2) with heating rate of 20 °C min^{-1}.

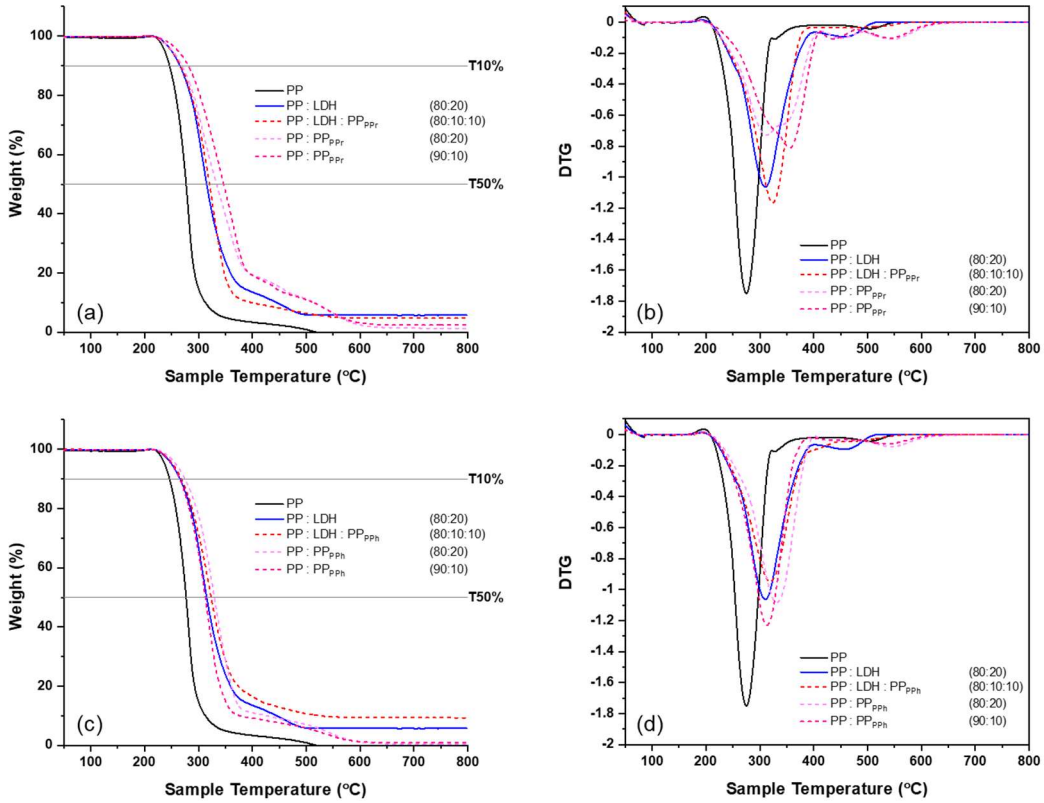

Figure A2.16 TGA curves and DTG plots of blends with modified polymers (6.84 mol%) and LDH. **PP$_{PPr}$** (a-b) and **PP$_{PPh}$** (c-d) with **PP** and LDH under a synthetic air atmosphere (20:80 O_2:N_2) with heating rate of 20 °C min^{-1}.

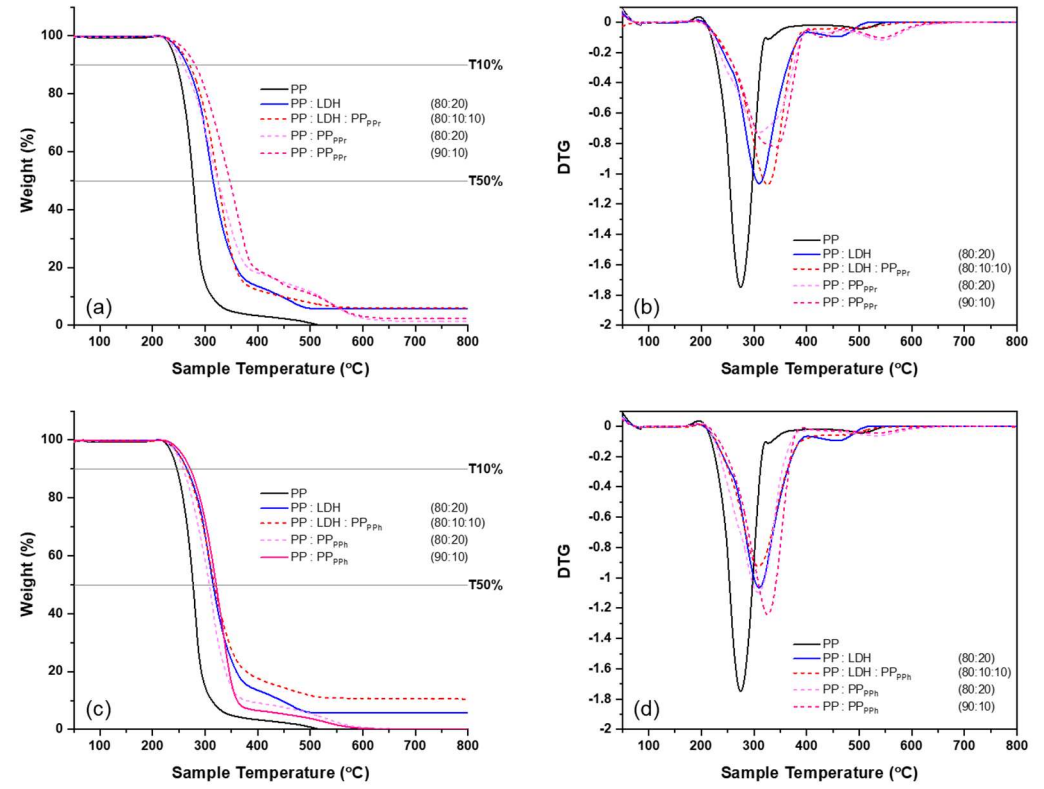

Figure A2.17 TGA curves and DTG plots of blends with modified polymers (7.98 mol%) and LDH. **PP$_{PPr}$** (a-b) and **PP$_{PPh}$** (c-d) with **PP** and LDH under a synthetic air atmosphere (20:80 O_2:N_2) with heating rate of 20 °C min^{-1}.

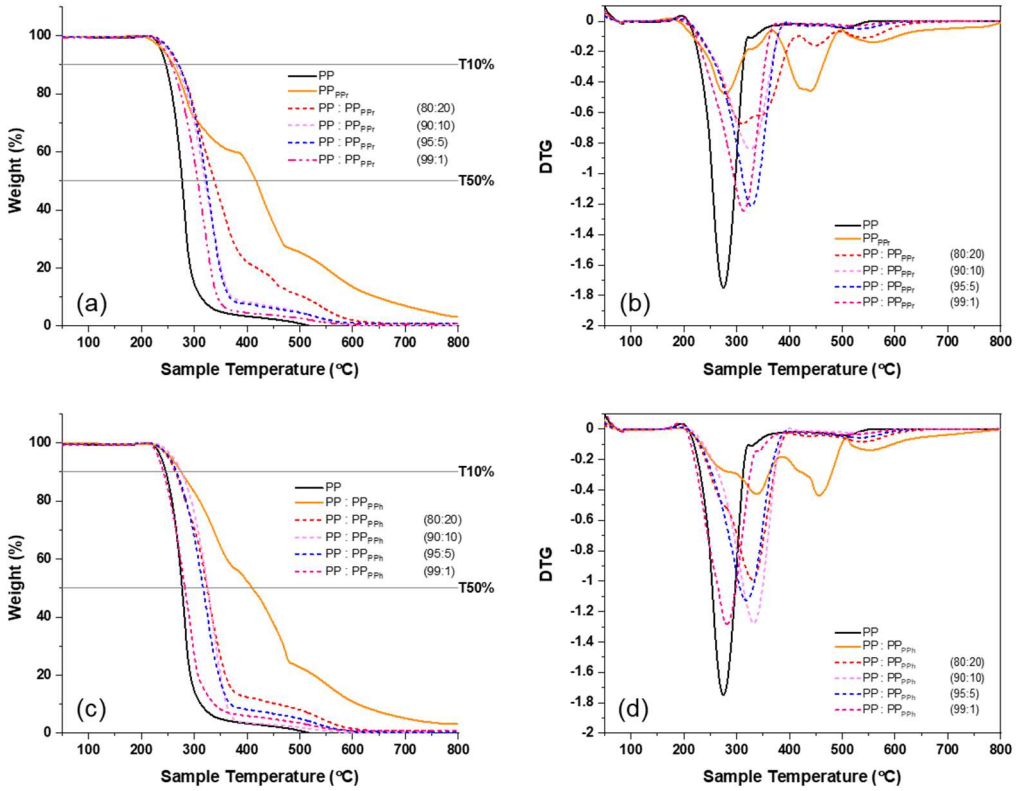

Figure A2.18 TGA curves and DTG plots of blends with modified polymers (3.99 mol%) and **PP**. **PP$_{PPr}$** (a-b) and **PP$_{PPh}$** (c-d) and associated blends with **PP** under a synthetic air atmosphere (20:80 O_2:N_2) with heating rate of 20 °C min^{-1}.

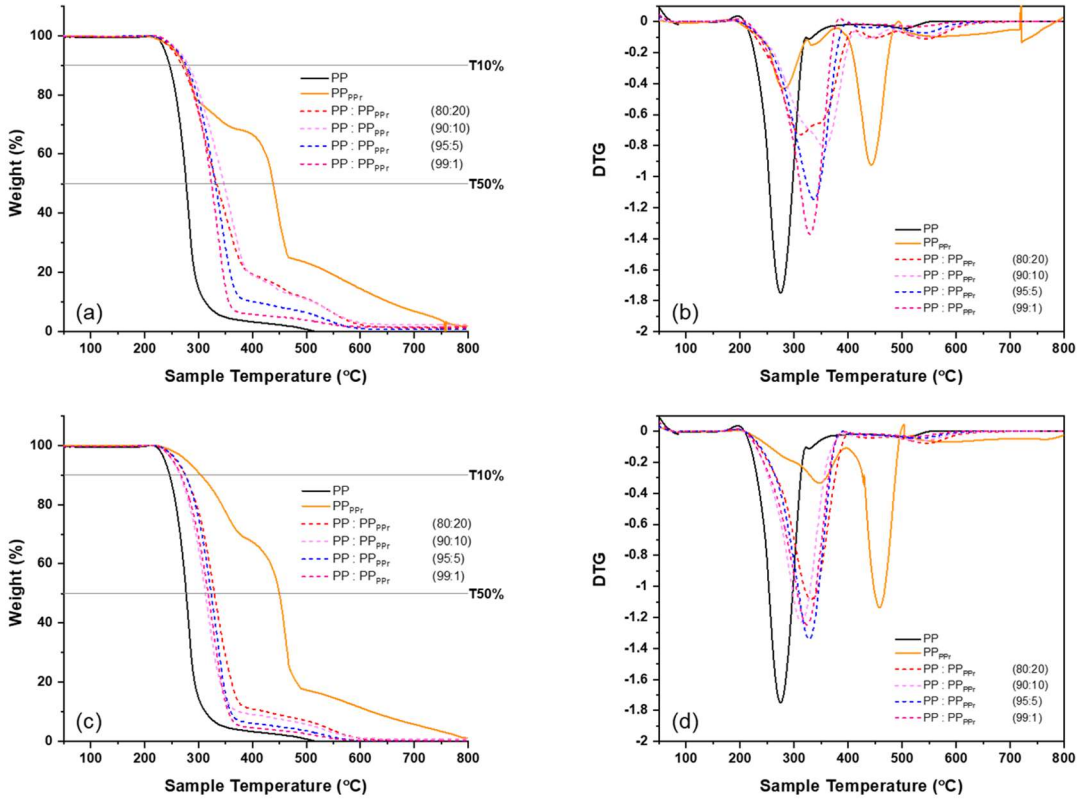

Figure A2.19 TGA curves and DTG plots of blends with modified polymers (6.84 mol%) and **PP**. **PP$_{PPr}$** (a-b) and **PP$_{PPh}$** (c-d) and associated blends with PP under a synthetic air atmosphere (20:80 O_2:N_2) with heating rate of 20 °C min^{-1}.

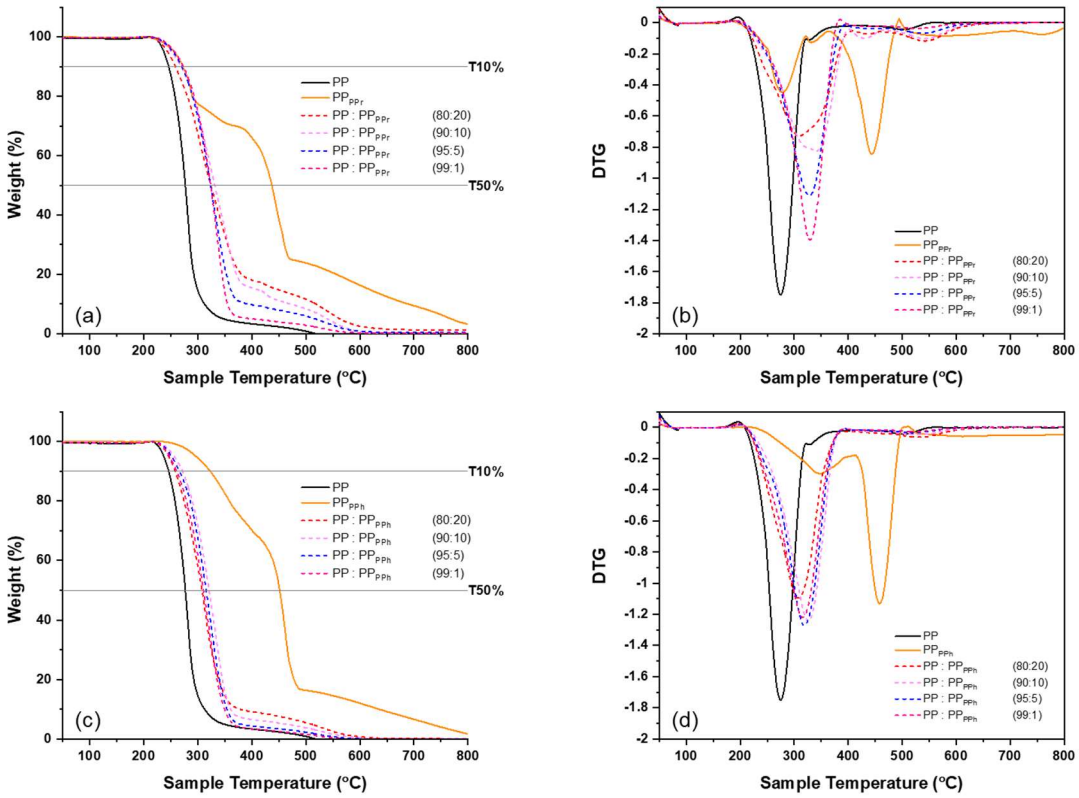

Figure A2.20 TGA curves and DTG plots of blends with modified polymers (7.98 mol%) and **PP. PP$_{PPr}$** (a-b) and **PP$_{PPh}$** (c-d) and associated blends with **PP** under a synthetic air atmosphere (20:80 O_2:N_2) with heating rate of 20 °C min^{-1}.

Table A2.6 Polymer blends thermal characterisation data.[a]

Sample	wt%	T_m[b] (°C)	Crystallinity[b] (%)	$T_{10\%}$[c]	$T_{50\%}$[c]	Residue[c,d] (%)	$T_{max\,(1)}$[c] (°C)	$T_{max\,(2)}$[c] (°C)
PP		111	38	246	277		275	
PP$_{PPr}$		77	20	274	438	6.93	281	443
PP$_{PPh}$		84	24	304	450	5.78	346	458
PP : PP$_{PPr}$	80 : 20	110	27	269	333	1.35	311	448
	90 : 10	110	35	281	347	2.37	355	
	95 : 5	111	38	277	331	0.72	337	
	99 : 1	111	36	274	324	1.65	329	
PP : PP$_{PPh}$	80 : 20	112	32	275	329	0.35	331	
	90 : 10	112	35	265	312	0.86	314	
	95 : 5	113	33	276	323	0.12	328	
	99 : 1	112	32	267	317	0.36	323	
PP : ATH	80 : 20	109	26	256	297	14.03	290	
PP : ATH : PP$_{PPr}$	80 : 10 : 10	113	29	265	317	6.78	314	
PP : ATH : PP$_{Ph}$	80 : 10 : 10	108	31	270	321	7.81	317	
PP : LDH	80 : 20	109	30	265	315	5.68	311	
PP : LDH : PP$_{PPr}$	80 : 10 : 10	114	27	267	321	4.76	323	
PP : LDH : PP$_{PPh}$	80 : 10 : 10	112	27	268	324	9.35	320	

[a]**PP$_{PPr}$** and **PP$_{PPh}$** phosphonate incorporation 6.84 % (mol%). Determined by ^{1}H NMR. [b]Determined by DSC. [c]TGA analyses were performed between 50-800 °C under a synthetic air atmosphere (20:80 O_2:N_2) with heating rate of 20 °C min^{-1} with values reported in °C. [d]Residue (%) at 700 °C.

Table A2.7 Polymer blends thermal characterisation data.[a]

Sample	wt%	T_m[b] (°C)	Crystallinity[b] (%)	$T_{10\%}$[c]	$T_{50\%}$[c]	Residue[c,d] (%)	$T_{max\ (1)}$[c] (°C)	$T_{max\ (2)}$[c] (°C)
PP		111	38	246	277		275	
PP_{PPr}		77	11	273	437	9.42	279	443
PP_{PPh}		76	26	323	452	6.60	346	458
PP : PP_{PPr}	80 : 20	113	29	258	324	1.34	310	
	90 : 10	111	36	269	331	0.00	341	
	95 : 5	111	42	270	324	0.43	328	
	99 : 1	111	36	274	324	0.18	330	
PP : PP_{PPh}	80 : 20	115	29	258	308	0.16	307	
	90 : 10	114	32	272	321	0.13	327	
	95 : 5	113	30	266	315	0.01	319	
	99 : 1	112	34	261	310	0.00	316	
PP : ATH	80 : 20	109	26	256	297	14.03	290	
PP : ATH : PP_{PPr}	80 : 10 : 10	110	37	254	306	7.08	301	
PP : ATH : PP_{PPh}	80 : 10 : 10	114	29	265	311	7.14	308	
PP : LDH	80 : 20	109	30	265	315	5.68	311	
PP : LDH : PP_{PPr}	80 : 10 : 10	110	29	270	324	5.99	327	
PP : LDH : PP_{PPh}	80 : 10 : 10	114	30	264	317	10.60	307	

[a]**PP_{PPr}** and **PP_{PPh}** phosphonate incorporation 7.98 % (mol%). Determined by ^{1}H NMR. [b]Determined by DSC. [c]TGA analyses were performed between 50-800 °C under a synthetic air atmosphere (20:80 O_2:N_2) with heating rate of 20 °C min^{-1} with values reported in °C. [d]Residue (%) at 700 °C.

A2.7. Higher molecular weight PP_{PPr} TGA analysis

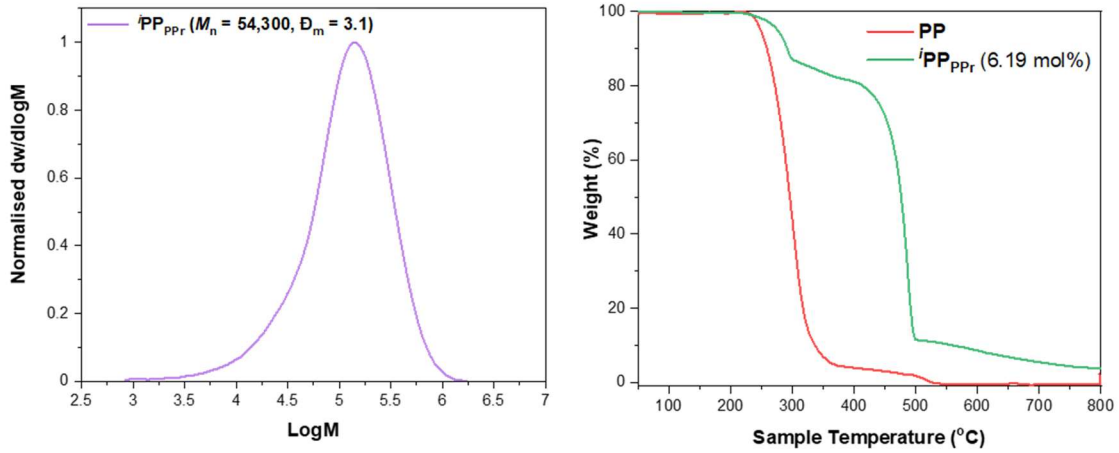

Figure A2.21 Synthesised higher M_n PP_{PPr}, **$^iPP_{PPr}$**, (left) showed increased thermal stability by TGA (right): $T_{10\%}$ = 292 °C, $T_{50\%}$ = 477 °C, $T_{max(1)}$ = 478 °C, $T_{max(2)}$ = 478 °C, Residue @700 °C = 5.52%.

A2.8. Reference

1 D. F. Shriver and M. A. Drezdon, *The Manipulation of Air-Sensitive Compounds*, 2 edn., Wiley, 1986.

A3. Supplementary data for Chapter Four

Functionalized polypropylene copolymers as mutli-substrate hot melt adhesives

Alexander Evans, Clement G. Collins Rice, Zoë R. Turner, and Dermot O'Hare

A3.1. General details and instrumentation

General procedures. Air- and moisture-sensitive compounds were manipulated under an inert atmosphere of nitrogen, using standard Schlenk line techniques[1] on a dual manifold vacuum/nitrogen line or in an MBraun Labmaster 100 glovebox.

Hexanes and toluene were dried using an MBraun SPS 800 solvent purification system, stored over a potassium mirror, and degassed under partial vacuum before use.

Commercially supplied materials. 11-Bromo-1-undecene (Sigma Aldrich) was dried over pre-activated 3 Å molecular sieves, filtered and freeze-pump-thaw degassed before use. Propylene (N2.5) was supplied by BOC Ltd. and was used as received. MAO was supplied by Chemtura Corporation as a slurry in toluene which was dried under vacuum before use. dimethylsilylene bis(2–methyl–4–phenyl–1–indenyl) zirconium (IV) dichloride was used as supplied by SGCC^{TM}. Diethylamine, ethyl(ethanol)amine, diethanol amine, 1,1,2,2-tetrachloroethane-d_2, triisobutylaluminium, were used as received from Sigma Aldrich. Plastic sheets were supplied from SCGC^{TM} (P722JO) and is a polypropylene copolymer resin. Steel sheets (QD23.5, smooth mill finish, Q-Panel) were employed as surfaces for adhesive experiments from Q-LAB.

Solution NMR spectroscopy. NMR spectra were recorded on a Bruker AVD 500 MHz. Spectra were recorded at 393 K and referenced internally to the residual *protio* solvent

resonance ($C_2D_2Cl_4$). Chemical shifts, δ, are reported in parts per million (ppm) relative to tetramethylsilane (δ = 0 ppm). Convection compensated diffusion experiment was carried out using Bruker pulse program "dstebpgp3s" on a Bruker AVD 500 MHz, $C_2D_2Cl_4$, 393 K.

Gel permeation chromatography. Gel permeation chromatography (GPC) was performed by Ms Liv Thobru, Ms Sara Rund Herum, and Ms Rita Jenssen (Norner AS, Norway) on a high temperature gel permeation chromatograph with an IR5 infrared detector (GPC-IR5). Samples were prepared by dissolution in 1,2,4-trichlorobenzene (TCB) containing 300 ppm of 3,5-di-*tert*-buty-4-hydroxytoluene (BHT) at 160 °C for 90 minutes and then filtered with a 10 μm SS filter before being passed through the GPC column. The samples were run under a flow rate of 0.5 mL min^{-1} using TCB containing 300 ppm of BHT as mobile phase with 1 mg mL^{-1} BHT added as a flow rate marker. The GPC column and detector temperature were set at 145 and 160 °C respectively.

Differential scanning calorimetry. Differential scanning calorimetry was performed on a Perkin Elmer DSC 4000 System, unless otherwise stated, within a temperature range of 30-200 °C at a rate of 5 K min^{-1}. Polymer samples were sealed in 50 μL aluminium crucibles. An empty crucible was used as a reference, and the DSC was calibrated using indium and zinc.

Lap shear strength. Samples were prepared *via* compression-molding the polymer. Propylene-based copolymers were loaded between the substrates: Steel QD35 and Plastic with overlap of 10 mm (127 mm^2 bonding area). Then, the compression-heating cycle was applied: (i) heating to 180 °C (ii) stabilizing for 5 min with no force applied, (iii) applying for 5 min with 25 kN normal force and cooling down to 40 °C under 25 kN

normal force. Before measurements, samples were conditioned for 7 days at room temperature. The measurements were performed using an Instron 5582 tensile tester equipped with a 5 kN load cell. The tests were performed on specimens (51 cm × 12.7 cm) with surface overlapping 10 mm at room temperature. A grip-to-grip separation of 140 mm was used. The samples were pre-stressed to 3 N, then loaded with a constant cross-head speed 100 mm/min. To calculate the lap shear strength the reported force value divided by the bonding surface (127 mm^2) of the specimens. The reported values are an average of at least 4 measurements of each composition.

Dynamic Rheology. Rheology was performed on a TA Instruments Discovery HR-2 hybrid rheometer using a temperature controlled stainless steel Peltier plate and a flat parallel plate geometry (20 mm diameter) with a working gap of 1000 μm. Approximately 180 mg sample polymer were pressed using a pellet press under 10 tons of pressure which was then placed on the rheometer plate at 25 °C. Measurements were performed at 180 °C, soaked for 300 s prior to start of test, under a flow of dry nitrogen in continuous oscillation (direct strain) mode at a strain of 1% and a logarithmic frequency sweep was performed from 0.01–100 rad s^{-1}.

A3.2. Polymer NMR, DSC, SEC, and FT-IR characterisation

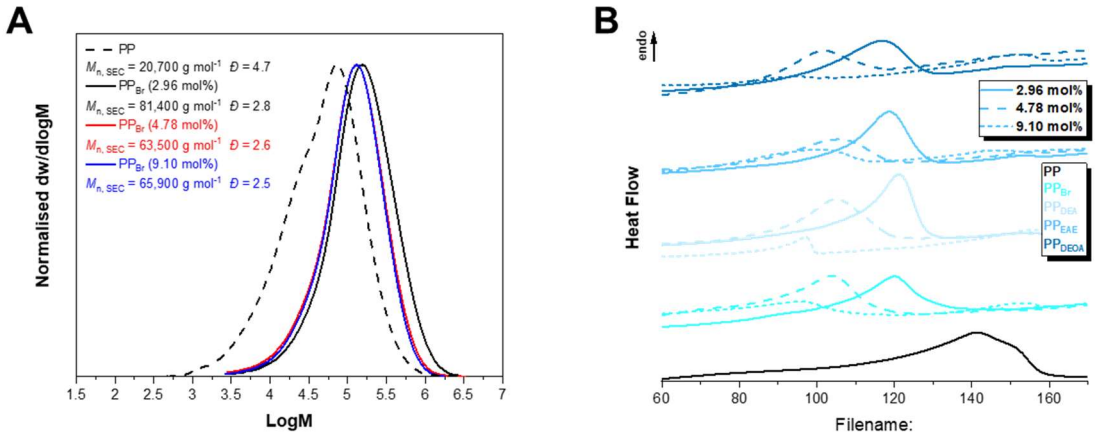

Figure A3.1 (**A**) SEC traces of **PP** and **PP$_{Br}$** at 2.96, 4.78, and 9.10 mol% incorporation. (**B**) DSC traces **PP**, **PP$_{Br}$**, **PP$_{DEA}$**, **PP$_{EAE}$**, and **PP$_{DEOA}$** at 2.96, 4.78, and 9.10 mol% incorporation.

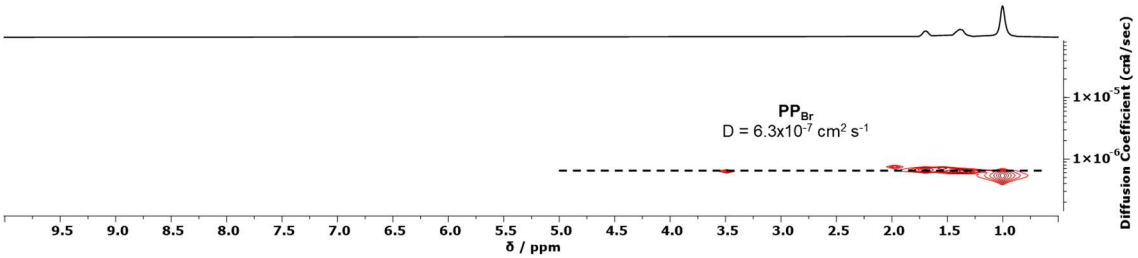

Figure A3.2 DOSY ^{1}H NMR spectra (500 MHz, $C_2D_2Cl_4$, 393 K).of **PP$_{Br}$**. For samples **PP$_{DEA}$**, **PP$_{EAE}$**, and **PP$_{DEOA}$** diffusion experiments were carried out with convection compensation, however due to the rapid relaxation of nitrogen adjacent protons –NC*H*$_2$R– it was impossible to measure accurate diffusion coefficients and evidence coupling by new characterisation methods. In previously reported work, peaks in ^{1}H NMR appeared broad and this observation was potentially explained by an increase in the relaxation rate caused by the adjacent quadrupolar ^{14}N. A lack of HMBC cross-peaks whilst still evidencing HSQC cross-peaks supported this. Additionally, when carrying out the diffusion experiment the relaxation times were fast (< ~20 ms) as observed in the T_1 inversion recovery experiment ran prior to the diffusion experiment. Previously experimentally HSQC equivalent delays were optimised for $^1J_{CH}$ 145 Hz coupling (3 ms delay) whereas HMBC experiments were optimised for a $^3J_{CH}$ 8 Hz (125 ms delay), giving the nuclei sufficient time to relax and preventing the appearance of any cross-peak to carbons adjacent to nitrogen, consequently this new evidence supports this hypothesis.[2-4]

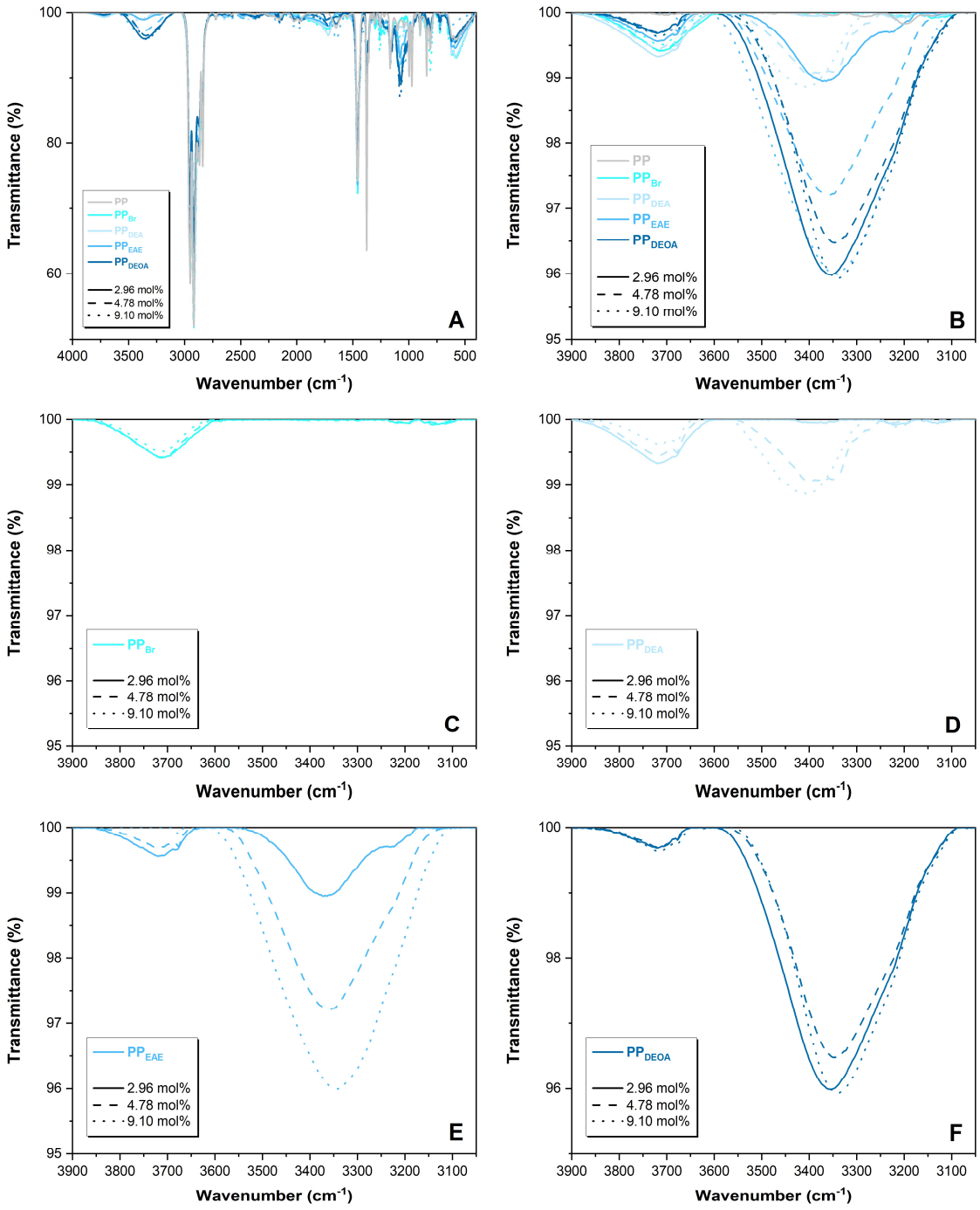

Figure A3.3 FT-IR spectrum of (**A**) **PP**, **PP$_{Br}$**, **PP$_{DEA}$**, **PP$_{EAE}$**, and **PP$_{DEOA}$** at 2.96, 4.78, and 9.10 mol% incorporation; (**B-F**) shown between 3050-3900 cm^{-1} of **PP$_{Br}$**, **PP$_{DEA}$**, **PP$_{EAE}$**, and **PP$_{DEOA}$** at 2.96, 4.78, and 9.10 mol% incorporation.

A3.3. Polymer Rheology

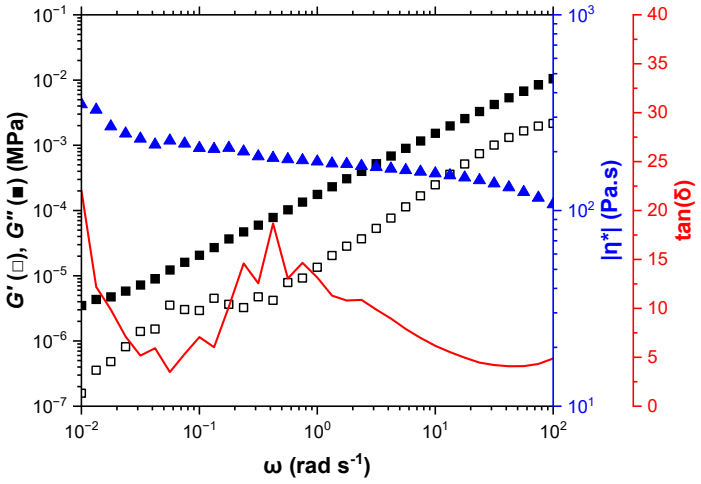

Figure A3.4 Frequency sweep rheometric curve measured at 180 °C for **PP**. Storage modulus, G′; loss modulus, G″; complex viscosity, |η*|; phase angle, δ; angular frequency, ω.

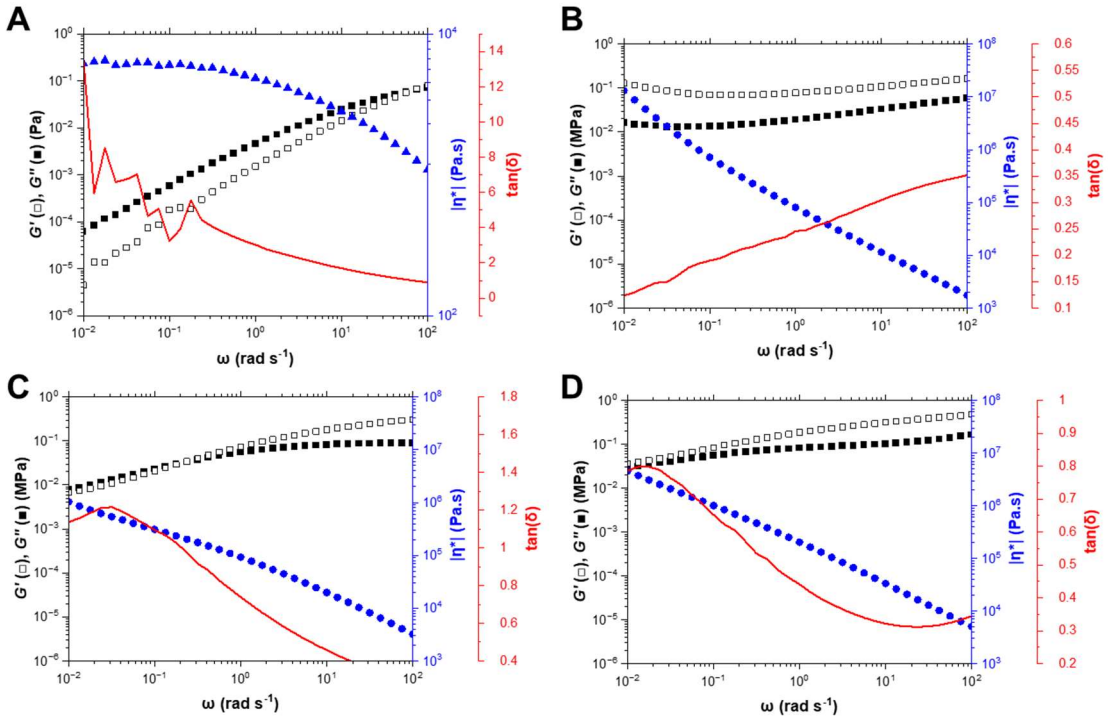

Figure A3.5 Frequency sweep rheometric curve measured at 180 °C for (**A**) **PP$_{Br}$**, (**B**) **PP$_{DEA}$**, (**C**) **PP$_{EAE}$**, and (**D**) **PP$_{DEOA}$**; 2.98 mol% incorporation. Storage modulus, G′; loss modulus, G″; complex viscosity, |η*|; phase angle, δ; angular frequency, ω.

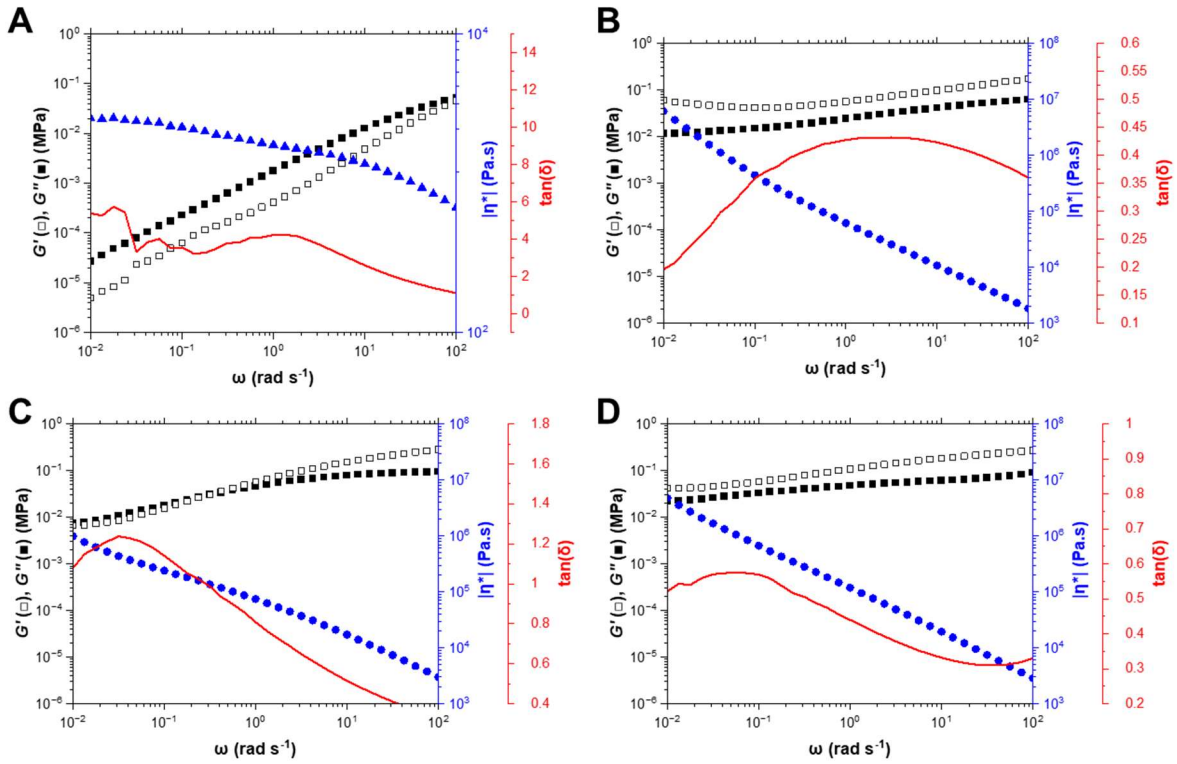

Figure A3.6 Frequency sweep rheometric curve measured at 180 °C for (**A**) **PP$_{Br}$**, (**B**) **PP$_{DEA}$**, (**C**) **PP$_{EAE}$**, and (**D**) **PP$_{DEOA}$**; 4.78 mol% incorporation. Storage modulus, G′; loss modulus, G″; complex viscosity, |η*|; phase angle, δ; angular frequency, ω.

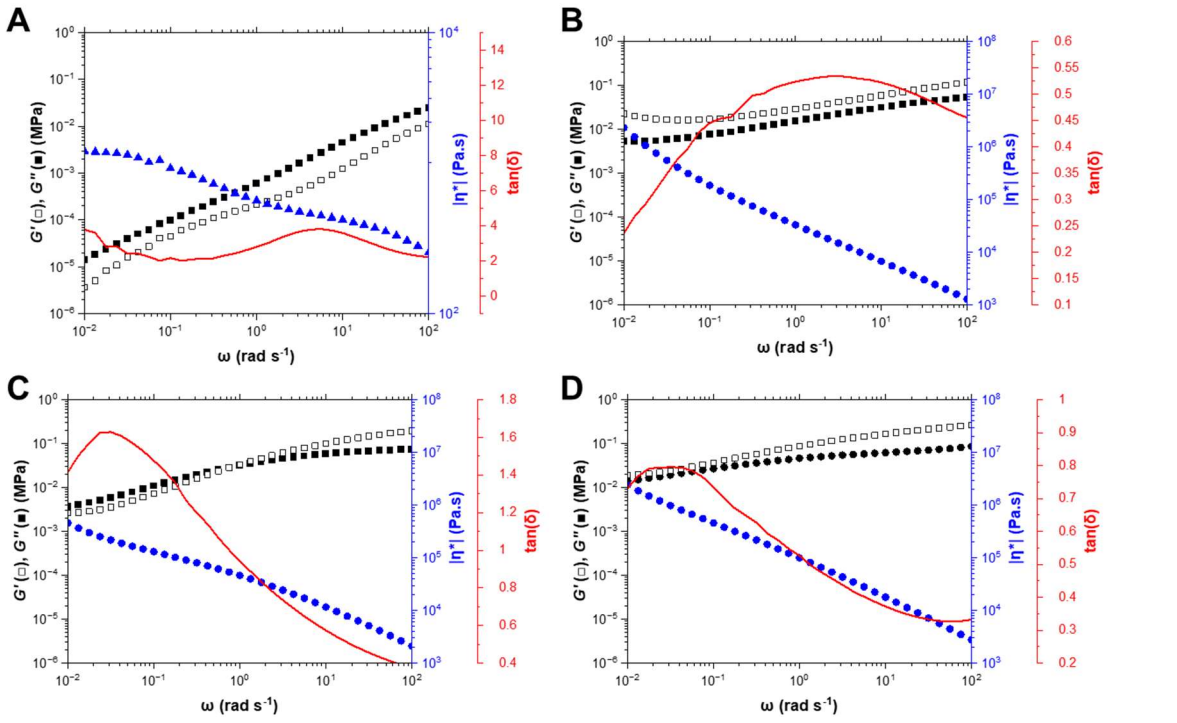

Figure A3.7 Frequency sweep small-amplitude oscillatory shear rheometry measured at 180 °C for (**A**) **PP$_{Br}$**, (**B**) **PP$_{DEA}$**, (**C**) **PP$_{EAE}$**, and (**D**) **PP$_{DEOA}$**; 9.10 mol% incorporation. Storage modulus, G′; loss modulus, G″; complex viscosity, |η*|; phase angle, δ; angular frequency, ω.

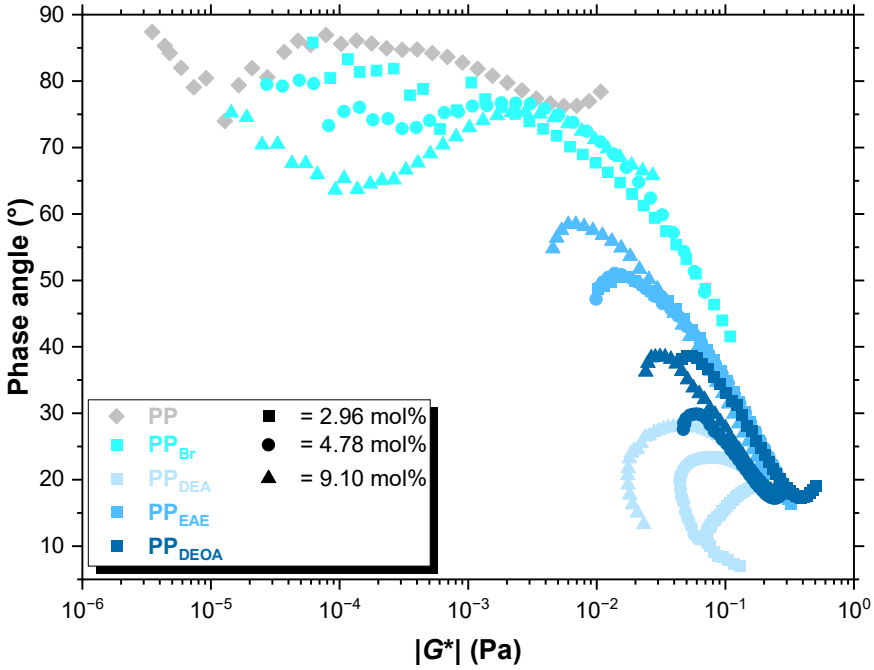

Figure A3.8 van Gurp-Palmen plot (phase angle as a function of the complex modulus), for propylene (co)polymers. A phase angle (δ) approaching 90 ° at low G^* indicates a material response dominated by viscous flow (**PP** and **PP$_{Br}$**), while decreasing δ with decreasing G^* is indicative of increased elasticity.[5] The enhanced elasticity of amine-functionalized PP can be rationalized through supramolecular network effects acting as physical crosslinks.

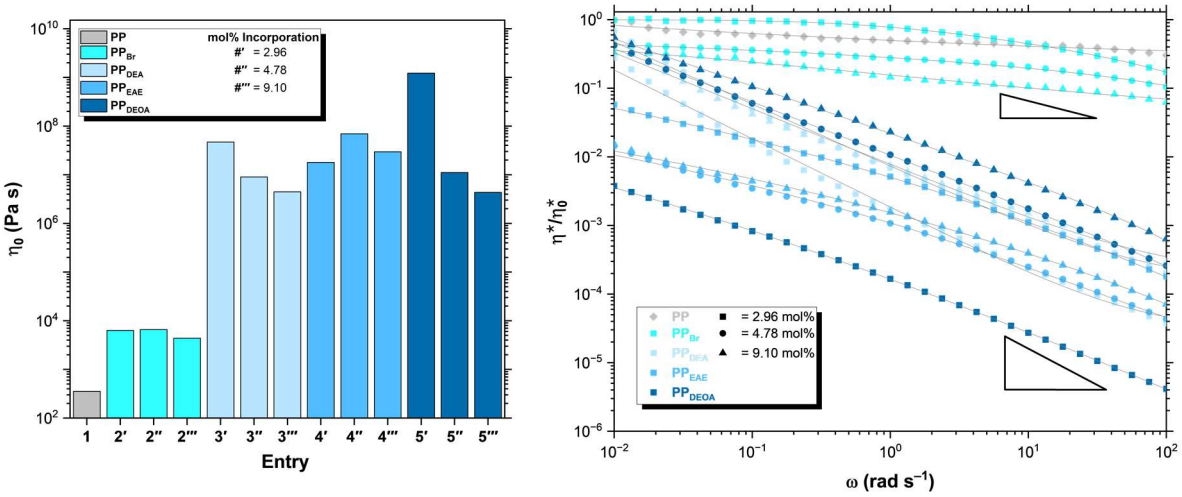

Figure A3.9 (Left) Zero-shear viscosity obtained from SAOS by fitting complex viscosity according to the Carreau equation, $\eta^*(\omega) = \eta_0^*[1 + (\lambda\omega)^2]^{\left(\frac{n-1}{2}\right)}$. (Right) Complex viscosity normalized by η^*_0 as a function of oscillation frequency. According to the Cox-Merz rule,[6] there is a direct correspondence between $\eta^*(\omega) \Leftrightarrow \eta(\dot{\gamma})$ though this generally holds more strongly for therorheologically simple materials, it has been demonstrated for virtually all single-phase polymer melts.[7, 8]

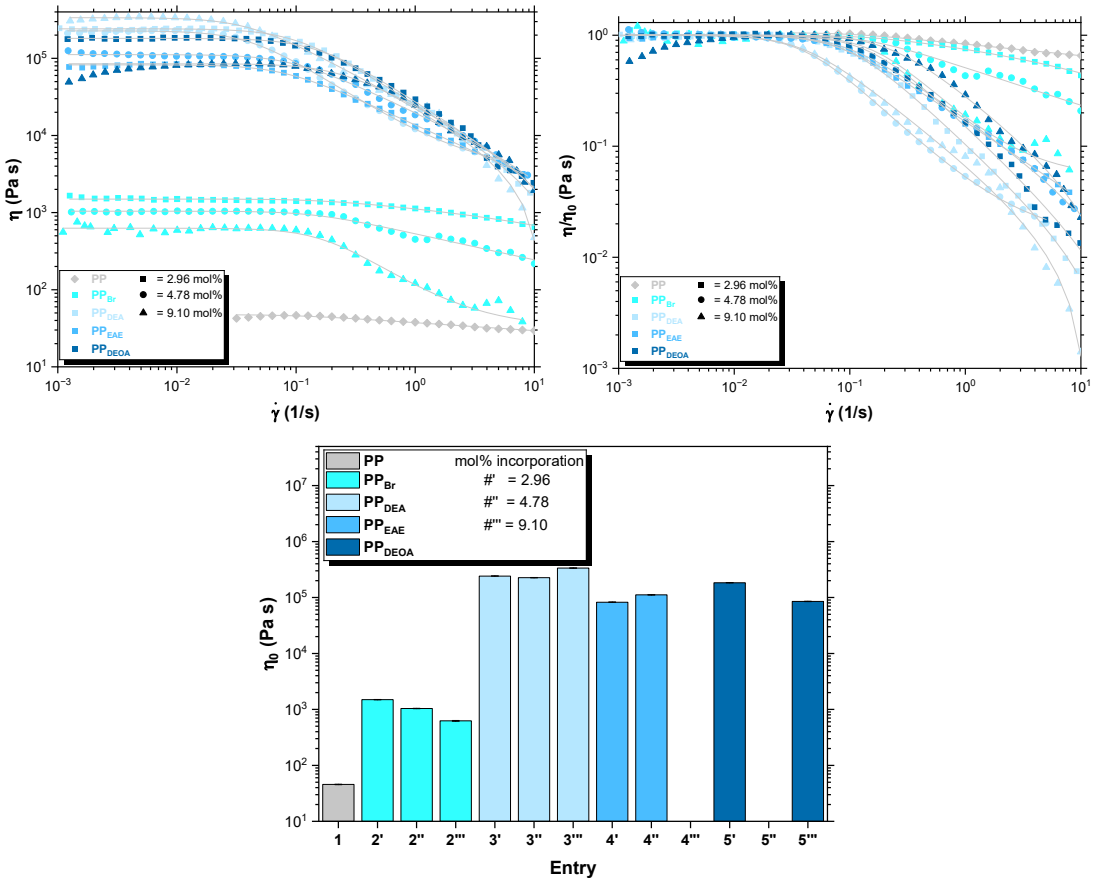

Figure A3.10 Steady-shear rheometry of **PP**, **PP$_{Br}$**, **PP$_{DEA}$**, **PP$_{EAE}$**, and **PP$_{DEOA}$**. (Top left) Viscosity, η, as a function of strain rate $\dot{\gamma}$ fitted according to the Carreau equation, $\eta(\dot{\gamma}) = \eta_0[1 + (\lambda\dot{\gamma})^2]^{\left(\frac{n-1}{2}\right)}$. (Top right) Viscosity normalized by the zero-shear viscosity. (Bottom) Zero-shear viscosity obtained from the Carreau equation. Normalization removes the effects of molecular weight and distribution with the shear sensitivity of the supramolecular network visible as shear thinning phenomena at high shear rate. At low $\dot{\gamma}$, the hydrogen bonds are quickly reformed and $\eta = \eta_0$, but at shear rates where the association time is slower than $\dot{\gamma}^{-1}$ the equilibrium between isolated and networked hydroxyls favours isolation and the measured viscosity decreases. The slope of the shear thinning therefore corresponds to the extent of the supramolecular network.

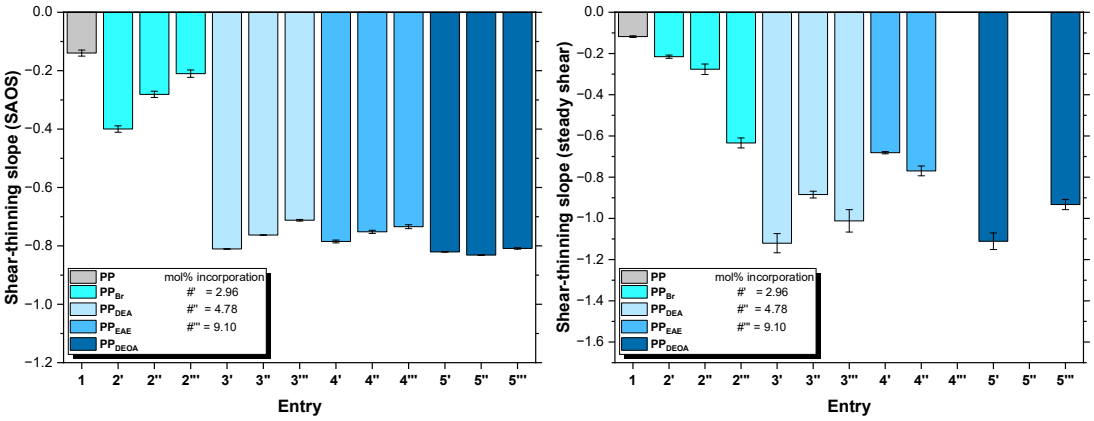

Figure A3.11 Shear-thinning slope obtained from (left) SAOS and (right) steady-shear rheometry, normalized according to the zero-shear viscosity and fitted linearly in the high-shear non-Newtonian region.

A3.4. Lap shear strength

Table A3.8 Lap shear strength measured adhesive forces

Entry	Modifier	Steel-Steel (MPa)	σ	Steel-Plastic (MPa)	σ
1		0.06906	0.04868	0.00000	0.00000
2′	Br	3.55460	1.83489	0.81125	0.29658
2″		1.80818	1.02841	3.37915	1.75443
2‴		7.58470	3.71846	0.67694	0.36955
3′	DEA	1.45805	0.86603	5.57859	0.81022
3″		7.63766	3.13881	5.91623	0.74907
3‴		6.06395	2.87239	5.50829	0.63862
4′	EAE	9.06078	2.61055	5.83722	0.42561
4″		15.16621	2.23874	6.09756	0.42094
4‴		16.83090	0.87655	5.58984	0.62375
5′	DEOA	6.66320	2.58160	3.39193	1.81558
5″		15.27748	1.41214	5.95097	0.66538
5‴		17.39507	1.57392	5.00538	0.29496

Determined by lap shear strength, mean adhesion ± one standard deviation reported.

A3.5. Modifier polarity assessment

A somewhat crude quantitative assessment of the effect of polarity, whereby incorporation is multiplied by a normalised coefficient related to any of modifier boiling point, electric dipole moment, summed heteroatom electronegativity or lone pairs, correlates fairly well to increasing adhesive strength. Importantly, this makes many assumptions and ignores a variety of intrinsic variables and should be interpretated generally and qualitatively with respect to the trends in adhesive forces.

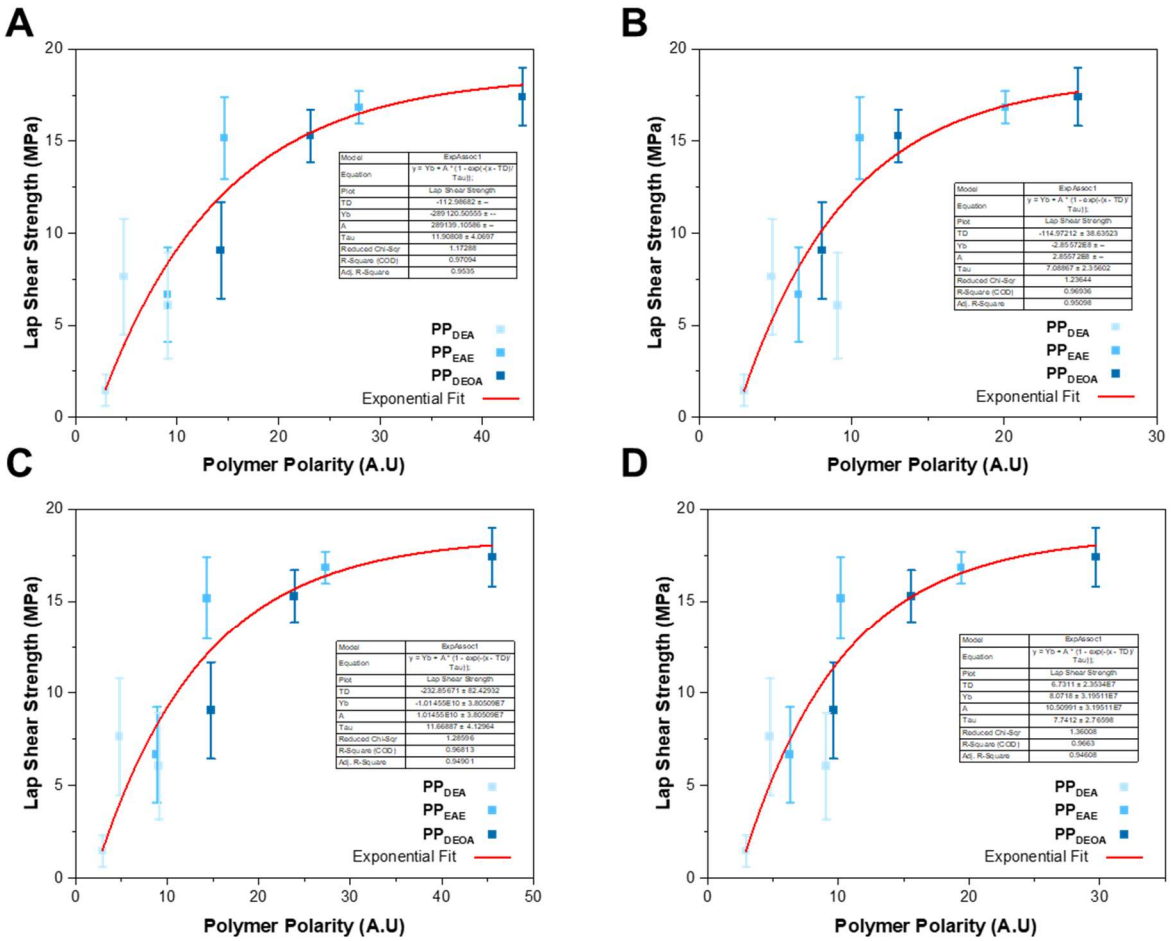

Figure A3.12 Evaluation of the relationship between lap shear strength and modifier polarity, where modifier is normalised from a physical constant: (A) modifier boiling point, (B) modifier electric dipole moment, (C) modifier summed lone pairs, and (D) modifier sum of heteroatom electronegativity.

A3.6. References

1. D. F. Shriver and M. A. Drezdon, *The Manipulation of Air-Sensitive Compounds*, 2 edn., Wiley, 1986.
2. T. C. Wong, L. R. Collazo, F. S. Guziec, *Tetrahedron*, 1995, **51**, 649-656.
3. J. A. Jarvis, I. M. Haies, P. T. Williamson, M. Carravetta, *Phys. Chem. Chem. Phys.*, 2013, **15**, 7613-7620.
4. A. Evans, O. Casale, L. J. Morris, Z. R. Turner, D. O'Hare, *Macromolecules*, 2024, **57**, 10778-10791.
5. Y. Li, Z. Yao, Z.-h. Chen, S.-l. Qiu, C. Zeng, K. Cao, *Ind. Eng. Chem. Res.*, 2013, **52**, 7758-7767.
6. W. P. Cox and E. H. Merz, *J. Polym. Sci.*, 1958, **28**, 619-622.
7. S. Gupta, X. Yuan, T. C. Mike Chung, M. Cakmak, R. A. Weiss, *Polymer*, 2016, **107**, 223-232.
8. J. Stange, C. Uhl, H. Münstedt, *J. Rheol.*, 2005, **49**, 1059-1079.

A4. Supplementary data for Chapter Five

Illuminating microplastics in cells: macro-problems for micro-barriers

Alexander Evans, Ríona M. Devereux, Zoë R. Turner, Angela J. Russell, and Dermot O'Hare

A4.1. General details and instrumentation

General procedures. Dichloromethane (DCM) were dried using an MBraun SPS 800 solvent purification system, stored over activated 3 Å molecular sieves, and degassed under partial vacuum before use.

Commercially supplied materials. *N*,*N*′-Dicyclohexylcarbodiimide (DCC), 4-(Dimethylamino)pyridine (DMAP), Rhodamine B (Rb), 1,1,2,2-tetrachloroethane-d_2, chloroform, toluene were used as received from Sigma Aldrich.

Solution NMR spectroscopy. NMR spectra were recorded on a Bruker NEO 600 (14.1 T, 600.4 MHz) with a broadband helium cryoprobe. Spectra were recorded at 393 K and referenced internally to the residual *protio* solvent resonance. Chemical shifts, δ, are reported in parts per million (ppm) relative to tetramethylsilane (δ = 0 ppm). Convection compensated diffusion experiment was carried out using Bruker pulse program "dstebpgp3s" on a Bruker AVD 500 MHz, $C_2D_2Cl_4$, 393 K.

Gel permeation chromatography. Gel permeation chromatography (GPC) was performed by Ms Liv Thobru, Ms Sara Rund Herum, and Ms Rita Jenssen (Norner AS, Norway) on a high temperature gel permeation chromatograph with an IR5 infrared detector (GPC-IR5). Samples were prepared by dissolution in 1,2,4-trichlorobenzene (TCB) containing 300 ppm of 3,5-di-*tert*-buty-4-hydroxytoluene (BHT) at 160 °C for 90 minutes and then filtered with a 10 μm SS filter before being passed through the GPC

column. The samples were run under a flow rate of 0.5 mL min^{-1} using TCB containing 300 ppm of BHT as mobile phase with 1 mg mL^{-1} BHT added as a flow rate marker. The GPC column and detector temperature were set at 145 and 160 °C respectively.

Differential scanning calorimetry. Differential scanning calorimetry was performed on a Perkin Elmer DSC 4000 System, unless otherwise stated, within a temperature range of 30-200 °C at a rate of 5 K min^{-1}. Polymer samples were sealed in 50 μL aluminium crucibles. An empty crucible was used as a reference, and the DSC was calibrated using indium and zinc.

Thermogravimetry. Thermogravimetric analysis was performed on a Perkin Elmer TGA 8000 thermogravimetric analyser within a temperature range of 50-800 °C. Polymer samples were loaded into pre-weighed ceramic pans and heated at a rate of 20 K min^{-1} unless otherwise stated. A purge gas of dry nitrogen was used.

Scanning Electron Microscopy. Scanning electron microscopy images were taken by adding samples as a solid powder to a carbon spot and placed on 12.5 mm aluminium stub before examining in a Jeol JSM6010. All samples were coated with platinum using a Quorum SC7620 Sputter Coater for 120 s before imaging. Accelerating voltages ranging from 5–15 kV were used.

Fourier-Transform Infrared Spectroscopy. Fourier-Transform Infrared Spectroscopy spectra were collected on a Bruker VERTEX 80 FT-IR spectrometer fitted with a DuraSamplIR Diamond ATR. Before the sample scans, 128 scans were taken as a background over the range 4000-400 cm^{-1}. Transmittance was recorded at a resolution of 4 cm^{-1} over the range 4000-400 cm^{-1} for 128 scans.

Ultraviolet–visible Spectroscopy. Optical measurement were conducted using UV-Vis-NIR spectrophotometer (PerkinElmer lambda 1050+). UV-Vis adsorption were measured by using a 150 mm diameter integrating sphere and 1 cm quartz cuvettes.

Dynamic Light Scattering. Hydrodynamic diameters (D_h) and size distributions were determined by dynamic light scattering on a MALVERN Zetasizer Nano ZS operating at 90 °C with a 4 mW He–Ne 633 nm laser module. Measurements were made at a detection angle of 173° (back scattering). Measurements were repeated three times with automatic attenuation selection and measurement position. The results were analysed using Malvern DTS 6.20 software. PDI values were calculated using eqn (1), where σ is the standard deviation and *d* is the diameter both obtained from the number, intensity, and volume distribution where relevant: (1) $PDI = \sigma^2/d^2$

Fluorescence Spectroscopy. Fluorescence intensity was monitored using a Shimadzu RF-6000 at an excitation wavelength of 558 nm and collection of emission at 581 nm based on using a quartz cuvette with a 1 cm path length.

Cell Culture. HEK293T cells (CRL-3216, ATCC, Manassas, VA, USA) were grown in Dulbecco's modified Eagle's medium (DMEM) containing high glucose (4.5 g/L, Sigma), 2 mM *L*-glutamine (Sigma), 10% heat-inactivated fetal bovine serum (FBS) (Sigma), 100 U/mL penicillin-streptomycin (Sigma) at 5% CO_2 and 37 °C.

AlamarBlue® cell viability assay. HEK293T cells were seeded in 96-well plates and allowed to adhere and grow for approximately 24 h in maintenance media (100 µL) at 37 °C and 5% CO_2. The cells were then treated with varying concentrations of **PP_{Rb}** for 24 h (final DMSO concentration <0.3%). AlamarBlue® reagent (Thermo Fisher Scientific) (10 µL) was added directly into the cell culture media, and the cells were

incubated in the dark for a further 4 h at 37 °C and 5% CO_2. The fluorescence (540-570 nm) and absorbance (570 and 600 nm) were then measured using a FLUOstar Omega plate reader.

Confocal imaging of Rb and PP_{Rb}. HEK293T cells were seeded onto fibronectin-treated coverslips and allowed to adhere for 24 h. The cells were then treated with 35 μM **Rb** or **PP_{Rb}** for various durations (1 or 24 h), after which the cells were washed with DPBS, fixed with 4% PFA for 10 min at RT, and washed thrice with DPBS. Coverslips were mounted on slides using Fluoromount-G™, with DAPI (Invitrogen) and allowed to set overnight at 4 °C. The cells were scanned using a Leica TCS SP5 confocal microscope (LysoTracker: λ_{ex} = 555/ λ_{em} = 567 nm, DAPI: λ_{ex} = 358/ λ_{em} = 461 nm) and acquired images were processed using Fiji software.

***In vitro* competition of PP_{Rb} with PP_{EAE}.** HEK293T cells were seeded onto fibronectin-treated coverslips and allowed to adhere for 24 h. The cells were then treated with 35μM **PP_{Rb}** and 35 μM **PP_{EAE}** for various durations, after which the cells were washed with DPBS, fixed with 4% PFA for 10 min at RT, and washed thrice with DPBS. Coverslips were mounted on slides using Fluoromount-G™, with DAPI (Invitrogen) and allowed to set overnight at 4 °C. The cells were scanned using a Leica TCS SP5 confocal microscope (LysoTracker: λ_{ex} = 647/ λ_{em} = 668 nm, DAPI: λ_{ex} = 358/ λ_{em} = 461 nm) and acquired images were processed using the Colocalisation Colourmap plugin for Fiji software.

***In vitro* staining of lysosomes.** HEK293T cells were seeded onto fibronectin-treated coverslips and allowed to adhere for 24 h. The cells were then treated with 35 μM **Rb** or **PP_{Rb}** for various durations, after which the cells were washed with DPBS and then incubated with pre-warmed DMEM with 50 nM of Lysotracker® Deep Red (Thermo

Fisher Scientific) for 30 min at 37 °C. The cells were washed with DPBS, fixed with 4% PFA for 10 min at RT, and washed thrice with DPBS. Coverslips were mounted on slides using Fluoromount-G™, with DAPI (Invitrogen) and allowed to set overnight at 4 °C. The cells were scanned using a Leica TCS SP5 confocal microscope (LysoTracker: λ_{ex} = 647/ λ_{em} = 668 nm, DAPI: λ_{ex} = 358/ λ_{em} = 461 nm) and acquired images were processed using Fiji software.

Statistical analysis. All experimental samples were run in triplicate with at least three biological repeats. Differences between samples were considered significant if $p < 0.05$ as determined using either a Student's T-test or a one-way Analysis of Variance (ANOVA). All graphs were created using OriginPro 2024b.

A4.2. Synthesis and characterisation

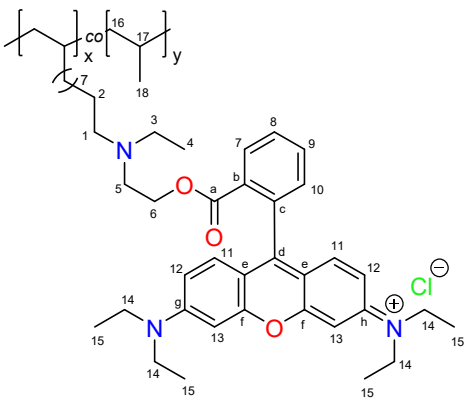

Synthesis of Rhodamine B modified PP$_{EAE}$, PP$_{Rb}$. PP$_{EAE}$ (0.5 g, 1.0 eq, 1.87 mol% [R-OH]), Rhodamine B (2.0 eq., Rb)), DCC (2.0 eq.), and DMAP (0.3 eq.) were dissolved in anhydrous DCM (50 ml) in an ampoule, sparged under N_2 and stirred for 30 min prior to sealing and heating to 80 °C for 72 h. Polymer was precipitated in methanol (2 wt%) before being collected by filtration, washed with methanol (20 mL), then acetone (2 x 20 mL), and dried *in vacuo* at 40 °C to a constant mass. Polymer was then purified by Soxhlet extraction (H_2O), ensuring polymer was trapped at the base of the thimble, until no residual Rb was observed in the solvent by thin layer chromatorgaphy (DCM). Polymer was then washed with acetone and dried *in vacuo* at 40 °C to a constant mass. **PP$_{Rb}$** (1.87 mol%). **^{1}H NMR (600 MHz, $C_2D_2Cl_4$, 393 K)**: δ 7.90 (1H, H^7), 7.48 (2H, $H^{8.9}$), 7.08 (1H, H^{10}), 6.56 (2H,

H^{12}), 6.53 (2H, H^{13}), 6.40 (2H, H^{11}), 4.00 (6H, br s, H^6), 3.58, 3.44 (8H. q, $^3J_{HH}$ = 7.0 Hz, H^{14}), 3.25-3.00 (18H, H^3, H^5, and H^1), 2.02-1.62 (217H, br m, H^{15}, H^2, H^{17}), 1.55-1.06 (432H, br m, H^b, H^{16} (*anti*), and H^4), 1.05-0.84 ppm (725H, br m, H^{18} and H^{16} (*syn*)).**^{13}C{^{1}H} NMR (151 MHz, $C_2D_2Cl_4$, 393 K)**: δ 201.02 (C^b), 190.84 (C^b), 158.16 (C^b), 156.16 (C^b), 156.24 (C^b), 132.93 (C^b), 131.79 (C^b), 130.52 (C^b), 130.19 (C^b), 130.03 (C^b), 123.94 (C^b), 120.54 (C^b), 116.68 (C^b), 116.47 (C^b), 116.27 (C^b), 114.12 (C^b), 111.24 (C^b), 100.31 (C^b), 99.88 (C^b), 96.97 (C^b), 65.50 (C^{14}), 58.73 (C^5), 56.79 (C^6), 54.17 (C^1), 49.45 (C^3), 46.22 (C^{17}), 28.58 (C^{16}), 23.47 (C^2), 21.66 (C^{18}), 8.81 (C^4).**FTIR**: *v* (cm^{-1}) = 2950, 2867, and 1456 (*v* (C-H, CH_3)), 2917, 2838, and 1377 (*v* (C-H, CH_2)), 1619 (*v* (C=O)), and 808 (*v* (C=C_{Ar})). **Fluorescence**: λ_{Ex} = 558 nm and λ_{Em} = 581 nm (0.5 mg mL^{-1}, chloroform). **UV-Vis**: λ_{Ex} = 558 nm (0.5 mg mL^{-1}, chloroform). [a]Nitrogen adjacent ^{1}H NMR peaks appear broad. This observation is potentially explained by an increase in the relaxation rate caused by quadrupolar Nitrogen.[1, 2] [b]Peaks corresponding to unassigned 20 carbons on Rb (7-13 and a-g). Due to the low levels of dye incorporation it was difficult to assign or integrate corresponding Rb moiety and comonomer -CH_2- peaks in the ^{13}C NMR spectrum; complimentary use of COSY and HSQC spectra afforded partial assignment.

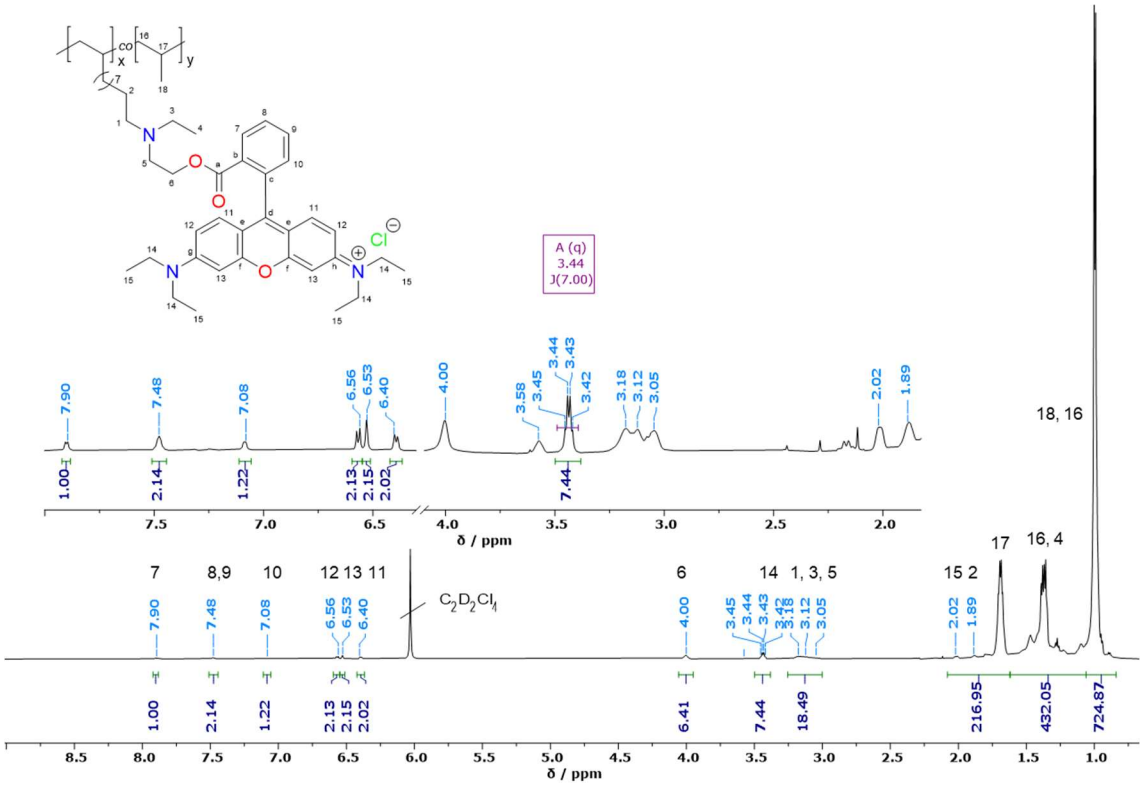

Figure A4.1 PP_{Rb} ^{1}H NMR (600 MHz, $C_2D_2Cl_4$, 393 K). Insert expanded region corresponding to polymer linker and dye moiety.

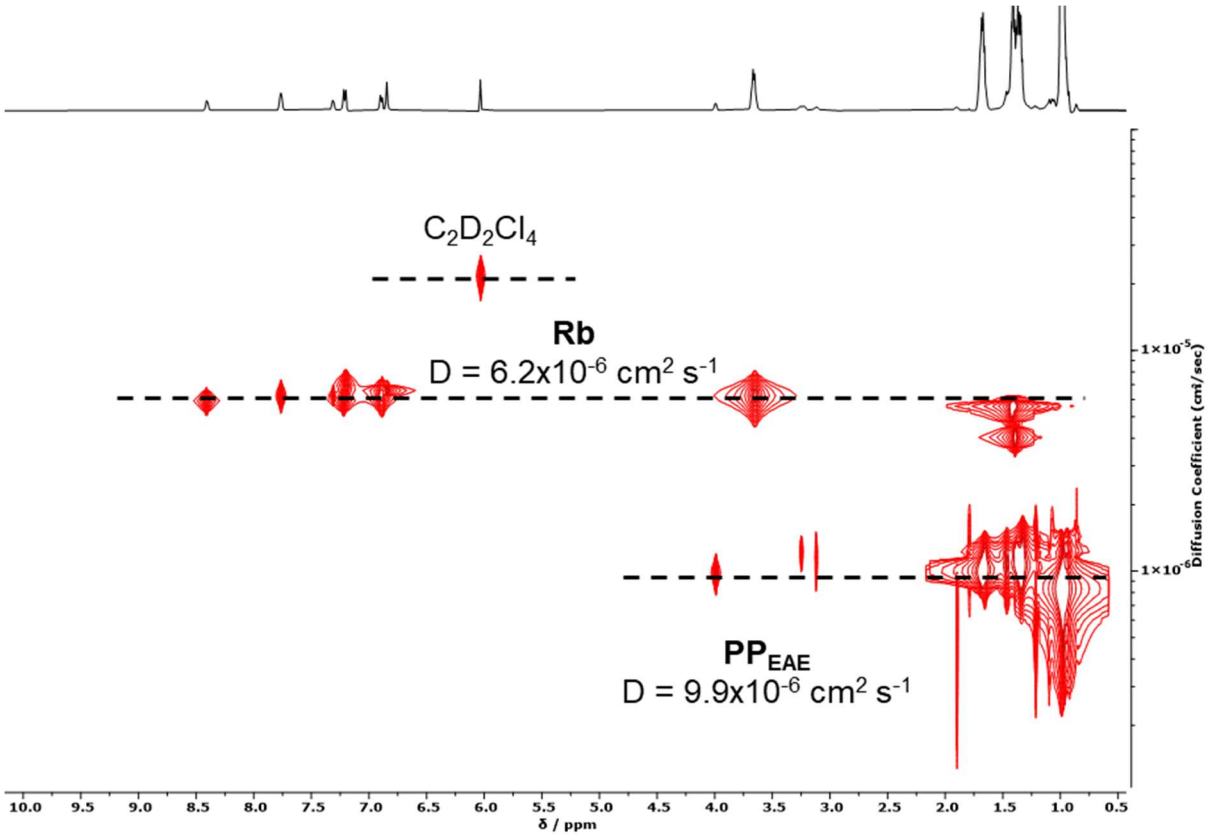

Figure A4.2 Convection compensated diffusion experiment using Bruker pulse program "*dstebpgp3s*" (500 MHz, $C_2D_2Cl_4$, 393 K). DOSY ^{1}H NMR spectra of parent polymer $\mathbf{PP_{EAE}}$ + **Rb**.

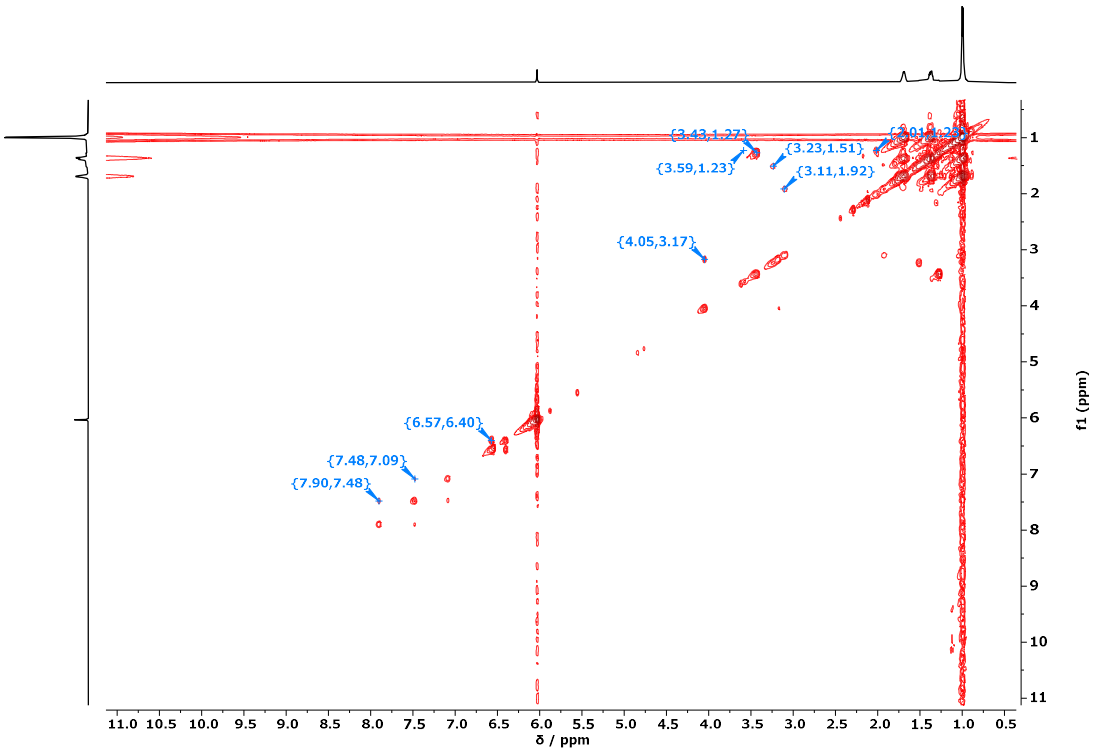

Figure A4.3 COSY ^{1}H-^{1}H NMR spectrum

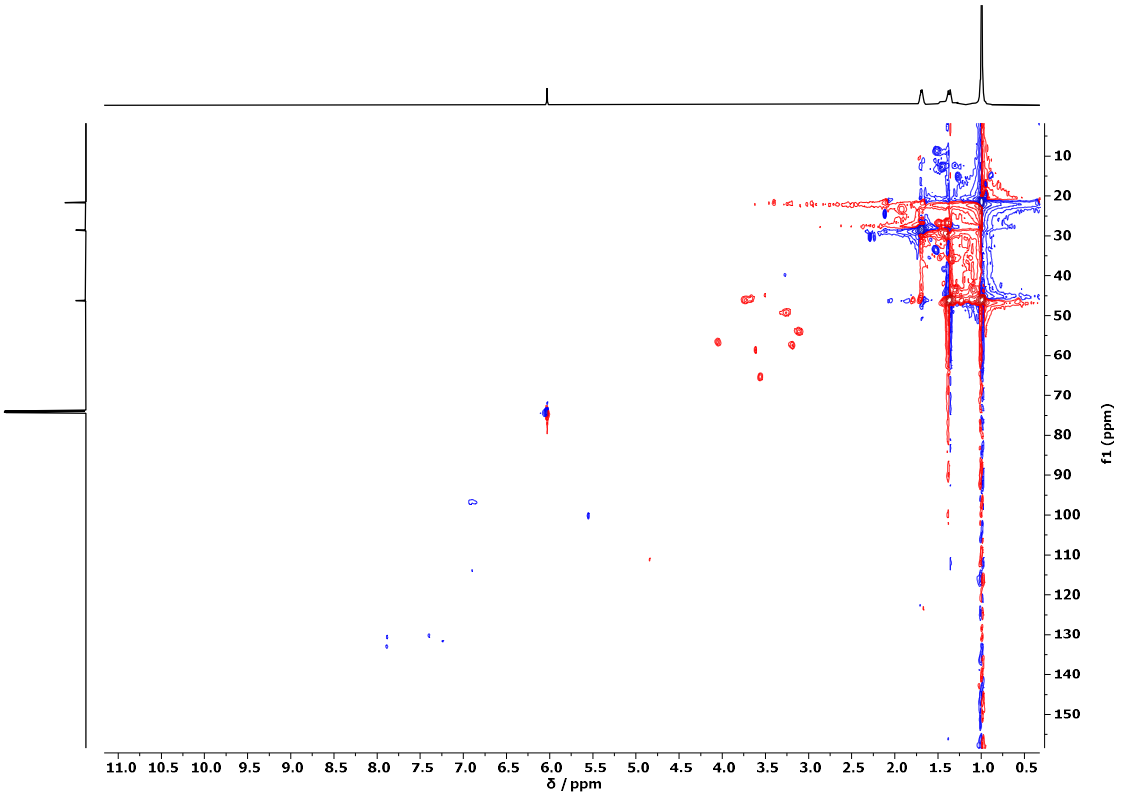

Figure A4.4 HSQC ^{1}H-^{13}C NMR spectrum

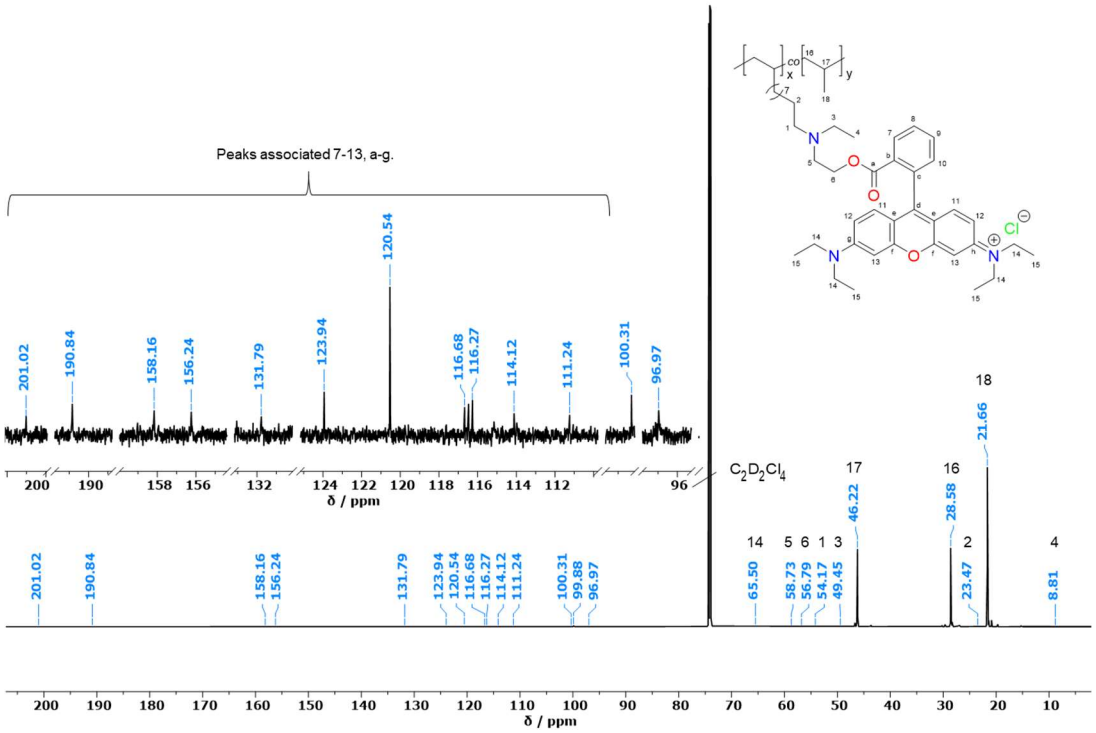

Figure A4.5 PP_{Rb} $^{13}C\{^1H\}$ NMR (151 MHz, $C_2D_2Cl_4$, 393 K), full spectrum.

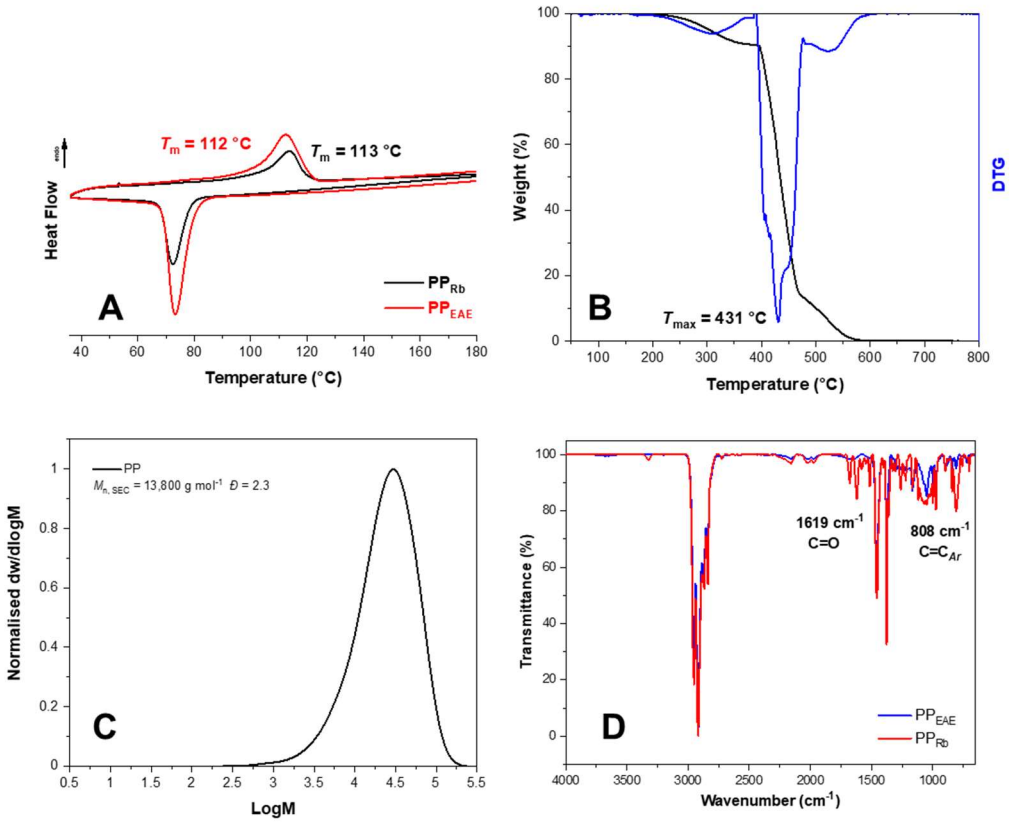

Figure A4.6 (**A**) DSC trace of **PP_{Rb}** and **PP_{EAE}**, temeperature scan rate 5 °C min^{-1}; observed decrease in crystallinity upon modification (**PP_{EAE}** = 35%, **PP_{Rb}** = 29%) (**B**) TGA thermograph of **PP_{Rb}** in a N_2 atmosphere, heating rate 20 °C min^{-1}. (**C**) **PP_{Br}** parent copolymer used to calculate **PP_{Rb}** $M_{n,\,th}$ = (13,800–(1.87×79.9)+(1.87×89.14)+(1.87×(479.02-2)) (g mol^{-1}))). (D) FT-IR of **PP_{Rb}** and **PP_{EAE}**.

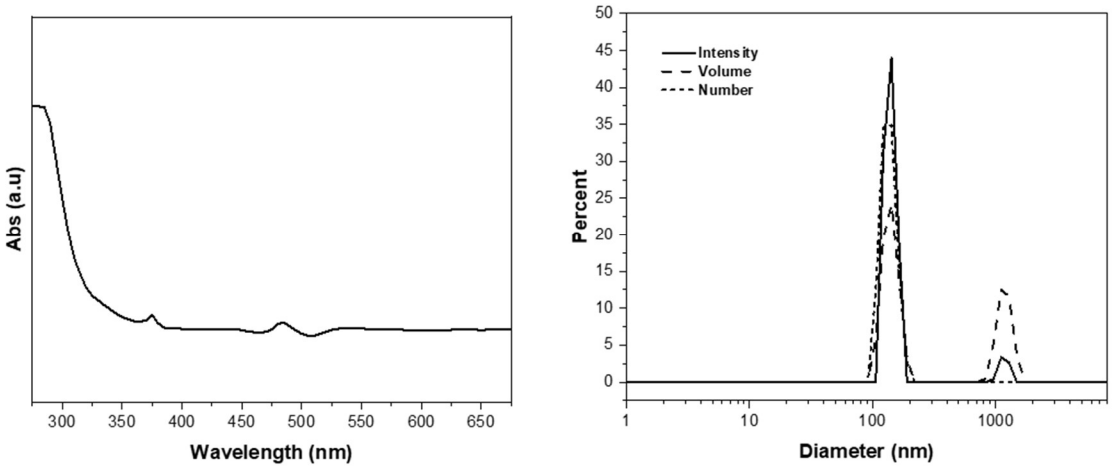

Figure A4.7 PP_{EAE} UV-Vis and DLS (1 mg ml^{-1}, toluene)

Table A4.9 Particle size data of **PP_{Rb}** and **PP_{EAE}** by dynamic light scattering (1 mg ml^{-1}, toluene)

Polymer	%	D_h	PDi
PP_{Rb}	Intensity	566.2	0.029
	Volume	588.1	0.039
	Number	547.6	0.039
PP_{EAE}	Intensity	139.9	0.011
		1,170	0.007
	Volume	139.8	0.022
		1,182	0.018
	Number	135.3	0.021
		1,155	0.019

$PDi = \sigma^2/D_h^2$

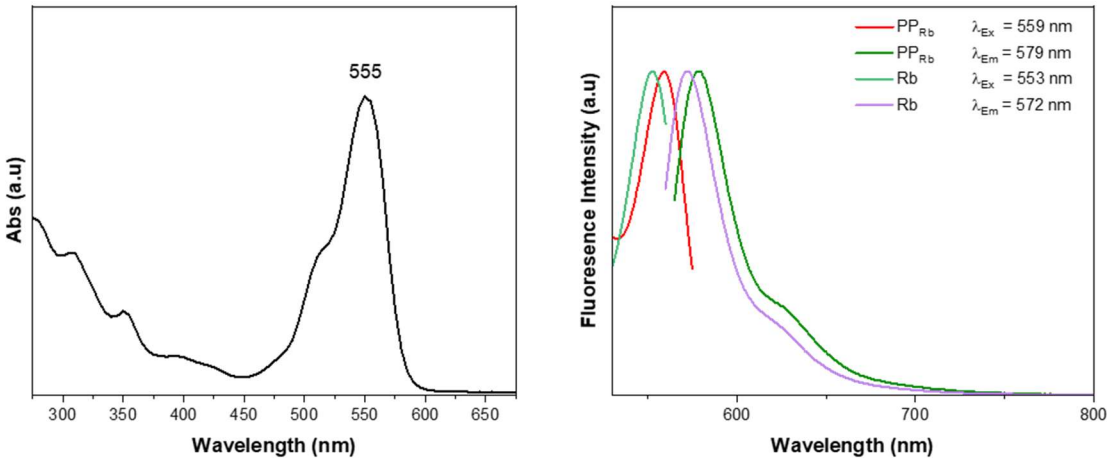

Figure A4.8 Rb (left) UV-Vis and (right) fluorescent spectra (0.522 nM, chloroform)

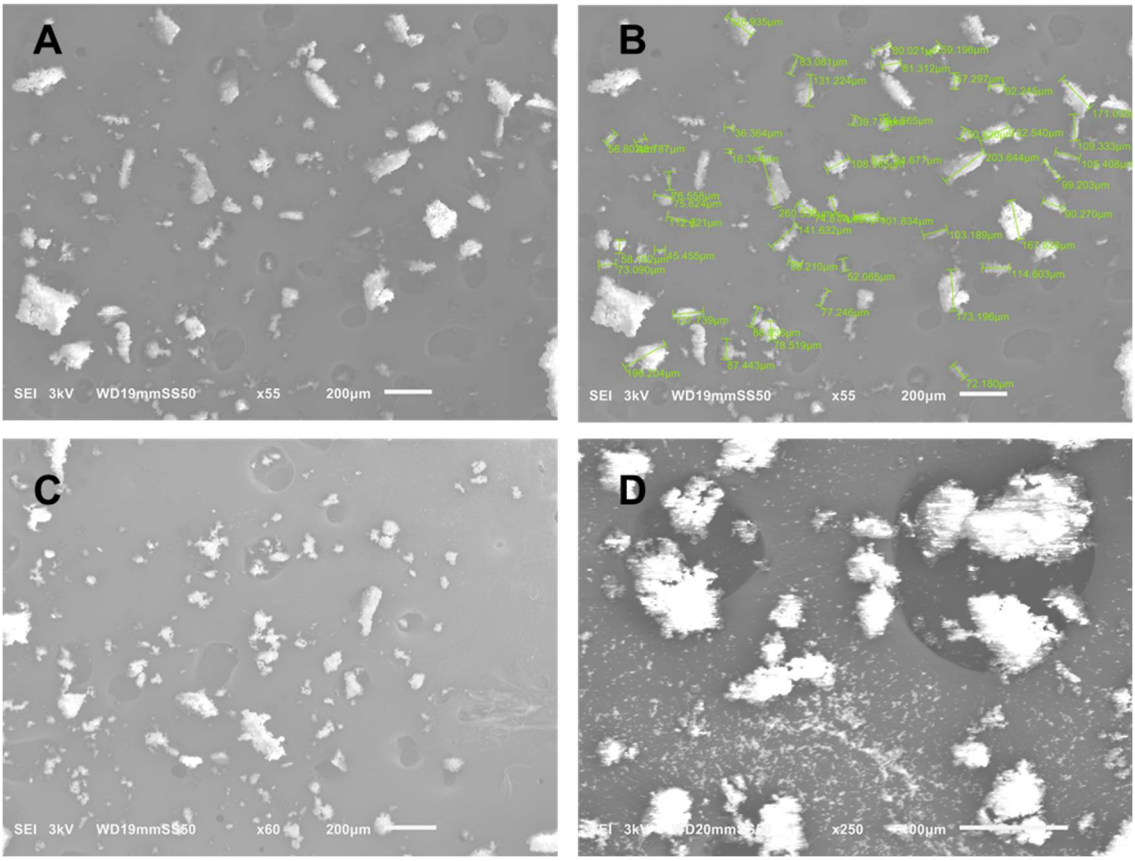

Figure A4.9 SEM images of $\mathbf{PP_{Rb}}$.

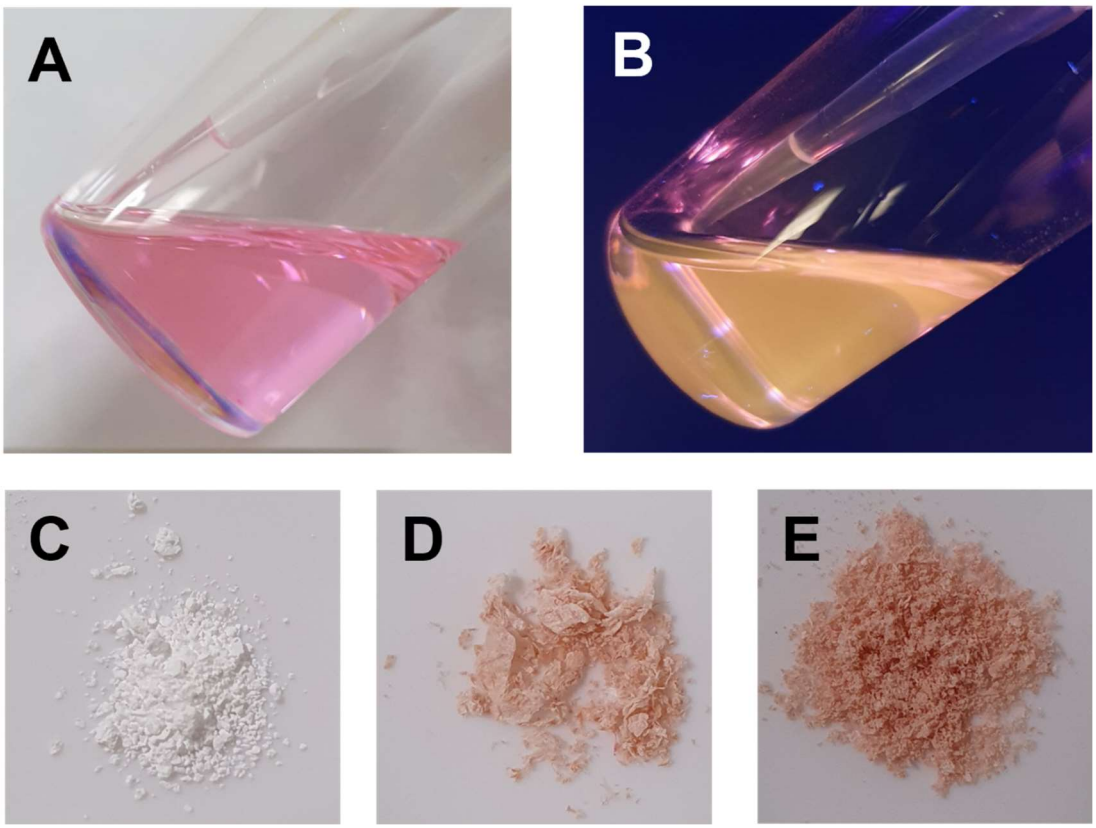

Figure A4.10 $\mathbf{PP_{Rb}}$ (0.5 mg mL^{-1}, chloroform) (A) visible light and (B) UV light. Photos of (C) $\mathbf{PP_{EAE}}$ (D) $\mathbf{PP_{Rb}}$ and (E) $\mathbf{^{c}PP_{Rb}}$.

A4.3. Cellular studies

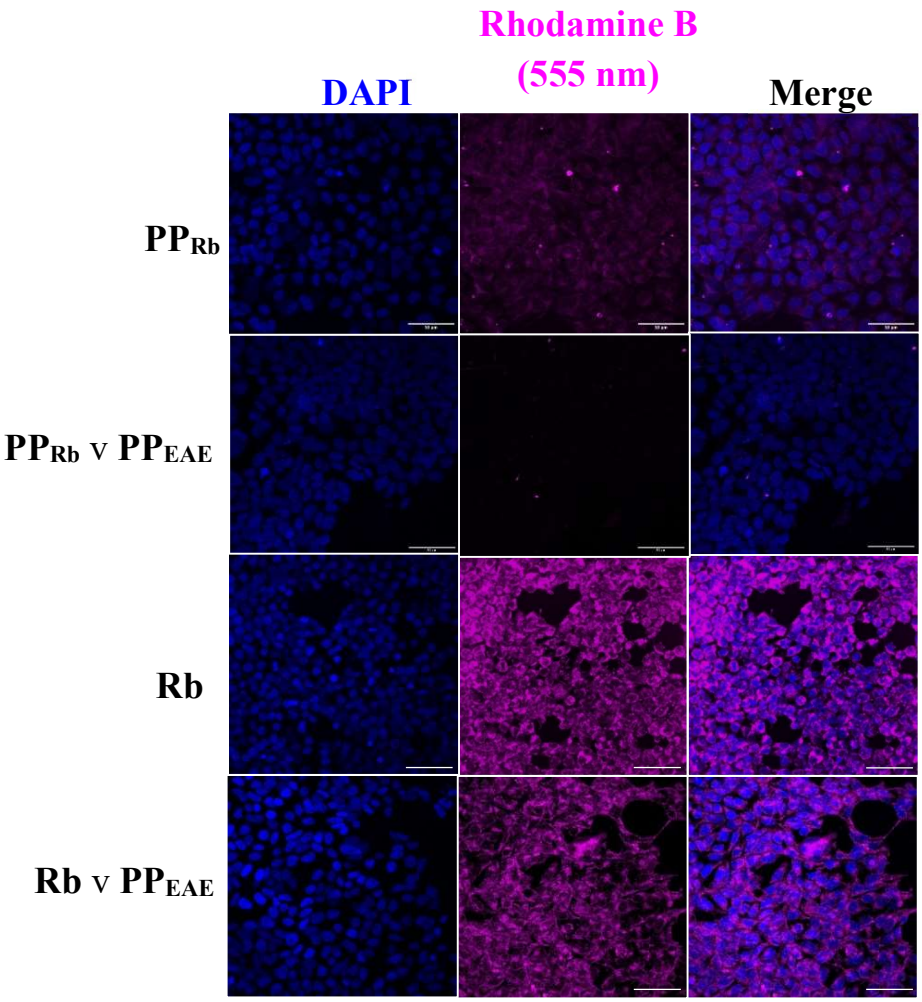

Figure A4.11 Fluorescence Competition Analysis of **PP$_{Rb}$** and free **Rb** co-treated with **PP$_{EAE}$** at 555 nm. Confocal microscopy images showing DAPI (nuclear stain), Rhodamine B fluorescence (555 nm), and merged channels for **PP$_{Rb}$**, **PP$_{Rb}$** vs **PP$_{EAE}$**, **Rb**, and **Rb** vs **PP$_{EAE}$** conditions. Scale bars 50 µm.

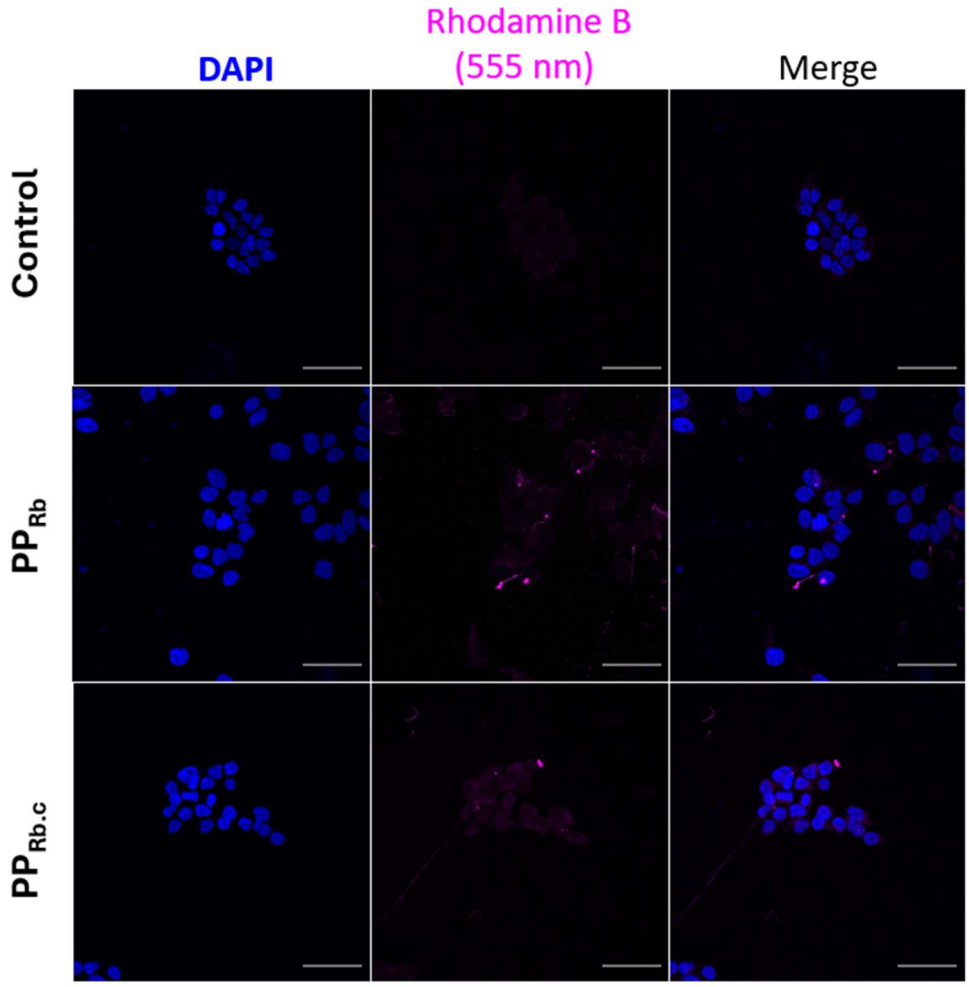

Figure A4.12 Comparable cellular localisation of both **PP$_{Rb}$** and **^{c}PP$_{Rb}$**. Confocal microscopy images showing DAPI (nuclear stain), Rb fluorescence (555 nm), and merged channels for Control, **PP$_{Rb}$**, and **^{c}PP$_{Rb}$** conditions after 24 h incubation. Scale bars 50 µm.

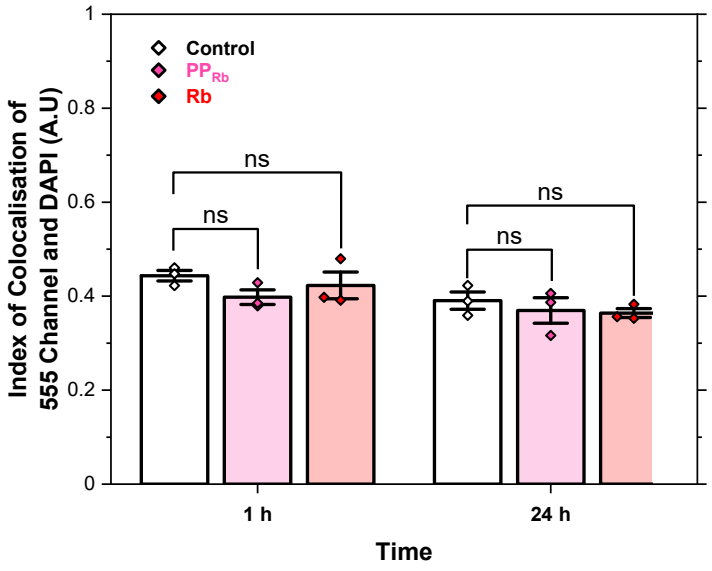

Figure A4.13 Analysis of Colocalisation between the 555 nm channel and DAPI for **PP$_{Rb}$** and **Rb**. The Index of Colocalisation between the 555 nm fluorescence signal and DAPI nuclear stain was statistically nonsignificant (ns) across all conditions (Control, **PP$_{Rb}$**, and **Rb**) and time points (1 and 24 h).

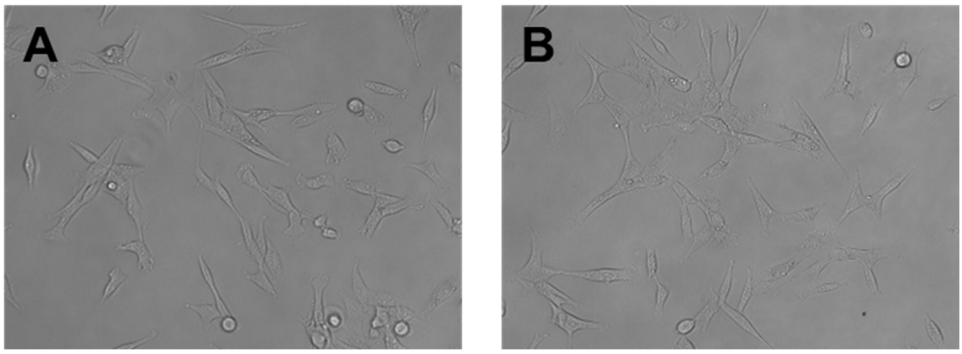

Figure A4.14 Representative bright-field microscopy images of HEK293 cells following 24 h exposure to 0 μM $\mathbf{PP_{Rb}}$ (**A**) and 35 μM $\mathbf{PP_{Rb}}$ (**B**), showing no observable signs of cell death or structural abnormalities between treated and untreated cells.

A4.4. References

1. T. C. Wong, L. R. Collazo and F. S. Guziec, *Tetrahedron*, 1995, **51**, 649-656.
2. J. A. Jarvis, I. M. Haies, P. T. Williamson and M. Carravetta, *Phys. Chem. Chem. Phys.*, 2013, **15**, 7613-7620.

A5. Supplementary data for Chapter Six

Synthesis, Characterisation, and Magnetic Properties of a Permethylated Manganocene

Alexander Evans, Thomas A. Q. Arnold, Paul Ransom, Samantha C. Binding, William K. Myers, Agamemnon E. Crumpton, Zoë R. Turner, Jean-Charles Buffet, and Dermot O'Hare

A5.1. Experimental

General methods and materials. Air and moisture sensitive reactions were performed on a dual-manifold vacuum/N_2 line using standard Schlenk techniques, or in a N_2 filled MBraun Unilab glovebox. Hexane was dried using a Braun SPS-800 solvent purification system and stored over a K mirror. THF was dried at reflux over Na/benzophenone and distilled under N_2. THF was stored over activated 3 Å molecular sieves. Benzene-d_6 (99%) was obtained from Goss Scientific, dried over Na and freeze-pump-thaw degassed three times, before being vac transferred prior to use.

Solution NMR spectroscopy. NMR samples were prepared in the glovebox under N_2 atmosphere in Young's tap NMR tubes. ^{1}H and ^{13}C{^{1}H} NMR spectra were recorded on 300 MHz Varian VX-Works spectrometers. All chemical shifts were expressed as δ, in parts per million (ppm) relative to TMS (δ = 0). Solution phase Evans' method NMR samples were prepared in both benzene-d_6 and toluene-d_8 as above and were run on the 500 MHz Bruker AVIII 500 spectrometer.

Single Crystal X-Ray Diffraction. Crystals were mounted on MiTeGen MicroMounts using perfluoropolyether oil and rapidly transferred to either a SuperNova A or Synergy DW diffractometer fitted with an Oxford Cryostreams Cryostream open-flow nitrogen

cooling device.[1] Data collections were carried out at low temperature, either 150 K or 100 K using Cu Ka radiation (= 1.54178 Å) and data were processed using CrysAlisPro.[2] Structures were solved using charge flipping algorithm (SUPERFLIP)4 and refined on F^2 by full-matrix lest-squares regression using the Olex-2 software suite.[3] Using Olex2, the structures were solved with the SHELXT[4] structure solution program using Intrinsic Phasing and refined on F^2 with the SHELXL[5] refinement package using least squares minimisation. Geometric calculations were performed using PLATON,[6] and illustrations were created using ORTEP-3.[7] The crystal structure solution of Ind*H was refined as a two-component twin, implementing the twin-law (-1 0 0 | 0 -1 0 | 0 0 1) with BASF = 0.4569.

Ultraviolet–visible Spectroscopy. Optical measurement were conducted using UV-Vis-NIR spectrophotometer (PerkinElmer lambda 1050+). UV-Vis adsorption samples were prepared in the glovebox and were run in dry, degassed *n*-hexanes in a cuvette sealed with a Young's tap. Spectra between 250 and 800 nm.

Fourier-Transform Infrared Spectroscopy. FT-IR spectroscopy samples were prepared in the glovebox as discs using KBr that had been dried at 150 K for eight hours under high vacuum. Discs were pressed in a custom made barrel and sealed while run on a Nicolet iS5 ThermoScientific IR spectrometer.

SQUID magnetomery details The magnetic susceptibility data was measured on a powdered sample with a Quantum Design MPMS-5 SQUID magnetometer. The accurately weighed (26 mg) sample was placed in a gelatine capsule and loaded into a non-magnetic plastic straw before being lowered into the cryostat. Experimental susceptibility data was collected in a temperature range of 1.8-300 K under an applied

field of 1000 G, and corrected for the underlying diamagnetism of $\chi_{dia} = -3.8376\times10^{-4}$ emu mol^{-1}, using Pascal's constants.[8]

EPR details. CW-EPR spectra were collected in the Center for Advanced ESR (CAESR) in the Inorganic Chemistry Laboratory at the University of Oxford. X-band measurements performed with a Bruker-Biospin Micro EMX^{plus} spectrometer equipped with a PremiumX microwave bridge, a cylindrical TE_{011}-mode resonator (SHQE-W), an ESR-900 liquid helium cryostat, and an Oxford Instruments ITC-503s temperature controller. Custom simulation scripts for matrix diagonalization were written in MatLab^{TM}.

A5.2. Synthesis and Characterisation

Updated ligand synthesis. The procedures are based upon a literature preparation.[9] Oxalyl chloride replaces thionyl chloride as the chlorinating agent and dichloromethane is introduced as the low boiling solvent, allowing the chlorination and Friedel-Crafts reactions to be combined in one pot. Methyllithium was found to be too basic to easily effect the ketone reduction and methylation and a softer cerium-based variant was introduced.[10-12] Iodine was succeeded by LiCl as the dehydrating agent, eliminating the need for column chromatography.[10]

Synthesis of 2,3,4,5,6,7-hexamethylindanone. 9.69 g (97 mmol, 1 eq.) trans-2-methylbutenoic acid was dissolved in 250 mL DCM and stirred under a flow of N_2 and 12.19 g (97 mmol, 1 eq.) oxalyl chloride added. A catalytic drop of DMF was added causing the reaction to effervesce vigorously and the reaction was stirred for 16 hours. The reaction vessel was cooled to <5 °C in an ice-bath and 13.16 g (98.5 mmol, 1.02 eq.) $AlCl_3$ was added. 12.3 g (92 mmol, 0.95 eq) 1,2,3,4-tetramethylbenzene was mixed with 25 mL DCM and was added in a slow dropw manner, and the reaction mixture allowed

to warm to room temperature, stirring, over four hours. 125 mL conc. HCl was mixed with 125 mL ice and was added to the reaction mixture, quenching it, before the DCM layer was decanted. The aqueous layer was extracted with two further portions of DCM and the combined organic phase washed with water, dried with $MgSO_4$, filtered, and removed in vacuo, affording the product as an off-white crystalline solid in 96 % yield (19 g, 88 mmol).

Synthesis of 1,2,3,4,5,6,7-heptamethylindan-1-ol. 20 g anhydrous $CeCl_3$ (81.1 mmol, 1.5 eq.) was activated by stirring in 300 mL dry, degassed THF under a nitrogen atmosphere for 16 h, before cooling to −78 °C. 47.3 mL methyllithium (1.6 M in Et_2O; 75.7 mmol, 1.4 eq.) was added fast dropwise to the white suspension turning it bright yellow. The solution was allowed to stir for a further hour warming to −35 °C before dropwise addition of 11.69 g 2,3,4,5,6,7-hexamethylindan-1-one (54.1 mmol, 1 eq.) in 100 mL THF, warming to room temperature and stirring for a further 12 h. The reaction mixture was quenched with 400 mL saturated aqueous ammonium chloride solution and was extracted in DCM (3 × 150 mL), dried over anhydrous $MgSO_4$ and reduced in vacuo affording a light brown oil. This oil was triturated with 2 mL hexane (4 °C), which was decanted after one hour affording an off-white crystalline solid in 96% yield (12.05 g, 51.9 mmol).

Synthesis of Ind*H. 9.21 g 1,2,3,4,5,6,7-heptamethylindan-1-ol (39.7 mmol, 1 eq.) was dissolved in 150 mL dry DMSO and allowed to stir under N_2. 2.53 g anhydrous lithium chloride (59.5 mmol, 1.5 eq) was quickly added to the pale brown solution, a reflux condenser was set up and the flask was heated to 110 °C and allowed to stir for 48 h, darkening in color. Upon cessation of stirring, a dark brown immiscible layer can be seen to form which solidifies to a pale-yellow wax on cooling of the reaction mixture to room

temperature. The product is extracted in pentane (3 × 150 mL), washed with distilled water (150 mL), dried over anhydrous $MgSO_4$ and removed under reduced pressure affording a pale brown crystalline solid in 92% yield (7.85 g, 36.6 mmol).

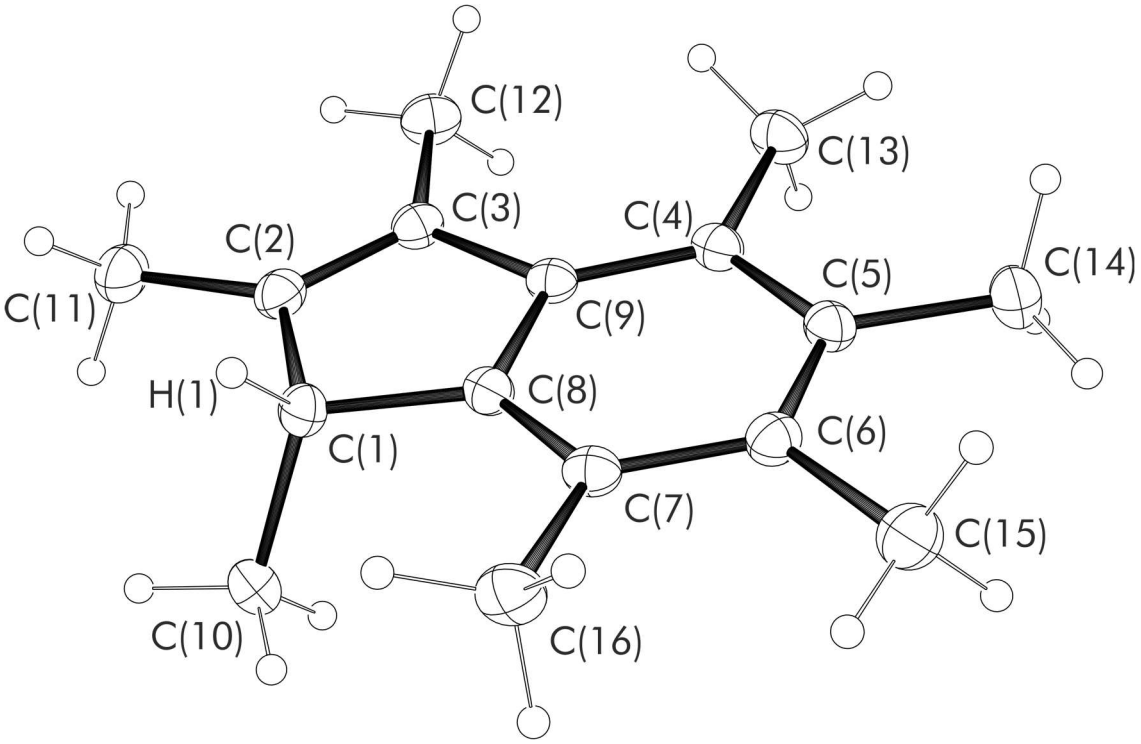

Figure A5.1 Molecular structure of Ind* (displacement ellipsoids are drawn at 30% probability). Selected distance, C_6-C_5 1.407(2) Å

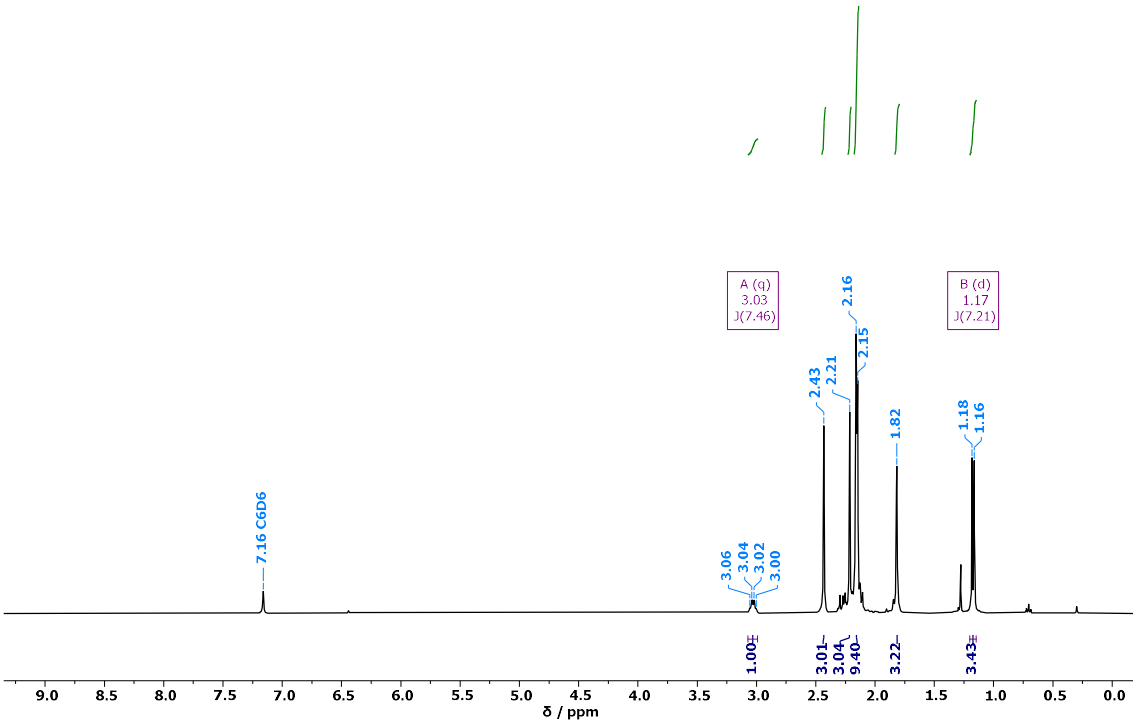

Figure A5.2 ^{1}H NMR Ind*(Benzene-d_6, 298 K, 400 MHz).

Table A5.1 Selected experimental crystallographic data for Ind*H.

Chemical formula	$C_{16}H_{22}$
M_r	214.33
Crystal system, space group	Monoclinic, $P2_1/c$
Temperature (K)	150
a, b, c (Å)	13.0353 (4), 10.9285 (4), 9.0453 (3)
β (°)	91.765 (3)
V (Å^3)	1287.95 (7)
Z	4
Radiation type	Cu $K\alpha$
μ (mm^{-1})	0.45
Crystal size (mm)	0.22 × 0.12 × 0.08
Diffractometer	SuperNova, Dual, Cu at home/near, Atlas
Absorption correction	Multi-scan *CrysAlis PRO* 1.171.42.72a (Rigaku Oxford Diffraction, 2022) Empirical absorption correction using spherical harmonics, implemented in SCALE3 ABSPACK scaling algorithm.
T_{min}, T_{max}	0.834, 1.000
No. of measured, independent and observed [$I > 2\sigma(I)$] reflections	5161, 5161, 4125
$(\sin \theta/\lambda)_{max}$ (Å^{-1})	0.630
$R[F^2 > 2\sigma(F^2)]$, $wR(F^2)$, S	0.047, 0.143, 1.09
No. of reflections	5161
No. of parameters	153
H-atom treatment	H-atom parameters constrained
$\Delta\rho_{max}$, $\Delta\rho_{min}$ (e Å^{-3})	0.25, −0.23
CCDC Deposition Number	2421030

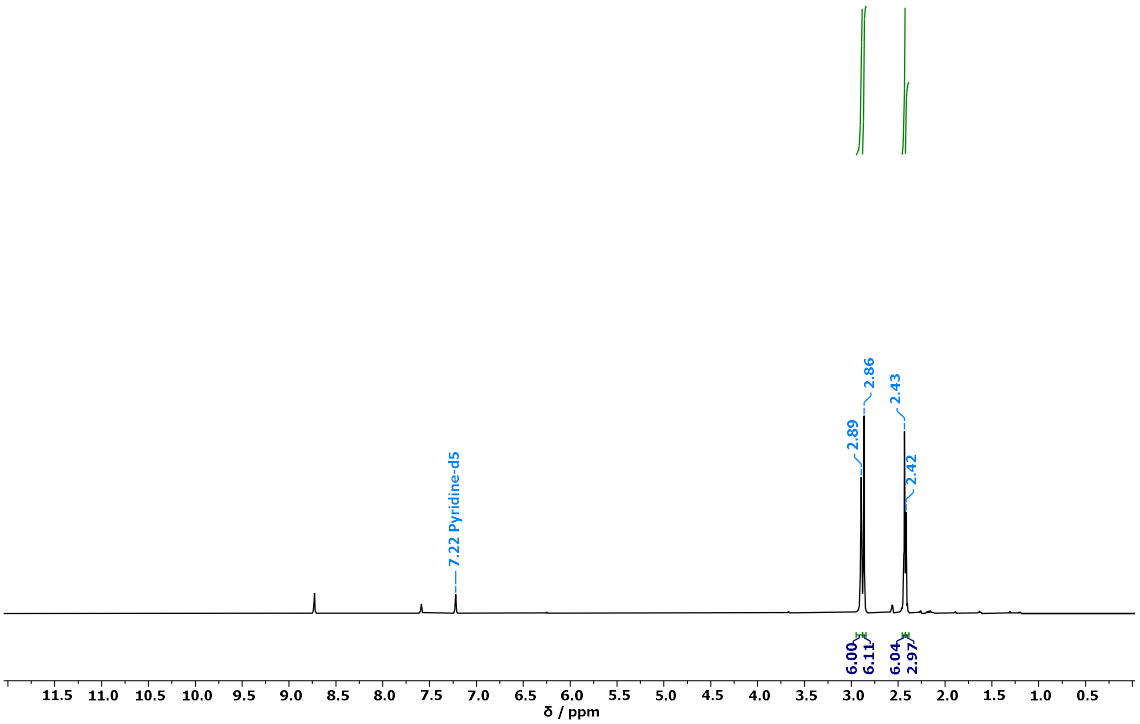

Figure A5.3 ^{1}H NMR Ind*(Pyridine-d_5, 298 K, 400 MHz).

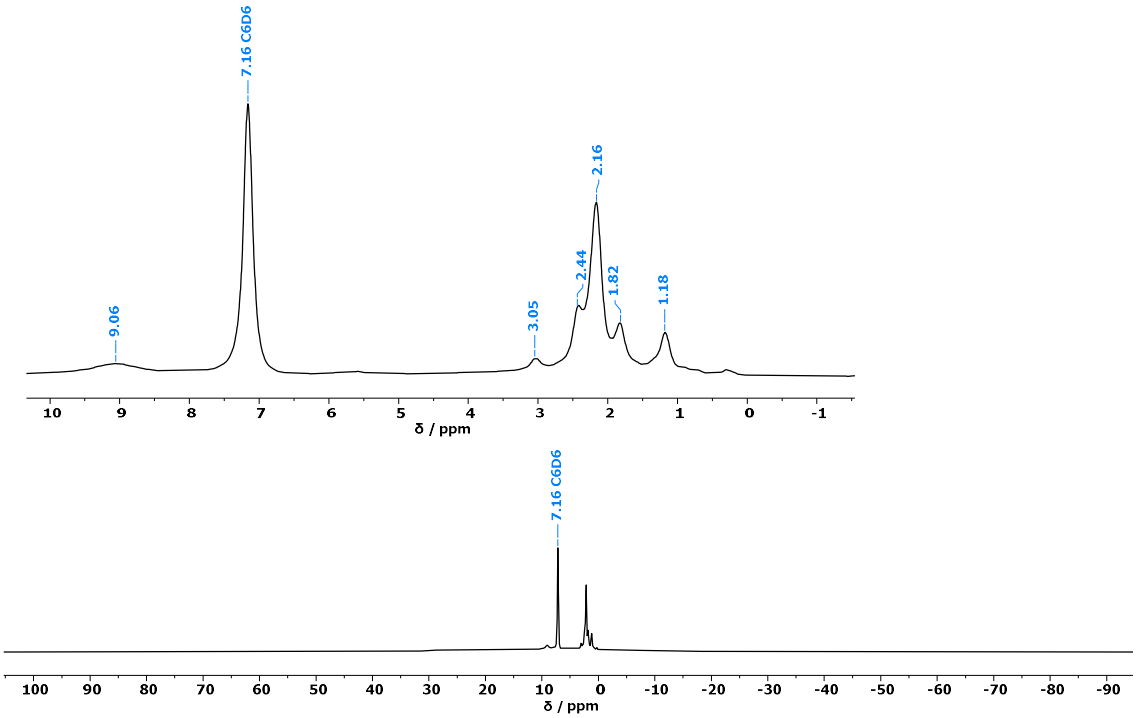

Figure A5.4 ^{1}H NMR full spectra of Ind*$_2$Mn and insert is of relevant region (Benzene-d_6, 298 K, 500 MHz).

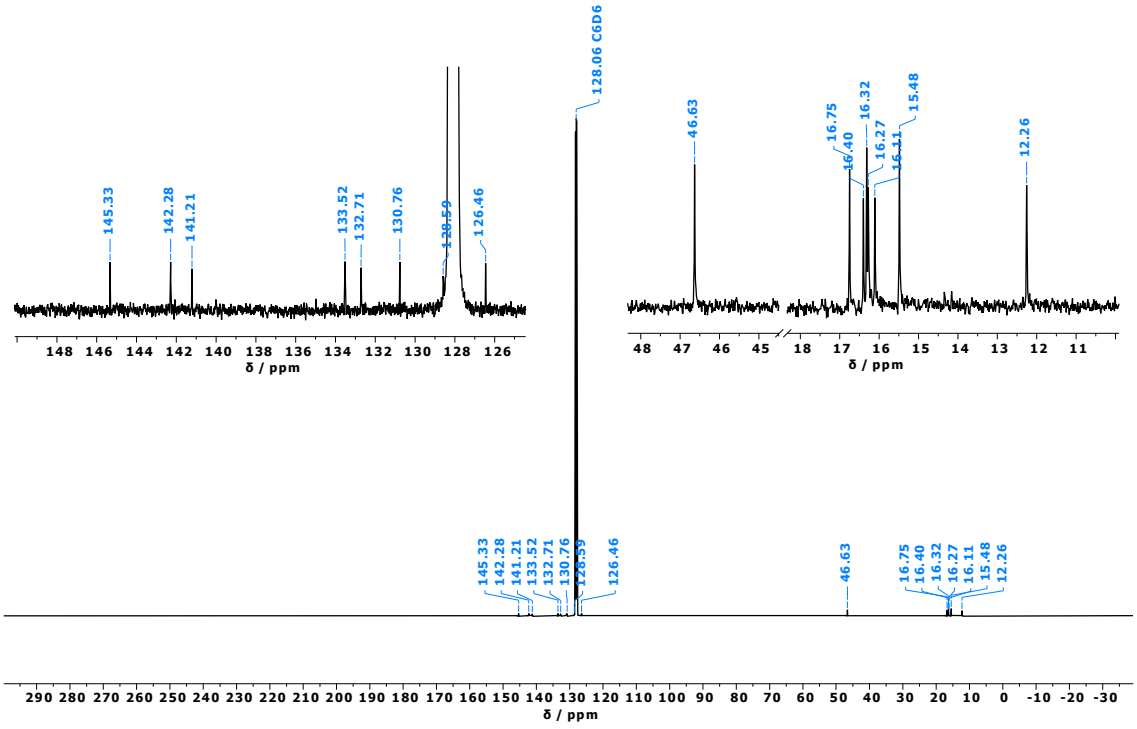

Figure A5.5 $^{13}C\{^{1}H\}$ NMR full spectra of Ind*$_2$Mn and inserts are of relevant regions (benzene-d_6, 298 K, 499.9 MHz).

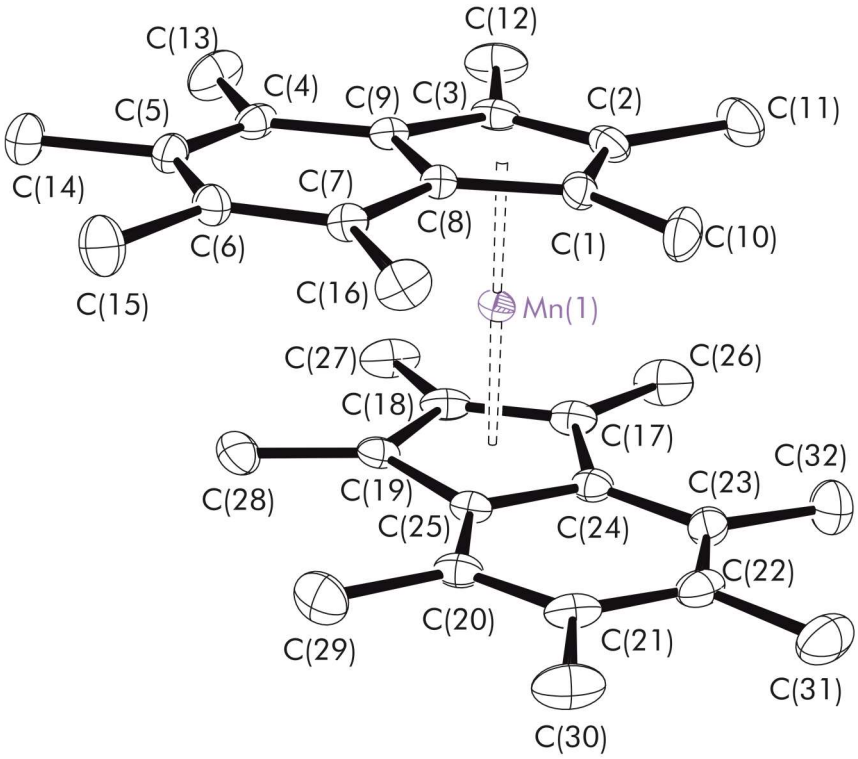

Figure A5.6 Fully labelled molecular structure of Ind*$_2$Mn. For clarity, hydrogens atoms were omitted (displacement ellipsoids are drawn at 30% probability).

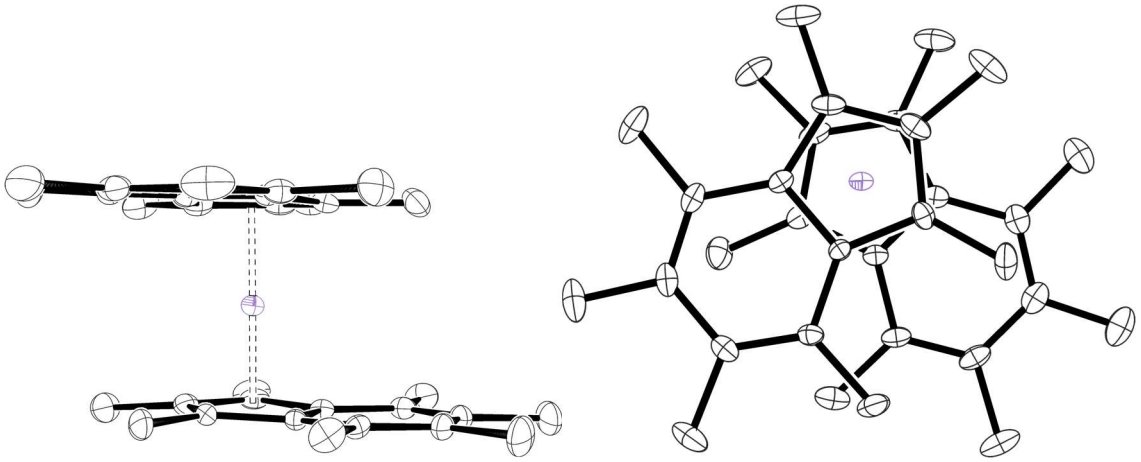

Figure A5.7 Alternate views of the molecular structure of Ind*$_2$Mn. For clarity, hydrogens atoms were omitted (displacement ellipsoids are drawn at 30% probability).

Table A5.2 Selected bond lengths (Å) and angles (°) for Ind*$_2$Mn.

M-C_{avg}	2.127
Cp_{cent}-M	1.7400(6)
Δ_{M-C}	0.073, 0.073
RA	85.2(2)
C_6-C_5	1.443(2)
C_{21}-C_{22}	1.441(2)

Definitions of structural parameters. The rotation angle (RA) and indeed torsion angles all measure the twist of the two indenyl rings relative to one another with 0° being eclipsed and 180° being staggered. However, these parameters are calculated in different ways but in this work RA is based on the torsion angle first introduced by Calhorda *et al*. [C(2)-Cp_{cent}-Cp_{cent}-C(18)] and adapted for Ind*$_2$Mn: [C(11)-C(2)-C(18)-C(27)].[9] Δ_{M-C}, also termed the ring-slip parameter is a measure of how far the metal distors from η^5 bonding towards η^3 and is a reasonable quantifier of the "indenyl effect". It is measured in angstroms and calculated according to Equation A5.1.

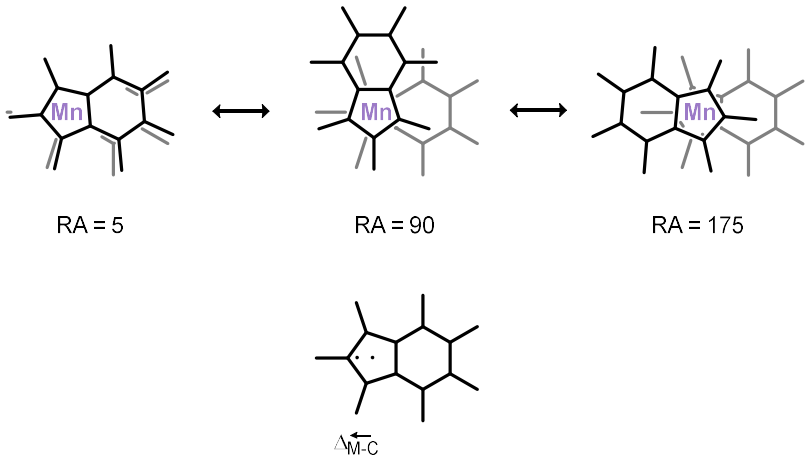

Figure A5.8 Visually defined structural parameters.

$$\Delta_{M-C} = \left\{\frac{C(8)+C(9)}{2}\right\} - \left\{\frac{C(1)+C(1)+C(3)}{3}\right\}$$

Equation A5.1 Definition of $\Delta_{M\text{-}C}$.

Table A5.10 Selected experimental crystallographic data for Ind*$_2$Mn.

Chemical formula	$C_{32}H_{42}Mn$
M_r	481.59
Crystal system, space group	Triclinic, *P*-1
Temperature (K)	100
a, *b*, *c* (Å)	9.0512 (1), 10.4398 (1), 15.8124 (1)
α, β, γ (°)	73.273 (1), 84.778 (1), 63.915 (1)
V (Å^3)	1284.09 (2)
Z	2
Radiation type	Cu *K*α
μ (mm^{-1})	4.28
Crystal size (mm)	0.3 × 0.13 × 0.04
Diffractometer	XtaLAB Synergy R, DW system, HyPix-Arc 150
Absorption correction	Multi-scan *CrysAlis PRO* 1.171.42.49 (Rigaku Oxford Diffraction, 2022) Empirical absorption correction using spherical harmonics, implemented in SCALE3 ABSPACK scaling algorithm.
T_{min}, T_{max}	0.548, 1.000
No. of measured, independent and observed [$I > 2\sigma(I)$] reflections	48167, 5238, 5064
R_{int}	0.028
$(\sin\theta/\lambda)_{max}$ (Å^{-1})	0.629
$R[F^2 > 2\sigma(F^2)]$, $wR(F^2)$, *S*	0.029, 0.081, 1.08
No. of reflections	5238
No. of parameters	312
H-atom treatment	H-atom parameters constrained
$\Delta\rho_{max}$, $\Delta\rho_{min}$ (e Å^{-3})	0.27, −0.34
CCDC Deposition Number	2421029

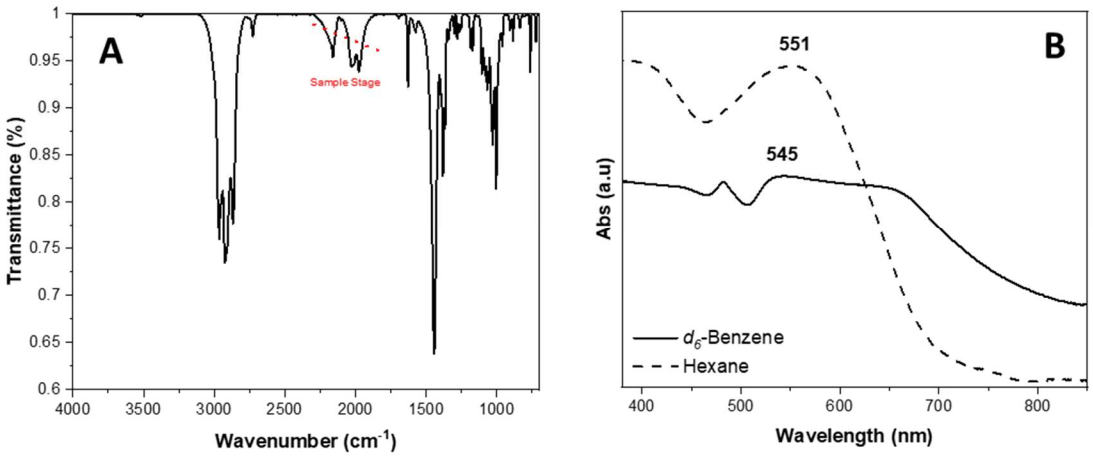

Figure A5.9 (**A**) FT-IR and (**B**) UV-Vis of Ind*$_2$Mn./

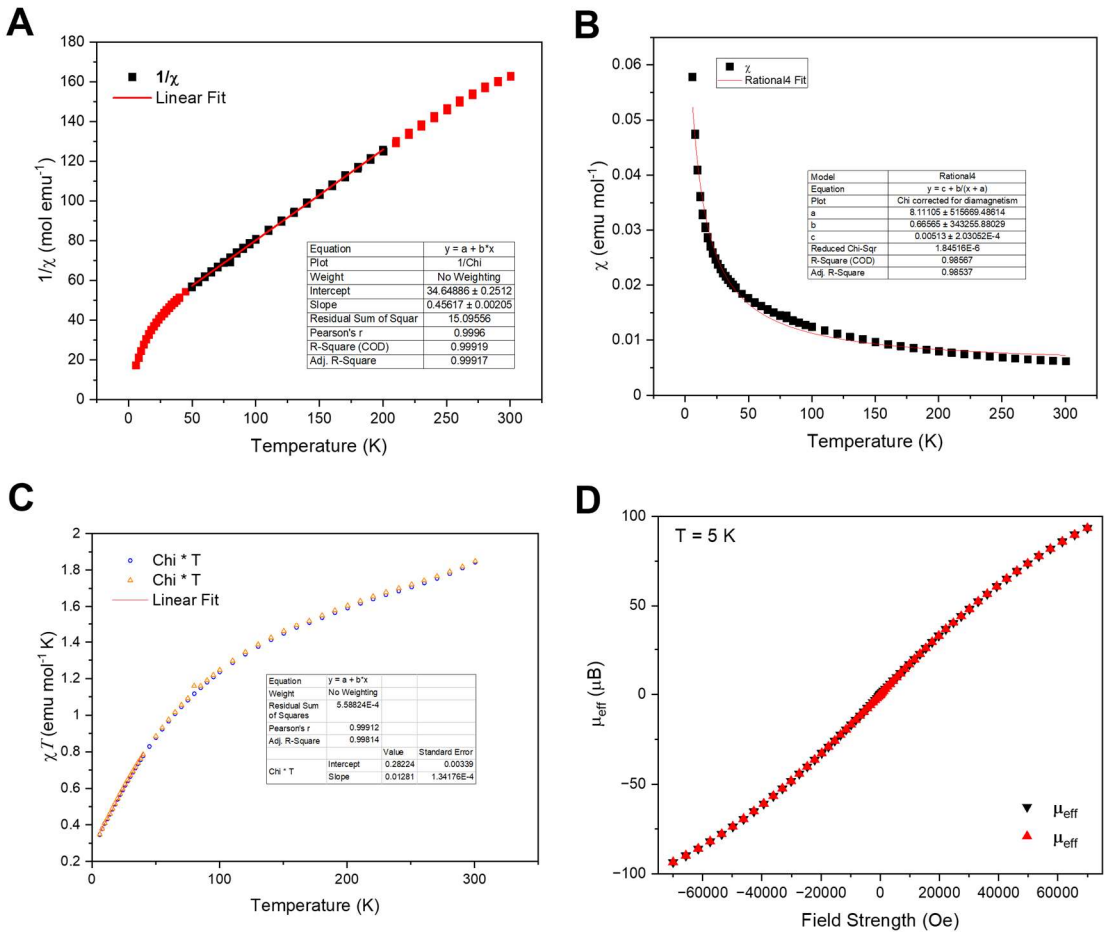

Figure A5.10 SQUID magnetronomy plots: (**A**) linear fit of 1/χ between 50-200 K calculated Weiss constant, θ = –44 K. Calculated f_{HS}: $\mu_{eff,exp}^2 = f_{HS}\cdot\mu_{eff,HS}^2 + f_{LS}\cdot\mu_{eff,LS}^2$. $(3.85)^2 = f_{HS}(5.92)^2 + (1 - f_{HS})(1.88)^2$. $f_{HS} \approx 0.358$;[14] (**B**) χ *vs* T, (**C**) χT *vs* T, and (**D**) a hysteresis loop (T = 5 K) classically describe a paramagnetic system.

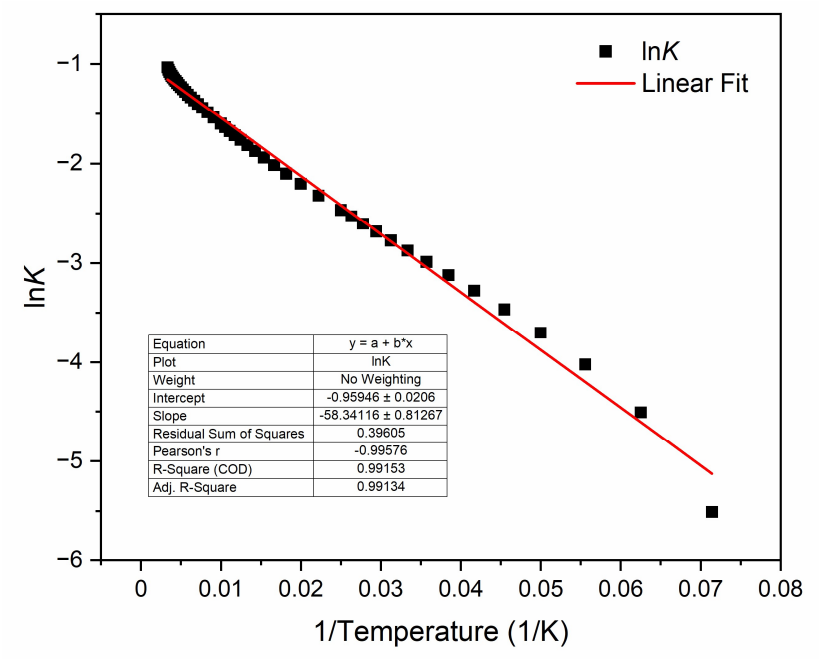

Figure A5.11 ln*K* *vs* T^{-1} plot for high-spin, low-spin equilibrium for Ind*$_2$Mn determined by solid-state magnetic susceptibility. $R^2 = 0.992$, $\Delta H = 0.485 \pm 0.007$ kJ mol^{-1}, and $\Delta S = -7.98 \pm 0.17$ J mol^{-1} .[15]

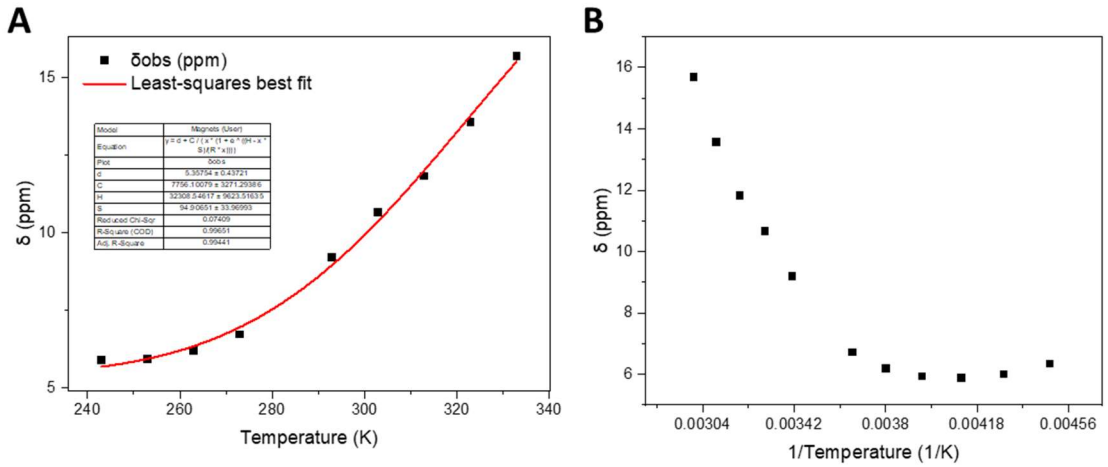

Figure A5.12 (**A**) Temperature variation and (**B**) reciprocal temperature variation of the ^{1}H NMR chemical shift for the resonance of the wing-tip methyl group between 243 K and 333 K (Me_2 in Figure 6.2) for Ind*$_2$Mn. Black squares represent experimental data and the red line is the least-squares best fit to $\delta_{obs} = \delta_{LS} + \frac{C}{T[1+e^{(\Delta H - T\Delta S/R)}]}$.[10,16,17] $R^2 = 0.997$, $\Delta H = 32 \pm 9$ kJ mol^{-1}, $\Delta S = 90 \pm 30$ J mol^{-1}, $C = 7000 \pm 3000$ K, and $f_{HS} = 17\%$ at 300 K, $f_{HS} = [HS]/[LS]$. The chemical shift measurements at 233 and 223 K are not included in this analysis, as they indicate an increasing shift upon decreasing temperature, which cannot be accounted for in the above model. This behaviour is most likely explained by a temperature dependence of the ^{1}H NMR shift of Me_2 due to the paramagnetic nature of the low spin complex. The result is a deviation from the above model, and correspondingly high errors in the derived thermodynamic parameters.

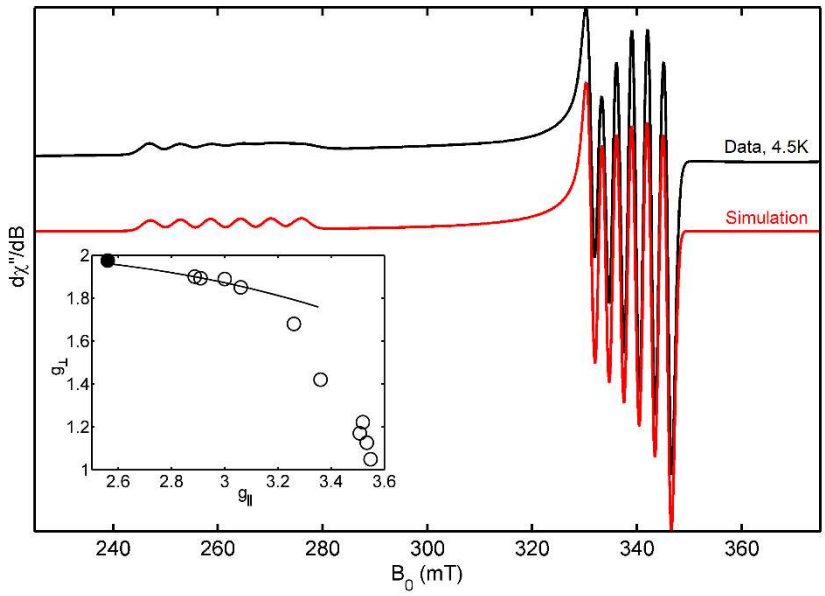

Figure A5.13 X-band EPR simulation of the low-spin species of Mn(II)Ind*$_2$ for data collected at 4.5 K. Simulation parameter values are $g_{\|} = 2.56$ and $g_{\perp} = 1.975$, $A_{\|}(^{55}\text{Mn})$=206MHz and $A_{\perp}(^{55}\text{Mn}) = 80$ MHz. *Inset*: parametric plot of literature g-values for low-spin Mn(II) sandwich compounds with this work in solid dot.[10] The inset line represents variation of axial symmetry distortion parameter, δ, in equations 1a-c. Acquisition conditions were as stated in the main text.

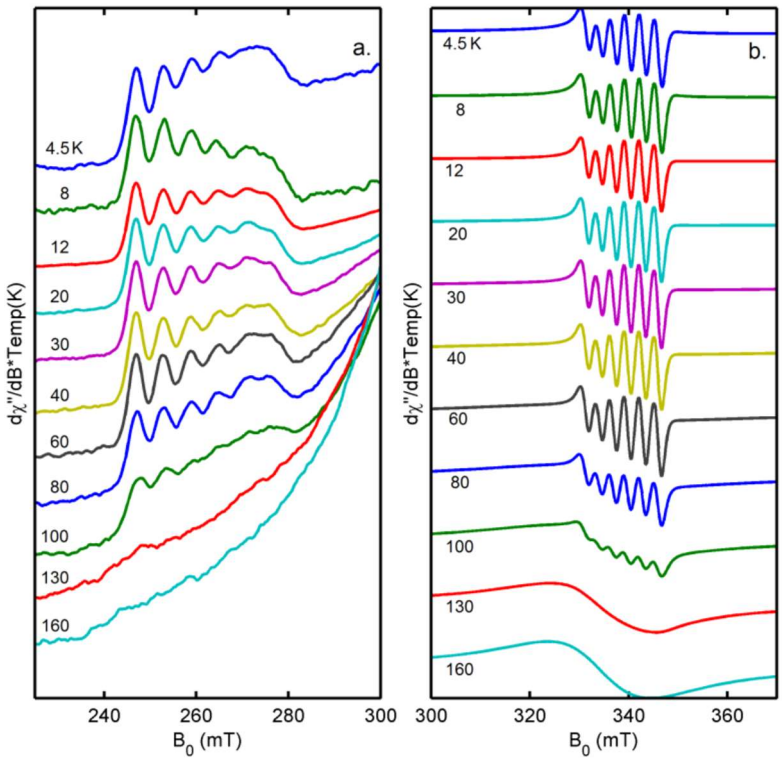

Figure A5.14 Temperature dependence of individual components of the low-spin signal in the transition to a high-spin signal. In the g|| region, 4.5 K and 8 K data represent acquisitions following a re-freezing of the sample, while the small decrease in the 12 K intensity is due to slight saturation at that temperature. Acquisition conditions were as stated in the main text.

A5.3. Computational details

General computation details. All calculations were performed using the ORCA software suite unless otherwise specified.[11] A range of functionals were used to probe the ΔE¬HL for the crystal structure geometry, all utilizing the def2-TZVP basis set.[12, 13] Specifically, we examined the following functionals: B3LYP,[14-17] R2SCAN,[18] M062X,[19] WB97X,[20] BP86,[21] PBE,[22] PBE0,[23] MN15L,[24] M06L,[25] M05,[25] M052X,[26] MN15,[27] TPSSH,[28] TPSS0,[28] M06, r2SCANh,[18] and OLYP.[29] The functionals and their corresponding ΔE values are shown in **Table S4**.

Table A5.4 Functionals

	Crystal stuctrure (kcal mol^{-1})
CCSD(T)	32.00623
CASSCF	27.633
MN15	33.39701

Functional	ΔE (kcal mol^{-1})
BP86	-52.7907
PBE	-52.744
TPSSh	-45.242
OLYP	-40.9621
WB97X	-37.826
B3LYP	-37.6495
R2SCAN	-37.0324
r2scan-3c	-36.508
wb97x-3c	-30.9477
r2SCANh	-28.4273
PBE0	-27.9945
pbeh-3c	-11.1639
M062X	-5.11955
M062X	5.119578
M052X	8.982872
MN15L	14.12748
M06	15.38958
M05	18.09392
TPSS0	30.55783
M06L	31.56466
MN15	33.39701
TPSSH	45.24218

We found that MN15 provided the best match with the CCSD(T) calculations detailed below. Geometry optimizations were performed on both the high and low spin electronic configurations, along with scanning the RA angle for both the high and low energy configurations. Single-point calculations were performed with the CCSD(T) procedure outlined below.

CCSD(T)-DLPNO. The coupled cluster single, double, and perturbative triple excitation (DLPNO-CCSD(T)) calculations were carried out using the BP86 functional to generate

reference orbitals.[30-39] This functional has been shown to provide reliable results for spin-splitting energetics and ground state predictions, as highlighted in reference [31]. The cc-pVDZ basis set[40] was used, with cc-pVTZ/C employed for correlated calculations to achieve better accuracy. VeryTightSCF thresholds were applied to ensure complete convergence of the self-consistent field (SCF) procedure, along with NormalPNO threshold, which provides a cost-effective balance between computational efficiency and accuracy.

The choice of BP86 orbitals was guided by literature precedence, which highlights their superiority in spin-state energetics and agreement with canonical CCSD(T) methods. For example, studies have shown that BP86 orbitals correctly predict the ground state for systems and offer mean deviations within 4 kcal/mol relative to canonical CCSD(T). These orbitals also exhibit an optimal balance in the number of pair natural orbitals (PNOs), as detailed in supplementary materials of prior studies.[41]

CASSCF/NEVPT. Complete active space self-consistent field (CASSCF) calculations followed by *N*-electron valence perturbation theory (NEVPT2) corrections were performed.[39, 42-44] The active space comprised 9 electrons in 12 orbitals, including 2 bonding orbitals, 5 metal-centered d orbitals, and 5 3 d' double-shell orbitals. This choice of active space is supported by previous studies, which demonstrate that inclusion of the d' double-shell orbitals enhances accuracy for systems of this type. The def2-TZVP basis set was employed for all atoms, with def2-TZVP/C used for correlated calculations.

Table A5.5 Orbital occupancy of CASSCF/NEVPT active space

Orbital Number	Occupancy	eH	eV
126	1.7975	-0.306212	-8.3325
127	1.7441	-0.277597	-7.5538
128	1.3899	-0.187782	-5.1098
129	1.3158	-0.168846	-4.5945
130	1.1748	-0.112336	-3.0568
131	0.7016	0.089904	2.4464
132	0.6009	0.106506	2.8982
133	0.1847	0.191967	5.2237
134	0.0301	0.551555	15.0086
135	0.0290	0.586597	15.9621
136	0.0235	0.703114	19.1327
137	0.0081	1.119556	30.4647

Table A5.6 Density matrix of CASSCF/NEVPT active space.

	1	**2**	**3**	**4**	**5**	**6**	**7**	**8**	**9**	**10**	**11**	**12**
1	1.797502	1.00E-06	2.00E-06	-1.00E-06	0	1.00E-06	-5.00E-06	0	0	0	-1.00E-06	0
2	1.00E-06	1.744138	1.00E-06	-1.00E-06	-1.00E-06	-2.00E-06	-1.00E-06	0	1.00E-06	0	0	-1.00E-06
3	2.00E-06	1.00E-06	1.389855	2.40E-05	-4.00E-06	1.00E-06	-1.00E-06	0	0	-4.00E-06	0	0
4	-1.00E-06	-1.00E-06	2.40E-05	1.315782	-1.20E-05	0	0	4.00E-06	1.00E-06	-2.00E-06	-1.00E-06	0
5	0	-1.00E-06	-4.00E-06	-1.20E-05	1.174842	1.00E-06	0	1.00E-06	-2.00E-06	0	-1.00E-06	0
6	1.00E-06	-2.00E-06	1.00E-06	0	1.00E-06	0.701563	-1.10E-05	-1.00E-06	-1.00E-06	0	0	1.00E-06
7	-5.00E-06	-1.00E-06	-1.00E-06	0	0	-1.10E-05	0.600895	-7.00E-06	0	-2.00E-06	0	0
8	0	0	0	4.00E-06	1.00E-06	-1.00E-06	-7.00E-06	0.184731	0	0	0	0
9	0	1.00E-06	0	1.00E-06	-2.00E-06	-1.00E-06	0	0	0.030124	0	0	0
10	0	0	-4.00E-06	-2.00E-06	0	0	-2.00E-06	0	0	0.028982	0	0
11	-1.00E-06	0	0	-1.00E-06	-1.00E-06	0	0	0	0	0	0.023499	0
12	0	-1.00E-06	0	0	0	1.00E-06	0	0	0	0	0	0.008088

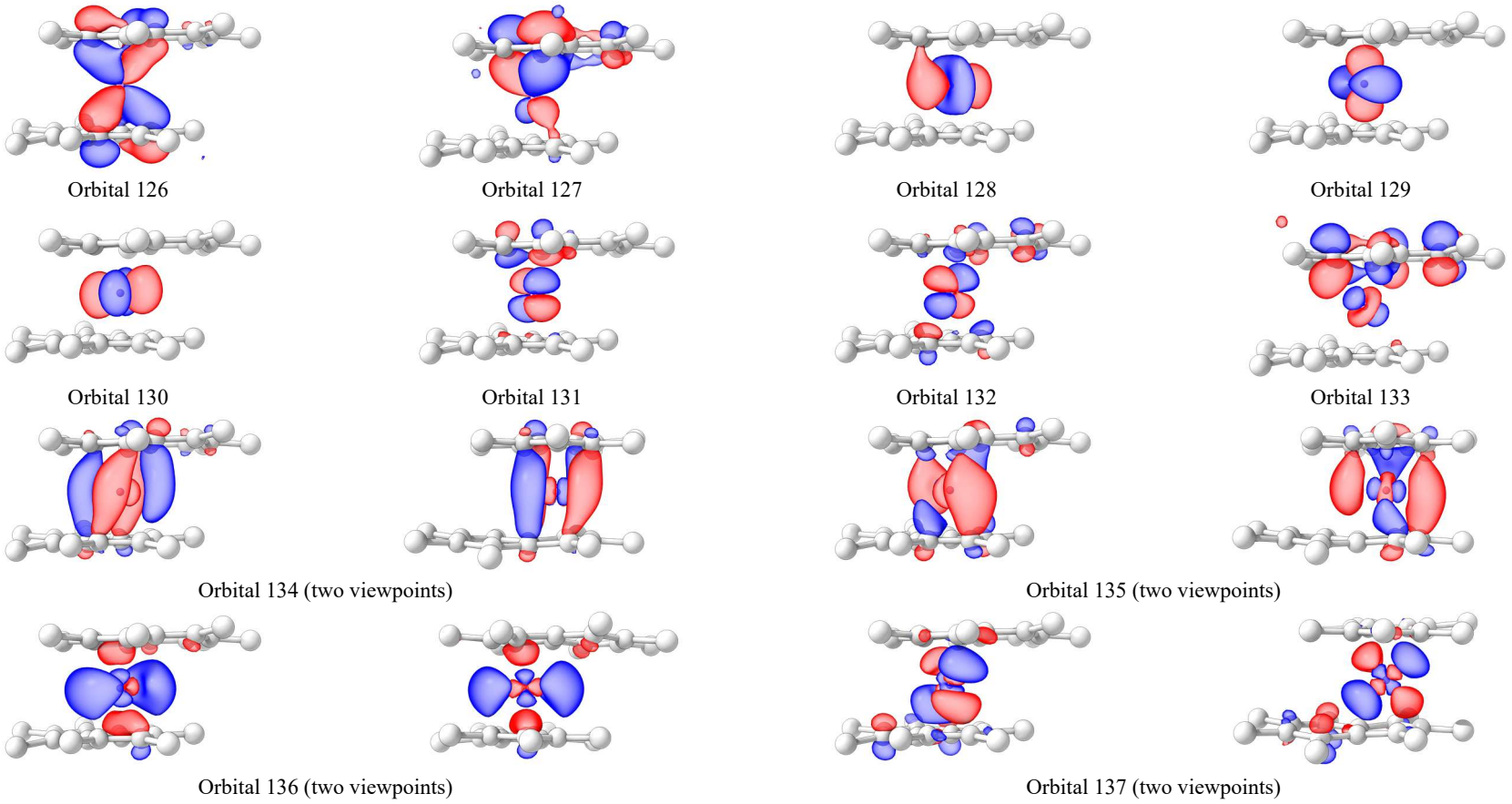

Figure A5.15 Active space comprising 9 electrons in 12 orbitals, including 2 bonding orbitals, 5 metal-centred d orbitals, and 5 3 d' double-shell orbitals.

EDA. Energy decomposition analysis (EDA) was performed to gain insight into the bonding interactions within the studied systems, comparing the Ind* system with that of the Cp* ligand system. The initial decomposition analysis was conducted using the sobEDA method[45] with the Gaussian 16.C program[46] and Multiwfn,[47, 48] employing the MN15 functional and the def2-TZVP basis set, consistent with the ORCA setup. Further decomposition of the E_{orb} term was carried out using the EDA-NOCV method[49, 50] in ORCA, allowing for detailed examination of pairwise deformation densities.

Figures. All molecular graphics and visualizations were generated using ChimeraX 1.9.[51] This software was employed to create high-quality figures that effectively represent the geometric and electronic properties of the systems studied.

Table A5.7 sobEDA energy partitioning.[a]

Ligand	Cp*	I*
Total interaction energy	-734.76	-717.47
Physical components of interaction energy derived by sobEDA		
Electrostatic (E_{els})	-1020.16	-1012.13
Exchange (E_x)	-80.59	-79.02
Pauli repulsion (E_{eep})	605.69	767.52
Exchange-repulsion ($E_{xrep} = E_x + E_{rep}$)	525.1	688.5
Orbital (E_{orb})	-605.69	-767.52
DFT correlation (E_{DFTc})	-76.03	-79.88
Dispersion correction (E_{dc})	0	0
Coulomb correlation ($E_c = E_{DFTc} + E_{dc}$)	-76.03	-79.88

[a]Units in kcal mol^{-1}.

Table A5.8 EDA-NOCV pair densities.

	I*			Cp*		
	α	β	Σ	α	β	Σ
E_{orb}	-324.3	-331.37	-655.67	-343.46	-349.56	-693.01
pair1	-181.61	-169.4	-351.01	-138.8	-167.33	-306.13
pair2	-62.71	-71.48	-134.19	-132.6	-102.94	-235.54
pair3	-19.04	-46.82	-65.86	-35.23	-20.2	-55.43
pair4	-17.63	-6.66	-24.29	-9.05	-10.86	-19.91

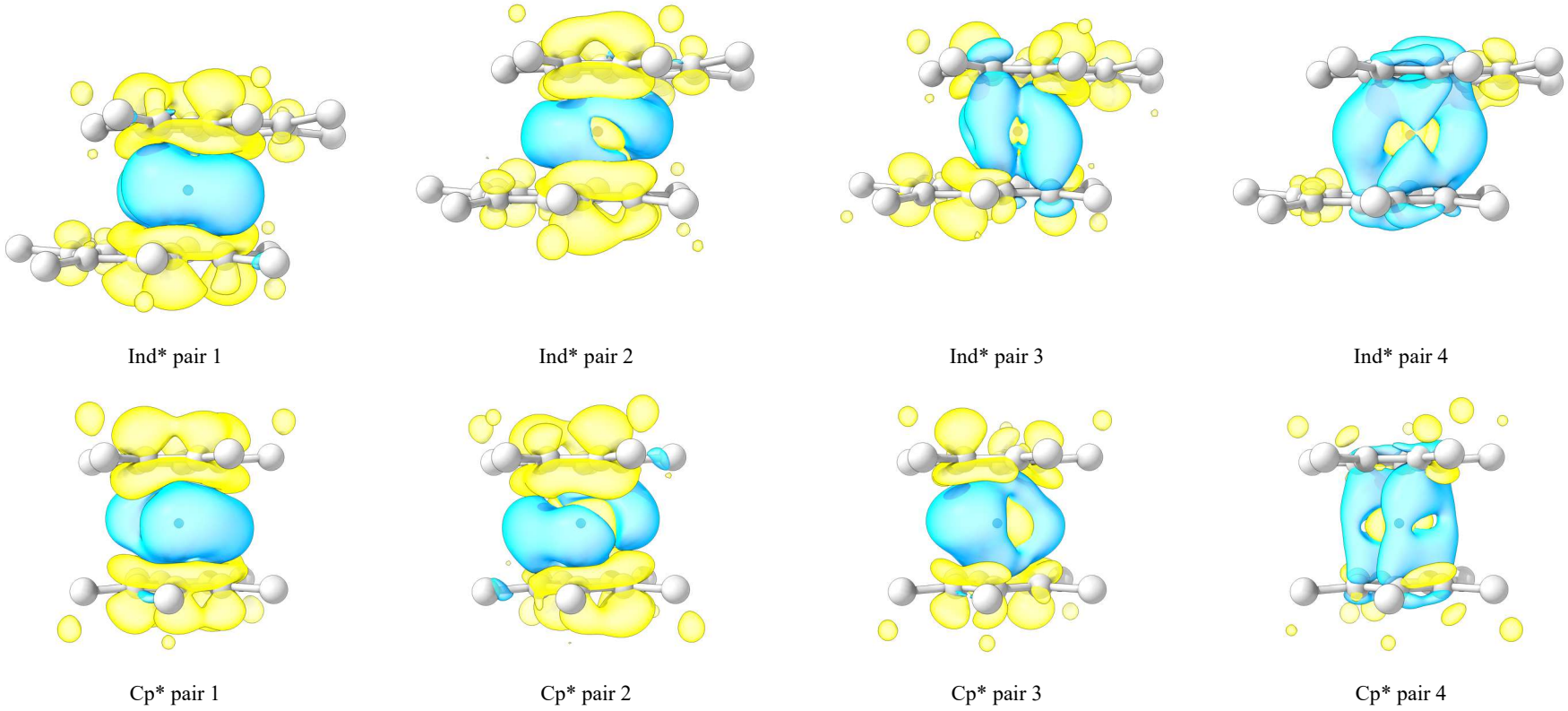

Figure A5.16 Pairwise deformation densities of Cp* and Ind*.

A5.4. References

1 J. Cosier and A. M. Glazer, *J. Appl. Crystallogr.*, 1986, **19**, 105-107.
2 CrysAlisPRO, Oxford Diffraction /Agilent Technologies UK Ltd, Yarnton, England.
3 O. V. Dolomanov, L. J. Bourhis, R. J. Gildea, J. A. K. Howard, H. Puschmann, *J. Appl. Cryst.*, 2009, **42**, 339-341.
4 G. Sheldrick, *Acta Crystallogr. Sect. A*, 2015, **71**, 3-8.
5 G. Sheldrick, *Acta Crystallogr. Sect. C*, 2015, **71**, 3-8.
6 A. Spek, *J. Appl. Crystallogr.*, 2003, **36**, 7-13.
7 L. J. Farrugia, *J. Appl. Crystallogr.*, 1997, **30**, 565-565.
8 G. A. Bain and J. F. Berry, *J. Chem. Educ.*, 2008, **85**, 532.
9 D. O'Hare, J. C. Green, T. Marder, S. Collins, G. Stringer, A. K. Kakkar, N. Kaltsoyannis, A. Kuhn, R. Lewis, *Organometallics*, 1992, **11**, 48-55.
10 A. E. Ashley, A. R. Cowley, D. O'Hare, *Eur. J. Org. Chem.*, 2007, **2007**, 2239-2242.
11 T. Imamoto, N. Takiyama, K. Nakamura, T. Hatajima, Y. Kamiya, *J. Am. Chem. Soc.*, 1989, **111**, 4392-4398.
12 T. Imamoto, Y. Sugiura, N. Takiyama, *Tet. Lett.*, 1984, **25**, 4233-4236.
13 M. J. Calhorda, V. Félix, L. s. F. Veiros, *Coord. Chem. Rev.*, 2002, **230**, 49-64.
14 M. E. Switzer, R. Wang, M. F. Rettig, A. H. Maki, *J. Am. Chem. Soc.*, 1974, **96**, 7669-7674.
15 M. D. Walter, C. D. Sofield, C. H. Booth, R. A. Andersen, *Organometallics*, 2009, **28**, 2005-2019.
16 W. L. Olson, A. M. Stacy, L. F. Dahl, *J. Am. Chem. Soc.*, 1986, **108**, 7646-7656.
17 M. E. Smith and R. A. Andersen, *J. Am. Chem. Soc.*, 1996, **118**, 11119-11128.
18 J. L. Robbins, N. M. Edelstein, S. R. Cooper, J. C. Smart, *J. Am. Chem. Soc.*, 1979, **101**, 3853-3857.
19 F. Neese, *Wiley Interdiscip. Rev. Comput. Mol. Sci.*, 2022, **12**, e1606.
20 F. Weigend, *Phys. Chem. Chem. Phys.*, 2006, **8**, 1057-1065.
21 F. Weigend and R. Ahlrichs, *Phys. Chem. Chem. Phys.*, 2005, **7**, 3297-3305.
22 A. D. Becke, *The Journal of Chemical Physics*, 1993, **98**, 5648-5652.
23 C. Lee, W. Yang, R. G. Parr, *Phys. Rev. B*, 1988, **37**, 785-789.
24 P. J. Stephens, F. J. Devlin, C. F. Chabalowski, M. J. Frisch, *J. Phys. Chem.*, 1994, **98**, 11623-11627.
25 S. H. Vosko, L. Wilk, M. Nusair, *Can. J. Phys.*, 1980, **58**, 1200-1211.
26 J. W. Furness, A. D. Kaplan, J. Ning, J. P. Perdew, J. Sun, *J. Phys. Chem. Lett.*, 2020, **11**, 8208-8215.
27 Y. Zhao and D. G. Truhlar, *Theor. Chem. Acc.*, 2008, **120**, 215-241.
28 N. Mardirossian and M. Head-Gordon, *Phys. Chem. Chem. Phys.*, 2014, **16**, 9904-9924.
29 J. P. Perdew, *Phys. Rev. B*, 1986, **33**, 8822-8824.
30 J. P. Perdew, K. Burke, M. Ernzerhof, *Phys. Rev. Lett.*, 1997, **78**, 1396-1396.
31 M. Ernzerhof and J. P. Perdew, *J. Chem. Phys.*, 1998, **109**, 3313-3320.
32 H. S. Yu, X. He, D. G. Truhlar, *J. Chem. Theory Comput.*, 2016, **12**, 1280-1293.
33 Y. Zhao, N. E. Schultz, D. G. Truhlar, *J. Chem. Phys.*, 2005, **123**.
34 Y. Zhao, N. E. Schultz, D. G. Truhlar, *J. Chem. Theory Comput.*, 2006, **2**, 364-382.
35 H. S. Yu, X. He, S. L. Li, D. G. Truhlar, *Chem. Sci.*, 2016, **7**, 5032-5051.
36 V. N. Staroverov, G. E. Scuseria, J. Tao, J. P. Perdew, *J. Chem. Phys.*, 2004, **121**, 11507-11507.
37 A. J. Cohen and N. C. Handy, *Mol. Phys.*, 2001, **99**, 607-615.
38 F. Neese, A. Hansen, D. G. Liakos, *J. Chem. Phys.*, 2009, **131**.
39 F. Neese, F. Wennmohs, A. Hansen, *J. Chem. Phys.*, 2009, **130**.
40 S. Kossmann and F. Neese, *Journal of Chemical Theory and Computation*, 2010, **6**, 2325-2338.
41 C. Riplinger and F. Neese, *J. Chem. Phys.*, 2013, **138**.
42 C. Riplinger, B. Sandhoefer, A. Hansen, F. Neese, *J. Chem. Phys.*, 2013, **139**.
43 C. Riplinger, P. Pinski, U. Becker, E. F. Valeev, F. Neese, *J. Chem. Phys.*, 2016, **144**.
44 G. Bistoni, C. Riplinger, Y. Minenkov, L. Cavallo, A. A. Auer, F. Neese, *J. Chem. Theory Comput.*, 2017, **13**, 3220-3227.
45 M. Saitow, U. Becker, C. Riplinger, E. F. Valeev, F. Neese, *J. Chem. Phys.*, 2017, **146**.
46 B. Helmich-Paris, B. de Souza, F. Neese, R. Izsák, *J. Chem. Phys.*, 2021, **155**.
47 F. Neese, *J. Comput. Chem.*, 2023, **44**, 381-396.
48 T. H. Dunning, Jr., *J. Chem. Phys.*, 1989, **90**, 1007-1023.
49 M. Drosou, C. A. Mitsopoulou, D. A. Pantazis, *Polyhedron*, 2021, **208**, 115399.
50 Y. Guo, K. Sivalingam, E. F. Valeev, F. Neese, *J. Chem. Phys.*, 2016, **144**.
51 C. Kollmar, K. Sivalingam, B. Helmich-Paris, C. Angeli, F. Neese, *J. Comput. Chem.*, 2019, **40**, 1463-1470.

52 M. Ugandi and M. Roemelt, *Int. J. Quantum Chem*, 2023, **123**, e27045.
53 T. Lu and Q. Chen, *J. Phys. Chem. A*, 2023, **127**, 7023-7035.
54 M. J. Frisch, G. W. Trucks, H. B. Schlegel, G. E. Scuseria, M. A. Robb, J. R. Cheeseman, G. Scalmani, V. Barone, G. A. Petersson, H. Nakatsuji, X. Li, M. Caricato, A. V. Marenich, J. Bloino, B. G. Janesko, R. Gomperts, B. Mennucci, H. P. Hratchian, J. V. Ortiz, A. F. Izmaylov, J. L. Sonnenberg, Williams, F. Ding, F. Lipparini, F. Egidi, J. Goings, B. Peng, A. Petrone, T. Henderson, D. Ranasinghe, V. G. Zakrzewski, J. Gao, N. Rega, G. Zheng, W. Liang, M. Hada, M. Ehara, K. Toyota, R. Fukuda, J. Hasegawa, M. Ishida, T. Nakajima, Y. Honda, O. Kitao, H. Nakai, T. Vreven, K. Throssell, J. A. Montgomery Jr., J. E. Peralta, F. Ogliaro, M. J. Bearpark, J. J. Heyd, E. N. Brothers, K. N. Kudin, V. N. Staroverov, T. A. Keith, R. Kobayashi, J. Normand, K. Raghavachari, A. P. Rendell, J. C. Burant, S. S. Iyengar, J. Tomasi, M. Cossi, J. M. Millam, M. Klene, C. Adamo, R. Cammi, J. W. Ochterski, R. L. Martin, K. Morokuma, O. Farkas, J. B. Foresman, D. J. Fox, Gaussian, Inc., Wallingford, CT, 2016.
55 T. Lu, *J. Chem. Phys.*, 2024, **161**.
56 T. Lu and F. Chen, *J. Comput. Chem.*, 2012, **33**, 580-592.
57 M. P. Mitoraj, A. Michalak, T. Ziegler, *J. Chem. Theory Comput.*, 2009, **5**, 962-975.
58 A. Altun, F. Neese, G. Bistoni, *J. Chem. Theory Comput.*, 2019, **15**, 215-228.
59 E. C. Meng, T. D. Goddard, E. F. Pettersen, G. S. Couch, Z. J. Pearson, J. H. Morris, T. E. Ferrin, *Protein Sci.*, 2023, **32**, e4792.

A6. Device fabrication

A6.1. Introduction

Understanding polymer physical properties is essential as they directly influence the material's performance, durability, and suitability for specific applications in diverse fields such as medicine, construction, and electronics. Mechanical testing enhances the impact of research by providing quantitative insights into a polymer's behaviour under stress, strain, and environmental conditions, enabling the optimisation of materials for practical and industrial use. This integration of fundamental property analysis and applied testing ensures the development of innovative, reliable, and high-performance polymer-based solutions. As a subset of various mechanical and physical bulk characterisation is tensile strength testing whereby investigations are frequently required for the characterisation of polymer materials. Evaluation of a material's ability to withstand tension provides critical data for assessing durability and performance under mechanical loads.

Working within a research laboratory setting, where sample quantity is often limited, creating specimens whilst minimising waste is ideal. Conventional preparation techniques utilise injection moulding devices that require > 100 g scale, wasting a lot of material in the process. Consequently, obtaining data from mg–g sample quantities, typical for preliminary and proof of concept research, is greatly beneficial for material understanding, sample screening, and industrial relatability. The added complexity of high T_m and low flowability when considering POs means moulding sample into specimens with minimal defects, such as entrapped voids, which severely disrupt the bulk mechanical performance, and of a defined and reproducible shape is difficult without the use of an extruder, itself requiring large sample volumes. Consistency in sample

preparation is of paramount importance for accurately assessing the material properties. Typically, mechanical testing is prone to error during measurement because of this; as such, most academic journals requiring samples to be tested in greater than quadruplicate.

Commercial vacuum compression moulding (VCM) devices enable lossless mg-to-g scale screening of thermoplastic formulations. An added benefit of an applied vacuum is that thermooxidative degradation is limited which can be a big problem in melt processing polymers. Consequently, two VCM devices were designed and fabricated for in-house sample preparation based on this concept, accounting for the properties of a wide range of materials studied within the research group. Devices were fabricated to produce both a pellet and dog bone which align with the common testing requirements of synthesised materials within the O'Hare group. Additionally, a third silicone mould for the preparation of dog bone specimens is described. Due to the fabrication of such apparatus, work described herein was published by co-workers and myself,[1-3] and by colleagues[4]; in each instance submitted manuscripts were required to provide mechanical evidence prior to publication.

A6.2. Vacuum compression moulding devices fabrication

Rheological, optical, and tensile measurements are now reliably accessible within the research group due to the development of VCM devices. Internal consistency with regards to reproducible sample preparation and additional compliance with standardised sample dimensions enables new routine characterisation and improved inter-laboratory comparison. Pellet (⌀ = 10 mm) and dog bone (ISO 37 Type 3; width b_1 = 4 mm, length, L_0 = 10 mm) devices were finalised and optimised through several iterations of each (Figure A6.1–4). Work could not have been completed without computer-aided design

(CAD) and mechanical work by Mr. Steven Barry (Mechanical Workshop, University of Oxford).

The devices themselves, made from aluminium for rapid heat transfer, can be heated on a hot plate in a controlled manner by inserting a thermocouple into the base of the device. This enables heating above the T_m of the polymer (tested up to 200 °C), although for accurate and repeatable results a protocol is required (optimising maximum temperature, residence time, and cooling rate) for each new polymer ensuring a homogenous sample and consistent preparation. A vacuum can be applied, preventing entrapped gas voids on sample cooling and limiting thermooxidative degradation, whilst also forcing a piston to press the sample and ensure a uniform specimen thickness and shape across a range of polymer viscosities. Due to the low sample mass required (> 50 mg, pellet; > 120 mg, dog bone), sufficient specimens could be prepared for rheology or tensile strength testing respectively from minimal quantity of sample.

The main challenge to overcome was samples with a low melt viscosity would escape the mould when normal force from the piston was applied at elevated temperatures. Thermal expansion differences between the aluminium body and initial aluminium or steel central compression chambers resulted in a poor seal. Initially, use of polytetrafluoroethylene (PTFE) sheets cut to size were used as liners to improve the seal within the device. However, there were several issues with the liners that prevented them from being appropriate for the job: (1) hard to cut accurately to size so that there was no overlap which created holes allowing sample to escape; (2) at high temperatures and under the compressive force of the piston the liner was not rigid enough, routinely deforming, again allowing sample to escape. Consequently, the use of PTFE spacers resolved this issue, thermally expanding and prevent sample escape during the moulding process whilst also

significantly more rigid, preventing deformation during use. Concerning the dog bone mould, a high temperature resin was used to 3D print the internal chamber using a Formlabs Form 3+ printer. The resin was chosen given the upper operating heat deflection temperature of 238 °C at 0.45 MPa. This way the device could be made with the required tolerances and precision (0.025 mm) that was impossible to achieve with metal counterparts made with available computer numerical control machinery. Several iterations regarding design were completed, the final design minimising resin use and also including cylindrical voids to aid specimen retrieval through the use of a specimen die release tool. Due to specimen length, it was difficult to remove the sample without damaging the mould as pushing on one end of the specimen to remove it would typically jam the specimen inside the mould. With the aid of the release tool, even force could be applied along the length of the specimen enabling efficient sample retrieval. It is worth noting that the resin has drawbacks, the major being brittleness, with the mould typically lasting ~30 uses before breaking.

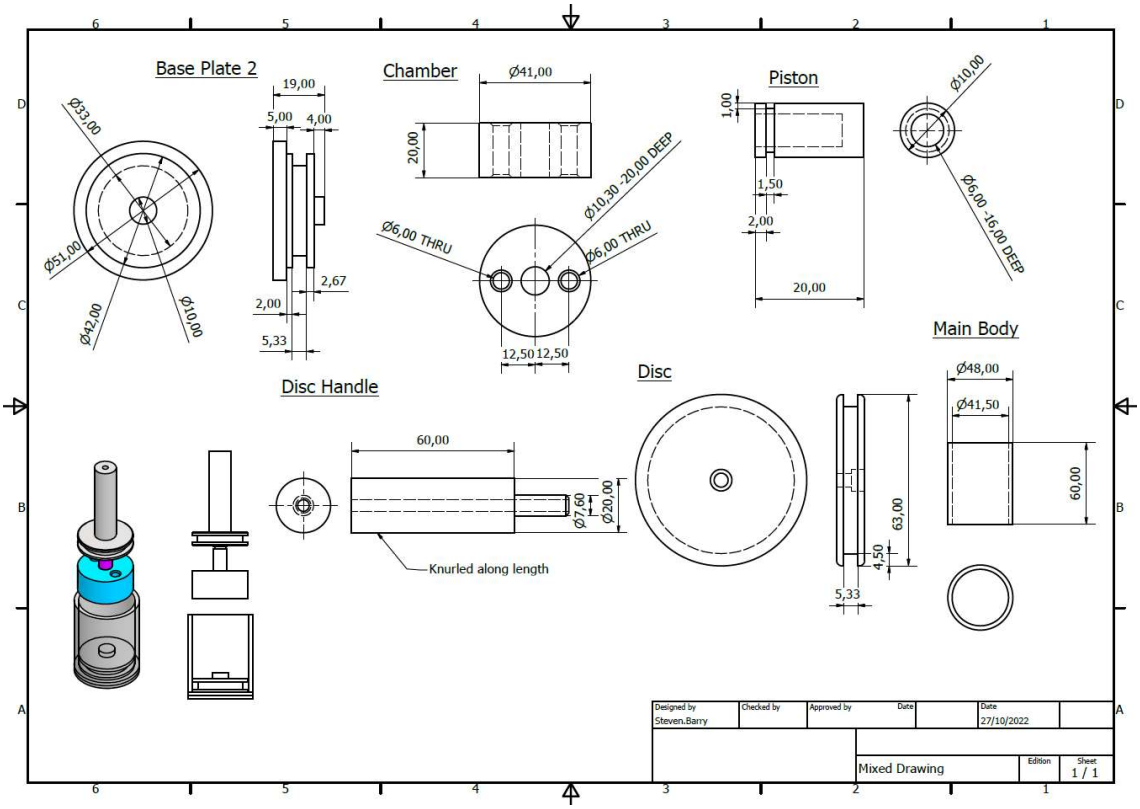

Figure A6.1 Pellet vacuum compression mould design.



Figure A6.2 (**A**) Assembled pellet vacuum compression mould and (**B**) dissassembled mould highlighting each part as designed in Figure A6.1. (**C**) Illustrative samples moulded from chapter 2, left to right: **PP**, **PP$_{Br}$**, **PP$_{PPr}$**, **PP$_{PPh}$**, **PP$_{DEA}$**, **PP$_{S}$**, **PP$_{OBn}$**.[3]

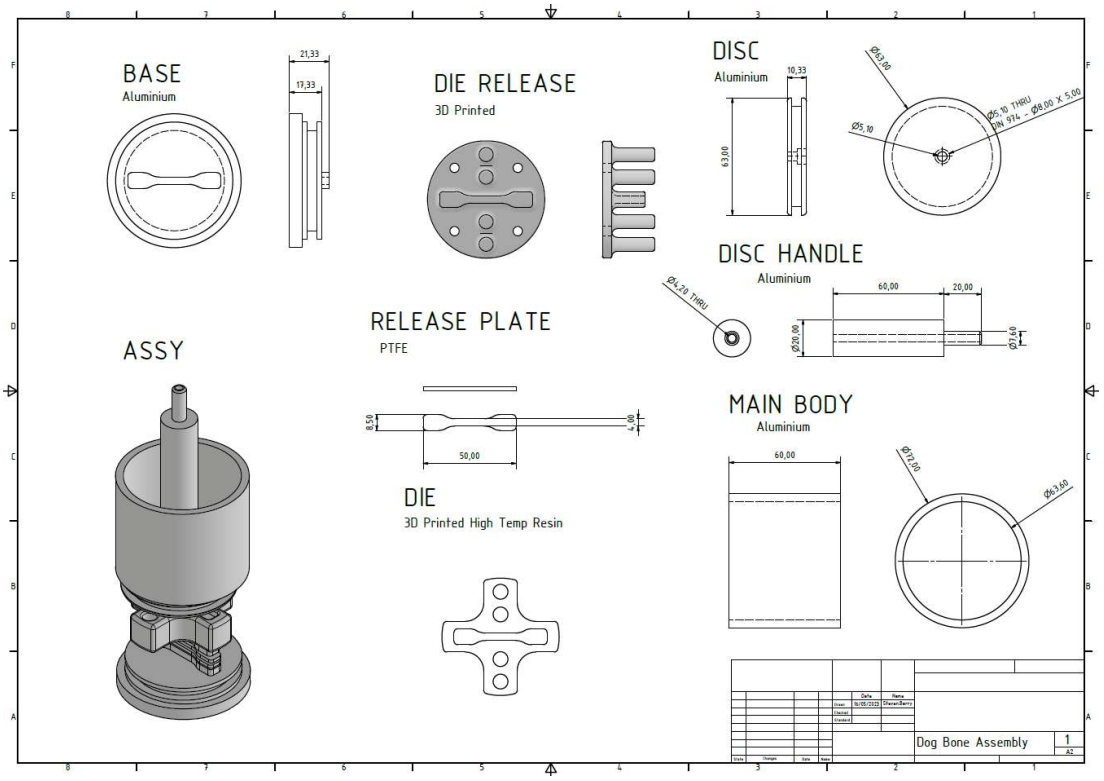

Figure A6.3 ISO 37 Type 3 dog bone vacuum compression mould.



Figure A6.4 (**A**) Assembled dog bone vacuum compression mould and (**B**) disassembled mould highlighting each part as designed in Figure A6.3.

A6.3. Silicone mould design and fabrication

In the instance of a liquid system, such as an epoxy resin that undergoes thermally induced curing, vacuum compression moulding is less necessary, and throughput is restricted, especially by the long curing times of epoxy resin. By designing an appropriate mould the specimen throughput can be drastically increased as sample can instead be loaded into the mould with a specific volume or mass to ensure uniform thickness of the final specimen and cured. Additionally, the flexibility of a silicone mould enables specimen isolation without damage to either component. Consequently, a silicone mould was fabricated after casting on a 3D printed inverse mould, made on a Formlabs Form 3+ printer using clear resin (Figure A6.6), with the capacity to produce 10 specimens per mould, drastically increasing throughput. Adhering to the procedures accompanying the commercial silicone is important, principally degassing the mould during curing. This subsequently prevents airflow through the liquid epoxy during sample preparation when placed under vacuum, consequently averting the generation of voids within the final specimen. CAD drawings were finalised using Autodesk Inventor Professional (Figure A6.5) with final dog bone dimensions in accordance with ISO 37 Type 3 (width b_1 = 4 mm, length, L_0 = 10 mm). A commercial two-component silicone was purchased that was stable at elevated temperatures (100 °C) once cured to account for varied formulation procedures of epoxy resins. It is worth noting however that some epoxy resins during curing can be inhibited by the silicone mould and that in specific use cases, an appropriate silicone should be selected.

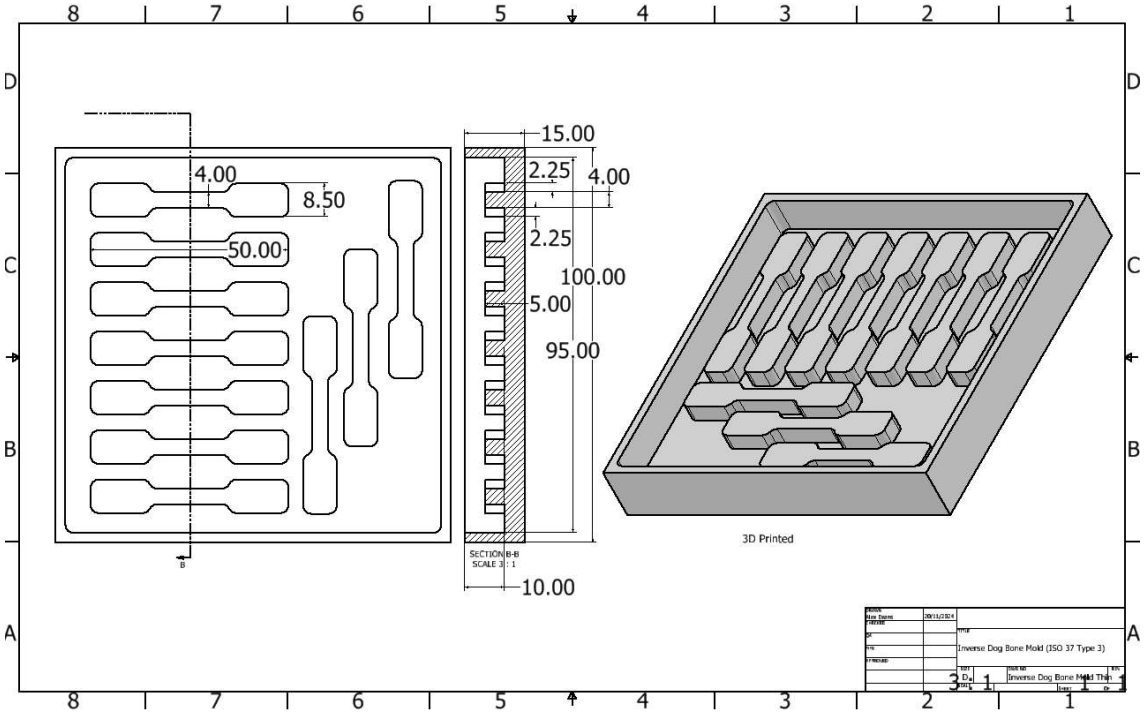

Figure A6.5 ISO 37 Type 3 inverse dog bone mould for silicone casting.

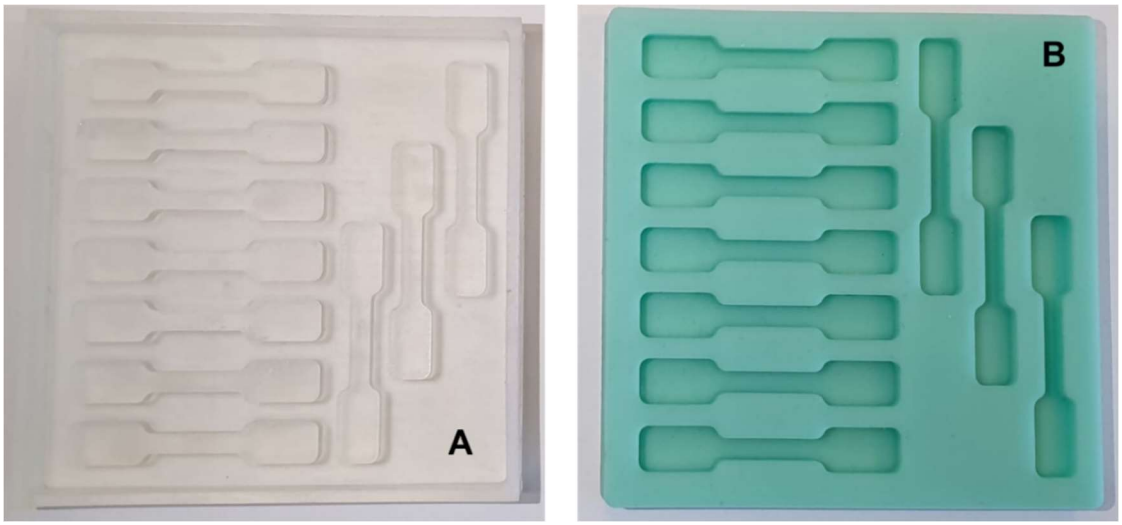

Figure A6.6 (**A**) 3D printed inverse dog bone mould according to drawings in Figure A6.5. (**B**) Silicone mould.

A6.4. Tensile strength testing

In order to illustrate the general applicability of the designed devices and moulds, two published works have been selected as case studies to exemplify their utility. Specimens were made from polyolefin and epoxy resin samples and tested in order to provide complimentary tensile characterisation data for the research of co-workers Chen[1] and Collins Rice,[2] in addition to the characterisation of samples within Chapters 2 and 4 of this thesis. The resulting tensile strength data is briefly surmised below for each use case with contextual information provided in the form of the published abstract. In each instance submitted manuscripts were required to provide mechanical evidence during peer review in order to support the conclusions and suitably elevate the impact. Without the developed methods for specimen production, it would have severely hampered the ability to publish the work.

A6.5. Boosting NIR Laser Marking Efficiency of a Transparent Epoxy Using a Layered Double Hydroxide[1]

A.6.5.1. Abstract

Efficient near-infrared (NIR) laser marking on transparent polymers like polypropylene, epoxy, and polyethylene has posed a big challenge due to their lack of absorption in the NIR. Currently, inorganic additives are used to improve NIR laser marking efficiency, but they come with issues such as toxicity, high loading requirement, adverse effects on colour/opaqueness, and the need for low laser head speeds. Herein, we report a new strategy of incorporating a food-grade, Mg_2Al-CO_3 LDH as a boosting co-additive alongside the commercial NIR laser marking additive (Iriotech 8815) in an epoxy system. Our findings demonstrate that the incorporation of Mg_2Al-CO_3 LDH can significantly increase both the darkness and contrast of marking even at high laser head speed (5000 mm s^{-1}), while minimizing surface damage. Notably, by replacing 95% of

Iriotech 8815 with Mg_2Al-CO_3 LDH, an epoxy plate can exhibit high transparency, while producing dark, sharply defined markings with excellent readable QR code markings at high laser speeds. This result offers a promising solution for enhancing high-speed NIR laser marking on transparent polymers with additional advantages of lower toxicity and cost and with minimal optical interference from high additive loadings.

A.6.5.2. Tensile strength results

Reviewers suggested that the incorporation of LDH, pre and post laser marking, may significantly impact the material properties. To verify the impact, it was suggested that mechanical testing be completed to ascertain the degree to which the specimens were altered. In the wider context of the work it was important not only to find a material which enhances laser markability, but one that does so without impacting the properties of the material.

Data presented in Figure A6.7 was gathered to evidence both the minimal impact of laser marking and the incorporation of LDH on max tensile strength. Specimens for tensile strength were prepared *via* high-speed mixing under vacuum and cast in the silicon dog bone mould. In conclusion, there is no statistically significant difference between any of these results and therefore neither laser marking, nor the additives, nor their combination meaningfully impact the underlying mechanical properties of the substrate under tension. The implication therefore is that the incorporation of LDH is a generally applicable technology that can be used in conjunction with existing materials and applications without having to consider the mechanical impact.

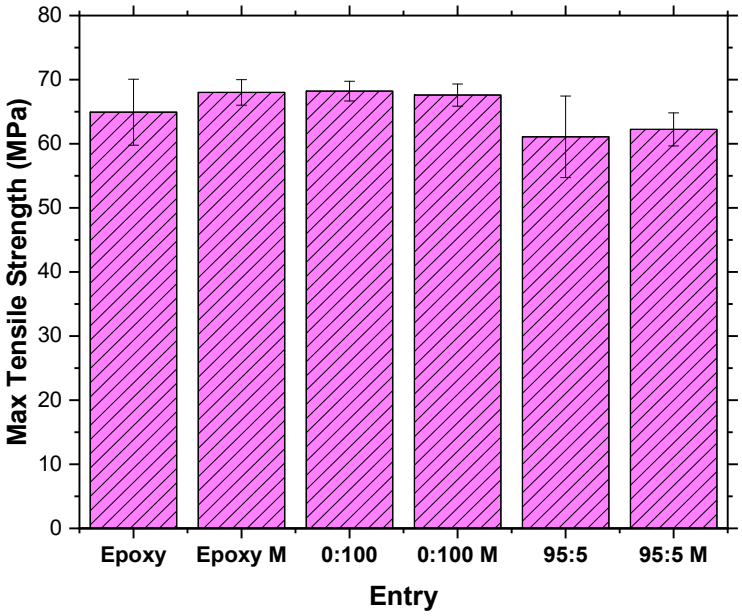

Figure A6.7 Tensile strength of LDH epoxy dog bone moulds as cast from ISO 37 Type 3 silicon mould. Epoxy dog bone samples containing LDH: Iriotech 8815 (0:0), (0:100), (95:5) and their laser marked analogues ((0:0 M), (0:100 M) and (95:5 M) at 40 kHz, 5000 mm s^{-1}. The reported values are an average of at least 5 measurements of each composition and reported error ± 1σ.[1]

A6.6. Strategies for enhancing the processability of UHMWPE[2]

A.6.6.1. Abstract

Ultra-high molecular weight polyethylene (UHMWPE, $M_w > 106$ g mol^{-1}) has been prepared using slurry phase titanium permethylindenyl-phenoxy (PHENI*) catalysts. Four strategies have been investigated for improving the melt processability of UHMWPE, which is the chief limiting factor to the applications of this high-performance polymer. 1) Active site engineering was used to explore the entanglement density in the resulting polymer, with substantially disentangled PE identified through thermal and rheological characterisation. 2) Hydrogen and $ZnEt_2$ were employed as chain transfer agents to modulate the polyethylene molecular weight and distribution (MWD). A sequential reactivity protocol using $ZnEt_2$ was able to produce bimodal UHMWPE with improved processability. 3) MWD tuning was further investigated using multisite catalysts, with the reaction conditions and Ti:Zr ratio able to control MWD to essentially arbitrary shapes. The inclusion of low molecular weight fractions into UHMWPE

improves the processability without compromising mechanical characteristics. 4) Polymer-reinforced composite blends of UHMWPE with either HDPE or LDPE as a highly processable matrix were extruded and explored, with polymer miscibility and mechanical properties studied in detail.

A.6.6.2. Tensile strength results

The submitted manuscript was determined by reviewers to require mechanical data. Initially the manuscript made arguments based solely on rheology and dynamic mechanical analysis; these were largely inconclusive as a measure of mechanical performance which was highlighted in review. As such, dog bone specimens of bimodal PE synthesised by multisite catalysts was prepared by vacuum compression moulding at 180–200 °C.

Unfortunately, small-scale mechanical characterisation presents challenges due to the influence of small imperfections that can act to concentrate stress. Consequently, there was quite a large error/inconsistency with some of the samples, partly because of the extreme viscosity of the polymers leading to non-uniformity in the mould and partly from edge defects. This makes the results much less precise than would be the case with large-scale injection moulded samples. However, obtaining data from g-scale samples was valuable with trends visible across the tested specimens and some statistically significant results reported in Figure A6.8.

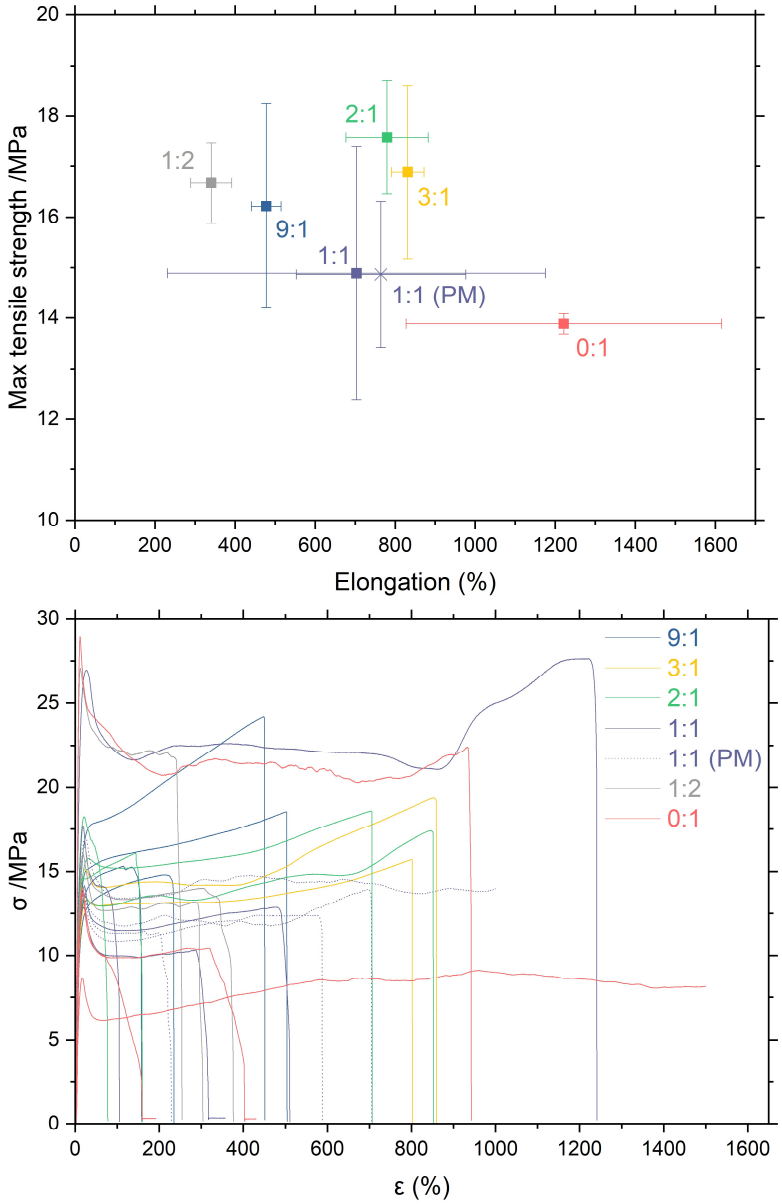

Figure A6.8 (**Top**) Tensile results of polyethylene produced at $T_p = 60$ °C by coimmobilised multisite catalysts $(1_n/2_m)_{sMAO}$ (or the physical mixture $1_{sMAO} + 2_{sMAO}$) as a function of [Ti]/[Zr], the samples were prepared by vacuum compression moulding into ISO 37 Type 3 dog bones. (**Bottom**) Corresponding stress-strain tensile curves. The reported values are an average of at least 4 measurements of each sample.[2]

Observed trends were demonstrated through tensile strength testing in relation to MWD tuning. Generally, the increasing high molecular weight fraction leads to increased tensile strength and decreased strain at break (ε_B) (Figure A6.8). Notably, when the ratio of Ti:Zr was equal to 3:1 and 2:1, resultant materials demonstrated greater tensile strengths (16.9 ± 1.7 and 17.3 ± 1.1 MPa respectively) and ε_B (830 ± 41 and 780 ± 100%

respectively) than would be expected from a simple mixing law, indicative of a synergistic enhancement in the mechanical properties of nanostructured all-polyethylene composites.[5] The MWD dependence is evident when the ratio of Ti:Zr was equal to 3:1 and 2:1, the resultant polymers have high molecular weight fractions of 49.9 and 55.2 wt% respectively (logM > 5.5) perhaps indicating a mechanically optimal composition.

A6.7. References

1. C. Chen, J. Wang, A. Evans and D. O'Hare, *ACS Appl. Polym. Mater.*, 2024, **6**, 8679-8686.
2. C. G. Collins Rice, A. Evans, Z. R. Turner, J. Wattoom and D. O'Hare, *Ind. Chem. Mater.*, 2024, DOI: 10.1039/D4IM00104D.
3. A. Evans, O. Casale, L. J. Morris, Z. R. Turner and D. O'Hare, *Macromolecules*, 2024, **57**, 10778-10791.
4. C. G. Collins Rice, L. J. Morris, J.-C. Buffet, Z. R. Turner and D. O'Hare, *Chem. Commun.*, 2023, **59**, 12128-12131.
5. M. Stürzel, A. G. Kurek, T. Hees, Y. Thomann, H. Blattmann and R. Mülhaupt, *Polymer*, 2016, **102**, 112-118.

A6.8. Statement of Authorship

Title of Papers	Boosting NIR Laser Marking Efficiency of a Transparent Epoxy Using a Layered Double Hydroxide Strategies for enhancing the processability of UHMWPE
Publication Status	Both published
Publication Details	Published respectively in: *ACS Appl. Polym. Mater.*, 2024, 6, 8679−8686 and *Ind. Chem. Mater.*, 2025,3, 178-190

Student Confirmation

Student Name:	Alexander Oscar Edward Evans
Contribution to the Paper	Performed tensile strength analysis and data interpretation on samples for the relevant publications. Contributed to the discussion within manuscripts, review, and editing.

Signature 	Date 02/01/2025

Supervisor Confirmation

Supervisor name and title: Professor Dermot O'Hare	
Supervisor comments: I can confirm that the candidate's contribution to this paper is as described above.	
Signature 	Date 19/01/2025

Appendix B

Crystallographic information file

B1. Ind*H

B2. Ind*$_2$Mn

Appendix C

For when I inevitably lose the cards gifted to me, containing such kind words from friends made along the way, upon passing my viva voce. Thank you.

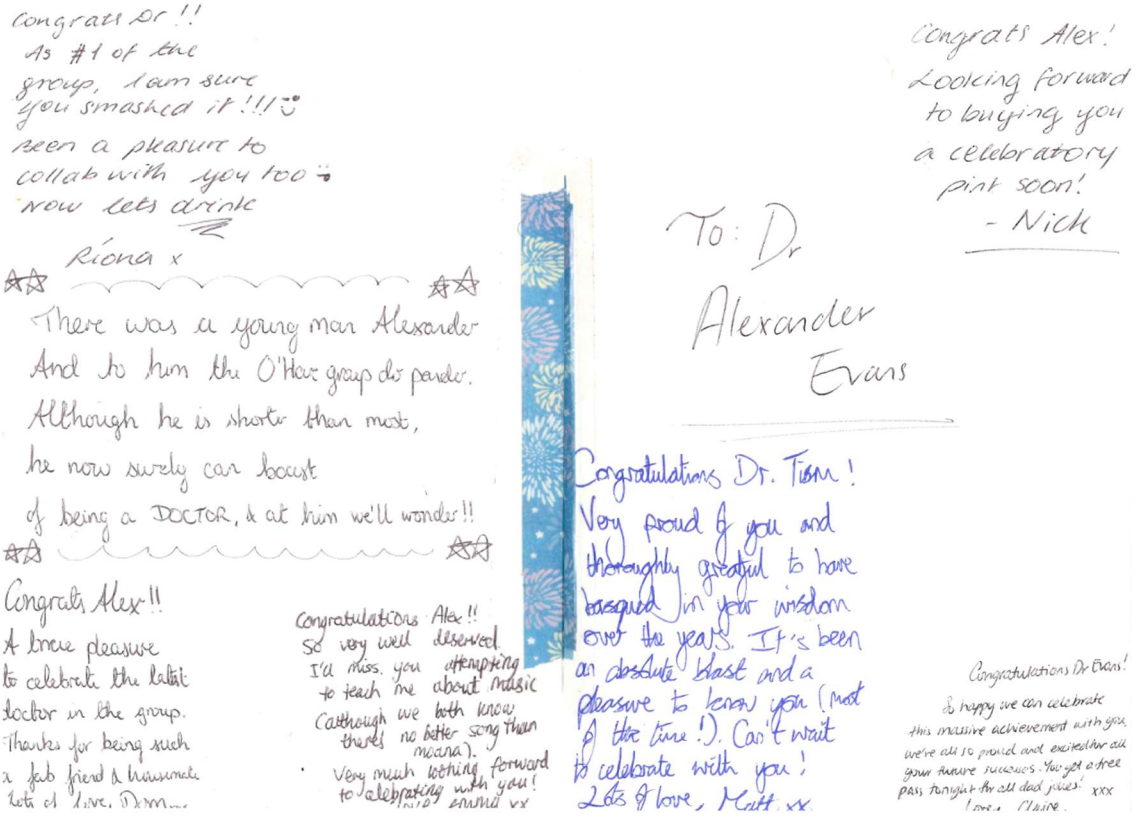

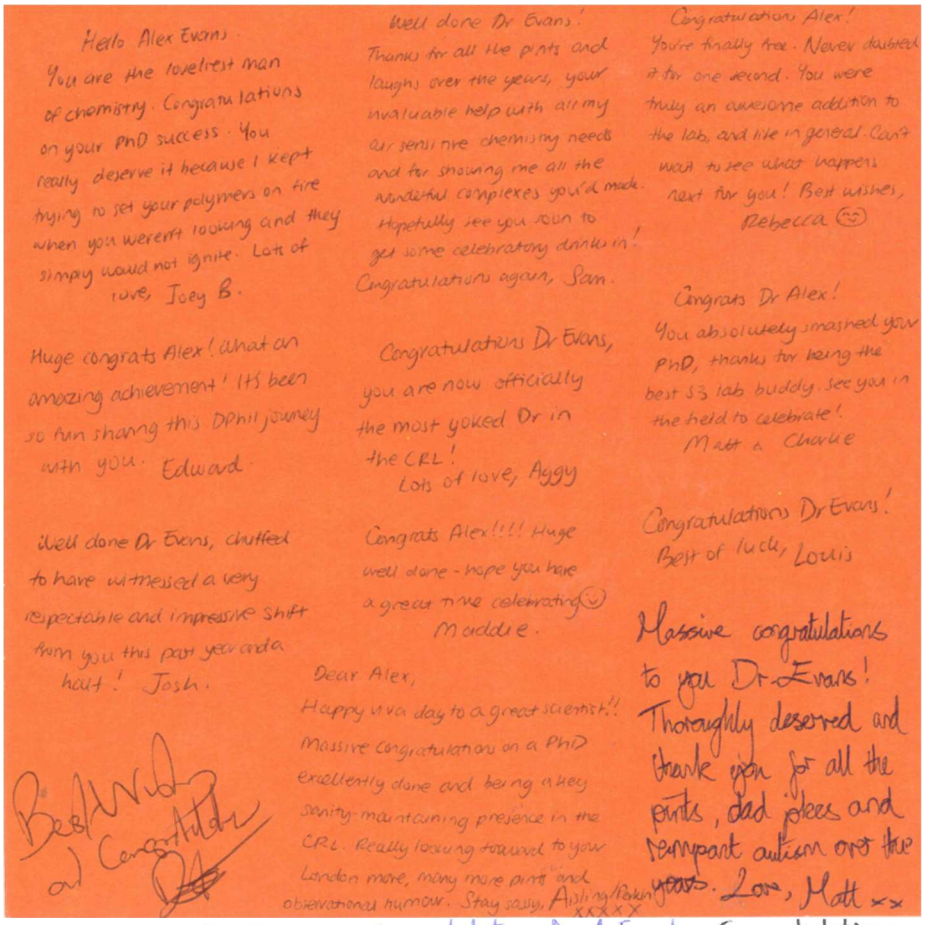

Hello Alex Evans.
You are the loveliest man of chemistry. Congratulations on your PhD success. You really deserve it because I kept trying to set your polymers on fire when you weren't looking and they simply would not ignite. Lots of love, Joey B.

Huge congrats Alex! What an amazing achievement! It's been so fun sharing this DPhil journey with you. Edward.

Well done Dr Evans, chuffed to have witnessed a very respectable and impressive shift from you this past year and a half! Josh.

Best Wishes and Congratulations

Well done Dr Evans!
Thanks for all the pints and laughs over the years, your invaluable help with all my air sensitive chemistry needs and for showing me all the wonderful complexes you'd made. Hopefully see you soon to get some celebratory drinks in!
Congratulations again, Sam.

Congratulations Dr Evans,
you are now officially the most yoked Dr in the CRL!
Lots of love, Aggy

Congrats Alex!!!! Huge well done - hope you have a great time celebrating
Maddie.

Dear Alex,
Happy viva day to a great scientist!! Massive congratulations on a PhD excellently done and being a key sanity-maintaining presence in the CRL. Really looking forward to your London move, many more pints and observational humour. Stay sassy, Aisling/Robin xxxxx

Congratulations Alex!
You're finally free. Never doubted it for one second. You were truly an awesome addition to the lab, and life in general. Can't wait to see what happens next for you! Best wishes,
Rebecca

Congrats Dr Alex!
You absolutely smashed your PhD, thanks for being the best 33 lab buddy. See you in the field to celebrate!
Matt & Charlie

Congratulations Dr Evans!
Best of luck, Louis

Massive congratulations to you Dr Evans! Thoroughly deserved and thank you for all the pints, dad jokes and rampant autism over the years. Love, Matt xx

Huge congrats Dr Alex!! Very well deserved - enjoy your celebrations!
Emma x

Congratulations Dr Evans!! Wish you all the best for the future! Tiger

Congrats Alex!
Very well deserved
Georgia

Massive congratulations, Dr Evans! So thoroughly earned - it's been such a pleasure working alongside you and all best wishes for your future!
Clem

Congrats Alex! So so proud of you. Can't wait to send it later
Claire xxx

Well done Alex! You're finally out! You've been a true role model for many of us over the past years and I can't wait to see you crush it in your next chapter xx Gabi

Congratulations Dr A. Evans!
Never in doubt. I hope you enjoyed the chat! Thanks for helping me get settled. Good luck! Roland

CONGRATS!

Congratulations Dr Evans.
Richly deserved. Celebrate abundantly.
All the best, Paul.

Congratulations Alex!! Thanks for always being approachable, incredible + genuine. All the best.
James SM

Alex, congratulations on finishing your PhD and never having to have another part II again :) Best of luck in your next adventure. -
Ollie.

Congratulations Alex!
Crazy to think all that time in the lab is over. I fondly remember the various tools you cooked up with the techs or asking how the chickens were going. Good luck, going forward to catch up soon!
All the best, Justin.

Wishing you the very best of luck. Hope you're a chess grandmaster by now!
Matt M.

Dr Alex, Congratulations are in order! Well done. Wish you the best that life has to offer. To more growth, learning, enthusiasm, and breakthrough. Linet -